Investigation and Prediction of Fundamental and PWM Frequency Induced Core Losses in PM Synchronous Traction Machines

by

Le Chang

A dissertation submitted in partial fulfillment of

the requirements for the degree of

Doctor of Philosophy

(Electrical Engineering)

at the

University of Wisconsin – Madison

2020

Date of final oral examination: 08/07/2020

The examination is approved by the following members of the Final Oral Committee:

Jahns, Thomas M., Professor, Electrical Engineering

Sarlioglu, Bulent, Associate Professor, Electrical Engineering

Schiferl, Rich, Adjunct Assistant Professor, Engineering Professional Development

Morgan, Dane, Professor, Materials Science and Engineering

Rahman, Khwaja, Director, Rivian Automotive

Abstract

During recent years, there are increasing demands to develop high-efficiency electric machines for traction applications to achieve a remarkable reduction of fossil fuel consumption and greenhouse gas emissions. Among a variety of machine topologies, the interior permanent magnet (IPM) synchronous machine is considered as one of the superior candidates owing to its high torque/power density and efficiency. However, inadequate understanding of the machine power loss phenomena in the electric machines compromises the loss prediction accuracy significantly, making it challenging to carry out reliable efficiency optimization and thermal analysis during the machine design stage.

This research program presents the development of a generalized dynamic hysteresis model for improved iron loss estimation of complex flux density waveforms caused by the fundamental excitation frequency and its associated low-order harmonics (e.g., machine slotting harmonics). The model has demonstrated a promising capability of intrinsically handling the harmonic-induced minor loops riding on top of the fundamental field as well as the minor loops influenced by the pre-magnetized dc-bias field in the machine rotor surface. The proposed model has been applied to investigate the fundamental field iron loss in baseline traction IPM machines.

In addition, considerable attention is devoted to developing a complete approach to conduct accurate and rapid assessments of the additional iron loss induced by pulsewidth modulation (PWM) switching with voltage-source inverters (VSIs). This work investigates the prediction and evaluation of the PWM-induced current ripple in IPM machines over broad ranges of operating conditions. In support of this work, magnetic material properties have been characterized over wide PWM switching frequencies and varying dc-bias fields. Using a modified dynamic Jiles-

Atherton (*J-A*) model and a unique frequency decomposition technique, a machine-level PWM-induced iron loss estimation algorithm has been developed for both existing and future ac traction machines.

Furthermore, this research investigates the total PWM power losses in IPM machines excited by VSIs using wide-bandgap (WBG) power devices (i.e., SiC or GaN) with different PWM modulation schemes over a wide range of PWM switching frequencies. Three enhanced power loss estimation models are utilized to determine the PWM-induced power losses in each of three major machine materials: the stator form-wound windings, the stator and rotor iron cores, and the permanent magnets in rotor cavities. The variation trend of each loss component versus PWM frequency and modulation scheme is provided, indicating that adopting the WBG-based inverters holds appealing potential for increasing the machine efficiency.

Experimental tests have been carried out during this research to evaluate the prediction accuracy and model scalability for both fundamental frequency and PWM-induced iron loss components, building confidence in the validity of the proposed iron loss estimation models. The results highlight the advantages of the standardized parameter identification process, feasible implementation procedure, wide application scope, and excellent prediction accuracy over the conventional models based on Steinmetz equation or iron loss separation theory. These features make the developed techniques appealing for use during machine design exercises to more accurately incorporate the iron loss into machine efficiency calculations and thermal analysis.

Acknowledgements

First of all, I would like to express my sincere gratitude to my advisor, Professor Thomas. M. Jahns, for his encouragement and continual support during my Ph.D. program at Wisconsin Electric and Power Electronics Consortium (WEMPEC). His knowledge, enthusiasm, and patience have inspired me to face technical challenges and move forward with courage. His rigorous work and research attitude will have invaluable impacts on my future career. I feel greatly honored and fortunate to be work with him.

I would also like to extend my thanks to all my committee members Professor Bulent Sarlioglu, Professor Rich Schiferl, Professor Dane Morgan, and Dr. Khwaja Rahman, for their valuable comments and suggestions to improve the quality of this research work. My special thanks go to Professor Rich Schiferl, who was kind and patient enough to do proofreading of this thesis, and lots of discussions with him during the course of this research is of great benefit to me.

Also, I would like to thank the entire WEMPEC faculty for offering great courses that help me to develop a better understanding of different power engineering areas. I am very grateful to the lectures given by Professor Robert Lorenz on the electric machine control theory. His dedication to teaching, research, and WEMPEC will inspire me throughout my career, and I wish I could learn more from him.

I also want to thank Kyle Hanson for his assistance and suggestions during the experimental work and to Helene Demont, Kathy Young, and Jim Sember for their works to keep WEMPEC a well-organized family. I want to thank all of my friends and colleagues at WEMPEC for making my stay in Madison a very pleasant and enjoyable experience, and it has been a great experience to work and interact with all of them.

My special thanks extend to Woongkul (Matt) Lee for his assistance and collaboration during this research project. He has always been very cooperative and helpful in troubleshooting the experimental challenges and providing interesting research ideas.

I would like to acknowledge the professional technical support provided by David Farnia for JMAG. I also want to thank Keith Cornacchia from Orchid Monroe for his help and arrangements to manufacture and process the magnetic materials used in this research.

I would like to thank Peter Link for his support and mentorship during my summer internship at Regal Beloit in the summer of 2015. I feel fortunate to have that valuable experience before starting my research work.

I am extremely grateful to General Motors Global Propulsion Systems for the financial support of this research program. I owe my sincere appreciation to Dr. Rolf Blissenbach and Dr. Khwaja Rahman, who provided many helpful suggestions and been the great support in the first few years of this research. I also deeply appreciate the help and support provided by Dr. Jihyun Kim and Michael C. Muir to complete this collaboration. I would also like to thank Joshua McCoskey and Dr. Sangyeop Kwak for their help in conducting the experimental tests during my visit at General Motors in 2016.

Lastly, I would like to express my deepest gratitude to my parents for their encouragement that kept me going. Without their unconditional support and love, I could not make it to the end.

Table of Contents

List of Figures

Chapter 1:

Chapter 2:

Chapter 3:

Chapter 4:

Chapter 5:

Chapter 6:

Chapter 7:

Chapter 8:

Chapter 9:

List of Tables

Chapter 2:

Chapter 3:

Chapter 4:

Chapter 5:

Chapter 8:

Chapter 9:

Nomenclature

Symbol	Description
B	Magnetic flux density [T]
d	Thickness of lamination sheet [m]
E	Everett function
f	Excitation frequency [Hz]
H	Magnetic field strength [A/m]
T	Timer period [s]
k_e	Hysteresis loss coefficient
k_h	Eddy-current loss coefficient
l_{core}	Stack length [m]
P_{iron}	Average power iron loss [W/kg]
i_d	d-axis current [A]
i_q	q-axis current [A]
L_d	d-axis inductance [H]
L_q	q-axis inductance [H]
ω	Angular velocity [rad/s]
θ	Angular position [rad]
R_s	Stator phase resistance [Ω]
P	Number of poles
T_e	Electromagnetic torque [N·m]

Abbreviations

FEA	Finite element analysis
MSE	Modified Steinmetz equation
GSE	Generalized Steinmetz equation
iGSE	Improved generalized Steinmetz equation
NSE	Natural Steinmetz equation
PM	Permanent magnet

IPM	Interior permanent magnet
NdFeB	Neodymium iron boron
IM	Induction machine
FSPM	Flux switching permanent magnet
DSPM	Doubly salient permanent magnet
NdFeB	Neodymium iron boron
SiFe	Silicon-iron
CoFe	Cobalt-iron
NiFe	Nickel-iron
SMC	Soft magnetic composite
VSI	Voltage source inverter
EMI	Electromagnetic interference
SVPWM	Space vector pulse width modulation
DPWM	Discontinuous pulse width modulation
IGBT	Insulated-gate bipolar transistor
SiC	Silicon carbide
GaN	Gallium nitride
WBG	Wide-bandgap
LMA	Levenberg-Marquart algorithm

Chapter 1
Introduction

1.1 Background and Motivation

During recent years, there are increasing demands to develop high-efficiency permanent magnet (PM) synchronous machines for various industrial and traction applications that must operate over a wide range of working conditions. In practice, the optimization of electrical machines to achieve the highest possible efficiency is largely dependent on an in-depth understanding of machine power loss phenomena, making accurate machine loss prediction critically important during the design stage.

Examples of machine power loss breakdown for two selected PM synchronous machines are presented in Figure 1-1. It can be seen that, when the machine operates under either high-speed conditions (Figure 1-1(a)) or light-load conditions (Figure 1-1(b)), the iron loss in the lamination steel represents a significant fraction of the total machine power loss. That is why the practical value of iron loss prediction has been widely recognized, and it has been investigated extensively for over a hundred years.

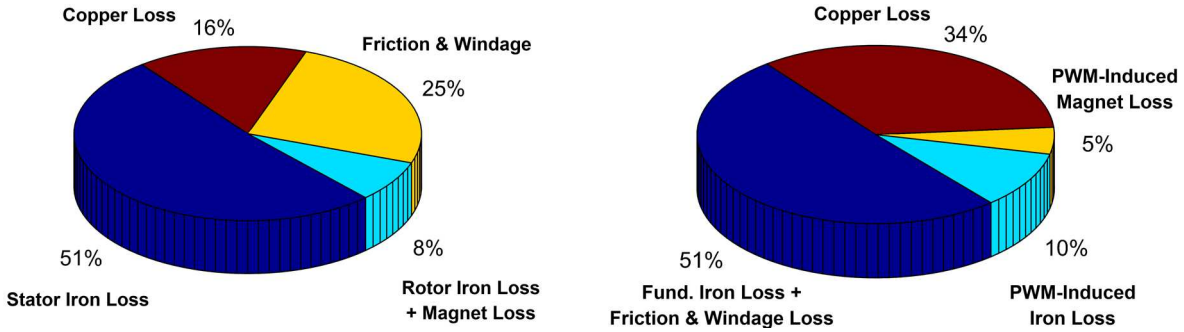

(a) 110 kW PM machine @ high-speed (b) 105 kW PM traction machine @ light-load

Figure 1-1: Examples of estimated power loss breakdowns for two PM synchronous machine operating under high-speed and light-load conditions.

Operation conditions*:* a) 110 kW permanent magnet synchronous machine (Speed = 51,000 rpm, T_{em} = 13 N·m, and P_{out} = 57.3 kW) [1]; and b) 105 kW permanent magnet synchronous machine designed for traction applications (I_{phase} = 35 Arms, f_{PWM} = 10 kHz, speed = 1,500 rpm, T_{em} = 45 N·m, and P_{out} = 7.1 kW) [2].

With the help of the classic Steinmetz equation-based model [3] and advanced finite element analysis (FEA) techniques, a popular approach for estimating the iron loss in the entire machine is to sum up the predicted loss in each analyzed mesh element. However, based on practical experience with this conventional model, large empirical correction factors (1.2 to 2 times the predicted iron loss) are needed for iron loss correction during the post-processing to adequately match the measured loss results. Moreover, identifying these empirical factors for each candidate design is impractical, and the scalability of correction factors is highly questionable when applied to newly designed machines with different sizes, topologies, and power ratings.

Therefore, development of improved iron loss models for future electric machine applications that offer higher accuracy compared to conventional models while retaining computational efficiency is critical for maximizing the efficiency of future machines during the machine design stage. In addition, the ability to accurately predict the iron loss in different physical regions of new electrical machine designs makes it possible to conduct more accurate thermal analyses and improve the cooling system design.

1.2 Statement of the Problem

The issue of iron loss prediction in high-performance PM synchronous traction machines has been receiving renewed attention by researchers in this field because of the recognized limitations of the classic Steinmetz equation. Furthermore, it is commonly recognized that the problem becomes more complicated when the machine is inverter-excited because the impact of high-frequency PWM-induced harmonics on the machine iron loss is not yet thoroughly understood. The introduction of new wide-bandgap power semiconductor switches that can raise PWM switching frequencies above 100 kHz further aggravates the difficulties associated with iron loss prediction since lamination material losses at such high frequencies are not well documented.

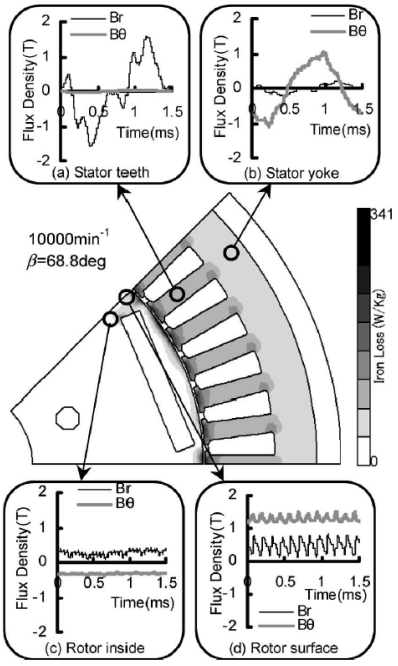

Figure 1-2: Calculated flux density waveforms at each point of an IPM motor and its iron loss distribution with 10,000 rpm rotating speed (f_{fund} = 666.67 Hz) and 68.8 deg current control angle γ [3].

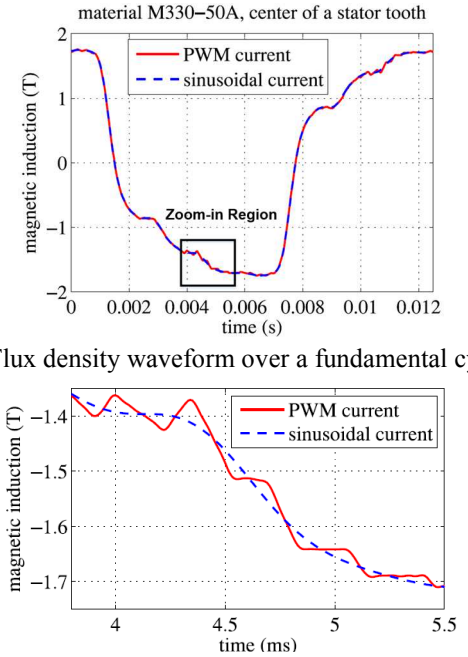

(a) Flux density waveform over a fundamental cycle

(b) Zoom-in region over a 1.75 ms period

Figure 1-3: Magnetic flux density waveforms computed in the center of the stator tooth with nominal current at 1950 Arms and rated speed at 1,600 rpm (f_{fund} = 80 Hz) for a surface PM synchronous machine [4].

1.2.1 Iron Loss Associated with the Fundamental & Low-Order Harmonics

Due to the intrinsically complicated nature of magnetic flux patterns in PM machines, the Fourier decomposition method is commonly adopted to segregate the complex flux waveforms into the different frequency components. Subsequently, the iron loss at each frequency is estimated individually before being summed to determine the total iron loss.

However, the mutual coupling between different orders of frequency components is highly nonlinear. This makes it unlikely that the linear superposition technique that lies at the heart of Fourier analysis is defensible for this application, casting doubt on the validity of loss predictions based on loss component summations of each of the frequency components in an expanded Fourier series. As can be observed in the calculated flux density waveforms in Figure 1-2 for an example IPM machine [3], the waveform associated with the middle of a stator tooth contains additional harmonic components attributable to multiple minor loops that are visible in the waveform.

Also, for high-performance interior PM (IPM) synchronous machines with neodymium-iron-boron (NdFeB) rare-earth magnets embedded in rotor cavities, the majority of the magnetic materials in the rotor are saturated magnetically, leading to an equivalent dc-bias field impact on the higher-order harmonics (i.e., slotting harmonics). As shown in Figure 1-2, flux density waveforms ride on top of the dc-bias field, especially for the point near the rotor surface. Unfortunately, the conventional Steinmetz equation cannot account for the effect of any dc-bias field, raising the risk of significant iron loss underestimation.

1.2.2 Additional Power Losses Due to PWM Switching

Interior permanent magnet (IPM) synchronous machines combined with VSIs are widely used in traction drives for hybrid- and battery-electric passenger vehicle applications. However, the high-frequency current ripple induced by PWM switching generates ac losses in each of the three major machine materials: the copper stator windings, the rotor permanent magnets, and the stator and rotor lamination cores. These additional ac losses can substantially degrade the machine's efficiency under some specific operating conditions (e.g., low-speed, light-load), creating circumstances in which the PWM-induced losses are comparable to the losses generated by the fundamental field. As presented in Figure 1-3(a)-(b) [4], high-frequency PWM-induced harmonics can be observed in the magnetic flux density waveform for a stator tooth when the studied surface PM machine is excited by PWM voltage waveforms.

In order to accurately predict and mitigate these losses during the machine design stage, accurate prediction of the PWM-induced current ripple is required under a wide range of drive and machine high-speed operating conditions. Although it is possible to model the stator current waveform with PWM-induced current ripple by nonlinear time-stepping FEA [5], very fine time steps and multiple fundamental periods are required to achieve converged steady-state simulation

results. The extended calculation time often poses serious problems, making this approach unattractive for practical applications.

Furthermore, under typical electric machine operating conditions, the fundamental frequency is much lower than the PWM switching frequency, and the PWM-induced flux ripple in the stator and rotor iron cores always rides on top of the fundamental field. Therefore, the amplitude of the fundamental field can be approximated as a constant dc-bias field during each PWM switching cycle. However, the iron loss data in the presence of pre-magnetized dc-bias field are not directly available from the steel manufacturer data sheets, and the proper inclusion of this impact in the process of iron loss estimation causes significant technical difficulties and challenges.

1.2.3 Opportunities and Challenges Created by WBG Power Devices for Machine-Side Efficiency in Motor Drive Applications

Adoption of the new-generation of WBG-based power semiconductor devices (i.e., SiC or GaN) in VSIs has exhibited promising capabilities for a variety of industrial and traction applications owing to their high efficiency, fast switching speeds, high-temperature operating capabilities, etc. [6], [7], making it possible to boost the drive system power density. Although increasing the PWM switching frequency helps to suppress the PWM-induced torque ripple in PM machines [8], the machine-side PWM power loss components are not yet well understood when the machines are exposed to significantly higher PWM switching frequencies.

Moreover, electric machines in the automotive industry have been moving to higher rotating speeds to boost machine power/torque density with smaller size and weight, leaving questions about the full impact of the WBG-based inverter on the iron loss in lamination steels with high fundamental and PWM switching frequencies. Also, it raises questions about the PWM power losses in IPM machines when excited by different PWM modulation schemes.

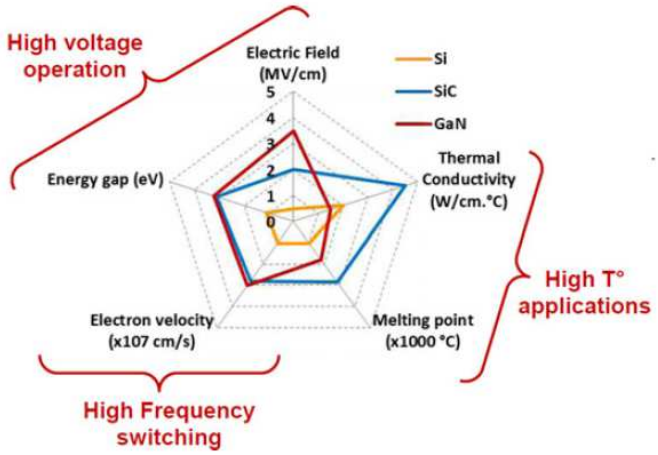

Figure 1-4: Comparison of Si, SiC, and GaN relative material properties for motor drive applications [6].

1.3 Objective of the Research Project

The overall objective of this research project is to develop improved iron loss models for calculating the iron loss in the stator and rotor iron cores of PM synchronous traction machines and to use the proposed models to shed light on the factors contributing to inaccurate iron loss estimation, providing deeper physical insights into iron loss phenomena.

Descriptions of the key tasks addressed during this research program are discussed in the following sub-sections:

1.3.1 Develop a Generalized Dynamic Hysteresis Model for Fundamental and Low-Order Harmonic Fields Iron Loss Estimation

The first objective has been to investigate the true nature of the iron loss induced by the complex magnetic flux waveforms. To achieve this objective, a versatile iron loss measurement system has been built, enabling characterization of magnetic materials over a wide range of ac and dc excitation. After collecting the measured iron loss and hysteresis loop data from the customized test setup, a generalized dynamic hysteresis model has been developed for estimating the nonlinear iron loss characteristics of magnetic materials by calculating the enclosed area of the dynamic hysteresis loop. Experimental verification has been carried out to evaluate the model's accuracy

and scalability over a broad range of operating conditions, building confidence in the developed iron loss estimation model.

1.3.2 Develop a Comprehensive Approach to Estimation of PWM-Induced Iron Loss in IPM Machines

The second major objective has been to develop a reliable and convenient approach to model and evaluate the PWM-induced iron loss in high-performance PM synchronous machines. An analytical model has been developed to achieve a fast and accurate estimation of PWM-induced current ripple, making it possible to predict the current ripple data for both existing and future PM synchronous machines. In order to analyze the iron loss characteristics of magnetic materials exposed to high-frequency ac magnetic fields under varying magnetization states, specially-designed toroidal cores have been tested using combinations of ac and dc current to provide the desired high-frequency flux waveforms as well as saturation levels. Moreover, a modified dynamic hysteresis model has been developed for PWM-induced iron loss estimation, permitting better emulation of the dc-bias field, asymmetrical waveforms, etc. Finally, experimental tests have been conducted to confirm the model performance using toroidal core tests. Additional testing has been carried out on an IPM machine, making it possible to apply special segregation techniques to isolate the measured PWM-induced losses for comparison with the model-predicted values.

1.3.3 Investigate the PWM Power Losses in IPM Machines Using WBG-Based Inverters with High Switching Frequencies

The third major objective has been to develop and build a new testing system using a GaN-based single-phase VSI to highlight the opportunities and address the concerns brought by WBG-based inverters. This new testing system has made it possible to fully characterize the lamination materials' magnetic and iron loss properties over a wide range of PWM switching frequencies and

varying dc-bias fields. A frequency-interconnected dynamic *J-A* model has been developed which is sufficiently generalized to incorporate the nonlinearities of magnetic materials with minimum input data requirement. Finally, an in-depth analysis of the PWM power losses in IPM machines has been conducted with different modulation schemes over a broad range of PWM switching frequencies enabled by the WBG-based VSI, providing deeper physical insights into the variation trend of each major power loss component. Experimental data collected from two IPM traction machines has been used to verify in the accuracy of the proposed model.

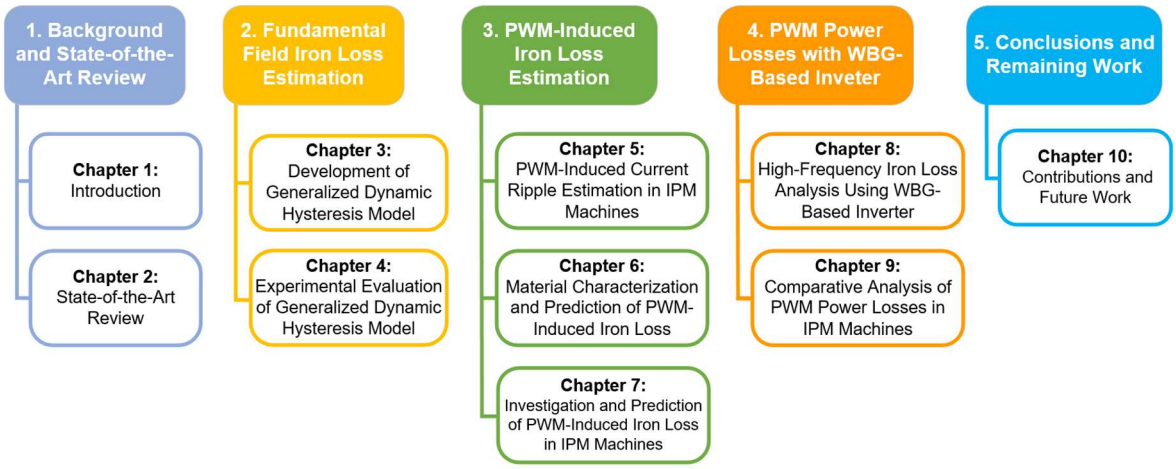

Figure 1-5: Summary of the thesis organization.

1.4 Thesis Organization

This thesis consists of five major parts that are highlighted in Figure 1-5, and each chapter is briefly summarized as follows:

Following this introductory chapter, Chapter 2 provides a thorough state-of-the-art review that examines a broad range of existing technical publications related to the topic of iron losses. Different types of material-level iron loss models are discussed together with a comparative study on their advantages and limitations. Next, several important issues associated with machine-level applications are discussed. In addition, past work reported in the literature regarding PWM-

induced current ripple and the associated power loss analysis are presented. Finally, key research opportunities are summarized.

Chapter 3 presents a generalized dynamic hysteresis model for estimating the iron loss of complex flux waveforms. The hysteresis loop and iron loss measurement system is first introduced to investigate the properties of the magnetic materials over a wide range of ac and dc excitation. With the measured hysteresis loop data available, an improved dynamic hysteresis model is proposed to properly incorporate the impact of several key factors on dynamic field modeling including the flux density changing rate, instantaneous magnetization state, and the time history of the magnetic flux.

Chapter 4 evaluates the proposed dynamic hysteresis model by comparing the predicted results with experimental data over broad ranges of operating conditions. These conditions include pure sinusoidal waveforms, non-sinusoidal flux waveforms with superimposed harmonics, and sine waves in the presence of pre-magnetized dc-bias fields. Finally, a preliminary machine-level iron loss analysis is provided.

Chapter 5 presents an improved analytical model for estimating the high-frequency current ripple of IPM machines caused by PWM switching. The proposed model accounts for the impact of slotting effects, magnetic saturation, and cross-coupling between the *d*- and *q*-axes. The model is subsequently used to investigate several factors that influence PWM-induced current ripple.

Chapter 6 investigates the iron loss properties of soft magnetic materials under conditions of high excitation frequency and varying pre-magnetized dc-bias fields. Using measured iron loss data, a modified dynamic Jiles-Atherton model is developed for PWM-induced iron loss estimation. Experimental results are provided to evaluate the iron loss variation under a wide range of ac flux amplitudes, excitation frequencies, and flux ripple waveshapes.

Chapter 7 presents an improved machine-level PWM-induced iron loss estimation model incorporating the impact of flux ripple waveshape and nonlinear magnetic characteristics. Experimental results are provided to evaluate the estimation accuracy and to investigate the effects of several factors on the PWM-induced iron and magnet loss in IPM machines.

Chapter 8 extends the PWM-induced iron loss characterization in different lamination steels to a much broader PWM frequency range (i.e., f_{PWM} up to 200 kHz) using WBG-based power devices. Experimental data confirm the model's promising ability to estimate the total iron loss under PWM voltage excitation with high fundamental and PWM switching frequencies and varying fundamental field amplitudes.

Chapter 9 provides a comparative analysis of PWM power losses in traction IPM machines with different PWM modulation schemes and a wide range of switching frequencies. The variation trends of three major power loss components in IPM machines are discussed, including the copper, iron, and magnet loss. In addition, test results collected from two traction IPM machines are utilized to verify the accuracy of the proposed model.

Chapter 10 summarizes the main research conclusions, key new contributions, and the suggested future work after this research program.

Chapter 2
State-of-the-Art Review

2.1 Introduction

It is widely acknowledged in both academia and industry that, although the conventional iron loss model either based on Steinmetz Equation or standard iron loss separation theorem is convenient for quick iron loss evaluation in the electric machines, it compromises the prediction accuracy significantly and the estimated values are always lower than the measured results. Therefore, the issues of iron loss modeling and investigation have been receiving renewed attention by researchers in this field.

Although achieving accurate iron loss prediction in the electric machines is still full of difficulties up to now, it has been concluded in [9], [10] that the principal factors leading to iron loss underestimation include inadequate understanding of microscopic magnetic phenomenon, lack of accurate iron loss prediction model, complex multidisciplinary nature (i.e., associated with mechanical and thermal effects), difficulties in machine-level iron loss segregation and estimation, and additional machine power losses due to PWM voltage excitation.

In general, as summarized in Figure 2-1, the efforts devoted to explaining the iron loss underestimation typically fall into three major categories, including material-level iron loss characterization, machine-level iron loss analysis, and investigations of the impact of PWM voltage excitation on machine power losses. In this chapter, the existing work involving iron loss background analysis is first presented to lay the foundation of iron loss phenomenon in the soft magnetic materials. Subsequently, various iron loss modeling approaches are discussed and compared regarding model accuracy, material data requirement, calculation effort, and

extendability to complex flux waveforms. Iron loss properties characterization and additional influencing factors on materials' magnetic properties and iron loss are evaluated, presenting a more comprehensive view of iron loss phenomena. Next, the existing works related to machine-level iron loss analysis are demonstrated. These include experimental segregation of iron loss in the electric machines as well as applying the material-level iron loss model to machine-level analysis. Moreover, available techniques for PWM-induced current ripple and power losses estimation are illustrated, highlighting the primary barriers hinder the fast and accurate PWM-induced iron loss estimation in IPM machines. Finally, key conclusions are presented to summarize the identified research opportunities.

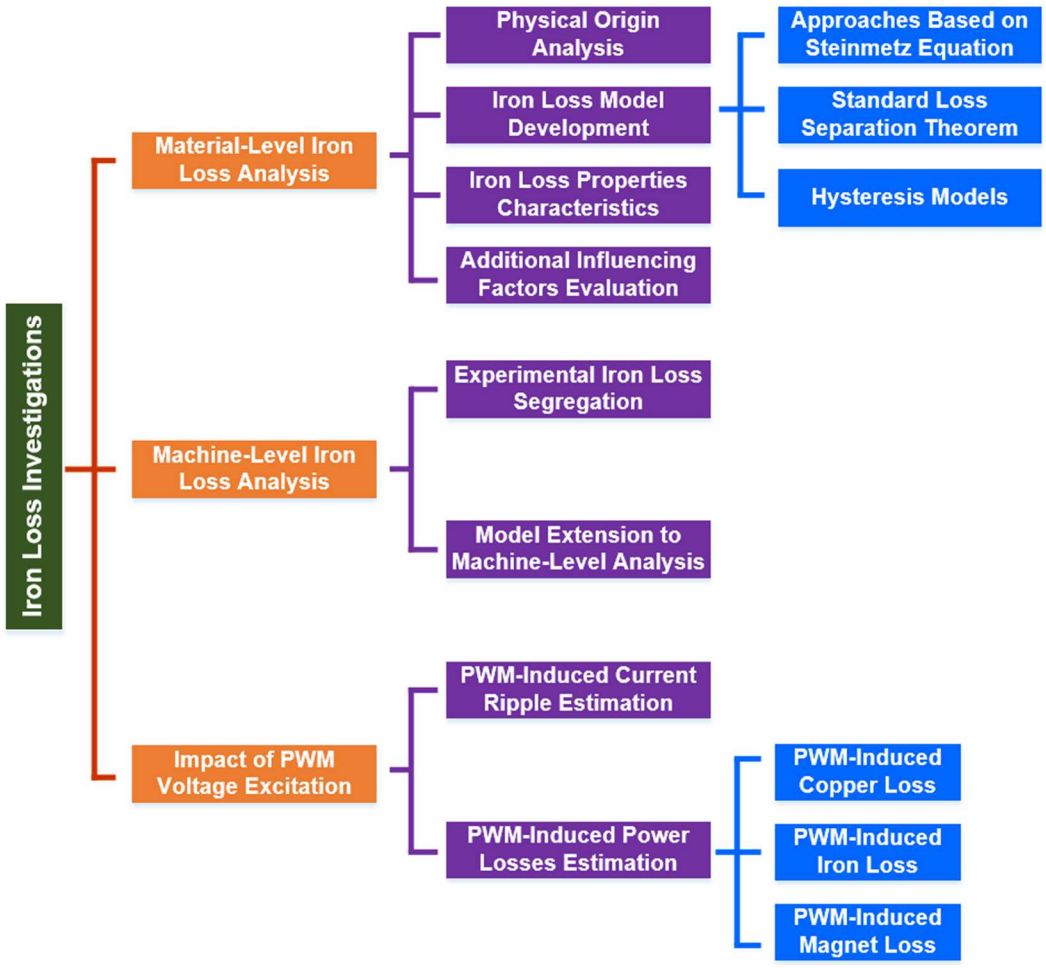

Figure 2-1: Overview of categorizations of iron loss investigations found in literature.

2.2 Material-Level Iron Loss Analysis and Prediction

Nowadays, the soft magnetic materials are ubiquitous and widely adopted by applications including transformers, electric machines, etc. Among a variety of material options, iron-silicon steel is one of the dominating choices due to its high permeability, high induction, and relatively low magnetic loss. Therefore, understanding the material-level iron loss mechanism is of great importance to diminish energy consumption and improve the efficiency of the overall system.

2.2.1 Physical Origin of Iron Loss Phenomenon

For engineering applications, it is commonly accepted that the total iron loss can be subdivided into two separate components, namely, the static hysteresis loss (i.e., no response to frequency) and dynamic eddy current loss. However, contradicted by specialists from material sciences and physics, this approach lacks theoretical justification, which is not adequate to explain the complex iron loss phenomenon [11].

From microscopic aspect, as the simplified domain structure shown in Figure 2-2 [12], the ferro- and ferrimagnetic materials consist of saturated domains, and the domain walls (i.e., Bloch walls) separate one domain from another. Moreover, Figure 2-3 [13] shows the orientation map of the microstructure of the non-oriented lamination steel. It further confirms that, rather than stay in a single magnetization state throughout the material, each domain points in a specific direction.

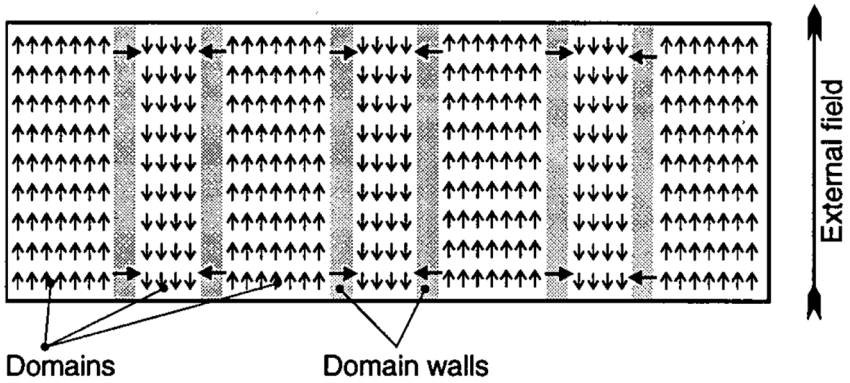

Figure 2-2: Magnetic domain structures in the ferro- and ferrimagnetic materials [12].

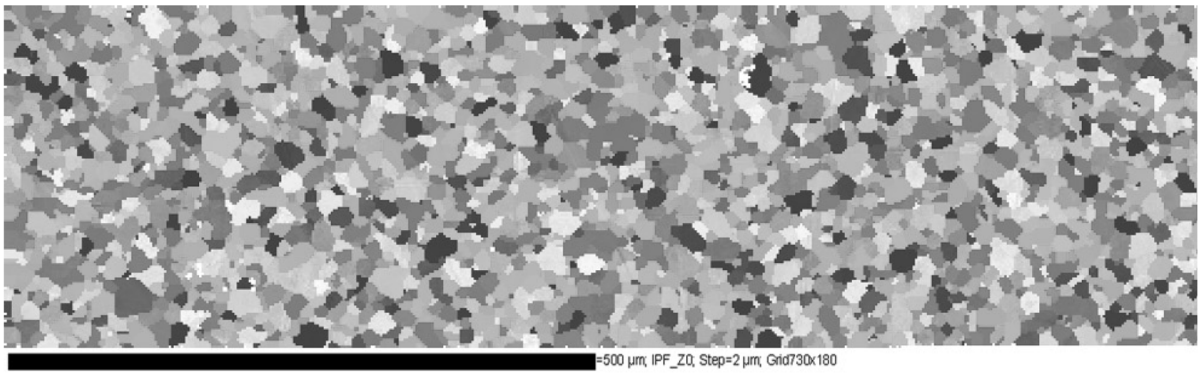

Figure 2-3: Orientation map of the microstructure of non-oriented electrical steel sheet [13].

Within each magnetic domain, it contains many magnetic dipole moments which aligned in the same direction. As shown in Figure 2-4(a), in the absence of external fields, all the magnetic domains inside the magnetic materials are randomly distributed, generating the zero net magnetic field. In response to the external magnetic field in Figure 2-4(b), the magnetic domains move towards the direction of the external field, and a smaller number of magnetic domains point against the external field. When all the domains are aligned in the same direction of the external field, the material reaches its saturation state (i.e., the relative permeability drops to 1). However, the magnetization process in ferromagnetic materials is not uniform but highly localized. A change in the global magnetization can only be achieved by movement of these domain walls. This physical interpretation has been experimentally verified and known as Barkhausen jumps [14].

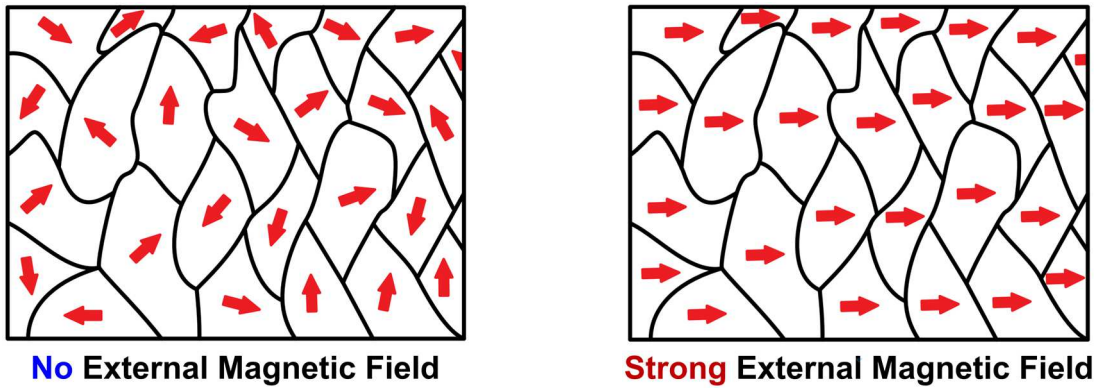

(a) Without external magnetic field (b) With external magnetic field

Figure 2-4: Orientation of magnetic domains with and without external magnetic field.
(**Sources**: https://www.allegromicro.com/ja-JP/Design-Center/Technical-Documents/Hall-Effect-Sensor-IC-Publications/Hysteresis-Mitigation-in-Current-Sensor-ICs-Using-Ferromagnetic-Cores.aspx

Consistent with magnetic domain theory, Williams *et al.* [15] pointed out that so-called anomalous loss, the difference between the predicted and measured values, is primarily due to the domain wall movement during the process of re-magnetization in the presence of external ac field.

To account for the domain structure of the magnetic material in the iron loss calculation, Pry and Bean [16] proposed an iron loss model incorporating a simple domain configuration, highlighting that anomalous loss arises from the non-uniform distribution of eddy currents which are much higher in the vicinity of moving domain walls.

However, Fish [17] pointed out that the uniform domain wall assumption adopted by Pry and Bean was greatly oversimplified. Furthermore, as presented by Haller *et al.* [18], during the re-magnetization process, there are different mobilities of existing domains walls as well as the dynamic nucleation of new walls especially when the magnetic materials fall into the saturated region (i.e., above the knee region of dc *B*-*H* curve).

Bertotti [19] discussed the basic principles of the magnetization process and the origin of iron loss in soft magnetic materials. Domain wall dynamics were investigated in well oriented single crystals, containing one or a few mobile 180˚ walls. However, characterization of microstructural models in different materials and various magnetization state remains challenging and not practical for engineering applications.

Graham [20] demonstrated that non-uniform magnetization is expected to have a profound effect on the eddy current distribution, and in turn, affect the resulting iron loss. Since magnetization is highly localized, the rate of change of magnetization, and local induced voltage, as well as localized eddy current, are significantly increased. The comparison of eddy current distribution between the classical model and domain-wall model is shown in Figure 2-5(a) and (b), respectively.

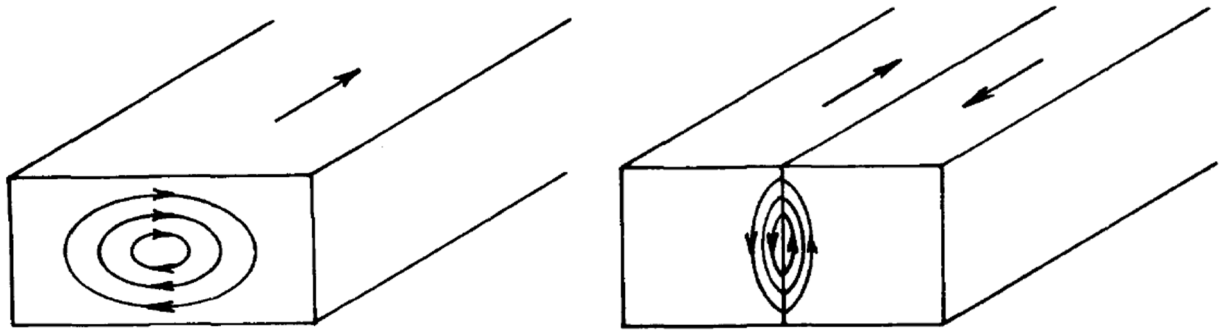

(a) Eddy current according to the classical model (linearized material)

(b) Eddy current based on the domain-wall model

Figure 2-5: Comparison of eddy current distribution in the linearized material and domain-wall model within a single sheet of lamination steel [20].

It was stated in [20] that there is no apparent physical distinction between the static hysteresis loss and dynamic eddy current loss. Therefore, only one physical origin of re-magnetization iron loss exists, namely the damping of domain wall movement by eddy currents and spin relaxation.

Becker [21] proposed a simple reversal model for eddy-current-controlled materials. However, as recognized by the author, the model is limited to some instances, which cannot be used at the power and audio frequencies in the presence of considerable magnetic field variation. Consistent with the conclusion drew by Graham in [20], only one loss mechanism exists in the magnetic materials, namely the eddy current induced by the domain walls movement. Furthermore, it has been found that the so-called static hysteresis loss could be frequency dependent once the collapsing wall region is reached at high frequencies, leading to an entirely different configuration.

Reinert *et al.* [12] reviewed and discussed the physical origin of iron loss and key characteristics of the re-magnetization process, highlighting the discrete nature of magnetization in terms of space and time. Nevertheless, it has been reported in [12], [20] that, although a good conceptual understanding of iron loss phenomenon has been developed, exact calculation or prediction of iron loss through microscopic magnetic domains modeling remains beyond our capacity. Therefore, macroscopic iron loss modeling techniques are highly preferred for engineering applications, and the existing estimation models will be investigated and compared in the following sections.

2.2.2 Iron Loss Model Development

As stated in the preceding subsection, it is infeasible to predict the iron loss on a microscopic scale. Instead, macroscopic techniques are more suitable, and as the overview given in Figure 2-6, these approaches can be classified into three main categories. The iron loss models in the first group are developed based on the original Steinmetz equation. In the second group, the total iron loss is subdivided into several terms based on physical interpretation and loss from each term is estimated individually. The models in the last group are proposed to emulate the actual magnetization process and then determine the loss from the enclosed area of the predicted hysteresis loop.

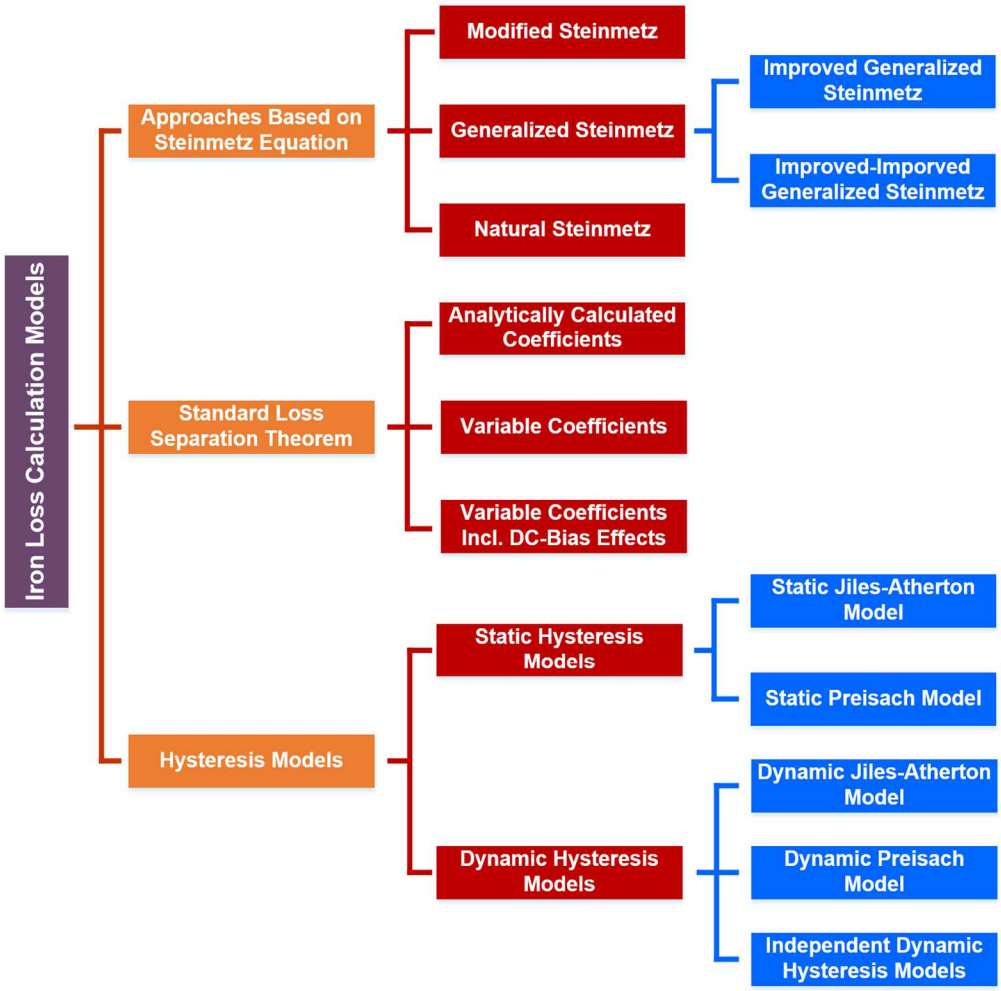

Figure 2-6: Classification of iron loss models in soft magnetic materials.

2.2.2.1 Iron Loss Models Based on the Steinmetz Equation

The well-known empirical equation for iron loss estimation in ferromagnetic materials traces back to an original equation developed by Steinmetz more than 130 years ago, and is formulated by means of the empirical formula as [22]:

$$P_{\text{iron}} = C_m f^{\alpha} \hat{B}^{\beta} \tag{2-1}$$

where P_{iron} is the iron loss, f is the excitation frequency of periodic waveform, and $\hat{B}$ is the peak value of flux density in the tested material.

The remaining three coefficients C_{m}, α, and β are determined by curve fitting the iron loss model to the measurement data. The obtained set of parameters are different for a given material and lamination thickness. However, (2-1) is only valid for sinusoidal flux waveform, which is a major limitation in electric machines applications.

Several modifications have been made to improve the estimation accuracy of the original Steinmetz equation and make the iron loss equation valid for non-sinusoidal flux waveform. Gradzki *et al.* [23] and Severns [24] tried to overcome this problem by introducing the Fourier expansion of arbitrary flux waveforms. Then (2-1) with identified parameters at each frequency is subsequently applied to the corresponding Fourier component and summed up for the total iron loss. However, the method of linear superposition is highly questionable due to the nonlinear properties of the ferromagnetic materials [25].

Reinert *et al.* [12] proposed the Modified Steinmetz Equation (MSE) for estimating the iron loss of arbitrary flux waveforms, in which the concept of equivalent frequency is introduced and defined in (2-2). Based on the physical understanding of the iron loss phenomena, the equivalent frequency is calculated as a function of averaged re-magnetization rate as well as the peak-to-peak flux density, making it possible to incorporate the waveshape properties into iron loss calculation.

$$f_{\text{eq}} = \frac{2}{B_{\text{peak}}^2 \pi^2} \int_0^T \left(\frac{dB}{dt}\right)^2 dt \tag{2-2}$$

where $B_{\text{peak}} = B_{\text{max}} - B_{\text{min}}$, and T is the time period of alternating flux waveform.

Combining (2-2) with the original Steinmetz equation in (2-1) gives the following expression:

$$P_{\text{iron}} = C_m f_{\text{eq}}^{\alpha-1} \hat{B}^{\beta} f \tag{2-3}$$

As can be seen from (2-3), without introducing any additional parameters compared to the original Steinmetz equation, it has been reported in [12] that the MSE model provides better extendability and estimation accuracy over the conventional model. However, a disadvantage of the MSE is that its accuracy degrades for flux waveforms with a small fundamental frequency part.

A general hypothesis for instantaneous iron loss was developed by Lancarotte *et al.* in [26], correlating the instantaneous power loss with magnetization rate *dB/dt* and induction level *B* as:

$$P_{\text{iron}}(t) = P_d\left(\frac{dB}{dt}, B\right) \tag{2-4}$$

where P_d is an unknown power dissipation function that reasonably describes the iron loss phenomenon for arbitrary flux density waveforms.

Although the importance of flux waveform time-history was noted by in [27], [28] direct modeling of P_d that matches well with the experimental results remains difficult and distant.

Based on the general hypothesis (2-4), Li *et al.* [29] proposed another version of Steinmetz equation so-called Generalized Steinmetz Equation (GSE), in which both the derivative of flux waveform *dB/dt* and instantaneous flux density *B* were included. The expression is given as:

$$\overline{P_{\text{iron}}} = \frac{1}{T} \int_0^T k_1 \left|\frac{dB}{dt}\right|^{\alpha} |B(t)|^{\beta-\alpha} dt \tag{2-5}$$

It has been proved [29] that (2-5) is intrinsically consistent with the original Steinmetz equation (2-1) for sinusoidal waveforms, and moreover, shows notable improvement for more complex flux

waveforms. However, based on the hypothesis that the energy loss is not sensitive to the minor loops riding on top of the fundamental field, the accuracy of GSE degrades when higher order harmonic components become significant. In addition, serval questions were raised in [30], pointing out the potential problems of modeling the iron loss only on the instantaneous parameters.

In order to eliminate the limitations of GSE, another modified iron loss model, the improved Generalized Steinmetz Equation (iGSE) was proposed by Venkatachalam *et al.* in [30]. The iGSE accounted for both the instantaneous factor and flux waveform history in the iron loss calculation while still being constant with Steinmetz equation for sinusoidal waveforms.

$$\overline{P_{\text{iron}}} = \frac{1}{T}\int_0^T k_1 \left|\frac{dB}{dt}\right|^{\alpha} |\Delta B|^{\beta-\alpha} \cdot dt \tag{2-6}$$

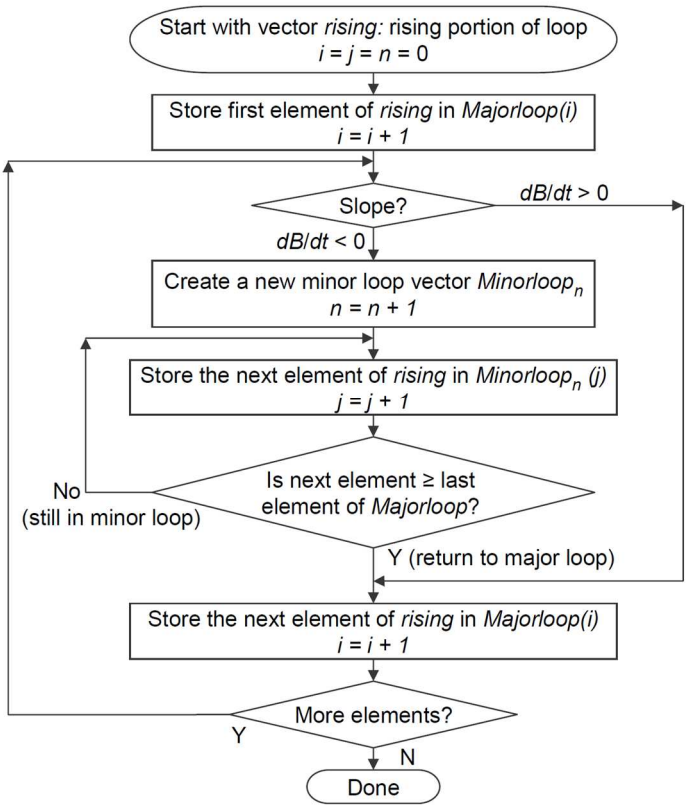

Figure 2-7: Flow chart for separation of minor loops from complex flux waveforms [30].

Different from the conventional Fourier expansion analysis, a flux waveform separation algorithm was proposed in [30] to separate the flux trajectory into the major and minor loops, where the iron loss of individual loop was estimated separately by (2-6). This decomposition process is summarized in the flow chart given in Figure 2-7. However, the iron loss has been known to vary significantly with pre-magnetized dc-bias field either for ferrimagnetic [31]–[34] or ferromagnetic materials [26], [35], whereas the iGSE ignores the dc-bias impact completely.

To further optimize the iGSE model, Mühlethaler *et al.* [36] developed an Improved-improved Generalized Steinmetz Equation (i^2GSE) to better emulate the magnetic relaxation phenomenon when zero voltage is applied across a transformer or inductor winding. Although the estimation accuracy increases in terms of trapezoidal waveforms over different frequencies and duty cycles, it requires five additional parameters and impact of dc-bias field remains neglected.

A similar approach to the iGSE was proposed in [37] as the Natural Steinmetz Extension (NSE)- (2-7) which was explicitly designed for square-shaped voltage waveforms with varying duty cycles, exhibiting certain improvement over the MSE. However, the major and minor loops were not differentiated, and the dc-bias field impact was ignored.

$$\overline{P_{\text{iron}}} = \left(\frac{\Delta B}{2}\right)^{\beta-\alpha} \frac{k_N}{T} \int_0^T k_1 \left|\frac{dB}{dt}\right|^{\alpha} \cdot dt \tag{2-7}$$

To sum up, there are various approaches based on the original Steinmetz equation developed for iron loss modeling, offering a simple and fast evaluation of iron loss of complex flux waveforms without requiring extra material characterization data. However, the parameters identification over wide frequency and flux amplitude range is challenging and lacks generality. Another significant limitation is that, except for the MSE proposed in [12], all the other models were originally designed and evaluated for ferrimagnetic materials instead of ferromagnetic materials.

2.2.2.2 Iron Loss Models Based on Standard Iron Loss Separation Theorem

In the last section, based on the original Steinmetz equation (2-1), various modeling approaches have been discussed, in which different input parameters are incorporated to achieve different objectives. However, no efforts have been devoted to explaining the physical loss mechanism. Distinguished from previous models, Jordan [38] attempted to estimate the iron loss by separating it into the static hysteresis loss and dynamic eddy-current loss as:

$$P_{\text{iron}} = P_{\text{hyst}} + P_{\text{eddy}} = k_h f \hat{B}^{\,2} + k_e f^2 \hat{B}^{\,2} \tag{2-8}$$

where k_h and k_e are the coefficients of hysteresis loss and eddy-current loss, respectively.

Under the assumptions of uniform magnetization (i.e., ignoring the magnetic domains), linearization, and homogeneity over each sheet of magnetic material, the eddy-current loss coefficient k_e can be derived and calculated analytically with knowledge of several physical parameters, as follows:

$$k_e = \frac{d^2 \left(\frac{dB}{dt}\right)^2}{12} = \frac{\pi^2 d^2}{6\rho_{\text{iron}}} \tag{2-9}$$

where d is the lamination sheet thickness, and ρ_{iron} is the material resistivity.

However, the hysteresis loss coefficient k_h can only be identified by the experimental tests under the quasi-static condition (i.e., low excitation frequency) which is generally assumed as a function of maximum flux density amplitude. Although this method has been adopted by varying engineering applications owing to its plausible physical backgrounds and ease of implementation, many papers have reported that the prediction results from (2-8) show substantial discrepancies compared to the measured results. In order to compensate the observed differences, a third artificial loss component has been introduced, normally referred as the excess or anomalous eddy-current loss P_{exc}, which has to be determined experimentally like the hysteresis loss coefficient.

In recognition that excess loss depends on empirical factors and experimental characterization prior to the iron loss estimation, a statistical theorem was proposed by Bertotti [39], introducing the magnetic objects to emulate the magnetic domain structures. Then the anomalous loss was calculated analytically based on the physical interpretation (i.e., domain walls motion) as follows:

$$P_{\text{iron}} = P_{\text{hyst}} + P_{\text{eddy}} + P_{\text{ano}} = k_h f \hat{B}^{\,2} + k_e f^2 \hat{B}^{\,2} + k_a f^{1.5} \hat{B}^{\,1.5} \tag{2-10}$$

$$k_a = \sqrt{S V_0 \sigma G} \tag{2-11}$$

where S is the cross-section area of the lamination sheet, V_0 determines the statistical distribution of the localized coercive fields and affected by the steel grain size [40], σ is the conductivity of the lamination sheet, and $G \approx 0.136$ is a dimensionless coefficient.

However, several problems with Bertotti's description were reported and discussed in [41]. First of all, the classical eddy-current loss term P_{eddy} shares the same limitation of (2-8), which is under the assumptions of uniform magnetization, linearity, and homogeneity. Although this assumption is acceptable at low frequency, it compromises the accuracy significantly as the frequency increases and the skin effect becomes critically important. It was reported in [42] that Bertotti's formula could be applied for frequencies lower than 225 Hz. Moreover, Bishop [43], [44] has proven that, due to the interaction between different magnetic objects, the P_{eddy} itself exhibits up to 30 % variations, destroying the attempts to physically explain the excess loss phenomenon. Also, several publications pointed out the frequency-dependent hysteresis loss [20], [45], [46], becoming a potential source of iron loss underestimation over the high-frequency range.

Ibrahim *et al.* [47] claimed that the excess eddy-current loss is mainly attributed to the non-uniform flux density distribution, and an improved model was proposed to take account for the skin effect. Adopting the analytical expression proposed in [48], the flux density at a given position y from the center of the lamination sheet is given as:

$$B_p(\hat{y}) = B_b \sqrt{\frac{\cosh\left(\frac{2\hat{y}}{\lambda}\right) + \cos(\frac{2\hat{y}}{\lambda})}{\cosh\left(\frac{2}{\lambda}\right) + \cos(\frac{2}{\lambda})}} \tag{2-12}$$

$$\lambda = \sqrt{\frac{2}{L^2 \omega \mu \sigma}} \tag{2-13}$$

where $\hat{y} = y/L$, which is the normalized value respect to the half lamination sheet thickness L. B_b is the flux density at the boundary, ω is the angular frequency, μ is the magnetic permeability.

The finite section method was proposed in [47] to achieve accurate quantification of the high frequency hysteresis loss, taking into account the actual flux density distribution. Figure 2-8(a) illustrates the basic idea behind this method, dividing each single lamination sheet into multiple segments and estimating the iron loss individually. The flow chart of the model implementation process is demonstrated in Figure 2-8(b).

Although the model exhibits acceptable performance for the unannealed laminations, in which the static hysteresis loss dominates, as acknowledged by the authors, the model accuracy degrades

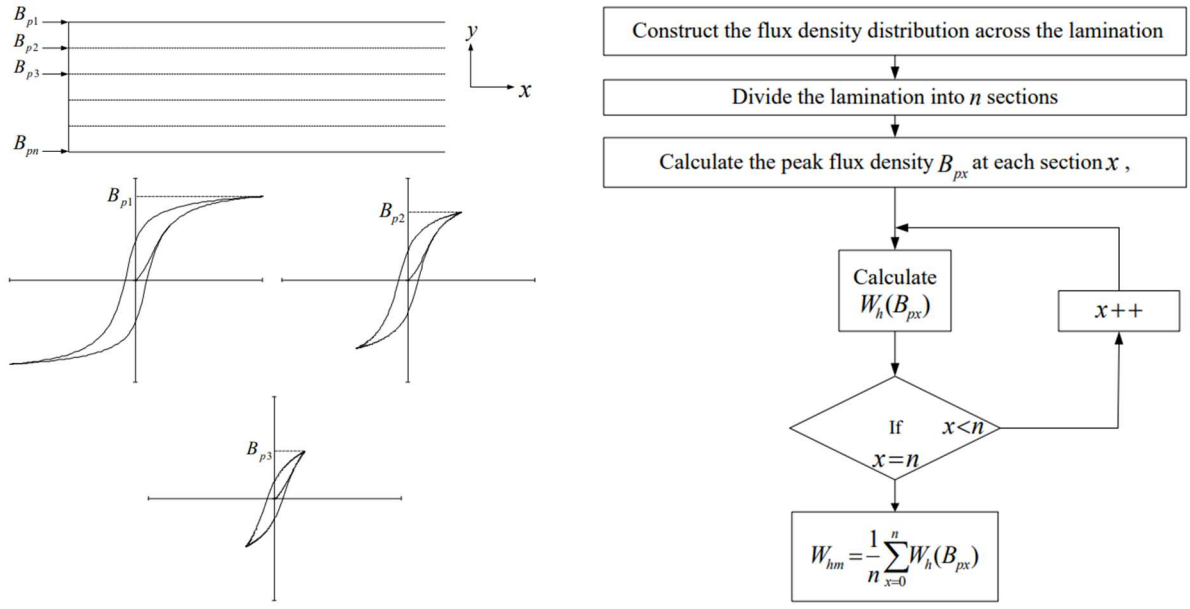

(a) Example of finite section method (b) Flow chart for hysteresis model estimation

Figure 2-8: Evaluation and analysis the impact of non-uniform flux density distribution on hysteresis loss [47].

for the annealed samples. It has been found that the effect of domain structure on eddy-current loss was ignored in [47], inevitably leading to iron loss underestimation at higher frequencies.

Gao *et al.* [49] introduced a simple numeric modeling of the excess eddy-current loss using the modified conductivity, including the skin effect with a 1-D nonlinear eddy current FEA.

Modified Iron Loss Equation:

$$P_{\text{iron}} = k_h(\hat{B})f + \frac{\pi^2 \hat{B}^{\,2} f^2 t^2}{6}\sigma^* \tag{2-14}$$

1-D Magnetic Field Analysis:

$$-\frac{\partial}{\partial z}\left(v\frac{\partial A_x}{\partial z}\right) + \sigma\frac{\partial A_x}{\partial t} = 0 \tag{2-15}$$

where σ^* is the modified conductivity to account for the short eddy-current loops around the domain walls.

Two different models, one neglecting the domain structure and another simple 1-D magnetic domain model are presented and compared in Figure 2-9(a) and (b), respectively. It has been discovered that the calculated iron loss results using the modified conductivity show the satisfied accuracy for non-oriented materials. However, identifying the σ^* requires sophisticated tests, and σ^* exhibits large variations over different frequencies and induction values. Furthermore, the proposed model calls for 1-D FEA, adding difficulties to implement practically.

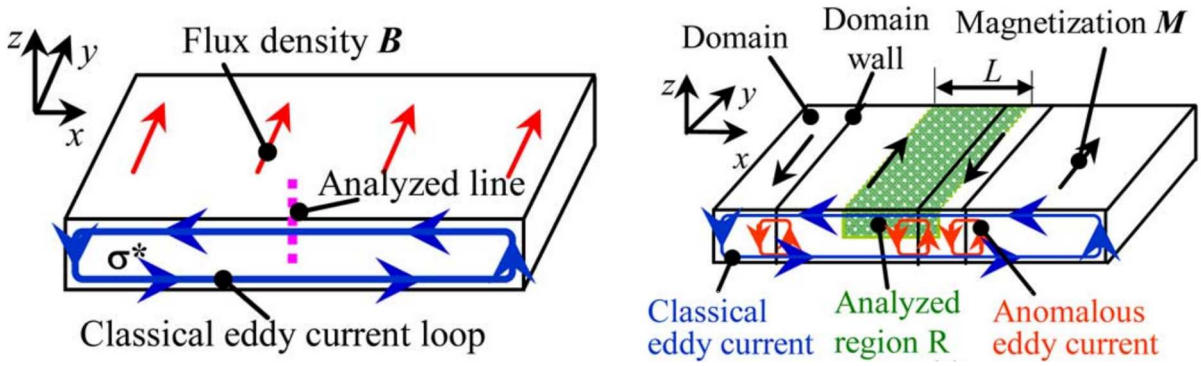

(a) Modeling without domain structure (b) Simple 1-D magnetic domain model

Figure 2-9: Comparison of eddy-current modeling with and without magnetic domains [49].

Over last few decades, instead of trying to explain and calculate the iron loss physically with constant parameters, some variability of the iron loss coefficients has been adopted to achieve higher estimation accuracy, sacrificing a portion of the physical basis of original loss separation theory and turning the iron loss model into a semi-empirical mathematical approach.

Ionel *et al.* [50] abandoned the excess loss concept and proposed a modified version of the iron loss equation based on (2-8), where the coefficients include frequency and induction dependencies.

$$P_{\text{iron}} = k_h(f) f \hat{B}^{\alpha(f,\hat{B})} + k_e\left(f, \hat{B}\right) f^2 \hat{B}^2 \tag{2-16}$$

The division of (2-14) by excitation frequency f yields a first-order polynomial equation, making it possible to identify these parameters through linear fitting process with the experimental data. However, the determined coefficients vary significantly with frequency and induction value, making it difficult and challenging for practical engineering applications in terms of data storage.

To further simplify the parameters identification process, another model with a constant value for the hysteresis loss power coefficient $\alpha = 2$ (CAL2) was also proposed in [50]:

$$P_{\text{iron}} = k_h\left(f, \hat{B}\right) f \hat{B}^2 + k_e\left(f, \hat{B}\right) f^2 \hat{B}^2 \tag{2-17}$$

where both k_h and k_e are functions of f and $\hat{B}$.

The division of (2-4) f by and $\hat{B}$ yields the following linear equation:

$$\frac{P_{\text{iron}}}{f \hat{B}^2} = k_h\left(f, \hat{B}\right) + k_e\left(f, \hat{B}\right) f \tag{2-18}$$

The parameters in (2-18) were characterized through the measured data over different frequencies (i.e., f = 25, 60, 120, 300 and 400 Hz) and induction values (i.e., up to 2 T). The determined coefficients were then expressed by the polynomial equations in (2-19) and (2-20). Overlaid with the polyfitted data, the variation of hysteresis loss coefficient k_e and eddy-current loss coefficient are presented in Figure 2-10(a) and (b), respectively.

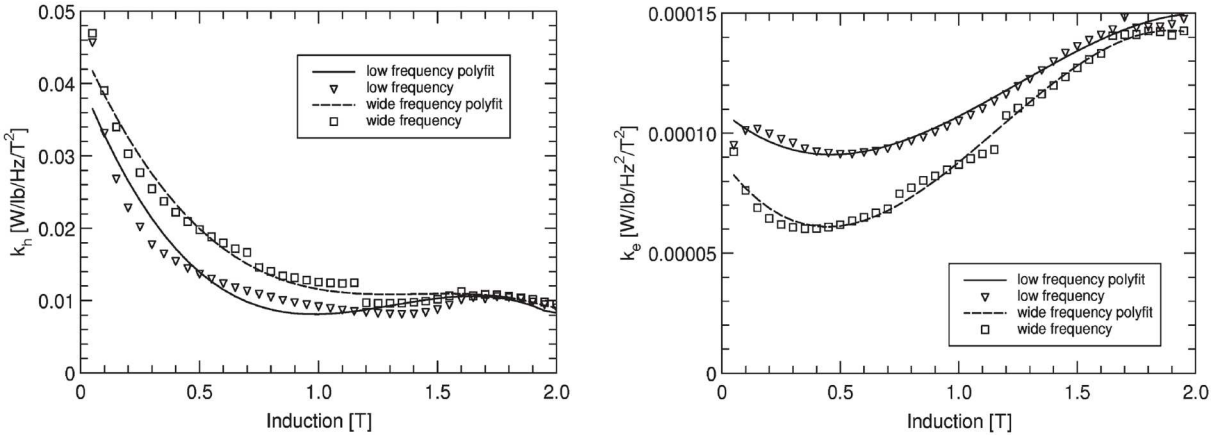

(a) Hysteresis loss coefficient k_h (b) Eddy-current loss coefficient k_e

Figure 2-10: Variation of the iron loss coefficients with induction and frequency in the CAL2 model [50].

$$k_e = k_{e0} + k_{e1}B + k_{e2}B^2 + k_{e3}B^3 \tag{2-19}$$

$$k_h = k_{h0} + k_{h1}B + k_{h2}B^2 + k_{h3}B^3 \tag{2-20}$$

Generally speaking, the CAL2 model offers serval desired advantages and appealing features for iron loss evaluation in the electric machines, including relatively simple parameters identification process, fast calculation speed, and satisfactory accuracy over broad operating conditions. Also, the required data are commonly available from typical lamination steel manufacturer, making this approach especially popular for engineering applications.

However, the accuracy of this model was only evaluated by the sinusoidal flux waveforms, raising skepticism whether the model can be extended to complex flux waveforms containing higher order harmonics. Moreover, the model parameters are determined through symmetrical loops excluding the dc-bias field impact on the iron loss.

Simão *et al.* [35] experimentally investigated the hysteresis loss of six different non-oriented industrial magnetic materials at 1 Hz (i.e., the eddy-current loss is negligible) over varying dc-bias fields, and a simple common rule was obtained in (2-21) to predict their behavior.

$$P_{\mathrm{iron}_{dc}}/P_{\mathrm{iron}(B_{\mathrm{dc}}=0)} = k_{\mathrm{dc}}B_{\mathrm{dc}}^{\lambda} + 1 \tag{2-21}$$

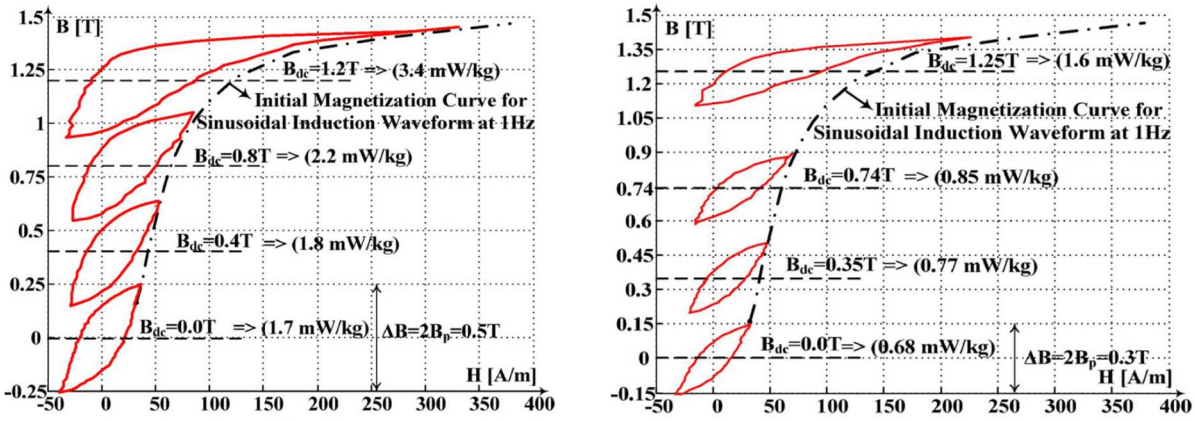

(a) ΔB = 0.5 T, and B_{ac} = 0.25 T (b) ΔB = 0.3 T, and B_{ac} = 0.15 T

Figure 2-11: Minor loops as function of dc-bias field with different ac flux densities [35].

Although the importance of the dc-bias field on iron loss has been demonstrated, the maximum amplitudes of the ac flux density B_{ac} of all the experimental data given by Simão *et al.* were limited to 0.25 T, and only static hysteresis loss (i.e., f = 1Hz) was evaluated, calling for more sophisticated material characterization over wider operating ranges.

Zhu *et al.* [51] extended similar test over a broader range of ac flux density (i.e., up to 0.75 T) and excitation frequency (i.e., up to 200 Hz) based on the traditional Epstein frame with dc-bias magnetization capability. Instead of using a lumped factor to describe the dc-bias field impact like (2-21), assuming the eddy-current loss is not affected by the dc-bias field, a correction factor $\varepsilon(B_{dc},B_{ac})$ was proposed in (2-22) to better emulate the impact of the dc-bias field on hysteresis loss. Improvement has been achieved compared to Simão's model especially in the region of the low dc-bias field, and the comparison data are shown in Figure 2-12.

$$P_{\text{iron}_{dc}} = k_e f^2 B_{\text{ac}}^2 + k_h \varepsilon(B_{\text{dc}}, B_{\text{ac}}) f B_{\text{ac}}^2 \tag{2-22}$$

In the past decade, the impact of the dc-bias field has gained wide attention and been researched extensively [52]–[55]. Generally, different versions of correction factors close to that in (2-22) were adopted for iron loss estimation in the presence of the dc-bias field. However, the issue of nonlinear cross-coupling between the fundamental and harmonic fields remains challenging.

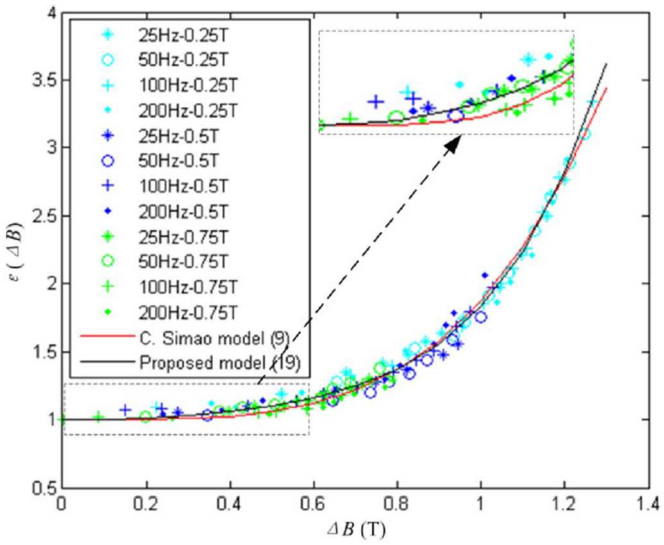

Figure 2-12: Comparison of measured and fitted data over different conditions [51].

Different from the conventional linear superposition method, Taitoda *et al.* [56] proposed an iron loss calculation method for a complex hysteresis loop including minor loops. The minor loops' losses and iron loss of the remained major loop were estimated separately using the modified equation (2-23), where both loss coefficients were considered as the functions of the ac flux density and dc-bias induction. The flux density terms were ignored for ease of parameters identification.

$$P_{\text{iron}} = k_h(B_{\text{ac}}, B_{\text{max}})f \ + k_e(B_{\text{ac}}, B_{\text{max}})f^2 \tag{2-23}$$

$$B_{\text{max}} = B_{\text{ac}} + B_{\text{dc}} \tag{2-24}$$

The characterized iron loss coefficients are shown in Figure 2-13(a) and (b), potentially with specific interpolation technique, the iron loss of complex flux waveform can be estimated following the calculation method demonstrated in Figure 2-13(c). It has been experimentally verified that, by employing the apparent frequency concept in addition to the coefficients identified under dc-biased excitation, the discrepancies between the predicted and measured iron losses are much diminished compared to the conventional method.

However, the characterization process of iron loss coefficients is complicated and time-consuming, requiring iron loss evaluation over varying dc-bias fields, ac flux density amplitudes,

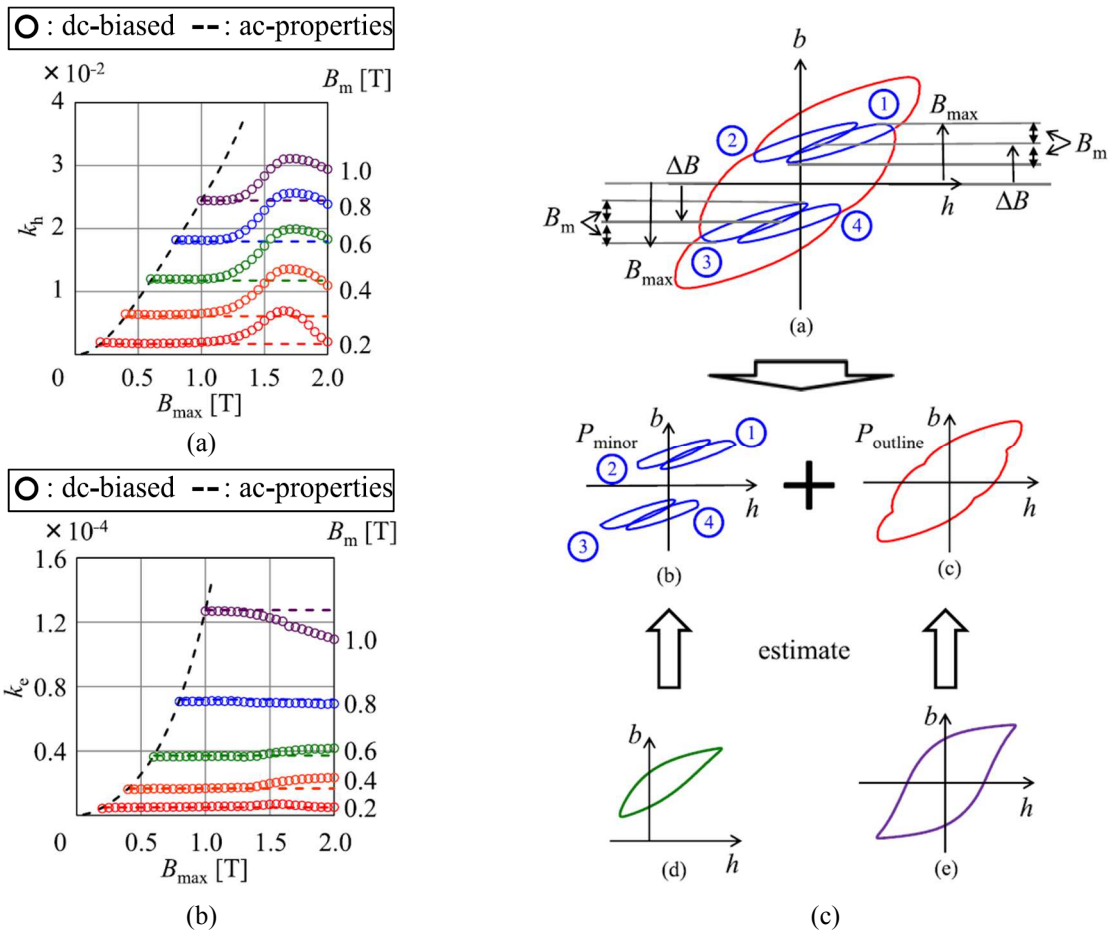

Figure 2-13: (a) Hysteresis loss coefficient, (b) Eddy-current loss coefficient, and (c) Flux waveform segregation [56].

and several excitation frequencies (in [56], f at 50, 150, and 750 Hz). Moreover, (2-23) is a frequency-domain iron loss model, which is not intrinsically compatible with the time-domain separation process shown in (c). The estimation accuracy likely degrades as the obtained waveform deviates from the sinusoidal shape.

In summary, various approaches based on iron loss separation theorem have been proposed. They can be mainly split into two categories, one with constant parameters derived from analytical interpretation, which is limited to ideal magnetic materials and low-frequency conditions. Another type of models introduces variable iron loss coefficients, expanding the application scope significantly. The dc-bias field impact can be incorporated appropriately by additional correction factors and physics-based hysteresis loop separation technique.

2.2.2.3 Hysteresis Models

To achieve more satisfactory estimation accuracy of the iron loss estimation and take physical insights into the magnetic mechanisms, hysteresis models are considered as the promising candidates that are able to predict the magnetization hysteresis loops accurately, whereby the iron loss can be subsequently determined from the enclosed loop area as:

$$P_{\text{iron}} = f \oint H \cdot dB \tag{2-25}$$

In the literature, there are two major categories of hysteresis models, namely the physics-based models and phenomenological (i.e., mathematical) models. The first ones are developed based on the knowledge of microscopic scale magnetization theory, where the widely acknowledged Jiles-Atherton model falls into this category. Regarding the second class, the hysteresis phenomenon is modeled by the interaction between the macroscopic scale magnetization state (i.e., magnetic flux density) and the resultant magnetic field strength (e.g., Preisach model and its descendants). Since the original introduction of these two models, they have received extensive attention to further improve the model performance, making them applicable to the electric machine applications. In this section, the state-of-the-art in hysteresis model development will be reviewed, discussed, and compared with iron loss models based on original Steinmetz equation and loss separation theorem.

A. Static Jiles-Atherton Model

Jiles and Atherton [57] proposed a theory of the magnetization process in ferromagnetic magnetic materials through sigmoid-shaped hysteresis loops. The model took the mean field approximation, assuming each domain interacts with the magnetic field strength *H* and a weighted mean of the overall magnetization. The imperfections of materials, as well as the regions of inhomogeneous strain, contribute to the opposition of domain wall movement, leading to an increase of hysteresis loss.

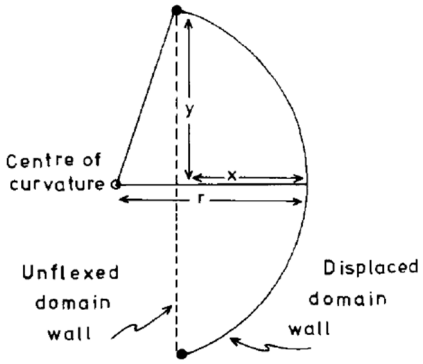

Figure 2-14: Bending of a magnetic domain wall between two pinning sites under the influence of an external magnetic field [57].

The hysteresis modeling is described with a macroscopic energy equation, which divides the overall magnetization process into reversible and irreversible changes. The irreversible change is responsible for the displacement of the domain walls, and the reversible changes in magnetization are due to the bending of domain walls between two pinning sites as shown in Figure 2-14, leading to a series of differential equations containing five physical parameters to identify [58]. The model performance has been experimentally investigated for ferromagnetic materials in terms of different types of magnetization curves, the anhysteretic, initial magnetization curve, and families of major hysteresis loops, highlighting the advantages of *J-A* model in accuracy as well as extendability.

Moreover, it is commonly acknowledged in the literature that the static *J-A* model is widely adopted owing to its simplicity in implementation, low computational effort, and low memory storage requirement.

It is worth noting that there are also some problems associated with the original *J-A* model, causing difficulties to implement it practically. First of all, the identification of *J-A* model parameters calls for availability of the regression curve and different mathematical modifications [59]–[62]. However, one of the model's equation involves differential calculation, making it necessary to introduce the iterative method to identify model coefficients. However, the standard procedure is sensitive to the selected initial values, likely leading to severe convergence problems.

Therefore, parameters identification plays a critical role in the practical implementation of *J-A* model. Various approaches have been proposed to optimize this process, such as Simulated Annealing Method [60], [61], [63], Genetic Algorithm [64]–[66], Neural Networks Method [67], [68], and Particle Swarm Optimization (PSO) [69], aiming to reduce the risk to exclude an acceptable solution.

Leite *et al.* [70] discovered that the data parameters obtained from the major hysteresis loop (i.e., outer loop in Figure 2-15(a)) only provide an accurate prediction of the major loop itself, but the comparison between the measured and simulated inner loops showed notable discrepancies.

As reported by Benabou *et al.* in [71] and Hamimid *et al.* in [72], the *J-A* model failed to provide closed non-centered minor loops using the parameters identified from the method described in [58], potentially leading to substantial iron loss underestimation of the complex flux waveforms containing minor loops (see Figure 2-15(b)). Although further attempts have been made to enforce the model to guarantee the closure of minor loops, they either call for a priori knowledge of field evolution [73] or extra parameters in addition to the original model [74].

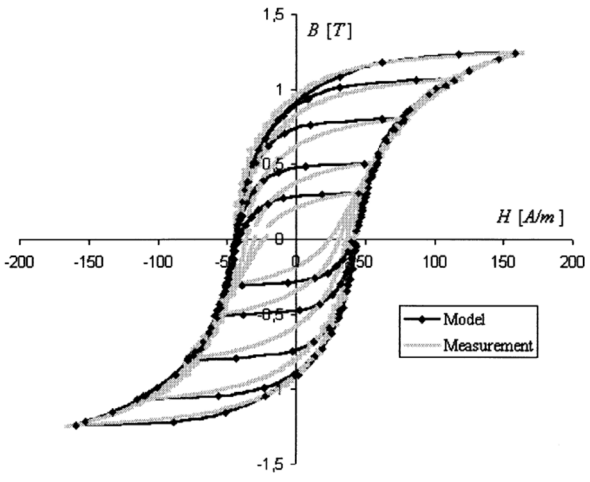

(a) Centered minor hysteresis loops [71]

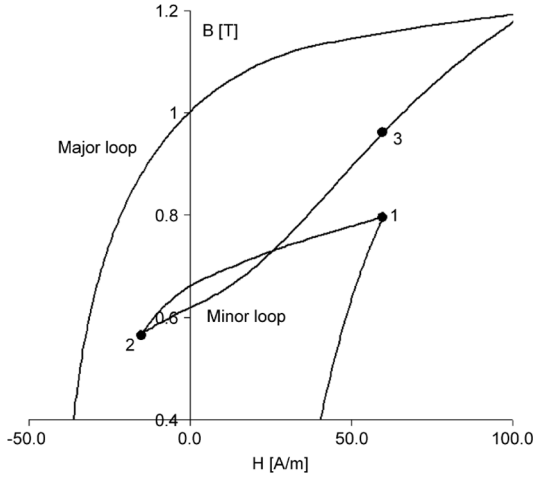

(b) Non-closure of non-centered minor hysteresis loops [72]

Figure 2-15: Typical problems of static *J-A* model with the parameters identified from major hysteresis loop.

B. Static Preisach Model

Another popular hysteresis model discussed in the literature is the Preisach model proposed by German physicist F. Preisach in 1935 [75]. Owing to its superior accuracy, stability, and generality, the Preisach model has been adopted by many researchers for the hysteresis modeling in many different applications, including the area of magnetics. It is a phenomenological model that can be utilized to model the Barkhausen effect (i.e., discontinuous magnetization) attributable to the existence of magnetic domains, which is often expressed by the following formula [76],

$$y(t) = \iint_{\alpha \geq \beta} \mu(\alpha, \beta)\, \hat{\gamma}_{\alpha,\beta}[u(t)] \cdot d\alpha d\beta \tag{2-26}$$

where $u(t)$ and $y(t)$ denote the system input and output respectively. In magnetic applications, $u(t) = H(t)$, $y(t) = B(t)$, $\mu(\alpha,\beta)$ is the weighted distribution function determined from experimental measurements, and $\hat{\gamma}_{\alpha,\beta}[u(t)]$ shown in Figure 2-16(a) is the hysteresis operator function represented by rectangular loops with α and β as the transition "up" and "down" switching values. The output of this function can be assumed only two values, +1 and -1.

As shown in Figure 2-16(b), the double integral process in (2-26) can also be interpreted as the superposition of elementary rectangular functions $\hat{\gamma}_{\alpha,\beta}$, weighted by distribution function $\mu(\alpha,\beta)$.

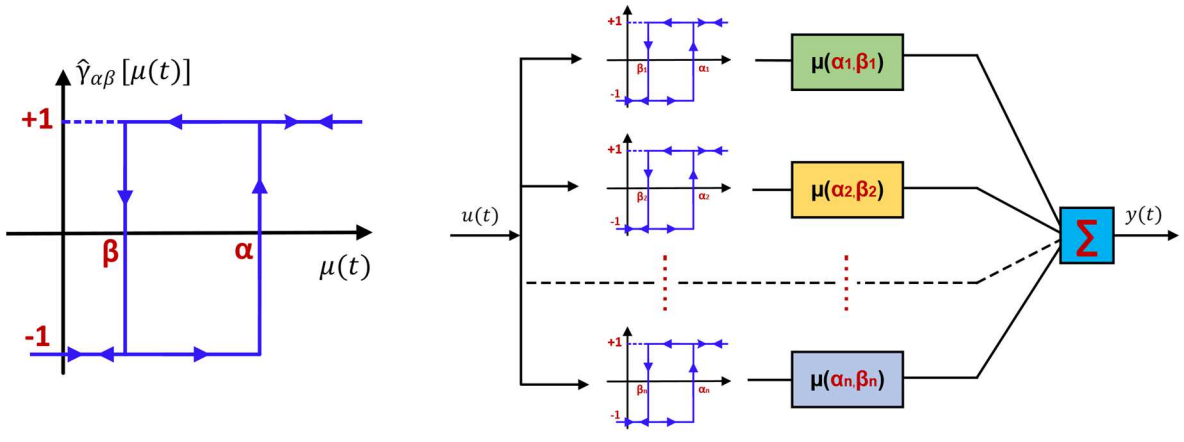

(a) Hysteresis operator $\hat{\gamma}_{\alpha,\beta}$ (b) Schematic of Preisach model

Figure 2-16: Overview of classical Preisach model structure.

After the early-stage analysis and development in terms of model understanding and stability evaluation, Krasnoselskii and Pokrovskii [77] separated the original Preisach model from its physical meaning and represented it in a purely mathematical form, establishing the limits of applicability of Preisach model.

Mayergoyz [28] thoroughly investigated the fundamental properties of the Preisach model, namely the wiping-out and congruency, stating that these intrinsic features are somewhat natural and consistent with experiments in the area of magnetics. In addition, he introduced the Everett function, which alternatively simplifies the double integral process and increases the computational efficiency significantly.

Zirka *et al.* [78] and Dlala *et al.* [79] analyzed the modeling accuracy of the Preisach model with the distribution function identified from the reversal curves. They pointed out that the Preisach model is generally sensitive to the position of the reversal points and the model does not produce closed minor loops. These problems are closely related to the identification techniques and generation of the first-order reversal curves.

Naidu [80] proposed a modified approach for Preisach model parameters identification. Instead of determining the parameters from first-order reversal curves, the major hysteresis loop was used, reducing the demands for testing waveforms generation. Furthermore, different techniques for identifying the distribution function were proposed and evaluated, including fuzzy logic and artificial neural network [81]–[83].

Dlala *et al.* [84] presented a method for modeling the symmetric minor loops in hysteresis magnetic materials. Combing the symmetrical minor loops around the origin and certain portions of initial magnetization curve (i.e., anhysteretic curve), the Preisach model was developed in terms of Everett function, omitting the need of higher-order reversal curves.

Furthermore, it has been proven in [84]–[86] that, under the quasi-static condition, the Preisach model is capable of accurately modeling hysteresis loops- Figure 2-17. Its ability to predict non-symmetric hysteresis loops make it an outstanding candidate for machine-level iron loss estimation.

As the *J-A* model and Preisach model become popular choices for hysteresis modeling, Philips *et al.* [87] and Benabou *et al.* [88] discussed and compared the strength and weakness of these two models. A general conclusion was reached that the *J-A* model shows appealing features in terms of calculation speed and simplicity, and the Preisach model exhibits better accuracy and generality. However, both models are inherently rate-independent, calling for additional efforts to take account of the frequency dependence of hysteresis effects.

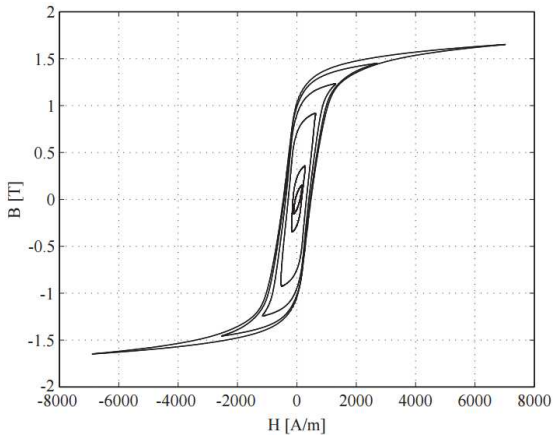

(a) Measured symmetrical loops to determine $\mu(t)$ [77]

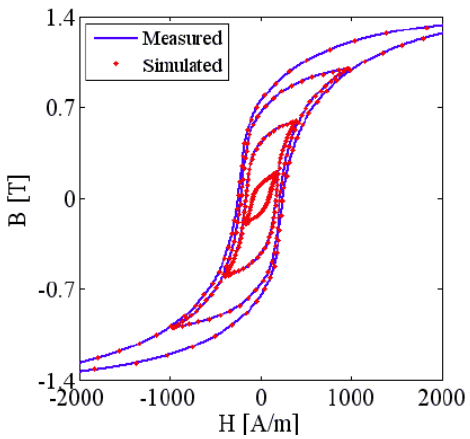

(b) Measured and simulated *B-H* curve of C19 [78]

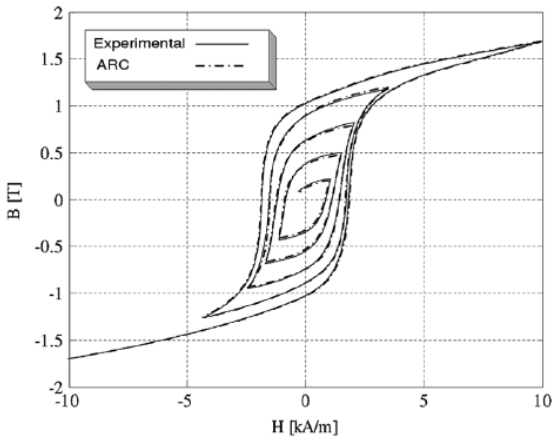

(c) Prediction results of symmetric minor loops [76]

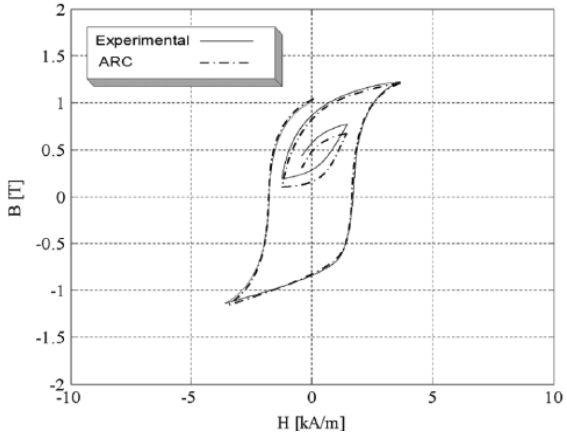

(d) Prediction results of non-symmetric minor loops [76]

Figure 2-17: Simulation results from Classical Preisach Model found in the literature.

C. Dynamic Jiles-Atherton Model

Based on the static version of *J-A* model, Jiles [89] proposed a scheme to include the dynamic losses in the ferromagnetic materials. Additional energy dissipation resulting from eddy-current losses were incorporated into the macroscopic energy balance equation. The classical eddy-current loss was considered proportional to the square of the rate of change of magnetization, given as:

$$\frac{dW_{EC}}{dt} = \frac{t^2}{2\rho_{\text{iron}}\beta}\left(\frac{dB}{dt}\right)^2 \tag{2-27}$$

where β is a geometrical factor (e.g., $\beta = 6$ in rectangular-shape lamination sheet).

The anomalous loss results from domain-wall motion were expressed as:

$$\frac{dW_A}{dt} = \left(\frac{GdwH_0}{\rho_{\text{iron}}}\right)^{1/2}\left(\frac{dB}{dt}\right)^{3/2} \tag{2-28}$$

where w is the width of laminations, and H_0 is a parameter representing the internal potential experienced by domain walls.

It is worth noting that both (2-27) and (2-28) are consistent with the loss separation theorem discussed in the previous section. With knowledge of energy consumption from eddy currents, the system energy-balance equation was rewritten, making it possible to predict the dynamic hysteresis loops. However, the accuracy of the original dynamic *J-A* model has been commonly adopted for real applications due to its relatively low accuracy.

Du and Robertson [90] proposed a modified dynamic *J-A* model to calculate the *B-H* curves and magnetic power loss in the lamination steels. The anomalous loss coefficient in (2-28) was determined based on a specific operating case instead of a pre-calculated constant. Two measured *B-H* curves were for any given flux density amplitude B_{ac} to simulate the dynamic properties of the selected lamination steel over a wide frequency. However, the model was only evaluated by simple sinusoidal cases.

Salvini *et al.* [67] proposed a method based on genetic algorithms and neural networks, making it possible to predict the dynamic hysteresis with five parameters that used in the static *J-A* model. However, the *J-A* model parameters have to be identified for each interesting frequency and ac flux density amplitude. In other words, the extendability of this model is very poor and limited. In addition, regarding the distorted excitations, the model is limited non-saturated minor loops.

Baghel *et al.* [91] improved the original dynamic *J-A* model by introducing an additional factor. However, it was reported that the model yields non-physical vertical lengthening of loops. Moreover, an alternative approach based on loss separation theory was discussed, which separated the static field and dynamic field estimation. This approach is fundamentally independent of the static *J-A* model, which will be reviewed later as a different category of dynamic hysteresis model.

D. Dynamic Preisach Model

Del Vecchio [92] stated that for non-oriented materials, ignoring the excess loss which is attributed to domain walls movement, the iron loss can be described in terms of the macroscopic magnetic fields. Taking into account the interaction of hysteresis and eddy-current phenomena, the well-known diffusion is expressed as:

$$\frac{\partial^2 H}{\partial z^2} = \sigma \frac{\partial B}{\partial t} \tag{2-29}$$

where t is the time and z is the axis perpendicular to the flux passing direction.

However, since (2-29) is nonlinear, hysteretic, and time- and space-dependent, the calculation of this diffusion typically calls for advanced numerical techniques (e.g., time-stepping analysis like Gillot-Calvert approach [93]), which is time-consuming and not favorable for the practical implementation. What is more, the excess loss cannot be included from the macroscopic scale, potentially leading to serious iron loss underestimation.

Mayergoyz [94] proposed a dynamic version of the Preisach model by introducing the time derivate of the output in (2-26). However, the parameters identification process is a bit complicated, and the estimation accuracy is relatively poor.

$$y(t) = \iint_{\alpha \geq \beta} \mu(\alpha, \beta, \frac{dy}{dt}) \hat{\gamma}_{\alpha,\beta}[u(t)] \cdot d\alpha d\beta \tag{2-30}$$

Bertotti [95] extended the classical Preisach model to a more generalized form. Instead of assuming that the elementary hysteresis operator switches instantaneously, in Bertotti's dynamic Preisach model, the time rate of hysteresis operator switching is proportional to the difference between the local magnetic field *H* and the elementary loop switching field, namely, α and β, taking into account the frequency impact. This method has been applied successfully for various operating cases, including estimating the iron loss in the electric machines. However, as noted by Philips *et al.* [96], after introducing the frequency dependence to the hysteresis operator, it then has more than two stable states, and the history storage becomes more difficult.

Rather than modify the hysteresis operator, Bernard *et al.* [97] expressed the distribution function of the Preisach model in terms of the derivative of flux density, and the flux density history was treated in the same way as the static Preisach model. The modified distribution function is expressed as:

$$\mu_{i,j}^{\text{inv}}\left(\frac{dB}{dt}\right) = \mu_{\text{stat}}^{\text{inv}}(i,j) + \tau(i,j)\frac{dB}{dt} \tag{2-31}$$

where $\mu_{\text{stat}}^{\text{inv}}$ is the static component of distribution function and τ is the slope value which describes the linear relationship between the rate-dependent distribution function and *dB/dt*.

Determining the μ_{stat}^{inv} and τ over the entire operating regions calls for the distribution function over different frequencies or *dB/dt* rates. As shown in Figure 2-18, several sets of centered cycles are used, yielding distinct distribution functions like two examples given in Figure 2-19.

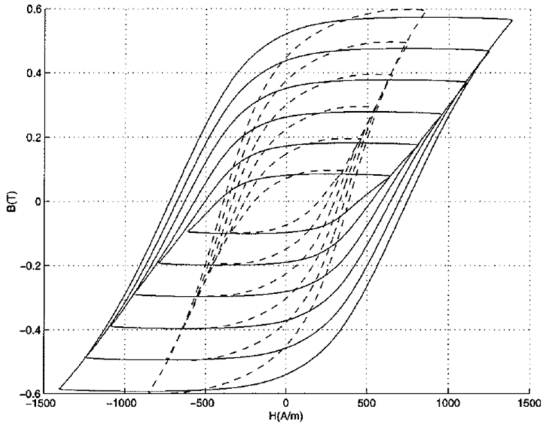

Figure 2-18: Two sets of symmetrical hysteresis loops measured with different *dB/dt* rates [97].
(Dashed lines: *dB/dt* = 5 T/s, full lines: *dB/dt* = 40 T/s)

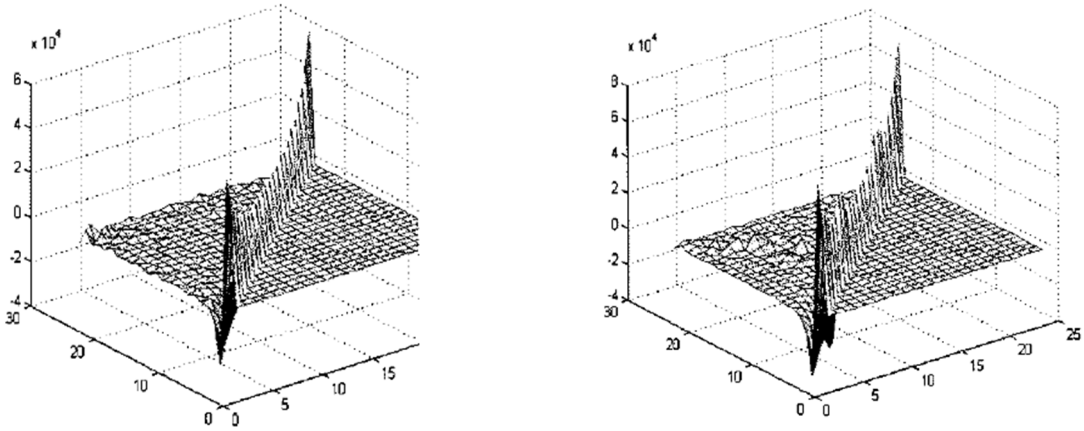

(a) *dB/dt* = 50 T/s (b) *dB/dt* = 200 T/s

Figure 2-19: Examples of obtained distribution functions under two flux density changing rates [97].

This method shows promising potential to model arbitrary magnetic flux trajectories with acceptable accuracy. In addition, the proposed model construction can be extended to include the impact of some other influencing factors, like temperature, mechanical stress, etc.

However, the experimental evaluation results presented in [97] was limited to relatively simple flux waveforms. The model performance in terms of complex waveforms containing high-order harmonics requires further investigation. Also, and the model resolution ΔB was at 0.1 T, which is too larger and not suitable for practical applications especially in terms of minor loops estimation (i.e., typically with small amplitudes).

E. Independent Dynamic Hysteresis Model

Another important class of dynamic hysteresis model enables the inclusion of eddy-current losses (i.e., both the classical and excess eddy-current loss) impact regardless of what kind of static hysteresis models are being used.

Under approximation that the iron loss separation theory is applicable and reasonably accurate, Zirka *et al.* [98] mathematically transformed the total magnetic field H_{tot} into separate field components, giving the total magnetic field expression as:

$$H_{\text{tot}}(t) = H_{\text{hyst}}(t) + H_{\text{eddy}}(t) + H_{\text{exc}}(t) \tag{2-32}$$

$$H_{\text{tot}}(t) = H_{\text{hyst}}(B) + \frac{d^2}{12\rho_{\text{iron}}}\frac{dB}{dt} + \delta\left|g(B)\frac{dB}{dt}\right|^{1/\alpha(B)} \tag{2-33}$$

where both $\alpha(B)$ and $g(B)$ are fitting parameters, and $H_{\text{hyst}}(B)$ can be determined through various static hysteresis modeling approaches (e.g., Static *J-A* and Preisach model).

However, as acknowledged by the authors, the model accuracy is largely determined by the fitting functions (i.e., $\alpha(B)$ and $g(B)$), especially under high-frequency (i.e., fundamental frequency $f_{\text{fund}} > 200$ Hz) conditions. Also the presented analysis in [98] is limited to the grain-oriented steels.

Steentjes *et al.* [99] introduced the saturation wave model to achieve estimation of classical eddy-current loss in the non-oriented materials by taking into account the skin effect,

$$H_{\text{tot}}(t) = H_{\text{hyst}}(B) + \frac{d^2(B - B_T)}{8\rho_{\text{iron}}B_{\max}}\frac{dB}{dt} + g(B)\left|\frac{dB}{dt}\right|^{1/\alpha(B)} \tag{2-34}$$

where B_T in (2-34) is equal to the coordinate of the initial point of the current curve stored in the memory of the static hysteresis model.

However, despite the efforts devoted to improving the classical eddy-current loss estimation, curve fitting the functions of $\alpha(B)$ and $g(B)$ remains indispensable and critical to model accuracy.

Dlala [100] proposed a simplified method for iron loss estimation based on the analytical solution of the diffusion equation and overcame the inadequacy of conventional model by introducing a function τ to enforce *dB/dt* to implicitly obey the magnetization law as:

$$H_{\mathrm{tot}}(t) = H_{\mathrm{hyst}}(B) + C_0\delta\left|\left(\frac{dB(t)}{dt}\right)^{\frac{1}{2}} + \overline{C_1}\delta\frac{dB(t)}{dt}\right|^{\tau(B(t))} \tag{2-35}$$

$$\tau\big(B(t)\big) = a_0 + a_1\delta\left(\frac{B(t)}{B_s}\right) + a_2\left(\frac{B(t)}{B_s}\right)^2 \tag{2-36}$$

where B_s predefines the magnetization saturation, and the remaining coefficients a_0, a_1, a_2, C_0, and $\overline{C_1}$ have to be estimated by curve fitting process.

Chevalier *et al.* [101] presented a dynamic hysteresis model by linking the excitation field on the sheet surface to the mean induction in the thickness of the sheet, the so-called Loss surface model. A characteristic surface function S was developed as:

$$S = H_{\mathrm{tot}}\left(B, \frac{dB}{dt}\right) = H_{\mathrm{stat}}(B) + H_{\mathrm{dyn}}(B, \frac{dB}{dt}) \tag{2-37}$$

As can be seen from (2-37), the *S* function divides the total magnetic field H_{tot} into two parts, namely a static part H_{stat} and a dynamic part H_{dyn}. This model offers freedom to select the static hysteresis model (Preisach model was used in [101]), and the dynamic part of the model contains two linear analytical equations describing the flux density derivatives in the low and high values respectively, requiring experimental characterization.

Zirka *et al.* [102] presented a viscosity-based Magnetodynamic model, which uses a viscous type differential equation to emulate the delay time between the input magnetic flux density and the output magnetic field strength. The excess eddy-current loss was included successfully through the following expression in (2-38) and the help of the finite-difference (FD) solver, However, the FD calculation is complicated, which is not convenient to implement in practice.

$$\frac{dB}{dt} = \frac{\delta}{g(B)} |H_{\text{tot}}(t) - H_{\text{stat}}(t)|^{\alpha(B)} \tag{2-38}$$

where $g(B)$ and $\alpha(B)$ control the shape of dynamic loops, and both factors requires experimental identification through measured dynamic hysteresis loops over different frequencies and ac flux amplitudes.

Bergqvist *et al.* [103] developed a friction-like model based on the assumption that hysteresis energies as the deviation from the anhysteretic curve due to the presence of pinning sites, producing a hysteresis mechanism similar to dry friction. Containing some appealing features in common with *J-A* model and Preisach model, the model is favorable in terms of both the physical background and calculation efficiency, but the problems related to parameters identification emerge as barriers to implement this model practically.

Among the existing dynamic methodologies for hysteresis modeling, the impact of dc-bias fields on high-frequency iron loss cannot be addressed directly. Therefore, proposing a more generalized dynamic hysteresis model so that it can adequately account for the impact of an external dc-bias field on high-frequency iron loss holds promise for standardizing the estimation procedure while maintaining high estimation accuracy.

2.2.2.4 Summary and Comparison of Investigated Iron Loss Models

To develop a more comprehensive understanding of the advantages and limitations of different iron loss models, Table 2-1 gives an overview of selected models in each main category that provide the superior performance in terms of several essential metrics of iron loss estimation for the purpose of machine design and optimization. These factors include the general prediction accuracy, extendability of complex waveforms, data requirement for parameters characterization, and complexity in practical implementation (e.g., calculation speed/memory of data storage).

TABLE 2-1: SUMMARY AND COMPARISON OF IRON LOSS MODELS FOUND IN THE LITERATURE

Iron Loss Model	Overall Accuracy	Extendability to Complex Waveforms	Material Data Requirement	Implementation Complexity
I- Iron Loss Models Based on Steinmetz Equation				
Steinmetz Equation [22]	**LOW**	**LOW**	**LOW**	**LOW**
Modified Steinmetz Equation [12]	**LOW-MED**	**LOW-MED**	**LOW**	**LOW**
Generalized Steinmetz Equation [29]	**LOW-MED**	**LOW-MED**	**LOW**	**LOW**
Improved Generalized Steinmetz Equation [30]	**LOW-MED**	**MED**	**LOW-MED**	**MED**
Improved-improved Generalized Steinmetz Equation [36]	**MED**	**MED**	**MED**	**MED-HIGH**
Natural Steinmetz Equation [37]	**LOW-MED**	**LOW**	**LOW**	**LOW**
II- Iron Loss Models Based on Iron Loss Separation Theorem				
Loss separation with constant coefficients [39]	**LOW-MED**	**LOW**	**LOW**	**LOW**
Loss separation with variable coefficients [50]	**MED**	**LOW-MED**	**LOW-MED**	**LOW-MED**
Loss separation with variable coefficients from dc-bias tests [56]	**HIGH**	**MED-HIGH**	**HIGH**	**MED-HIGH**
III- Hysteresis Models				
Dynamic Jiles-Atherton model [91]	**MED**	**LOW-MED**	**MED**	**MED**
Dynamic Preisach model [95]	**HIGH**	**MED**	**MED-HIGH**	**HIGH**
Dynamic model based on loss separation [100]	**HIGH**	**MED**	**MED**	**MED**
Loss Surface model [101]	**MED-HIGH**	**MED**	**MED-HIGH**	**MED-HIGH**
Viscosity-based Magnetodynamic model [102]	**HIGH**	**MED-HIGH**	**MED-HIGH**	**HIGH**
Friction-like model [103]	**MED-HIGH**	**MED**	**MED-HIGH**	**HIGH**

In summary, there is a wide variety of iron loss models available for estimating the iron loss of the non-oriented lamination steels which commonly used in the area of electric machines, each having distinct strengths and weaknesses.

In order to provide a comprehensive comparison between different iron loss models, four important metrics that play crucial roles in securing accurate iron loss estimation in electric machines are summarized in Table 2-1, including the model's overall accuracy, extendability to complex waveforms (i.e., flux density waveforms with additional harmonics), the requirement for input material data, and implementation complexity.

More specifically, the general accuracy indicates the model performance when it is applied for iron loss analysis in magnetic materials over a broad range of flux density amplitudes and excitation frequencies. Secondly, whether the model can reasonably incorporate the impact of non-linear coupling between different frequency components mainly determines its rating for complex waveforms extendability. However, even though some models exhibit superior performance in minor loop modeling, they require a large amount of input data (e.g., iron loss testing in the presence of dc-bias fields) as a side effect. In comparison, minimal input data are necessary for particular models, making them more suitable for rough iron loss analysis. At last, the model's implementation complexity is evaluated. The frequency-domain approaches (e.g., Fourier analysis) are generally easier to implement regardless of excitation conditions, whereas the time-domain models (e.g., hysteresis models) call for longer calculation time and are sensitive to the waveform quality, time step selection, presence of additional minor loops, etc.

As demonstrated in Table 2-1, even with very limited data available for the analyzed materials, iron models based on the original Steinmetz equation are capable of providing a rough approximation of iron loss. However, the accuracy of these models is typically not satisfactory

under the high-frequency conditions or when the analyzed waveforms deviate from the sinusoidal shape. Moreover, as mentioned in the preceding subsection, the applicability to ferromagnetic materials remains unclear and requires further experimental investigation.

Owing to its reasonable accuracy and ease of implementation, the models based on iron loss separation theory appear to be the most mature and widespread tools for the iron loss estimation in the ferromagnetic materials, making it possible to conduct iron loss minimization analysis as well as a comparative study of different magnetic materials for a particular application. However, unless taking significant efforts to characterize the model parameters in the presence of dc-bias fields, the model behavior in terms of complex waveforms is relatively weak. Lacking sufficient insights into iron loss mechanism, it is hard to make further improvements.

In contrast to the iron loss model either based on original Steinmetz equation or loss separation theorem, the complex hysteresis model exhibits higher estimation accuracy with the requirement of more sophisticated material data (i.e., dynamic hysteresis loops) rather than simple power loss values. Although the hysteresis loop prediction might seem to be unnecessary and unimportant where there is only interest in iron loss value, it can provide deeper physical insights of iron loss mechanism especially in terms of complex flux waveforms, offering opportunities to minimize and even eliminate the estimation errors by comparing the predicted and measured hysteresis loops.

Even though these models differ in several aspects, depending on the complexity and specific type of iron loss model, they more or less require measured iron losses/hysteresis loops data to identify the model parameters. It is natural that these parameters vary significantly for the magnetic materials with different grades, thickness, and manufacturing processes. Thus, it is of great importance to determine the model parameters under the condition that is close to the actual operating environment (e.g., static transformer or rotating electric machines). In the following

subsections, the methodologies for iron loss characterization and serval influencing factors on material degradation will be reviewed and discussed.

2.2.3 Characterization of Iron Loss in Soft Magnetic Materials

Various approaches have been proposed to characterize the magnetic properties and iron loss of lamination steels. The commonly adopted power analysis method depends on the loss separation scheme, which divides the total dissipative power loss into the copper loss consumed by the excitation winding and the iron loss induced in the core material. As a result, this method requires adequate knowledge of the winding resistance to evaluate the resulting losses. However, due to the skin and proximity effect, the winding resistance (i.e., ac resistance) increases substantially as the excitation frequency increases, posing an enormous obstacle to accurately secure the effective winding resistance under broad operating conditions.

In terms of the accuracy and generality in power dissipation measurement, calorimetric method [104] is considered as a universal approach, guaranteeing the satisfied accuracy over wide frequency and operating conditions. However, several disadvantages reported in [105] emerge as profound barriers to practical implementation:

- The measurement process is time consuming and it takes a long time to get the temperature stabilized, making it difficult to sweep over large testing cases,
- The winding loss segregation issue remains troublesome and can be problematic when the skin or proximity effect is significant,
- The temperature variation potentially exerts large influences on the material properties,
- The accuracy degrades substantially when the temperature variation is unnoticeable.

In contrast, the two-winding iron loss measurement method presented in [106], commonly known as the *B*-*H* loop measurement, have been widely implemented for determining the magnetic

and iron loss characteristics. Employing this method on a toroidal core tester, Figure 2-20 [107] gives a typical schematic of the test setup, containing an excitation source, testing core, main winding, and sensing winding. The product of secondary-side open circuit voltage V_{sense} and primary-side current I_{main} gives the iron loss experienced by the core material as:

$$P_{\text{iron}} = \frac{N_{\text{main}}}{N_{\text{sense}}} \int_0^T V_{\text{sense}} I_{\text{main}} \cdot dt \tag{2-39}$$

Where N_{main} is the number of turns in the primary winding, N_{sense} is the number of turns in the secondary sensing winding, and T is the time period of alternating flux waveform.

Furthermore, the magnetic flux density B and the magnetic field strength H can be expressed with knowledge of the toroidal core dimensions, giving an alternative expression of iron loss.

$$H(t) = \frac{N_{\text{main}} I_{\text{main}}(t)}{l_{\text{core}}} \tag{2-40}$$

$$B(t) = \frac{1}{A_{\text{core}} N_{\text{sense}}} \int V_{\text{sense}} \cdot dt \tag{2-41}$$

$$P_{\text{iron}} = V_{\text{core}} f \int_0^T H \frac{dB}{dt} \cdot dt \tag{2-42}$$

where l_{core} is the mean magnetic path, A_{core} is the cross-section area of the toroidal core, and V_{core} is the total volume of the toroidal core.

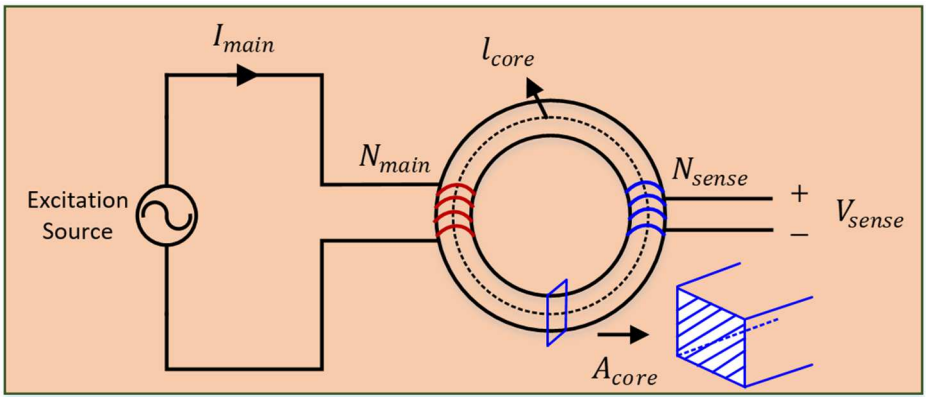

Figure 2-20: Schematic of *B*-*H* loop measurement using the toroidal core tester.

A disadvantage of this approach is that the estimation accuracy becomes susceptible to the phase shift error (e.g., phase lag caused by the current sensor) when the phase discrepancy θ between the secondary-side voltage V_{sense} and primary-side current I_{main} is close to 90°. The percent error in the measured loss due to phase shift error η_{error} is given by [106]:

$$Percent\ error = \frac{[\cos(\theta + \eta_{\text{error}}) - \cos(\theta)]}{\cos(\theta)} \times 100\% \tag{2-43}$$

As can be seen from Figure 2-21 (calculated by (2-43)), even with a minimal phase shift error (i.e., η_{error} = 1°), the resultant power loss measurement error is over 100 % percent when the phase shift is significant (i.e., θ = 89°). Therefore, for either the high-frequency or low material permeability applications (i.e., large phase shift), the impact of phase shift error requires careful attention. To resolve this problem, the capacitive voltage cancellation method proposed by Mu *et al.* [108] can effectively eliminate the measurement errors caused by phase shift discrepancy.

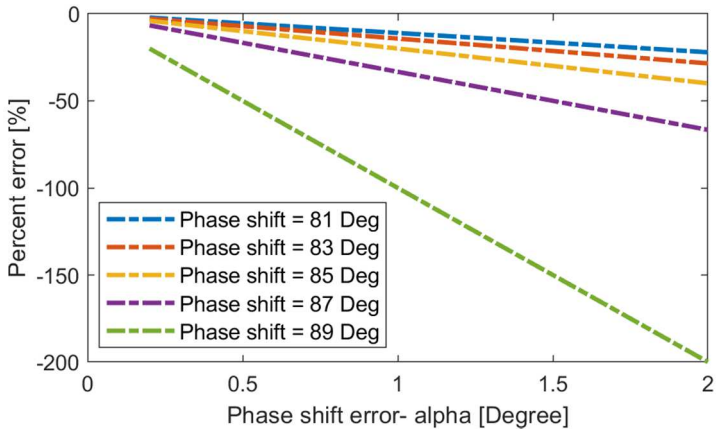

Figure 2-21: Calculated percent error in iron loss measurement versus α for different values of θ [106].

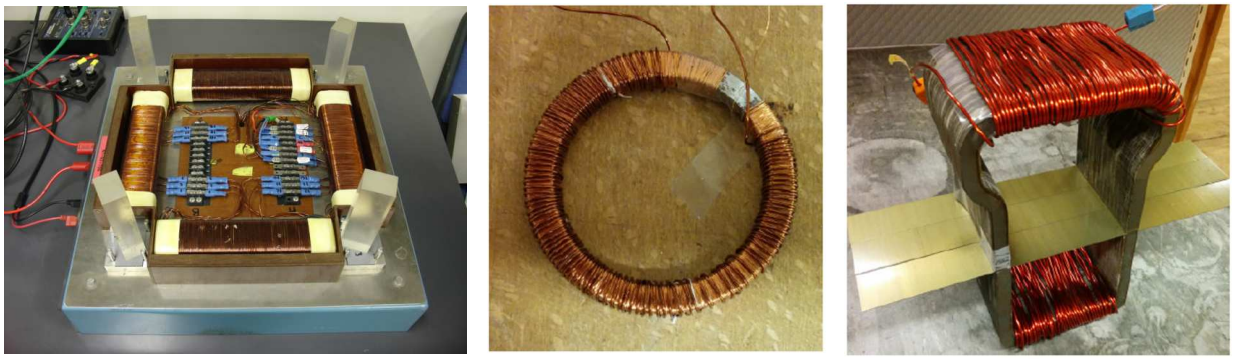

(a) Epstein frame [109] (b) Toroidal core tester [10] (c) Single sheet tester [10]

Figure 2-22: Test arrangement for *B-H* loop measurement.

Not just for the toroidal core tester shown in Figure 2-20, the *B-H* loop measurement scheme can be applied to other two types of standardized iron loss testers, including the Epstein frame and single sheet tester. Examples of these three test structures are shown in Figure 2-22. Detailed evaluation and comparison of all three standardized measurement methods have been conducted by Mthombeni *et al.* in [110], and Fiorillo [111] gave a comprehensive guide of magnetic measurements. Key conclusions can be drawn as follows:

***Epstein frame*:** The Epstein frame has been widely adopted by the steel manufactures for material characterization. However, several shortcomings make this method less desirable to evaluate the materials commonly used in the electric machines, namely the non-oriented steel. As shown in Figure 2-20(a), there are four arms in the typical Epstein frame, and the magnetic flux passing in each arm is unidirectional, which cannot mimic the rotating flux nature in the electric machines. What is more, the magnetic flux distribution in the regions of joints is not uniform. Also, the conventional Epstein frame is limited to the low-frequency range.

***Toroidal core tester*:** In contrast to Epstein frame, the toroidal core tester better emulates the geometric shape of electric machines, and the closed magnetic path makes it possible to eliminate the needs for the correction factor. In addition, the toroidal core tester allows the iron loss evaluation over wide frequency ranges. However, the sample preparation time is long.

Single sheet tester: Single sheet tester offers a method with easy preparation and simple test setup. The excitation windings are pre-wound around the double yoke as shown in Figure 2-20(c), and a *B*-field sensor or few turns of sensing winding can be used to identify the magnetic field flowing inside the testing sheet, making this method preferable to quickly evaluate a large number of candidate steels. However, the double yoke itself is heavy, costly, and large. Another disadvantage of this method is that it requires pre-calibration with either Epstein frame or toroidal core tester for purpose of estimating the equivalent magnetic path, and this calibration process may have to be repeated when evaluating a new type of lamination steel or testing a known steel with different manufacturing procedures (i.e., cutting or assembly process).

Different from three standardized iron loss measurement methods, Clerc [112] directly utilized the machine stator core (See Figure 2-23(a)) for material characterization. By wrapping the windings around the static back iron, the impact of the manufacturing process at various stages was evaluated experimentally, providing more profound insights into the material degradation phenomena during the steel manufacturing process. However, as shown in Figure 2-23(b)), additional correction factors identified from FEA are indispensable to account for the fringing flux near the top of stator teeth. On the other hand, the effective magnetic path along the back iron is very close to that in the toroidal core tester, making the stator teeth structure not very useful.

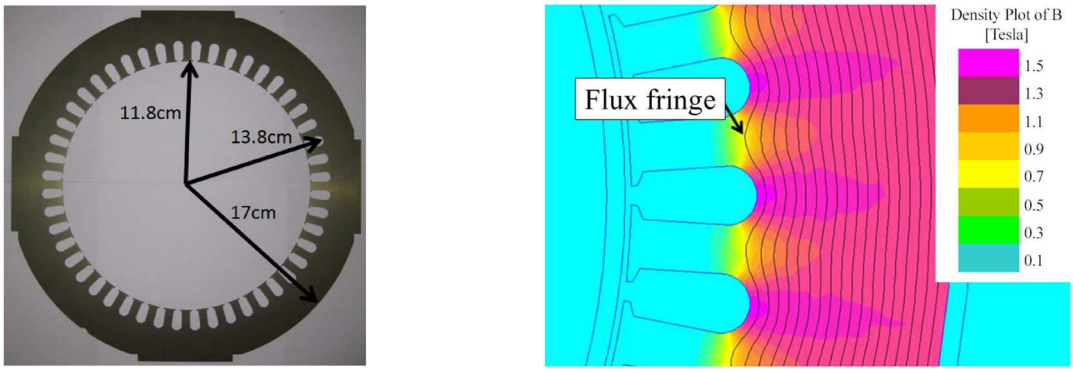

(a) Single lamination sheet (b) Plot of fringing flux effect

Figure 2-23: Overview of ring test of a machine stator [112].

Although each approach has its advantages and limitations, for the purpose of extensively characterizing a limited number of steels, toroidal core tester is preferred due to its similar geometrical structure compared to the machine stator as well as the adjustable size, being able to meet power capability of available testing equipment.

Another critical challenge during the magnetic measurement is ensuring the sinusoidal shape of the flux density waveform. Due to the nonlinear nature of magnetic materials, a sinusoidal voltage input signal in Figure 2-20, for a lot of operating conditions, cannot generate a desired sinusoidal output signal (i.e., the waveform obtained from sensing winding), requiring additional feedback control to regulate the flux density in the sinusoidal shape.

Nowadays, the adaptive digital feedback system initially proposed by Zurek *et al.* [113] has been widely adopted and demonstrated superior performance in terms of stability and generality for different materials and types of testers (e.g., toroidal core and single sheet tester) compared to the conventional analog electric circuit method. As the block diagram presented in Figure 2-24, a given reference waveform can be achieved by iteratively modifying the magnetization current without any prior knowledge of the analyzed magnetization system.

Based on the theory described above, Anderson [114] greatly simplified the control process by directly manipulating the output voltage based on the sensing voltage and stored output data from the last iteration, achieving about 75 % overall test time reduction compared to the previous one.

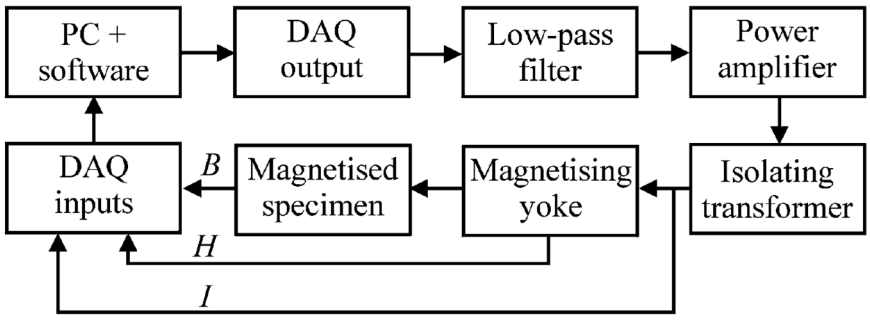

Figure 2-24: Block diagram of digital feedback system with adaptive control capability [113].

Geisinger and Knight [115] presented a flux density controller based on the real-imaginary control of high-order harmonics for Epstein frame, creating both single and mixed frequency flux density waveforms. It was observed that iron loss varies drastically with the amplitude, phase, and frequency of the superimposed harmonics. Also, as acknowledged by the authors, there is a need to develop a universal approach to accurately predict the iron loss under non-sinusoidal excitation.

In short, experimental characterization of magnetic materials serves a critical role to understand the properties of a given material and most importantly, generating the iron loss/hysteresis loop data for the iron loss models described in the proceeding subsections. Regardless of the physical basis and complexity of an iron loss model, accurate data input are absolutely necessary and indispensable to all of them.

2.2.4 Influencing Factors on Magnetic Properties and Iron Loss

As already mentioned, the sources of iron loss underestimation are heterogeneous and interconnected. Therefore, beyond the ideal material (i.e., loose lamination sheets), investigating the impact of several influencing factors on the degradation of magnetic properties and iron loss is of great importance for achieving accurate field analysis and iron loss estimation in the high-performance electric machines.

With the availability of raw lamination sheet after the rolling process (In rectangular shape), various approaches have been utilized to cut the sheet into the desired shape (e.g., electric machine stator). These cutting technologies include mechanical stamping, laser cutting, water-jet cutting, etc. However, additional mechanical or thermal stress (i.e., localized heating and melting) are induced inside the sheets, and in turn, affect the materials' magnetic properties and iron loss. Although the influencing region can go up to 10 mm from the cutting edge [116], the material degradation can be recovered as much as possible by stress-relief annealing (SRA) process [117].

Similar material deterioration phenomena are caused by the stacking and welding process during the machine core assembly process and thus, degrade the magnetic properties (i.e., lower permeability) and induce higher iron loss. The stacking and welding process introduce additional mechanical stress in the axial direction of stacked sheets, and the materials near the welding beams suffer from the high thermal stress. Furthermore, the non-conductive insulation layers between the stacked sheets are destroyed by welding seams, creating closed-loop short circuit paths for the eddy currents induced by the alternating magnetic flux [118], [119].

Another significant source of external mechanical stress applied to the stator core is the heat shrink fitting process. Daikoku *et al.* [120] experimentally investigated the impact of external stress using a single sheet tester equipment with the stress-applying mechanism shown in Figure 2-25(a). As the measured results presented in Figure 2-25(b), the relative permeability versus applied stress of the selected magnetic steel (50A800) are plotted for two magnetic flux density amplitudes. Permeability under the stressed condition is inferior to the unstressed state. In particular, the compressive stress (i.e., with negative stress value) exerts a more significant detrimental impact compared to that under tensile stress (i.e., with positive stress value).

Yamazaki and Takeuchi [121] further evaluated the impact of mechanical stress on the iron loss characteristics caused by both the stator shrink fitting and the rotor centrifugal force.

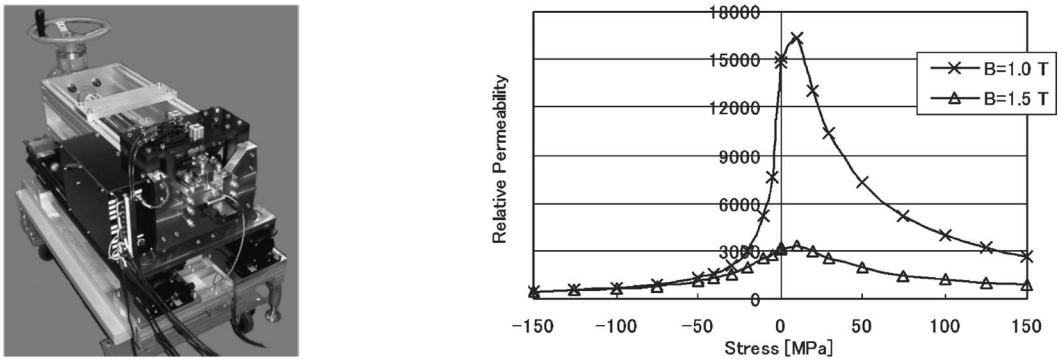

(a) (b)

Figure 2-25: (a) Equipment with stress-applying mechanism; (b) Measured results of relative permeability [120].

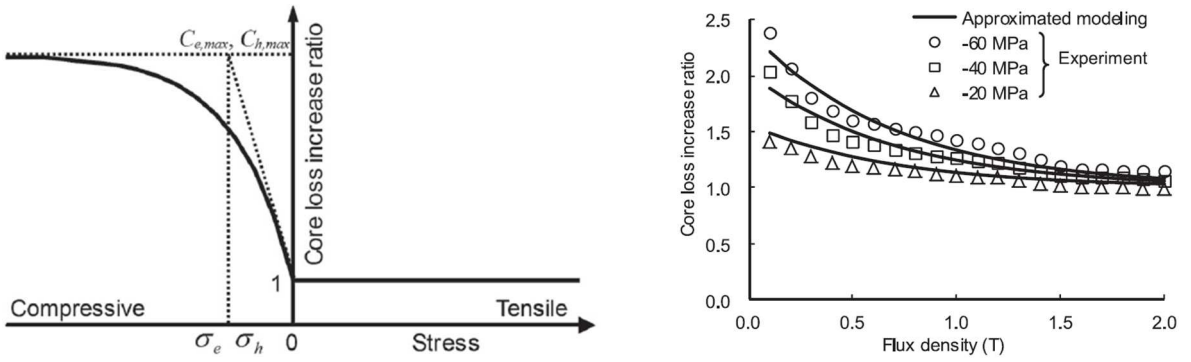

(a) (b)

Figure 2-26: Impact of mechanical stress on iron loss: (a) Outline of variation in iron loss increase with stress; (b) Measured and modeled iron loss increase ratio with different values of compressive stress [121].

As can be seen from Figure 2-26(a), similar to the impact on magnetic permeability, it is the compressive stress that results in a larger iron loss, whereas the tensile stress impact on iron loss is negligible. The measured results given in Figure 2-26(b) suggest that the iron loss increasing ratio due to compressive stress is much more significant at low flux density region (i.e., $B_{ac} < 0.5$ T) and it becomes almost ignorable as the material is driven into the heavy saturation region.

Aside from the mechanical and thermal stress, the characteristics of magnetic materials are also found temperature dependent. Figure 2-27(a) [122] and (b) [123] demonstrate that the variation trend of the *B-H* curve over a wide temperature range. Although a slight permeability reduction is observed as the temperature increases, within the normal operating temperature of traction machines (i.e., - 40˚C to 160˚ C), the impact of temperature is negligible.

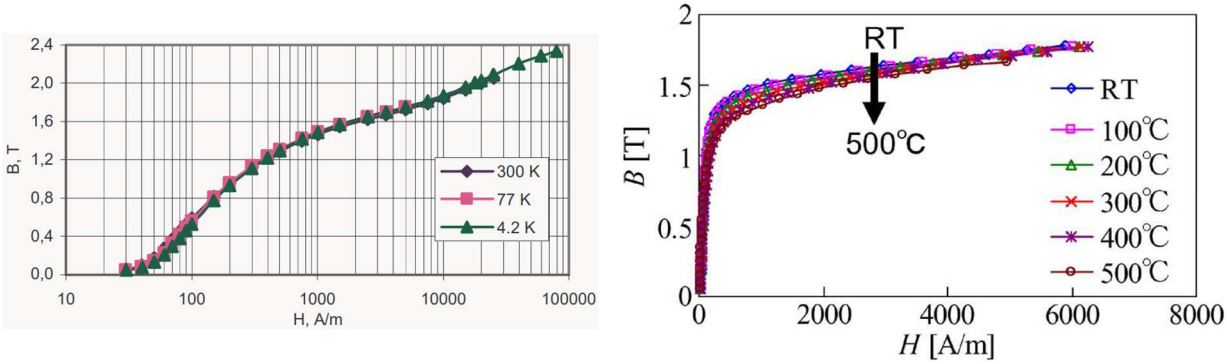

(a) NO steel 2212 (1.31% Si and < 0.04 % C) [122] (b) NO steel 35A360 (0.35 mm thickness) [123]

Figure 2-27: Variation of quasi-static dc *B-H* curve versus temperature for two different lamination sheets.

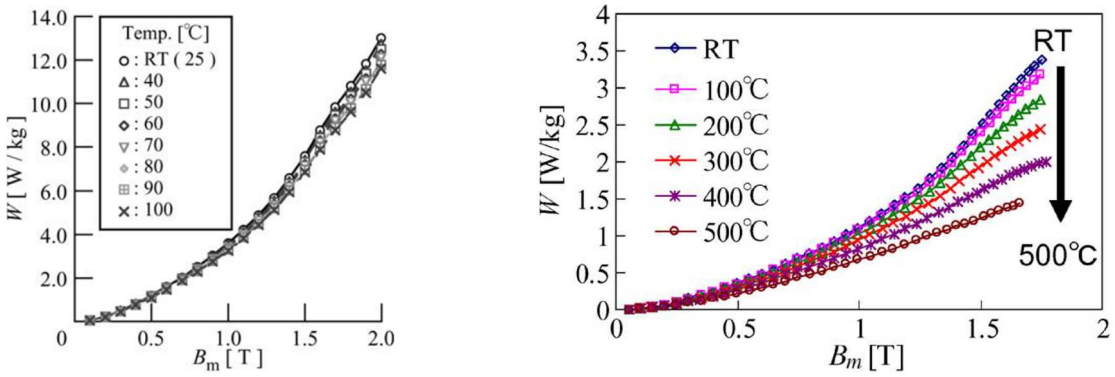

(a) NO steel 50A1300 (thickness 0.5 mm) [124] (b) NO steel 35A360 (0.35 mm thickness) [123]

Figure 2-28: Change of iron loss due to temperature for two different lamination sheets at 50 Hz frequency.

Similarly, the iron loss properties of lamination steels vary with the temperature. Figure 2-28(a) [124] shows the iron loss of 50A1300 lamination sheets at 50 Hz up to 2 T maximum magnetic field. From the room temperature (i.e., 25 ˚C) to 100 ˚C, iron loss reduction up to 12 % is observed. Moreover, iron loss evaluation over a broader temperature range has been conducted in [123], as shown in Figure 2-28(b), the variation of 35A360 material at 50 Hz below 200 ˚C is very small. From what has been discussed above, a conclusion can be drawn that the temperature only has secondary effects on the characteristics of magnetic materials.

2.3 Machine-Level Iron Loss Analysis and Prediction

Even though the iron loss phenomena in soft magnetic materials have been investigated for a long time and various approaches are available for different degrees of accuracy, there are considerable differences when it comes to machine-level analysis.

First of all, unless inserting a large number of magnetic field sensors in the specially designed machine, *B-H* loop measurement technique is no longer applicable to the electric machines for iron loss segregation. As a result, the loss separation process is typically employed to determine the iron loss by subtracting other loss terms (either from prediction or experimental results) from the measured total power loss value.

Moreover, although the flux linkages can be measured from the stator windings, the detailed magnetic field distribution data are unavailable and complicated inside the electric machines, calling for FEA simulation to predict the magnetic field in each mesh element. Taking the PM machines as an example, due to the existence of stator slots and rotor magnets, the flux density waveforms inside electric motor are highly distorted compared to sinusoidal waveform or waveform with superimposed harmonics (e.g., 3rd or 5th harmonics). Also, rather than flow in a single direction in the standardized iron loss testers (e.g., Epstein frame), another complexity is introduced by the rotating magnetic flux which mainly occur at the inner periphery of stator teeth (tooth tips), as well as along the inner portions of the stator yoke and the rotor surfaces, potentially yielding different iron loss characteristics compared to that under the unidirectional condition.

In this section, the existed approaches for iron loss segregation techniques based on PM machines are reviewed and discussed. Subsequently, a summary of different iron loss models adopted and proposed for machine-level analysis is provided.

2.3.1 Iron Loss Segregation in PM Synchronous Machines

Generally, in the PM synchronous machines, the total core losses P_{core} including the magnet eddy current loss and the iron loss in the stator and rotor lamination steels is estimated from the electrical input power P_{in}, mechanical output power P_{out}, armature copper loss P_{copper}, and mechanical loss P_{mech} (i.e., friction and windage loss), as follows [3]:

$$P_{\text{core}} = P_{\text{in}} - P_{\text{out}} - P_{\text{copper}} - P_{\text{mech}} \tag{2-44}$$

$$P_{\text{out}} = T_{\text{em}}\omega \tag{2-45}$$

where T_{em} is the mechanical output torque recorded by the digital torque meter and ω is the machine rotating speed.

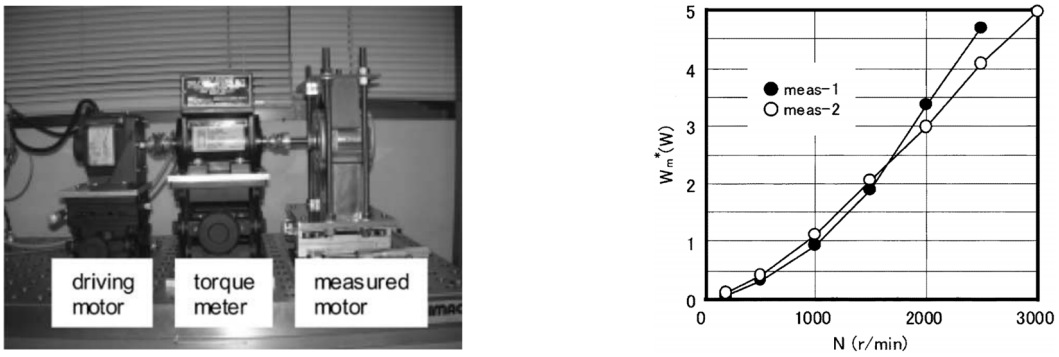

(a) (b)

Figure 2-29: (a) Torque measuring equipment, and (b) Measured mechanical loss with machine speed [125].

The mechanical loss is commonly measured by rotating the machines under the no-load condition. However, for PM machines, rotating the magnetized magnets will induce an additional iron loss in the stator and rotor cores, and in turn, pose barriers to measure the mechanical loss. With torque measuring equipment shown in Figure 2-29(a), Domeki *et al.* [125] measured the mechanical loss of the SPM machine by rotating a rotor with non-magnetized permanent magnets (i.e., keep the rotor weight and structure unchanged). Furthermore, as can be seen from mechanical loss results presented in Figure 2-29(b), it varies as a function of machine rotating speed and the results measured by two institutes (i.e., meas- 1 and meas- 2) are very similar to each other.

The power dissipated by the motor windings is generally calculated using the winding dc resistance R_{dc} and corresponding phase currents I_{phase} as:

$$P_{\mathrm{copper}} = nR_{\mathrm{dc}}I_{\mathrm{phase}}^2 \tag{2-46}$$

where n is the number of machine phases.

It is worth noting that (2-46) is only applicable under room temperature and when the frequency dependent effects are negligible (i.e., skin effect and proximity effect). This issue becomes more significant for form-wound windings which are experiencing popularity for traction applications [126]. Although the low dc resistance property is favorable, form-wound windings potentially lead to higher ac copper loss, which further complicates the copper loss prediction.

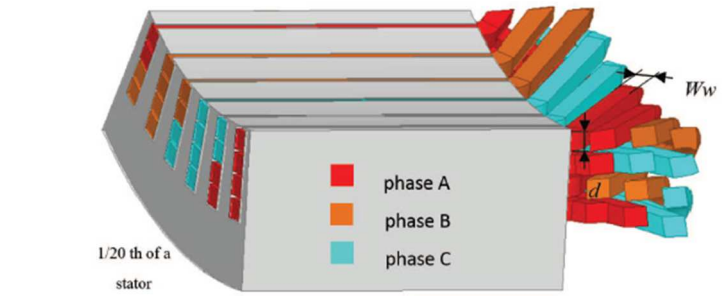

(a)

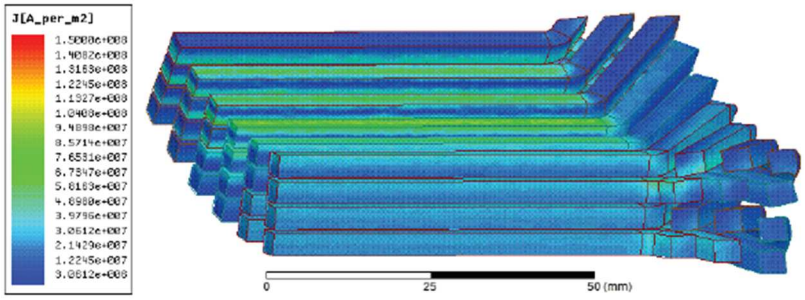

(b)

Figure 2-30: (a) 3-D finite element model, and (b) Calculated current density distribution with 400 Hz 300 A current excitation using 3-D FEA [127].

Considering the complex nature of winding loss with form-wound windings, it typically calls for advanced 3-D FEA with fine mesh structures (See Figure 2-30) to achieve accurate copper loss prediction. However, 3-D FEA is very time-consuming. Alternatively, Zhang *et al.* [127] proposed a sophisticated analytical model to evaluate the ac copper loss, enabling the rapid analysis of a large number of candidate designs.

With the knowledge of mechanical loss, copper loss, and total power loss, the machine core losses (i.e., the sum of iron and magnet loss) can be determined subsequently. Further experimental segregation between the iron loss and magnet loss is very challenging since both of them cannot be measured directly. Yamazaki *et al.* [128] tried to separate them by conducting the locked rotor tests with and without the permanent magnets in the rotor cavities. Although the loss measurement process is valid, the magnetic conditions vary substantially, leading to inconsistent test conditions. Instead, as the results demonstrated in Figure 2-31 [129], the 3-D FEA serves as a useful tool for estimation of magnet eddy-current loss, and the prediction accuracy has been verified in [130].

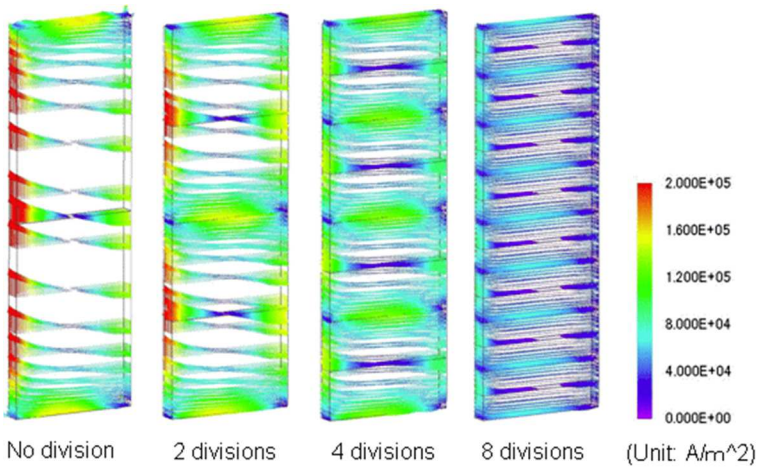

Figure 2-31: JMAG Application Note - Analysis of Eddy Current in the Magnet of an IPM Machine [129].

As described above, the iron loss segregation process in the PM machines is complicated, requiring sophisticated efforts to secure the measurement accuracy. Alternatively, under an assumption that the iron loss is not sensitive to the armature currents and load conditions [131], the iron loss under the no-load condition can be determined by driving the open-circuited PM machines with a dynamometer, and the measured shaft torque gives total no-load power loss including the no-load iron loss as well as the mechanical loss. After subtracting the mechanical loss following the procedure described in [125], the no-load iron loss $P_{\text{iron}no\text{-}load}$ is given as:

$$P_{\text{iron}_{no-load}} = T_m\omega - P_{\text{mech}} \tag{2-47}$$

Based on the same assumption, Jardan *et al.* [132] proposed a machine-level calorimetric method for fast and accurate assessment of iron loss in the PM machines, describing the iron loss as a function of machine speed only. Although the iron loss characterization based on (2-47) is free from complex loss separation and ease of implementation, ignoring the armature currents potentially leads to severe underestimation of iron loss under loaded conditions especially for the high-performance traction machines, which are excited with large stator currents to meet desired torque/power performance. Also, the additional losses induced by the PWM switching cannot be considered by driving the machine under the no-load condition.

2.3.2 Iron Loss Estimation in Electrical Machines

As aforementioned, the flux waveforms in the electric machines can deviate from the sinusoidal shape significantly, and to a considerable extent, depend on the machine topologies and driving conditions (e.g., the high-speed condition under flux-weakening control). Moreover, the material-level iron loss models reviewed in the preceding sections assume that all magnetic fluxes are in a single direction. Therefore, to account for the harmonic and rotating magnetic fields in the electric machines, (2-8) is extended by the following expressions with the Fourier decomposition of the simulated flux density waveform in each mesh element from 2-D FEA simulation [3]:

$$P_{\text{iron}} = \int_{\text{iron}} \sum_{n} k_e D \cdot (nf)^2 \cdot \left\{B_{r,n}^2 + B_{\theta,n}^2\right\} \cdot dv + \int_{\text{iron}} \sum_{n} k_h D \cdot (nf) \cdot \left\{B_{r,n}^2 + B_{\theta,n}^2\right\} \cdot dv \tag{2-48}$$

where D is the density of lamination steel, n is the order of Fourier transformation, k_e and k_h are the iron loss coefficients characterized from the standardized iron loss testers (e.g., Epstein frame), and $B_{r,n}$ and $B_{\theta,n}$ are the n^{th} harmonics of the radial and circumferential magnetic flux density.

This method is intrinsically based on linear superposition assumption, which cannot differentiate the major and minor hysteresis loops during the loss modeling. As the limitation is recognized, Yamazaki [133] proposed an equivalent time domain model using the same coefficients that used in (2-48):

$$P_{\text{iron}} = \frac{k_e D}{2\pi^2} \int_{\text{iron}} \frac{1}{N} \sum_{n} \left\{ \left(\frac{B_r^{k+1} - B_r^k}{\Delta t} \right)^2 + \left(\frac{B_\theta^{k+1} - B_\theta^k}{\Delta t} \right)^2 \right\} \cdot dv + \frac{k_h D}{T} \sum_{i=1}^{NE} \frac{\Delta V_i}{2} \left(\sum_{j=1}^{N_{pr}^i} \left(B_{mr}^{ij}\right)^2 + \sum_{j=1}^{N_{p\theta}^i} \left(B_{m\theta}^{ij}\right)^2 \right) \tag{2-49}$$

where Δt is the time interval of flux density waveform, N is the total number of time steps per one fundamental period, ΔV_i is the volume of the i^{th} mesh element, and B_{mr} and $B_{\text{m}\theta}$ are the amplitudes of segregated hysteresis loops (i.e., including major and minor loops) in two orthogonal directions.

However, (2-49) estimates the hysteresis loss under the assumption that the major and minor loops share similar shapes and the excess loss is ignorable, likely leading to iron loss underestimation. Based on iron loss models (2-17) that employ the variable loss coefficients, an improved version of frequency-domain iron loss models was presented by Seo *et al.* [134],

$$\begin{aligned} P_{\text{iron}} = & \int_{\text{iron}} \sum_{n} D \cdot (nf)^2 \cdot \left\{ k_e\left(nf, B_{r,n}\right) B_{r,n}^2 + k_e\left(nf, B_{\theta,n}\right) B_{\theta,n}^2 \right\} \cdot dv \\ & + \int_{\text{iron}} \sum_{n} D \cdot (nf) \cdot \left\{ k_h\left(nf, B_{r,n}\right) B_{r,n}^2 + k_h\left(nf, B_{\theta,n}\right) B_{\theta,n}^2 \right\} \cdot dv \end{aligned} \tag{2-50}$$

Similarly, (2-50) can be transformed into its time-domain version adopting the same variable coefficients and the hysteresis loop separation technique used in (2-49),

$$\begin{aligned} P_{\text{iron}} = & \frac{D}{2\pi^2} \int_{\text{iron}} \frac{1}{N} \sum_{n} \left\{ k_e(f_d, B_r) \left(\frac{B_r^{k+1} - B_r^k}{\Delta t} \right)^2 + k_e(f_d, B_\theta) \left(\frac{B_\theta^{k+1} - B_\theta^k}{\Delta t} \right)^2 \right\} \cdot dv \\ & + \frac{D}{T} \sum_{i=1}^{NE} \frac{\Delta V_i}{2} \left(\sum_{j=1}^{N_{pr}^i} k_{hr}(f_d, B_{mr}^{ij}) \left(B_{mr}^{ij}\right)^2 + \sum_{j=1}^{N_{p\theta}^i} k_{hr}(f_d, B_{m\theta}^{ij}) \left(B_{m\theta}^{ij}\right)^2 \right) \end{aligned} \tag{2-51}$$

where f_{d} is the dominant frequency of the analyzed waveform. For the stator side, it is referred to the fundamental frequency. On the rotor side, the frequency related to slotting harmonics is used:

$$f_{d_{\text{rotor}}} = f_{\text{fund}} \times \frac{S}{P/2} \tag{2-52}$$

where f_{fund} is the machine fundamental frequency, S is the number of stator slots, and P is the number of poles.

Although (2-51) exhibits better performance in capturing the nonlinear iron loss characteristics of complex flux waveforms, there are still some imperfections worth further improvement:

- Parameters (i.e., k_e and k_h) selection process is ambiguous and questionable for the complex flux waveforms deviating from the sinusoidal shape,
- All the segregated minor loops are considered symmetric to the origin point, and the impact of external average field (e.g., dc-bias field) on the iron loss of minor loops is not included,
- The major and minor components of the rotating magnetic fields are not always corresponding to the radial and circumferential components.

To overcome the first two limitations, a more generalized iron loss model is preferred to provide satisfactory accuracy for complex flux waveforms. Regarding the third issue, rather than decompose the field in cylindrical coordinate system, Hargreaves *et al.* [135] and Zhu *et al.* [51] presented a method to separate the field along the local major and minor axes of magnetization ellipse, and these axes might vary for the fields in different mesh elements. As shown in Figure 2-32(a), the alternating flux components are predominantly along a single line. While for the rotating fields, the major field components can be well consistent with the cylindrical coordinate system (See Figure 2-32(b)), but more generally, they can correlate to an arbitrary direction angle φ relative to the circumferential-axis, like the plot given in Figure 2-32(c).

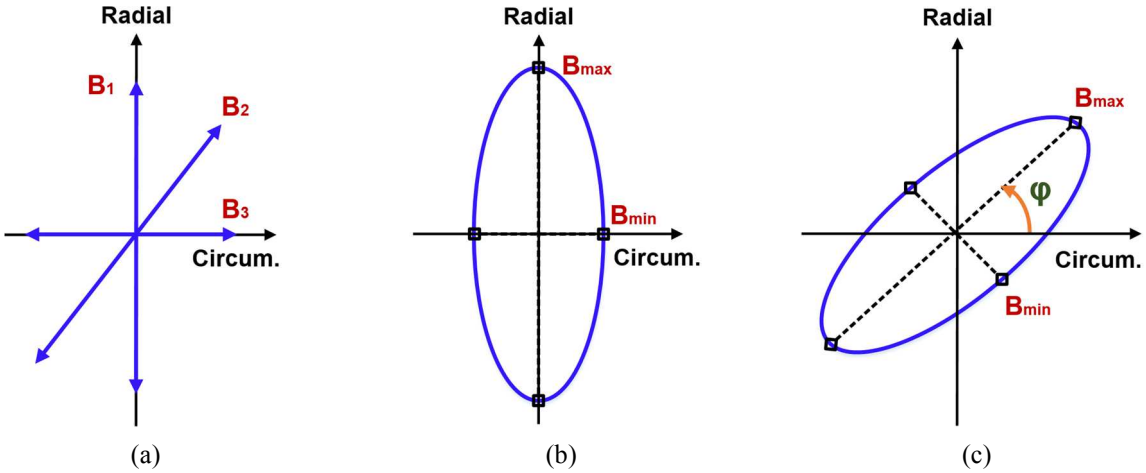

(a) (b) (c)

Figure 2-32: Different loci of magnetic fields: (a) Alternating magnetic field, (b) Rotating magnetic field (Major component is at radial direction), and (c) Rotating magnetic field with an arbitrary angle φ relative to axis.

It is worth noting that the major axis selection requires vector information from 2-D FEA simulation, and the axis of major flux component is identified through the full loop loci on an element level, resulting in additional calculation time compared to the models using the default Cartesian or cylindrical coordinate system.

Different from the iron loss models based on loss separation theory, some versions of dynamic hysteresis model [136], [137] apply to the machine-level analysis and are being implemented with time-stepping FEA. However, these techniques are not sufficiently general to predict the iron loss of complex waveforms influenced by the dc-bias or ac average field effects.

Tekgun [138] proposed a special technique for iron loss estimation in the electric machines based on the actual flux density waveforms in various regions. As the illustration shown in Figure 2-33(a), the stator of the studied IPM machine is subdivided into seven different regions, where the magnetic field within each region is assumed uniformly distributed. The extracted flux waveform of each region from 2-D FEA is subsequently reproduced in the toroidal core iron loss tester (See Figure 2-33(b) and (c)). The same procedure is applied to the machine rotor side, and then sum up with the stator side loss for total iron loss in the electric machine.

Although this method has been implemented to yield successful results for analyzing the iron loss of an IPM machine under both the no-load condition as well as a selected loaded condition, the iron loss characterization procedure is too cumbersome, and thus, cannot be used to predict the iron loss for a given machine over varying operating conditions or evaluate and compare a large number of candidate machine designs. On the other hand, this approach offers an alternative way to conduct the preliminary evaluation of different iron loss models instead of implementing the machine-level loss segregation to determine the iron loss component.

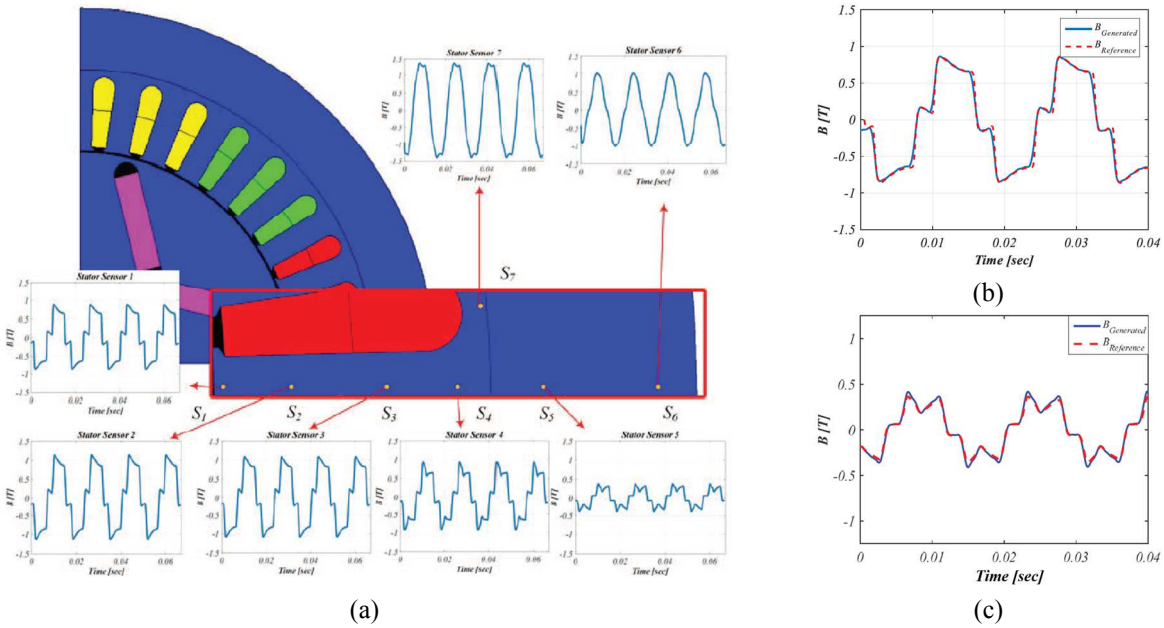

Figure 2-33: (a) Simulated stator flux density waveforms of an IPM machine at unloaded condition using 2-D FEA, (b) Reference and generated flux waveform at region S1 (stator tooth body), and (c) Reference and generated flux waveform at region S5 (stator back iron) [138].

2.4 PWM-Induced Current Ripple and Parasitic Machine Losses under PWM Voltage Excitation

Three-phase voltage-source PWM converters are widely implemented for power conversion applications, including the ac motor drives, grid-connected converters, renewable energy, etc. However, under PWM voltage excitation, additional high-frequency current ripple will be induced on top of the fundamental component, leading to extra machine power losses compared to that under the sinusoidal supply. Therefore, it is of great importance to take into account these losses in the process of loss estimation/segregation.

In this section, existed techniques devoted to addressing two crucial aspects of PWM related phenomena will be reviewed and discussed, including:

- Prediction and characterization of PWM-induced current ripple,
- Technical approaches to evaluate and predict the parasitic losses induced by the PWM switching in the electric machines.

2.4.1 Prediction and Analysis of PWM-Induced Current Ripple

When the voltage-source inverters (VSIs) are used to drive an ac machine (e.g., IPM machine), unlike the fundamental input current, the PWM-induced current ripple information is not directly available, which will vary substantially when driven by varying PWM switching frequencies, switching algorithms (e.g., Space-vector PWM), load operating conditions, etc. Therefore, current ripple prediction has drawn considerable attention for the purpose of minimizing the current ripple amplitude as well as the electromagnetic interference (EMI) induced by PWM harmonics.

The modulation scheme that is used to control the inverter switching events exerts a crucial impact on the resulting inverter loss, current ripple amplitude, and its frequency composition [139]–[141]. Among available modulation schemes, space vector PWM (SVPWM) and discontinuous PWM (DPWM) are popular choices owing to their high dc-bus voltage utilization capability compared to the conventional sinusoidal PWM (SPWM). Also, the DPWM scheme leads to reduced inverter switching losses by clamping each of the output phase voltages to the positive or negative inverter bus for one-third of the fundamental cycle, resulting in increased current ripple and conduction loss as a side effect.

Close-form analysis of PWM-induced current ripple has been presented in [139], [142]–[144] to analyze the current ripple's rms value or total harmonic distortion (THD) over a full fundamental cycle. Different pulsewidth modulation techniques and switching algorithms have been proposed to minimize the inverter switching loss and improve system efficiency. However, those analytical methods are not real-time current ripple prediction. For applications such as PWM-induced iron loss estimation, detailed ripple waveshape information is desired during each switching cycle.

Jiang and Wang [145] developed the analytical current ripple expressions for three-phase PWM converters depicted in Figure 2-34(a) as the basis for the design and implementation of

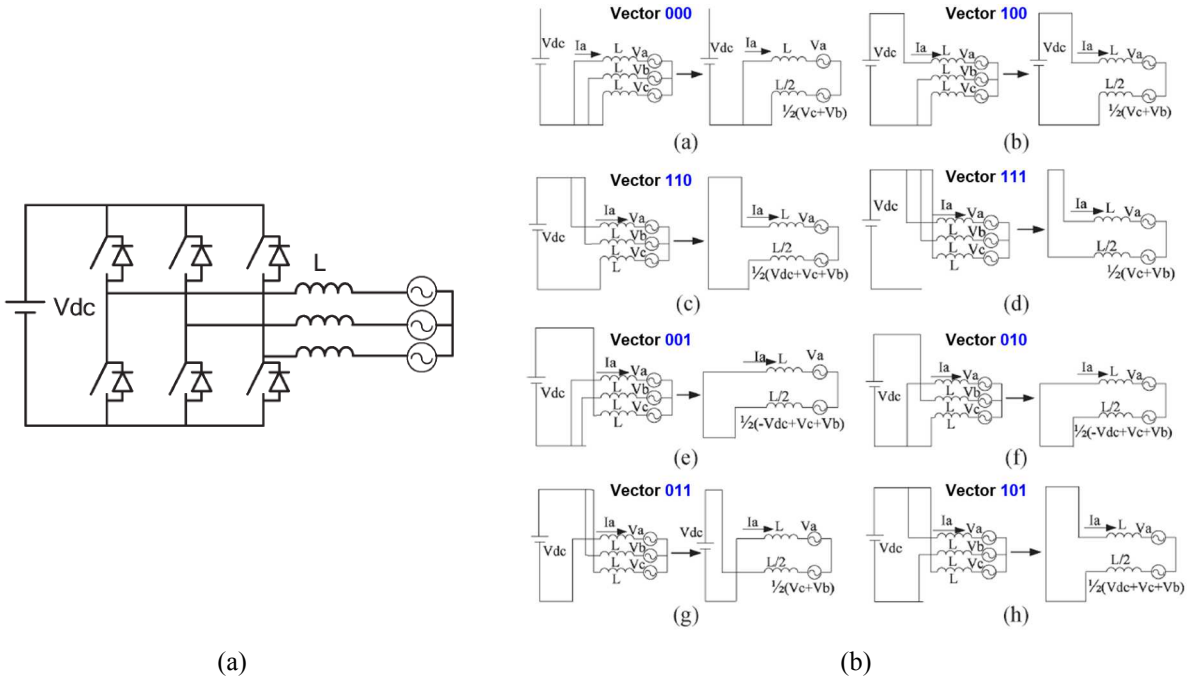

(a) (b)

Figure 2-34: (a) Three-phase PWM converter and load, and (b) Thevenin equivalent circuits under different voltage vectors [145].

variable switching PWM (VSPWM). Based on the eight different voltage vectors shown in Figure 2-34(b), the corresponding Thevenin equivalent circuit for each case was modeled, providing the expression of the current ripple slope individually. The method was applied successfully to evaluate the current ripple using either the SVPWM or DPWM algorithms. In addition, the authors introduced a general current prediction method [146] for multiphase (e.g., five-phase system) PWM converters based on the single-phase equivalent circuit. However, sharing the same limit, simple *L*-*R*-*C* loads were used under the assumption that the load inductance remained unchanged and operated within in the linear region.

Grandi and Loncarski [147] proposed a similar analytical approach to predict the peak-peak output current ripple of a *R*-*L* load system in the whole fundamental period as a function of inverter the modulation index. Furthermore, Grandi *et al.* [148] extended the current ripple analysis to an induction machine driven by three-level inverters. Similar to the *R*-*L* load, it is the leakage

inductance that primarily determines the current ripple in the induction machines. Unless driving the machine into saturated conditions, the machine leakage inductance can be assumed constant.

Yang *et al.* [149] presented a current ripple prediction method using the *d*-*q* transformation to account for the time-varying phase windings in IPM machines as the rotor rotates. However, constant inductance values measured for a single load condition were used for the current ripple prediction, which cannot accurately account for the high-order spatial harmonics (i.e., slotting harmonics), mutual coupling, and magnetic saturation.

In short, despite the progress made for PWM-induced current ripple prediction, there is still a need to improve the current ripple prediction in IPM machine over broad operating conditions.

2.4.2 Parasitic Losses Induced by PWM Switching

Under the excitation of PWM switched voltage waveforms, although the electric machine itself behaves as an inductive filter that attenuates the harmonic components, there are still PWM-induced ripple components that survive this filtering and appear in the phase currents. Taking the PM machines as an example, parasitic losses will be induced in each of three major machine materials: stator copper windings, stator and rotor iron cores, and permanent magnets.

2.4.2.1 PWM-Induced Copper Loss

Compared the DC/low fundamental frequency excitation, the high-frequency PWM-induced harmonics further exacerbate the copper losses increase due to the skin and proximity effects. In a machine with parallel wires, four influencing ac loss effects in the current conductors have been identified [150]: skin and proximity effects inside individual strand, as well as the skin and proximity effects across different parallel wires (i.e., circulating current).

Van der Geest *et al.* [151] evaluated the strand current distributions as the function of frequency for one straight and one twisted winding. Figure 2-35(a) shows the cross-section view of a slot

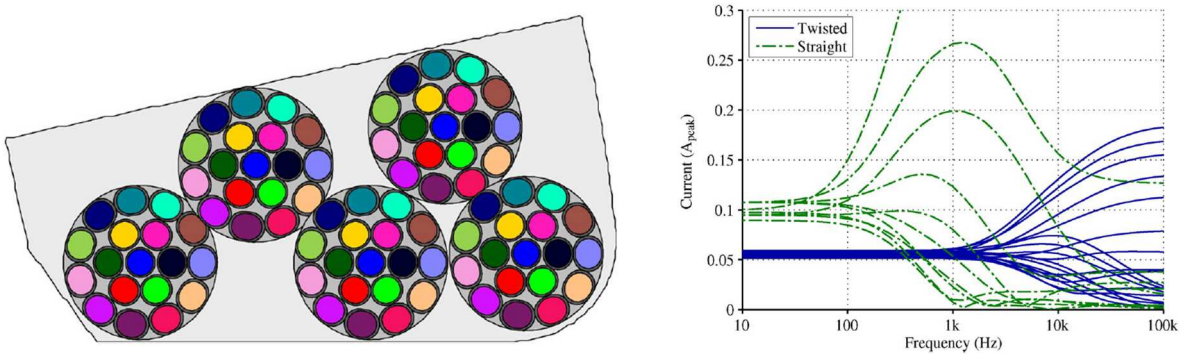

(a) (b)

Figure 2-35: (a) Cross-sectional view of a slot side, and (b) Strand currents as functions of frequencies [151].

side containing five 18-strand bundles, where each color represents the same conductor in different parallel connected turns. Figure 2-35(b) presents that the current distribution becomes unequal as the frequency increases between different strands, likely leading to a much higher copper loss.

In addition, the impact of PWM switching frequency on the copper loss of random-wound windings were investigated in [152]. It was concluded that using a higher switching frequency is beneficial to reduce the copper loss, since the current ripple amplitude goes down linearly with the PWM frequency, while the AC/DC loss ratio saturates at higher frequencies.

Islam and Arkkio [153] investigated the effects of PWM voltage excitation on the additional ac copper losses in an inverter-fed cage rotor induction machine using 2-D FEA. The study of a 1,250-kW induction motor demonstrated the notable loss contribution due to PWM harmonics in the stator winding compared to the sinusoidal supply. Similarly, it has been reported that increasing the PWM switching frequency might decrease the additional ac copper losses.

Zhang [127] further expanded the application range of analytical for modeling the current conductors' ohmic losses under arbitrary periodic excitation waveforms, including the PWM-induced harmonics. It has been experimentally confirmed that the PWM-induced copper loss decreases as the PWM switching frequency, which is proportional to $f_{\mathrm{PWM}}^{-1.6}$ and very close to the prediction trend given from the analytical model- $f_{\mathrm{PWM}}^{-1.5}$ with some simplifying assumptions.

2.4.2.2 Magnet Eddy-Current Loss

Sintered rare-earth PM materials are widely used in the PM machines, providing high power and torque densities for varying demanding applications. However, due to the relatively low resistivity, the spatial slotting harmonics and time harmonics (i.e., PWM-induced harmonics) contribute to nonnegligible Joule losses and temperature rise in the PM materials, increasing the risk of magnets demagnetization. Therefore, taking into account the PM eddy-current loss is of great importance in the machine design stage.

Various techniques have been proposed to conduct the PM eddy-current loss prediction, including the analytical approaches, 3-D time stepping FEA, and some hybrid methods.

The existing analytical models [154]–[157] more or less require some simplifying assumptions regarding the magnetic field distribution, and the impact of magnet eddy-current on the magnetic field distribution is ignored. Also, those models are not sufficiently general and limited to specific machine topologies and machine operating conditions. Moreover, the analytical models are developed to address the eddy-current loss induced by either the armature current reaction or slotting harmonics (e.g., surface PM machines), limiting the scalability and accuracy.

In contrast, considering the fact that hysteresis loss in the PM materials is negligible [158] and it is acceptable to adopt the linearized material assumption, the 3-D time-stepping FEA [5], [130], [159], [160] has been considered as the most accurate and general solution for prediction of magnet eddy-current loss under the supply switched voltage waveforms.

Yamazaki and Abe [5] investigated the PM eddy-current loss using the 3-D nonlinear time-stepping FEA, and the outline of the calculation procedure is given in Figure 2-36. It has been found that the magnet loss in IPM machines is primarily caused by the PWM harmonics and loss

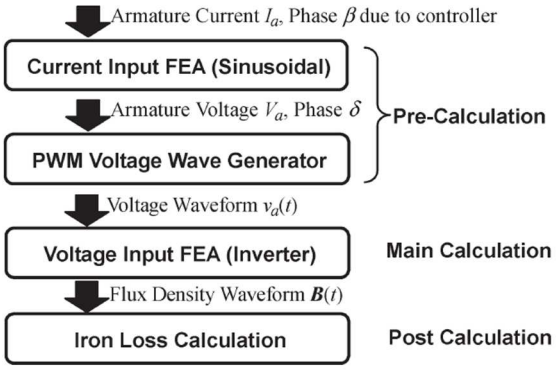

Figure 2-36: Core losses calculation outline in an IPM machine using 3-D FEA [5].

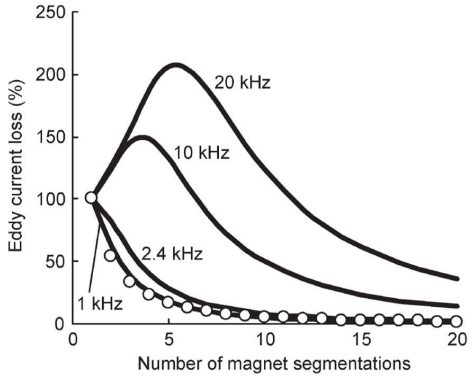

Figure 2-37: Relative magnet eddy-current loss variation versus number of segmentations [160].

values vary substantially with a number of magnet segmentation. However, the 3-D FEA typically takes long calculation time for solving a full fundamental cycle.

Furthermore, Yamazaki and Fukushima [160] presented an analytical model to estimate the magnet eddy-current loss variation versus the number of magnet segmentations. As the results given in Figure 2-37, the resulting magnet eddy-current loss reaches its maximum value when the length of the segmented magnet equals to the two-time skin depth.

Huang *et al*., [161] proposed an analytical model to optimize the magnet segmentation in both the circumferential and axial directions. It is concluded that when the skin effect is negligible, any circumferential or axial segmentation is helpful to reduce the magnet eddy-current loss. Otherwise, there is a risk in enhancing the eddy current dissipation for certain schemes of magnet's division, agreeing with the conclusion drawn in [160]. However, the frequency level of the studied harmonics is relatively low, leaving questions about the full impact of skin effect with a large number of segments with very high harmonic frequencies.

Cheng and Zhu [162] proposed a hybrid a method incorporating the 2-D FEA and analytical calculation approach, requiring a shorter time compared to the 3-D FEA. However, the calculation accuracy is limited by the simplifying assumptions and selected machine topology. Moreover, the implementation procedure is complicated and tedious.

2.4.2.3 PWM-Induced Iron Loss

The current waveforms including the PWM harmonics generate the rotating magnetic fields inside the electric machines, and in turn, yield additional iron losses in both the stator and rotor iron cores. The standard approach uses linear Fourier transformation to analyze the complex flux waveform and decompose that into different frequency components. Subsequently, the iron loss equation based on (2-17) with loss varying coefficients (i.e., a function of ac flux amplitude B_{ac} and excitation frequency f) is commonly used to predict the iron loss of each discretized mesh element in 2-D FEA and then sum up for the total iron loss in the electric machine. However, even when the advanced FEA is being used, due to the complex nonlinearities of magnetic materials, the prediction accuracy PWM-induced iron loss is not satisfactory.

As the major limitations of conventional estimation method are recognized, Krings *et al.* [163] experimentally investigated the influence of PWM switching frequency and modulation index on the iron loss of silicon-iron (SiFe) lamination sheets of a slotless PM machine.

Figure 2-38(a) shows the measured *B-H* curve of the stator core at 50 Hz and a fundamental flux density peak value at 1.2 T. As the zoom-in plot around zero flux density depicted in Figure 2-38(b), the enclosed area of PWM-induced minor loop (i.e., iron loss) decreases with both the PWM switching frequency and modulation index. It is shown in [163] that the iron loss under

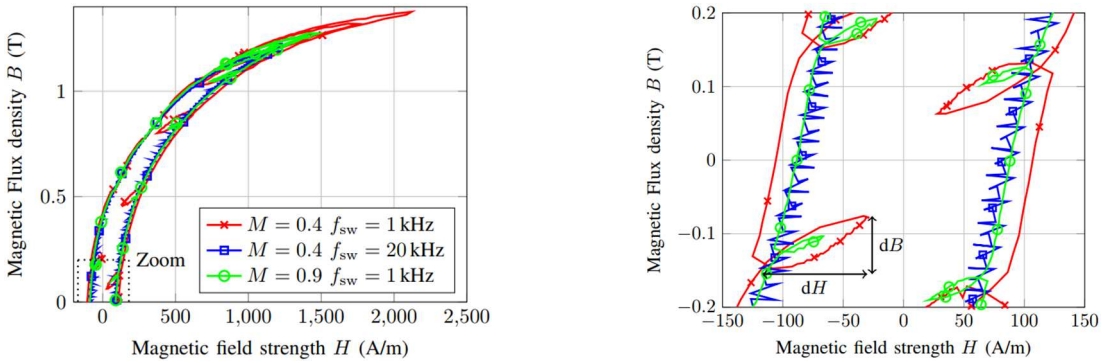

Figure 2-38: (a) *B-H* curve at 50 Hz and 1.2 T flux density, (b) Zoom-in region around zero flux density [163].

PWM supply increases substantially (up to 80 %) in the case of a low modulation index and low switching frequency compared to the pure sinusoidal condition.

Boglietti *et al.* [164] presented an investigation into the impact of PWM harmonics on the iron loss of an induction motor with a non-conducting rotor cage to eliminate additional Joule losses consumed by the rotor-side conductors due to both the spatial and PWM harmonics. However, as recognized by the authors, with a non-conductive rotor, the induction motor itself cannot run by itself, adding difficulties to segregate the additional losses due to PWM voltage excitation. Although it is possible to run the rotor under the standstill condition, the impact of machine operating conditions cannot be included (i.e., a machine with different slip values and speeds).

Masisi *et al.* [165] investigated the iron losses resulting from the two- and three-level inverters for the same dc-bus voltage and PWM switching frequency using the stator toroid core used in the synchronous reluctance machine (SynRM). The iron loss with three-level inverter exhibits approximately 60% loss reduction compared to the two-level inverter, where the most significant reduction is at high flux densities and fundamental frequencies. Also, the three-level inverter has better dc-bus voltage utilization (i.e., lower modulation index). However, extra cost and system volume make the three-level inverter less appealing compared to the two-level inverter.

Although the PWM-induced iron loss has been quantitatively evaluated via experimental tests for a variety of ac machine topologies, the additional iron loss due to PWM switching was not experimentally segregated or analyzed separately from the total machine loss in IPM machines.

Compared to the major magnetic field, the PWM-induced flux ripple contains some distinctive characteristics, making the conventional approach developed for major field analysis not suitable anymore. Since the PWM switching frequency is typically much higher than the fundamental

frequency and flux ripple amplitude is much smaller than the fundamental field, within each PWM switching period, the flux ripple experiences equivalent dc-bias field impact from the major field.

Lancarotte *et al.* [166] proposed a methodology to estimate the iron loss under PWM voltage excitation or dc-bias field. An experimental setup was built to investigate the minor loop losses in both the oriented and non-oriented ferromagnetic materials. The results shown in Figure 2-39(a) and Figure 2-39(b) demonstrated that the minor loops produced by PWM voltage do not affect the major hysteresis loop loss nor the minor loop losses measured at different points of the major loop. In other words, the iron loss of major and minor loops induced by PWM harmonics can be estimated separately. However, the amplitude of flux ripple analyzed in [166] is a bit large (e.g., $B_{\text{minor}} > 0.1$ T) and maximum frequency is limited to 500 Hz.

Gmyrek [167] extended the testing frequency to 4 kHz with much smaller harmonic amplitude (i.e., $B_{\text{minor}} = 5$ mT). The variation trends of iron losses of minor loops over varying ac and dc bias fields are given in Figure 2-40(a) and Figure 2-40(b), respectively.

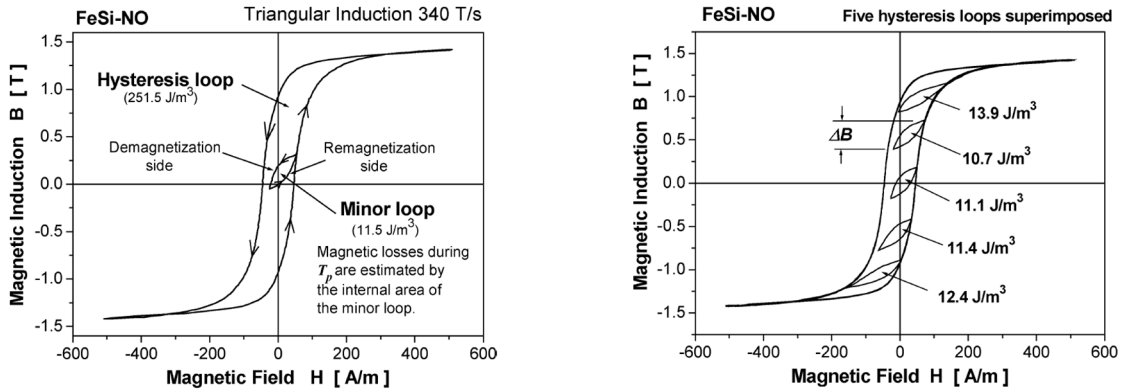

(a) (b)

Figure 2-39: (a) Experimental hysteresis loop with a single minor loop, and (b) Five hysteresis loops each with a single minor loop, superimposed [166].

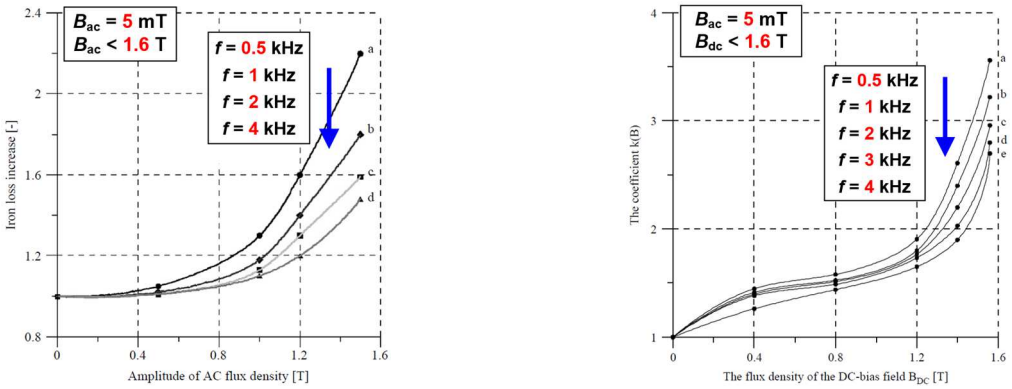

(a) (b)

Figure 2-40: (a) Iron loss increase vs. ac flux density B_{ac}, and (b) Iron loss increase vs. dc flux density B_{dc} [167].

A polynomial equation was proposed in [168] to emulate the iron loss increasing trend versus dc-bias flux density value B_{dc}:

$$k(B_{dc}) = 1 + A_1 B_{dc} + A_2 B_{dc}^2 + A_3 B_{dc}^3 + A_4 B_{dc}^4 \tag{2-53}$$

where $k(B_{dc})$ is the relative iron loss increase factor compared to the iron loss without the dc-bias field, and the remaining polynomial coefficients are fitted parameters. However, the iron loss increase factor is difficult to determine when the shape of the fundamental field becomes distorted or when the harmonic spectrum is complicated.

Xue *et al.* [169] adopted the coefficient k_{minor} to describe the ratio of hysteresis loss with and without the minor loops. However, a constant factor k between the 0.6 and 0.7 is used in (2-54) to predict the iron loss of minor loops, lacking scalability and generality over wide operating regimes.

$$k_{minor} = 1 + k \frac{1}{B_{major}} \sum_{i=1}^{N} \Delta B_i \tag{2-54}$$

where B_{major} is the amplitude of major field, and ΔB_i is segregated minor loop amplitude.

Takeda *et al.* [170] proposed a more generalized prediction model that combines a hysteresis model and 3-D FEA for toroidal core analysis. However, the calculation time is long and still not practical for machine-level PWM-induced iron loss analysis.

Recently, new-generation of wide-bandgap (WBG) power semiconductors (i.e., SiC or GaN) are becoming increasingly popular in a variety of industrial and traction applications. In addition to several promising advantages including but not limited to high-temperature operating capability and high efficiency, the fast-switching speed of those devices makes it possible to drive the electric machine loads with elevated fundamental frequencies while maintaining high inverter-side efficiency with low switching losses [6], [7]. However, it raises questions about the iron loss properties of lamination steels when they are exposed to such a considerably higher switching frequency (e.g., f_{PWM} > 20 kHz).

Martinez *et al*., [171] developed a GaN-based full-bridge inverter in Figure 2-41(a) to investigate the high-frequency iron loss properties of electrical steels, enabling a wide PWM switching frequency range from 5 up to 500 kHz. As depicted in Figure 2-41(b), the measured iron loss versus f_{PWM} results reported in [171] indicates that the total iron loss under PWM voltage excitation is not sensitive to switching frequency when f_{PWM} is below 100 kHz, whereas the total iron loss increases dramatically beyond 100 kHz f_{PWM}. Also, it is found that the total iron loss shows a negligible change with the inverter deadtime. However, the analysis presented in [171] is limited to a very low fundamental frequency (f_{fund} = 50 Hz) and a small flux density amplitude (B_{ac}

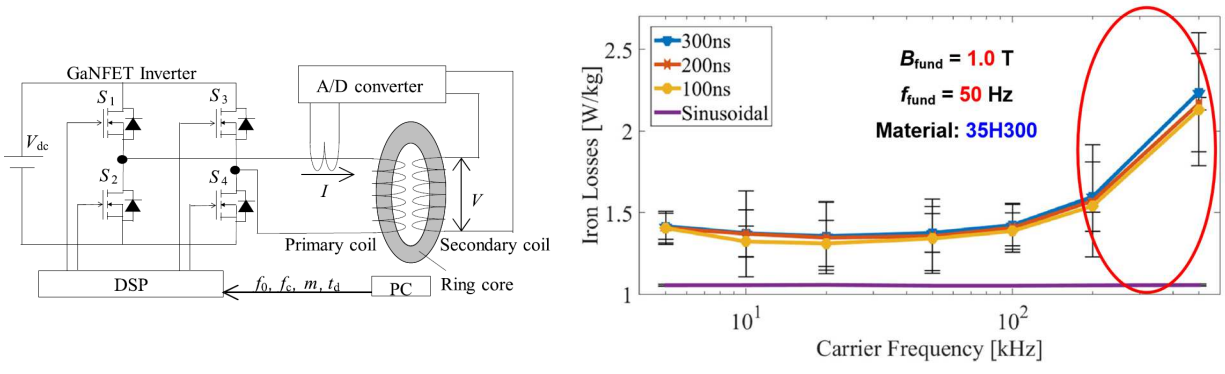

(a) (b)

Figure 2-41: (a) Iron loss measurement circuit with a GaN-based inverter, and (b) Iron loss versus PWM switching frequency with the 1.0 T and 50 Hz fundamental field excitation [171].

= 1.0 T). Moreover, the PWM-induced iron loss is not segregated from the total iron loss, lacking sufficient insights into the PWM iron loss behaviors operating with high PWM frequency.

Millinger *et al*., [172] measured the high-frequency iron loss in a two-pole slotless permanent magnet motor using a linear amplifier combining with a signal generator. The dc-bias coil shown in Figure 2-42(a) enables the iron loss characterization over varying dc-bias fields. For a given steel- NO20, the iron loss versus the dc-bias field is evaluated and depicted in Figure 2-42(b) by maintaining the primary winding voltage constant at 50 Vrms. The iron loss reaches the peak point around 1.4 T for this particular material and then drops as the dc-bias field continues increasing. However, since the test is conducted with a constant voltage supply, as the winding current goes up in the saturated region (i.e., B_{dc} > 1.4 T), the voltage drop on the winding resistance increases considerably, which in turn, result in a smaller flux density amplitude in the saturated region. Therefore, it is not yet well understood how the high-frequency iron loss varies with a constant flux density amplitude.

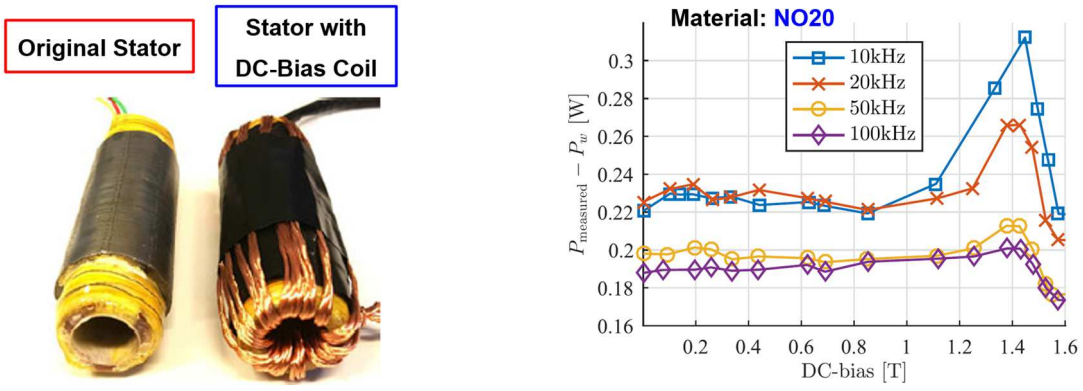

(a) (b)

Figure 2-42: (a) Original stator core of a two-pole slotless PM motor and the stator core with dc-bias coil for high-frequency iron loss measurement, and (b) Iron loss results of the NO20 material versus dc-bias field B_{dc} at varying excitation frequencies with 50 Vrms primary winding input.

2.5 Conclusions and Identified Research Opportunities

Various approaches developed for modeling the iron losses of fundamental and low-order harmonic components have been compared and discussed in this chapter. Although the iron loss models based on the Steinmetz Equation or loss separation theorem are preferred for fast iron loss investigation, they compromise the accuracy significantly when they are applied to complex flux waveforms containing rich harmonics or affected by the external fields. In contrast, the hysteresis models exhibit promising potential for modeling the dynamic hysteresis loops over varying operating conditions. However, the existing hysteresis models lack sufficient generality for modeling the dynamic field, maintaining the congruency of minor loops over broad conditions, and emulating the impacts of dc-bias fields on minor loops. Therefore, this research project is aimed at developing a more generalized dynamic hysteresis model suitable for iron loss estimation in IPM machines.

Furthermore, as the VSIs are widely employed to drive the electric machines over a wide range of operating conditions, the system efficiency degradation attributable to PWM switching has drawn considerable attention during the past couple of decades. Finite-element analysis (FEA) serves as a useful tool for estimation of PWM-induced copper and magnet losses. However, due to the non-linearities of the magnetic materials, the estimation accuracy is limited even when the FEA is being used. Although several studies have been devoted to raising the awareness about PWM-induced iron loss in electrical steels and experimentally investigating these PWM losses, a comprehensive approach for PWM-induced iron loss in electric machines has not been developed yet in the literature. Great efforts are made during this research program to aggressively attack two of the critical weaknesses of currently available PWM-induced iron loss models, including: 1) accurate prediction of PWM-induced current ripple for varying machine and inverter operating

conditions; and 2) improved physics-based modeling of PWM-induced iron loss that includes the nonlinear impact of the equivalent dc-bias fields.

More recently, the new-generation of wide-bandgap power semiconductor devices (i.e., SiC or GaN) in VSIs are becoming increasingly popular in various industrial and traction applications. Besides several promising advantages brought by those new devices (e.g., high inverter efficiency, fast switching speed, etc.), they raise questions about the iron loss properties of lamination steels when exposed to such elevated switching frequencies. Existing studies have presented experimental analysis of high-frequency iron loss in selected electrical steels. However, only the total iron loss is studied for some particular testing conditions. Also, no accurate and convenient iron loss model has been found in the literature that can be applied for PWM iron loss estimation over broad excitation frequencies, flux density amplitudes, and dc-bias fields. To resolve these issues, an in-depth analysis of PWM-induced iron loss in lamination steels is presented in this dissertation. The results of this research include development of an estimation model that is suitable for PWM iron loss analysis under high-frequency excitation conditions with WBG-based inverters, shedding some light on the impact of WBG devices on electric machine efficiencies.

Chapter 3
Development of Generalized Dynamic Hysteresis Model

3.1 Introduction

Accurate iron loss modeling of ferromagnetic materials (e.g., lamination steels) is of great importance for use in the electric machine optimization tool. Although the materials' iron loss properties can be well characterized using the Epstein frame test to evaluate the iron losses of sinusoidal waveforms over different excitation frequencies and ac flux densities amplitudes, the flux waveforms in the electric machines deviate substantially from the pure sinusoidal shape due to the magnetic saturation, MMF harmonics, etc.

Minor loops riding on top of the fundamental field are induced in the stator and rotor surface regions due to the slotting harmonics, contributing to additional losses. Also, since the rotor rotates synchronously with the frequency of the supply current, the main magnetic field in the rotor side is the dc field. In other words, the iron losses of minor loops in the rotor surfaces are influenced by the dc-bias fields. Therefore, having a generalized iron loss estimation tool applicable to complex flux waveforms is of great importance during the process of machine design optimization.

This chapter begins with the development of the measurement system for hysteresis loops and iron loss data collection over a wide range of ac and dc excitation. With the measured data available, an improved generalized hysteresis model is proposed to properly include the impact of the flux density changing rate, instantaneous magnetization state, and time history of magnetic flux on dynamic field modeling. Special minor loop compensation and dc-bias field correction methods are developed to emulate the actual characteristics of minor loops with the low measurement data requirement.

3.2 Measurement of Hysteresis Loop and Iron Loss Data

3.2.1 Test Configuration A: dSPACE Controller Board with Power Amplifier

To investigate the iron loss properties of the studied non-oriented soft magnetic materials, the toroidal core iron loss tester is selected due to its simple structure, closed magnetic path, and improved geometry emulation of electric machines compared to the conventional Epstein frame.

As the test configuration shown in Figure 3-1, the primary winding of the toroidal core is connected to the power amplifier, generating ac magnetic flux in the toroidal core, and the corresponding magnetic field strength can be determined using (3-1). An additional isolating transformer is placed in between them to eliminate any remained dc components generated by the power amplifier.

$$H = \frac{N_{\text{main}} I_{\text{main}}}{l_{\text{core}}} \qquad l_{\text{core}} = \frac{\pi \cdot (OD - ID)}{\ln(\frac{OD}{ID})} \tag{3-1}$$

where I_{main} is the primary winding current, N_{main} is the number of turns in the primary winding, and l_{core} is the mean magnetic path with OD and ID equal to the toroidal core's outer and inner diameter, respectively.

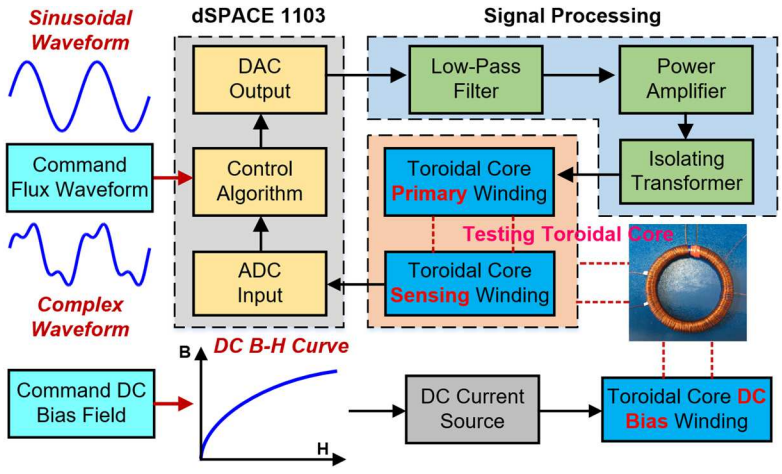

Figure 3-1: Test configuration A for hysteresis loops and iron loss data measurement with dSPACE controller and power amplifier.

According to (3-2), the open-circuit sensing voltage V_{sense} is used to measure the time waveform of the ac magnetic flux density B_{ac} in the testing iron core.

$$V_{\text{sense}}(t) = N_{\text{sense}} A_{\text{core}} \frac{dB_{\text{ac}}(t)}{dt} \tag{3-2}$$

where N_{sense} is the number of turns in the secondary sensing winding, A_{core} is the cross-section area of the toroidal core, and the key parameters and dimensions of the thin-gauge silicon steel toroidal core are provided in Table 3-1.

However, due to the inherent nonlinearities (e.g., saturation) of the magnetic materials and the voltage drop across the winding resistance, the actual magnetic field observed from the sensing winding can deviate from the command flux waveform, making it necessary to implement a close-loop flux waveshape regulation control. As the limitations of the conventional analog control circuit are widely recognized, digital feedback control schemes are generally adopted for flux waveform control. The early version of the digital system [113] requires complex phase adaption to account for the nonlinear phase delay caused by the low-pass passive *R*-*C* filter and power amplifier. More recently, the advanced data acquisition device [114] enables the data storage of

TABLE 3-1: KEY PARAMETERS AND DIMENSIONS OF MANUFACTURED TOROIDAL CORE FOR LOW-FREQUENCY ANALYSIS

Primary winding turns N_{main}	375
Sensing winding turns N_{sense}	155
DC-bias winding turns N_{dc}	260
Lamination thickness	0.3 mm
Toroidal core thickness	5.1 mm
Number of sheets	17
Outer diameter (**OD**)	76.2 mm
Inner diameter (**ID**)	64.77 mm
Material mass density ρ_{iron}	7600 kg/m^3
Stress relief annealing process	Yes

the previous generation of digital-to-analog output, removing the demand for adaption code. Therefore, the primary winding output voltage waveform V_{out} can be updated iteratively by (3-3) with a proportional controller based on the given command voltage V_{cmd} calculated using (3-2). The output voltage waveform at each discretized sampling point can be determined as,

$$V_{\text{in}}(i) = V_{\text{in}}(i-2) + k_p(V_{\text{mea}}(i-2) - V_{\text{cmd}}) \tag{3-3}$$

where i is the current iteration index of the fundamental period, V_{mea} is the measured voltage waveform from the secondary sensing winding, and k_p is the error gain of the proportional controller.

Figure 3-2 depicts the sequencing of the data collection and output voltage generation. Within each fundamental period, there are multiple sampling points and larger the number of data points, better the regulation accuracy. Moreover, it always requires at least one full fundamental cycle to process the measured data in the previous period and generate the new output voltage for the coming period. Therefore, the output voltage of the current iteration (i.e., i) is calculated based on the output command and measurement errors that lag two iterations behind (i.e., i - 2).

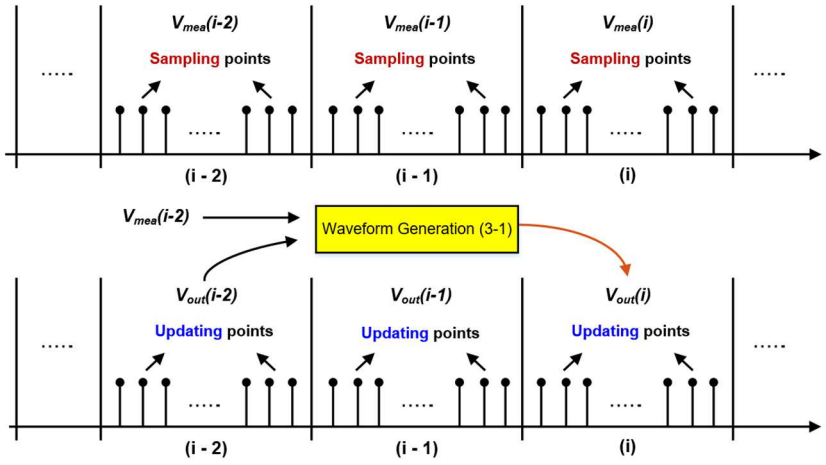

Figure 3-2: Sequencing of data sampling and updating for flux waveshape regulation control

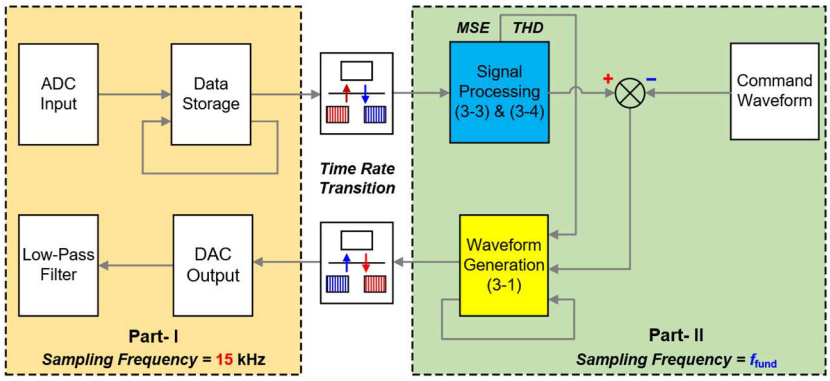

Figure 3-3: Block diagram of the flux waveform regulation control.

Figure 3-3 shows the overall block diagram of the flux waveform regulation control. The system can be subdivided into two parts with different sampling frequencies. The left part of the control system- Part I is responsible for the instantaneous data collection which operates at the maximum sampling frequency (i.e., f_{sample} = 15 kHz) of the available controller. Since the data over a full fundamental cycle is needed for the voltage command update given in (3-3), the sampling frequency of Part II is the same as the fundamental frequency of the command voltage waveform, and two parts of the control system are connected by time rate transition blocks. A second-order low-pass filter is connected to the DAC output, filtering out additional high-frequency harmonics remained in the latched voltage output waveforms.

For each discretized data point with index k over one full fundamental cycle, the error $e(k)$ can be determined by subtracting the corresponding value of the command voltage waveform as:

$$e(k) = V_{\text{cmd}}(k) - V_{\text{mea}}(k) \tag{3-4}$$

Subsequently, the mean square error (MSE) can be calculated by (3-5), which is considered as the key control criteria of the flux waveform generation.

$$\text{MSE} = \sqrt{\frac{1}{N}\sum_{k=1}^{N} e_k^2} \tag{3-5}$$

where N is the total number of the discretized data points in one fundamental cycle.

Furthermore, for the purpose of achieving pure sinusoidal waveforms, the total harmonic distortion (THD) expressed by (3-6) is another important metric for waveform quality evaluation.

$$\mathrm{THD} = \frac{\sqrt{B_2^2 + B_3^2 + B_4^2 + \cdots}}{B_1} \times 100\% \tag{3-6}$$

where B_n is the n^{th} order of the Fourier decomposed component.

If the value of MSE is smaller than 0.005 and THD is smaller than 0.5 %, the control algorithm will be switched off and maintain the output voltage waveform unchanged.

Figure 3-4 shows the measured voltage waveforms of the primary winding and the sensing winding over three different amplitudes of magnetic flux density at 50 Hz. Also, the primary winding current of each case is presented. As can be seen from Figure 3-4(b) and (d), owing to the high permeability of ferromagnetic materials in the linear region, a small amount of primary winding current (i.e., magnetic field strength) is needed to achieve the command magnetic flux. Therefore, the primary winding voltage waveforms given in Figure 3-4(a) and (c) are very close to the sinusoidal shape. In other words, even without flux waveshape regulation control, a sinusoidal input voltage can lead to a sinusoidal output voltage across the sensing winding with relatively low THD. However, a much larger excitation current is needed to drive the material into the heavy saturation region, like the results depicted in Figure 3-4(e) and (f). As a result, the voltage drop over the resistive component (i.e., winding resistance) increases significantly, leading to a voltage spike in phase with the current maxima in the primary winding voltage waveform. That is why the flux regulation control is indispensable when the material is the region of saturation.

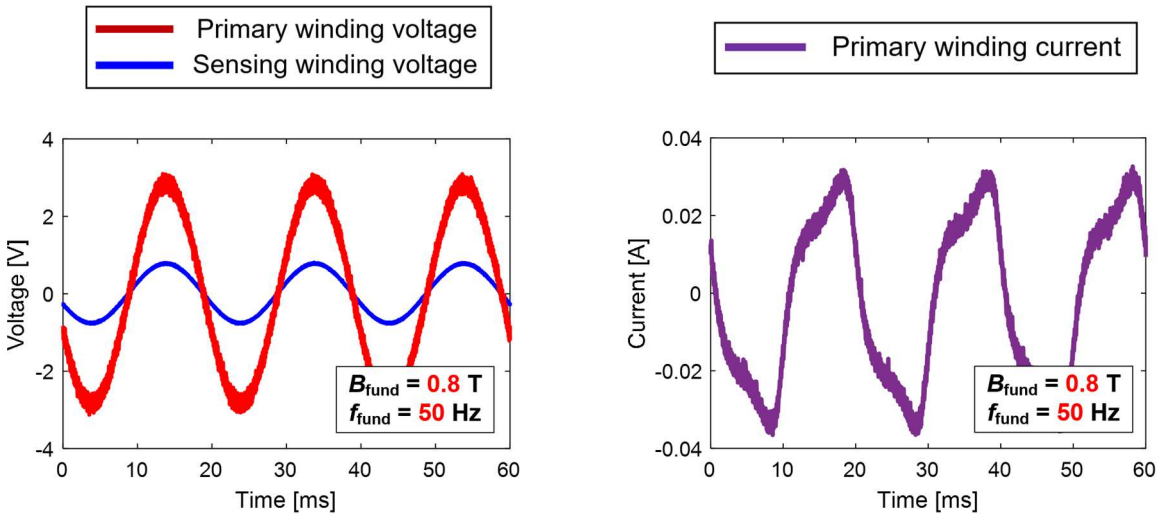

(a) Primary and sensing winding voltage waveforms (b) Primary winding current waveform

Operating condition: AC flux density amplitude B_{fund} = 0.8 T, excitation frequency f_{fund} = 50 Hz

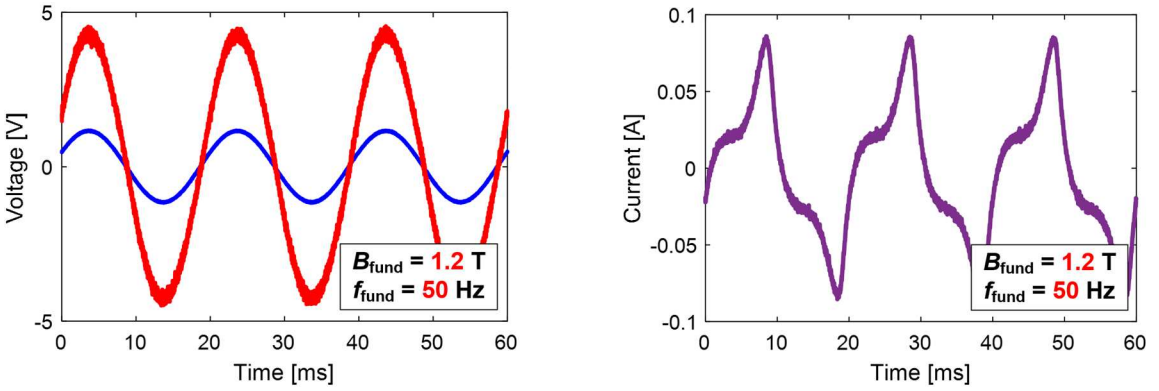

(c) Primary and sensing winding voltage waveforms (d) Primary winding current waveform

Operating condition: AC flux amplitude B_{fund} = 1.2 T, frequency f_{fund} = 50 Hz

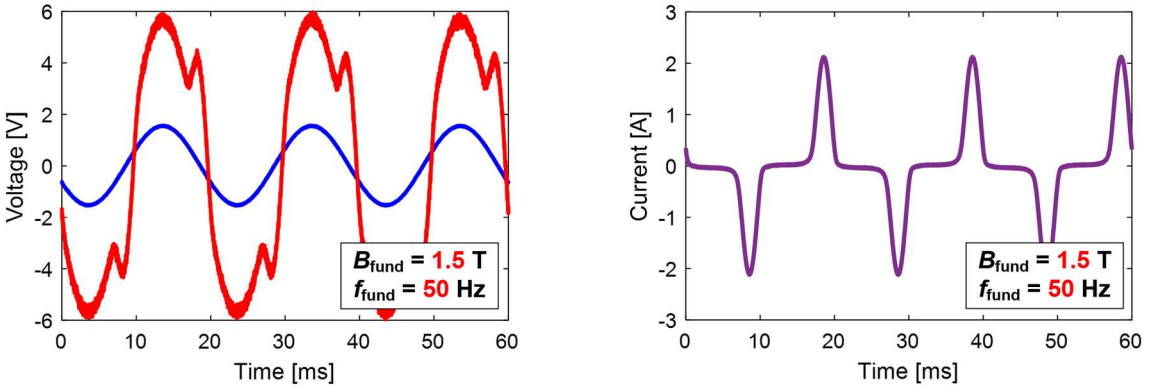

(e) (f)

Operating condition: AC flux amplitude B_{fund} = 1.5 T, and excitation frequency f_{fund} = 50 Hz

Figure 3-4: Measured voltage and current waveforms for three selected iron core operating conditions.

3.2.2 Test Configuration B: WBG-Based VSI with *L-C* Sinewave Filter

Although the test configuration discussed in the preceding section offers a good controlling capability, due to limited sampling and output frequency of the ADC and DAC module for the available dSPACE controller, the maximum achievable frequency is 200 Hz which restricts the iron loss evaluation to a relatively low-frequency range. Even for machines operating under low-speed conditions, the slotting harmonics appearing in the stator tooth tips and soft iron loss pole shoes of electric machines are at much higher frequencies. Therefore, extending the appliable frequency range of the material characterization system is of great importance.

To extend the fundamental frequency range of input characterization data, an improved inverter-based hysteresis loop and iron loss measurement system has been built, and its equivalent circuit configuration is shown in Figure 3-5. Two GaN half-bridge boards operate under control of PWM gate signals to generate the PWM voltage excitation waveform with the desired fundamental component. Key inverter parameters are provided in Table 3-2. Depending on the requirements of specific applications, the output voltage waveforms can be generated using either a unipolar modulation algorithm with three voltage levels ($+V_{dc}$, 0, $-V_{dc}$) or bipolar modulation with two voltage levels ($+V_{dc}$, $-V_{dc}$). Since the proposed dynamic hysteresis model requires the

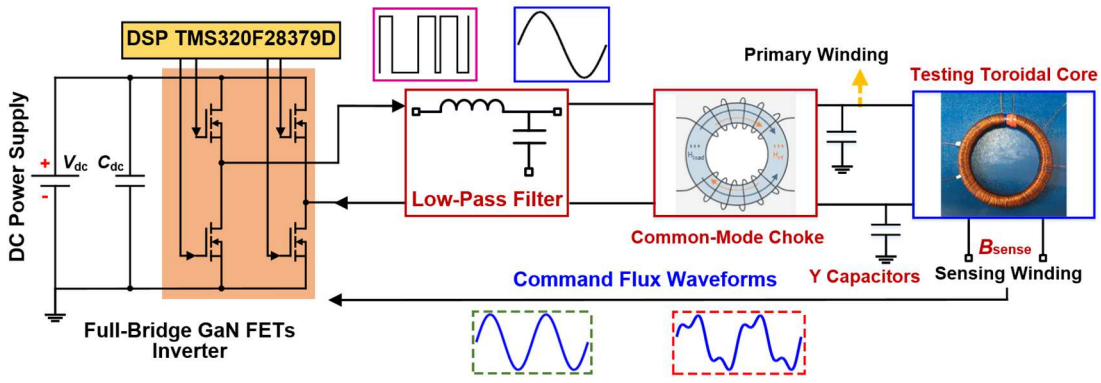

Figure 3-5: Test configuration B for hysteresis loop and iron loss data measurement using a GaN-based VSI with *L-C* low-pass filter.

TABLE 3-2: KEY PARAMETERS OF GAN FETS VOLTAGE SOURCE INVERTER

Maximum dc-bus voltage	140 V
Maximum output current	12 A
Turn-on deadtime	< 20 ns
Output voltage rise time	< 10 ns
Output voltage fall time	< 10 ns
PWM switching frequency	10- 200 kHz

input hysteresis loop data to have a purely sinusoidal waveshape, the unipolar switching scheme has been adopted because its switching harmonics have lower amplitudes and are easier to suppress.

A low-pass *L-C* filter is placed at the inverter output, filtering out the high-order PWM switching harmonics. The availability of wide bandgap (WBG) switches makes it possible to raise the PWM switching frequency significantly (e.g., $f_{PWM} > 100$ kHz). This creates sufficiently large frequency differences between the desired fundamental frequency f_{fund}, the filter cut-off frequency f_c, and the PWM switching frequency f_{PWM} to eliminate the undesired PWM harmonics without attenuating the fundamental frequency to any significant degree.

It is worth noting that, since the material data over a wide fundamental frequency range are necessary for dynamic hysteresis model characterization, three low-pass *L-C* filters have been built with different cut-off frequencies, making it possible to "customize" the low-pass filter in Figure 3-5 for the desired fundamental frequency test range. This approach guarantees excellent filtering performance over the entire frequency range that is being investigated. Figure 3-6(a)-(c) show the manufactured filter boards with cut-off frequency f_c values of approx. 10, 20, and 50 kHz, respectively. The minimum ratio between the fundamental frequency and its corresponding cut-off frequency is maintained over 20, making it possible to selectively introduce low-order harmonics (e.g., 3rd or 5th harmonic component) into the excitation waveform when desired.

(a) f_c = 10 kHz (b) f_c = 20 kHz (c) f_c = 50 kHz

Figure 3-6: Three fabricated *L-C* low-pass filters with different cut-off frequencies for use in the Figure 3-5 test configuration B.

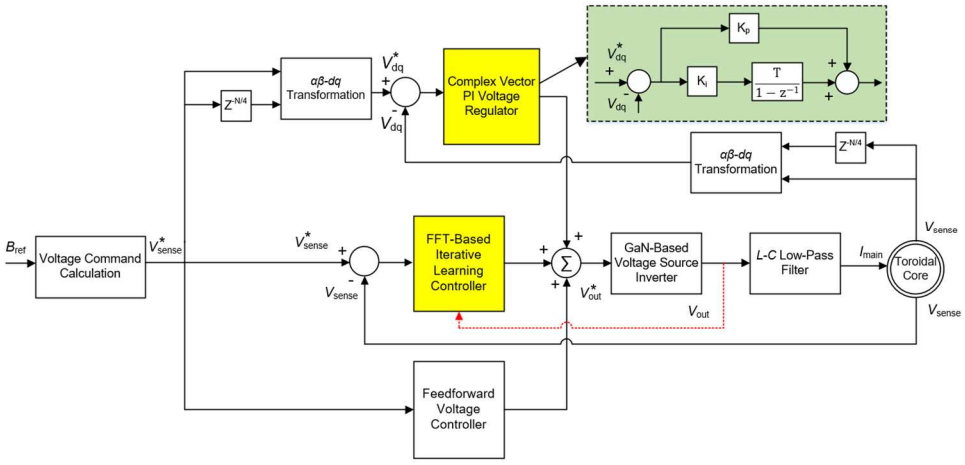

(a) Complete block diagram of the overall control system

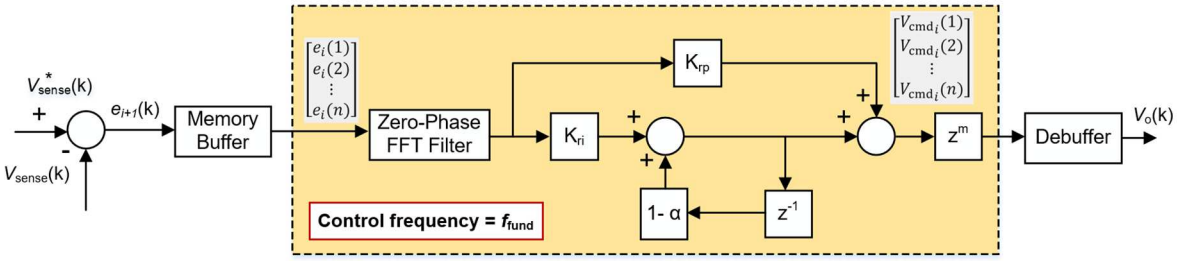

(b) FFT-based iterative learning controller

Figure 3-7: Block diagram of the proposed hybrid flux waveshape regulation control system.

As presented in Figure 3-7(a), the proposed hybrid flux waveshape control system consists of three voltage controllers, including a feedforward voltage controller, a complex vector PI voltage regulator, and a modified FFT-based iterative learning controller (ILC). The feedforward controller provides the dominant component of the inverter output voltage when the toroidal core operates in the linear region, and its command value is calculated based on the turns ratio between the primary and sensing winding

$$V_{\mathrm{ff}}(t) = \frac{N_{\mathrm{main}}}{N_{\mathrm{sense}}} A_{\mathrm{core}} \frac{dB_{\mathrm{ac}}(t)}{dt} \tag{3-7}$$

Yet, even ignoring the impact of nonlinear magnetic saturation, the existence of the low-pass *L-C* filter introduces a voltage drop as well as the phase delay, making it necessary to include the flux waveshape regulation control. In addition to the feedforward controller, a complex vector PI voltage regulator [173] is used to minimize the control errors while improving the system dynamic performance. However, at least two static voltage signals are necessary to transform them into the *d-q* rotating frame. To solve this problem, a second quadrature voltage waveform is created for the β axis by purposely delaying the measured voltage in the α axis by 90 degrees [174], [175].

The single-phase *d-q* frame voltage V_{dq} can be then calculated using the following rotary transformation:

$$V_{\mathrm{dq}} = T \cdot V_{\alpha\beta}, \text{ where } T = \begin{bmatrix} \sin(\theta) & -\cos(\theta) \\ \cos(\theta) & \sin(\theta) \end{bmatrix} \tag{3-8}$$

$$V_{\alpha} = V_{\mathrm{sense}} \tag{3-9}$$

$$V_{\beta} = V_{\mathrm{sense}} \cdot z^{-n/4} \tag{3-10}$$

where $\theta = \omega t$ is the rotating angle in [rad], $\omega = 2\pi f_{\mathrm{fund}}$ is the electrical angular frequency in [rad/s], and n is the total number of sensing points in the full fundamental cycle, corresponding to 90 degrees (i.e., $\pi/2$ rad).

As a result, the *q*-axis command is a dc variable equal to the peak value of the reference sensing voltage, while the *d*-axis command is always zero. However, the PI regulator is still not capable of adequately suppressing the higher-order periodic disturbances which are mainly induced by the nonlinear primary winding current. Therefore, a modified FFT-based iterative learning controller shown in Figure 3-7(b) has been developed for this project and added to the control system. Unlike the conventional repetitive or iterative learning controller [176], [177] that works at the system

control frequency, the proposed controller first saves all of the measured data for a full fundamental cycle using a memory buffer and processes all of this data at a much lower rate (i.e., once per cycle of the fundamental frequency) which reduces the calculation complexity and cost substantially. In the absence of this modified iterative learning controller, the heavy computational burden makes it challenging to implement closed-loop control at high fundamental frequencies (i.e., $f_{\text{fund}} \geq 500$ Hz).

Another advantage of the proposed control system, in addition to the low computational cost, is the zero-phase delay FFT filter that appears in Figure 3-7(b). By collecting the measured data for a full cycle, the high-frequency noise (e.g., noise that is close to the Nyquist frequency) can be filtered out in the frequency domain without leading to any undesired phase shifts.

The critical design decisions include selecting a proper iterative learning gain K_{ri}, a forgetting factor α, and the time-advance step m. In general, the error decay speed is proportional to the amplitude of the gain factor K_{ri}, and therefore, having a unity gain factor is desirable to achieve fast error convergence. However, it was found during the experiments that having a large gain value can easily lead to instability, especially under high-frequency conditions where the number of sampling points per cycle is limited. Hence, the value of K_{ri} is tuned depending on the specific sampling-to-fundamental frequency (S2F) ratio. When implementing the proposed control algorithm in the available DSP, the maximum control frequency is 32 kHz. As long as the S2F ratio is equal or larger than 128, the learning gain value $K_{\text{ri}} = 0.5$ is used. When the S2F ratio drops below 64, a lower learning gain value in the vicinity of 0.05 is selected to ensure system stability, which in turn, degrades the error convergence rate and waveform quality.

Including a positive forgetting factor α provides an effective means to enhance the system stability and protect it from nonperiodic disturbances, dynamic load changes, etc. The value of α

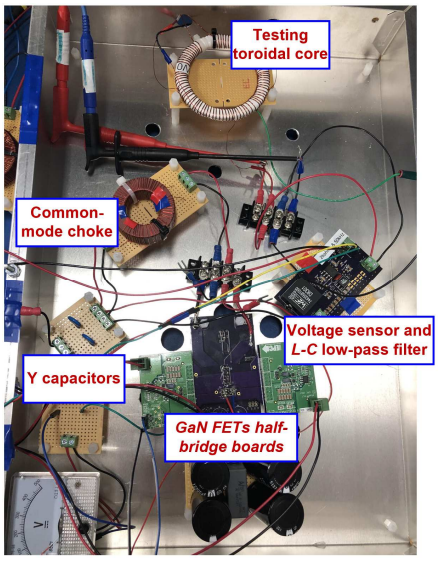

Figure 3-8: Experimental test configuration B based on the GaN FETs single-phase VSI for high-frequency magnetic materials characterization.

TABLE 3-3: KEY PARAMETERS AND DIMENSIONS OF FABRICATED TOROIDAL CORE FOR HIGH-FREQUENCY ANALYSIS

Primary winding turns N_{main}	343
Sensing winding turns N_{sense}	95
DC-bias winding turns N_{dc}	-
Lamination thickness	0.3 mm
Toroidal core thickness	3.0 mm
Number of sheets	10
Outer diameter (**OD**)	76.2 mm
Inner diameter (**ID**)	64.77 mm
Material mass density ρ_{iron}	7600 kg/m^3
Stress relief annealing process	Yes

is typically maintained in the range of 0.001 to 0.005. Similar to the sensitivity of the learning gain value to S2F ratio, a larger forgetting value is used under high-fundamental-frequency conditions to further improve the robustness of the control system while resulting in higher residual errors.

Next, there are multiple factors that can cause phase delay in the control system, including control signal propagation delay (i.e., one step delay), inverter phase lag, and the low-pass *L*-*C* filter delay. The specific delay induced by the latter two factors changes with operating conditions, including the fundamental frequency, filter cut-off frequency, and PWM switching frequency. For the proposed system, a time-advance block of z^m is included in the Figure 3-7(b) block diagram. In practice, $m = 3$ has typically been used as an initial starting value during testing, and its value is then experimentally tuned if any instability issues are observed during operation.

Figure 3-8 shows the experimental test configuration of the proposed testing system, and the key specifications of the manufactured toroidal core are given in Table 3-3. It should be noted that the number of winding turns and lamination sheets can be adjusted accordingly to match the inverter output capability. (See Table 3-2 for the detailed inverter specifications)

Figure 3-9(a)-(c) depict the collected primary and sense winding waveforms for different material saturation conditions. As can be seen from Figure 3-9(a), when the material operates in the linear region (i.e., B_{fund} = 1.0 T), both the primary winding input voltage and the sensing output voltage are sinusoidal in shape, indicating that the voltage drop across the winding resistance is almost negligible. However, as the material is driven to the heavily saturated region (i.e., B_{fund} = 1.6 T) in Figure 3-9(b), the waveform quality becomes poorer due to the distortion in the region where the peak current occurs. As a result, the iterative learning control is indispensable to achieve

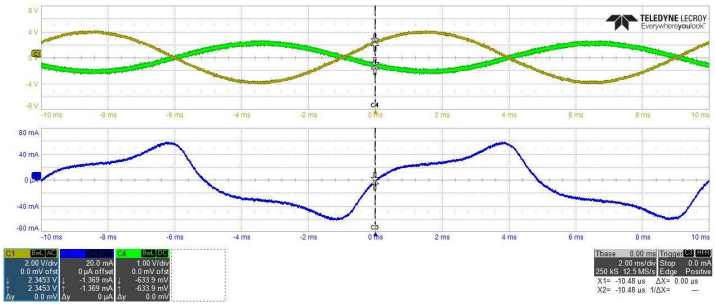

(a) B_{fund} = 1.0 T, f_{fund} = 100 Hz (**With** iterative learning control)

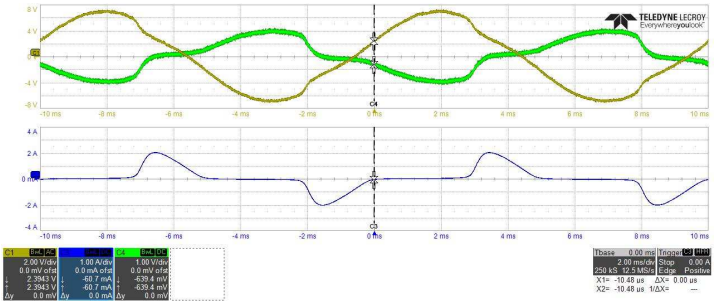

(b) B_{fund} = 1.6 T, f_{fund} = 100 Hz (**Without** iterative learning control)

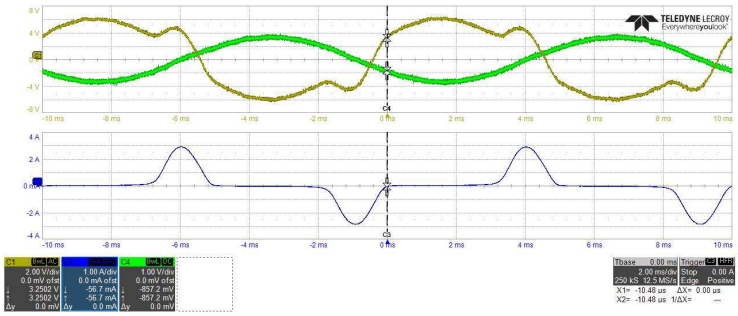

(c) B_{fund} = 1.6 T, f_{fund} = 100 Hz (**With** iterative learning control)

Legend:

Toroidal core primary winding input voltage waveform after the low-pass *L*-*C* filter

Toroidal core sense winding voltage waveform

Toroidal core primary winding current waveform

Figure 3-9: Example primary and sensing winding waveforms over different material saturation conditions with and without implementing the iterative learning control.

high waveform quality. Figure 3-9(c) shows that the iterative learning control algorithm is effective for delivering the appropriately-shaped non-sinusoidal input primary winding current waveform that is needed to generate the desired sinusoidal sense winding voltage. To date, the maximum fundamental frequency has been successfully extended to 1 kHz, and the collected dynamic hysteresis loop data over a broad frequency range will subsequently be utilized to characterize the proposed dynamic hysteresis model.

In addition to the sinusoidal flux waveforms, the availability of the flux waveshape regulation control system makes it possible to explore the magnetic characteristics of the complex flux waveforms containing higher order harmonic components or the flux waveforms influenced by the external dc-bias fields, which lays a solid foundation for iron loss investigation.

As discussed in the preceding chapter, the measurement system is capable of separating the iron loss from the copper loss in the primary winding by integrating the product of primary winding current and sensing winding voltage as:

$$\overline{P_{\text{iron}}} = \frac{N_{\text{main}}}{N_{\text{sense}}} \int_0^T V_{\text{sense}} I_{\text{main}} \cdot dt \tag{3-11}$$

where T is the time period of the alternating flux waveform.

Furthermore, expressing the sensing voltage and primary current in terms of the magnetic flux density and magnetic field strength gives an equivalent expression of iron loss:

$$\overline{P_{\text{iron}}} = V_{\text{core}} \frac{1}{T} \int_0^T H \frac{dB}{dt} \cdot dt \tag{3-12}$$

where V_{core} is the total volume of the toroidal core.

3.2.2 Hysteresis Loop and Iron Loss Data at Low-Frequency Range

Figure 3-10 depicts the measured dc *B-H* curve identified from a group of symmetrical hysteresis loops under low excitation frequency (i.e., f_{fund} = 10 Hz) using the test configuration A overlaid with the data provided by the steel manufacturer. The great agreement between the test results and *B-H* provided steel manufacturer confirms the validity of the proposed measurement system.

Moreover, using the material's *B-H* curve shown in Figure 3-10, the corresponding dc-bias field B_{dc} can be generated in the test core based on the supplied dc magnetic field strength H_{dc} given in (3-13), enabling the iron loss evaluation in the presence of dc-bias fields.

Similar to the symmetrical hysteresis loop measurement, flux waveshape regulation control is needed to guarantee the desired flux waveshape (e.g., sinusoidal shape).

$$H_{\text{dc}} = \frac{I_{\text{dc}} N_{\text{dc}}}{l_{\text{core}}} \tag{3-13}$$

where I_{dc} is the constant excitation current provided by the dc current source (See Figure 3-1), and N_{dc} is the number of turns in the dc winding.

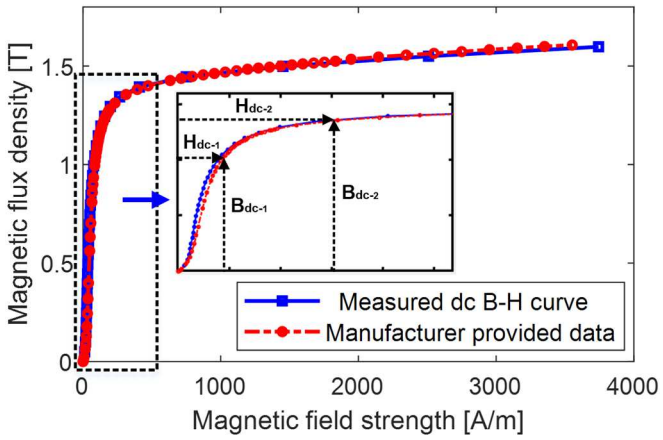

Figure 3-10: Measured and steel manufacturer provided dc *B-H* curve of lamination steels used in Table 3-1.

Next, the developed measurement system is applied to characterize the material's magnetic and iron loss properties over varying excitation frequencies (i.e., f_{fund} = 30, 100, and 200 Hz) and ac flux density amplitudes (i.e., B_{fund} = 0.6, 1.2, and 1.5 T). As presented in Figure 3-11, the areas of dynamic hysteresis loops at varying flux amplitudes expand as the frequency goes up, and in turn, yield much larger iron loss per re-magnetization cycle (i.e., P_{iron}/f). The identified iron losses from the measured dynamic hysteresis loops are subsequently compared to the iron loss data from the steel manufacturer. The excellent agreement in Figure 3-12 again validates the measurement system's accuracy.

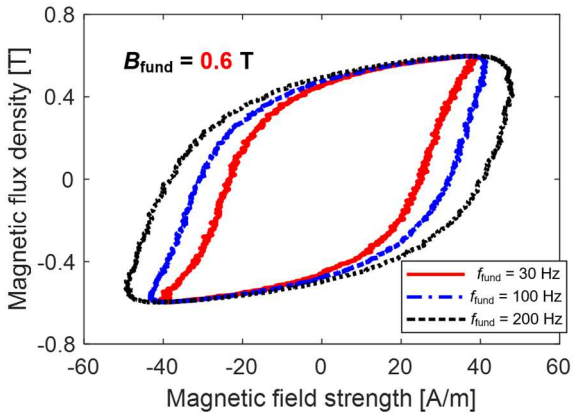

(a) AC flux density amplitude B_{fund} = 0.6 T

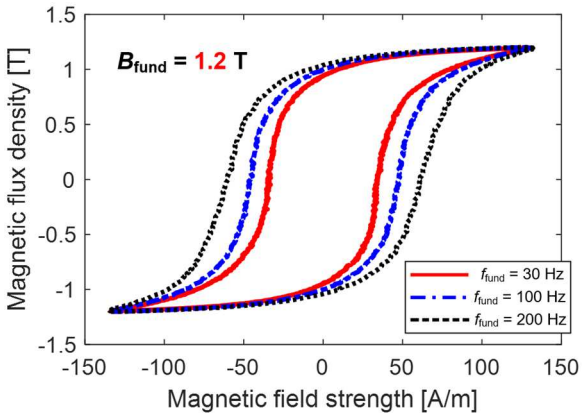

(b) AC flux density amplitude B_{fund} = 1.2 T

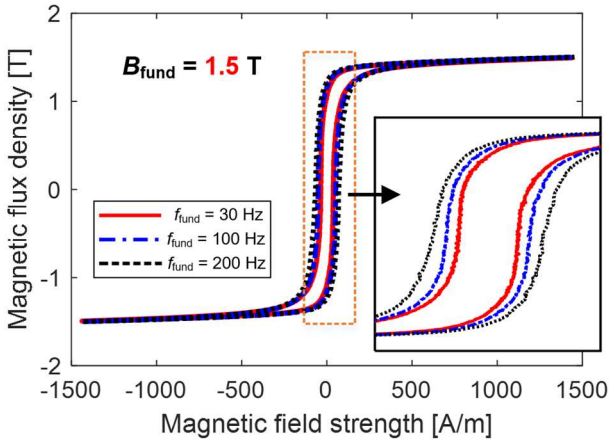

(c) AC flux density amplitude B_{fund} = 1.5 T

Figure 3-11: Measured dynamic hysteresis loops over varying ac flux density amplitudes and excitation frequencies.

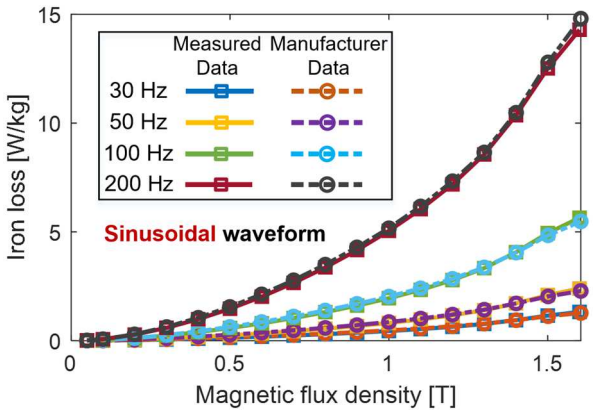

Figure 3-12: Comparison of measured and manufacturer provided iron loss results over varying ac flux density amplitudes and within low fundamental frequencies range (i.e., f_{fund} from 30 to 200 Hz) using test configuration A.

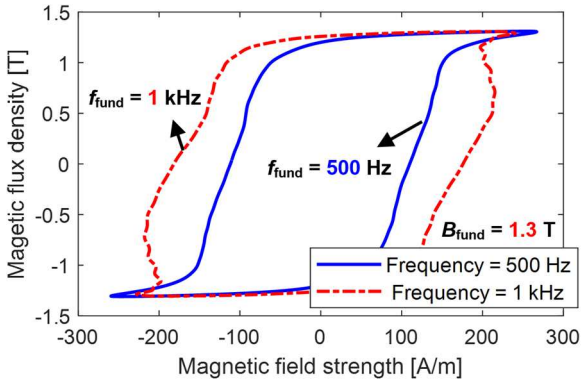

Figure 3-13: Example of measured dynamic hysteresis loops at 1.3 T for two high fundamental frequency cases using the test configuration B.

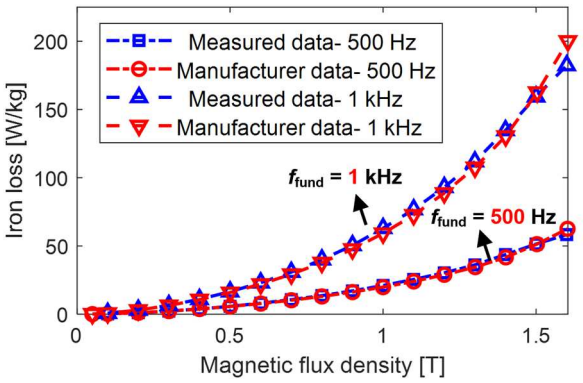

Figure 3-14: Comparison of measured iron loss results with data provided by the steel manufacturer at 500 Hz and 1 kHz over different flux density amplitudes.

Furthermore, the test configuration B (i.e., GaN-based inverter system) is applied to characterize the material's iron loss and dynamic hysteresis loop properties at high excitation frequencies and varying ac flux density amplitudes. As presented in Figure 3-13, with a selected magnetic field amplitude B_{fund} at 1.3 T, the enclosed area (i.e., energy loss per cycle) of dynamic hysteresis loops expands substantially as the excitation frequency goes up, indicating that the dynamic eddy current loss becomes more dominant at higher frequencies.

Similarly, the collected high-frequency iron loss results have been compared to iron loss data provided by the steel manufacturer. The excellent agreement in Figure 3-14 at 500 Hz and 1 kHz builds confidence in the system's accuracy. In the next section, the measured dynamic hysteresis loops over different frequencies will be applied for model parameters identification.

3.3 Model Development

As aforementioned, the flux waveforms in IPM machines deviate from the sinusoidal shape substantially in the area of stator and rotor surfaces. Therefore, the frequency-domain iron loss estimation approach is less desirable, which cannot capture the magnetic materials' nonlinearities. Rather than linearly decompose the complex flux waveforms using the Fourier analysis, the waveform can be segregated into its major and minor loop components [30], [56] as shown in Figure 3-15, where each minor loop is influenced by a specific ac average field that is cross-coupled with the major field. However, the impact of the ac average field and dc-bias field shown in Figure 3-16 have not been compared and differentiated in the iron loss modeling.

In this section, a generalized dynamic hysteresis model is developed to emulate the shape and enclosed area of hysteresis loops over broad operating conditions, in which the total magnetic field strength is subdivided into the static and dynamic field component. Minor loop compensation method is proposed to guarantee the closure of minor loops affected by either the ac average field coupled with the major field (See Figure 3-15) or the pre-magnetized dc-bias field (See Figure 3-16). Subsequently, the impacts of these two external fields on minor loops' magnetic conditions are evaluated and compared. At last, a 2-D look-up table is built for dc-bias field correction, improving the extendability of the proposed dynamic hysteresis model.

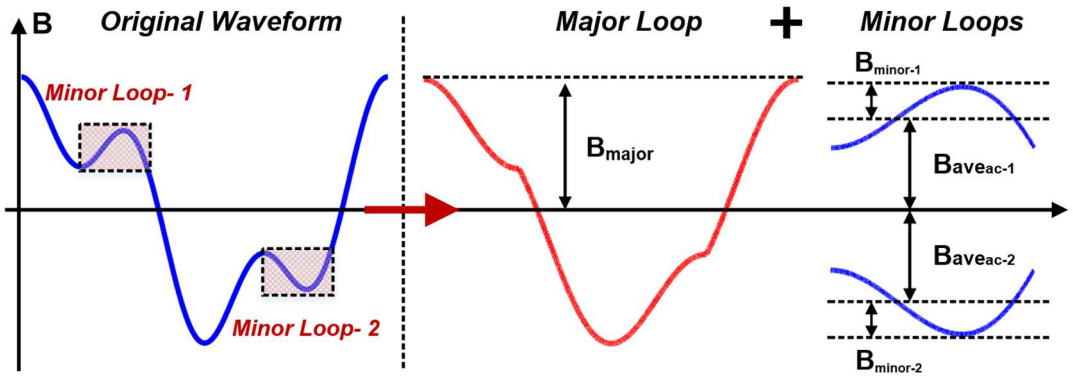

Figure 3-15: Segregation of major and minor loops affected by the ac average fields coupled with the major field.

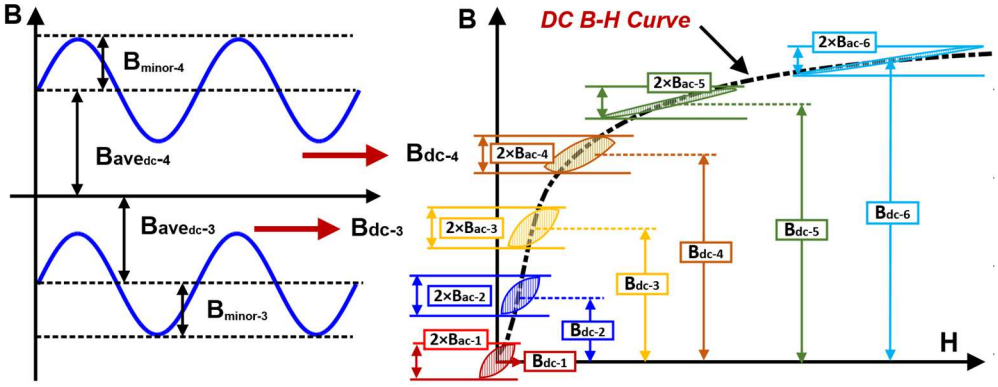

Figure 3-16: Minor loops affected by the pre-magnetized dc-bias fields.

3.3.1 Static Inverse Preisach Model

The static Preisach model [75] has been widely adopted for hysteresis loop modeling under quasi-static conditions owing to its accuracy as well as minor loops congruency. In this analysis, the static Preisach model is used in its inversed form to take the magnetic flux density B as the input variable, and the magnetic field strength H_{stat} can be calculated through a double integral

$$H_{\text{stat}}(t) = \iint_{\alpha \geq \beta} \mu(\alpha, \beta) \hat{\gamma}_{\alpha\beta}[B(t)] \cdot d\alpha d\beta \tag{3-14}$$

where α is the transition 'up' operator, β is the transition 'down' operator, $\mu(\alpha,\beta)$ is the distribution function, and $\hat{\gamma}_{\alpha\beta}[B(t)]$ is the Preisach operator.

For a complex flux waveform with multiple localized extrema shown in Figure 3-17(a), the

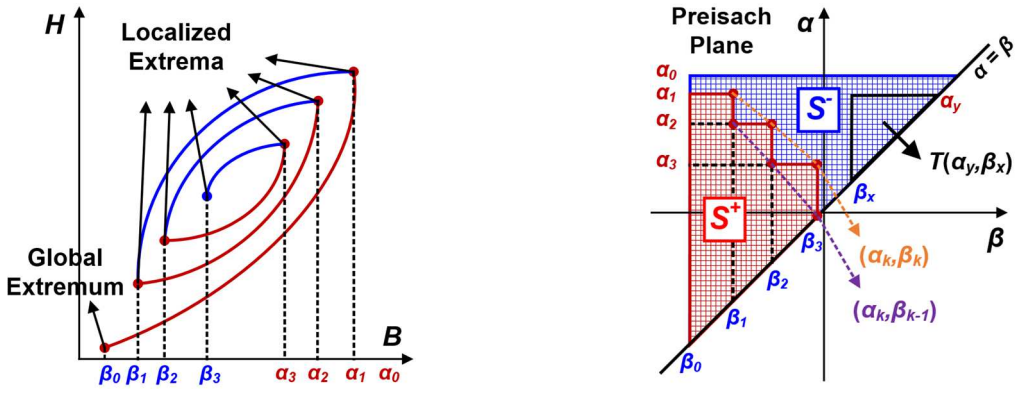

(a) (b)

Figure 3-17: (a) A complex waveform with multiple localized extrema; and (b) Geometrical interpretation of double integral process in Preisach plane.

double integral in (3-14) can be geometrically interpreted in Figure 3-17(b), where the red area S^{+} (i.e., $\hat{\gamma}_{\alpha\beta}$ = + 1) contributes to the positive value and vice versa for the S^{-1} (i.e., $\hat{\gamma}_{\alpha\beta}$ = - 1). Moreover, the area of each triangular block is determined by the distribution function $\mu(\alpha,\beta)$, giving an alternative expression of (3-14) as:

$$H_{\text{stat}}(t) = \iint_{S^{+}} \mu(\alpha,\beta)\cdot d\alpha d\beta - \iint_{S^{-}} \mu(\alpha,\beta)\cdot d\alpha d\beta \tag{3-15}$$

However, the double integral process is not computationally efficient, and instead, the Everett function [76] is commonly used to directly represent the double integral results. Taking the triangular area $T(\alpha_y,\beta_x)$ in Figure 3-17(b) as an example, the net area of this block (i.e., double integration) is expressed as:

$$E(\alpha_y,\beta_x) = \frac{1}{2}\left(H_{\alpha_y} - H_{\alpha_y\beta_x}\right) = \iint_{T(\alpha_y,\beta_x)} \mu(\alpha_y,\beta_x)\cdot d\alpha d\beta \tag{3-16}$$

$$H_{\text{stat}}(t) = -E(\alpha_0,\beta_0) + 2\sum_{k=1}^{N}[E(\alpha_k,\beta_{k-1}) - E(\alpha_k,\beta_k)] \tag{3-17}$$

where the value of Everett function over the entire Preisach plane can be experimentally identified by a group of concentric hysteresis loops [84] at a certain interval value (ΔB is maintained at 0.05 T in this analysis) up to a large magnetization state (e.g., B_{max}= 1.6 T) with low excitation frequency, α_k and β_k correspond to the localized extrema on the ascending and descending paths, respectively, and N is the number of horizontal links in the Preisach plane.

Figure 3-18 presents the value of Everett function for the non-oriented lamination steel described in Table 3-1. Although the identified Everett function is intrinsically discretized by the selected flux density interval ΔB, this limitation can be easily addressed by 2-D interpolation, making it possible to determine the value of Everett function for an arbitrary operating point within the characterized Preisach plane.

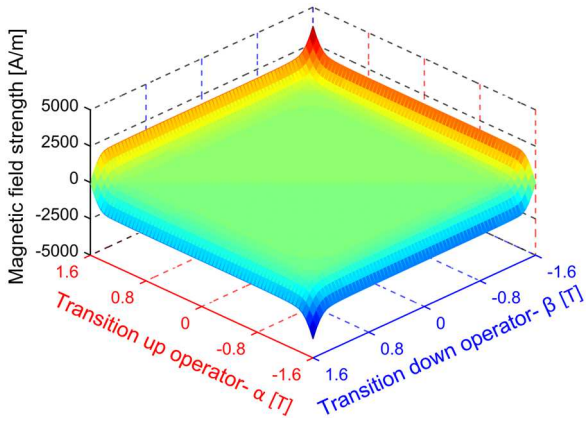

Figure 3-18: Parameters of inverse static Preisach model- Everett function.

3.3.2 Generalized Dynamic Field Modeling

Subtracting the static loop component H_{stat} either from the measured data or the predicted values of static Preisach model, the dynamic field H_{dyn} can be segregated sequentially from the total magnetic field H_{tot},

$$H_{\mathrm{dyn}}(t) = H_{\mathrm{tot}}(t) - H_{\mathrm{stat}}(t) \tag{3-18}$$

Conventionally, on the basis of statistical theory [39], the dynamic field is represented by the fields induced by the classical eddy-current loss H_{cl} and anomalous loss H_{ano},

$$H_{\mathrm{dyn}}(t) = H_{\mathrm{cl}}(t) + H_{\mathrm{ano}}(t) = C_{\mathrm{cl}}\delta\left|\frac{dB(t)}{dt}\right|^{v} + C_{\mathrm{ano}}\delta\left|\frac{dB(t)}{dt}\right|^{1/2} \tag{3-19}$$

where $C_{cl} = d^2/12\rho$ is derived analytically under the linear material and uniform flux distribution assumptions, v equals to 1, d is the thickness of lamination sheet, ρ is the material's resistivity, δ is the sign of $dB(t)/dt$, and C_{ano} is the parameter which fitted through the experimental data.

To achieve a better match with the experimental results, a modified approach is available [100] to enforce the v as a function of instantaneous magnetic flux density B(t) and predefined material saturation state B_{sat},

$$v\big(B(t)\big) = a_0 + a_1\delta\left(\frac{B(t)}{B_{\mathrm{sat}}}\right) + a_2\left(\frac{B(t)}{B_{\mathrm{sat}}}\right)^2 \tag{3-20}$$

where all the coefficients including C_{cl}, C_{ano}, a_0, a_1, and a_2 are fitted experimentally by the sinusoidal waveforms with large amplitude (e.g., B_{fund} = 1.5 T) and different excitation frequencies.

However, the model lacks generality in terms of modeling the flux waveforms with different amplitudes (e.g., B_{fund} < 1 T), multiple localized extrema (e.g., Figure 3-17(a)), or minor loops influenced by the external fields (e.g., Figure 3-15 and Figure 3-16). Therefore, a more general hypothesis is developed to describe the dynamic field, incorporating the impact of flux density changing rate *dB/dt*, instantaneous magnetization state $B(t)$, and magnetic history of flux waveform B_{hist} which defined by the previous extreme values (either the global or localized extreme values) that consistent with the Preisach plane,

$$H_{\mathrm{dyn}}(t) = g\left(\frac{dB(t)}{dt}, B(t), B_{\mathrm{hist}}\right) \tag{3-21}$$

where *g* is a hypothetical model that is sufficiently generalized to describe the dynamic hysteresis phenomenon.

Due to the complex microscopic structures of the ferromagnetic materials [20], exact modeling of energy loss caused by domain wall motions remains unrealistic. Therefore, imitating the basic structure of the Preisach model, two dynamic field modeling approaches are proposed in this research analysis, with different interpretations of the dynamic magnetic field phenomena.

3.3.2.1 Time-Derivative Dynamic Field Modeling

First, a second-order polynomial expression is employed to uniquely define the time-derivative of discretized dynamic field strength $\Delta H_{dyn}/\Delta t$ expressed by:

$$\begin{aligned}\frac{\Delta H_{\mathrm{dyn}}}{\Delta t} = {} & k_0(B_{\mathrm{inst}}, B_{\mathrm{hist}}) + k_1(B_{\mathrm{inst}}, B_{\mathrm{hist}})\frac{\Delta B}{\Delta t} \\ & + k_2(B_{\mathrm{inst}}, B_{\mathrm{hist}})\delta\left|\frac{\Delta B}{\Delta t}\right|^2\end{aligned} \tag{3-22}$$

where B_{hist} represents the discretized form of instantaneous flux density expressed by:

$$\begin{cases} \text{if } dB/dt \geq 0, B_{\text{hist}} = \Delta B \times \lceil B(t)/\Delta B \rceil \\ \text{if } dB/dt < 0, B_{\text{hist}} = \Delta B \times \lfloor B(t)/\Delta B \rfloor \end{cases} \quad (3\text{-}23)$$

The dynamic model parameters in (3-22) including k_0, k_1, and k_2 are determined by the concentric hysteresis loops in sinusoidal shape over varying frequencies (see Figure 3-11 and Figure 3-13) with the flux density inverter ΔB at 0.05 T, and the amplitude of each symmetrical hysteresis loop defines its corresponding magnetic history. Owing to the symmetry in the ascending and descending path, either one can be utilized for model characterization. Considering the descending path of flux waveform at 1.3 T and 100 Hz as an example, the discretized hysteresis loop after linearization is presented in Figure 3-19, where the total field variation in each discretized segment can be identified. Since the sinusoidal flux waveforms are used for parameters identification, the time interval Δt for a given flux density interval ΔB varies with the value of instantaneous flux density amplitude. Therefore, as shown in Figure 3-20, similar discretization technique is employed to determine the time interval of each linearized segment over the entire analyzed waveform.

Figure 3-21 shows the discretized magnetic flux waveforms over varying excitation frequencies from 10 to 200 Hz at 1.3 T, and the waveform measured at 10 Hz is approximated as the static reference case. As can be seen from the different zoom-in regions with the same magnetic history, the total magnetic field strength changes with the frequency, indicating the substantial variations of dynamic fields with different instantaneous flux amplitudes. Subtracting the static value ΔH_{stat} (i.e., ΔH_{tot} at 10 Hz) from the total field change ΔH_{tot} in each region gives the value of discretized dynamic field ΔH_{dyn}, and the generalized expression is given by:

$$\Delta H_{\text{dyn}}(B_{\text{hist}}, B_{\text{inst}}, \Delta B, \Delta t) = \Delta H_{\text{tot}}(B_{\text{hist}}, B_{\text{inst}}, \Delta B, \Delta t) - \Delta H_{\text{stat}}(B_{\text{hist}}, B_{\text{inst}}, \Delta B) \quad (3\text{-}24)$$

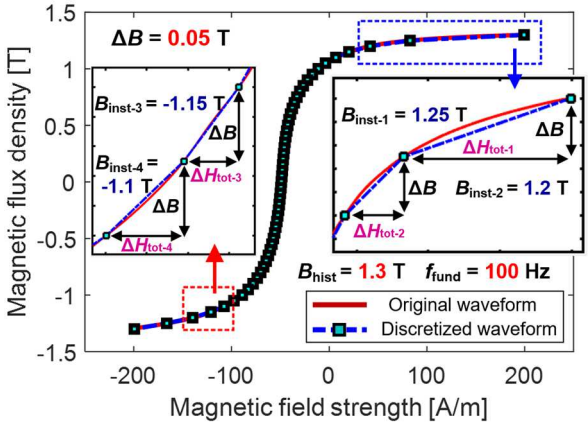

Figure 3-19: Discretized flux waveform at 1.3 T B_{hist} and 100 Hz f_{fund} with ΔB = 0.05 T for total field strength identification in each segment.

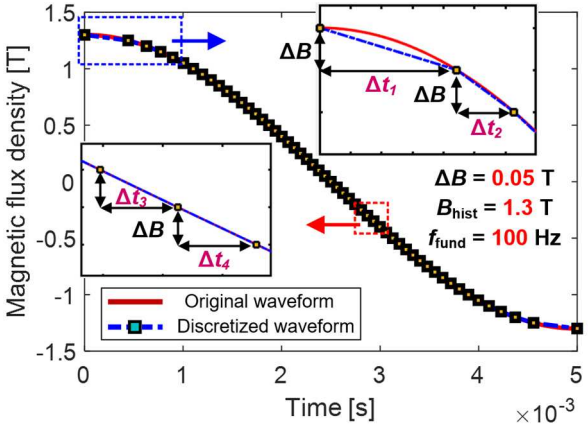

Figure 3-20: Time-domain discretized flux waveform at 1.3 T B_{hist} and 100 Hz f_{fund} with ΔB = 0.05 T for time interval identification in each segment.

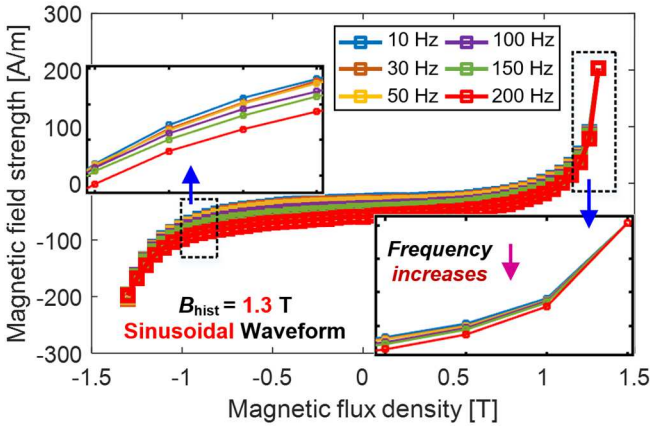

Figure 3-21: Discretized magnetic flux waveforms at 1.3 T B_{hist} for six excitation frequencies f_{fund} from 10 Hz (approximated as the static reference case) to 200 Hz.

The measured data calculated from (3-24) can be subsequently used to identify the coefficients in (3-22) via the polynomial least squares fitting process. Since the beginning and end regions of ascending/descending path typically experience the most significant magnetic field variations over the entire path, comparison of the measured and fitted time-derivative dynamic field strengths over varying time-derivative of magnetic flux density for first and last two discretized segments are presented in Figure 3-22(a)-(b) and Figure 3-22(c)-(d), with the magnetic history B_{hist} at 0.6 and 1.3 T, respectively. Generally, the fitted data using the second-order polynomial equation provide a great emulation of dynamic magnetic field strengths over varying magnetization states and flux density changing rates. Also, it clearly indicates that three basic variables in adopted in (3-21) are all critical and essential to adequately define an operating condition of a discretized field segment.

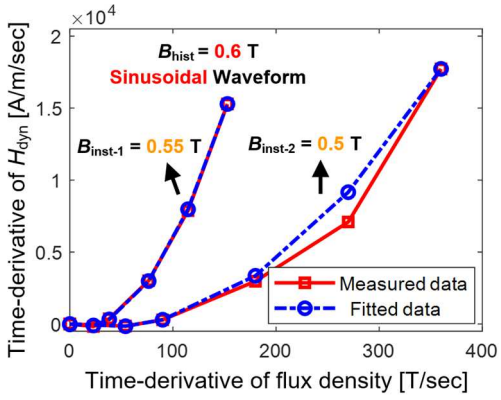

(a) B_{hist} = 0.6 T, B_{inst} = 0.55 and 0.5 T

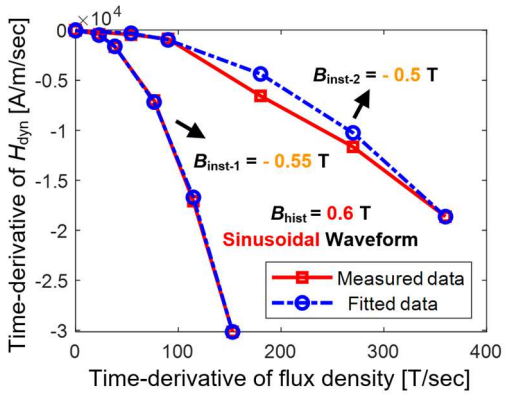

(b) B_{hist} = 0.6 T, B_{inst} = - 0.55 and - 0.5 T

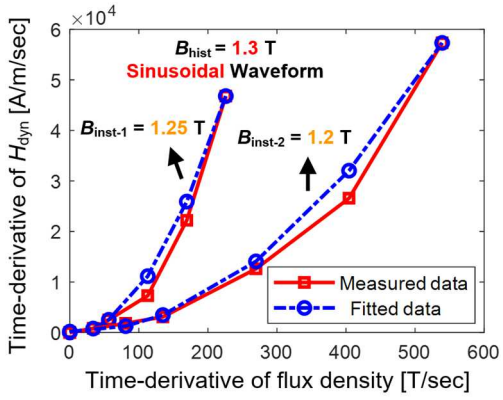

(c) B_{hist} = 1.3 T, B_{inst} = 1.25 and 1.2 T

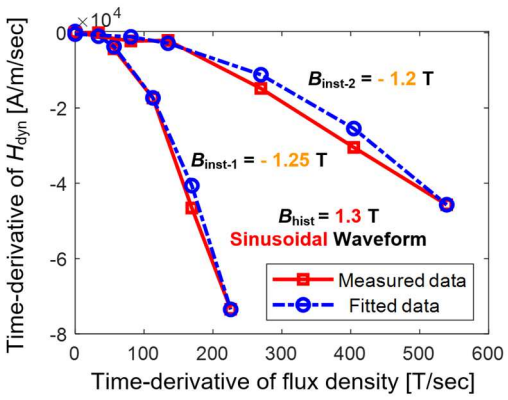

(d) B_{hist} = 1.3 T, B_{inst} = -1.25 and -1.2 T

Figure 3-22: Comparison of measured and fitted discretized dynamic field strengths over varying time-derivative of flux density for first and last two segments with magnetic history B_{hist} at 0.6 T and 1.3 T.

However, the discretized waveform in Figure 3-19 deviates noticeably from the original waveform near the beginning and end of the studied hysteresis loop, making it necessary to decrease the value of flux density interval. Rather than increase the measured cases and add extra burdens to material characterization, the linear interpolation technique presented in Figure 3-23(a) is employed while keeping the original flux density interval unchanged (i.e., $\Delta B = 0.05$ T), yielding a much smaller value of $\Delta B = 0.01$ T. Comparing the discretized waveform at 1.3 T with that in Figure 3-19, the discrepancies between the discretized and original waveforms diminish significantly. Figure 3-23(b) shows the comparison of the measured hysteresis loop at 1.27 T and the interpolated hysteresis loops determined from two adjacent loops at 1.25 and 1.3 T. The good agreement confirms the sufficient accuracy of the linear interpolation.

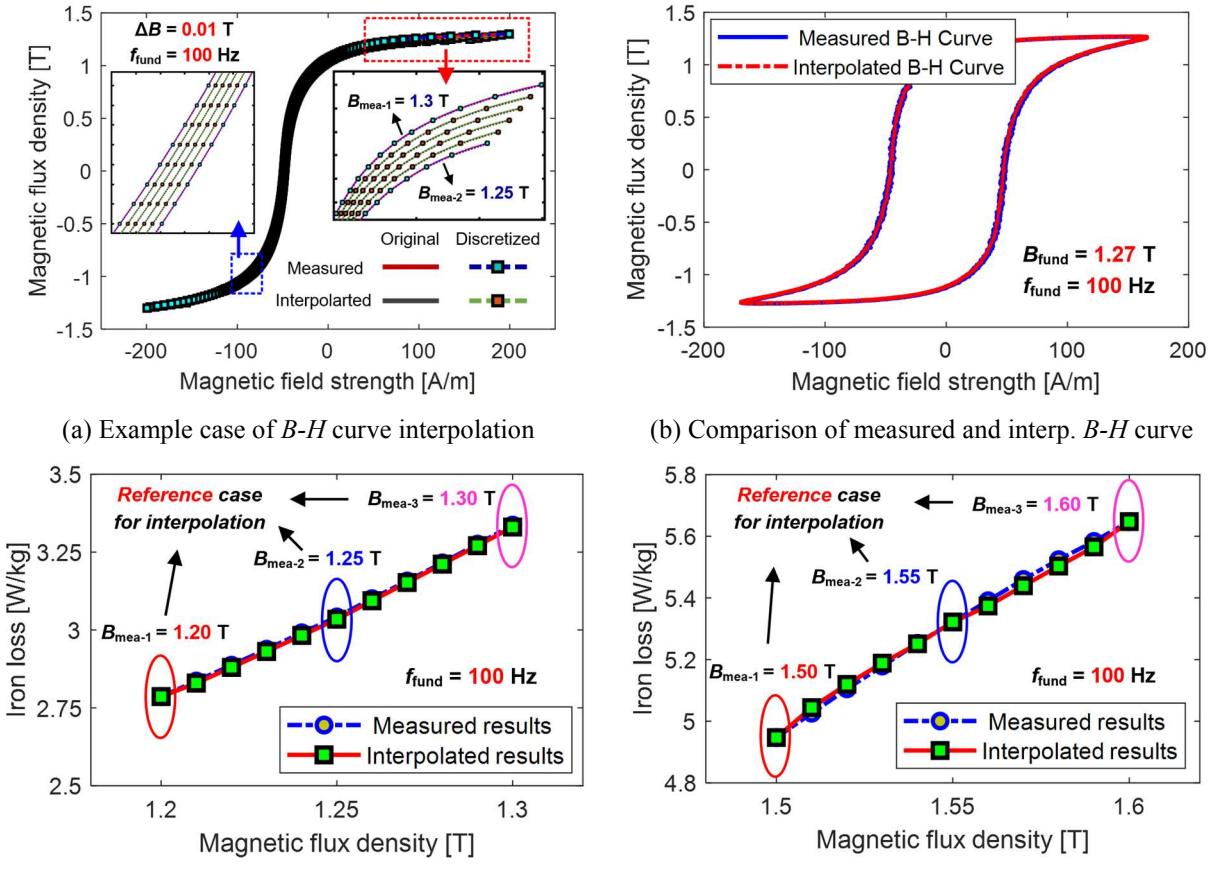

(a) Example case of *B-H* curve interpolation

(b) Comparison of measured and interp. *B-H* curve

(c) Example case- 1, B_{mea} = 1.20, 1.25, and 1.30 T

(d) Example case- 2, B_{mea} = 1.50, 1.55, and 1.60 T

Figure 3-23: Linear interpolation using the available measured hysteresis loops.

Furthermore, Figure 3-23(c) and (d) show the evaluation of the measured iron loss results and the interpolated values over two different regions of magnetic flux density. The close agreement further validates the applicability of linear interpolation on hysteresis loop generation. Therefore, this linear interpolation technique is employed to analyze and process the full range of the originally measured waveforms, providing more comprehensive hysteresis loop data for dynamic parameters characterization given in Figure 3-22.

Figure 3-24 shows the characterized dynamic model coefficients which share the same structure of static Preisach model. With the static field component estimated by (3-17), the total magnetic field strength is determined by:

$$H_{\mathrm{tot}}(t) = H_{\mathrm{stat}}(t) + \sum_{n=1}^{N_{\mathrm{seg}}} \Delta H_{\mathrm{dyn}}\left(B_{\mathrm{hist}}, B_{\mathrm{inst}_n}, \Delta B, \Delta t_n\right) \tag{3-25}$$

where N_{seg} is the number of discretized segments in the analyzed flux waveforms. If the magnetic history of analyzed waveform is in between two discretized values (e.g., B_{inst} = 1.275 T) and the waveform is not influenced by any external fields, with linear interpolation, the hysteresis loop can be determined by weighting the predicted results using two adjacent values of discretized magnetic history (i.e., B_{inst} = 1.27 and 1.28 T).

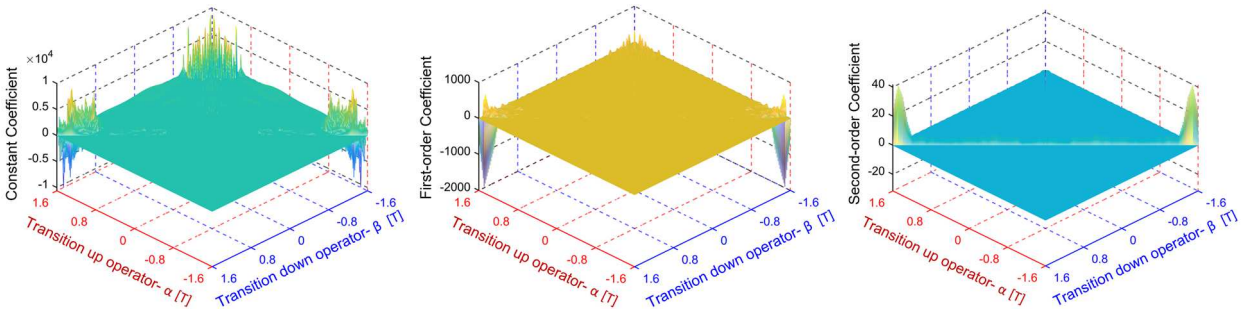

(a) (b) (c)

Figure 3-24: Characterized parameters of the proposed dynamic hysteresis model based on time derivative dynamic field $\Delta H_{\mathrm{dyn}}/\Delta t$ modeling: (a) Constant coefficient: $k_0(B_{\mathrm{inst}}, B_{\mathrm{hist}})$; (b) First-order coefficient: $k_1(B_{\mathrm{inst}}, B_{\mathrm{hist}})$; and (c) Second-order coefficient: $k_2(B_{\mathrm{inst}}, B_{\mathrm{hist}})$.

3.3.2.2 Instantaneous Dynamic Field Modeling

Although (3-22) provides a proper interpretation of the general dynamic field solution given in (3-21), it is under an intrinsic assumption that the trajectory between the instantaneous modeling point and the previous flux density reversing point (i.e., magnetic history B_{hist}) has a purely sinusoidal waveshape. Rather than estimate the $\Delta H_{\text{dyn}}/\Delta t$ rate, another possible approach is to directly model the instantaneous dynamic field H_{dyn} following the same hypothesis given in (3-21). The resulting expression is given by

$$H_{\text{dyn}} = k_0(B_{\text{inst}}, B_{\text{hist}}) + k_1(B_{\text{inst}}, B_{\text{hist}})\frac{\Delta B}{\Delta t} + k_2(B_{\text{inst}}, B_{\text{hist}}) \cdot \delta \left|\frac{\Delta B}{\Delta t}\right|^2 \tag{3-26}$$

where the magnetic history definition is the same as (3-23).

Compared to the modeling approach that calculates $\Delta H_{\text{dyn}}/\Delta t$ rate, this new model assumes that the instantaneous dynamic field H_{dyn} is not affected by the magnetic field travel trajectory between the current modeling point and the previous flux reversing point. Instead, the dynamic field solely depends on the instantaneous flux density amplitude B_{inst}, flux density reversing point B_{hist}, and time derivative of the localized flux density waveform *dB/dt*. Similarly, all the model parameters can be curve-fitted using the measured dynamic hysteresis loop data over a wide input frequency range (i.e., 10 Hz to 1 kHz), following the implementation procedure described in the preceding section. The comparison of measured and fitted dynamic field values versus the input frequency for four selected operating points are presented in Figure 3-25(a)-(d). In general, the fitted data present excellent agreement with the measured values for different magnetic history and instantaneous flux density amplitudes, confirming the validity of this approach. The characterized model parameters within the scope of this study are depicted in Figure 3-26(a)-(c).

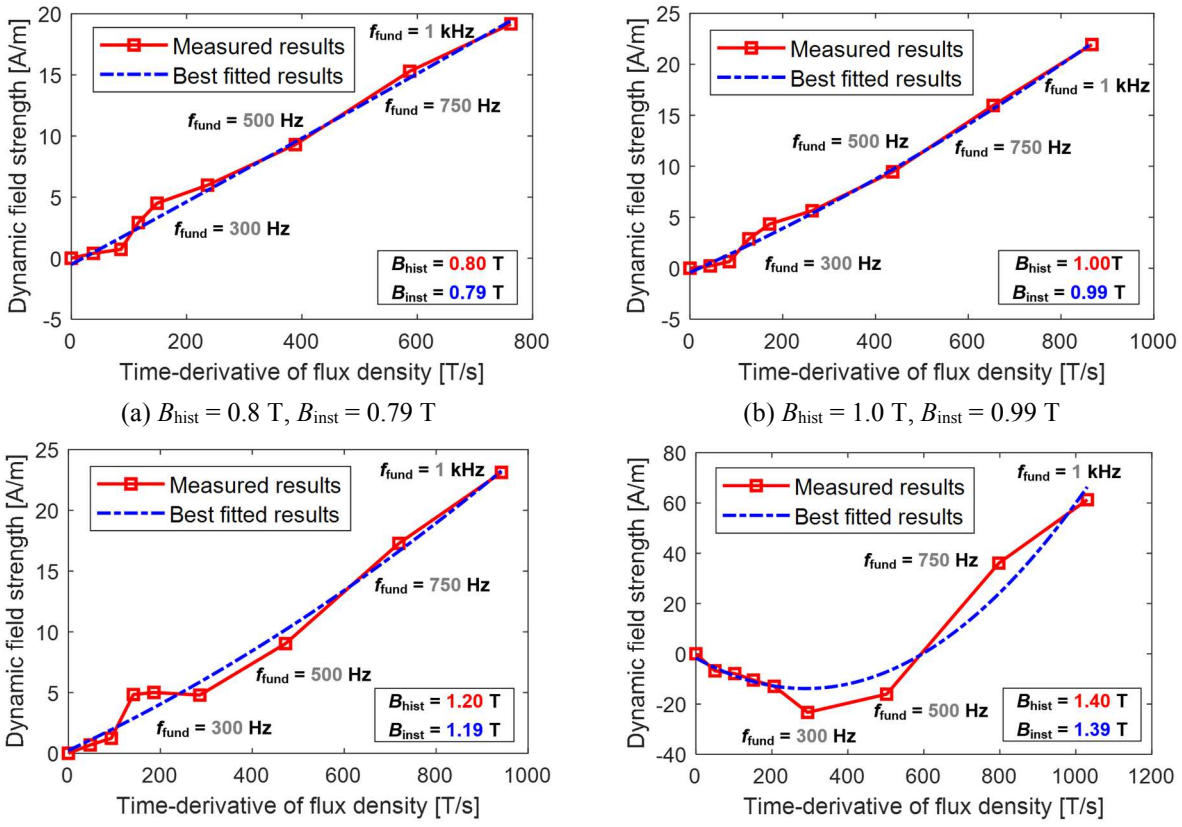

(a) B_{hist} = 0.8 T, B_{inst} = 0.79 T (b) B_{hist} = 1.0 T, B_{inst} = 0.99 T

(c) B_{hist} = 1.2 T, B_{inst} = 1.19 T (d) B_{hist} = 1.40 T, B_{inst} = 1.39 T

Figure 3-25: Comparison of measured and fitted discretized dynamic field strengths over varying time-derivative of flux density for different testing conditions based on the instantaneous dynamic field modeling approach.

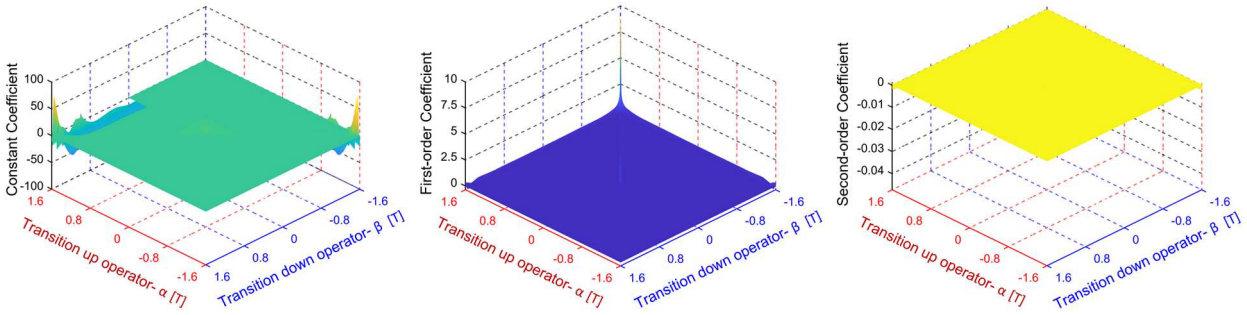

(a) (b) (c)

Figure 3-26: Characterized parameters of the proposed dynamic hysteresis model based on instantaneous dynamic field H_{dyn} modeling: (a) Constant coefficient: $k_0(B_{inst}, B_{hist})$; (b) First-order coefficient: $k_1(B_{inst}, B_{hist})$; and (c) Second-order coefficient: $k_2(B_{inst}, B_{hist})$.

Nevertheless, due to the degraded input waveform quality (i.e., higher total harmonic distortion (THD)) at higher saturation levels (i.e., input flux density amplitude B_{ac} > 1.5 T), the measured dynamic field data exhibit much larger fluctuations, making it more challenging to fit the measured

data for both dynamic field modeling approaches. Therefore, switching to a conventional iron loss model with varying coefficients [50], [56] in high-saturation regions is expected to provide more stable results. Also, since the maximum iron loss and hysteresis loop data are constrained to 1.6 T in this analysis due to instrumentation and controller limitations, conventional models based on iron loss equations according to have the advantage of working with extrapolated iron loss data for extremely high saturation levels (i.e., $B_{\mathrm{ac}} > 1.8$ T) where measured hysteresis loop data are rarely available.

$$P_{\mathrm{iron}} = k_h(B_{\mathrm{ac}})f_{\mathrm{ac}} + k_e(B_{\mathrm{ac}})f_{\mathrm{ac}}^2 \tag{3-27}$$

where k_h and k_e are the iron loss coefficients based on the flux density amplitude B_{ac}. The detailed parameter identification process can be found in [50], [56] and is not provided in this thesis.

It should be noted that the accuracy of the extrapolated data is susceptible to the order of the curve-fitting function. Typically, a higher-order polynomial function (e.g., 5$^{\mathrm{th}}$ or 7$^{\mathrm{th}}$ order) shows an advantage in matching the available measured data within the limit. However, an abrupt change might occur in the extrapolated region. Therefore, adopting a lower-order fitting function (e.g., 2$^{\mathrm{nd}}$ or 3$^{\mathrm{rd}}$ order) is expected to provide a more reasonable iron loss estimation beyond the data limit with acceptable but slightly larger discrepancies within the data limit as a side effect.

Moreover, when the input model characterization data are limited to sinusoidal flux density waveforms, neither of those two models discussed above can fully represent the dynamic field properties given the fact that magnetic history is defined as the value of the previous flux density reversing point B_{hist}. In addition to the *dB(t)/dt* rate, instantaneous field B_{inst}, and magnetic history B_{hist}, the dynamic field variation also depends on the specific flux density trajectory B_{traj} from the last magnetic history point to the current magnetic field position. Based on that, an improved dynamic field definition is proposed to be:

$$H_{\mathrm{dyn}}(t) = g(\frac{dB(t)}{dt}, B(t), B_{\mathrm{hist}}, B_{\mathrm{traj}}) \tag{3-28}$$

However, in reality, there could be an infinite number of feasible trajectories as the magnetic field moves from one point to another (e.g., sinusoidal waveform, triangular waveform, etc.), making it impractical to come up with a generalized solution of (3-28) with a limited number of input data points. Although the flux density waveforms in electric machines contain higher-order harmonics, the dominant magnetic field component is still close to the sinusoidal shape. Therefore, modeling approaches expressed in (3-22) and (3-26) are more suitable for practical applications without causing extra burdens on input data collection. The performance and accuracy of each model will be examined and compared in the next chapter.

3.3.3 Parameters Approximation and Compensation Method for Minor Loop Analysis

Unlike the Everett function identified for static Preisach model in Figure 3-18, the dynamic model coefficients contain no physical meanings and are limited to concentric hysteresis loops that are not affected by any external fields including the ac average field coupled with the major field or the pre-magnetized dc-bias field.

Figure 3-27 demonstrates the typical operating condition of a minor loop in the presence of an external field B_{ave} and with ac flux density B_{minor}. The maximum and minimum values of B_{max} and B_{min} corresponds to the magnetic history of the descending and ascending path, respectively. The dynamic model data are intrinsically applicable to the descending path. However, regarding the ascending path with magnetic history at B_{min}, the available coefficients are limited to the range of B_{min} and $-B_{\mathrm{min}}$, not covering the operating region of the analyzed waveform (i.e., from B_{min} to B_{max}).

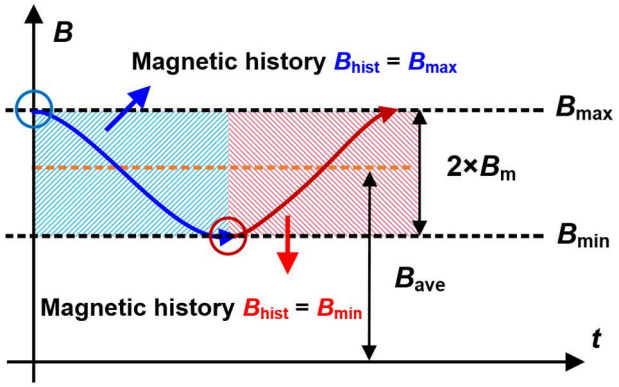

Figure 3-27: Typical operating conditions of minor loops affected by the external average fields.

This problem can be partially solved by measuring the hysteresis loops in the presence of pre-magnetized dc-bias fields. However, it also carries significant limitations for practical applications:

- The data collection process is very tedious which requires sweeping over a wide range of ac and dc flux density amplitudes for multiple excitation frequencies,
- As the number of testing conditions increases, a table containing a large number of dynamic coefficients is needed,
- This approach is based on the assumption that the impact of the ac average fields that couple with the major field and the pre-magnetized dc-bias field for minor loops are identical.

Temporarily ignoring the potential differences between the two sources of the average field, a flux waveform (1.0 T and 30 Hz) superimposed with 3rd harmonic (0.5 T), and 180 degree phase shift is generated in the toroidal core tester to evaluate the physical properties of the minor loop influenced by an external average field. The measured hysteresis loop is given in Figure 3-28.

Taking the minor loop with a positive average field as an example, the descending path of the minor loop aligns well with the major loop in the same region, indicating that the known major loop data can offer acceptable accuracy in terms of modeling the initial half path of the minor loop. On the other hand, the minor loop ascending path is consistent with the major loop when it

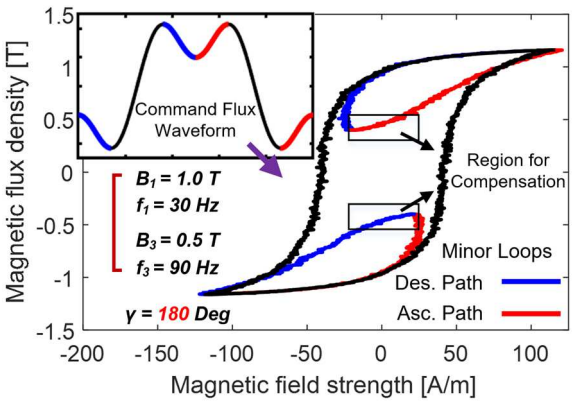

Figure 3-28: Measured hysteresis loop with superimposed minor loops.

approaches its maximum value. Therefore, the magnetic history for the ascending path can be considered the same as that of the major loop (i.e., $B_{hist} = - B_{max}$).

However, especially for the model based on $\Delta H_{dyn}/\Delta t$ rate estimation, the total dynamic field variations in each path might not be consistent in most cases, leading to non-closed minor loops. To take advantage of accurate dynamic field modeling in half of the minor loop path while guaranteeing the stability and closure of all minor loops, a special minor loop compensation method is proposed by attributing the difference of predicted dynamic field between the two paths H_{comp} to the beginning of the unknown minor loop half path, which corresponds to the ascending path for the positive average field case. The same technique is applicable to the minor loop with a negative average field where, conversely, the ascending path serves as the reference path and the compensation is made at the beginning of the descending path.

$$H_{\text{comp}} = \left| \sum_{n=1}^{N_m} \Delta H_{\text{dyn}_n}^{\text{Des.}} - \sum_{n=1}^{N_m} \Delta H_{\text{dyn}_n}^{\text{Asc.}} \right| \tag{3-29}$$

where N_m is the number of discretized segments in the descending or ascending path, and the first five segments are considered as the compensation region unless the amplitude of minor loop is smaller than 0.05 T.

In contrast, the model based on instantaneous dynamic field modeling is expected to provide a smaller discrepancy between the ascending and the descending path as the *dB/dt* rate shrinks to zero near the starting and ending regions of minor loops, ensuring the convergence of the predicted minor loops.

In summary, the availability of the proposed compensation technique makes it possible to predict the minor hysteresis loops for broad operating conditions, and more experimental results are presented and discussed in the next chapter to evaluate the model performance and accuracy.

3.3.4 2-D Look-Up Table for DC-Bias Field Correction

As discussed above, an external average field B_{ave} can be generated by either the ac average field or dc-bias field. Although the proposed dynamic hysteresis model applies to either one, it is natural that the model characterized by ac symmetrical hysteresis loops is preferable in terms of modeling the minor loop affected by the ac average field. Therefore, in this section, the influence of each average field on minor loops' magnetic conditions are experimentally investigated.

The dc-bias field can be created by the dc winding current from (3-13) and interpolated correspondingly from the dc *B-H* curve given in Figure 3-10. To secure the desired waveshape of the testing waveform, the flux waveshape regulation control is employed when the minor loops are affected by the dc-bias fields.

On the other hand, to emulate the magnetic conditions of minor loops affected by the ac average field, a fundamental field is superimposed with a 3rd harmonic field with 180 degree phase shift. As a result, two minor loops can be generated on the top and bottom region of the combined flux waveform, and each minor loop is affected by the same ac average field.

$$B(t) = B_1 \cos(2\pi f_1 t) + B_3 \cos(2\pi f_3 t + \pi) \tag{3-30}$$

where B_x and f_x are the ac flux amplitude and frequency of *x*-order component, respectively.

Taking the time-derivative on both sides of (3-30) gives

$$\frac{dB(t)}{dt} = -2\pi f_1 B_1 \sin(2\pi f_1 t) - 2\pi f_3 B_3 \sin(2\pi f_3 t + \pi) \tag{3-31}$$

To identify the flux density reversing points in the flux waveform, the *dB(t)/dt* on the left side is set to zero, and then (3-31) is simplified into:

$$0 = -2\pi f_1 B_1 \sin(2\pi f_1 t) - 2\pi f_3 B_3 \sin(2\pi f_3 t + \pi) \tag{3-32}$$

$$B_1 \sin(2\pi f_1 t) = 3B_3 \sin(2\pi f_3 t) \tag{3-33}$$

If we define:

$$x = 2\pi f_1 t \tag{3-34}$$

Then (3-34) reduces to:

$$B_1 \sin(x) = 3B_3 \sin(3x) \tag{3-35}$$

Representing sin(3x) in terms of sin(x) results in:

$$\sin(3x) = 3\sin(x) - 4\sin^3(x) \tag{3-36}$$

$$B_1 \sin(x) = 3B_3(3\sin(x) - 4\sin^3(x)) \tag{3-37}$$

Dividing both sides of (3-37) by sin(x) leads to:

$$B_1 = 9B_3 - 12\sin^2(x) \tag{3-38}$$

$$x = \pm \sin^{-1}\left(\sqrt{\frac{3}{4} - \frac{B_1}{12B_3}}\right) \tag{3-39}$$

Note that x at either 0 or π are two universal solutions of (3-37).

It is clear from (3-39) that the minor loops exist if $B_1/B_3 \leq 9$.

Assume $B_1/B_3 \leq 9$, there are six potential solutions over one fundamental cycle for (3-37). including two universal solutions at 0 and π. These six solutions are corresponding to the peak points of two minor loops- either at the top or bottom region of the analyzed flux waveform. Owing to the symmetry of two minor loops, only the one with the positive average value is considered.

Define the first solution of (3-39) over 0 to 2π as:

$$x_1 = \sin^{-1}\left(\sqrt{\frac{3}{4} - \frac{B_1}{12B_3}}\right), x_1 \le \frac{\pi}{2} \tag{3-40}$$

For the minor loop with positive average value, the minor loop ac flux amplitude B_{minor} and the average field B_{ave} can be calculated by (3-41) and (3-42), respectively,

$$\begin{aligned} B_{\text{minor}} &= \frac{1}{2}\left(-B(t=0) + B\left(t = \frac{x_1}{2\pi f_1}\right)\right) \\ &= \frac{1}{2}((\cos(x_1) - 1)B_1 + (1 - \cos(3x_1))B_3) \end{aligned} \tag{3-41}$$

$$\begin{aligned} B_{\text{ave}} &= \frac{1}{2}\left(B(t=0) + B\left(t = \frac{x_1}{2\pi f_1}\right)\right) \\ &= \frac{1}{2}((\cos(x_1) + 1)B_1 - (1 + \cos(3x_1))B_3) \end{aligned} \tag{3-42}$$

Cross solving (3-41) and (3-42) gives the solution of the 3rd harmonic field for a give fundamental field and a command minor loop as:

$$\begin{aligned} B_3 &= \frac{B_1}{12\lambda^2 - 3} \\ \lambda &= \frac{2B_1 + 3B_{\text{minor}} - \sqrt{6B_1B_{\text{minor}} + 9B_{\text{minor}}^2}}{2B_1} \end{aligned} \tag{3-43}$$

In addition, the resultant average field is expressed as:

$$B_{\text{ave}} = B_1\cos(x_1) - B_3\cos(3x_1) - B_{\text{minor}} \tag{3-44}$$

However, if the frequencies of the fundamental and 3rd harmonic component maintain constant, the minor loop frequency f_{minor} varies slightly with the level of the average field,

$$f_{\text{minor}} = \frac{1}{\Delta T_{\text{minor}}} = \frac{\pi}{x_1} \times f_1 \tag{3-45}$$

where ΔT_{minor} is the time span of the minor loop.

Therefore, the properties of these two sources of average field cannot be compared using the collected iron loss values due to the inconsistent excitation frequencies. Also, although the minor loops created by the superimposed ac magnetic fields are close to the sinusoidal waveform, small deviations do exist, adding additional difficulties for direct comparison. On the other hand, it has been discovered that, although the enclosed area (i.e., P_{iron}/f) of minor loop is sensitive to the excitation frequency, and flux waveshape (e.g., sinusoidal or triangular waveform), the peak-to-peak amplitude of magnetic field strength $H_{p\text{-}p}$ is primarily determined by the ac flux amplitude. As a result, by maintaining the minor loop amplitude B_{minor} identical and frequency f_{minor} in a similar range, $H_{p\text{-}p}$ is considered as the key metric to specify a unique magnetic condition and then used to differentiate two sources of the external average field.

Figure 3-29 shows the measured hysteresis loops with different amplitudes of fundamental (30 Hz) and 3rd (90 Hz) harmonic fields, and the minor loop amplitude is maintained at 0.3 T. As the amplitude of fundamental field increases, both the 3rd field component given in (3-43) and the average field from (3-44) go up correspondingly, creating different magnetic conditions of minor loops. It is clear that the shapes of minor loops vary significantly especially in the heavy saturation region, indicating that the external magnetic fields can exert significant impacts on minor loops.

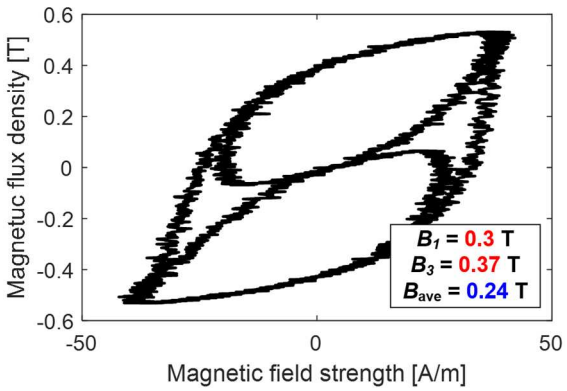

(a) B_1 = 0.3 T and B_3 = 0.37 T

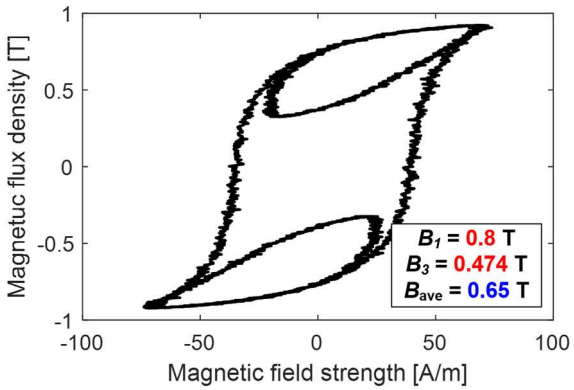

(b) B_1 = 0.8 T and B_3 = 0.474 T

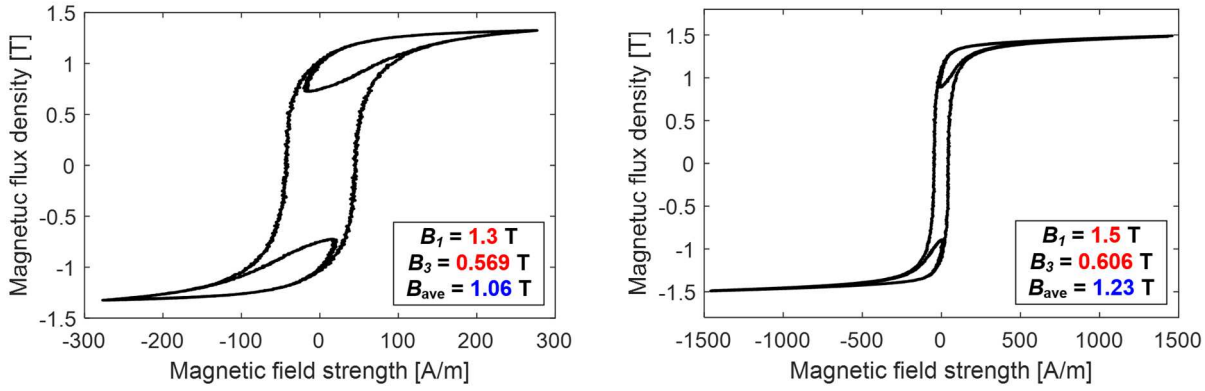

(c) B_1 = 1.3 T and B_3 = 0.569 T (d) B_1 = 1.5 T and B_3 = 0.606 T

Figure 3-29: Superimposed flux waveforms with different fundamental (30 Hz) and 3rd harmonic field (90 Hz) combinations with the induced minor loop amplitude B_{minor} at 0.3 T.

Furthermore, the minor loop of each operating condition shown in Figure 3-29 can be segregated from the total hysteresis loop, making it possible to investigate the enclosed area and the peak-to-peak magnetic field strength $H_{p\text{-}p}$ of minor loop individually. To confirm the impact of the frequency on minor loop magnetic condition, Figure 3-30 shows the variation trends of measured peak-to-peak field strengths of minor loops with three different amplitudes (i.e., B_{minor} = 0.1, 0.2 and 0.3 T) over a wide range of external average fields. For each case, the minor loops are generated with fundamental frequencies at 30 and 50 Hz. Although the fundamental frequency and the minor loop frequency increase by 80 %, the values of peak-to-peak magnetic field strength $H_{p\text{-}p}$ are not sensitive to the frequency regardless of the minor loop amplitudes. In other words, it has been verified that the peak-to-peak magnetic field strength can be used to represent the localized magnetic conditions of minor loops influenced by the external fields.

Similarly, the impact of dc-bias fields on minor loop characteristics can be evaluated and compared with the ac average fields. However, since the dc-bias field is provided by additional dc winding and not directly observable from the sensed flux waveforms, the amplitude of the dc-bias field can only be interpolated from the dc *B*-*H* curve.

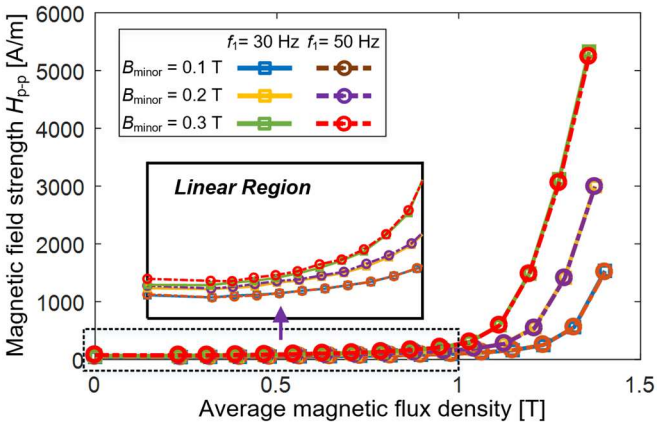

Figure 3-30: Variation trends of measured peak-to-peak magnetic field strengths of minor loops affected by the external ac average field over different amplitudes (i.e., B_{minor} = 0.1, 0.2, and 0.3 T) and frequencies.

Figure 3-31 depicts the comparison of the measured minor loops affected by two different sources of external average fields, namely, the ac average field and the dc-bias field. The excitation frequencies of the two cases are in the vicinity of 100 Hz, and the amplitudes of minor loops are kept constant at 0.3 T. Even ignoring the potential differences in the enclosed areas (i.e., iron losses), the peak-to-peak magnetic field strengths of minor loops exhibit substantial variations under the same average field level, indicating that these two average fields can exert different impacts on the magnetic conditions of minor loops. To more comprehensively investigate the differences of these two average fields, the peak-to-peak field strengths are compared with each other for four amplitudes presented in Figure 3-32, covering the small- (B_{minor} = 0.05 T), medium (B_{minor} = 0.1 and 0.15 T), and large-amplitude (B_{minor} = 0.3 T) minor loop conditions.

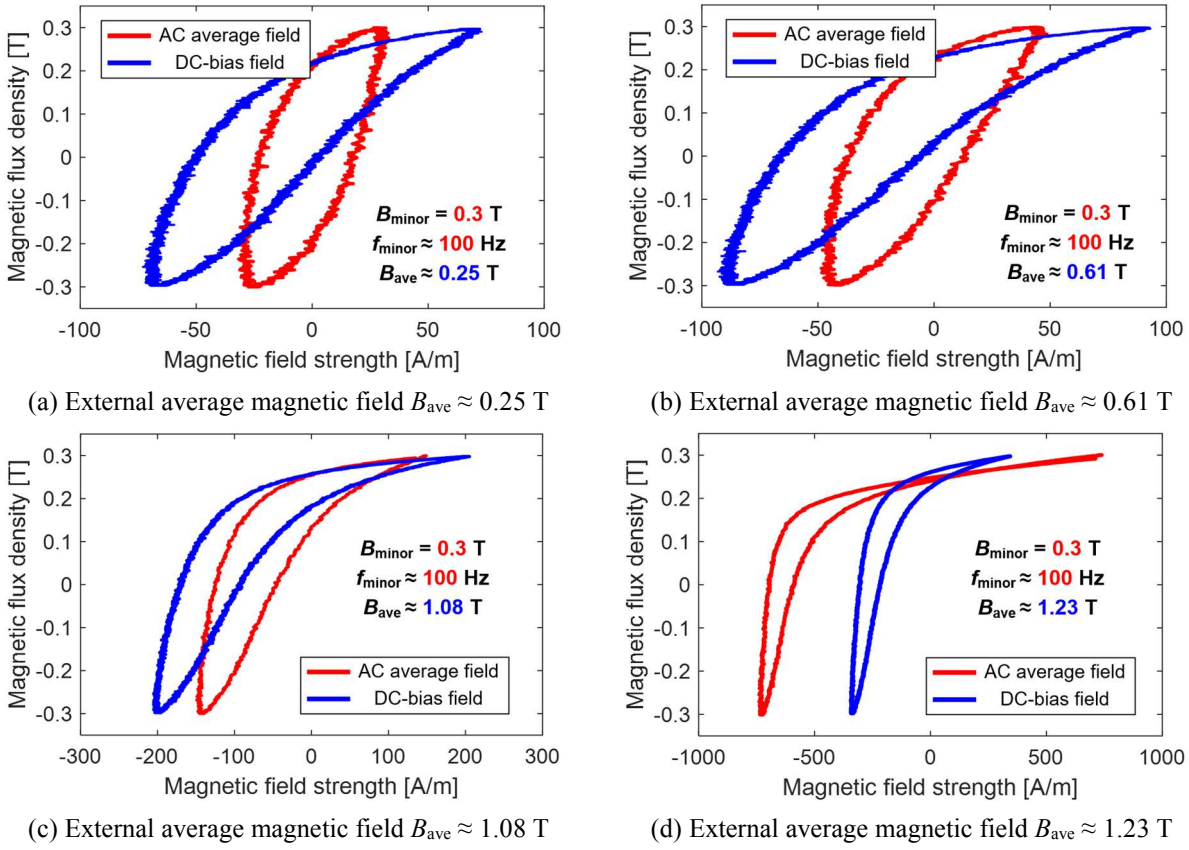

(a) External average magnetic field $B_{ave} \approx 0.25$ T

(b) External average magnetic field $B_{ave} \approx 0.61$ T

(c) External average magnetic field $B_{ave} \approx 1.08$ T

(d) External average magnetic field $B_{ave} \approx 1.23$ T

Figure 3-31: Comparison of minor loop waveshapes of two different external average fields with varying average field amplitudes and constant minor loop amplitude B_{minor} at 0.3 T.

As can be seen from all four cases, when the amplitude of the average field is relatively small (i.e., linear region), the dc-bias field exerts a more significant impact on the minor loops' magnetic conditions, demanding larger field strength to achieve the same minor loop amplitude. As the average increases and drives the material into the saturated region, different variation trends are observed. For the small-amplitude case (B_{minor} = 0.05 T or 0.1 T), a great agreement between two average fields indicates that the small-amplitude minor loop would not affect the magnetic condition. While for the minor loop with a larger amplitude- 0.3 T, much larger field strength is needed for the minor loop affected by the ac average field. In summary, as the amplitude of minor loop increases, the minor loop itself exercises a more significant influence on the magnetic condition. Therefore, it is indispensable to take into account the actual magnetization state in the minor loop iron loss modeling.

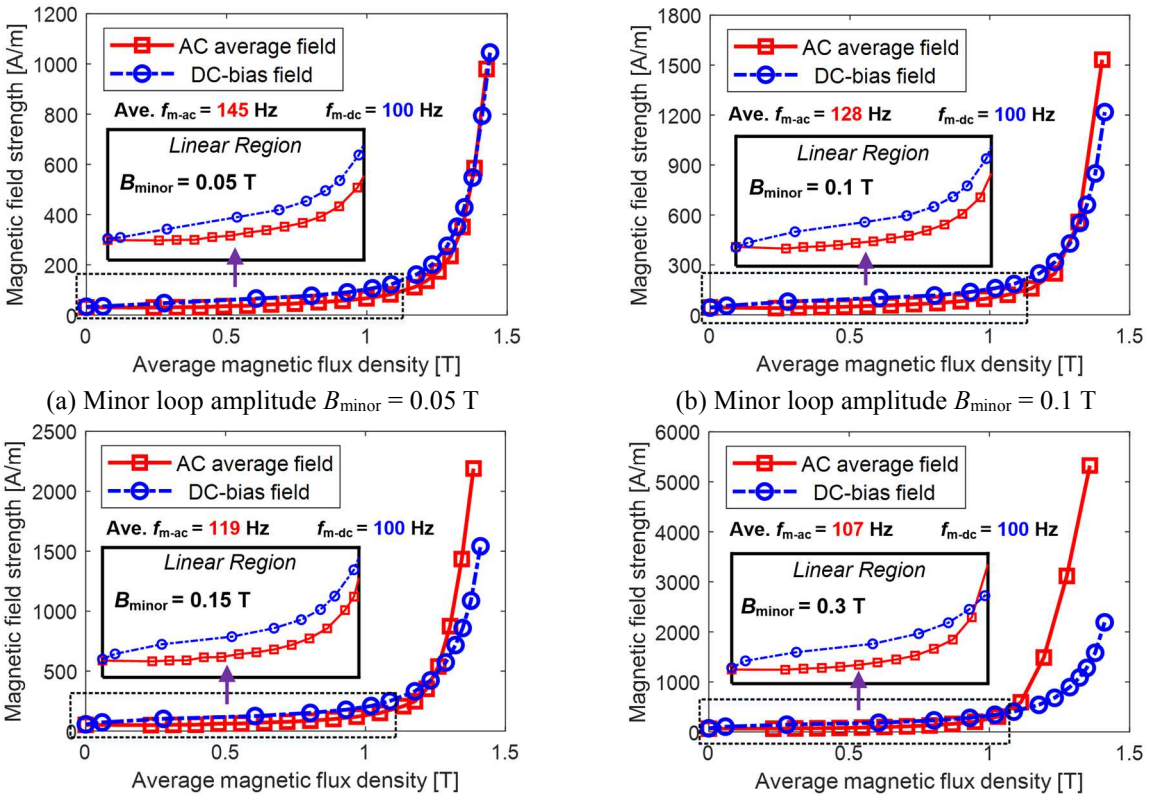

(a) Minor loop amplitude B_{minor} = 0.05 T

(b) Minor loop amplitude B_{minor} = 0.1 T

(c) Minor loop amplitude B_{minor} = 0.15 T

(d) Minor loop amplitude B_{minor} = 0.3 T

Figure 3-32: Comparison of magnetic conditions of average fields induced by the ac average field B_{ave} and the dc-bias field B_{dc} over varying minor loop amplitudes.

Since the proposed dynamic hysteresis model is developed and characterized by concentric ac hysteresis loops, the magnetic condition of the analyzed minor loop is intrinsically consistent with the ac average field rather than the dc-bias field. To determine the equivalent ac average field for a given combination of minor loop amplitude and dc-bias field, a 2-D look-up table is constructed in Figure 3-33, where the comparison presented in Figure 3-32 is conducted every 0.05 T ranging from 0.05 to 0.3 T. In the 2-D look-up table, a minor loop for each ac average field value consumes the same amount of peak-to-peak magnetic field strength $H_{p\text{-}p}$ (i.e., identical magnetic condition) as it would with the corresponding dc-bias field value. Furthermore, if the minor loop amplitude is smaller than 0.05 T, the relationship of two average fields can be assumed identical to that for the 0.05 T since the impact of a small-amplitude minor loop on magnetic condition is negligible.

Provided the minor loop amplitude falls within the characterized range (i.e., $B_{minor} < 0.3$ T), 2-D interpolation can be used to correlate ac average and dc-bias field values with a given minor loop amplitude. As a result, the minor hysteresis loop in the presence of the dc-bias field can be directly predicted using the data characterized from symmetrical hysteresis loops. Additional testing data is required if the minor loop is larger than 0.3 T.

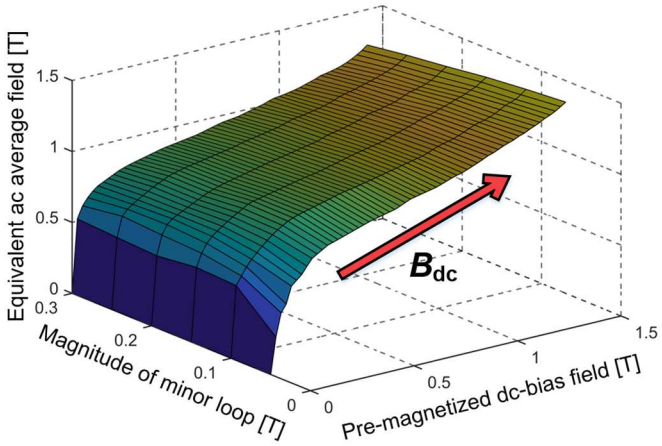

Figure 3-33: 2-D look-up table for dc-bias field correction.

3.4 Summary

In this chapter, a generalized dynamic hysteresis model has been developed for estimating the real hysteresis phenomena of complex flux density waveforms. Two versatile *B-H* measurement systems are developed to experimentally investigate the magnetic and iron loss properties of the studied soft magnetic materials over a wide range of ac and dc excitation conditions. Using the measured hysteresis loop data, two dynamic hysteresis models are proposed in this research based on a generic dynamic field solution, incorporating the impact of the magnetic flux density changing rate dB/dt, instantaneous magnetization state B_{inst}, and time history of the magnetic flux density B_{hist} on dynamic field modeling.

Furthermore, a unique minor loop compensation method is proposed to bypass the intrinsic limitation of input symmetrical hysteresis loops, making it possible to guarantee the congruency of the minor loops without conducting any additional tests involving pre-magnetized dc-bias fields.

Finally, the impacts of the ac average field and dc-bias field on the magnetic conditions of minor loops are compared and differentiated experimentally. It has been concluded that the differences between these two sources of external field are accentuated as the minor loop amplitude increases, and the relationship remains almost unchanged as the excitation frequency varies. A 2-D look-up table is proposed, serving as a useful tool to determine the equivalent ac average field based on the minor loop and dc-bias field amplitudes.

Chapter 4
Experimental Evaluation of Generalized Dynamic Hysteresis Model

4.1 Introduction

This chapter focuses on the experimental evaluation of the proposed generalized dynamic hysteresis model for the flux waveforms over varying conditions. These include the pure sinusoidal flux waveform, complex flux waveform with different orders of the harmonic field, and flux waveform influenced by the pre-magnetized dc-bias field, which to a great extent emulate the actual operating conditions of the flux waveform in IPM machines. In addition, the flux waveforms in the different regions of the studied IPM machines designed for traction applications are predicted by 2-D FEA and subsequently synthesized in the toroidal core iron loss tester, building confidence in the usefulness of the proposed model for machine-level iron loss investigation.

4.2 Pure Sinusoidal Flux Waveform

For typical three-phase electric machine applications (e.g., induction or synchronous machines), the sinusoidal current waveform is fed to each phase to deliver constant output torque/power. Even though the flux waveforms deviate from the pure sinusoidal shape due to the magnetic saturation, the flux waveforms are intrinsically close to the sinusoidal shape for a bigger portion of the electric machines. Therefore, the performance of the proposed model is first evaluated using the sinewaves.

As demonstrated in the preceding chapter, the input data of the proposed hysteresis model is the measured dynamic hysteresis loops over varying excitation frequencies. Nevertheless, after the linearization process presented in Figure 3-19, the input waveforms are transformed into multiple

discretized segments for parameters characterization. Furthermore, even for sinewave prediction, the input waveform is first represented by a set of discretized components with the same amplitude ΔB at 0.01 T, and the magnetic field strength of each part is predicted individually.

Figure 4-1(a)-(d) presents the comparison of predicted and measured dynamic hysteresis loops using $\Delta H_{dyn}/\Delta t$-based dynamic hysteresis model over a variety of magnetic conditions, including 0.5 T (i.e., linear region), 1.0, 1.2 T (i.e., intermediate region), and 1.5 T (i.e., saturated region). For each flux density amplitude, tests have been conducted to sweep over three frequency levels (i.e., 200 Hz, 500 Hz, and 1 kHz). Overall, the proposed model has exhibited excellent capability for estimating the dynamic hysteresis loops over different flux density amplitudes and excitation frequencies, where the hysteresis loop expansions (i.e., iron loss increase per cycle) and the dynamic field induced losses are accurately modeled. Small discrepancies are observed when the excitation frequency is at 1 kHz, mainly due to degraded input data quality at that frequency case.

For the large amplitude waveform, Figure 4-1(d), it is the magnetic field strength in the knee region that experiences the most significant variation at higher frequencies. In contrast, both the shape and enclosed area in the heavy saturation region are less sensitive to the excitation frequency. Next, the same analysis is conducted by using the H_{dyn}-based dynamic hysteresis model, where the instantaneous dynamic field strength is model directly. As the results given in Figure 4-2(a)-(d), H_{dyn}-based also exhibits very promising capability in modeling dynamic hysteresis loop with sinusoidal flux density excitation over broad testing conditions. However, since both models are fed with sinusoidal input waveforms for parameter characterization, the good match between the predicted and measured data only confirms that the proposed polynomial equation can emulate the dynamic field properties with sinusoidal input in different magnetic flux density amplitudes over the studied frequency range.

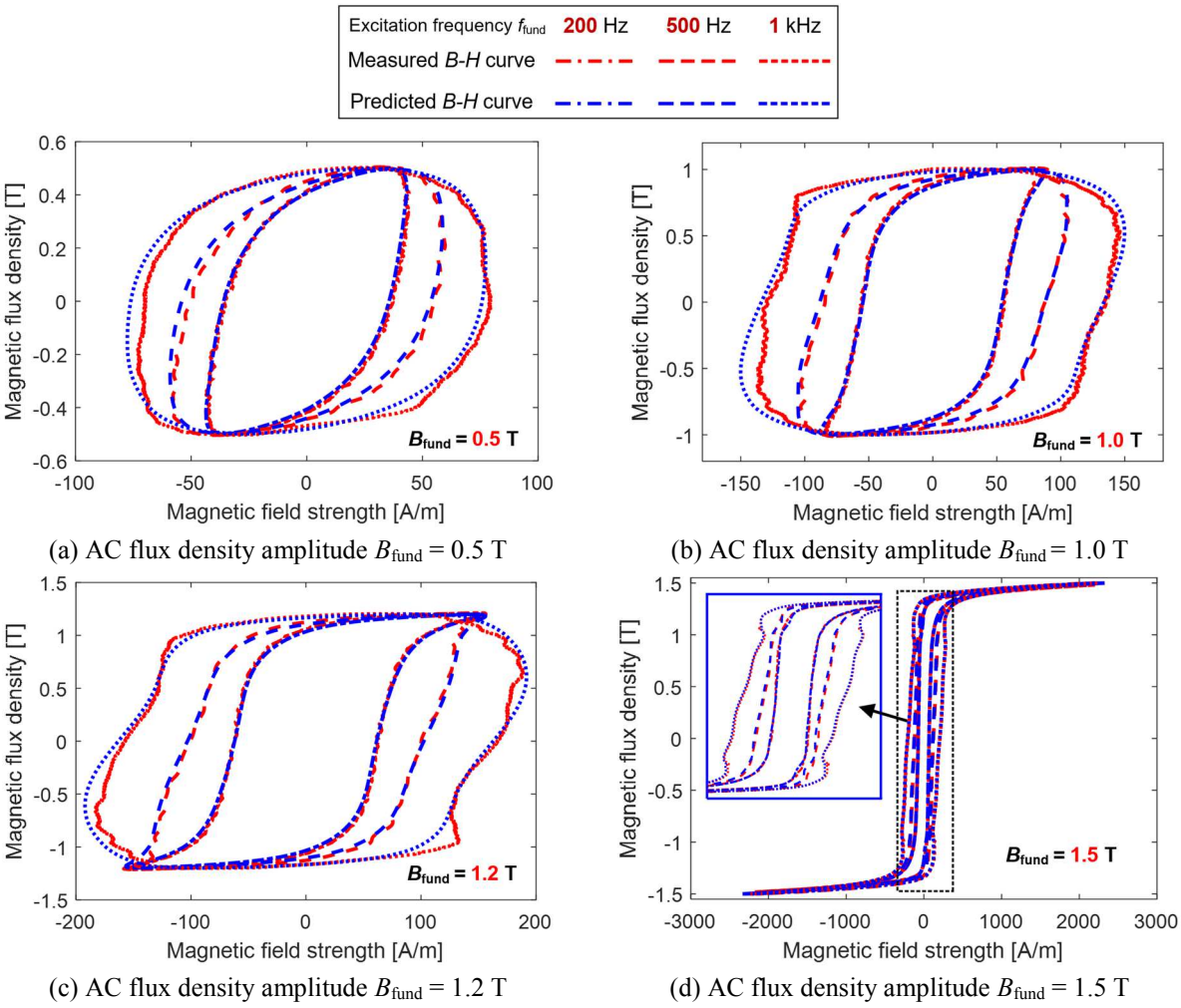

(a) AC flux density amplitude B_{fund} = 0.5 T

(b) AC flux density amplitude B_{fund} = 1.0 T

(c) AC flux density amplitude B_{fund} = 1.2 T

(d) AC flux density amplitude B_{fund} = 1.5 T

Figure 4-1: Comparison of measured and predicted hysteresis loops using $\Delta H_{dyn}/\Delta t$-based dynamic hysteresis model for three ac flux density amplitudes (i.e., B_{fund} = 0.5, 1.0, 1.2, and1.5 T) and three excitation frequencies (i.e., f_{fund} = 200 Hz, 500 Hz, and 1 kHz).

As aforementioned, the dissipated power loss for a periodic flux waveform is determined by the product of the enclosed area of the dynamic hysteresis loop and the fundamental excitation frequency. Hence, having the dynamic hysteresis loops data available makes it possible to determine the total iron loss (i.e., the sum of static and dynamic losses). Figure 4-3(a)-(d) compares the measured and predicted iron loss data for both available models over different frequencies and wide flux density amplitude ranges within the frequency limit of characterized data (i.e., f = 1 kHz). The excellent agreement (i.e., average error < 2 %) raises the confidence of two proposed dynamic hysteresis model for sinusoidal waveform analysis.

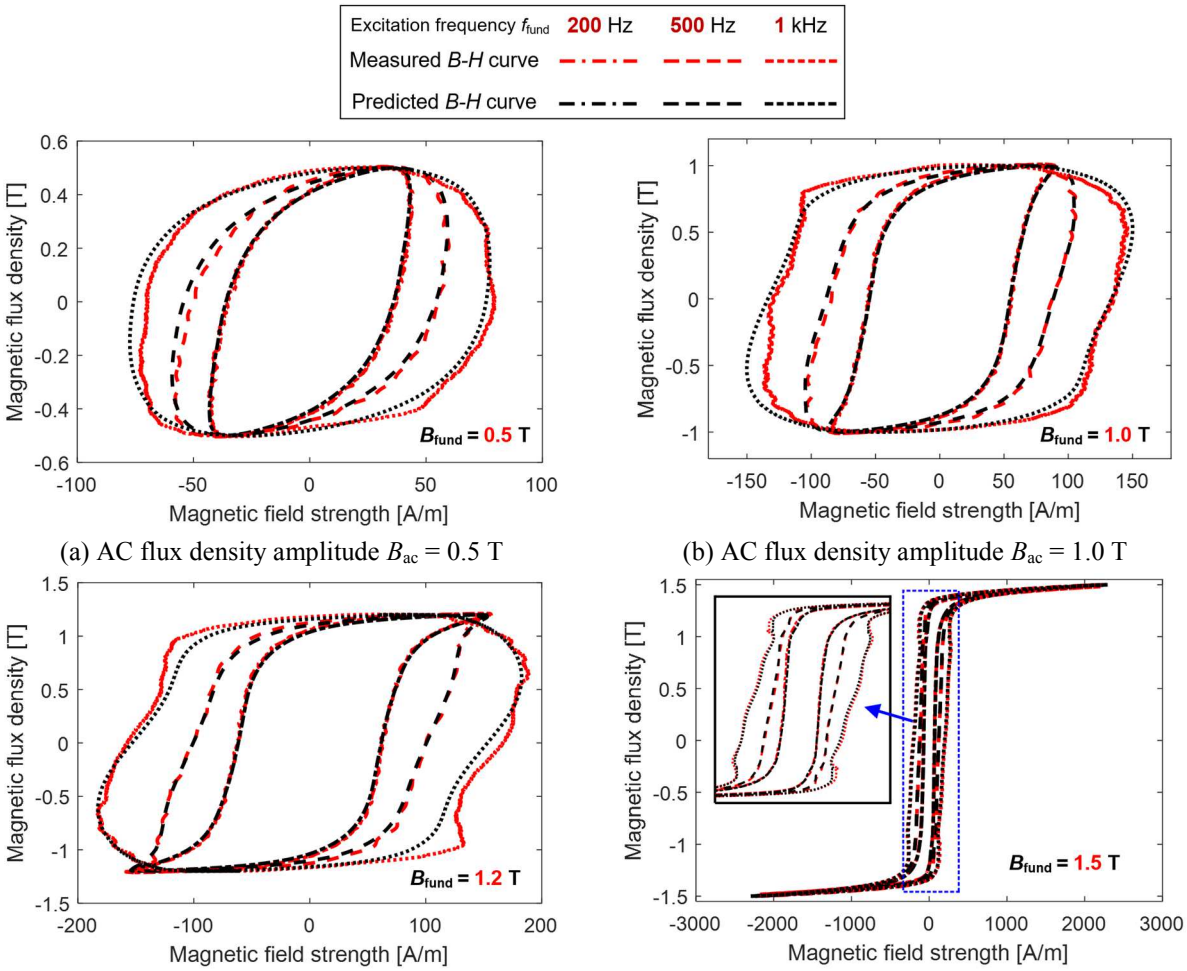

(a) AC flux density amplitude B_{ac} = 0.5 T

(b) AC flux density amplitude B_{ac} = 1.0 T

(c) AC flux density amplitude B_{ac} = 1.2 T

(d) AC flux density amplitude B_{ac} = 1.5 T

Figure 4-2: Comparison of measured and predicted hysteresis loops using H_{dyn}-based dynamic hysteresis model for three ac flux density amplitudes (i.e., B_{fund} = 0.5, 1.0, 1.2, and1.5 T) and three excitation frequencies (i.e., f_{fund} = 200 Hz, 500 Hz, and 1 kHz).

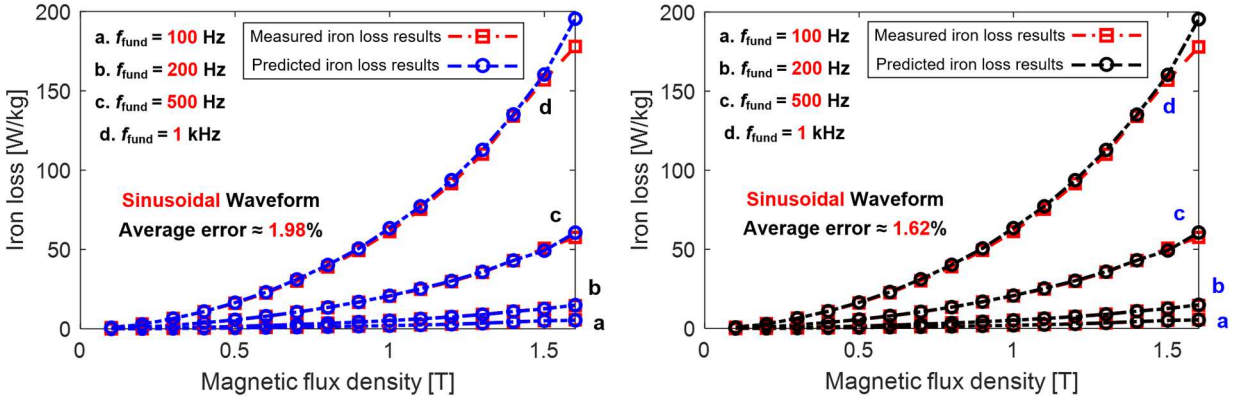

(a) $\Delta H_{dyn}/\Delta t$-based dynamic hysteresis model

(b) H_{dyn}-based dynamic hysteresis model

Figure 4-3: Comparison of measured and predicted iron loss results of sinusoidal flux waveforms within the frequency limit (f = 1 kHz) of available model parameter characterization data.

It should be noted that, in the above cases, the studied frequencies are within the input frequency limit of 1kHz. Although it is expected that the proposed model will exhibit desirable performance when the frequency is below the input data limit, it is necessary to re-evaluate the model's accuracy when the frequency exceeds that threshold. Instead of conducting interpolation, the characterized second-order polynomial equations in (3-22) and (3-26) are used to extrapolate beyond the range of the available data.

Figure 4-4(a)-(b) shows a comparison of predicted iron loss results and the manufacturer-provided loss data for $\Delta H_{dyn}/\Delta t$-based and H_{dyn}-based dynamic hysteresis model, respectively. The three studied frequencies falling with the range from 2 kHz to 5 kHz, five times the maximum frequency used for model characterization. As can be observed, the estimation errors for both models remain acceptable at 2 kHz, but there is an obvious trend that the error increases quickly as the frequency is raised beyond that value to 5 kHz. Due to the nonlinearity of material iron loss characteristics, measured dynamic hysteresis loop data at higher frequencies are needed to improve the model accuracy in those regions. Moreover, the H_{dyn}-based model shows higher estimation errors at frequencies beyond the input data, suggesting it is more preferable to use $\Delta H_{dyn}/\Delta t$-based with high input frequency, in which the model parameters have a better frequency extendability.

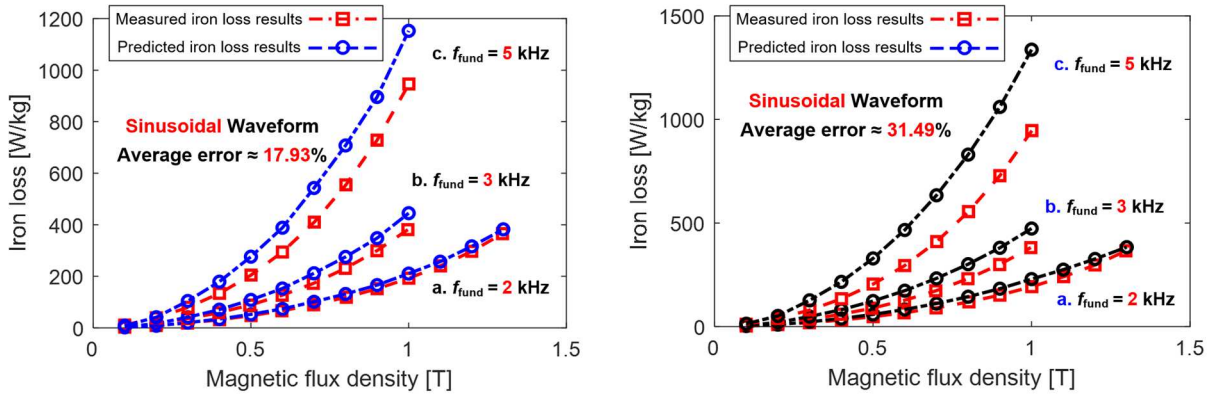

(a) $\Delta H_{dyn}/\Delta t$-based dynamic hysteresis model (b) H_{dyn}-based dynamic hysteresis model

Figure 4-4: Comparison of measured and predicted iron loss results of sinusoidal flux waveforms beyond the frequency limit (f = 200 Hz) of available model parameter characterization data.

4.3 Non-Sinusoidal Flux Waveform with Superimposed Harmonic Field

4.3.1 Variation of Flux Waveform as a Function of Harmonic Field Phase Shift

Next, the experimental investigations are further extended to the non-sinusoidal flux waveform containing a higher order harmonic field with varying phase shift angles (i.e., 0- 180 degree), and the flux density waveform is expressed as:

$$B(\varphi_{\text{shift}}) = B_1 \cos(2\pi f_1 t) + B_x \cos(2\pi f_x t + \varphi_{\text{shift}}) \quad (4\text{-}1)$$

where φ_{shift} is the phase shift angle between the fundamental and harmonic field, and B_x and f_x are the ac flux density amplitude and frequency of the x-order component, respectively.

Taking the 30 Hz fundamental field at 1.0 T and its 3rd harmonic field at 0.5 T as an example, flux density waveforms with four different phase shift angles are demonstrated in Figure 4-5.

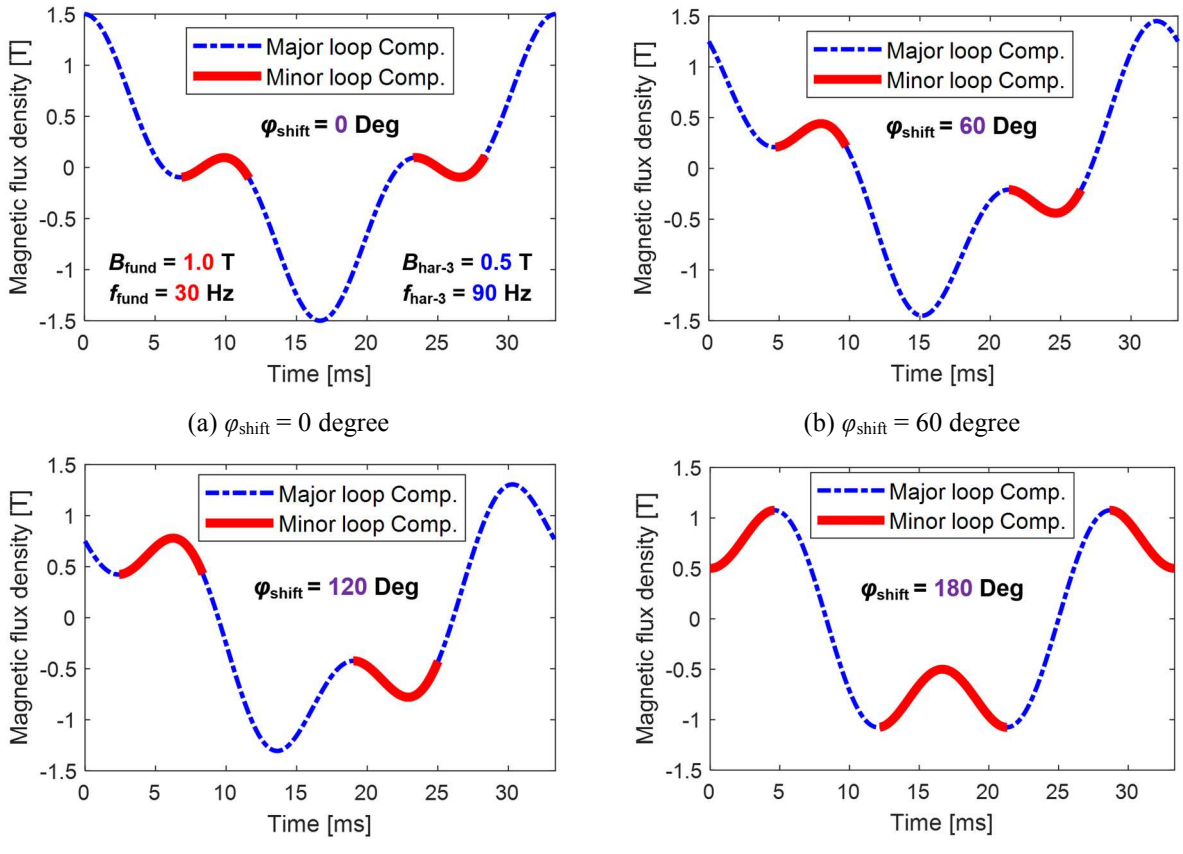

(a) φ_{shift} = 0 degree

(b) φ_{shift} = 60 degree

(c) φ_{shift} = 120 degree

(d) φ_{shift} = 180 degree

Figure 4-5: Variation of flux density waveshapes over varying phase shift angle φ_{shift}.

As can be seen from Figure 4-5, the waveshape and peak flux density amplitude both change significantly as the phase shift angle varies, indicating that the conventional linear decomposition technique (i.e., Fourier analysis) is not applicable to study the non-sinusoidal flux waveforms. Moreover, the occurrence of the minor loops is observed (See the red color lines), which are induced by the localized flux density reversing points riding on top of either the ascending or descending path of the major loop. Each minor loop is cross-coupled with the major loop, which in turn results in an external average field on the minor loop. That is why considering the impact of external average field is of the great importance of modeling the iron loss of minor loop.

Figure 4-6(a) shows the segregated minor loops with 60 degree phase shift angle. Owing to the waveform symmetry, two minor loops are identical in amplitude and frequency but opposite sign

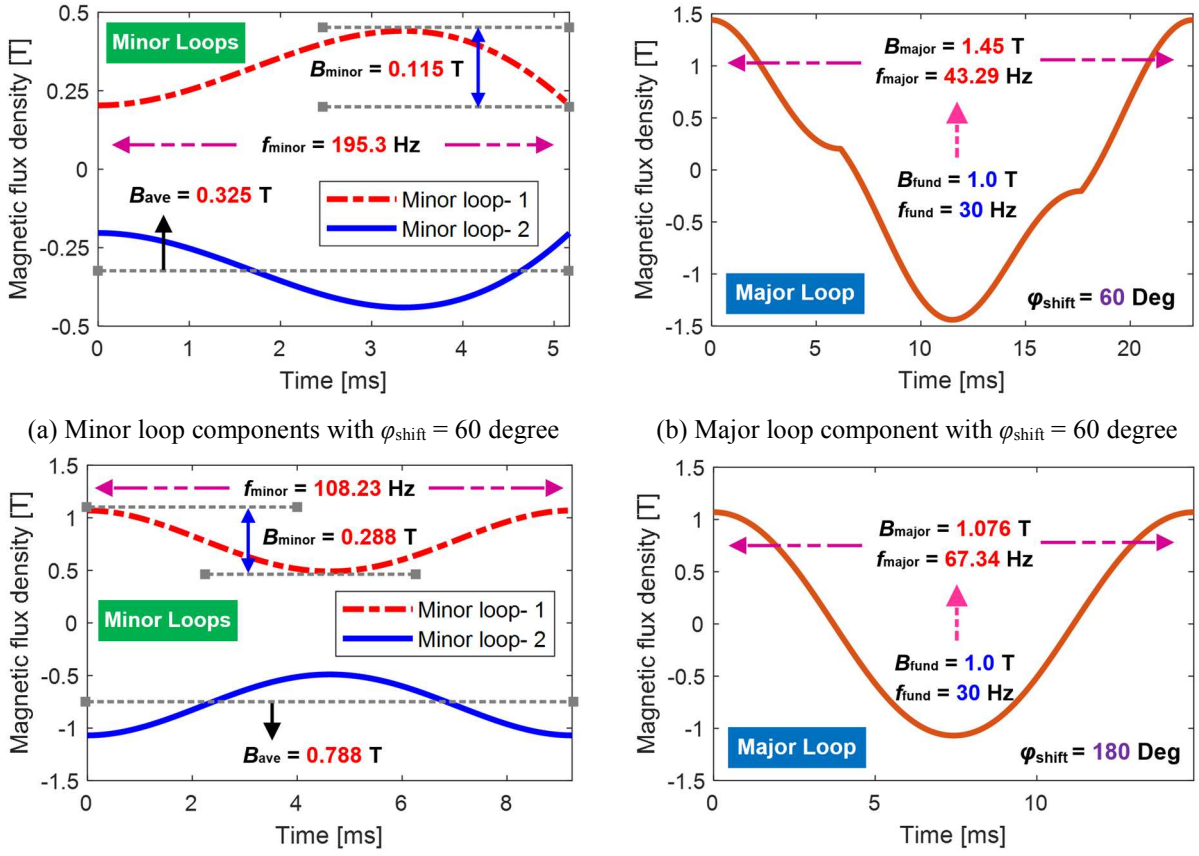

(a) Minor loop components with φ_{shift} = 60 degree

(b) Major loop component with φ_{shift} = 60 degree

(c) Minor loop components with φ_{shift} = 180 degree

(d) Major loop component with φ_{shift} = 180 degree

Figure 4-6: Segregation of major loop and minor loops affected by the ac average fields.

of the external average field. The frequency of the induced minor loop is calculated based on its time span, which is substantially different from the original 3rd harmonic field- 90 Hz.

In addition, removing the minor loops from the combined flux waveform, the major loop component can be obtained as shown in Figure 4-6(b). Also, both the peak flux density amplitude and frequency are different from the fundamental component. Therefore, estimating the iron losses of major and minor loop separately can better emulate the physical properties of the real waveform.

Similarly, the same decomposition technique is applied to the flux waveform shown in Figure 4-5(d) with 180 degree phase shift value. As can be seen from Figure 4-6(c) and (d), both the major and minor loops are under different operating conditions, making the field separation process indispensable. More generally, when analyzing an arbitrary flux waveform with multiple harmonics, separating the waveform into its major loop and minor loop components is always applicable and critical to the estimation accuracy.

Furthermore, as the phase shift angle goes up, the peak amplitude of major loop component decreases, and its frequency increases inversely. Regarding the minor loops, the amplitudes of both the ac flux density and average field become bigger with the larger value of phase shift angle. Therefore, changing the phase shift angle possibly lead to a notable impact on the iron loss, and the impact of several influencing factors on the iron loss of complex flux waveform will be explored in the following sections.

4.3.2 Effect of Harmonic Field Phase Shift on Total Iron Loss

As indicated from preceding section, although the frequency composition of a complex flux density waveform maintains unchanged, the mutual interaction between the fundamental and harmonic field varies with the phase shift angle, leading to substantial variations of the resulting flux density waveforms. To shed some light on its impact of the phase shift angle on the iron loss value, Figure 4-7(a)-(f) demonstrates the comparison of the measured and predicted dynamic hysteresis loops using $\Delta H_{dyn}/\Delta t$-based model with the fundamental component at 1.0 T B_{fund}, 100 Hz f_{fund} and 3rd harmonic field $B_{har\text{-}3}$ at 0.5 T for six different phase shift angles φ_{shift}, ranging from 0 to 180 degree. The measured and predicted iron loss values determined by the hysteresis loop enclosed area are given in figure.

It can be observed that maximum iron loss value occurs at 0 degree φ_{shift}, where the peak points of two fields align with each other in the same spot. While the 3rd component counteracting with the fundamental field at large phase shift values, the iron loss decreases about 50 % (e.g., φ_{shift} = 180 degree) compared to that under 0 degree φ_{shift}. It is worth noting that the proposed $\Delta H_{dyn}/\Delta t$-based dynamic hysteresis model offers an appealing estimation accuracy over a wide range of phase shift values. Only modest overestimations of the major loop are observed in the regions where the minor loops are induced.

On the other hand, consistent with the conclusions drawn from the prior section, the amplitudes of induced minor loops reach their maximum values at 180 degree, leading to much larger iron loss contribution compared to that under 0 degree. Moreover, as depicted in Figure 4-7(e)-(f) where the minor loops exert a considerable impact on total iron loss, the minor loops have been modeled accurately, building confidence in the proposed minor loop estimation method. Also, the developed minor loop compensation approach guarantees the congruency of minor loops.

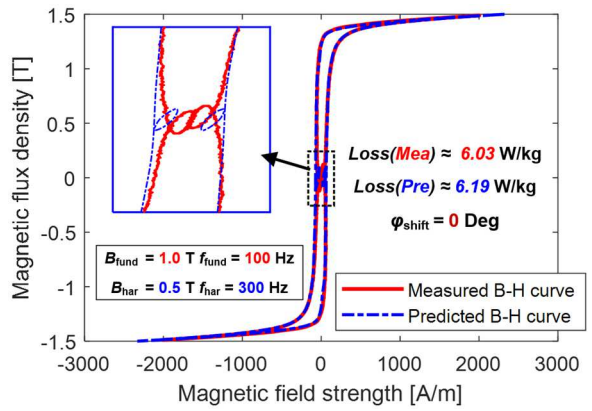

(a) B_{fund} = 1.0 T, f_{fund} = 100 Hz, $B_{har\text{-}3}$ = 0.5 T, $f_{har\text{-}3}$ = 300 Hz, and φ_{shift} = 0 Degree

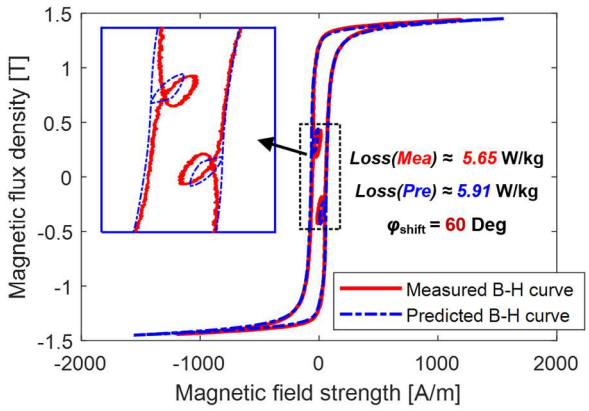

(b) B_{fund} = 1.0 T, f_{fund} = 100 Hz, $B_{har\text{-}3}$ = 0.5 T, $f_{har\text{-}3}$ = 300 Hz, and φ_{shift} = 60 Degree

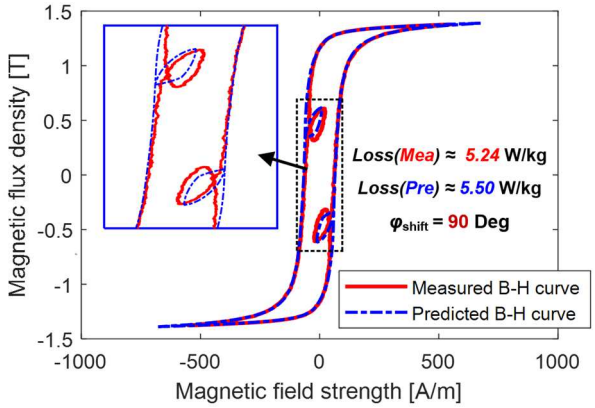

(c) B_{fund} = 1.0 T, f_{fund} = 100 Hz, $B_{har\text{-}3}$ = 0.5 T, $f_{har\text{-}3}$ = 300 Hz, and φ_{shift} = 90 Degree

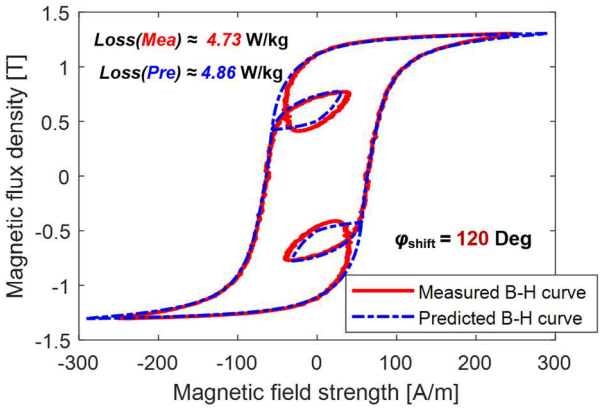

(d) B_{fund} = 1.0 T, f_{fund} = 100 Hz, $B_{har\text{-}3}$ = 0.5 T, $f_{har\text{-}3}$ = 300 Hz, and φ_{shift} = 120 Degree

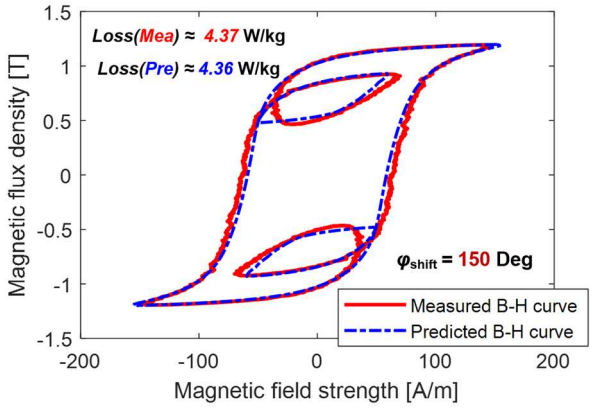

(e) B_{fund} = 1.0 T, f_{fund} = 100 Hz, $B_{har\text{-}3}$ = 0.5 T, $f_{har\text{-}3}$ = 300 Hz, and φ_{shift} = 150 Degree

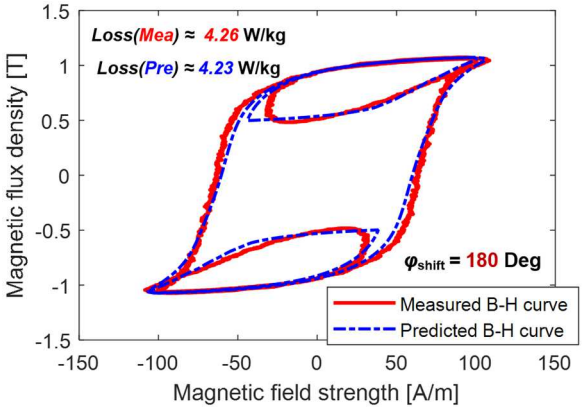

(f) B_{fund} = 1.0 T, f_{fund} = 100 Hz, $B_{har\text{-}3}$ = 0.5 T, $f_{har\text{-}3}$ = 300 Hz, and φ_{shift} = 180 Degree

Figure 4-7: Comparison of measured and predicted non-sinusoidal hysteresis loops with 3rd harmonic components for six phase shift values (a to f) using the $\Delta H_{dyn}/\Delta t$-based dynamic hysteresis model.

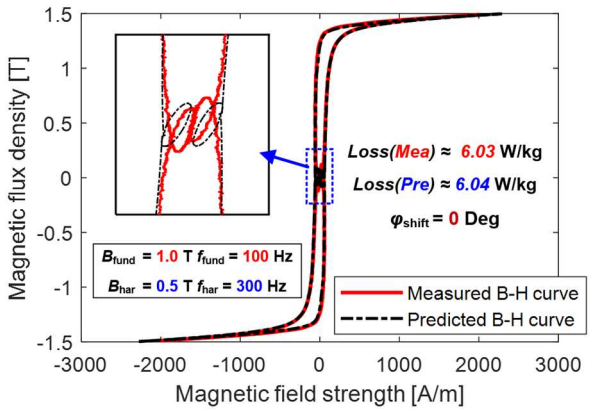

(a) B_{fund} = 1.0 T, f_{fund} = 100 Hz, $B_{har\text{-}3}$ = 0.5 T, $f_{har\text{-}3}$ = 300 Hz, and φ_{shift} = 0 Degree

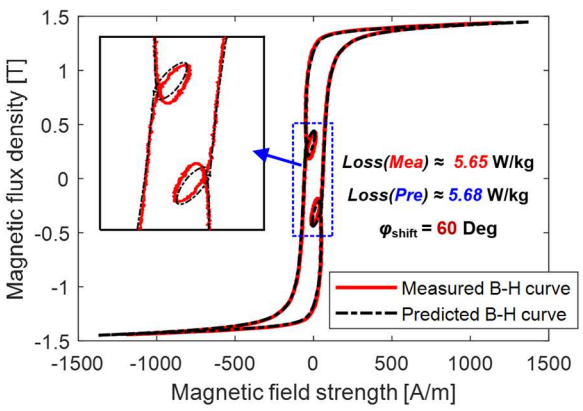

(b) B_{fund} = 1.0 T, f_{fund} = 100 Hz, $B_{har\text{-}3}$ = 0.5 T, $f_{har\text{-}3}$ = 300 Hz, and φ_{shift} = 60 Degree

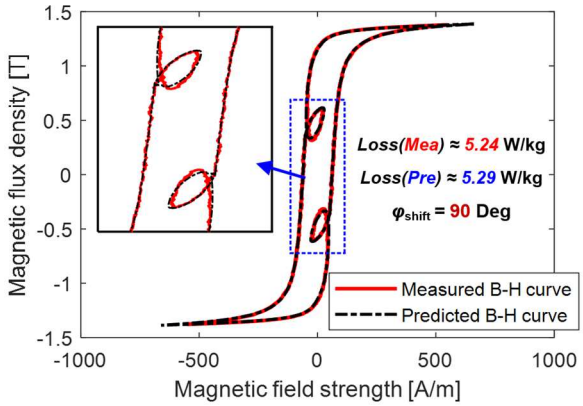

(c) B_{fund} = 1.0 T, f_{fund} = 100 Hz, $B_{har\text{-}3}$ = 0.5 T, $f_{har\text{-}3}$ = 300 Hz, and φ_{shift} = 90 Degree

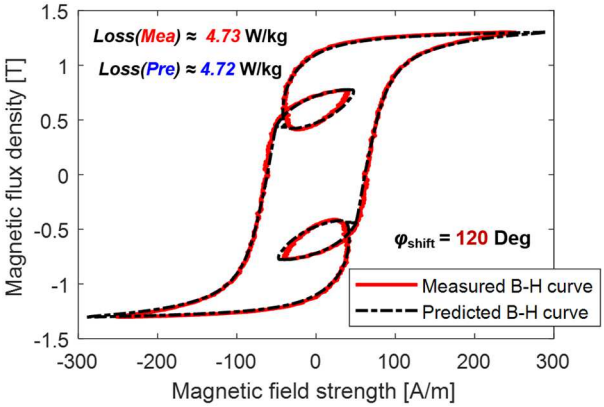

(d) B_{fund} = 1.0 T, f_{fund} = 100 Hz, $B_{har\text{-}3}$ = 0.5 T, $f_{har\text{-}3}$ = 300 Hz, and φ_{shift} = 120 Degree

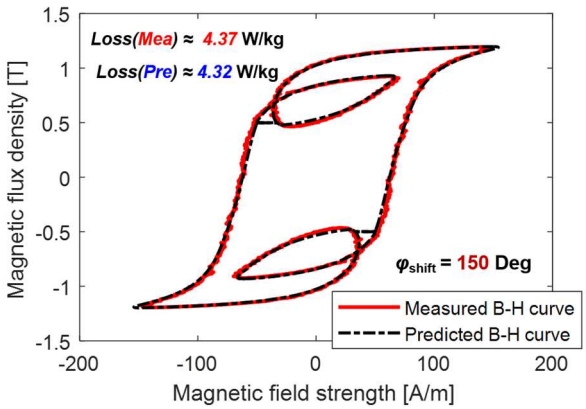

(e) B_{fund} = 1.0 T, f_{fund} = 100 Hz, $B_{har\text{-}3}$ = 0.5 T, $f_{har\text{-}3}$ = 300 Hz, and φ_{shift} = 150 Degree

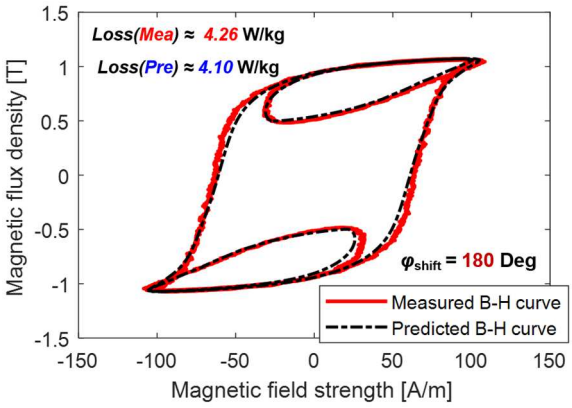

(f) B_{fund} = 1.0 T, f_{fund} = 100 Hz, $B_{har\text{-}3}$ = 0.5 T, $f_{har\text{-}3}$ = 300 Hz, and φ_{shift} = 180 Degree

Figure 4-8: Comparison of measured and predicted non-sinusoidal hysteresis loops with 3rd harmonic components for six phase shift values (a to f) using the H_{dyn}-based dynamic hysteresis model.

Next, the H_{dyn}-based dynamic hysteresis model is applied to estimate the dynamic hysteresis loops over the same operating conditions, where the evaluation results are presented in Figure 4-8(a)-(f). Compared to the $\Delta H_{dyn}/\Delta t$-based model, when the dynamic field strength H_{dyn} is modeled directly, a greater match with the measured waveforms is observed, especially in the regions where the minor loops occur.

The model is subsequently applied to estimate the total iron loss of waveforms with varying phase shift angles φ_{shift} for the same condition. As the results depicted in Figure 4-9, both models exhibit a promising capability in addressing the impact of a superimposed 3rd harmonic field on the resulting iron loss, where the average error for each is below 3%. It can be observed that, as the phase shift angle increases, the total iron loss gradually goes down, which is primarily due to the reduction of iron loss contribution from the major loop component and iron loss increase from minor loop components has less impact. Nevertheless, accurate modeling of both parts is equally important for estimating the total iron loss. In addition, the predicted results based on conventional Fourier analysis are overlaid in the same figure, where the iron loss at 100 Hz and 300 Hz are estimated individually and summed up for the total iron loss. However, the iron loss value remains the same for each angle, resulting in a considerably higher average estimation error (≈ 12.26%).

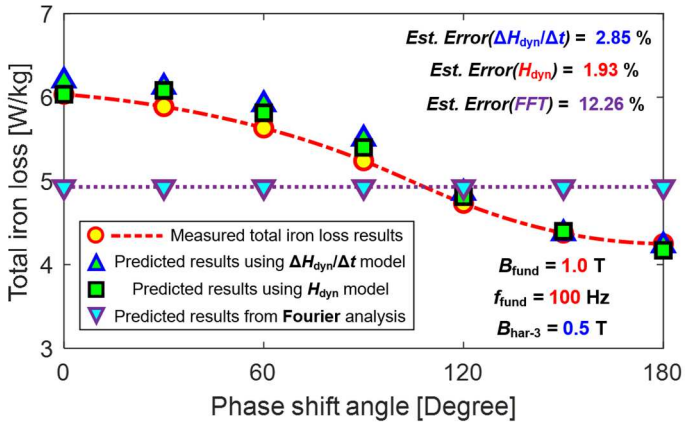

Figure 4-9: Comparison of measured and predicted total iron loss vs. phase shift angle φ_{shift} with fundamental field B_{fund} at 1.0 T and f_{fund} at 100 Hz superimposed with the 3rd harmonic field $B_{har\text{-}3}$ at 0.5 T.

The 50% 3rd harmonic components (i.e., $B_{\text{har-3}}$ = 0.5 T) with varying phase shift angles φ_{shift} have exhibited considerable impact on the resulting hysteresis loops, which, in turn, change the total iron loss significantly, indicating an obvious shortcoming of the conventional frequency-domain iron loss models that takes no account of the phase shift angles on nonlinear mutual-coupling between different frequency components. Next, in order to facilitate the understanding of the harmonic field impact in other amplitudes and frequencies, 3rd harmonic fields with some other amplitudes (i.e., B_{fund} = 0.2, 0.3 and 0.4 T) and at a significantly higher frequency (i.e., $f_{\text{har-3}}$ = 1.5 kHz) with varying phase shift angles φ_{shift} are superimposed with the same fundamental field amplitude (i.e., B_{fund} = 1.0 T), and the obtained hysteresis loops using two available dynamic hysteresis models are shown in Figure 4-10(a)-(b), overlaid with measured *B*-*H* curves.

As observed in those figures, $\Delta H_{\text{dyn}}/\Delta t$-based model can accurately emulate the dynamic hysteresis loops in their maximum amplitude regions. However, the measured hysteresis loops move inward in the middle region, whereas the proposed model fails to follow that inward path. As a result, the enclosed areas of predicted hysteresis loops are significantly larger than the measured waveforms, resulting in considerable iron loss overestimation.

On the other hand, the H_{dyn}-based dynamic hysteresis model exhibits a very promising ability to estimate the major loop component in the presence of the 3rd harmonic component even at extremely high fundamental and harmonic field frequencies, considering the fact that the harmonic frequency is beyond the input data limit (i.e., 1 kHz). The reasonably good guarantees a close match of the measured and predicted iron loss values.

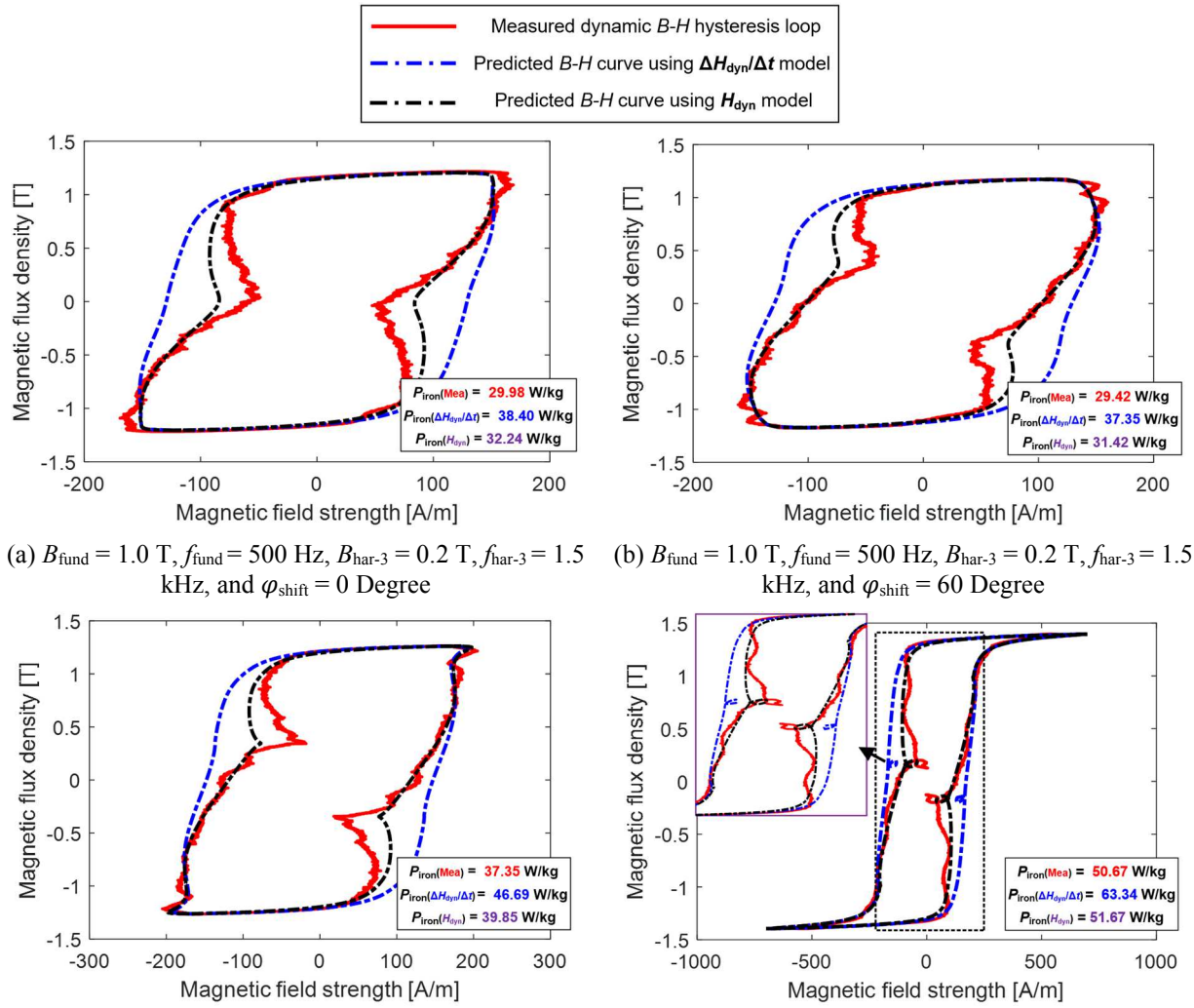

(a) B_{fund} = 1.0 T, f_{fund} = 500 Hz, $B_{har\text{-}3}$ = 0.2 T, $f_{har\text{-}3}$ = 1.5 kHz, and φ_{shift} = 0 Degree

(b) B_{fund} = 1.0 T, f_{fund} = 500 Hz, $B_{har\text{-}3}$ = 0.2 T, $f_{har\text{-}3}$ = 1.5 kHz, and φ_{shift} = 60 Degree

(c) B_{fund} = 1.0 T, f_{fund} = 500 Hz, $B_{har\text{-}3}$ = 0.3 T, $f_{har\text{-}3}$ = 1.5 kHz, and φ_{shift} = 60 Degree

(d) B_{fund} = 1.0 T, f_{fund} = 500 Hz, $B_{har\text{-}3}$ = 0.4 T, $f_{har\text{-}3}$ = 1.5 kHz, and φ_{shift} = 30 Degree

Figure 4-10: Comparison of measured and predicted non-sinusoidal hysteresis loops with 3rd harmonic components over varying conditions with high fundamental and injected harmonic field frequency.

The key difference between those models lies mainly in the modeling variable. The $\Delta H_{dyn}/\Delta t$-based model emulates the variation of ΔH_{dyn} over time Δt compared to the previous discretized flux density unit. Also, this model intrinsically assumes that flux density waveform between the current modeling point and the previous flux density reversing point is in sinusoidal shape. In other words, for the region of the major waveform where minor loop occurs (i.e., *dB/dt* approaches zero), the $\Delta H_{dyn}/\Delta t$-based model assumes the current modeling point and the whole trajectory is at a low frequency, giving the $\Delta H_{dyn}/\Delta t$ value close to zero. However, as the major waveform experiences

a considerable variation of the *dB/dt* rate and shows significant deviation from the sinusoidal waveform, it violates the underlying assumption of the $\Delta H_{dyn}/\Delta t$-based model, where the $\Delta H_{dyn}/\Delta t$ actually goes negative. In contrast, the H_{dyn}-based model ignores the travel trajectory between the modeling point and the previous flux density reversing point. Therefore, as the *dB/dt* rate gradually diminishes, the resulting H_{dyn} value also decreases, giving a negative $\Delta H_{dyn}/\Delta t$ variation, which shows an improved agreement with the measured data.

Taking the $B_{har\text{-}3}$ at 0.3 T as an example, the predicted total iron loss results versus the phase shift angle φ_{shift} from two dynamic hysteresis models and Fourier analysis are compared with the measured data in Figure 4-11. Consistent with hysteresis loop results given in Figure 4-10, the predicted iron loss results from $\Delta H_{dyn}/\Delta t$-based model are overestimated, especially when the phase shift angle is relatively small (i.e., $\varphi_{shift} \leq 90$ degree), leading to a large estimation error around 18.89%. In contrast, the H_{dyn}-based model presents very promising accuracy over the entire φ_{shift} range, with the average error below 5%. The predicted results using Fourier analysis again are invariant with φ_{shift}, and the accuracy (average est. error > 10%) is not comparable to the H_{dyn}-based model, confirming that it is critically important to incorporate the nonlinear coupling into iron loss modeling regardless of the excitation frequencies and harmonic field amplitudes.

It is worth noting that the *dB/dt* rate of the minor loop typically does not experience significant variations, meeting the critical prerequisite of the $\Delta H_{dyn}/\Delta t$-based model. In addition, as indicated in Figure 4-4(b), the accuracy and stability of the H_{dyn}-based model drop as the studied frequency exceeds the input data limit (i.e., 1 kHz). That is why, the $\Delta H_{dyn}/\Delta t$-based dynamic hysteresis model is more preferable in this analysis for high-frequency minor loop analysis, and a hybrid dynamic hysteresis model is formulated, in which the H_{dyn}-based model is responsible for major loop analysis and the $\Delta H_{dyn}/\Delta t$-based model is applied to emulate the minor loop characteristics.

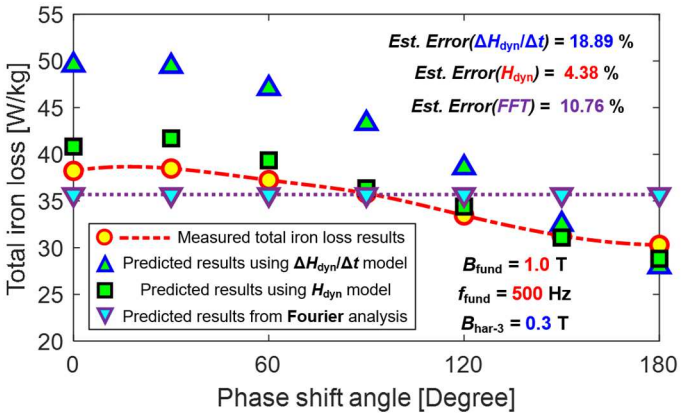

Figure 4-11: Comparison of measured and predicted total iron loss vs. phase shift angle φ_{shift} with fundamental field B_{fund} at 1.0 T and f_{fund} at 500 Hz superimposed with the 3rd harmonic field $B_{har\text{-}3}$ at 0.3 T.

4.3.4 Effect of Harmonic Field Amplitude and Frequency on Total Iron Loss

Next, the impact of harmonic field excitation frequency on the iron loss of complex flux waveform is investigated using the proposed hybrid dynamic hysteresis model. Maintaining the fundamental field at 1.0 T B_{fund} with 100 Hz f_{fund}, Figure 4-12(a)-(f) present the comparison of measured and predicted non-sinusoidal hysteresis loops with two amplitudes of 5th harmonic field (i.e., $B_{har\text{-}5}$ = 0.3 and 0.5 T) and three phase shift angles (i.e., φ_{shift} = 0, 90 and 180 degree).

For each harmonic field amplitude, even though the frequency composition of complex waveform maintains identical, the shape of resulting hysteresis loop changes considerably with phase shift angle. However, compared to the results given in Figure 4-7, the 3rd and 5th harmonic field at the same amplitude (i.e., 0.5 T) can lead to a different impact on the obtained hysteresis loop. When the phase shift angle changes from 0 to 180 degree, the reduction of peak magnetic flux density reduces from 28.53 % to 12 %, indicating that the 5th harmonic field exerts much less impact on the major loop component compared to the 3rd harmonic field. Nevertheless, for the non-sinusoidal waveform affected by higher order harmonics, more minor loops are induced and riding on top of the major field component. Besides, as the amplitude of the 5th harmonic field increases from 0.3 to 0.5 T, the peak-to-peak amplitudes and enclosed areas of minor loops become

much larger, leading to more significant minor loop iron loss contributions. Therefore, modeling the minor loops affected by the external ac average field that coupled with the major loop is of great importance, which, in turn, plays a critical role in achieving satisfied total iron loss estimation.

As the comparison results shown in Figure 4-22(a)-(f), the proposed model exhibits promising performance in emulating the shapes and enclosed areas of both the symmetrical major loop as well as the asymmetrical minor loops with different amplitudes over a wide range of ac average fields, building confidence in the proposed minor loop estimation method. Having this approach available successfully bypasses the need for additional tests involving external dc-bias fields.

Furthermore, the frequency impact analysis is further extended to non-sinusoidal waveform containing the 7th harmonic field (i.e., $f_{\text{har-7}} = 700$ Hz), and the evaluation results are demonstrated in Figure 4-13(a)-(f). Similarly, in the presence of the additional harmonic field, the hysteresis loop becomes much distorted, where multiple minor loops are observed inside the major hysteresis loop and contribute to a significant amount of iron loss. Even though the phase shift angle mainly determines the peak-to-peak amplitude and position (i.e., ac average field) of the individual minor loop, the shape and amplitude of major loop component almost maintain unchanged over varying phase shift angles φ_{shift}. As the phase shift angle of the 7^{th} harmonic field at 0.3 and 0.5 T changes from 0 to 180 degree, the reduction of major loop flux density amplitudes is diminished to 7.5 % and 6.1 %, respectively. Furthermore, the harmonic field with higher harmonic order (e.g., 9^{th} or 11^{th}) is expected to continue this trend, making the impact of phase shift angle on both the major and minor loops much less influential.

Here again, the proposed dynamic hysteresis model exhibits the excellent capability in predicting the actual hysteresis loops of the non-sinusoidal flux waveforms over a wide range of

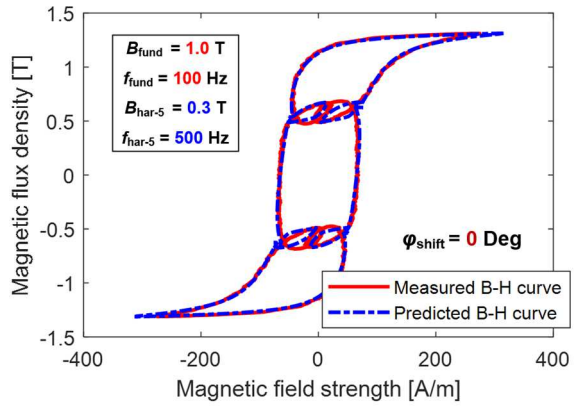

(a) B_{fund} = 1.0 T, f_{fund} = 100 Hz, B_{har-5} = 0.3 T, f_{har-5} = 500 Hz, and φ_{shift} = 0 Degree

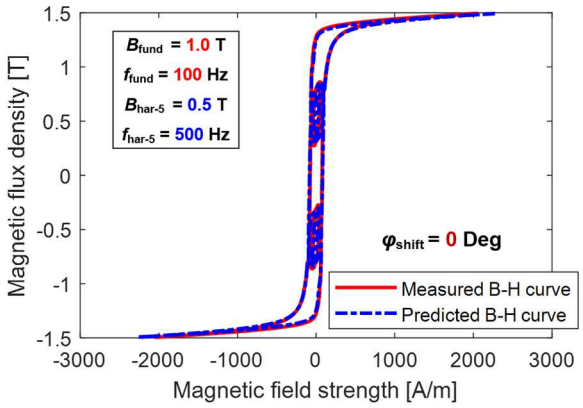

(b) B_{fund} = 1.0 T, f_{fund} = 100 Hz, B_{har-5} = 0.5 T, f_{har-5} = 500 Hz, and φ_{shift} = 0 Degree

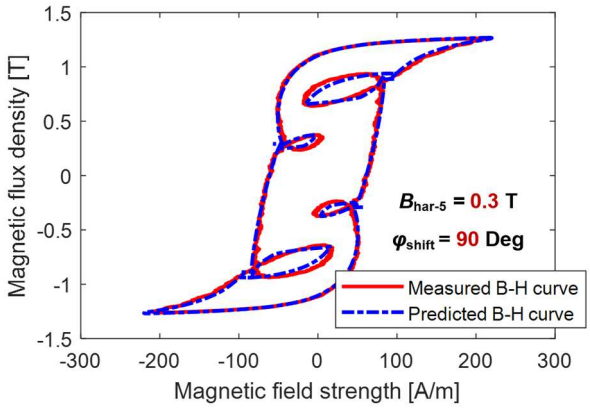

(c) B_{fund} = 1.0 T, f_{fund} = 100 Hz, B_{har-5} = 0.3 T, f_{har-5} = 500 Hz, and φ_{shift} = 90 Degree

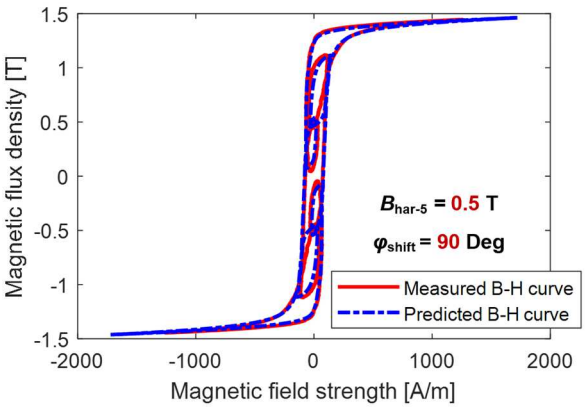

(d) B_{fund} = 1.0 T, f_{fund} = 100 Hz, B_{har-5} = 0.5 T, f_{har-5} = 500 Hz, and φ_{shift} = 90 Degree

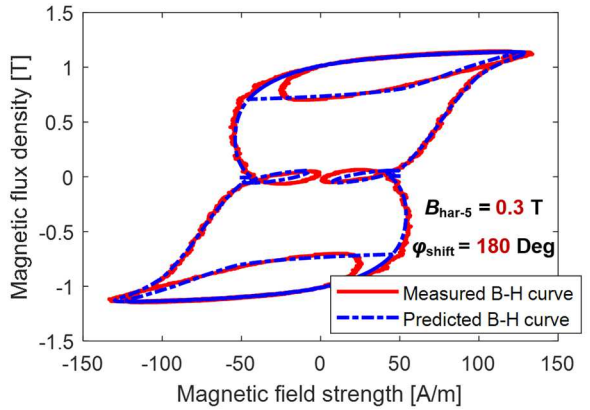

(e) B_{fund} = 1.0 T, f_{fund} = 100 Hz, B_{har-5} = 0.3 T, f_{har-5} = 500 Hz, and φ_{shift} = 180 Degree

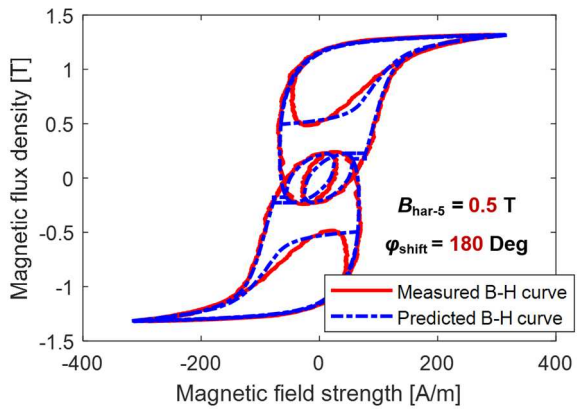

(f) B_{fund} = 1.0 T, f_{fund} = 100 Hz, B_{har-5} = 0.5 T, f_{har-5} = 500 Hz, and φ_{shift} = 180 Degree

Figure 4-12: Comparison of measured and predicted non-sinusoidal hysteresis loops with 5th harmonic components for different harmonic field amplitudes and phase shift angles.

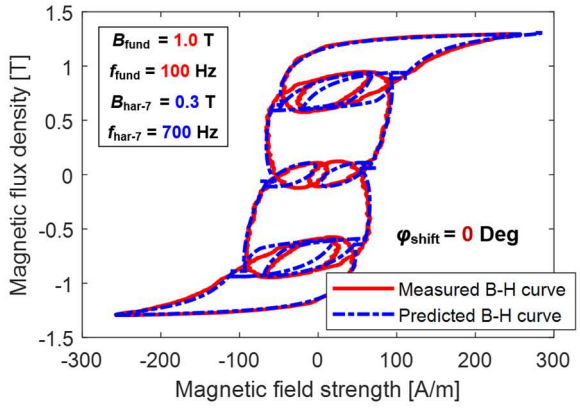

(a) B_{fund} = 1.0 T, f_{fund} = 100 Hz, B_{har-7} = 0.3 T, f_{har-7} = 700 Hz, and φ_{shift} = 0 Degree

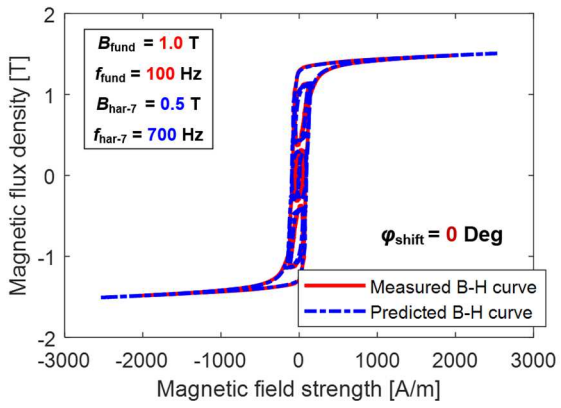

(b) B_{fund} = 1.0 T, f_{fund} = 100 Hz, B_{har-7} = 0.5 T, f_{har-7} = 700 Hz, and φ_{shift} = 0 Degree

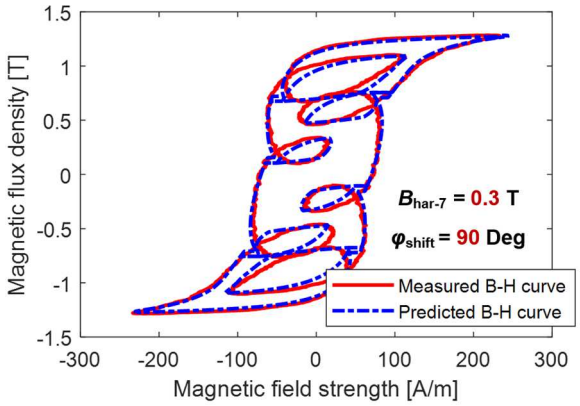

(c) B_{fund} = 1.0 T, f_{fund} = 100 Hz, B_{har-7} = 0.3 T, f_{har-7} = 700 Hz, and φ_{shift} = 90 Degree

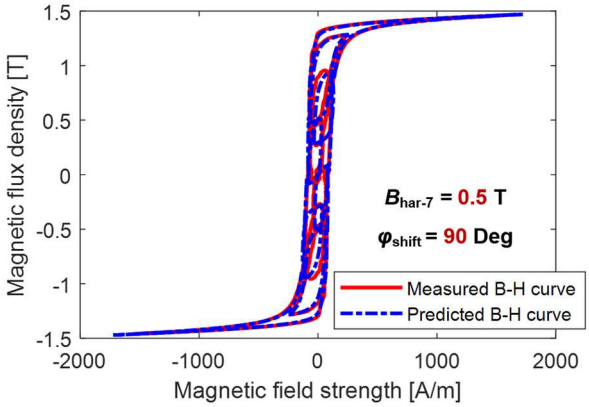

(d) B_{fund} = 1.0 T, f_{fund} = 100 Hz, B_{har-7} = 0.5 T, f_{har-7} = 700 Hz, and φ_{shift} = 90 Degree

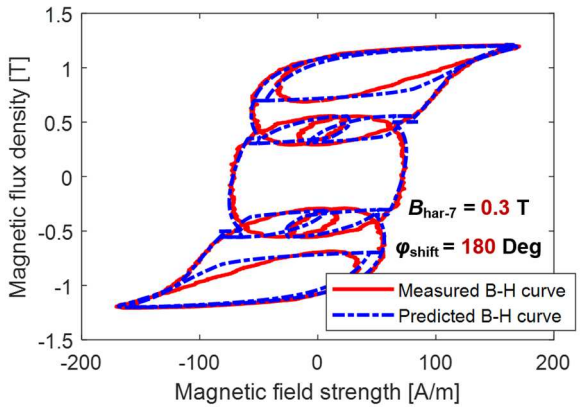

(e) B_{fund} = 1.0 T, f_{fund} = 100 Hz, B_{har-7} = 0.3 T, f_{har-7} = 700 Hz, and φ_{shift} = 180 Degree

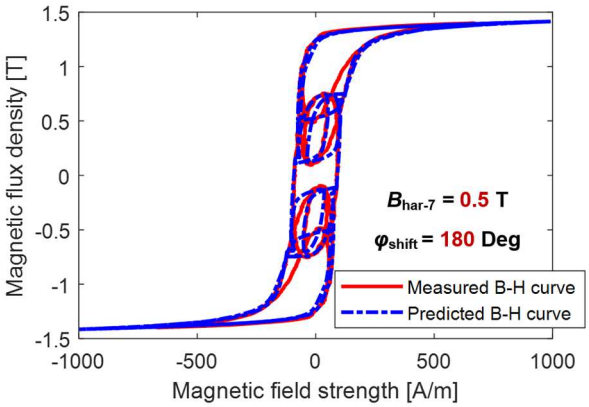

(f) B_{fund} = 1.0 T, f_{fund} = 100 Hz, B_{har-7} = 0.5 T, f_{har-7} = 700 Hz, and φ_{shift} = 180 Degree

Figure 4-13: Comparison of measured and predicted non-sinusoidal hysteresis loops with 7th harmonic components for different harmonic field amplitudes and phase shift angles.

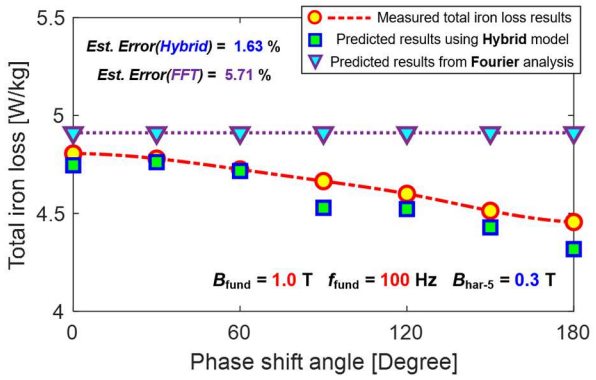

(a) B_{fund} = 1.0 T, f_{fund} = 100 Hz, and $B_{har\text{-}5}$ = 0.3 T

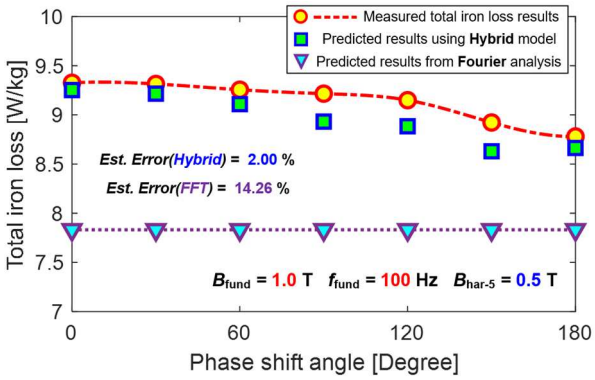

(b) B_{fund} = 1.0 T, f_{fund} = 100 Hz, and $B_{har\text{-}5}$ = 0.5 T

Figure 4-14: Comparison of measured and predicted total iron loss results versus phase shift angle φ_{shift} for two amplitudes of 500 Hz 5th harmonic field at 0.3 and 0.5 T.

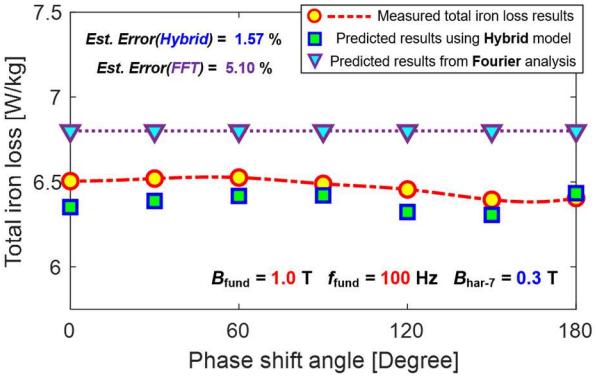

(a) B_{fund} = 1.0 T, f_{fund} = 100 Hz, and $B_{har\text{-}7}$ = 0.3 T

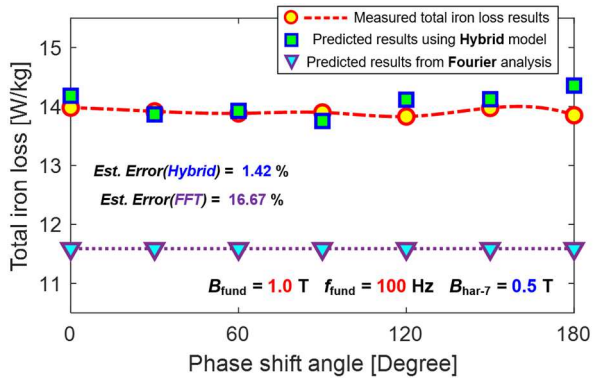

(b) B_{fund} = 1.0 T, f_{fund} = 100 Hz, and $B_{har\text{-}7}$ = 0.5 T

Figure 4-15: Comparison of measured and predicted total iron loss results versus phase shift angle φ_{shift} for two amplitudes of 700 Hz 7th harmonic field at 0.3 and 0.5 T.

operating conditions, and the minor loop compensation method always guarantees the congruency of minor loops affected by the ac average field.

Moreover, having the predicted hysteresis loops and their enclosed areas data available gives the iron loss of the non-sinusoidal flux density waveform under each operating condition. Figure 4-14(a)-(b) present the comparison of the measured and predicted total iron loss results with 5th harmonic field ($f_{har\text{-}5}$ = 500 Hz) at 0.3 and 0.5 T versus the phase shift angle φ_{shift}. It can be seen that the predicted and measured losses match within 2% over the studied phase shift angle, validating the model's capability in estimating the iron loss values for different phase shift angles and harmonic field amplitudes. On the other hand, although the accuracy of the iron loss model

based on Fourier analysis seems acceptable when the $B_{\text{har-5}}$ is at 0.3 T (See Figure 4-14(a)), considerable discrepancies between the predicted and measured results are observed in Figure 4-14(b), and the average estimation error exceeds 14%, which suggest that the nonlinear coupling between two frequency components is more substantial with a larger harmonic field amplitude. Also, the iron loss from minor loops become more significant in the latter case. That is why the frequency-domain model, which fails to take the external average field into account, leads to a severe iron loss underestimation.

Next, the proposed dynamic hysteresis model is exercised to calculate the total iron loss values when 7$^{\text{th}}$ harmonic fields (i.e., f_{fund} = 700 Hz) at 0.3 and 0.5 T are superimposed with the 100 Hz fundamental field at 1.0 T with varying phase shifts angles. As depicted in Figure 4-15(a)-(b), the measured total iron loss almost maintains constant regardless of the phase shift angle, whereas a relatively small but noticeable decline trends are observed in Figure 4-14(a)-(b) when 5$^{\text{th}}$ harmonic field is injected. Although the total iron loss is no longer sensitive to the phase shift variation, the frequency-domain model cannot offer desirable estimation accuracy. Instead, a constant estimation error is observed for each studied phase shift angle. What is worse, regarding the case with a lager harmonic field amplitude (i.e., $B_{\text{har-7}}$ = 0.5 T in Figure 4-15(b)), the average error reaches 16.67%, which again indicates that the model based on Fourier analysis is not capable of calculating the iron loss of complex flux density waveforms in the presence of minor loops. In comparison, the proposed dynamic hysteresis model accurately models the total iron loss in both cases, where the average error for each case is below 2%. Moreover, even for the harmonic field with a higher harmonic order (e.g., 9$^{\text{th}}$, 11$^{\text{th}}$, or PWM-induced harmonics.) is expected to apply a similar impact. In other words, the mutual coupling between fundamental and harmonic field exerts a critical influence on the resulting iron loss, making it necessary to model the major and each minor loop

individually and take the material nonlinear characterization into account during the iron loss analysis.

Finally, model estimation errors with different combinations of fundamental and superimposed harmonic field amplitudes, frequencies, and phase shift angles are plotted in Figure 4-16(a)-(f). With the fundamental field amplitude held constant at 1.0 T, three different fundamental frequency cases have been studied, including 100, 250, and 500 Hz. It has been verified that the proposed hybrid dynamic hysteresis model exhibits an excellent ability to estimate the total iron loss with different combinations of low-order harmonics. For most studied cases, the average error is below 5%. However, estimation errors increase as the frequency is raised. The primary sources of errors can be attributed to the following possible causes:

- The dynamic hysteresis loop data are identified from the linearized sinusoidal waveforms over different excitation frequencies with limited original resolution (i.e., $\Delta B = 0.05$ T). Even after the linear interpolation process developed in this analysis, there could be some remaining errors.
- The second-order polynomial equations are deployed to emulate the behavior of dynamic field component over varying operating conditions. However, certain errors are inevitably introduced by either the measured data or least squares curve fitting process. Especially at higher frequencies (e.g., $f_{\text{input}} = 500$ Hz or 1 kHz), the input data contain larger noises as the control system performance degrades in those frequencies, making it more challenging to secure desired fitting performance over a wide frequency range.
- As the shape of waveforms becomes complicated, the localized flux density changing rate *dB/dt* might exceed the upper limit of input data, which, in turn, leads to larger estimation errors for Figure 4-16(e)-(f). Expanding the frequency range of the input data is considered as the one of key solutions to further enhance the model performance in higher frequencies.

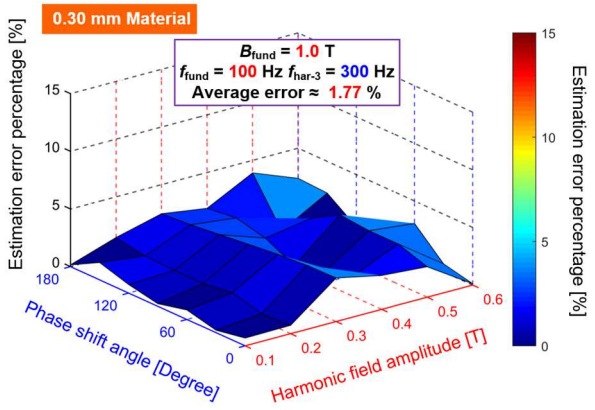

(a) B_{fund} = 1.0 T, f_{fund} = 100 Hz, and f_{har-3} = 300 Hz

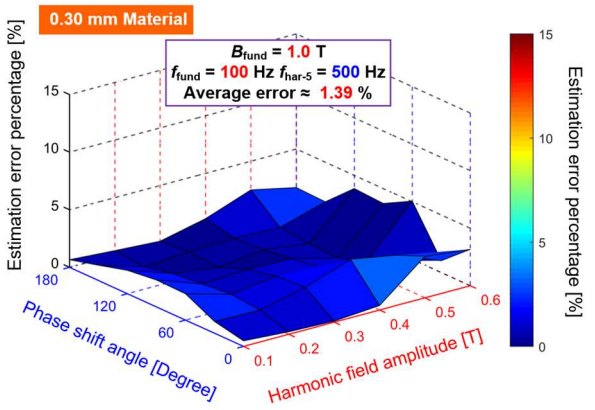

(b) B_{fund} = 1.0 T, f_{fund} = 100 Hz, and f_{har-5} = 500 Hz

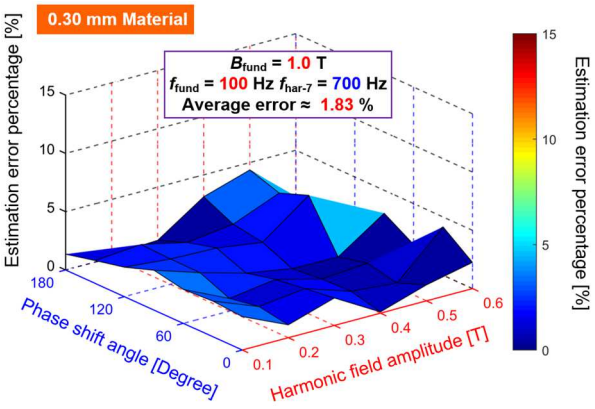

(c) B_{fund} = 1.0 T, f_{fund} = 100 Hz, and f_{har-7} = 700 Hz

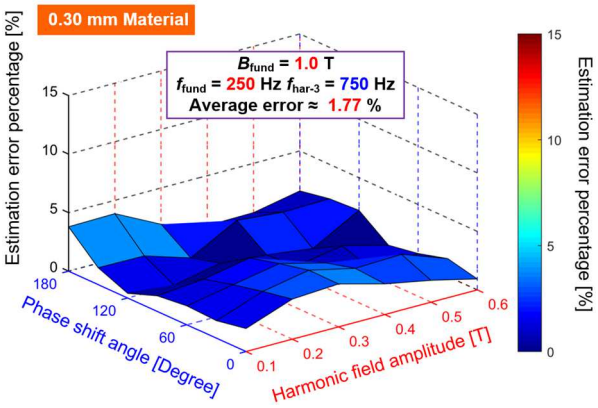

(d) B_{fund} = 1.0 T, f_{fund} = 250 Hz, and f_{har-3} = 750 Hz

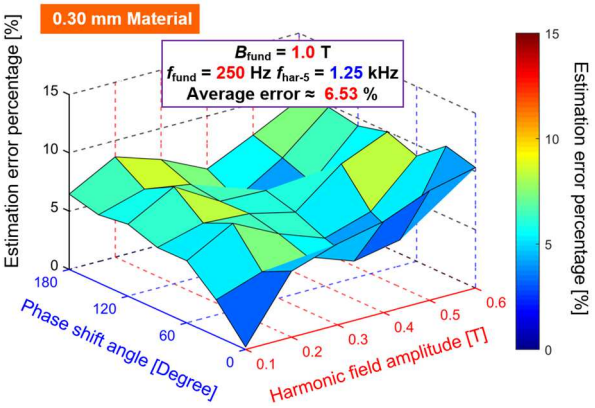

(e) B_{fund} = 1.0 T, f_{fund} = 250 Hz, and f_{har-5} = 1.25 kHz

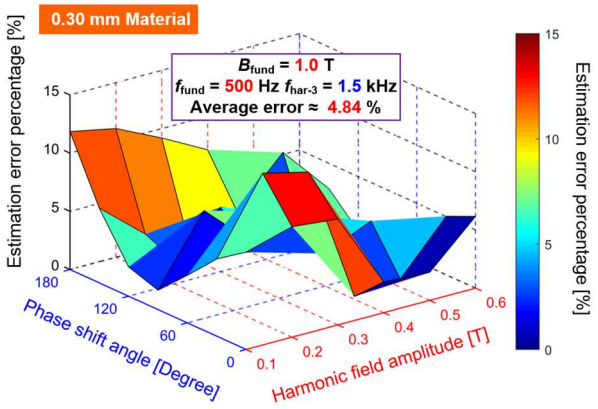

(f) B_{fund} = 1.0 T, f_{fund} = 500 Hz, and f_{har-3} = 1.5 kHz

Figure 4-16: Evaluation of percentage core loss estimation errors for 0.30 mm material with different combinations of fundamental and low-order harmonic field amplitudes B_{har}, excitation frequencies f_{har}, and phase shift angles φ_{shift}.

4.3.5 Model Accuracy Evaluation using Different Lamination Steels

The proposed dynamic hysteresis model has been successfully applied to estimate the iron loss of the 0.30 mm material over a variety of different operating conditions with excellent accuracy. To further evaluate the model's scalability to other magnetic materials, two newer lamination steels with 0.25 and 0.27 mm sheet thickness are investigated, and detailed characterization results are presented in this section.

As shown in Figure 4-17(a)-(b), two toroidal cores have been prepared for each material. The core designed for fundamental field testing has a sufficiently large number of turns (i.e., >300 turns), making it possible to achieve a high saturation level (i.e., B_{max} = 1.6 T). The key specifications for those cores are provided in Table 4-1 and Table 4-2. In contrast, the other two cores have fewer turns to minimize the winding-to-winding stray capacitance, making them more suitable for high-frequency PWM-induced iron loss evaluation which will be discussed in later chapters.

TABLE 4-1: KEY SPECIFICATIONS OF FUND. FIELD 0.25 MM TOROIDAL CORE

Primary winding turns N_{main}	355
Sensing winding turns N_{sense}	85
Lamination thickness	0.25 mm
Number of sheets	12
Outer diameter (**OD**)	76.2 mm
Inner diameter (**ID**)	64.7 mm

TABLE 4-2: KEY SPECIFICATIONS OF FUND. FIELD 0.27 MM TOROIDAL CORE

Primary winding turns N_{main}	325
Sensing winding turns N_{sense}	84
Lamination thickness	0.27 mm
Number of sheets	11
Outer diameter (**OD**)	76.2 mm
Inner diameter (**ID**)	64.7 mm

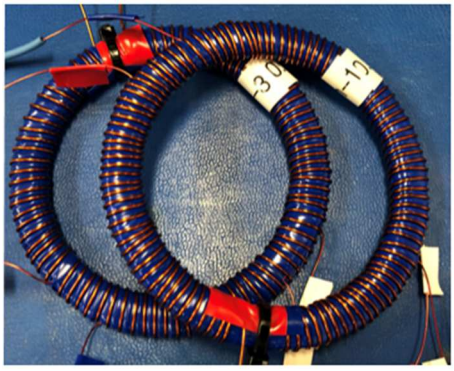

(a) Toroidal core sample with 0.25 mm material

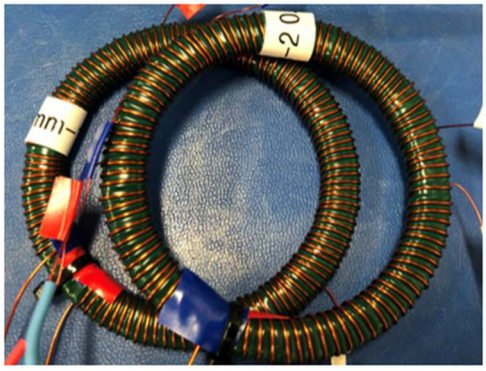

(b) Toroidal core sample with 0.27 mm material

Figure 4-17: Fabricated toroidal cores for magnetic material characterization of two new lamination steel materials with different sheet thicknesses at 0.25 and 0.27 mm.

It is worth noting that both new materials have been pre-characterized and compared to the manufacturer provided data. The measured material dc *B*-*H* curves, as well as the measured iron loss results over a wide range of frequencies, agree well with the manufacturer data, validating the accuracy of the proposed material testing system that discussed in the last chapter in other magnetic materials. Therefore, this system can be considered as a generalized measurement system.

Following the identical material characterization procedure that was implemented for the 0.30 mm material, the measured input hysteresis loop data over a wide frequency range (i.e., 10 Hz to 1 kHz) for both new lamination steels have been used to calculate the H_{dyn}-based dynamic hysteresis model coefficients, as well as the $\Delta H_{dyn}/\Delta t$-based model parameters that are adopted for minor loop estimation.

Since the performance of the H_{dyn}-based model degrades at higher frequencies, the predicted dynamic hysteresis loops are compared to the measured data in Figure 4-18 and Figure 4-19 for two new materials for two selected conditions with high fundamental and harmonic frequencies. In contrast to the 0.30 mm material results, excellent agreement is observed for all of these 4 test cases even when the fundamental frequency reaches 500 Hz. It is possible that a thinner sheet thickness reduces the impact of the dynamic eddy current on the resulting hysteresis loop, to some degree, improving the frequency extendability of the proposed dynamic hysteresis model. Nevertheless, it also suggests that the dynamic hysteresis model is intrinsically more susceptible to measurement fluctuations /errors compared to the conventional models based on the Steinmetz iron loss equation. However, significantly higher accuracy and in-depth physical insights make the dynamic hysteresis model a much-preferred solution to resolve the discrepancies between the measured and predicted the iron loss values for high-performance electric machine applications.

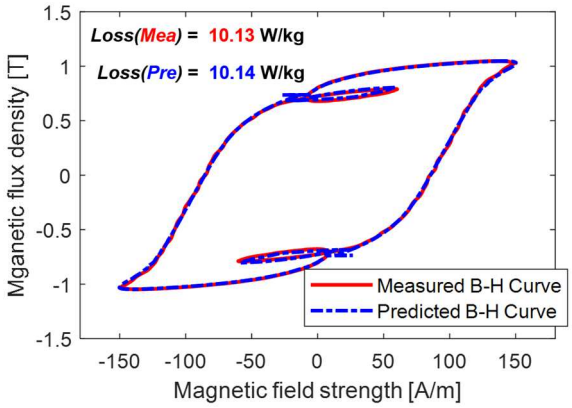

(a) **0.25** mm material: B_{fund} = 1.0 T, f_{fund} = 250 Hz, $B_{\text{har-3}}$ = 0.4 T, $f_{\text{har-3}}$ = 750 Hz, and φ_{shift} = 150 Degree

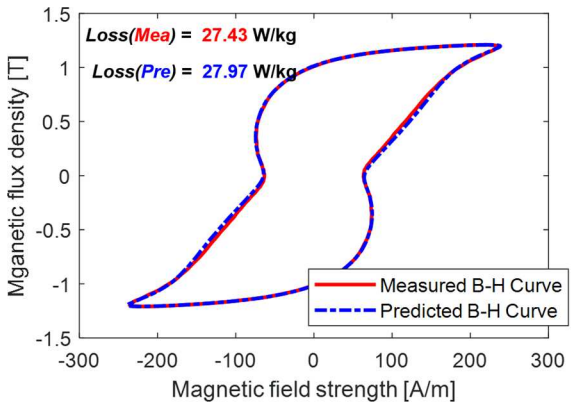

(b) **0.25** mm material: B_{fund} = 1.0 T, f_{fund} = 500 Hz, $B_{\text{har-3}}$ = 0.2 T, $f_{\text{har-3}}$ = 1.5 kHz, and φ_{shift} = 0 Degree

Figure 4-18: Comparison of measured and predicted dynamic hysteresis loops over selected operating conditions for 0.25 mm lamination steel.

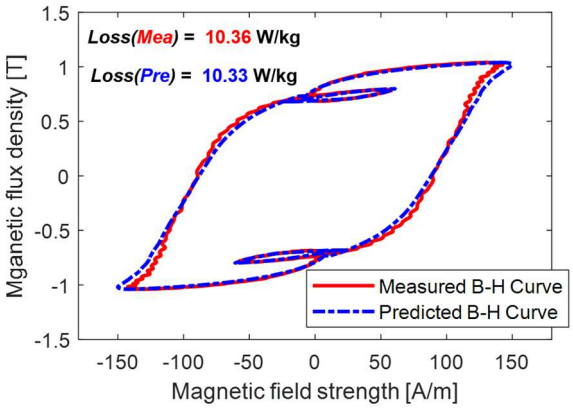

(a) **0.27** mm material: B_{fund} = 1.0 T, f_{fund} = 250 Hz, $B_{\text{har-3}}$ = 0.4 T, $f_{\text{har-3}}$ = 750 Hz, and φ_{shift} = 150 Degree

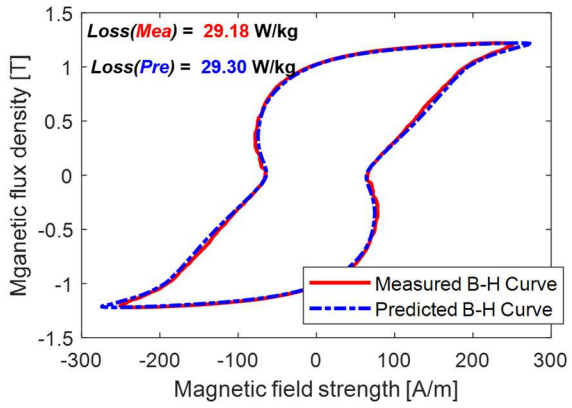

(b) **0.27** mm material: B_{fund} = 1.0 T, f_{fund} = 500 Hz, $B_{\text{har-3}}$ = 0.2 T, $f_{\text{har-3}}$ = 1.5 kHz, and φ_{shift} = 0 Degree

Figure 4-19: Comparison of measured and predicted dynamic hysteresis loops over selected operating conditions for 0.27 mm lamination steel.

Next, model accuracy evaluation results for the new materials are presented in Figs. 10(a)-(f) and Figs. 11(a)-(f) by sweeping different fundamental and harmonic field combinations. These results confirm that the H_{dyn}-based dynamic hysteresis model exhibits an excellent ability to emulate the material nonlinearities for different material thicknesses, and the average error for each of the cases is below 5%. This agreement also builds confidence in the H_{dyn}-based model for evaluating the iron loss of other magnetic materials with different thicknesses and compositions.

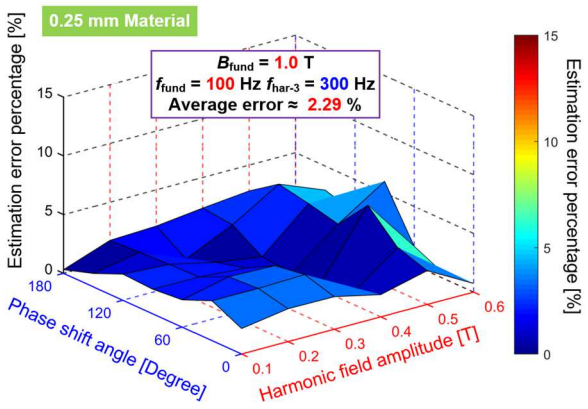

(a) B_{fund} = 1.0 T, f_{fund} = 100 Hz, and f_{har-3} = 300 Hz

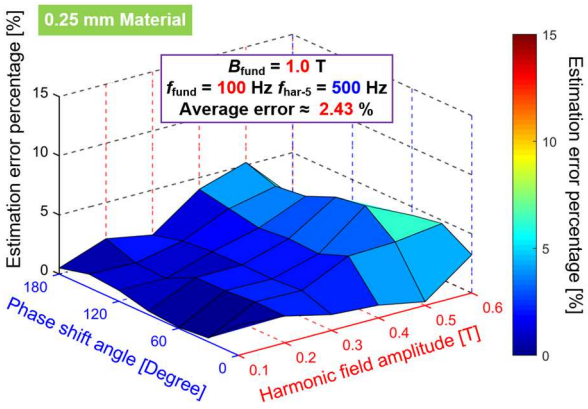

(b) B_{fund} = 1.0 T, f_{fund} = 100 Hz, and f_{har-5} = 500 Hz

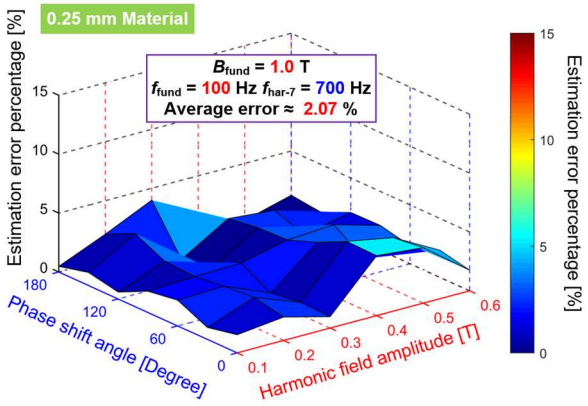

(c) B_{fund} = 1.0 T, f_{fund} = 100 Hz, and f_{har-7} = 700 Hz

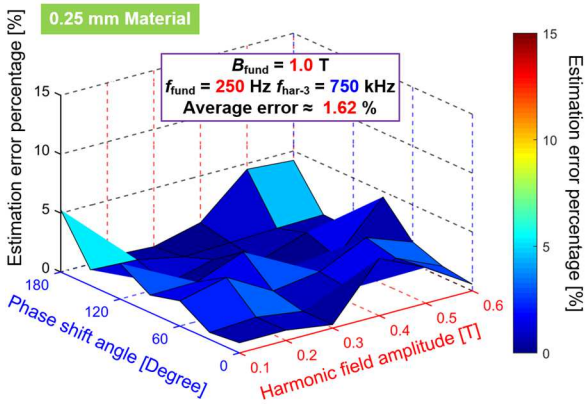

(d) B_{fund} = 1.0 T, f_{fund} = 250 Hz, and f_{har-3} = 750 Hz

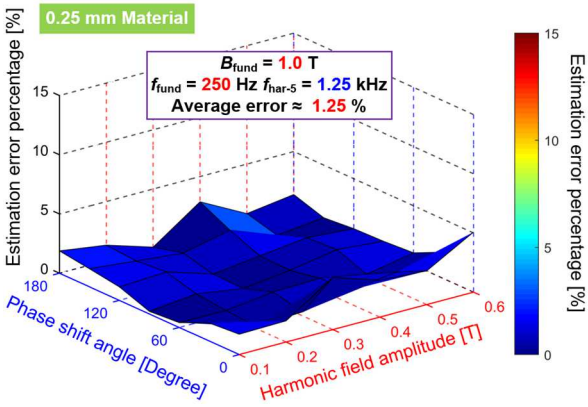

(e) B_{fund} = 1.0 T, f_{fund} = 250 Hz, and f_{har-5} = 1.25 kHz

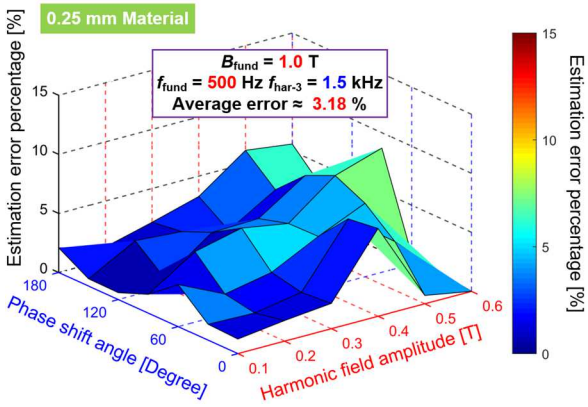

(f) B_{fund} = 1.0 T, f_{fund} = 500 Hz, and f_{har-3} = 1.5 kHz

Figure 4-20: Evaluation of percentage core loss estimation errors for 0.25 mm material with different combinations of fundamental and low-order harmonic field amplitudes B_{har}, excitation frequencies f_{har}, and phase shift angles φ_{shift}.

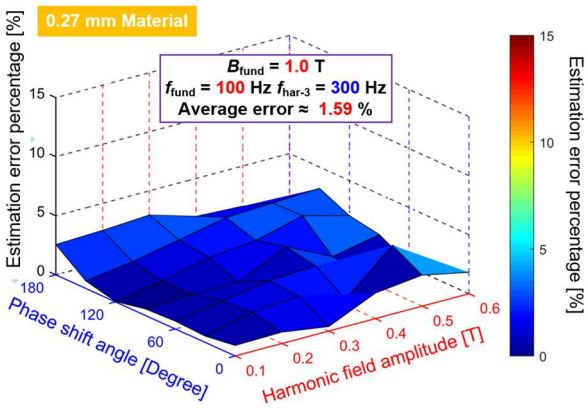

(a) B_{fund} = 1.0 T, f_{fund} = 100 Hz, and f_{har-3} = 300 Hz

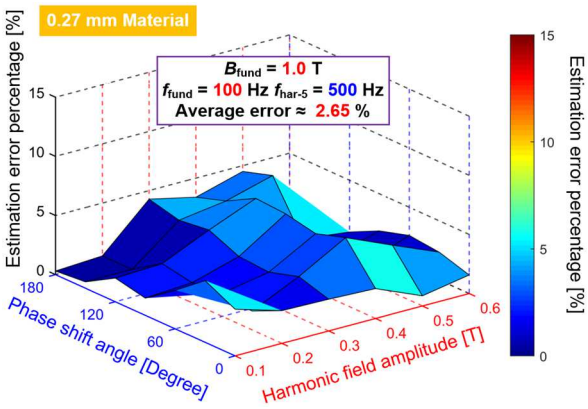

(b) B_{fund} = 1.0 T, f_{fund} = 100 Hz, and f_{har-5} = 500 Hz

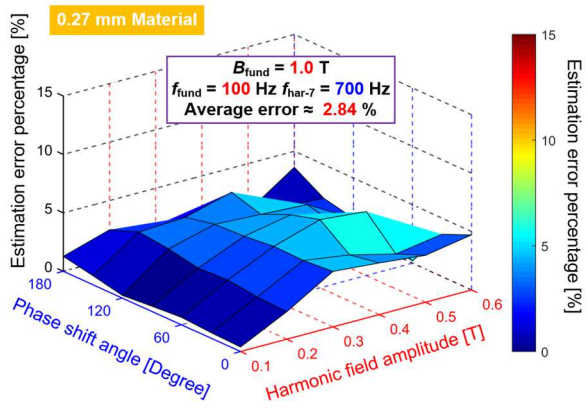

(c) B_{fund} = 1.0 T, f_{fund} = 100 Hz, and f_{har-7} = 700 Hz

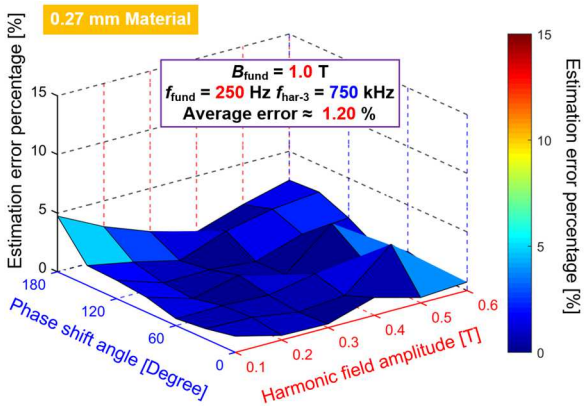

(d) B_{fund} = 1.0 T, f_{fund} = 250 Hz, and f_{har-3} = 750 Hz

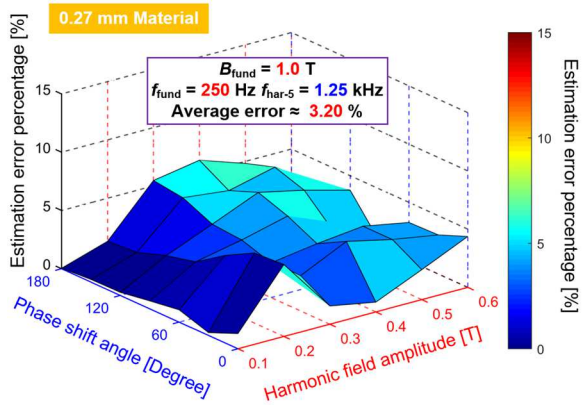

(e) B_{fund} = 1.0 T, f_{fund} = 250 Hz, and f_{har-5} = 1.25 kHz

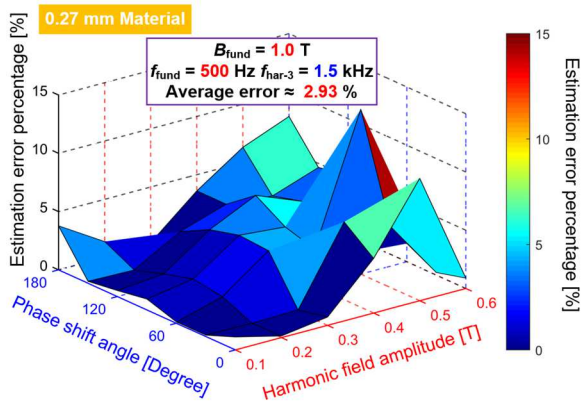

(f) B_{fund} = 1.0 T, f_{fund} = 500 Hz, and f_{har-3} = 1.5 kHz

Figure 4-21: Evaluation of percentage core loss estimation errors for 0.27 mm material with different combinations of fundamental and low-order harmonic field amplitudes B_{har}, excitation frequencies f_{har}, and phase shift angles φ_{shift}.

4.4 Sinusoidal Flux Waveform in the Presence of DC-Bias Field

As demonstrated in the preceding section, the proposed dynamic hysteresis model can be directly applied to estimate the minor hysteresis affected by the ac average field that coupled with the major field. Similarly, the proposed minor loop compensation approach applies to dc-bias field condition as well, providing the intrinsically closed minor loop. However, as displayed in Figure 3-32, the magnetic condition of the average field induced by the dc-bias field is different from that of ac average field, and the deviation exaggerates as the minor loop amplitude increases. In this section, the iron loss of minor loop affected by dc-bias field is investigated.

To account for the potential differences between the ac average field and dc-bias field, a 2-D look-up table is proposed in Figure 3-33 to correlate those two sources of external field with a given minor loop amplitude. Since the accuracy of the proposed model for estimating the minor loop in the presence of ac average field is verified, once the actual magnetic field influenced by dc-bias field is secured, the proposed model can be extended for dc-bias field analysis.

Figure 4-22(a)-(d) depict the measured minor hysteresis loops at 0.1 T, 200 Hz in the presence of four different external dc-bias fields, including both the linear and saturated region. The predicted values with and without conducting the dc-bias field correction are overlaid with the measured results. As discussed previously, the peak-to-peak field strength data $H_{p\text{-}p}$ serves as a critical metric to specify the magnetic condition when the material is influenced by the external field. Seen from Figure 4-22(a)-(c), without field correction, the values of $H_{p\text{-}p}$ are smaller than measured values, resulting, in turn, in the conservative estimation of the enclosed areas of minor loops. Moreover, those two external fields can be assumed identical when the dc-bias field reaches 1.32 T (i.e., saturated region). In comparison, the proposed dc-bias field correction has exhibited great agreement with the measured hysteresis loop data over a wide range of dc-bias field.

Furthermore, in Figure 4-23(a)-(d), the minor loop amplitude is extended to 0.3 T, where those two external fields are much more different. When the dc-bias field is small (i.e., $B_{dc} \leq 0.93$ T), the dc-bias field applies a more substantial impact on the material's magnetic condition. On the other hand, the actual magnetization state caused by the dc-bias field in the saturated region is smaller than that of the ac average field, making the field correction indispensable in both regions. Even though the differences between two external field become exaggerated at 0.3 T minor loop amplitude, the proposed model with field correction has shown the promising capability of addressing the impact dc-bias field on minor loops.

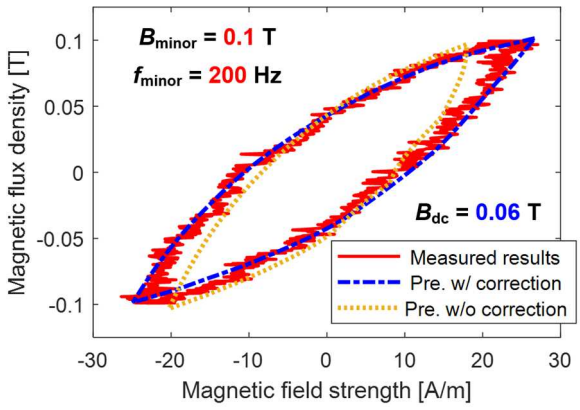

(a) B_{minor} = 0.1 T, f_{minor} = 200 Hz, and B_{dc} = 0.06 T

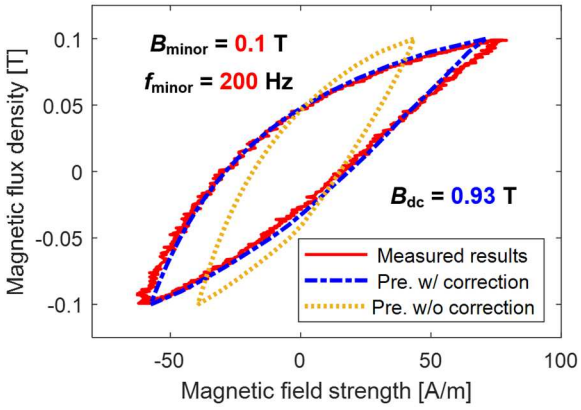

(b) B_{minor} = 0.1 T, f_{minor} = 200 Hz, and B_{dc} = 0.93 T

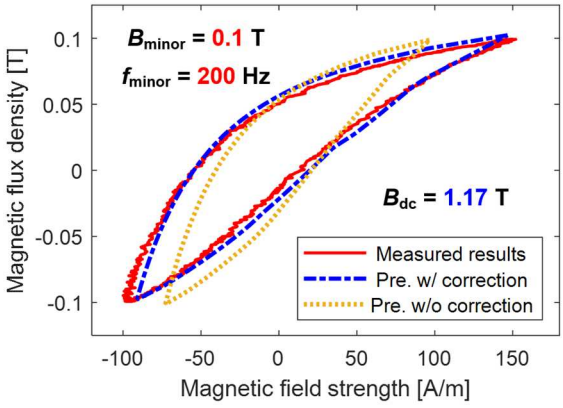

(c) B_{minor} = 0.1 T, f_{minor} = 200 Hz, and B_{dc} = 1.17 T

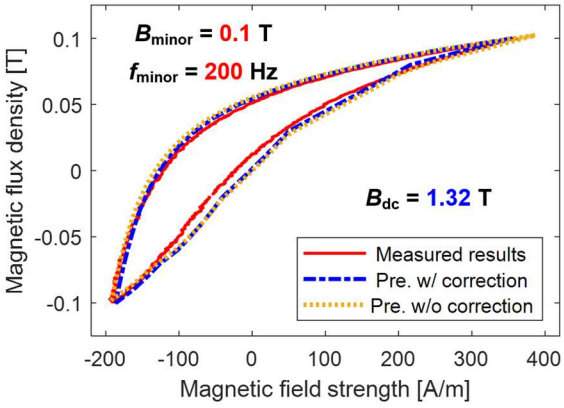

(d) B_{minor} = 0.1 T, f_{minor} = 200 Hz, and B_{dc} = 1.32 T

Figure 4-22: Comparison of measured and predicted minor loops affected by dc-bias fields with and without dc-bias field correction with flux density amplitude B_{minor} at 0.1 T.

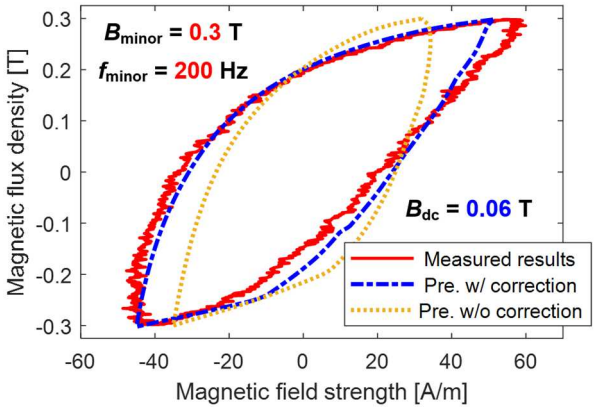

(a) B_{minor} = 0.3 T, f_{minor} = 200 Hz, and B_{dc} = 0.06 T

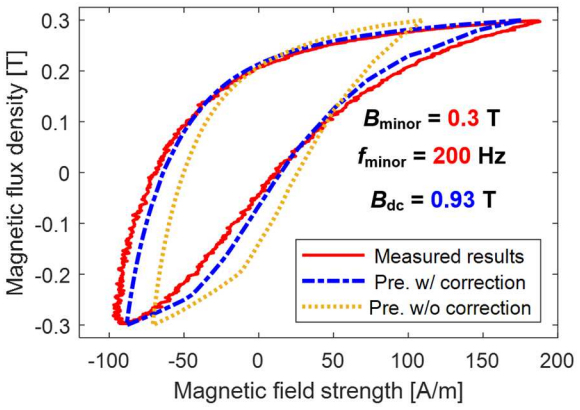

(b) B_{minor} = 0.3 T, f_{minor} = 200 Hz, and B_{dc} = 0.93 T

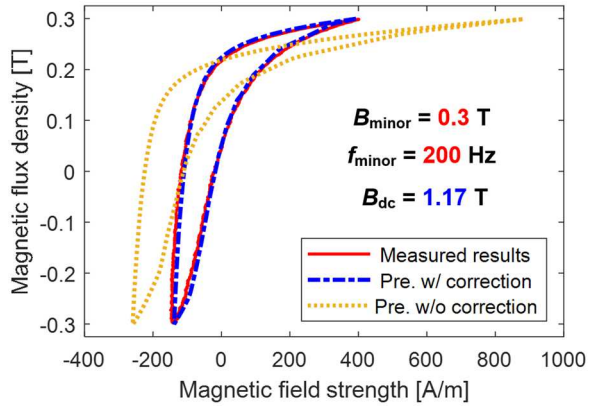

(c) B_{minor} = 0.3 T, f_{minor} = 200 Hz, and B_{dc} = 1.17 T

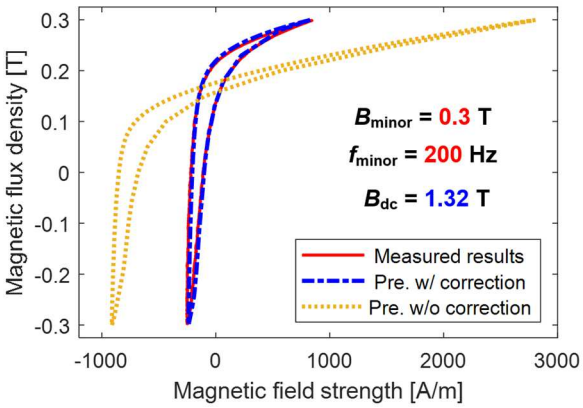

(d) B_{minor} = 0.3 T, f_{minor} = 200 Hz, and B_{dc} = 1.32 T

Figure 4-23: Comparison of measured and predicted minor loops affected by dc-bias fields with and without dc-bias field correction with flux density amplitude B_{minor} at 0.3 T.

Figure 4-24(a) depicts the measured iron loss versus dc-bias field at 200 Hz with ac flux density at 0.15 T. The prediction results with and without the dc-bias field correction are overlaid with each other for comparison. Although the predicted results without dc-bias field correction basically follow the same variation trend of measured results, the estimation accuracy is compromised noticeably in both the linear and saturated regions. In contrast, the proposed model with field correction has offered much-improved estimation accuracy, and the residual error- 10.3 % mainly attributes to the limited resolution of input characterization data- ΔB = 0.05 T. This can be improved in the future by introducing a larger number of measurement data or optimizing the interpolation scheme rather than the linear interpolation technique.

Next, the amplitude of the minor loop is increased 0.3 T. As the results shown in Figure 4-24(b), the proposed model with dc-bias field correction offers superior performance, where the average error is reduced from 13.3 % to 2.7 %. Also, it again indicates that the proposed model has higher accuracy when modeling the large-amplitude minor loops.

In addition, the relationship of ac average field and dc-bias field for a minor loop within the characterized 2-D look-up table can be determined through the interpolation. That is why the validity of this process is explored in Figure 4-24(c) with the selected amplitude different from the original input characterization data (i.e., B_{minor} = 0.225 T). The high agreement further confirms that the proposed model can be deployed to predict the iron loss of minor loop affected by the dc-bias field with the help of developed 2-D look-up table for dc-bias field correction. On the other hand, having the iron loss data measured with dc-bias fields is not capable of adequately describing the properties of minor loops influenced by the ac average field, especially when the minor loop amplitude becomes large (e.g., B_{minor} = 0.3 T) and the magnetic condition affected by the ac average field deviates significantly from that of the dc-bias field.

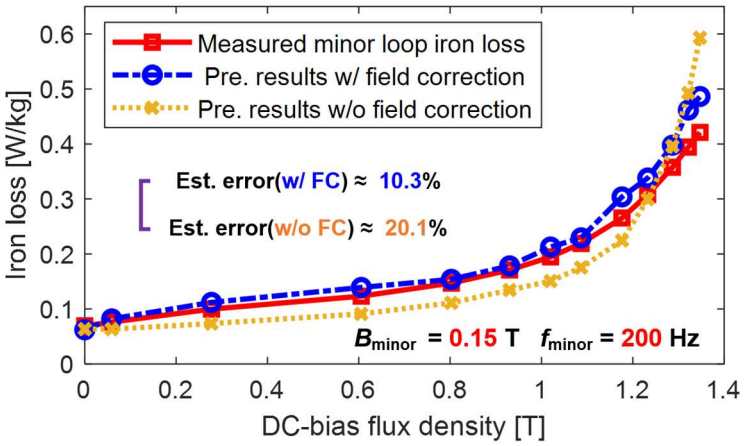

(a) Minor loop flux density amplitude B_{minor} = 0.15 T

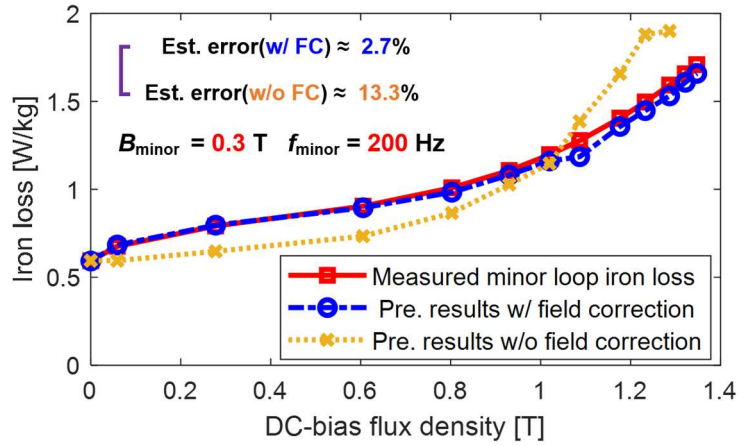

(b) Minor loop flux density amplitude B_{minor} = 0.3 T

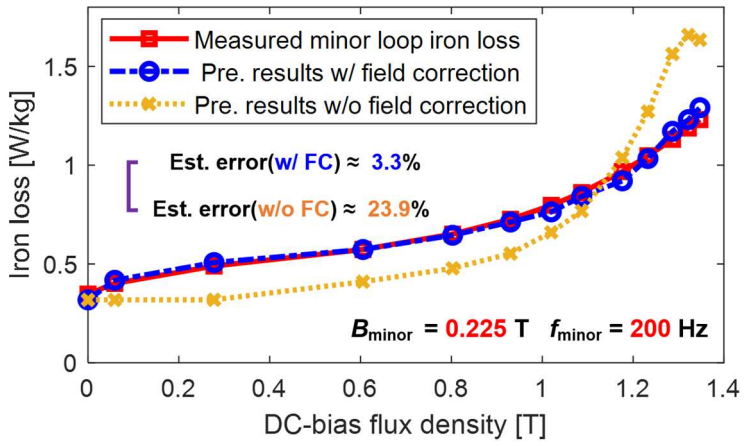

(c) Minor loop flux density amplitude B_{minor} = 0.225 T

Figure 4-24: Comparison of measured and predicted minor loop iron loss results with and without the dc-bias field correction at three ac flux density amplitudes (B_{minor} = 0.15, 0.3, and 0.225 T) and 200 Hz.

4.5 Machine-Level Iron Loss Model Evaluation

In the preceding sections of this chapter, the proposed model has been evaluated against the flux density waveforms that are commonly observed in IPM machines, including purely sinusoidal waveshapes (i.e., no harmonics) as well as non-sinusoidal waveshapes that include a single low-order harmonic field component. Next phase of the investigation presented in this section in focused on machine-level iron loss model evaluation. However, since the machine-level iron loss segregation process is challenging and tedious, and its accuracy is susceptible to various factors and measurement disturbances. An alternative approach to machine-level model evaluation is implemented here [138]. By dividing the studied machine into a couple of lumped regions, the average flux density waveform in each region is first calculated using 2-D FEA. Next, the resulting flux density waveforms from these 2-D FEA results are synthesized and applied to the toroidal core in the iron loss test equipment to acquire the measured hysteresis loop and iron loss data. Finally, comparisons of the predicted and measured results for the toroidal test results provide valuable preliminary insights into the behavior of the proposed iron loss model when it is applied to a machine-level problem.

Moreover, an element-by-element machine-level iron loss estimation scheme is presented in this section, including a generalized complex waveform segregation technique and an approach to better decompose the rotating magnetic fields in electric machines. After the introduction of these two improvements, a complete framework has been constructed to evaluate the fundamental field-induced iron loss in the selected baseline IPM traction machine. The comparison results between the predicted loss results using the new model and FEA-simulated data from JMAG are provided to shed some light on the accuracy of the proposed model.

4.5.1 Emulation of Simulated Flux Density Waveforms in the Stator-Side of Baseline IPM Machine

A baseline high-performance IPM machine designed for traction applications is used for iron loss investigation. The cross-sectional view of the studied IPM machine is provided in Figure 4-25(a), and the key specifications and dimensions of the machine are documented in Table 4-3. Moreover, Figure 4-25(b) identifies the basic repeating unit of the machine stator core consisting of a half stator tooth tip, a half tooth body, and a half back iron region. The single-pole slice of the studied IPM machine in Figure 4-25(a) includes twelve of these basic repeating units (i.e., two per stator slot). The basic repeating unit in Figure 4-25(b) is further subdivided into seven regions distinguished by the observation that flux density distribution is relatively uniform in each region. As shown on the right side of Figure 4-25(b), each region area is fitted with a sufficiently fine triangular mesh elements to secure the accuracy of 2-D FEA within the boundaries of each region.

TABLE 4-3: KEY IPM MACHINE SPECIFICATIONS AND DIMENSIONS [126]

Peak torque	540 N·m
Maximum speed	4,500 rpm
Nominal dc-bus voltage	350 Volts
Rated current	450 Arms
Stator outer diameter	213 mm
Active stack length	125 mm

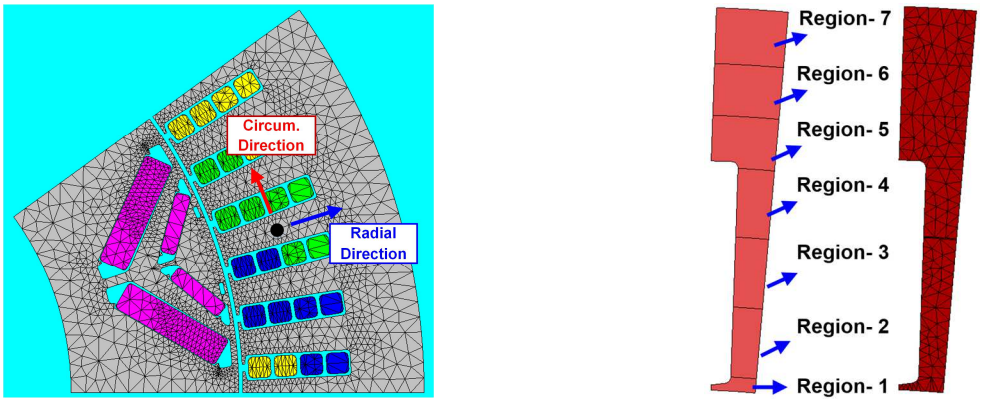

(a) (b)

Figure 4-25: (a) Cross-sectional view of studied IPM machine, and (b) Least repeatable units in the stator side.

TABLE 4-4: SUMMARY OF REGION NUMBER AND FLUX DIRECTION FOR EACH CASE INDEX NUMBER

Case Index #	Region #	Direction	Case Index #	Region #	Direction
1	1	Radial	6	5	Radial
2	1	Circum.	7	5	Circum.
3	2	Radial	8	6	Radial
4	3	Radial	9	6	Circum.
5	4	Radial	10	7	Circum.

In addition, the flux density in each element is decomposed into its radial and circumferential direction, respectively. The sum of the iron loss contributions from each of these orthogonal directions (calculated separately) is considered to be the predicted total iron loss in a given element.

It should be noted that 4 of the 14 orthogonal flux density components associated with the seven regions have negligible amplitudes (e.g., the circumferential component in stator tooth body). As a result, only 10 out of the 14 simulated field components have been selected for inclusion in the stator-side iron loss analysis. Definitions of each of the 10 case index numbers consisting of the region number and flux density orientation are provided in Table 4-4.

In order to adequately reproduce the simulated flux density waveforms in the tested toroidal core, the command flux density waveform B_{cmd} is expressed by the expansion of Fourier series up to 13$^{\text{th}}$ harmonic component as follows:

$$B_{cmd}(t) = B_1 \cos(2\pi f_1 t + \varphi_1) + B_3 \cos(2\pi f_3 t + \varphi_3) + \cdots + B_{13}\cos(2\pi f_{13} t + \varphi_{13}) \quad (4\text{-}2)$$

Due to the limited controller calculation speed, the maximum machine speed has been limited to 3,000 rpm, corresponding to 250 Hz machine fundamental frequency. The machine-level analysis is carried out under light-load condition with 20 Arms phase current and 10 degree current control angle. The selected testing condition is consistent with the machine operating at relatively high speed, where the machine stator core is not heavily saturated. Also, only sinusoidal current has been considered in this analysis, excluding any of the PWM-induced harmonics.

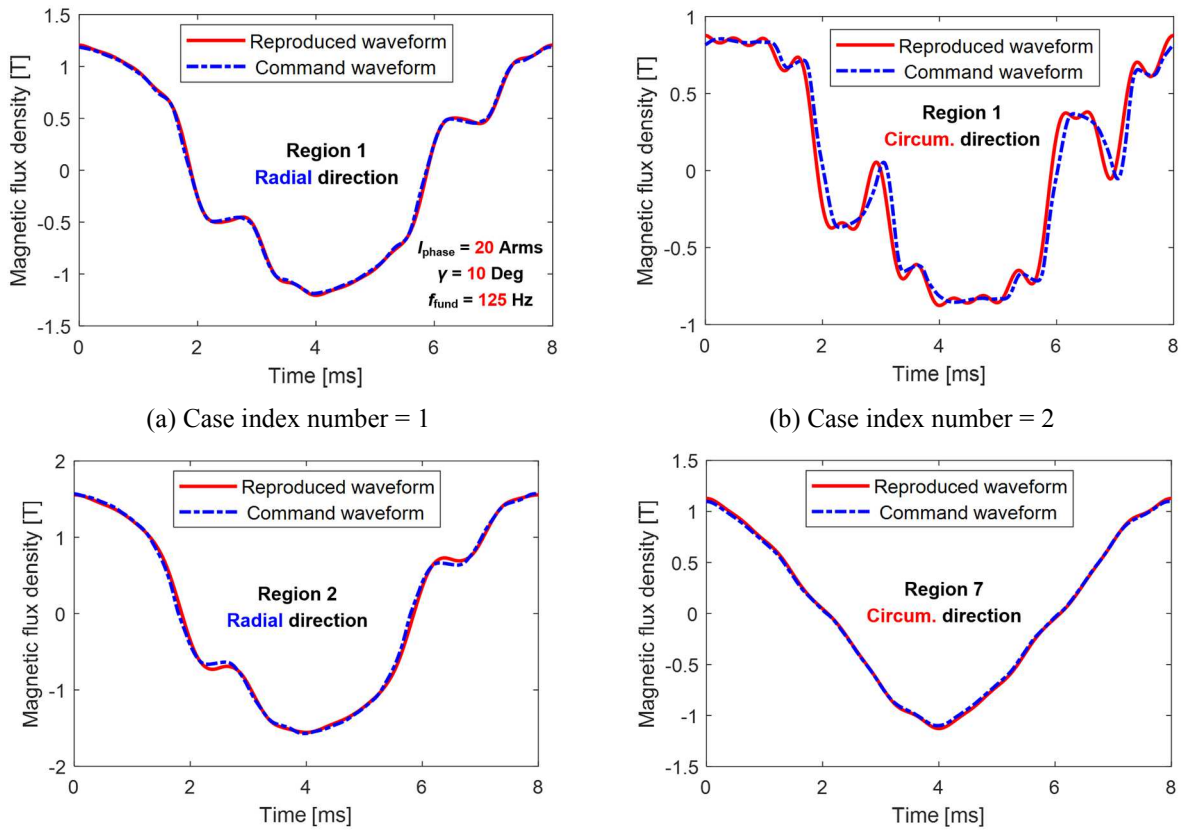

(a) Case index number = 1

(b) Case index number = 2

(c) Case index number = 3

(d) Case index number = 10

Figure 4-26: Comparison of command flux density waveforms and the measured flux density waveforms from the toroidal core iron loss test for four selected cases.

***Test conditions**:* fundamental current I_{phase} = 20 Arms, machine speed = 1,500 rpm (f_{fund} = 125 Hz), and current control angle γ = 10 degree.

Figure 4-26(a)-(d) confirm that the reproduced flux density waveforms in the toroidal core have achieved excellent agreement with the input flux density command waveforms derived from the 2-D FEA results in the seven regions and orthogonal orientations at 1,500 rpm machine speed. Since the flux density control performance is improved at lower speeds (i.e., lower fundamental frequencies), the waveform quality for those conditions is even better than the results shown in Figure 4-26(a)-(d), whereas it degrades at higher machine rotating speeds.

4.5.2 Model Evaluation over Different Machine Positions and Operating Conditions

With the proposed dynamic hysteresis model, the measured and predicted *B*-*H* curves are plotted in Figure 4-27(a)-(d) of four selected case indexes with 20 Arms phase current, 125 Hz fundamental frequency, and a current control angle γ at 10 degree.

As aforementioned, the complex flux density waveforms are first decomposed into its major and minor loop components, and then they are estimated separately. As depicted in Figure 4-27(a)-(d), the predicted hysteresis loops agree reasonably well with the measured data, which emulate the major loop waveshapes in the presence of multiple low-order harmonic fields. In most regions, the flux density waveforms in the machine stator side do not contain large-amplitude minor loops (e.g., stator tooth body or back iron region). However, as the results presented in Figure 4-26(b), the flux density waveform in the stator tooth tip region along the circumferential direction deviates considerably from the purely sinusoidal shape, and the slotting harmonics exert a significant impact and induce multiple minor loops. Also, since the input flux density waveform for this particular case is quite different from the input reference waveform, relatively larger discrepancies are observed compared to the measured data. For the remaining three cases, since the waveforms are closer to sinewaves, the proposed model agree quite well with the measured results.

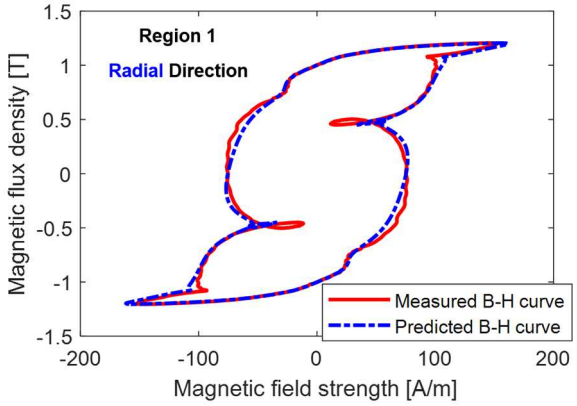

(a) Case index number = 1

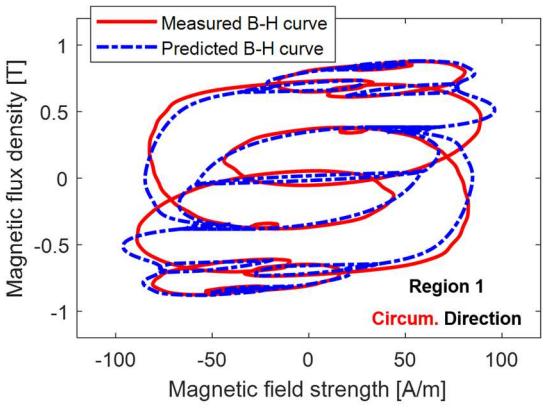

(b) Case index number = 2

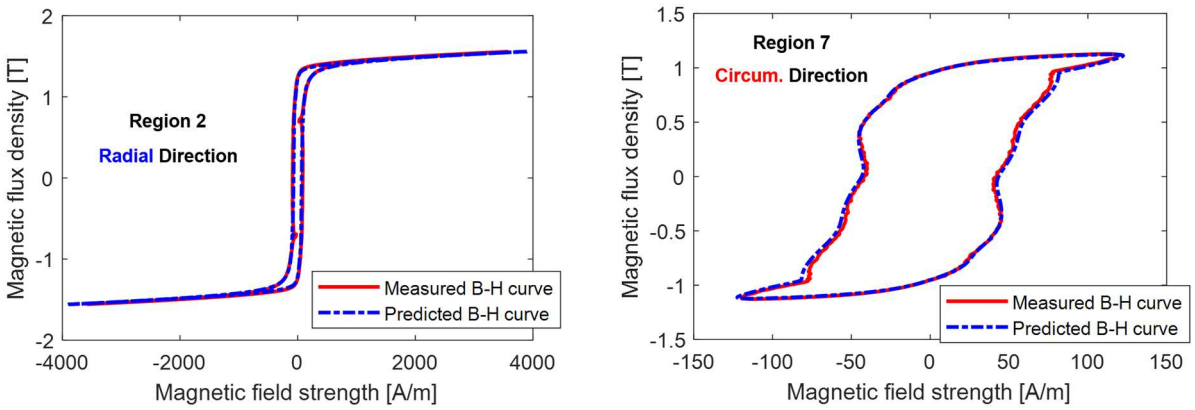

(c) Case index number = 3 (d) Case index number = 10

Figure 4-27: Comparison of measured and predicted *B-H* curves of four selected cases in the machine stator side.
***Test conditions**:* fundamental current I_{phase} = 20 Arms, machine speed = 1,500 rpm (f_{fund} = 125 Hz), and current control angle γ = 10 degree.

Figure 4-28(a)-(c) show the evaluation of iron loss prediction in different case indexes for three selected machine speed conditions (i.e., 500, 1,500, and 3,000 rpm). The volume of each region is taken into consideration and then scaled to the full structure of machine stator to determine the total iron loss in the stator side. It can be concluded that the proposed model has exhibited good agreement with the measured data over varying machine positions and decomposed flux directions, where the average error for each speed case is below 5%.

Next, estimated total stator-side iron loss based on the model-based predictions and the toroidal core loss measurements for the 10 cases are plotted versus the speed in Figure 4-29 for the same test conditions as in Figure 4-28. Despite higher errors in particular case index numbers (e.g., stator tooth tips (#2) and back iron region (#10) with 3,000 rpm machine speed)), the average estimation error drops to 1.61% since the stator iron loss is predominantly concentrated in the tooth body region where the errors are generally smaller.

In conclusion, these presented results based on toroidal core loss predictions and measurements have raised expectations for the model's ability to accurately the stator core loss over a wide range of speeds.

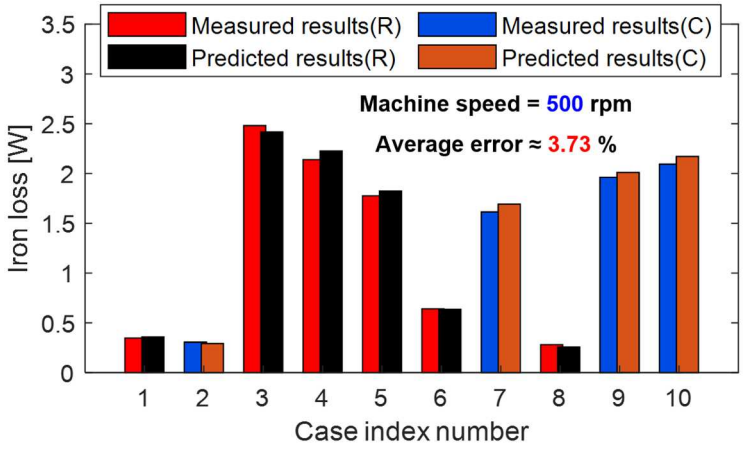

(a) Machine rotating speed = 500 rpm

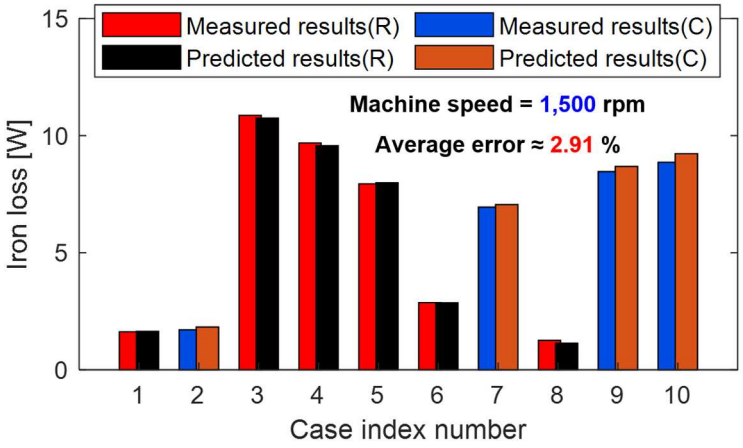

(b) Machine rotating speed = 1,500 rpm

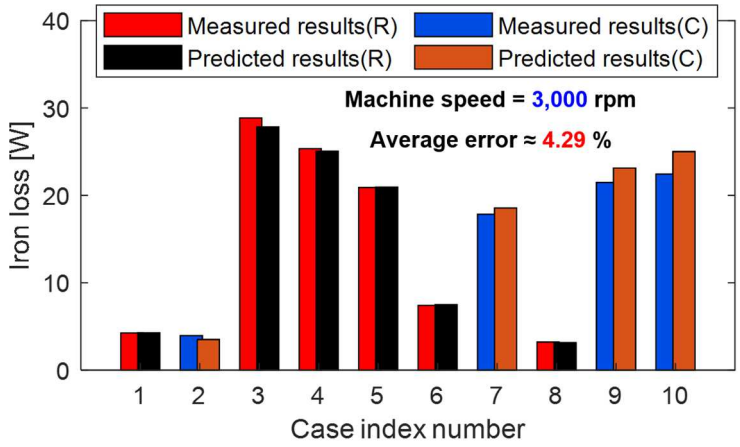

(c) Machine rotating speed = 3,000 rpm

Figure 4-28: Comparison of measured and predicted iron loss over different studied cases index numbers for three selected machine rotating speeds.

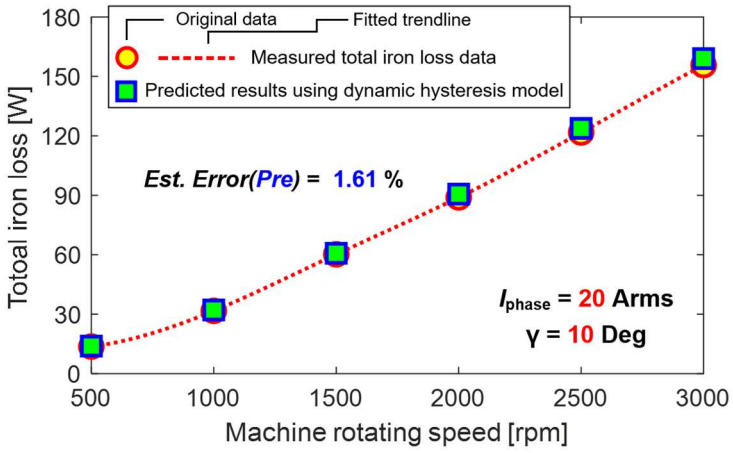

Figure 4-29: Estimates of machine total stator-side iron loss vs. machine rotating speed based on model-based loss prediction and measurements from the toroidal core test equipment.

4.5.3 High-Frequency Iron Loss Investigation in the Presence of DC-Bias Fields

The same approach discussed above could theoretically be extended to the rotor core iron loss analysis. However, when (4-2) is applied to the rotor side, the lowest significant frequency for the ac flux density components in the rotor occurs at the 12th harmonic of the machine fundamental frequency for the analyzed IPM machine since it is attributed to the stator slot harmonics. That is, 12 stator slots pass a given point on the rotor for each pole pass. As a result, the rotor-side 'fundamental' frequency rises to 500 Hz for even the lowest studied speed condition of 500 rpm corresponding to an excitation fundamental frequency of 41.67 Hz. This makes it very challenging to control the flux density waveforms via closed-loop control with the available testing equipment for rotor core iron loss estimation. Moreover, the machine rotor structure is more complicated compared to the stator side, calling for a much larger number of subdomain regions to emulate the flux density distribution.

As a compromise, high-frequency ac flux density waveforms with sinusoidal waveshapes are evaluated in the presence of external dc-bias fields to mimic the operating conditions of machine rotor-side harmonics. As discussed before, the pre-determined 2-D look-up table given in Figure 3-33 is used for magnetic condition compensation for as given minor loop amplitude.

Next, experimental tests have been conducted to develop a comparison of the measured and predicted iron loss in the toroidal core for ac flux ripple with varying amplitudes and frequencies together with varying dc-bias fields. As can be seen from Figure 4-30(a)-(b), the model-predicted iron loss results when the ac frequency is at 500 Hz closely match the measured values. More specifically, the average error for each of the two ripple amplitudes is below 10%, building confidence in the ability of the proposed scheme to predict the high-frequency rotor core iron loss in the presence of a dc-bias field. When the ac frequency is raised to 1 kHz, the estimation accuracy degrades as shown in Figure 4-30(c)-(d). However, the proposed model predicts a similar trend of iron loss variation vs. dc-bias field as the measured loss, supporting a conclusion that ignoring the impact of the dc-bias field in the rotor core iron loss analysis will lead to serious iron loss underestimation. A likely explanation for the above phenomena is that, since the 2-D look-up table in Figure 3-33 is developed for low ac excitation frequency values ($f_{minor} \approx 100$ or 200 Hz), this table cannot accurately predict the impact of the dc-bias field on the iron loss when the ac ripple frequency is considerably higher. As a result, it calls for further model characterization in the future in terms of the impact of bias fields on resulting iron loss in extended frequencies (e.g., f_{minor} ranges from 2 to 5 kHz).

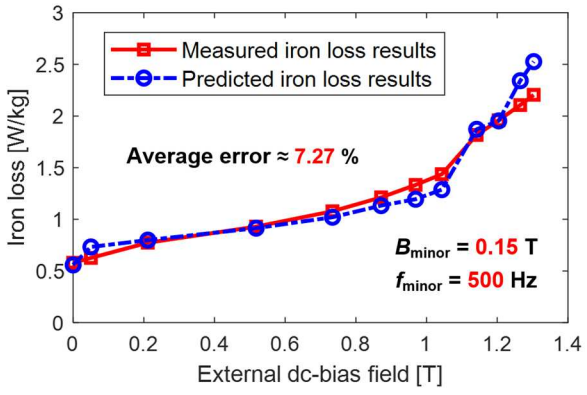

(a) B_{minor} = 0.15 T, f_{minor} = 500 Hz

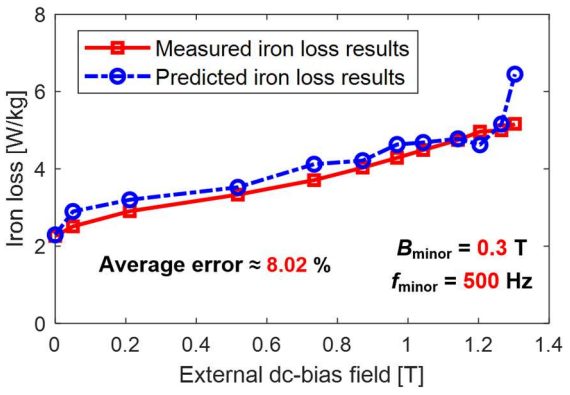

(b) B_{minor} = 0.3 T, f_{minor} = 500 Hz

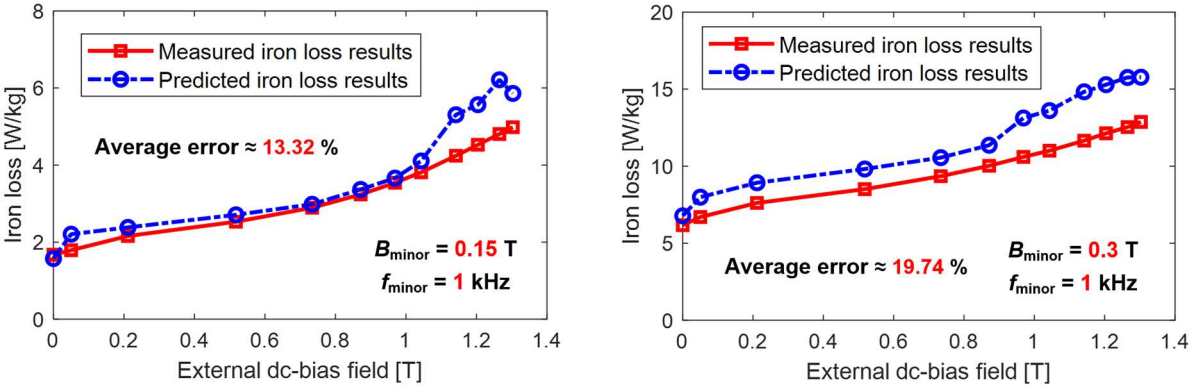

(c) B_{minor} = 0.15 T, f_{minor} = 1 kHz (d) B_{minor} = 0.3 T, f_{minor} = 1 kHz

Figure 4-30: Evaluation of the high-frequency ac iron loss at 500 Hz and 1 kHz with different ac flux ripple amplitudes (B_{minor} = 0.15 and 0.3 T) in the presence of external dc-bias fields.

4.5.4 Development of the Generalized Flux Density Waveform Segregation Algorithm

The existence of the external field has been shown to exert a substantial impact on the shape and the enclosed areas (i.e., iron loss) of the minor loops for a variety of magnetic materials with varying thicknesses and compositions. Therefore, it is of great importance to properly take the external field impact into consideration using the proposed dynamic hysteresis model.

However, the previous minor loop segregation technique implemented in Matlab requires a very small time step, making its accuracy and stability highly susceptible to the positions and amplitudes of the minor loops. As the flux density waveforms become more complicated in certain regions of the machine cores, it calls for a more generalized approach, and Figure 4-31 shows the flow chart of the proposed minor loop segregation algorithm. For a given simulated flux density waveform from 2-D FEA, all of the localized and global peak points are first determined via the first derivative. Then the minor loop identification problem is resolved by analytically solving for the position of the end point, which shares the same peak value as the studied localized peak point. More specifically, to locate each end point, the whole waveform is shifted downward/upward by the same value as the localized peak point depending on its polarity, making the end point identification process equivalent to that of the eigenvalue calculation discussed in [178], [179]

using a FFT-based mathematical approach. Since it is possible that there are multiple embedded minor loops inside a large-amplitude minor loop (frequently observed for elements located in the rotor surface), a repetitive process is applied to ensure that all of the embedded minor loops are separated out, guaranteeing accurate major and minor loop segregation for arbitrary waveshapes. By combining this segregation process with the proposed dynamic hysteresis model, the total iron loss in the studied machine can be determined element-by-element.

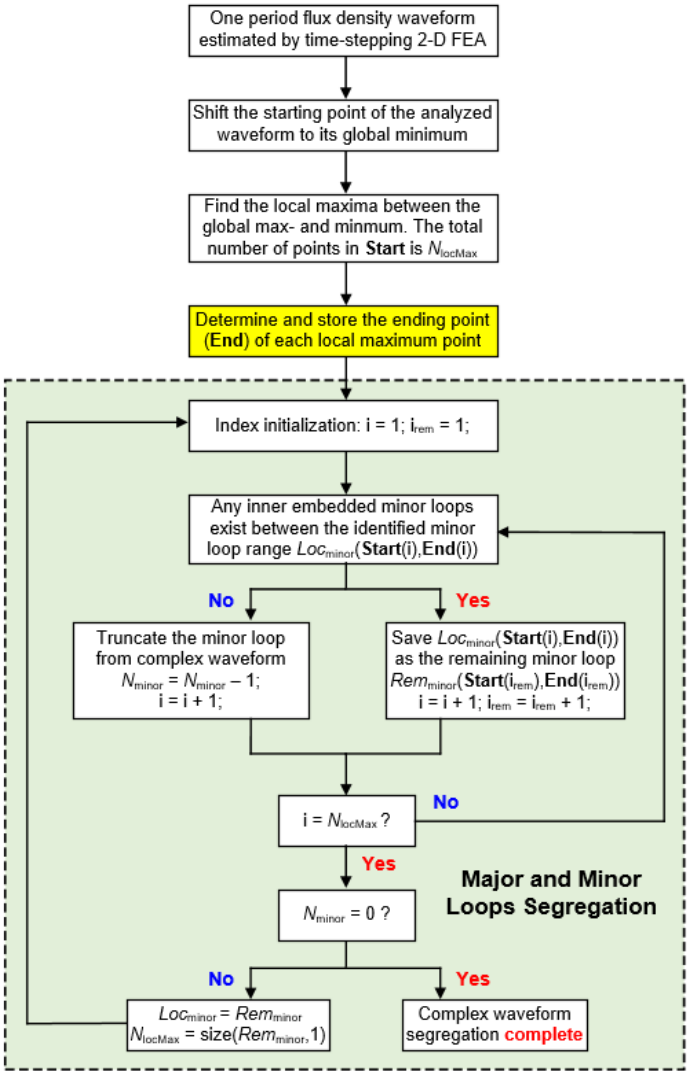

Figure 4-31: Flow chart of the proposed generalized flux density waveform segregation algorithm.

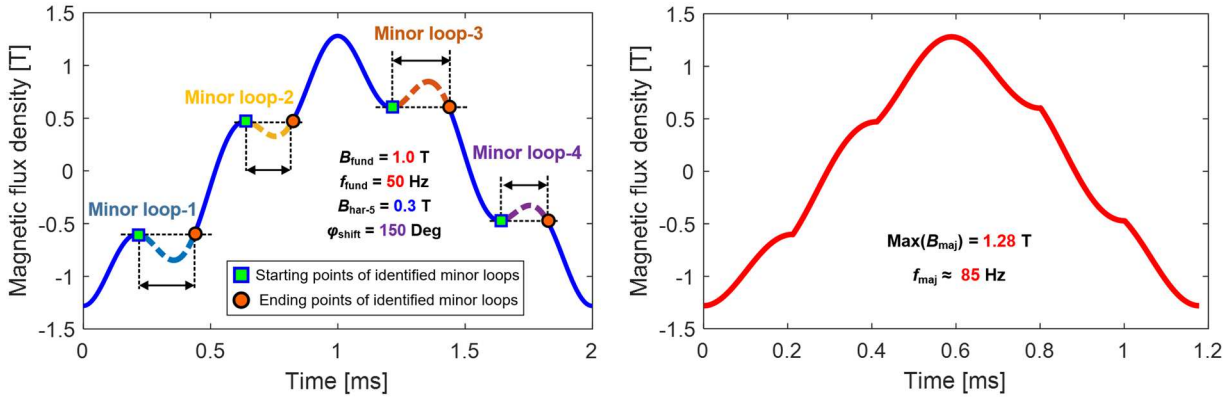

(a) Original flux density waveform (b) Segregated major loop component

Figure 4-32: Example flux density waveform with superimposed harmonic components, illustrating process for segregating minors loops from the original input flux density waveform.

An example case of the minor loop segregation is depicted in Figure 4-32(a)-(b). As shown in Figure 4-32(a), each minor loop in dashed lines starts with a localized peak point (i.e., square-shape marker) and an end point (i.e., circle-shape marker), which both are solved analytically. All of the minor loops are subsequently truncated from the original waveform, leaving the major loop component displayed in Figure 4-32(b). It is worth noting that, after the segregation process, the frequency of the major or minor loop components can deviate significantly from the fundamental frequency. In the example case, the major loop frequency increases to 85 Hz from 50 Hz f_{fund}, which clearly suggests that conventional FFT-based iron loss models are not suitable to evaluate the iron loss of complex waveforms that contain rich harmonics and minor loops.

4.5.5 Rotating Flux Density Waveform Decomposition

It has been demonstrated earlier in this chapter that the predicted magnetic field from 2-D FEA in each studied region is typically decomposed into the radial and circumferential direction to reflect the rotating nature of the flux density distribution in electric machines. Although the dominant field components align well with those two orthogonal directions, in some specific regions (e.g., the junction of the stator tooth and stator back-iron), the major (i.e., B_{max} axis) and minor (i.e., B_{min} axis) can deviate significantly from the radial and circumferential directions. As

a result, a modified technique proposed in [51], [135] has been adopted to decompose the simulated magnetic field into major and minor axes that are adjusted to align with the calculated magnetization ellipse. These axes vary for the specific field distributions in different machine regions. It has been widely acknowledged [180] that non-oriented magnetic materials which are primarily adopted for electric machine applications are less sensitive to rotating field effect compared to the grain-oriented materials, making it a reasonably accurate approximation.

A general expression of the rotating field $\boldsymbol{B}_{\mathbf{rot}}$ is given as:

$$\boldsymbol{B}_{\mathbf{rot}} = B_{\mathrm{rad}} + 1i \cdot B_{\mathrm{cir}} \tag{4-3}$$

where the B_{rad} and B_{cir} are the simulated magnetic flux density from the 2-D FEA in the radial and circumferential direction, respectively, where the radial component is aligned with the real axis.

The major field axis $\varphi_{\max}$ can be determined from the following expression:

$$\varphi_{\max} = \mathrm{angle}(\mathrm{Max}(\boldsymbol{B}_{\mathbf{rot}})) \tag{4-4}$$

After obtaining the major axis information, the simulated field in the radial and circumferential directions can be transformed to the major and minor axes using a rotational transformation expressed by the following matrix equation:

$$\begin{bmatrix} B_{\mathrm{major}} \\ B_{\mathrm{minor}} \end{bmatrix} = \begin{bmatrix} \cos(\varphi_{\max}) & \sin(\varphi_{\max}) \\ -\sin(\varphi_{\max}) & \cos(\varphi_{\max}) \end{bmatrix} \cdot \begin{bmatrix} B_{\mathrm{rad}} \\ B_{\mathrm{cir}} \end{bmatrix} \tag{4-5}$$

An example case is given in Figure 4-33(a)-(b), where the major and minor axis field component-B_{major} and B_{minor} are determined using (4-3)-(4-5). Once the decomposed field components are calculated, the proposed dynamic hysteresis model can be employed to calculate the iron loss contributions separately from the major and minor axis components before summing them to estimate the total iron loss in the analyzed region. This approach makes it possible to better incorporate the impact of the rotating field on the resulting machine iron loss without requiring additional measurement data or introducing extra calculation burdens.

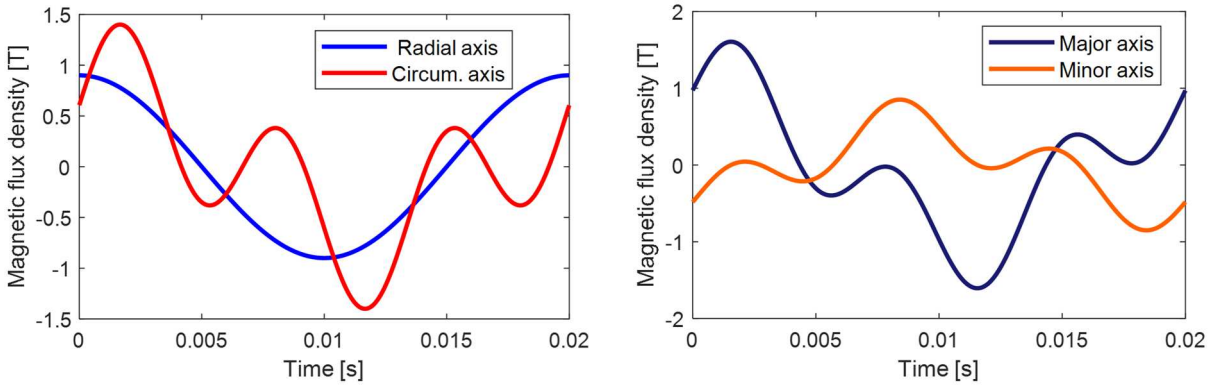

(a) Original flux density waveforms in radial and circumferential direction

(b) Decomposed field components in the major and minor axes

Figure 4-33: Example of the rotating field decomposition applied to a set of field waveforms expressed in the orthogonal radial and circumferential directions.

4.5.6 Element-by-Element Machine-Level Iron Loss Analysis

With the availability of the complex waveform segregation and rotating field decomposition techniques demonstrated in the preceding sections, an element-by-element machine total iron loss estimation framework has been constructed, and the flow chart of the proposed algorithm is summarized in Figure 4-34.

To investigate the iron loss induced by the fundamental field and low-order harmonic components (e.g., slotting harmonics), a sinusoidal current command is fed to the 2-D FEA to determine the flux density distribution in the studied IPM machine. Based on the simulated results in the orthogonal radial and circumferential directions, the rotating magnetic fields are decomposed into the corresponding major- and minor-axis components, where the iron loss in each axis is evaluated separately before summing them to obtain the total iron loss in a mesh element.

For the decomposed field components in either the major- or minor-axis, the flux density waveform is further segregated into the major and minor loop components, which are subsequently analyzed by the proposed dynamic hysteresis model. The same process is repeated for all the mesh elements in a single-pole model with sufficiently fine mesh properties to ensure accurate magnetic flux density estimation. Moreover, since this approach relies on material-level characterization and

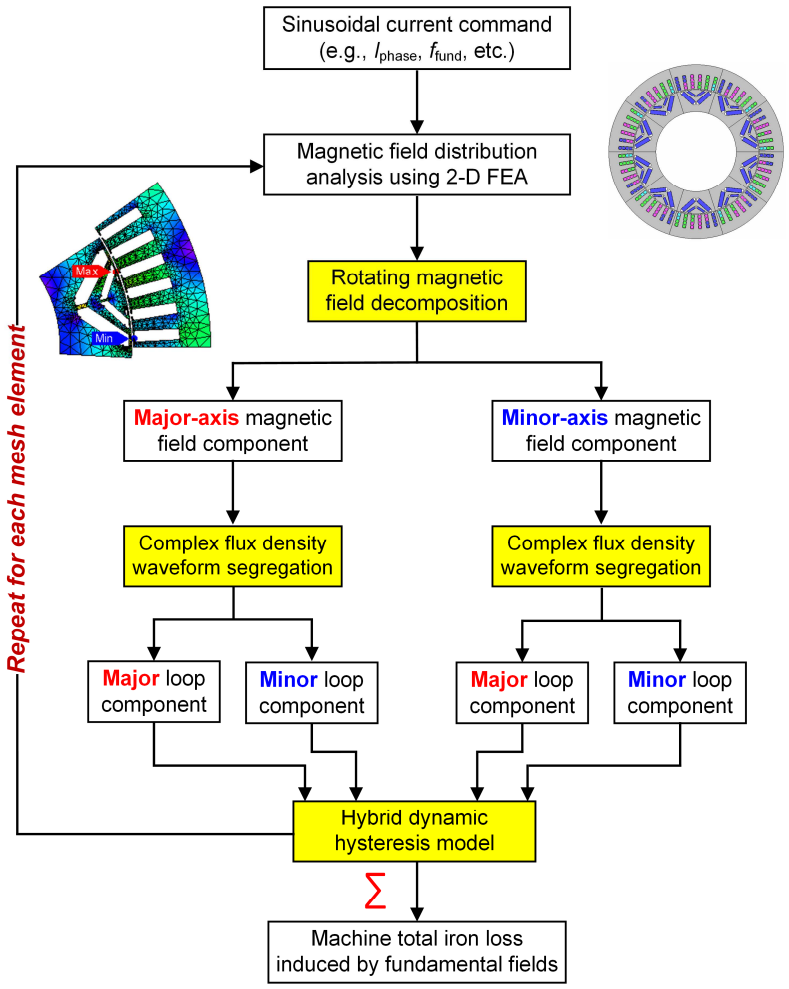

Figure 4-34: Flow chart of the proposed machine-level total iron loss estimation algorithm.

machine-level FEA simulation, it can be easily extended to a wide range of either existing or future electric machine topologies (e.g., induction machines).

The proposed iron loss estimation scheme has been applied to study the iron loss in the same baseline IPM machine specified in Table 4-3 for two selected loading conditions over a wide range of machine speeds. To provide a preliminary insights into the validity of the proposed model's performance, the prediction results are compared to the loss predictions provided by the embedded iron loss model in JMAG, where the total iron loss is segregated into the static hysteresis loss, classical eddy current loss, and excess loss. However, since the JMAG model is fundamentally based on Fourier analysis, it is widely acknowledged that this class of iron loss model cannot

properly evaluate all of the loss characteristics of dynamic hysteresis loops. Furthermore, the additional impact introduced by the external magnetic fields is ignored in the JMAG iron loss model, potentially leading to a major iron loss underestimation when the stator armature current deviates from the sinusoidal waveform (i.e., six-step voltage mode) or when the machine rotor-side iron loss induced by slotting harmonics becomes more significant at higher rotating speeds.

Figure 4-34(a)-(d) presents a comparison of the predicted stator core iron losses using the proposed dynamic hysteresis model and the iron loss model embedded in the JMAG FEA simulation software. For this particular light-load condition (i.e., I_{phase} = 20 Arms, γ = 10 deg), most field components in the machine stator core elements are quite sinusoidal in shape without heavy saturation since pure sinusoidal current waveforms with relatively low amplitudes are supplied to the Spark machine. As a result, close agreement in the defined stator regions is observed between the losses predicted using the proposed dynamic hysteresis model and the JMAG FEA iron loss model. This suggests that that the performance of the conventional FFT-based iron loss model is acceptable when the field component waveforms are close to sinusoidal.

However, the results in the machine rotor core are much different. Figure 4-35(e) overlays the FEA-simulated rotor iron loss with the dynamic hysteresis model's predicted values with and without including the dc-bias field impact. If the dc-bias field effect is ignored, the predicted and measured values are very close, and the small deviation is likely caused by the different methods used for rotating field decomposition.

In JMAG, the rotating field is separated into radial and circumferential components, whereas an improved rotating field decomposition approach is adopted for the proposed dynamic hysteresis model's predictions. Furthermore, once the dc-bias field impact is considered, the estimated rotor-side iron loss is significantly higher than that resulting from ignoring the bias field effect. The

substantial difference indicates that the existence of external bias fields plays a critical role in rotor-side iron loss. As a result, the predicted machine total iron loss in Figure 4-35(e) with dc-bias field effect included is higher than the loss predictions provided by JMAG due to the latter model's much lower rotor-side iron loss contribution. This suggests that the iron loss underestimation at high machine speeds which has been often observed is likely attributable to ignoring the dc-bias field in conventional iron loss models.

In addition, the same analysis has been extended to another condition with a higher stator current (i.e., I_{phase} = 35 Arms, and γ = 10 Deg). In general, a similar conclusion can be drawn from the comparison results presented in Figure 4-36(a)-(e). Excellent agreement of the loss predictions provided by the dynamic hysteresis loss model and the FEA iron loss model is observed in most stator regions, and the total stator core iron loss values are almost identical over the studied machine speed range. However, ignoring the dc-bias field in the machine rotor side leads to a substantial estimation error. Although the rotor core iron loss is less significant compared to the stator core contribution in the studied PM synchronous machine with distributed windings, it is apparent that the predicted total iron loss results are higher with the proposed new dynamic hysteresis model than with the more conventional iron loss model used in the JMAG FEA software.

In conclusion, the proposed dynamic hysteresis iron loss model exhibits similar performance compared to the embedded iron loss model in JMAG to determine the stator-core iron loss with sinusoidal current supplied to the windings. More importantly, the new model provides a much-improved solution for incorporating the dc-bias field effect on iron losses into the minor loop iron loss estimation calculations in the machine rotor core.

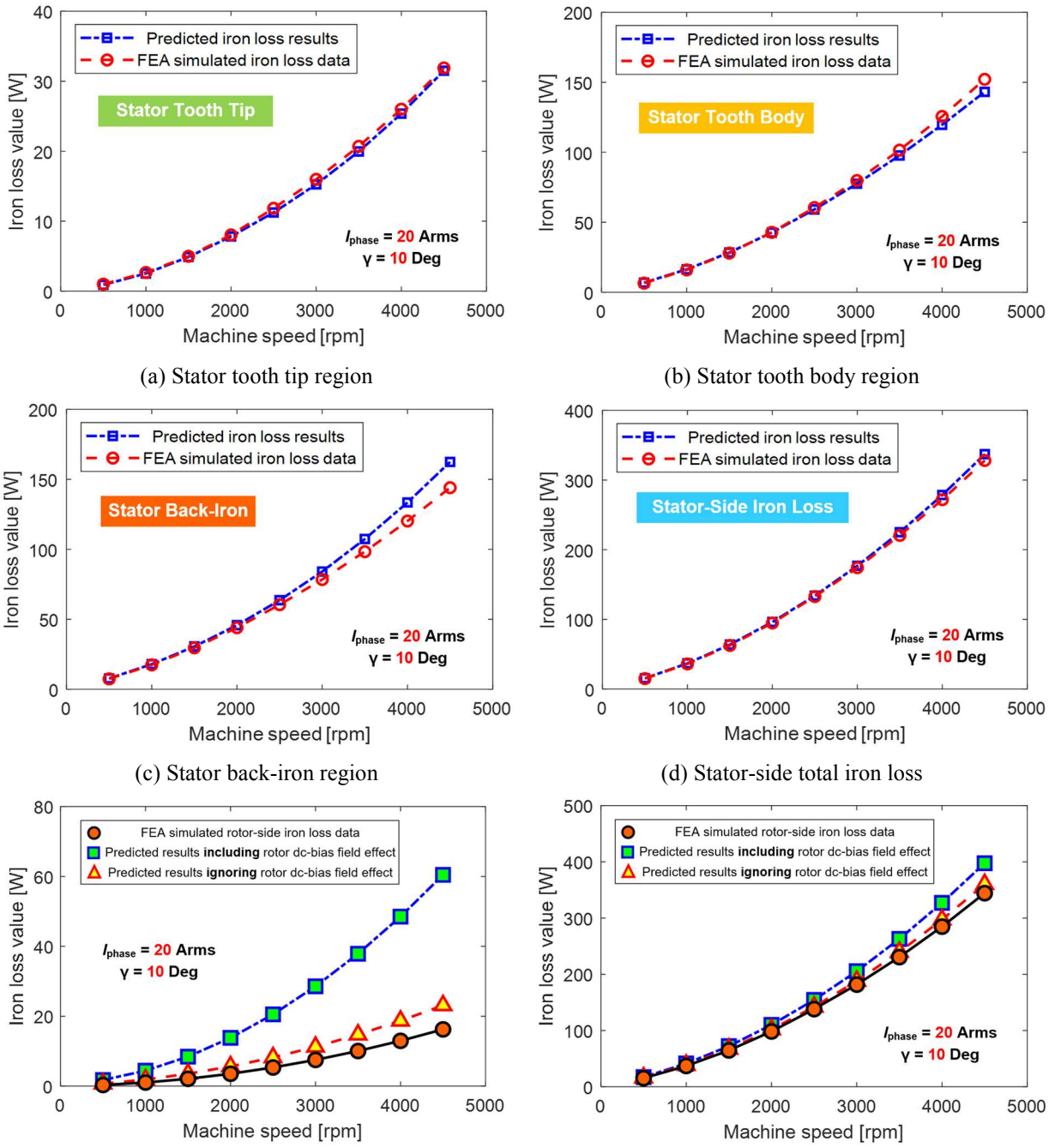

(a) Stator tooth tip region

(b) Stator tooth body region

(c) Stator back-iron region

(d) Stator-side total iron loss

(d) Rotor-side total iron loss

(e) Machine total iron loss under sinusoidal supply

Figure 4-35: Comparison of predicted iron loss results using the proposed dynamic hysteresis loss model and the JMAG FEA loss model in different regions of the studied IPM traction machine (Case I).

(***Test conditions***: I_{phase} = 20 Arms, γ = 10 deg, and machine speed = 500 to 4,500 rpm)

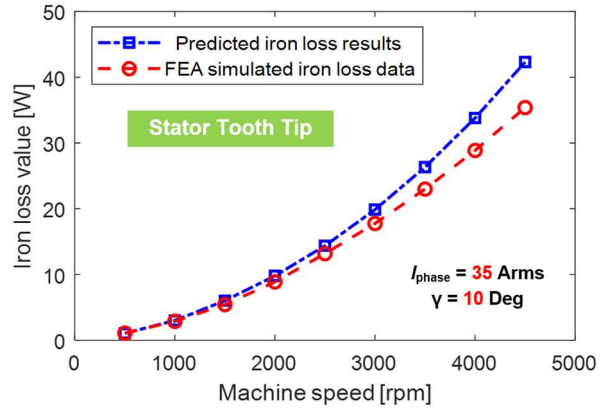

(a) Stator tooth tip region

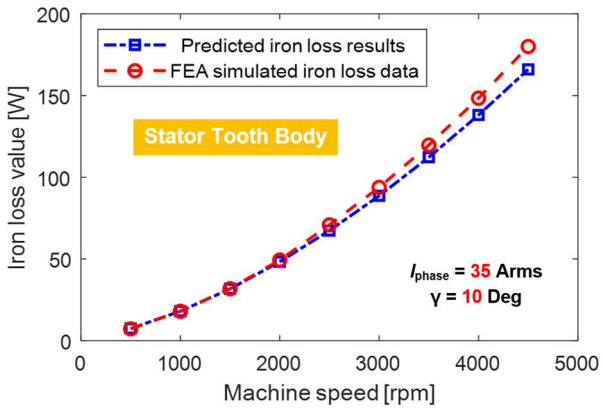

(b) Stator tooth body region

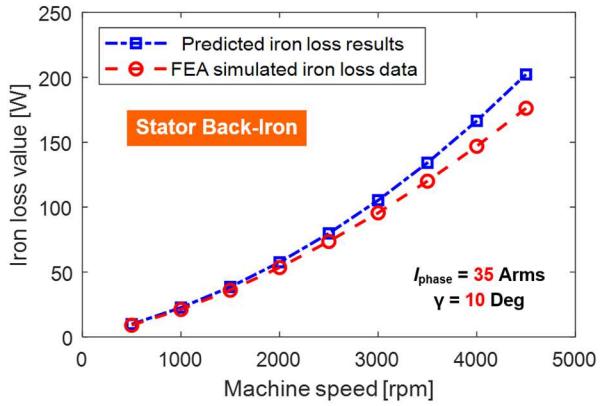

(c) Stator back-iron region

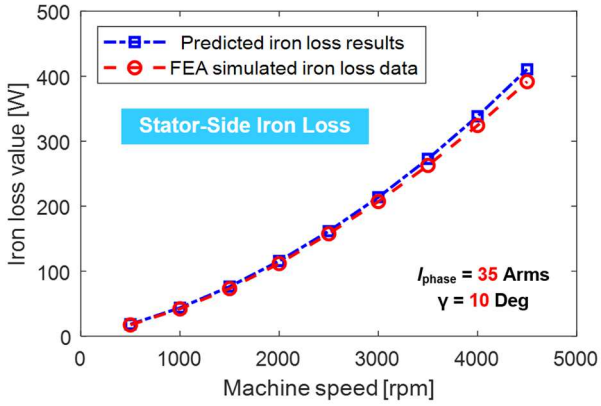

(d) Stator-side total iron loss

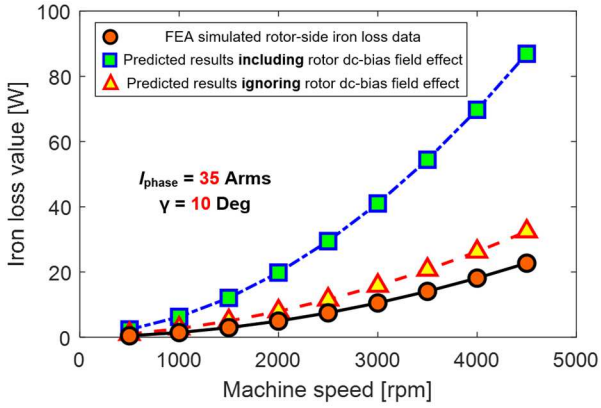

(d) Rotor-side total iron loss

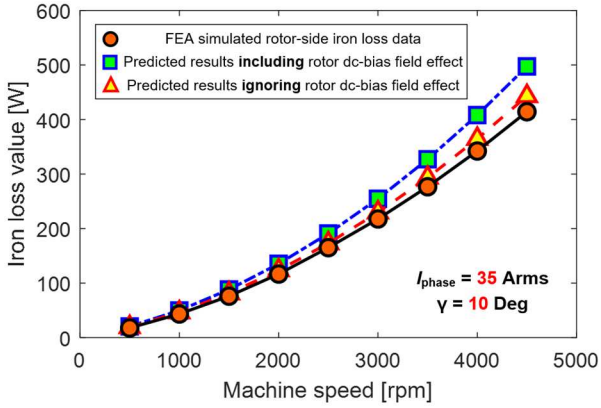

(e) Machine total iron loss under sinusoidal supply

Figure 4-36: Comparison of predicted iron loss results using the proposed dynamic hysteresis loss model and the JMAG FEA loss model in different regions of the studied IPM traction machine (Case II).

(***Test conditions***: I_{phase} = 35 Arms, γ = 10 Deg, and machine speed = 500 to 4,500 rpm)

4.6 Summary

In this chapter, experimental verification of the proposed $\Delta H_{dyn}/\Delta t$-based and H_{dyn}-based dynamic hysteresis models has been conducted by evaluating different flux waveforms that are commonly observed in IPM machines. These include the sinusoidal flux waveforms, non-sinusoidal flux waveforms with superimposed higher-order harmonics, and sinusoidal flux waveforms in the presence of pre-magnetized dc-bias fields. It has been confirmed that both models can accurately estimate the iron loss of the flux density waveform for sinusoidal waveshapes when the frequency is within the input data limit. They also exhibited some extrapolation capabilities for frequencies outside input data range, but errors generally grow monotonically as the extent of the extrapolation is increased. In comparison, the $\Delta H_{dyn}/\Delta t$-based model performs better outside the input data limit at 1 kHz.

When the models are applied to non-sinusoidal waveforms with superimposed harmonics, the $\Delta H_{dyn}/\Delta t$-based model gives overestimated results due to complex *dB/dt* profiles in specific conditions, whereas the H_{dyn}-based model exhibits promising capabilities for emulating the *B-H* curves of the major loop components over varying testing conditions, including the cases with very high fundamental frequency (i.e., f_{fund} = 500 Hz). Taking advantages of each proposed model, a hybrid dynamic hysteresis model is formulated in this analysis. The H_{dyn}-based model is adopted for major loop analysis, and the $\Delta H_{dyn}/\Delta t$-based model is responsible for minor loop estimation. The accuracy of this model has been validated for 0.30 mm material over a broad testing range.

Furthermore, two new lamination steels have been characterized in this report with sheet thickness values of 0.25 and 0.27 mm. Following the same model characterization procedure, the newly proposed hybrid dynamic hysteresis model has been employed to predict the dynamic hysteresis loop and corresponding iron loss data for different testing conditions with both new

materials. The excellent agreement between the predicted and measured data confirms that the proposed model can be extended to analyze magnetic materials with different sheet thicknesses and compositions, making it a sufficiently generalized tool for iron loss analysis.

In light of the uncertainties in machine iron loss segregation, machine-level model evaluation has been conducted by reproducing the simulated flux density waveforms from the stator side of the baseline IPM machine and then using the toroidal test results to develop estimates of the stator core losses. The predicted results in different defined regions of the stator core exhibit excellent agreement with the measured data, and the average error of the total stator core iron loss estimate when comparing a prediction based on the characterized model with another based on the measured toroidal core test results is approx. 1.61% over a range of machine speeds from 500 to 3,000 rpm. Also, high-frequency iron loss in the presence of external dc-bias fields has been investigated to mimic the operating conditions of rotor-side harmonics. The results indicate that incorporating the dc-bias field effect into iron loss estimation is vital to achieve acceptable accuracy.

Finally, an element-by-element machine-level iron loss estimation scheme has been developed, including a generalized complex waveform segregation technique and an approach to better decompose the rotating magnetic fields in electric machines. With the introduction of these two improvements, a complete framework has been constructed to evaluate the fundamental field-induced iron loss in the baseline IPM machine. The comparison results between the predicted loss results using the new model and FEA-simulated data from JMAG indicate that the rotor-side iron loss can be severely underestimated if the dc-bias field impact is not properly included. In contrast, if the input stator currents have sinusoidal waveshapes and small amplitudes (i.e., light-load conditions), the predicted loss results are very close to the predictions calculated by the embedded iron loss model in JMAG over a wide machine speed range (i.e., from 500 to 4,500 rpm).

Chapter 5
Prediction and Evaluation of PWM-Induced Current Ripple

5.1 Introduction

Interior permanent magnet synchronous machines combined with three-phase voltage source inverters (VSIs) are widely used for traction applications owing to their high torque/power density and efficiency. However, the high-frequency current ripple induced by pulsewidth modulation (PWM) switching generates ac losses in each of three major machine materials: the copper stator windings, the rotor magnets, and the stator and rotor laminated cores. These additional ac losses can degrade the machine's efficiency substantially under some specific operating conditions when the PWM-induced losses are comparable to the losses generated by the fundamental component. In order to accurately predict and mitigate these losses during the machine design stage, accurate prediction of the PWM-induced current ripple is required under a wide range of drive and machine high-speed operating conditions.

After the introduction, the analytical prediction model is discussed based on the instantaneous inverter-side voltage waveforms during each PWM switching cycle combined with a dynamic model of the IPM machine in the *d-q* rotor reference frame. The model is subsequently used to investigate the impact of several influencing factors on the current ripple's rms value and frequency spectrum. Experimental results are presented to verify the proposed analytical model. Issues associated with the practical applications of the proposed model are discussed. Finally, conclusions summarizing key points are presented.

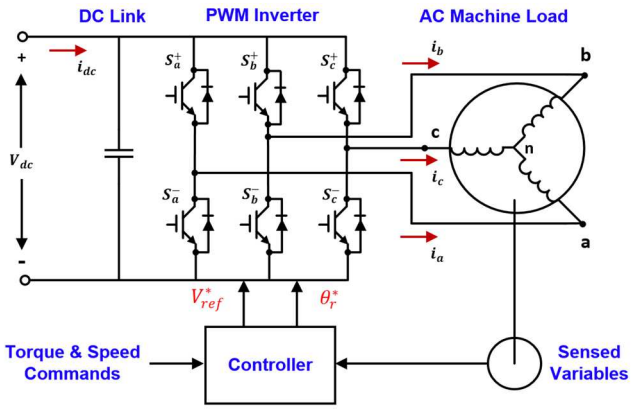

Figure 5-1: Conventional three-phase VSI-based ac drive configuration.

5.2 Analytical Prediction Model Derivation

5.2.1 PWM-Induced Current Ripple Definition

For the typical three-phase ac machine supplied by a VSI with current-regulated phase currents (see Figure 5-1), the phase voltage waveforms with the desired sinusoidal fundamental frequency component are delivered corresponding to the torque/speed commands.

It is assumed that space vector pulsewidth modulation (SVPWM) is used for the switching algorithm, and the reference voltage vector $\vec{V}_{\text{ref}}$ is within linear modulation range. The switching sequence of VSIs is based on the position of the commanded voltage vector in the space vector diagram and its amplitude $|\vec{V}_{\text{ref}}|$ compared to the dc-bus voltage V_{dc}, as shown in Figure 5-2. The ratio between $|\vec{V}_{\text{ref}}|$ and V_{dc} is known as the modulation index. The time duration of each switching state can be determined analytically as [181]

$$T_1 = \frac{\sqrt{3}T_s|\vec{V}_{\text{ref}}|}{V_{\text{dc}}} \cdot \sin\left(\frac{n}{3}\pi - \alpha\right) \tag{5-1}$$

$$T_2 = \frac{\sqrt{3}T_s|\vec{V}_{\text{ref}}|}{V_{\text{dc}}} \cdot \sin\left(\alpha - \frac{n-1}{3}\pi\right) \tag{5-2}$$

$$T_0 = T_s - T_1 - T_2 \tag{5-3}$$

where n is the sector where the voltage vector is located and α is the angle between $\vec{V}_{\text{ref}}$ and phase a axis, as indicated in Figure 5-2.

For symmetrical SVPWM, each PWM switching cycle can be sub-divided into seven symmetrically distributed sections. Since the PWM switching frequency is generally much higher than the machine fundamental frequency, the machine-side voltage is assumed unchanged within each switching cycle. The instantaneous inverter output phase voltages, and the average voltage during each PWM cycle are plotting in Figure 5-3 when the reference voltage resides in the first sector.

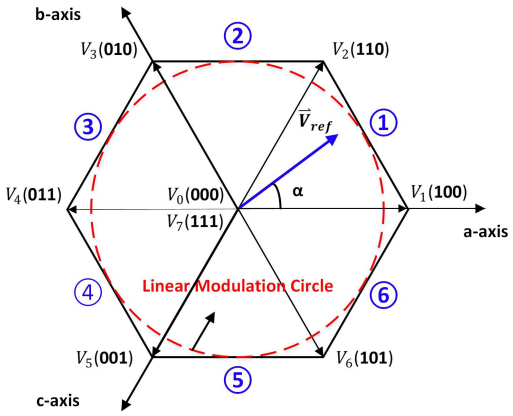

Figure 5-2: Space vector diagram and eight voltage states.

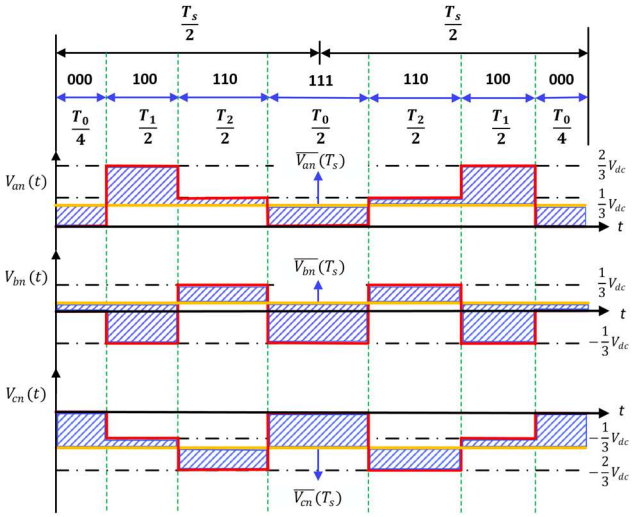

Figure 5-3: Instantaneous (—) and average (—) voltage waveforms for the three phases during one PWM switching cycle in the first sector.

TABLE 5-1: INVERTER SWITCH STATES AND PHASE LINE-TO-NEUTRAL VOLTAGES FOR THE EIGHT INVERTER OUTPUT VOLTAGES STATES

Voltage	V_{an}	V_{bn}	V_{cn}	Voltage	V_{an}	V_{bn}	V_{cn}
V_0(000)	0	0	0	V_4(001)	$\frac{-2V_{dc}}{3}$	$\frac{V_{dc}}{3}$	$\frac{V_{dc}}{3}$
V_1(100)	$\frac{2V_{dc}}{3}$	$\frac{-V_{dc}}{3}$	$\frac{-V_{dc}}{3}$	V_5(001)	$\frac{-V_{dc}}{3}$	$\frac{-V_{dc}}{3}$	$\frac{2V_{dc}}{3}$
V_2(110)	$\frac{V_{dc}}{3}$	$\frac{V_{dc}}{3}$	$\frac{-2V_{dc}}{3}$	V_6(101)	$\frac{V_{dc}}{3}$	$\frac{-2V_{dc}}{3}$	$\frac{V_{dc}}{3}$
V_3(010)	$\frac{-V_{dc}}{3}$	$\frac{2V_{dc}}{3}$	$\frac{-V_{dc}}{3}$	V_7(111)	0	0	0

The inverter switch states and phase line-to-neutral voltages corresponding to each of the eight output voltage vectors are summarized in Table 5-1.

The red-outlined envelopes of the shaded areas in Figure 5-3 voltage waveforms highlight the ac components of the three-phase voltage waveforms. This ac component is defined as the voltage difference between the instantaneous $v_{xn}(t)$ and the average phase voltage $\bar{v}_{xn}(t)$ during each PWM switching cycle.

Considering phase-*a* as an example and ignoring (for now) the mutual coupling between the phases, the slope of current ripple with constant load inductance L can be calculated by (5-4), where the average machine-side voltage $\bar{v}_{an}$ is approximated as the voltage in the center of the switching cycle to account for changes in either the machine's resistive voltage or back-emf during one switching cycle.

$$\frac{di}{dt} = \frac{v_{an}(t) - \overline{v}_{an}(T_s)}{L} = \frac{\overline{v}_{an}}{L} \tag{5-4}$$

Within each PWM switching cycle, the current ripple can be approximated as the concatenation of seven linear segments, as depicted in Figure 5-4.

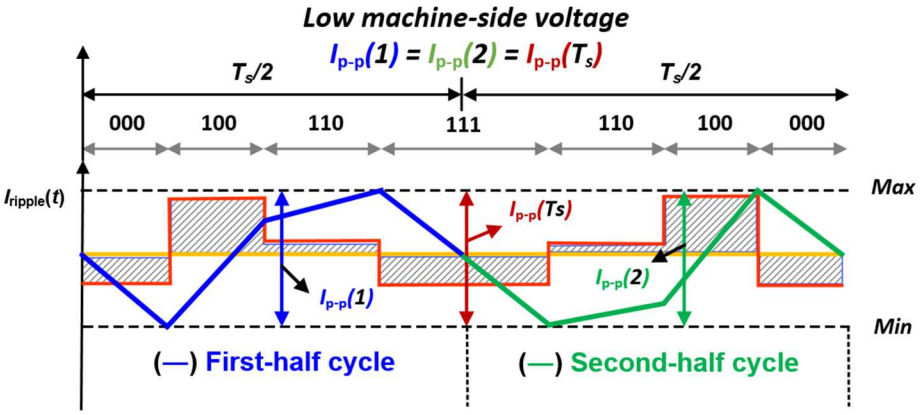

Low machine-side voltage case: $\overline{v}_{an}(T_s) < V_{dc}/3$

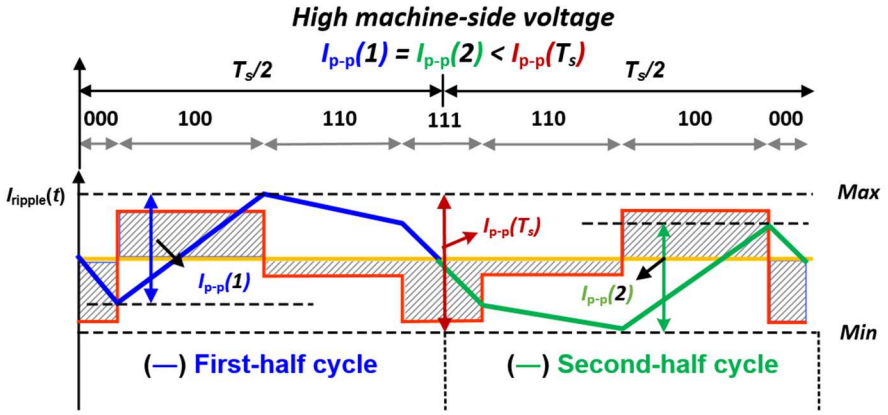

High machine-side voltage case: $\overline{v}_{an}(T_s) > V_{dc}/3$

Figure 5-4: Phase-*a* current ripple waveform for a PWM switching cycle with different machine-side voltages.

The shape and peak-to-peak value of the current ripple waveforms are determined by both the time duration and current slope of each state. Therefore, the resultant PWM-induced current ripple is inherently determined by the inverter switching state, dc-bus voltage, load inductance, and average load voltage (i.e., machine operating condition).

The actual switching patterns of VSIs could be slightly different from the ideal condition due to the deadtime effect or the voltage drop across the power device. However, the deadtime adopted by commercial drives (e.g., 150 ns) is typically much smaller than one PWM switching period, and deadtime compensation is often added to the drive controls to cancel its effects, as is the case in the experimental evaluation discussed in a later section of this chapter. Similarly, the voltage

drop across the power device is typically small and negligible compared to the inverter dc-bus voltage or machine-side average voltage. Therefore, the impact of deadtime and on-state switch voltage drop are ignored in this analysis. If necessary, those voltage terms could be added to the equations to incorporate both effects.

Figure 5-4(a) and (b) shows the waveshape properties under two different machine-side voltage conditions. When $\bar{v}_{an}(T_s)$ is smaller than $V_{dc}/3$, the peak-to-peak values of current ripple in the first- and second-half of the PWM switching cycle are equal to the value across the full cycle (i.e., $I_{p\text{-}p}(1) = I_{p\text{-}p}(2) = I_{p\text{-}p}(T_s)$), which drives the dominant frequency of current ripple toward 2x PWM frequency. As the machine-side voltage increases and becomes larger than $V_{dc}/3$, although the first-and second-half cycles are still inversely symmetrical across the mid-point of one PWM cycle (i.e., $I_{p\text{-}p}(1) = I_{p\text{-}p}(2)$), the peak-to-peak value in each half cycle is smaller than the peak-to-peak value across the full cycle. Therefore, a larger amount of harmonic components in the vicinity of 1x PWM frequency will be observed during operation with higher machine-side voltage. To sum up, not only the current ripple's rms value varies with the inverter and machine operating conditions, but the frequency spectra also change, which, in turn, can have a significant impact on the frequency-sensitive losses.

5.2.2 Static and Dynamic Inductances of IPM Machines

In contrast to the *L-R-C* load bank with a constant inductance value, the phase winding inductances of IPM machines can vary significantly as the machine moves into its highly saturated region or deep flux-weakening region. Moreover, for the IPM machines under PWM excitation, it is the dynamic inductance rather than the static inductance that determines the slop and amplitude of the PWM-induced current ripple. The static and dynamic inductances are defined as:

$$L^{Sta} = \frac{\psi}{I} \tag{5-5}$$

$$L^{Dyn} = \frac{d\psi}{dI} \tag{5-6}$$

The variation trends for the *d*- and *q*-axis flux linkages ψ_d, ψ_q versus stator *dq* currents i_d, i_q are shown in Figure 5-5 without considering any cross-coupling effects.

Figure 5-5 shows that the flux linkage curve for the *q*-axis can be divided into two parts: its linear and saturated regions. When the machine operates in a low-excitation Point-A, the static inductance is very close to its dynamic inductance. However, as the *q*-axis current increases and moves to Point-B where the machine is heavily saturated, the dynamic inductance decreases sharply and exhibits a significant difference from its static inductance value.

On the other hand, owing to the large equivalent air gap created by the permanent magnets in the *d*-axis, there is much less magnetic saturation in the *d*-axis. Therefore, the static and dynamic inductances in the *d*-axis are intrinsically close to each other over a wide range of operating conditions, including the saturated region like the Point-C plotted in Figure 5-5.

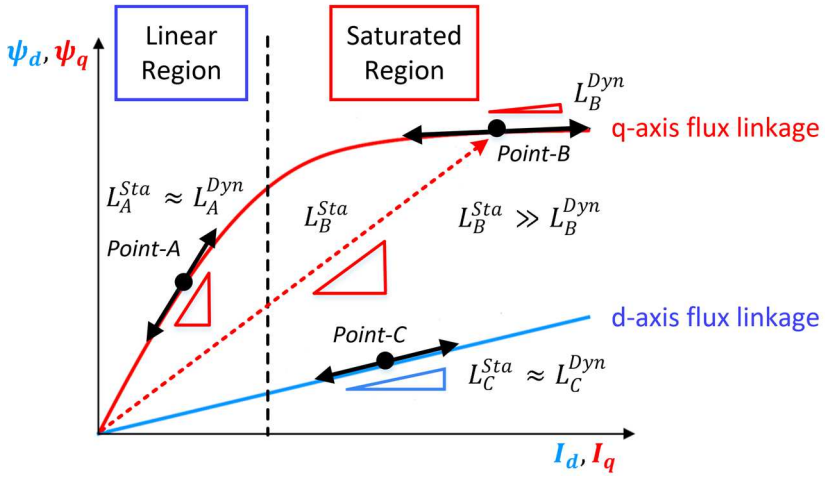

Figure 5-5: *d*- and *q*-axis flux linkages versus *dq* stator currents and comparison of static and dynamic inductances in the linear and saturated regions.

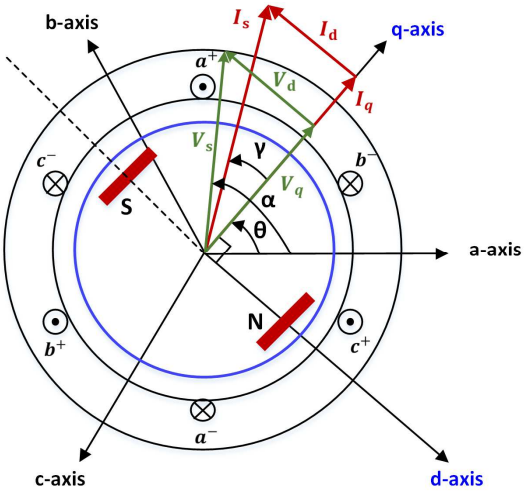

Figure 5-6: Axis and angle conversions for three-phase, two-pole IPM machine.

5.2.3 Current Ripple Prediction Model for IPM Machines

A three-phase, two-pole IPM machine is shown in Figure 5-6 serving as the basis for the model derivation. In the stationary reference frame, the machine voltage equation incorporating the non-linear machine characteristics is described by the following:

$$\boldsymbol{v}_{abc}(t) = R_s \boldsymbol{i}_{abc}(t) + \frac{d\boldsymbol{\psi}_{abc}(t)}{dt} \tag{5-7}$$

where $\boldsymbol{v}_{\text{abc}}$ is the stator complex voltage vector, R_s is the stator winding resistance, $\boldsymbol{i}_{\text{abc}}$ is the stator current vector, and $\boldsymbol{\psi}_{\text{abc}}$ is the stator flux linkage vector.

By transforming these equations from the *abc* stationary frame to rotor *dq* reference frame where the *d*-axis is aligned with the flux linkage generated by the permanent magnets, the machine voltage equation can be expressed by the following:

$$v_d(t) = R_s i_d(t) + \frac{d\psi_d(t)}{dt} - \omega_e \psi_q(t) \tag{5-8}$$

$$v_q(t) = R_s i_q(t) + \frac{d\psi_q(t)}{dt} + \omega_e \psi_d(t) \tag{5-9}$$

where v_d and v_q are the *d*- and *q*-axis voltage, respectively.

To account for the stator slotting effect, magnetic saturation, and the effects of cross-coupling between the *d*- and *q*-axis, the flux linkages are considered to be functions of i_d, i_q, and the machine/rotor position θ. Therefore, the machine *dq* voltage can be modified to be

$$v_d(t) = R_s i_d(t) + \frac{d\psi_d(i_d, i_q, \theta)}{dt} - \omega_e \psi_q(i_d, i_q, \theta) \tag{5-10}$$

$$v_q(t) = R_s i_q(t) + \frac{d\psi_q(i_d, i_q, \theta)}{dt} + \omega_e \psi_d(i_d, i_q, \theta) \tag{5-11}$$

Through the total differential theorem, the derivative terms in (5-10) and (5-11) can be further expanded to three partial derivative parts

$$\begin{aligned} v_d(t) = R_s i_d(t) &+ \frac{\partial \psi_d(i_d, i_q, \theta)}{\partial i_d}\frac{di_d}{dt} + \frac{\partial \psi_d(i_d, i_q, \theta)}{\partial i_q}\frac{di_q}{dt} \\ &+ \frac{\partial \psi_d(i_d, i_q, \theta)}{\partial \theta}\frac{d\theta}{dt} - \omega_e \psi_q(i_d, i_q, \theta) \end{aligned} \tag{5-12}$$

$$\begin{aligned} v_q(t) = R_s i_q(t) &+ \frac{\partial \psi_q(i_d, i_q, \theta)}{\partial i_d}\frac{di_d}{dt} + \frac{\partial \psi_q(i_d, i_q, \theta)}{\partial i_q}\frac{di_q}{dt} \\ &+ \frac{\partial \psi_q(i_d, i_q, \theta)}{\partial \theta}\frac{d\theta}{dt} + \omega_e \psi_d(i_d, i_q, \theta) \end{aligned} \tag{5-13}$$

The partial derivatives of flux linkages with respect to the *d*- and *q*-axis current are defined as either the dynamic self- or mutual-inductance using expressions shown in (5-14)-(5-17).

$$L_{dd}^{Dyn}(i_d, i_q, \theta) = \frac{\partial \psi_d(i_d, i_q, \theta)}{\partial i_d} \approx \left.\frac{\Delta \psi_d}{\Delta i_d}\right|_{i_q = \text{const.}} \tag{5-14}$$

$$L_{dq}^{Dyn}(i_d, i_q, \theta) = \frac{\partial \psi_d(i_d, i_q, \theta)}{\partial i_q} \approx \left.\frac{\Delta \psi_d}{\Delta i_q}\right|_{i_d = \text{const.}} \tag{5-15}$$

$$L_{qd}^{Dyn}(i_d, i_q, \theta) = \frac{\partial \psi_q(i_d, i_q, \theta)}{\partial i_d} \approx \left.\frac{\Delta \psi_q}{\Delta i_d}\right|_{i_q = \text{const.}} \tag{5-16}$$

$$L_{qq}^{Dyn}(i_d, i_q, \theta) = \frac{\partial \psi_q(i_d, i_q, \theta)}{\partial i_q} \approx \left.\frac{\Delta \psi_q}{\Delta i_q}\right|_{i_d = \text{const.}} \tag{5-17}$$

The dynamic inductance values can be approximated as the localized flux variation versus a small perturbation of excitation current in either axis while maintaining the current in the other axis constant.

When the machine operates under steady-state conditions, the commanded i_d and i_q currents maintain constant. In other words, the only source of current variations is PWM switching. The instantaneous voltage differences $\tilde{V}$ between the inverter-side phase voltages and fundamental component of machine-side phase voltages in the *abc* stationary frame are given by

$$\tilde{v}_{abc} = \begin{bmatrix} \tilde{v}_{an} \\ \tilde{v}_{bn} \\ \tilde{v}_{cn} \end{bmatrix} = \begin{bmatrix} v_{an}(t) - \left|\vec{V}_{\text{ref}}\right|\cos(\alpha) \\ v_{bn}(t) - \left|\vec{V}_{\text{ref}}\right|\cos(\alpha - \frac{2}{3}\pi) \\ v_{cn}(t) - \left|\vec{V}_{\text{ref}}\right|\cos(\alpha + \frac{2}{3}\pi) \end{bmatrix} \tag{5-18}$$

The value of $\left|\vec{V}_{\text{ref}}\right|$ for a given load condition is determined from (5-12) and (5-13) with constant *d*- and *q*-axis command current values I_d^{Cmd} and I_q^{Cmd} (i.e., $\frac{di_d}{dt} = \frac{di_q}{dt} = 0$), where the impact slotting effect on the flux linkages in both axes is included

$$V_d^{\text{Cmd}}(\theta) = R_s I_d^{\text{Cmd}} + \frac{\partial \psi_d}{\partial \theta}\frac{d\theta}{dt} - \omega_e \psi_q(\theta) \tag{5-19}$$

$$V_q^{\text{Cmd}}(\theta) = R_s I_q^{\text{Cmd}} + \frac{\partial \psi_q}{\partial \theta}\frac{d\theta}{dt} + \omega_e \psi_d(\theta) \tag{5-20}$$

$$\left|\vec{V}_{\text{ref}}(\theta)\right| = \sqrt{\left(V_d^{\text{Cmd}}(\theta)\right)^2 + \left(V_q^{\text{Cmd}}(\theta)\right)^2} \tag{5-21}$$

The voltage differences in the *abc* stationary frame are subsequently transformed to the *dq* rotor frame according to

$$\tilde{v}_{dq0} = \frac{2}{3}\begin{bmatrix} \sin(\theta) & \sin(\theta - \frac{2}{3}\pi) & \sin(\theta + \frac{2}{3}\pi) \\ \cos(\theta) & \cos(\theta - \frac{2}{3}\pi) & \cos(\theta + \frac{2}{3}\pi) \\ \frac{1}{\sqrt{2}} & \frac{1}{\sqrt{2}} & \frac{1}{\sqrt{2}} \end{bmatrix} \cdot \tilde{v}_{abc} \tag{5-22}$$

As indicated in (5-4), it is the inductive component that determines the slope of the current ripple. Substituting the dynamic inductance terms from (5-14) to (5-17) into (5-12) and (5-13) while eliminating the noninductive terms, the relationship between the inverter-machine voltage differences and the current ripple slopes can be derived as

$$\begin{bmatrix}\tilde{v}_d(t)\\ \tilde{v}_q(t)\end{bmatrix} = \begin{bmatrix}L_{dd}^{Dyn} & L_{dq}^{Dyn}\\ L_{qd}^{Dyn} & L_{qq}^{Dyn}\end{bmatrix} \cdot \begin{bmatrix}\frac{di_d}{dt}\\ \frac{di_q}{dt}\end{bmatrix} = L_{IPM}^{Dyn} \cdot \begin{bmatrix}\frac{di_d}{dt}\\ \frac{di_q}{dt}\end{bmatrix} \tag{5-23}$$

Finally, the slope of the current ripples in the *dq* frame for three-phase IPM machine can be derived from (5-23) to be the product of the inverse of the dynamic inductance matrix in (5-23) and the instantaneous voltage differences. The current ripple in the *abc* stationary reference frame can be determined using the *dq0-abc* transformation, where the zero-sequence current is ignored for the assumed floating-wye winding configuration

$$\begin{bmatrix}\frac{di_d}{dt}\\ \frac{di_q}{dt}\end{bmatrix} = \left(L_{\mathrm{IPM}}^{\mathrm{Dyn}}\right)^{-1} \cdot \begin{bmatrix}\tilde{v}_d(t)\\ \tilde{v}_q(t)\end{bmatrix} \tag{5-24}$$

$$\begin{bmatrix}\frac{di_a}{dt}\\ \frac{di_b}{dt}\\ \frac{di_c}{dt}\end{bmatrix} = \begin{bmatrix}\sin(\theta) & \cos(\theta) & 1\\ \sin(\theta-\frac{2}{3}\pi) & \cos(\theta-\frac{2}{3}\pi) & 1\\ \sin(\theta+\frac{2}{3}\pi) & \cos(\theta+\frac{2}{3}\pi) & 1\end{bmatrix} \cdot \begin{bmatrix}\frac{di_d}{dt}\\ \frac{di_q}{dt}\\ 0\end{bmatrix} \tag{5-25}$$

5.3 Experimental Verification and Evaluation of PWM-Induced Current Ripple in IPM Machines

To verify the estimation accuracy of the proposed current ripple estimation of the proposed current ripple prediction model and investigate the impact of several influencing factors on current ripple, a baseline IPM machine designed for traction applications was selected for machine-level

analysis. The key parameters of the studied IPM machine are documented in Table 4-3. The schematic of the test configuration and a close-up view of the test machine used for current measurements are shown in Figure 5-7(a) and (b). During the experiment, the coolant temperature is kept constant at 85ºC for all of the studied cases.

A silicon-based IGBT inverter power module is used to drive the traction motor [182]. A 12-bit high-resolution oscilloscope with high sampling capability (up to 2 GS/s) and wide bandwidth current probes are used for phase current measurements. In these experiments, the oscilloscope sampling rate was set at 5 MS/s to achieve sufficient measurement accuracy without storing excessive amounts of data.

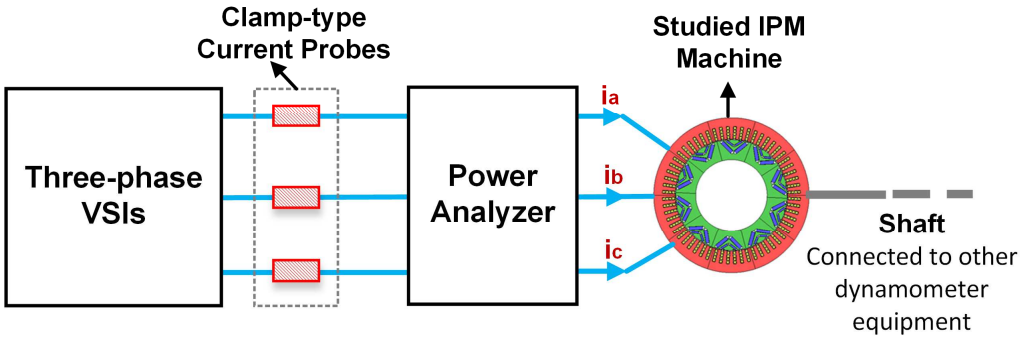

(a)

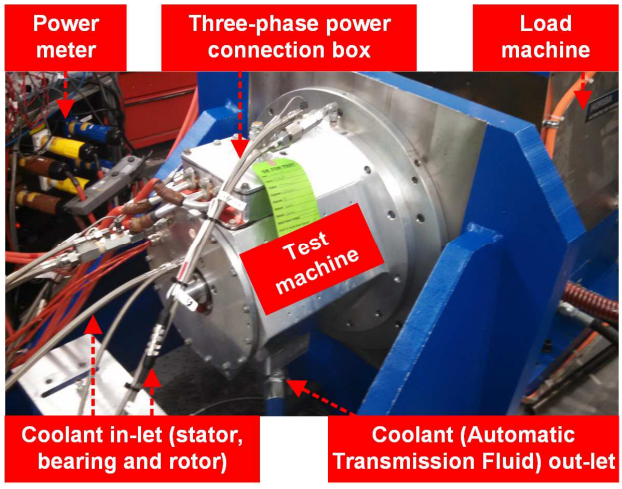

(b)

Figure 5-7: Experiment setup for current measurement. (a) Schematic of test configuration for current measurement, and (b) Close-up view of the IPM machine under test.

For a given machine operating condition (i.e., I_{phase} = 100 Arms and γ = 10°), the flux linkage of each phase can be estimated by FEA and then transferred to the synchronous dq frame, as shown in Figure 5-8(a). To determine the corresponding dynamic self- and mutual-inductance, a small current perturbation set at 5% of the d- and q-axis current is applied to either axis while maintaining the current in the other axis unchanged. The availability of the predicted flux linkages with and without the current perturbations makes it possible to calculate the dynamic inductances of IPM

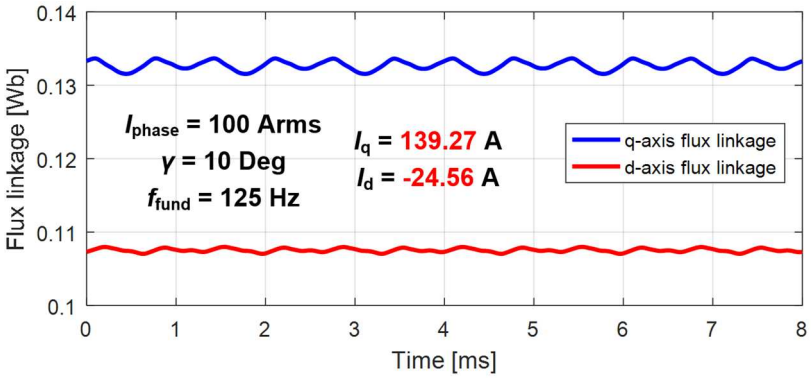

(a) Predicted d-axis flux linkage ψ_d and q-axis flux linkage ψ_q

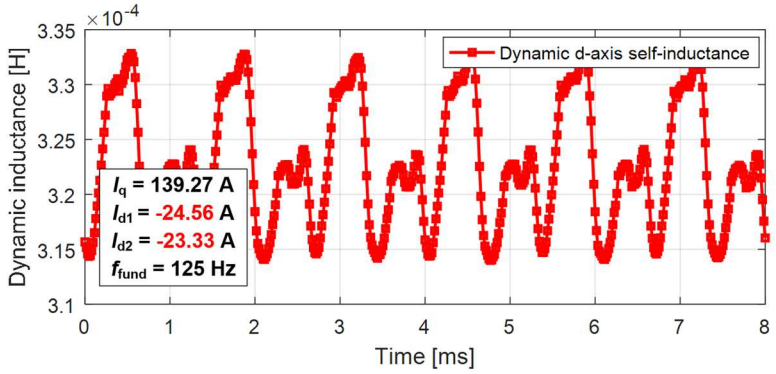

(b) Predicted dynamic d-axis self-inductance L_{dd}^{Dyn}

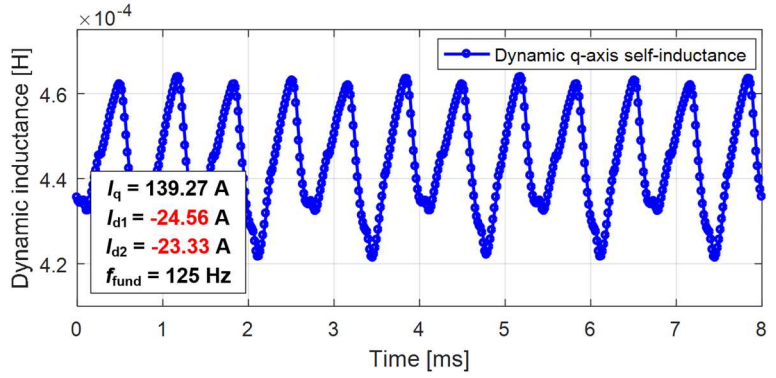

(c) Predicted dynamic q-axis self-inductance L_{qq}^{Dyn}

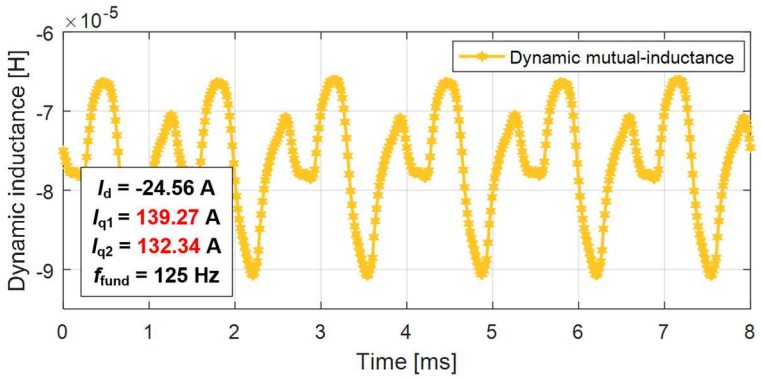

(d) Predicted dynamic mutual-inductance $L_{dq}^{Dyn} = L_{qd}^{Dyn}$

Figure 5-8: Predicted stator flux linkages and dynamic inductances.

Test conditions: fundamental phase current I_{phase} = 100 Arms, fundamental frequency f_{fund} = 125 Hz, and current control angle γ = 10°.

machines using the definition provided in (5-14)-(5-17). Taking the L_{qq}^{Dyn}- dynamic q-axis self-inductance calculation as ab example, the d-axis current held constant at – 24.56 A and the q-axis current is varied from 139.27 to 132.34 A. Then the variation of q-axis flux linkage $\Delta\psi_q$ over Δi_q determines the value of L_{qq}^{Dyn}.

The impact of stator slotting on the predicted current ripple is incorporated into the model using the time-varying dynamic inductances presented in Figure 5-8(b)-(d), which depend on rotor instantaneous position. Since the reciprocity holds for the nonlinear magnetic coupling, L_{dq}^{Dyn} is assumed to be identical to L_{qd}^{Dyn}. The dynamic inductances can alternatively be identified via experimental tests following the same procedure. However, that approach requires a prototype machine as well as a fully calibrated drive system which is not available during the initial machine design state.

5.3.1 PWM Switching Frequency

The proposed model is first employed to investigate the PWM-induced current ripple for different PWM switching frequencies f_{PWM} from 3.5 to 10 kHz. It should be noted that the current ripple analysis has been purposely focused on light-load (i.e., I_{phase} = 35 Arms) and low speed (i.e., < 2,000 rpm) conditions to constrain the reference voltage vector within its linear region. Since a major reason for developing this model is to investigate PWM-induced iron loss, it was also preferable to focus on low-speed, light-load conditions to maximize the proportion of total machine losses attributable to the PWM effects. The PWM losses are much more difficult to segregate during the experimental tests if the fundamental-frequency iron or copper loss dominates.

As the PWM switching frequency f_{PWM} changes, the machine operating condition (e.g., L_{IPM}^{Dyn} and $\left|\vec{V}_{\mathrm{ref}}\right|$) and the inverter dc-bus voltage V_{dc} are not affected. Therefore, all of the parameters in (5-24) that determine the slope of each linear current segment in the current ripple waveform for the same operating point are unaffected by f_{PWM}. However, since the time duration of each switching state (5-1)-(5-3) varies inversely with f_{PWM}, the resultant current ripple amplitude follows the trend and decreases inversely as the PWM switching frequency increases. The accuracy of this inverse relationship suffers at low ratios between f_{PWM} and fundamental frequency f_{fund} because the machine's fundamental voltage component can vary significantly during one PWM switching period under these circumstances.

The current ripple is calculated under the assumption that the initial position of reference voltage vector $\vec{V}_{\mathrm{ref}}$, shown in Figure 5-2, is aligned with the phase-*a* axis. However, this could lead to a small phase error (as large as one switching cycle) between the predicted and measured ripple components. Therefore, in order to investigate the detailed waveshape properties, the predicted current ripple is shifted within one PWM cycle to match the actual phase of the measured data.

Despite this adjustment, the rms value and frequency composition of the predicted results are intact with or without the phase shift. Figure 5-9(a) shows the overlaid phase current waveforms including the ripple components for one fundamental period. The predicted ripple waveform is shifted rightward approximately one-half PWM cycle, 0.14 ms ($T_s \approx 0.2866$ ms corresponding to f_{PWM} at 3.5 kHz), to synchronize it with the measured waveform. All of the following waveform comparison results are presented after this phase-shift post-processing.

The predicted current ripple is overlaid with the measured data for two selected f_{PWM} values, namely 3.5 and 10 kHz in Figure 5-9(b) and (c), respectively. It should be noted that the machine operating conditions- torque and rotating speed are maintained identical for these current ripple comparisons with different f_{PWM} values. As shown in the expanded plots embedded in Figure 5-9(b) and (c)m the measured and predicted current ripple waveforms match very closely for the two investigated PMW switching frequencies. As depicted in the zoom-in plots in Figure 5-9, current spikes (i.e., high-frequency ringing) at the switching instants are observed in the measured waveforms for both PWM switching frequencies. Although this effect is ignored in the prediction model considering its limited impact on the current ripple waveshape within the range of the studied PWM frequency (i.e., $f_{PWM} \leq 10$ kHz), larger load capacitances including cable capacitance and parasitic capacitance between the motor windings and frame as well as higher *dv/dt* rates could further exaggerate this ringing. As the PWM switching frequency increases in the machine drive inverters using wide bandgap power semiconductors (e.g., SiC and GaN) the effects of these parasitic capacitances will require further investigation.

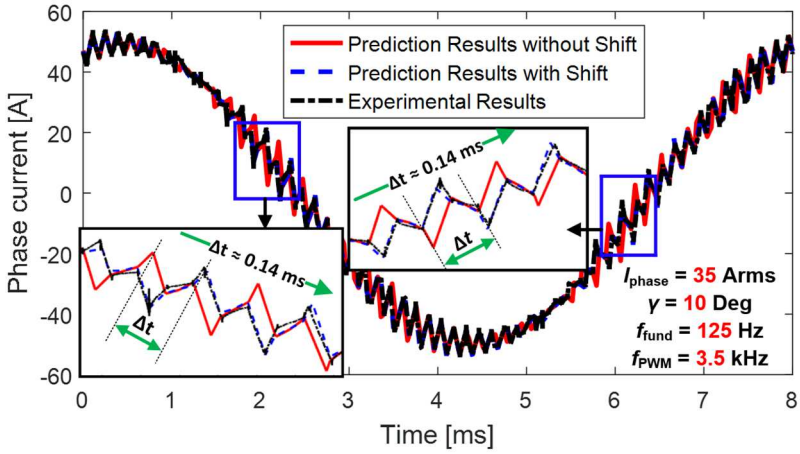

(a) PWM switching frequency: f_{PWM} = 3.5 kHz

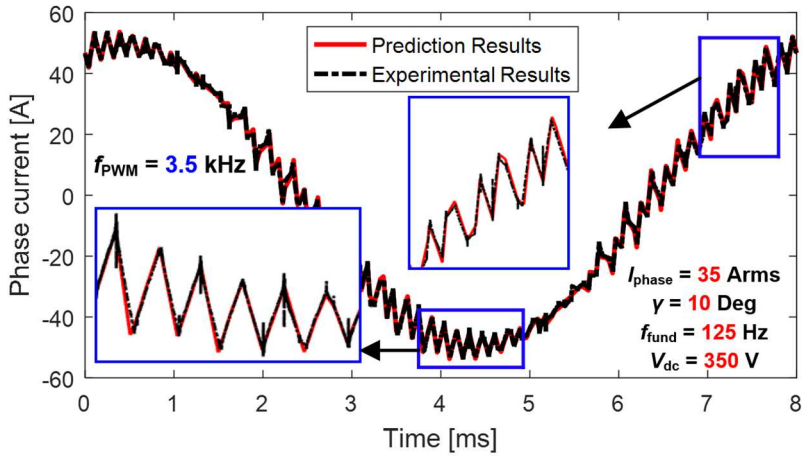

(b) PWM switching frequency: f_{PWM} = 3.5 kHz. Same measured current waveform as in (a) but with different zoom-in plots

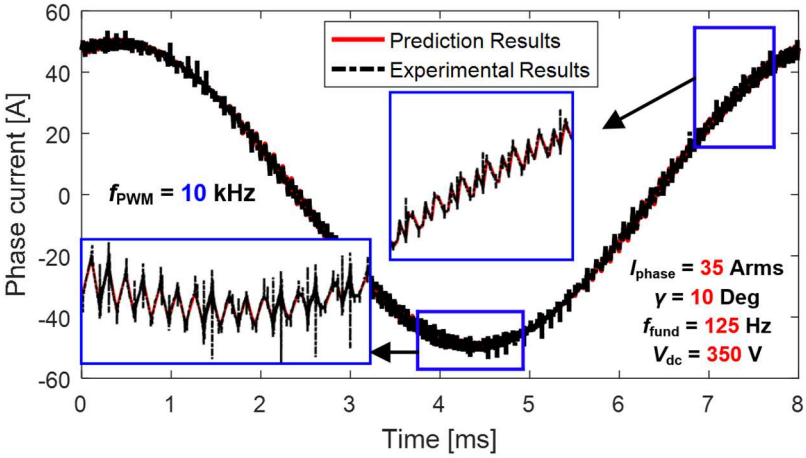

(c) PWM switching frequency: f_{PWM} = 10 kHz

Figure 5-9: Comparison of predicted and measured phase current waveforms for two values of f_{PWM}.

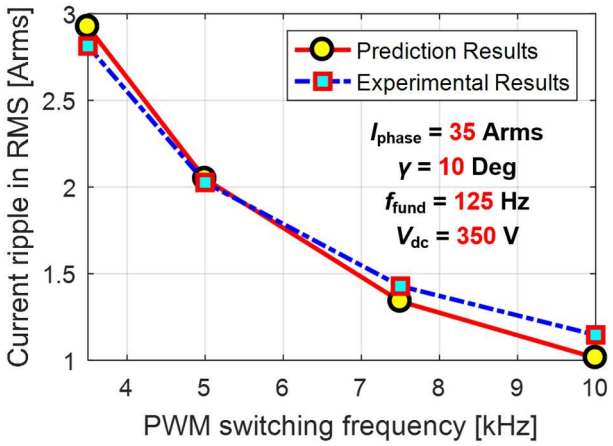

Test conditions:

Fundamental current I_{phase} = 35 Arms

Fundamental frequency f_{fund} = 125 Hz

Current control angle γ = 10 degree

Inverter dc-bus voltage V_{dc} = 350 V.

Figure 5-10: Predicted and measured rms ripple versus PWM switching frequency f_{PWM}.

Figure 5-10 shows a comparison of the predicted and measured rms values of PWM-induced current ripple for different values of f_{PWM}. This plot confirms that the current ripple amplitude decreases inversely with f_{PWM}. Both Figure 5-9 and Figure 5-10 demonstrate the current ripple prediction accuracy of the proposed model over a wide PWM frequency range.

5.3.2 Machine Rotating Speed (i.e., Fundamental Frequency)

Next, the impact of machine speed on current ripple is investigated. Figure 5-11(a) and (b) show the predicted phase current overlaid with the measured waveform for two machine speeds, 500 and 2,000 rpm. As in the preceding section, all of the key operating conditions including current amplitude and angle are maintained identical for the two speeds, including the PWM frequency (i.e., f_{PWM} = 5 kHz). Figure 5-11(a) and (b) show that the amplitude of current ripple increases as the machine speed (i.e., fundamental frequency) increases for these operating points. This increase is affected by both the increase in the phase voltage amplitude as a fraction of the dc-link voltage V_{dc} as the frequency increases, as well as the reduced ratio of the fundamental frequency to f_{PWM}. Excellent agreement between the predicted and measured current ripple waveforms can be observed for both machine speeds.

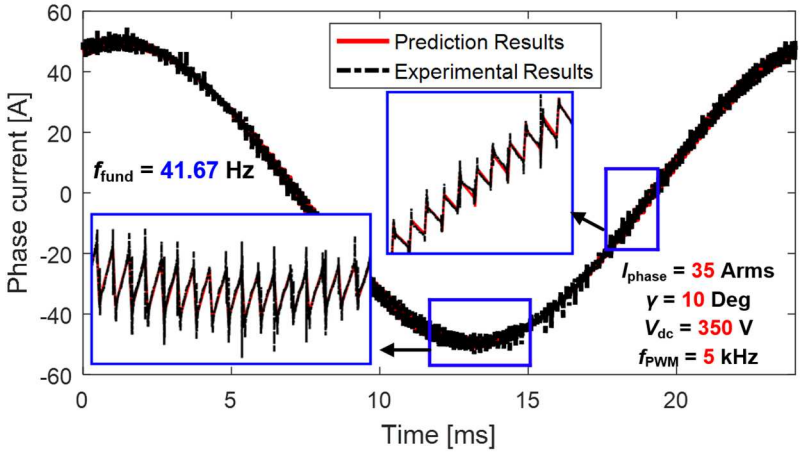

(a) Machine rotating speed = 500 rpm (f_{fund} = 41.67 Hz)

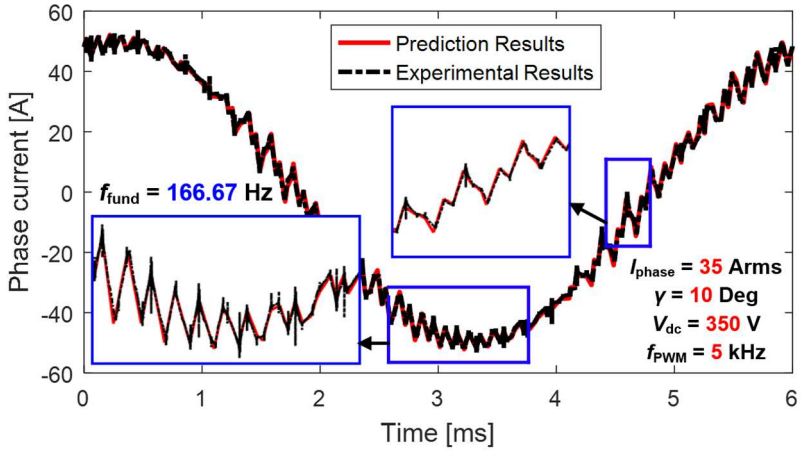

(b) Machine rotating speed = 2,000 rpm (f_{fund} = 166.67 Hz)

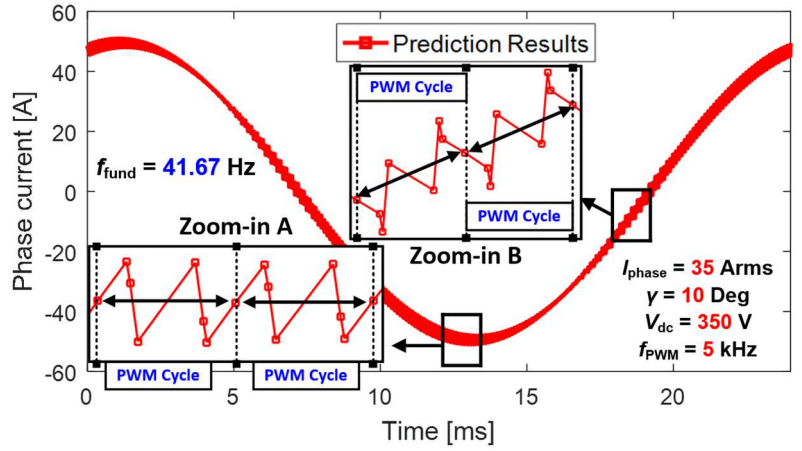

(c) Machine rotating speed = 500 rpm (f_{fund} = 41.67 Hz)

Figure 5-11: Comparison of predicted and measured current waveforms at two speeds.

By comparing the current ripple in the zoomed time windows, it is apparent that not only the ripple amplitude changes with the machine speed but also the shape of the current ripple waveform varies significantly. To better observe the current ripple slope variation within each PWM cycle, only the predicted ripple waveform for the 500 rpm case is shown in Figure 5-11(c), where each square-shape marker represents a switching instant. Consistent with the low machine-side voltage condition described in Figure 5-4(a), there are two inversely symmetrical ripple components during each PWM cycle.

The current ripple spectra shown in Figure 5-12(a)-(e) reveal the important shift of the harmonic distribution in the frequency domain. For low machine speeds (e.g., 500 rpm), the dominant PWM harmonic components are concentrated around 10 kHz (2x the PWM frequency). As the speed increases, increasing harmonics are observed in the vicinity of 5 and 10 kHz (1x and 2x the PWM frequency). After the speed passing 1,500 rpm, the dominant harmonic frequency shifts to 5 kHz (1x the PWM frequency).

As the rotor speed increases, the speed voltage terms in (5-19) and (5-20) increase in direct proportion, resulting in monotonically increasing modulation index values, as shown in Figure 5-12(f). As aforementioned, it is the modulation index (reference voltage divided by dc-bus voltage) that determines the switching patterns of the SVPWM which, in turn, determine the harmonic spectrum. With higher modulation index values, the time duration of the zero-state (**000** and **111** states) decreases and drives the harmonics to 1x PWM switching frequency.

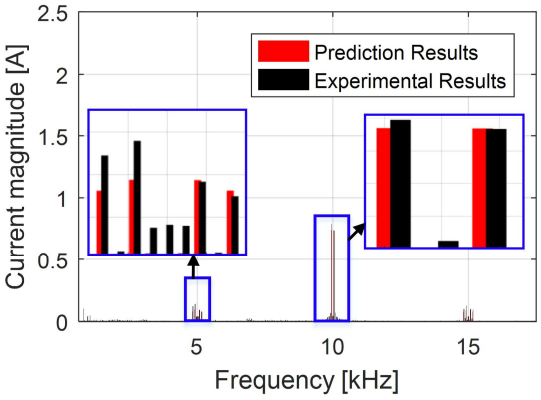

(a) Machine rotating speed = 500 rpm.

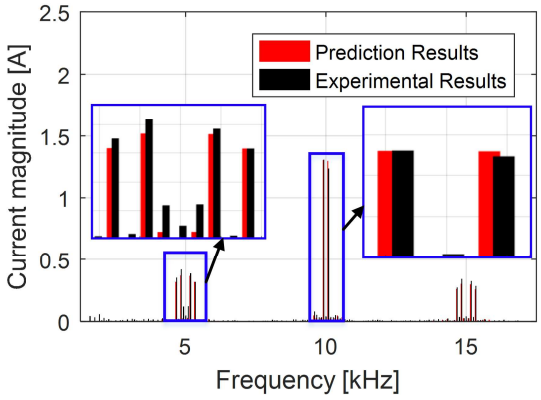

(b) Machine rotating speed = 1,000 rpm.

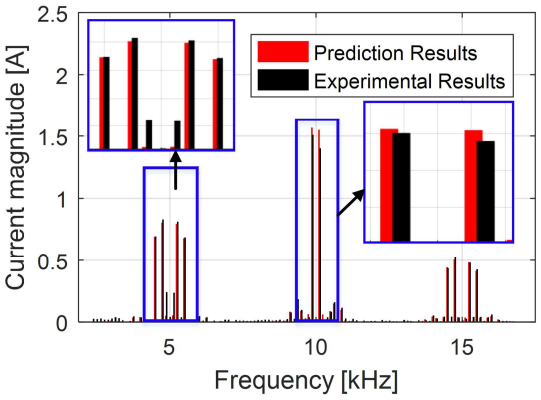

(c) Machine rotating speed = 1,500 rpm.

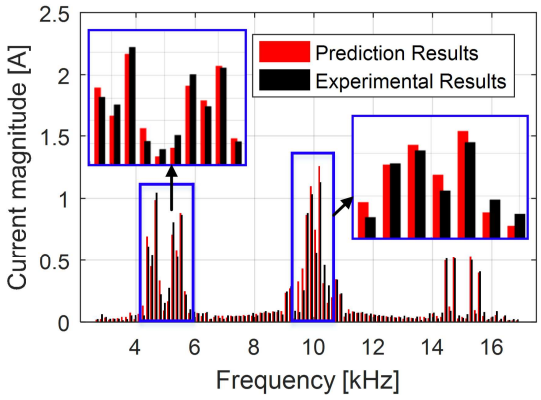

(d) Machine rotating speed = 1,700 rpm.

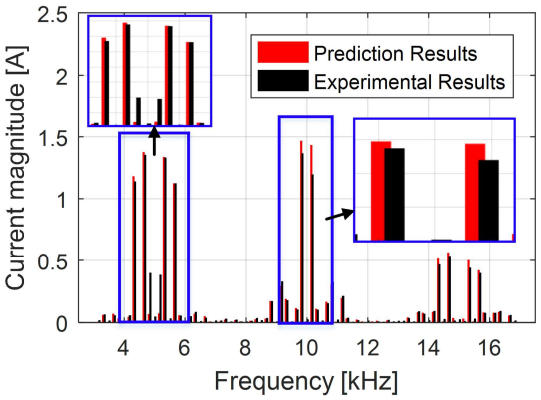

(e) Machine rotating speed = 2,000 rpm.

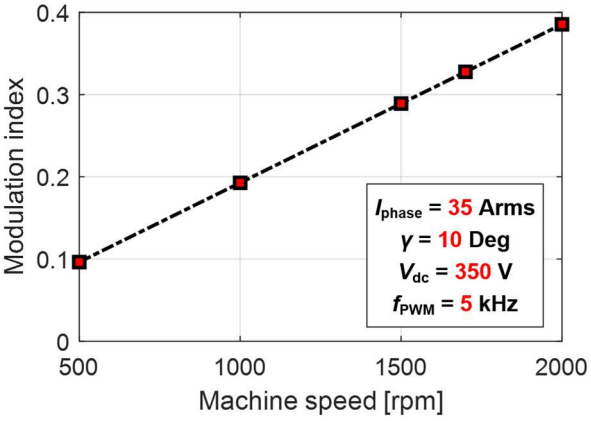

(f) Predicted modulation index.

Figure 5-12: Predicted and measured current ripple spectra and modulation index versus speed.

Test conditions: fundamental phase current I_{phase} = 35 Arms, current control angle γ = 10 degree, inverter dc-bus voltage V_{dc} = 350 V, and PWM switching frequency f_{PWM} = 5 kHz.

5.3.3 Inverter DC Bus Voltage

The impact of inverter dc-bus voltage V_{dc} on current ripple shares some similarities with the impact of machine speed since V_{dc} directly affects the value of modulation index.

Figure 5-13 highlights the changing frequency spectra of the measured current for five V_{dc} values. By maintaining the machine speed, current amplitude, and γ angle identical for each case, the machine's reference voltage $|\vec{V}_{ref}|$ is constant. As V_{dc} varies from a small value, 200 V, to a larger value, 400 V, the modulation index value decreases in inverse proportion, which shifts the dominant harmonic frequency from 10 kHz (1x the PWM frequency) to 20 kHz (2x the PWM frequency). Since the current properties are very similar to the results in the prior case, detailed comparisons of the predicted and measured waveforms are not provided.

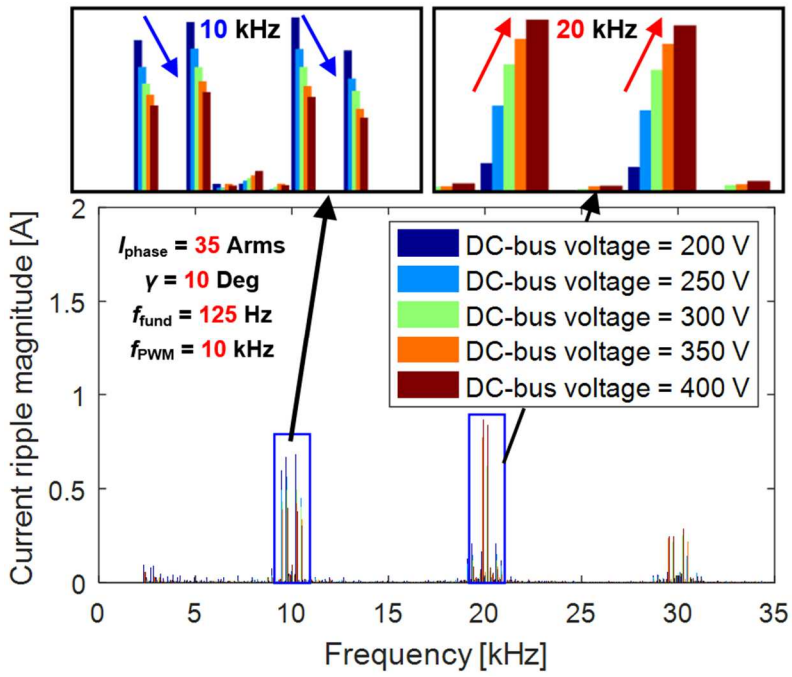

Figure 5-13: Measured current ripple spectra for five dc-bus voltage values.

Test conditions: fundamental phase current I_{phase} = 35 Arms, fundamental frequency f_{fund} = 125 Hz, current control angle γ = 10 degree, inverter dc-bus voltage V_{dc} = 350 V, and PWM switching frequency f_{PWM} = 5 kHz.

5.3.4 Current Control Angle γ

In contrast to the previous factors, the flux density distribution changes with the current angle γ for a fixed current amplitude. This affects the saturation level as well as the mutual coupling between the d- and q-axis.

Figure 5-14 shows the average value of dynamic self-inductance versus γ in both axes (i.e., averaged for a full rotation to filter out slotting effects). Due to magnetic saturation, the dynamic inductances are functions of both the excitation current amplitude I_{phase} and control angle γ.

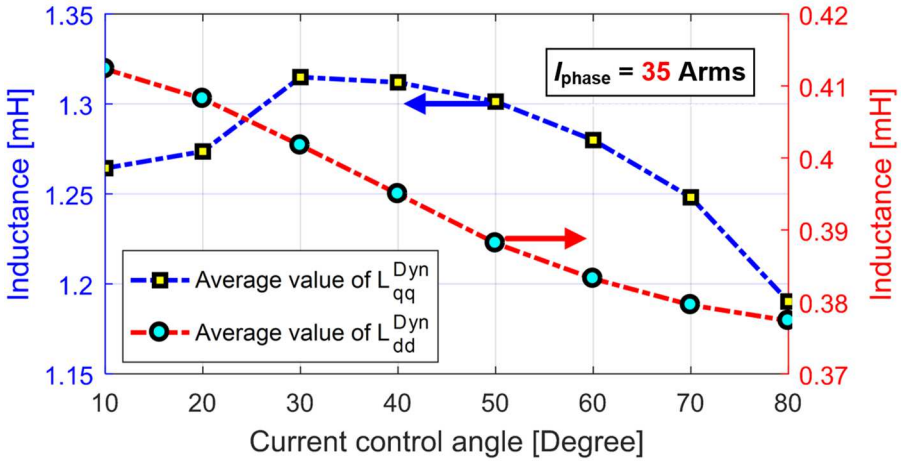

Figure 5-14: Predicted average values d- and q-axis dynamic self-inductance, L_{qq}^{Dyn} and L_{qq}^{Dyn} (I_{phase} = 35 Arms).
Note: Different scales are used for two curves.

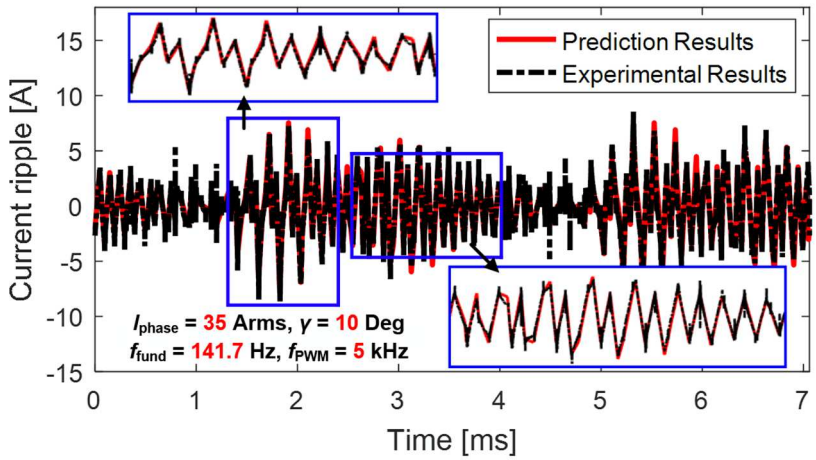

(a) Current control angle γ = 10 degree

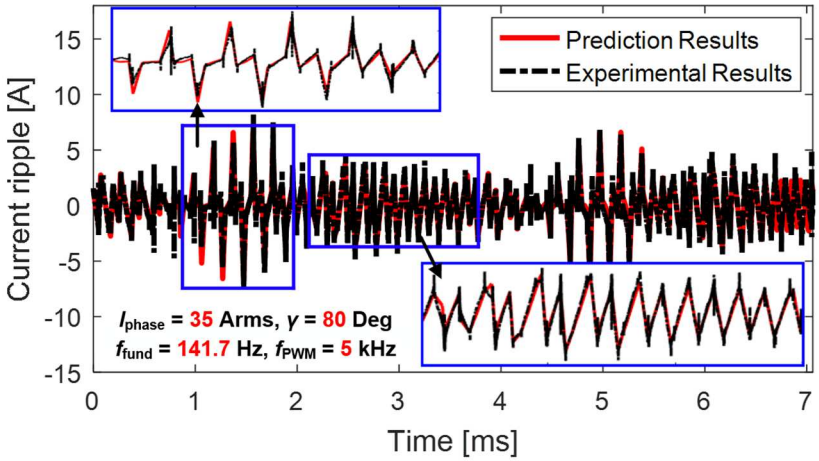

(b) Current control angle γ = 80 degree

Figure 5-15: Predicted and measured current ripple waveforms for two values of current control angle γ.

Results from two-dimensional FEA have shown that changes in angle γ exhibit a more substantial impact on the machine's dynamic self-inductance as the current amplitude increases (e.g., I_{phase} = 100 Arms). Although the mutual-inductance varies with the γ angle as well, the value is much smaller than the self-inductance, and its impact on the current ripple is limited. Figure 5-15(a) and (b) show the current ripple waveforms for γ = 10 and 80 degree, respectively. These waveforms suggest that as γ increases, both the shape and amplitude of the current ripple experience large variations. Moreover, as depicted in the zoom-in plots, the details of the current ripple waveshape are accurately captured by the proposed prediction model for these two values of control angle γ.

Figure 5-16 confirms the monotonically decreasing rms value of PWM-induced current ripple versus angle γ. Although the phase current and other machine operating condition are maintained constant, the increase of the negative d-axis current leads to smaller reference voltage values. As a result, the time durations of zero states increase, limiting the peak values of the current ripple.

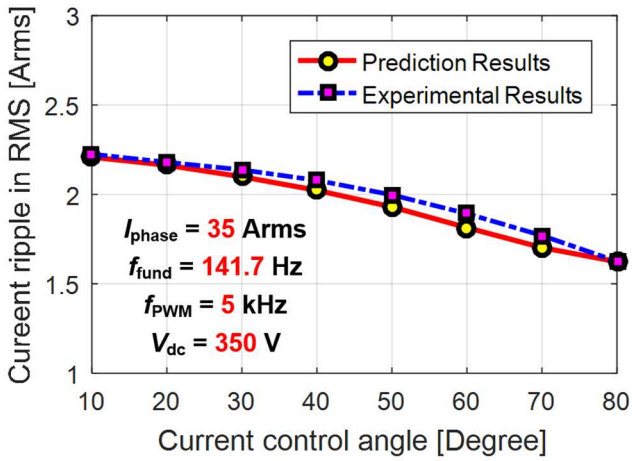

Test conditions:

Fundamental current I_{phase} = 35 Arms

PWM frequency f_{PWM} = 5 kHz

Fundamental frequency f_{fund} = 141.7 Hz

Inverter dc-bus voltage V_{dc} = 350 V

Figure 5-16: Predicted and measured rms current ripple amplitude versus current control angle γ.

5.3.5 Excitation Current Amplitude (i.e., Saturation Level)

In the previous section, the dynamic inductances do not change significantly in either axis since the selected current amplitude is relatively small. In this section, the current ripple is evaluated over a wide range of current amplitudes.

As can be seen in Figure 5-17, the average value of the static q-axis self-inductance (i.e., $L_{qq}^{Sta} = \psi_q/i_q$) and the dynamic q-axis inductance L_{qq}^{Dyn} are close in the linear region up to 50 Arms phase current. However, as the machine moves into the saturated region, the dynamic inductance drops much faster than the static value. Furthermore, since the q-axis can be easily saturated, the q-axis dynamic inductance in the saturated region decreases significantly compared to its linear region value. The d-axis dynamic inductance L_{dd}^{Dyn} exhibits a slower declining trend due to the impact of the magnet cavities along the d-axis of the machine. Since saturation is low, the static and dynamic d-axis inductances are nearly identical over the full current range.

Furthermore, Figure 5-17 shows that the dynamic q-axis inductance values drop below the corresponding dynamic d-axis inductance values for elevated current values in the saturated region. It is important to note that the dynamic inductance values represent the incremental slopes of the flux versus current curves. In contrast, the static q-axis inductance remains higher than the static

d-axis inductance throughout the plotted current range as the two static inductance curves gradually converge as saturation increases.

Figure 5-18 shows the current ripple spectra of the measured current data with five current amplitudes ranging from 20 to 100 Arms. The harmonics around both the 1x and 2x the PWM frequencies (i.e., f_{PWM} = 10 and 20 kHz) increase monotonically with current, but less than in direct proportion to the current amplitude.

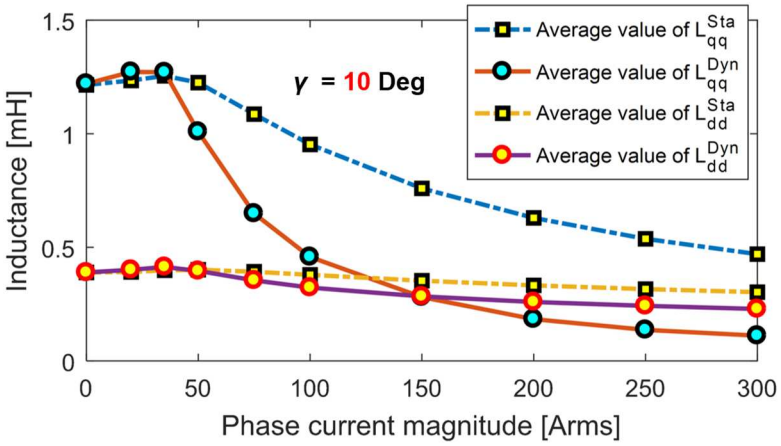

Figure 5-17: Predicted average values of self-inductances versus current amplitude at 10 degree γ.

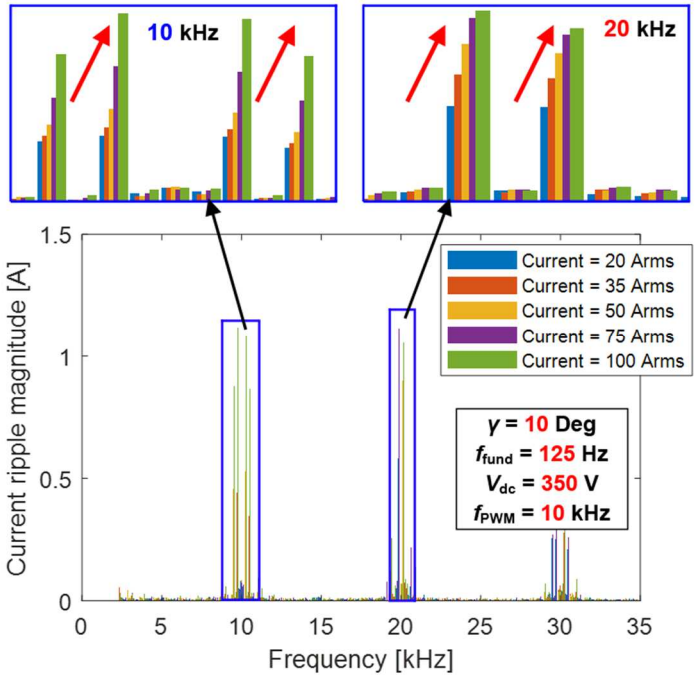

Figure 5-18: Measured current ripple spectra versus current rms amplitude, with zoomed-in plots in the vicinity of 1x f_{PWM} and 2x f_{PWM}.

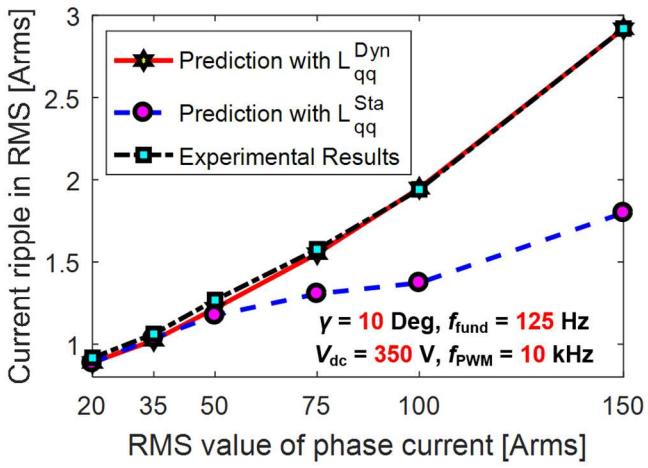

Test conditions:

PWM frequency f_{PWM} = 10 kHz

Fundamental frequency f_{fund} = 125 Hz

Current control angle γ = 10 degree

Inverter dc-bus voltage V_{dc} = 350 V.

Figure 5-19: Predicted and measured current ripple rms amplitude versus rms phase current using either static or dynamic inductances in calculations.

Figure 5-19 compares the predicted rms current ripple amplitude calculated using the static or dynamic q-axis self-inductance values. Each is calculated in combination with the dynamic d-axis self-inductance and dynamic mutual-inductance. The measured results are overlaid. The predictions using the static q-axis self-inductance highly underestimate the current ripple when the phase current is >50 Arms. With 150 Arms phase current, the predicted static q-axis self-inductance (L_{qq}^{Sta} = 0.7593 mH) is approximately three times the dynamic value (L_{qq}^{Dyn}= 0.2808 mH), leading to 60 % underestimation of PWM-induced current ripple when the static value is used. In contrast, the agreement is very good when the q-axis dynamic self-inductance is used.

5.3.6 Current Ripple with Constant Modulation Index

Changing the values of any of the factors investigated above (except for the PWM switching frequency) is accompanied by changes in the modulation index because these factors affect either the machine or inverter-side operating conditions. In this section, the current ripple properties versus machine speed and excitation current amplitude are evaluated with constant modulation index values by adjusting the dc-bus voltage.

Figure 5-20 shows the predicted current ripple for three different excitation current amplitudes which span both the linear and saturated regions. The modulation index is maintained constant at 0.5 for each case, corresponding to maximum current ripple. The square-shaped markers shown in the waveform represents the time instant when the inverter switch state changes and results in a slope change in the current ripple. As depicted in the zoom-in plots, the PWM switching instants are identical for the three current amplitudes. This is expected because the value of the modulation index determines the switching pattern and the voltage harmonic distribution in the frequency domain. Although the switching pattern is the same, the magnitude of current ripple exhibits large deviations. As the excitation current increases, the slope of each linear current ripple segment increases considerably, especially when the machine operates in the heavy-saturation region.

The impact of machine speed with constant modulation index on current ripple is shown in Figure 5-21. The machine speed varies from 1,000 to 3,000 rpm while the modulation index is held constant at 0.5. Inspection shows that the envelopes of the current ripple waveforms are very similar for the three speeds over one fundamental period. The zoom-in plots indicate that the detailed waveshapes and PWM switching patterns are also very similar when compared in equivalent time intervals for the three speed cases. Unlike the preceding case that varied the current amplitude, the machine dynamic inductances are the same when the speed is varied because the current amplitude is held constant. Instead, both the inverter dc-bus voltage and machine-side average voltage increase in direct proportion to the machine speed (ignoring the small voltage drop across the stator resistance and the slotting effect). Therefore, the slopes of all of the current ripple segments also increase in direct proportion, causing the rms current amplitude to increase linearly with speed.

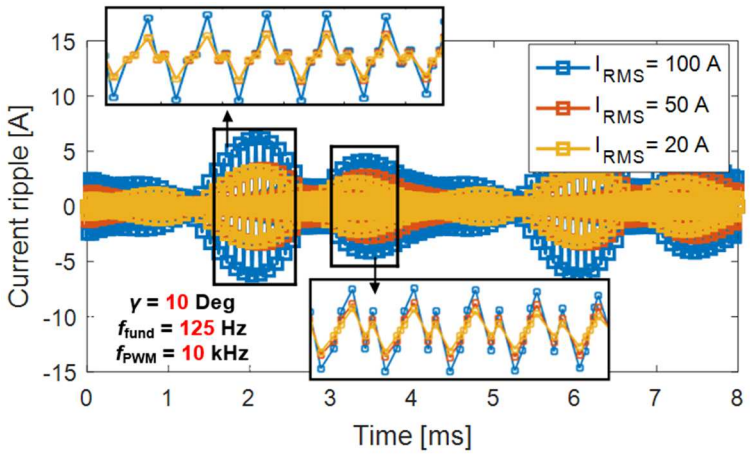

Figure 5-20: Predicted current ripple versus current amplitude with constant modulation index at 0.5.

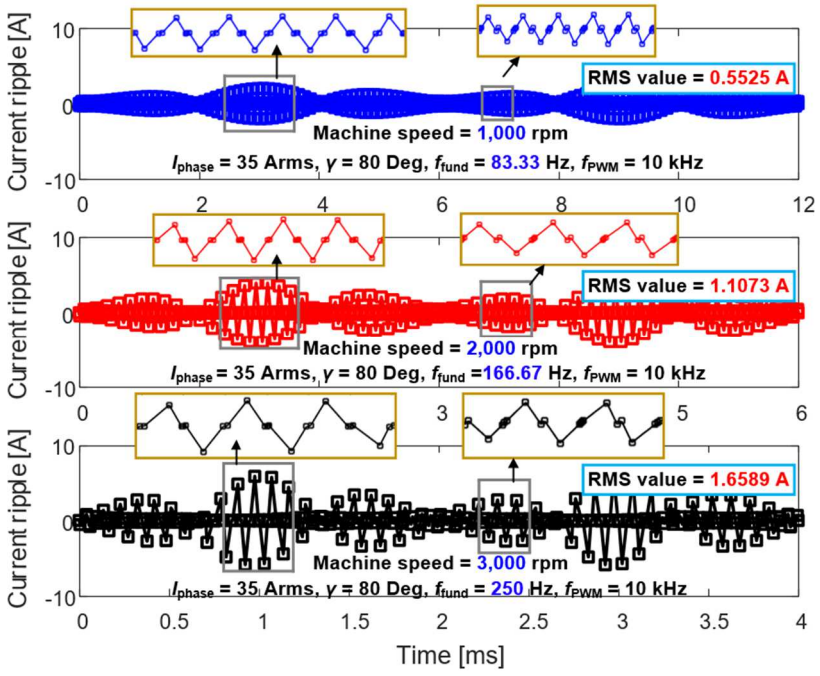

Figure 5-21: Predicted current ripple at three speeds with fixed modulation index at 0.5.

5.4 Time-Stepped Finite Element Simulation of the PM Traction Machine with PWM Voltage Excitation

Besides the proposed analytical current ripple estimation model, an alternative approach is time-stepped FEA that combines a Simulink-based model of the inverter and machine load with a numerical machine model (i.e., JMAG-RT model) generated using fast and accurate FEA. Key results of an investigation on time-stepped FEA simulation are presented in this section.

5.4.1 Overview of time-stepped FEA simulation

Accurate modeling of the stator current waveform with PWM-induced current ripple typically calls for nonlinear time-stepped finite element analysis coupled with numerical simulation of the governing nonlinear differential equation using Simulink, which requires an extended calculation time. With JMAG-RT, it is possible to create an equivalent machine model that matches the behavior of a real machine and accounts for nonlinear spatial harmonics and magnetic saturation characteristics that are included in the model without significantly lengthening the simulation time. Importing this machine model into Simulink makes it possible to carry out current ripple simulations that account for a machine's magnetic saturation and spatial harmonics as well as the inverter drive's excitation and control characteristics.

Figure 5-22 shows the schematic of a time-stepped simulation in Simulink using a JMAG-RT FEA model. The voltage command generator including a closed-loop PI current regulator and SVPWM gate signal generator are built into the Simulink model to control the studied IPM machine.

Figure 5-23(a)-(b) shows results of the time-stepped FEA simulation that confirm that the proposed system is capable of accurately regulating the *d*- and *q*-axis current in both the machine's linear and saturated region. This time-stepped FEA simulation model has subsequently been

applied to investigate the impact of machine and inverter conditions on PWM-induced current ripple, as discussed in the next subsection.

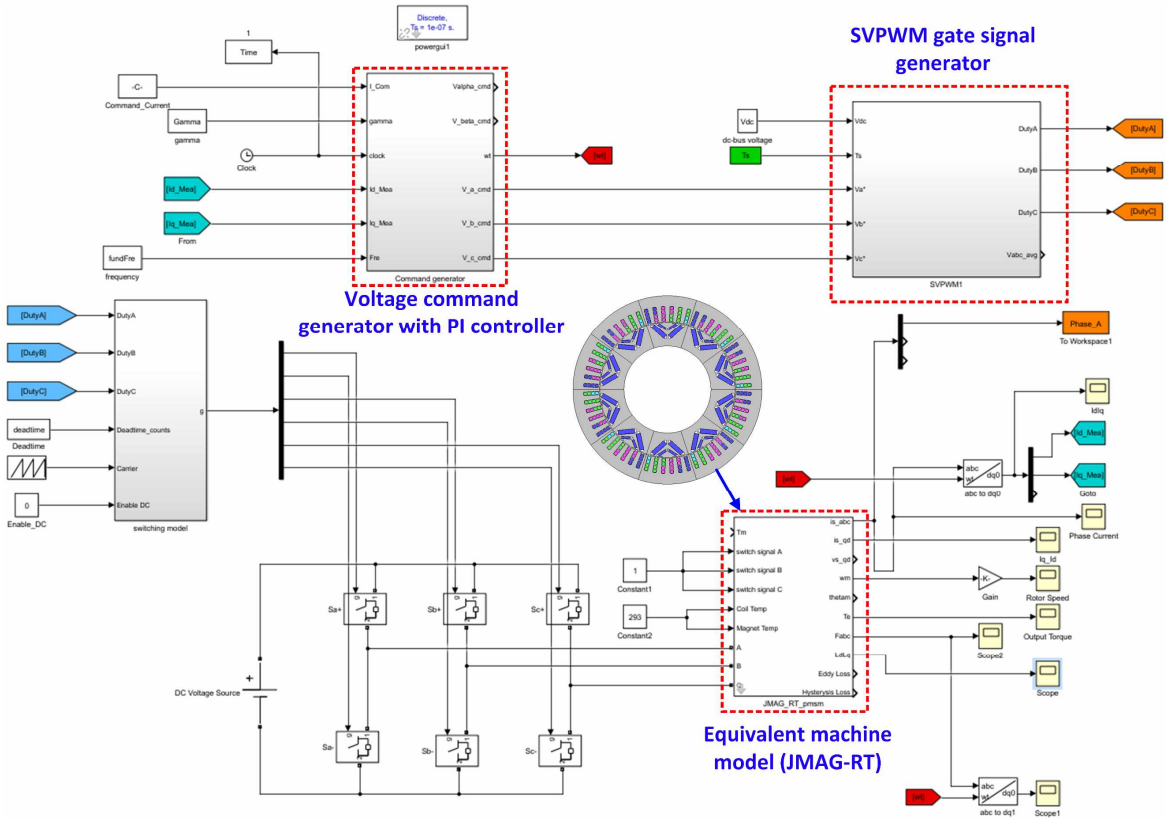

Figure 5-22: Schematic of simulation setup in Simulink with JMAG-RT model.

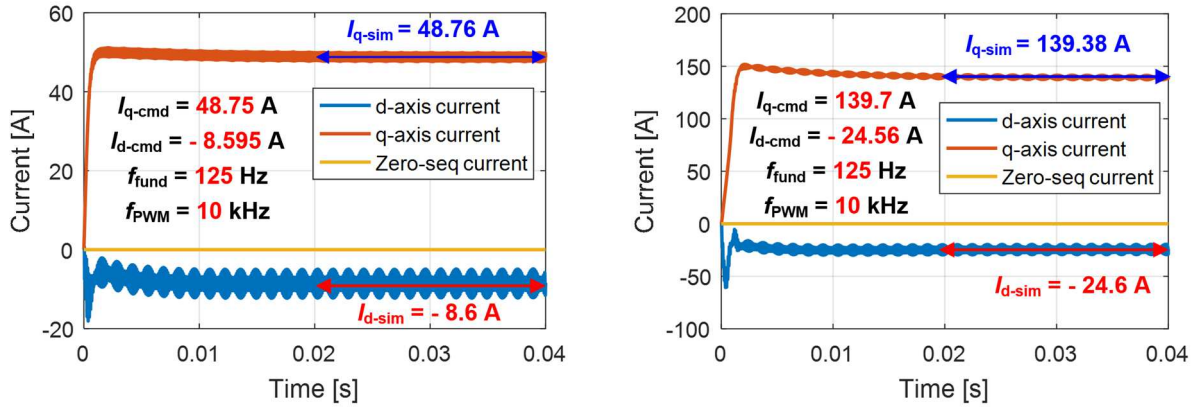

(a) Command I_{phase} = 35 Arms, and γ = 10 degree (b) Command I_{phase} = 100 Arms, and γ = 10 degree

Figure 5-23: Example waveforms of *d*- and *q*-axis current trajectories compared to the command phase current.

5.4.2 Experimental evaluation of time-stepped FEA simulation

To verify the accuracy of this model, the time-stepped FEA simulation has first been employed to investigate the PWM-induced current ripple for different PWM switching frequencies f_{PWM}. The same set of experimental data obtained by the baseline IPM given in Figure 5-7 is used to evaluate the model performance. Although the measured data is limited to a maximum f_{PWM} value of 10 kHz, the time-stepped FEA simulation has been run with PWM frequencies up to 30 kHz and compared with prediction results from the analytical current ripple model proposed in this chapter.

Figure 5-24(a)-(b) show comparisons of the RMS values and Fourier decomposition of the PWM-induced current ripple from three available sources including time-stepped FEA simulation, the analytical model, and measured data. The time-stepped FEA simulation exhibits excellent current ripple prediction accuracy when the machine operates in the linear region. In addition, the analytical and simulation prediction models exhibit very good agreement of their current ripple predictions beyond 10 kHz, which builds confidence in the ability of these models to predict the current ripple waveforms for high PWM switching frequencies using wide bandgap devices (e.g., SiC or GaN).

Figure 5-25(a) confirm the prediction accuracy of time-stepped FEA simulation for modeling the current ripple for varying speeds. However, as shown in Figure 5-25(b), the time-stepped FEA simulation fails to capture the correct current ripple variation trend when the machine operates in the heavy saturation region (i.e., phase current $I_{phase} > 100$ Arms). It is suspected that the equivalent machine model generated by JMAG-RT cannot properly take the dynamic inductances into consideration. In comparison, the proposed analytical model provides accurate current ripple prediction over varying conditions, making it a much preferred model for practical applications.

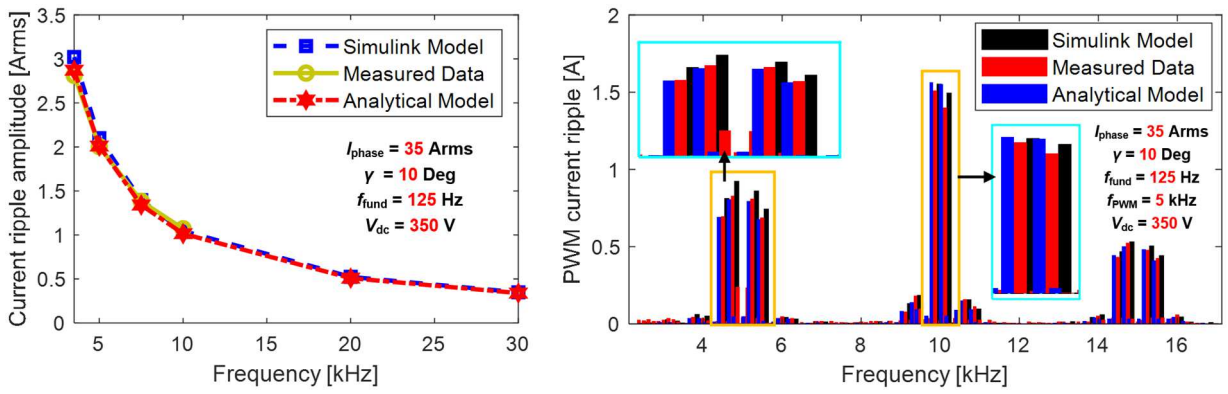

(a) (b)

Figure 5-24: RMS values of prediction and measured current ripple with different values of PWM switching frequencies f_{PWM}; and (b) Fourier decomposition of predicted and measured waveform at f_{PWM} = 5 kHz

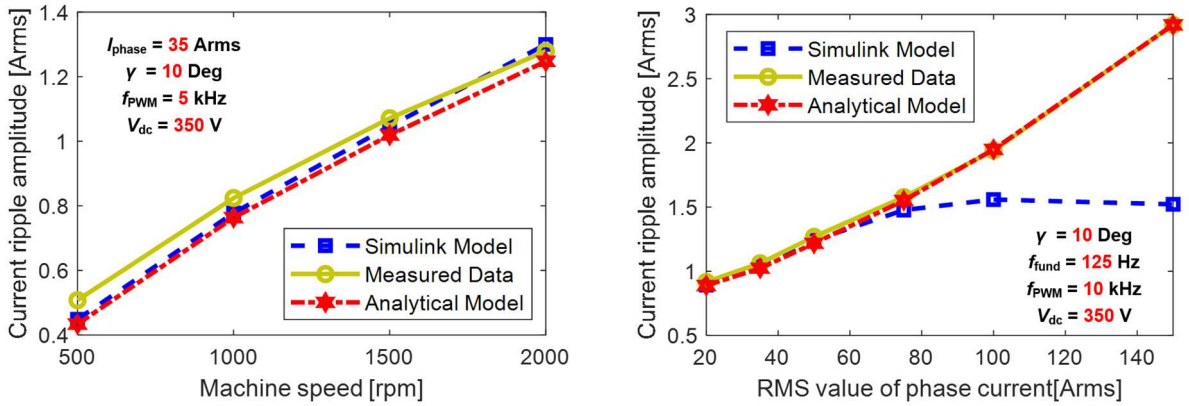

(a) (b)

Figure 5-25: (a) RMS values of prediction and measured current ripple with different machine speeds; and (b) RMS values of prediction and measured current ripple with different excitation current amplitudes

5.5 Application of Proposed Method on PWM-Induced Iron Loss Estimation

The ability to accurately predict current ripple has been utilized to implement variable PWM switching frequency schemes to increase the inverter efficiency and improve the electromagnetic interference performance [145], [148], [149]. Beyond that, the proposed current ripple estimation model can serve a valuable purpose to enable more accurate predictions of the PWM-induced iron loss in IPM machines. Compared to ideal sinusoidal excitation conditions, electric machines inevitably experience higher iron loss in the presence of PWM-induced current ripple, accounting for as much as 20– 30% of the total iron loss [163]. Therefore, estimation of the PWM-induced iron loss is of great practical value to better optimize the machine design by having knowledge of the potential efficiency reduction attributable to this loss mechanism during the initial machine design stage.

Using estimated dynamic inductances derived from FEA, the proposed model is capable of carrying out fast (i.e., typical calculation time < 1 s) and accurate assessments of the PWM-induced current ripple for a wide range of operating conditions, making it possible and practical to evaluate large numbers of candidate designs. Furthermore, the in-depth discussion of frequency and shape properties of PWM-induced current ripple presented in this thesis can facilitate the development of a physics-based iron loss model with higher estimation accuracy. More detailed analysis of PWM-induced iron loss using the predicted current ripple data will be presented in the following chapters.

5.6 Summary

A promising analytical model using machine dynamic inductances derived from either FEA predictions or experimental tests has been developed to predict the PWM-induced current ripple in IPM machines. The impact of slotting, magnetic saturation, and cross-coupling effects are considered. Several influencing factors on current ripple have been thoroughly investigated and verified using measured results, including PWM switching frequency, machine speed, dc-bus voltage, current control angle γ, and the excitation current amplitude. Since most of these factors are closely related to the modulation index, the current ripple variation properties have been further explored with constant modulation index.

It has been found that the value of the modulation index determines the switching pattern of SVPWM and plays a key role in determining the amplitude and frequency spectra of the current ripple. In particular, the amplitude of the current ripple component at 1x PWM frequency increases monotonically as the modulation index increases, while the corresponding component at 2x PWM frequency initially increases and then falls back when the modulation index is beyond 0.3. In addition, The IPM machine's dynamic self- and mutual-inductances in both axes are functions of rotor position, current angle γ, and the phase current amplitude. The dynamic inductance must be used when calculating the current ripple, while the use of the static inductance leads to substantial estimation errors when the IPM machine is saturated.

The availability of this improved model for predicting the current ripple in IPM machines with varying machine parameters and operating conditions is expected to provide a valuable tool in the investigation of PWM-induced iron loss.

Chapter 6
Characterization and Modeling of Soft Magnetic Materials for PWM-Induced Iron Loss Estimation

6.1 Introduction

Collecting high-frequency toroidal core iron loss data under conditions of pre-magnetized dc-bias flux density is critical to understanding the PWM-induced iron loss phenomenon in electric machine applications. More specifically, the dc-bias field can exert considerable influence on the magnetic domain distribution, significantly affecting the ac iron loss. As a result, it would be critical to evaluate the iron loss characteristics over a wide range of PWM switching frequencies in the presence of varying external dc-bias fields.

Existing PWM-induced iron loss models typically use a combination of Fourier analysis and some version of the Steinmetz equation. As presented in Chapter 4, Fourier decomposition cannot provide adequate accuracy in terms of modeling the non-sinusoidal waveforms. The PWM-induced ripple induced in the nonlinear magnetic material, sharing the similar properties to the PWM-induced current ripple, deviates from the sinusoidal shape significantly (i.e., concatenation of multiple linear segments). Therefore, the hysteresis model is preferable to analyze and model each minor loop individually.

On the other hand, the generalized dynamic hysteresis model proposed in Chapter 3 suffers from limited operating frequency range and less desirable prediction accuracy when the amplitude of the analyzed waveform is small compared to the input data resolution- $\Delta B = 0.05$ T. That is why a modified dynamic Jiles-Atherton (*J-A*) model is proposed in this Chapter for estimating the PWM-induced iron loss over a wide operating range of excitation conditions.

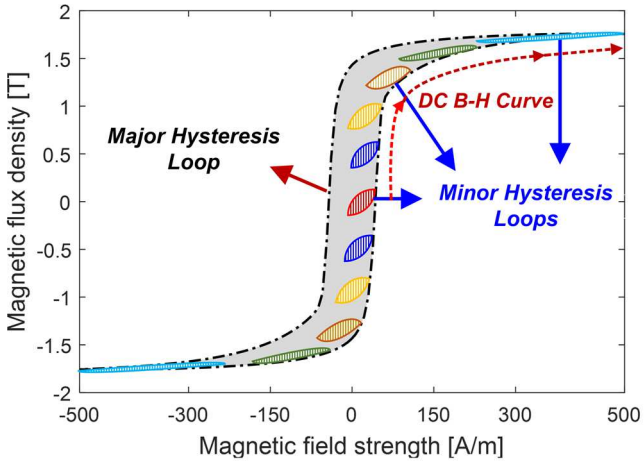

Figure 6-1: Relationship of major and small-amplitude minor hysteresis loops.

6.2 Additional Iron Loss Induced by PWM Harmonics

The experiments reported in [166] show that each minor loop encountered during PWM voltage excitation can be approximated as an individual minor loop superimposed on the fundamental field. In other words, the iron loss induced by the fundamental and PWM harmonic components can be calculated separately. As illustrated in the sketched hysteresis loop in Figure 6-1, as long as the amplitude of each minor is much smaller than the major loop, the shape and enclosed area of the major hysteresis loop is unchanged by the presence of the minor loops, making it possible to decouple the PWM harmonics. As a result, the total iron loss can be estimated by summing the areas of the major and minor loops:

$$P_{\text{iron}} = P_{\text{major}} + P_{\text{minor}} \quad \text{[W]} \qquad (6\text{-}1)$$

$$P_{\text{major}} = V_{\text{vol}} f_{\text{fund}} \int_0^{1/f_{\text{fund}}} H_{\text{major}} \frac{dB_{\text{major}}}{dt} \cdot dt \quad \text{[W]} \qquad (6\text{-}2)$$

$$P_{\text{minor}} = V_{\text{vol}} f_{\text{fund}} \cdot \left(\sum_{n=1}^{n=n_{\text{minor}}} \int H_n \frac{dB_n}{dt} \cdot dt \right) \quad \text{[W]} \qquad (6\text{-}3)$$

where f_{fund} is the fundamental frequency of the major hysteresis loop, n_{minor} is the total number of minor loops occurred during one fundamental period, and V_{vol} is the volume of the material.

Since the PWM switching frequency is typically much higher than the fundamental frequency, the fundamental field during each PWM switching cycle can be considered as a constant dc-bias field B_{dc}. A different value of B_{dc} is required for each of the minor loop integral evaluated in (6-3). B_{dc} can be calculated as follows for each minor loop:

$$B_{\mathrm{dc}} = \frac{1}{\Delta T_{\mathrm{minor}}} \int_{0}^{\Delta T_{\mathrm{minor}}} B_{\mathrm{major}} \cdot dt \qquad [\mathrm{T}] \qquad (6\text{-}4)$$

where B_{major} is the fundamental frequency magnetic flux density waveform, and $\Delta T_{\mathrm{minor}}$ is the time period of a given minor loop.

Figure 6-2 shows the equivalent dc-bias field for each minor loop. As reviewed in Chapter 2, the external dc-bias field exerts a substantial influence on both the shape and iron loss of the minor loop. Using the iron loss data measured in the absence of dc-bias fields leads to significant errors in the iron loss estimation. Therefore, both the enclosed area and corresponding iron loss for each minor loop are evaluated as a function of the minor loop's ac flux density amplitude B_{minor}, external dc-bias field amplitude B_{dc}, excitation waveshape (e.g., sinusoidal or triangular waveform), and minor loop (i.e., PWM switching) frequency f_{minor}.

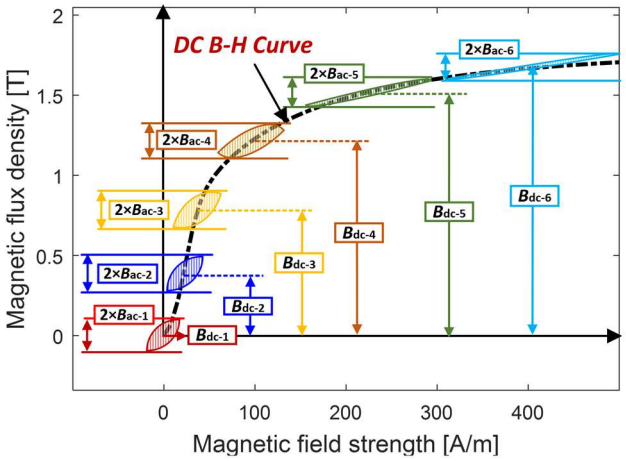

Figure 6-2: Equivalent dc-bias field for each individual minor loop.

6.3 Measurement of Iron Loss for High Frequency Excitation and Pre-Magnetization with DC-Bias Fields

A toroidal-core iron loss measurement system serves as a valuable tool for investigating the iron loss properties of non-oriented soft magnetic materials (e.g., silicon-iron lamination steel) for high excitation frequencies and varying dc-bias fields. The test configuration used to conduct the iron loss measurement is shown in Figure 6-3. It is designed to excite the toroidal core with ac flux density waveforms superimposed with adjustable dc-bias fields. Different from magnetic material characterization involving large flux density amplitudes, the minor loop iron loss evaluation in the PWM frequency range typically operates in the small-amplitude range (i.e., $B_{\text{minor}} \leq 50$ mT). Therefore, the material's magnetic condition can be assumed unaffected by the ac flux component, but dominant by the dc-bias field. In other words, the magnetic material operating at a given dc-bias field is close to linear material with varying permeabilities and iron loss properties (i.e., magnetic domain distributions).

As a result, the flux waveshape regulation control is no longer needed, and the open-circuit sensing-winding voltage V_{sense} is used to measure and adjust the peak amplitude of the minor loop

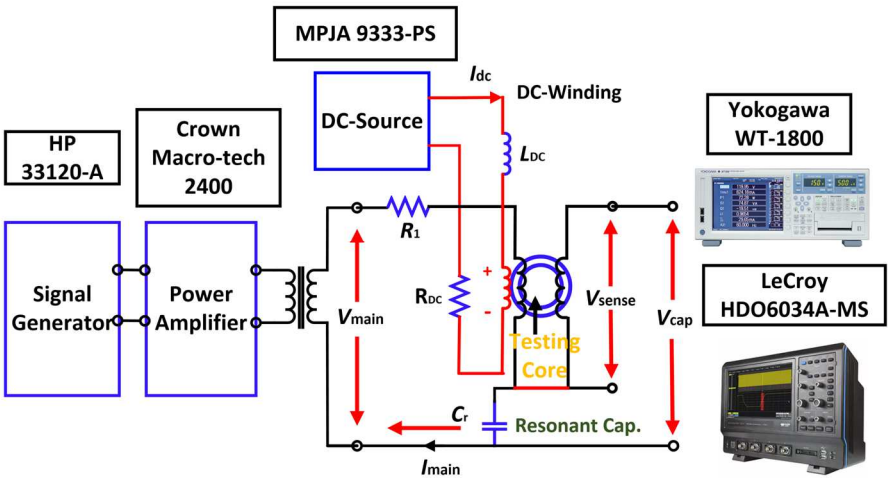

Figure 6-3: Basic circuit configuration of iron loss measurement test equipment.

ac flux density B_{minor} by controlling the rms value of induced open-circuit voltage $V_{\text{sense}_{rms}}$ across the secondary sensing winding, which is given by (6-5). According to (6-6), this system is capable of separating the iron loss from the copper loss in the primary winding by integrating the product of primary winding current and sensing-winding voltage.

$$V_{\text{sense}_{rms}} = \frac{N_{\text{sense}} A_{\text{core}} 2\pi f_{\text{minor}} B_{\text{minor}}}{\sqrt{2}} \tag{6-5}$$

$$\overline{P_{\text{iron}}} = \frac{N_{\text{main}}}{N_{\text{sense}}} \int_0^{1/f_{\text{minor}}} V_{\text{sense}} I_{\text{main}} \cdot dt \tag{6-6}$$

Similar to the procedure presented in Chapter 3, the level of dc-bias field B_{dc} can be adjusted by changing the output of dc current source, which is connected to a third bias winding with N_{dc} turns to provide constant current excitation I_{dc}. An inductor bank L_{dc} is connected in series with the dc current source to suppress the ac ripple induced in the bias winding as much as possible. Otherwise, the ac losses consumed by the dc winding resistance will be inherently included as the iron loss of the testing core, which, in turn, result in an overly measured loss value. Using the material's dc *B*-*H* curve such as the one plotted in Figure 6-2, the corresponding dc-bias field B_{dc} can be determined.

The key parameters and dimensions of the thin-gauge silicon-steel toroidal core are provided in Table 3-1. The primary and dc-bias field windings are shown in Figure 6-4(a) and (b), respectively. Using a high number of turns in both windings enables the system to drive the core into the heavily-saturated region where the maximum value of dc-bias field B_{dc} reaches 1.8 T.

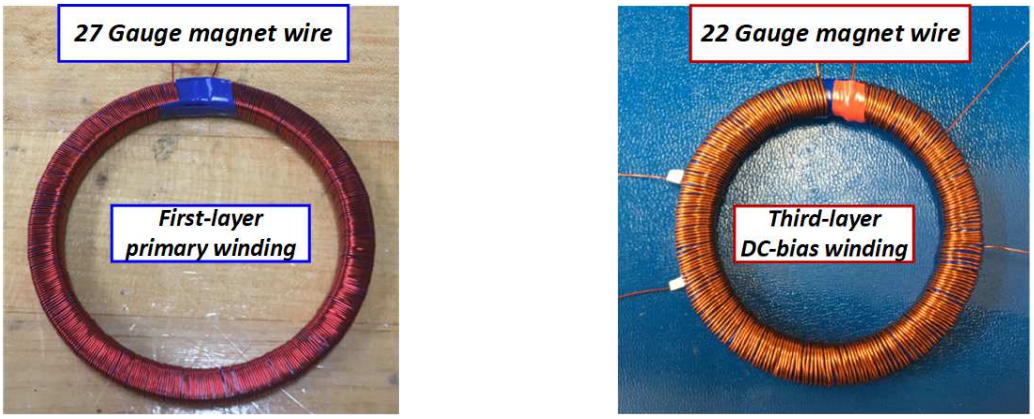

(a) Toroidal core primary winding (b) Toroidal core dc-bias winding

Figure 6-4: Manufactured toroidal core for iron loss characterization.

Figure 6-5(a) shows an overall view of the iron loss measurement test equipment. As shown in the close-up view of the cooling fixture in Figure 6-5(b), the toroidal core is immersed in mineral oil during the test, giving it improved ability to dissipate the additional heat produced in the dc-bias winding. A feedback control circuit has been utilized that can regulate the oil temperature to be constant with the external cooling fan. Therefore, the core temperature rise due to the dc-bias winding current is negligible. To better monitor the instantaneous surface temperature of the dc-bias winding, a thermocouple is mounted on the toroidal core surface. It has been experimentally verified in Figure 6-6 that the steady-state toroidal core surface temperature is within the safe operating limits of the selected magnet wire over the entire range of dc winding current.

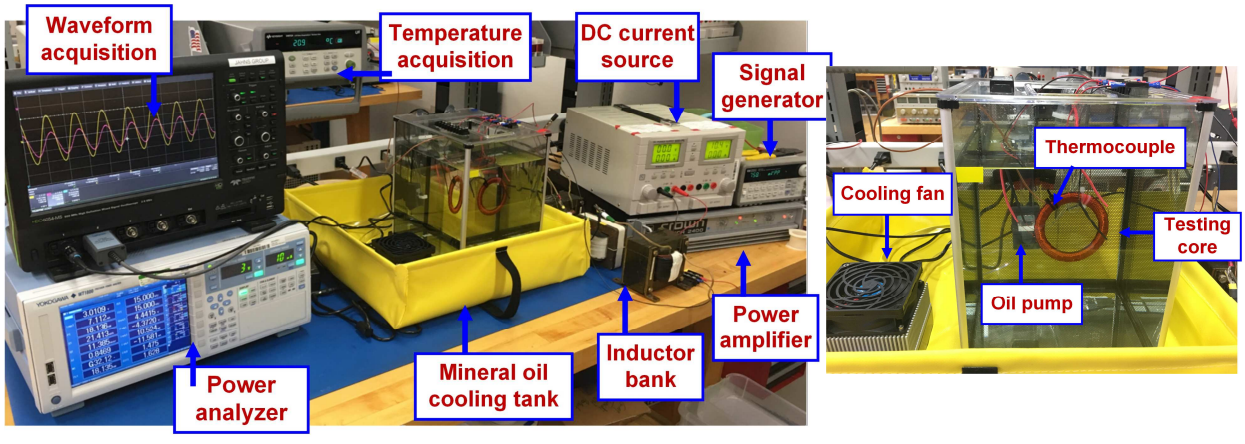

(a) Overall test configuration (b) Close-up view of cooling system

Figure 6-5: Experimental test configuration for toroidal core iron loss test.

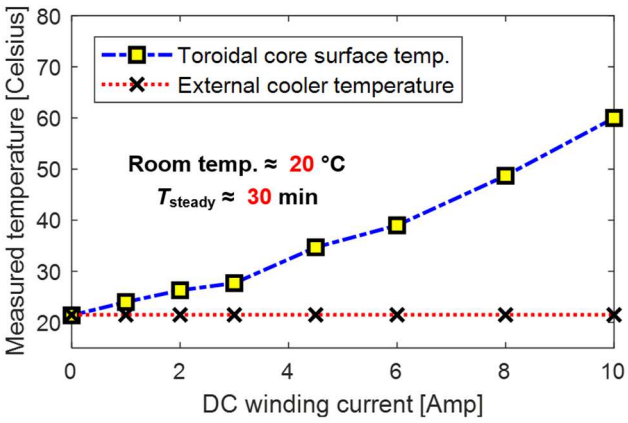

Figure 6-6: Measured temperature at the testing core surface and external cooler vs. dc winding current.

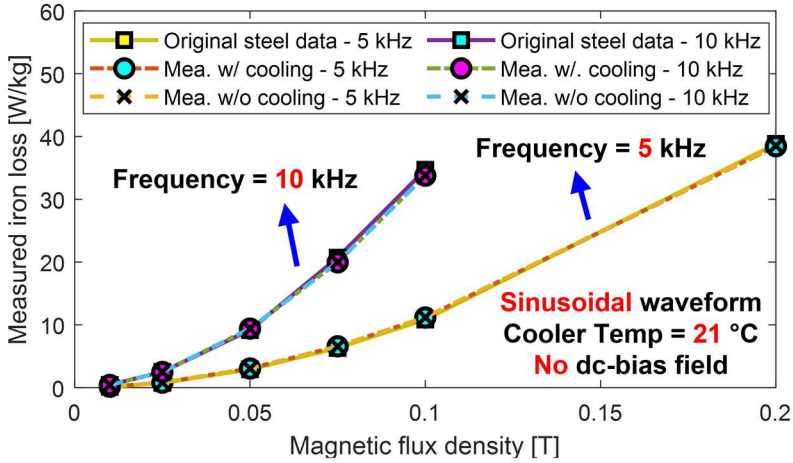

Figure 6-7: Measured iron loss test results without dc-bias field provided by the steel manufacturer and toroidal core test configuration with two excitation frequencies (f_{minor} = 5 & 10 kHz).

Figure 6-7 presents a comparison of the measured high-frequency iron loss results provided by the steel manufacturer and the proposed toroidal core system with and without immersing the testing core into mineral oil. The generally good agreement between these measured data supports the assumption that the proposed cooling system does not affect the magnetic environment of the toroidal core or induce additional iron loss.

Figure 6-8 depicts the measured iron loss versus the dc-bias field at 5 and 10 kHz, respectively. Consistent with the previous assumption that the amplitude of the PWM-induced ripple is much smaller than the fundamental field, the ac flux density B_{minor} is fixed at 10 mT.

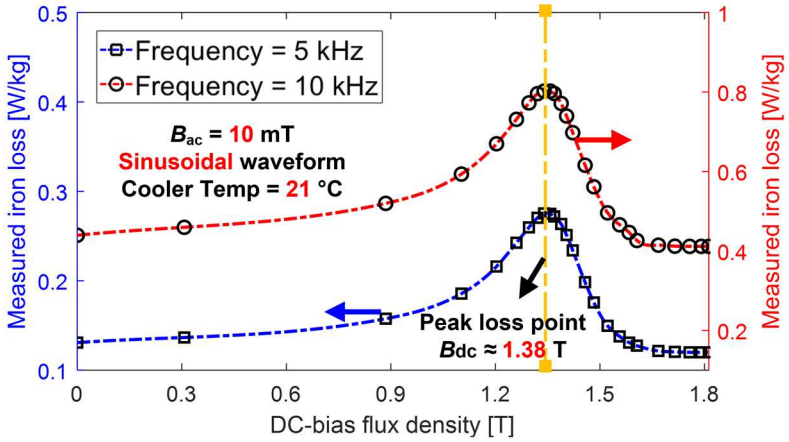

Figure 6-8: Measured iron loss versus external dc-bias field with small minor loop flux density amplitude B_{minor} at 10 mT, and two excitation frequencies f_{minor} = 5 & 10 kHz.

As can be seen from Figure 6-8, the iron loss exhibits a similar response to the dc-bias field at both excitation frequencies. In the low dc-bias field region, the iron loss is relatively small. As the dc-bias field increases, the iron loss gradually increases and reaches its maximum value in the vicinity of 1.38 T. Consistent with the sketched minor loop in Figure 6-2, the peak loss point falls in the knee region of the material's *B*-*H* curve, suggesting that the magnetic domain distribution determined by the dc-bias field plays a major role in deciding the iron loss. After passing the peak point, the iron loss decreases sharply and then remains at a nearly constant value in the heavily saturated region (i.e., $B_{dc} \geq 1.6$ T). This result is consistent with the observation that the magnetic properties of the iron core remain almost unchanged as the dc-bias field increases beyond 1.6 T.

It is worth noting that when supplying a large dc-bias current to drive the iron core into its heavily saturated condition, the phase shift φ_{shift} between the primary current and secondary voltage is very close to 90 degree, which pushes the power factor towards zero. As demonstrated in [106], if the power factor is nearly 90 degree, even a very small phase measurement error less than 1 degree results in significant active power (i.e., iron loss) measurement errors. Therefore, the accuracy of the measurement results when the tested iron core falls into the heavy saturation region requires special attention and confirmation.

An interesting capacitive voltage cancellation methodology is proposed in [108] to cancel the reactive voltage generated by the magnetizing inductance. As shown in the equivalent circuit provided in Figure 6-3, connecting a resonant capacitor C_r in series with the primary winding makes it possible to minimize the phase shift between the voltage V_{cap} and primary-side current if the capacitance is selected carefully as follow:

$$C_r = \frac{N_{\text{main}}}{N_{\text{sense}}(2\pi f)^2 L_m} \tag{6-7}$$

However, changing the amplitude of the dc-bias field alters the permeability of the iron loss, which, in turn, changes the value of the magnetizing inductance L_m. As a result, it is impractical to achieve zero phase shift at each dc-bias field tested in Figure 6-8. Therefore, the primary role of C_r in these tests is to provide a means to verify the accuracy of the power analyzer.

Based on the availability of low-loss film capacitors with ESR below 10 mΩ, the entire dc-bias field testing range has been divided into five operating regions with different C_r capacitance values in each region to cancel the reactive voltage induced by magnetizing inductance as much as possible. For the most cases, the phase shift is kept lower than 60 degrees, where the error percentage caused by a 1 degree phase discrepancy is below 3%. A comparison of measured iron loss versus dc-bias field with and without the resonant capacitor is shown in Figure 6-9. The good agreement raises confidence in the measurement accuracy of the power analyzer even when the phase shift is close to 90 degrees. Also, plotting the iron loss variation versus the dc magnetizing force H_{dc} provides another perspective, suggesting that the studied magnetic material exhibits different responses to dc-bias field in the linear region (i.e., Region- I) compared to other saturated regions.

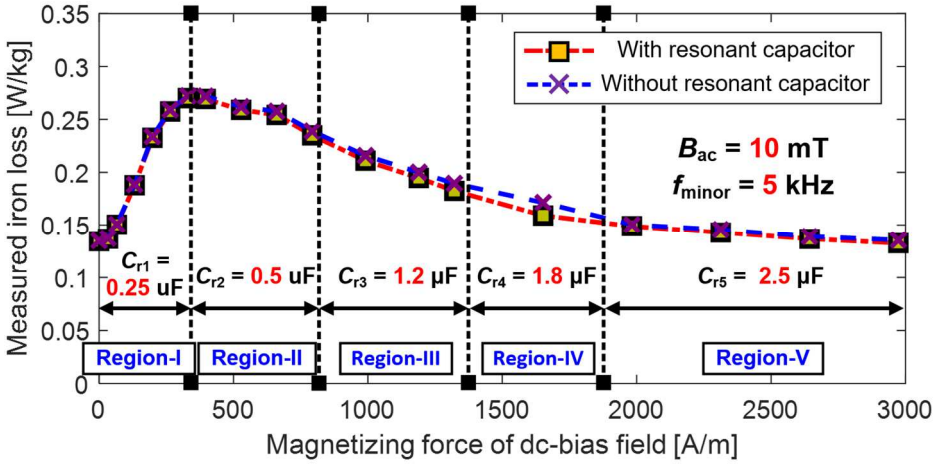

Figure 6-9: Comparison of measured iron loss versus dc magnetizing force with and without connecting the series resonant capacitor C_r.

Note: Five zones are identified with different C_r values.

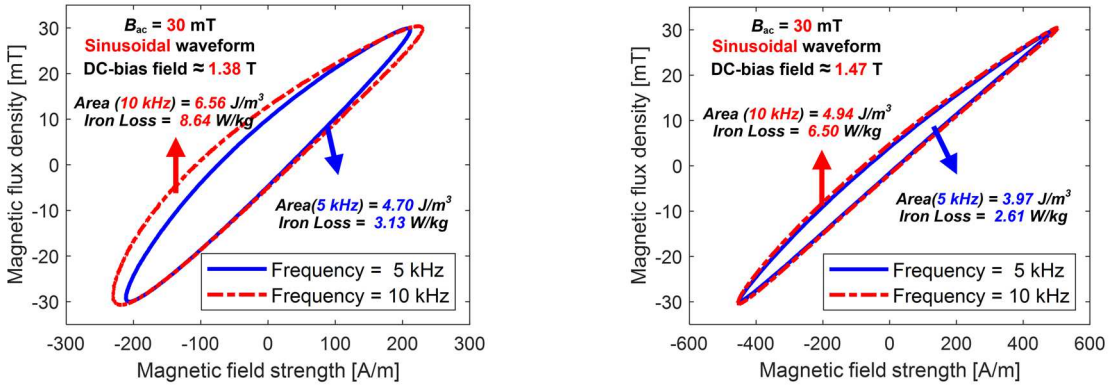

(a) DC-bias flux density B_{dc} = 1.38 T (b) DC-bias flux density B_{dc} = 1.47 T

Figure 6-10: Measured hysteresis loops for two values of external dc-bias flux density at 5 & 10 kHz

Measured hysteresis loops, together with the calculated net-enclosed areas and iron losses for two selected dc-bias fields are presented in Figure 6-10 (a) and (b). It has been observed from these tests that, if the amplitude of the minor loop ac magnetic flux is relatively small (i.e., $B_{minor} \leq 30$ mT), the hysteresis loops maintain their symmetrical shapes even in the presence of the dc-bias field. These results support the conclusion that the magnetic condition of the material is dominated by the dc-bias field and the impact of small-magnitude ac ripple is negligible.

In summary, the availability of this test configuration makes it possible to comprehensively evaluate the high-frequency iron loss for a much broader range of test conditions, and more results are presented in the later section discussing the experimental investigation of the proposed model.

6.4 Modified Dynamic Jiles-Atherton Model for PWM-Induced Iron Loss Estimation

The iron loss in the ferromagnetic materials is generally divided into three terms including static hysteresis loss, classical eddy current loss, and anomalous loss. However, it has been long recognized that the loss decomposition method cannot provide sufficient accuracy for modeling the high-frequency or non-sinusoidal flux density waveforms. Considering the issue of PWM-induced iron loss in electric machines, the PWM switching frequency of modern inverters give rise to high-frequency components of magnetic flux density in the laminations that is typically beyond the range of frequencies where the classical Steinmetz equation can be used. This situation is almost certain to worsen during coming years as the availability of wide bandgap power semiconductor switches (i.e., SiC and GaN) will make it possible to significantly raise the PWM switching frequency, further degrading the usefulness of the Steinmetz equation for evaluating PWM-induced iron losses in the machine core.

As a result, a dynamic hysteresis model appears as a better candidate for PWM-induced iron loss estimation. Although the proposed generalized dynamic hysteresis model in Chapter 3 exhibits promising capability for modeling the minor loop affected by the dc-bias field, it intrinsically requires full hysteresis loop data at the interested minor loop frequency (e.g., f_{minor} = 5 or 10 kHz), which is typically not feasible to collect. Also, its accuracy degrades as the minor loop amplitude becomes small, making it less desirable for PWM frequency range applications. Among the existing hysteresis models, the Jiles-Atherton (*J-A*) model is considered to be a practical and conventional tool for predicting the major hysteresis loops under quasi-static conditions. Although the original static *J-A* model has been extended for dynamic conditions to include the impact of eddy current loss contributions [91] and dc-bias fields [183], these models have not been designed

or evaluated for PWM-induced iron loss estimation. Therefore, the development of an improved dynamic *J-A* model for PWM-induced iron loss estimation will be demonstrated in this section.

6.4.1 Static Jiles-Atherton Model

The original *J-A* model [57] was designed for analyzing the major hysteresis loop of magnetic materials under static conditions without considering the dynamic field impact including the classical eddy current loss and anomalous loss. The formulation of the original *J-A* model can be represented by five fundamental equations, presented below in equations from (6-8) to (6-12):

$$M_{\text{an}} = M_s \left[\coth\left(\frac{H_e}{a}\right) - \frac{a}{H_e} \right] \tag{6-8}$$

where M_{an} is the anhysteretic magnetization, M_{s} is the saturation magnetization of the major loop, H_e is the effective field, and a denotes the density of magnetic domain distribution.

$$H_e = H + \alpha \cdot M \tag{6-9}$$

where M is the total magnetization, H is the magnetization force, and α is the parameter associated the inter-domain coupling.

$$M = M_{\text{rev}} + M_{\text{irr}} \tag{6-10}$$

where M consists of the sum of a reversible component M_{rev} and an irreversible component M_{irr}.

$$M_{\text{rev}} = c(M_{\text{an}} - M_{\text{irr}}) \tag{6-11}$$

where c is the coefficient of proportionality associated with the initial differential susceptibilities of the normal and anhysteretic magnetization curves.

$$\frac{dM_{\text{irr}}}{dH_e} = \frac{M_{\text{an}} - M_{\text{irr}}}{k\delta} \tag{6-12}$$

where k is the model parameter related to coercive field, and δ is the directional parameter that takes the value $+1$ when $dH/dt > 1$ and -1 when $dH/dt < 1$.

In [184], a modified version of the *J-A* model is proposed with an additional parameter to avoid the non-physical behavior reconstructed *B-H* curves when the incremental susceptibility becomes negative. According to this modified, (6-12) can be updated as:

$$\frac{dM_{\text{irr}}}{dH_e} = \delta_M \cdot \frac{M_{\text{an}} - M_{\text{irr}}}{k\delta} \tag{6-13}$$

where $\delta_M = 1/2 \cdot [1 + \text{sgn}(M_{\text{an}} - M) \cdot \frac{dH}{dt}]$, and *sgn* is the signum function that deliver either + 1 or − 1 depending on the polarity of the expression in the parentheses.

Combining (6-8) to (6-13), the differential equation summarizing the general magnetization process can be reduced to:

$$\frac{dM}{dH_e} = \delta_M \cdot \frac{M_{\text{an}} - M_{\text{irr}}}{k\delta} + c\frac{dM_{\text{an}}}{dH_e} \tag{6-14}$$

Since the magnetic flux density *B* is generally considered as the input variable instead of the magnetizing force *H*, the so-called inverse *J-A* model has been proposed with the following relationship:

$$B = \mu_0 \cdot (H + M) \tag{6-15}$$

After several steps of algebraic simplification, the final differential equation for the inverse *J-A* model is expressed as:

$$\frac{dM}{dB} = \frac{\delta_M(M_{\text{an}} - M) + ck\delta\frac{dM_{\text{an}}}{dH_e}}{\mu_0[k\delta + (1-\alpha)\cdot\left(\delta_M(M_{\text{an}} - M) + ck\delta\frac{dM_{\text{an}}}{dH_e}\right)]} \tag{6-16}$$

Summarizing, modeling the hysteresis loop of a particular magnetic material requires the pre-knowledge of five physical parameters including a, α, c, k, and M_s. These parameters can be identified via an identification process based on the experimentally-measured hysteresis loop.

6.4.2 Inclusion of Dynamic Eddy Current Loss

As the excitation frequency increases, the enclosed area and shape of hysteresis loop can be substantially affected by the dynamic loss components reflected in the measured dynamic hysteresis loops for a series of frequencies shown in Figure 6-11. Owing to the physical nature of dynamic hysteresis loop, the enclosed area is equivalent to the energy dissipation during a single hysteresis loop excursion, including the loss contribution from the static hysteresis loop and dynamic eddy current loss.

Moreover, as can be seen from Figure 6-11, the net area of each loop increases significantly with the excitation frequency, indicating that loss per magnetization cycle goes up while the magnetic permeability drops. The expanding area of these loops as the frequency increases makes the dynamic loss the dominant loss component over the static hysteresis loss for high-frequency conditions (i.e., the frequency range of PWM-induced ripple). Therefore, proper inclusion of dynamic eddy current loss is of great importance to fully understand and emulate the PWM-induced iron loss phenomenon.

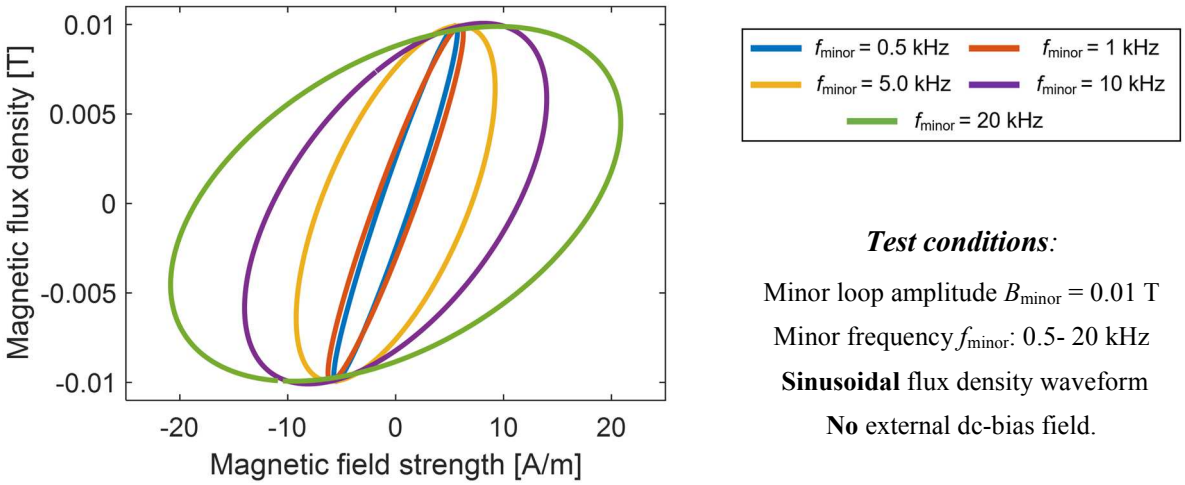

Figure 6-11: Measured dynamic hysteresis loops over different minor loop excitation frequencies.

The dynamic *J-A* model has been discussed and implemented in [67], [89]–[91]. Three kinds of dynamic *J-A* model are commonly adopted in the literature, including (1) Conventional static *J-A* model, (2) Dynamic *J-A* model based on energy balance theorem, and (3) Dynamic *J-A* model based on field separation theory.

Conventional Static *J-A* Model: The key idea behind this method is to emulate the measured dynamic hysteresis loop as an equivalent static hysteresis but referring to a new hypothetical magnetic material. This model has the advantage of not requiring any additional parameters except five original parameters given in (6-16). However, the model applicability in the high-frequency range has not been verified yet in [67], and its performance will be evaluated and compared with the proposed model in the following section.

Dynamic *J-A* Model based on Energy Balance or Field Separation Theorem: To achieve a better match with the measured dynamic hysteresis loops over a broad frequency range, additional terms related to dynamic eddy current loss are introduced in the dynamic *J-A* models based on energy balance or field separation theorem.

The core equation of energy balance theorem is to include the dynamic energy dissipation in the magnetization process as:

$$\begin{aligned}\mu_0 \int M_{\mathrm{an}} \cdot dH_e \\ &= \mu_0 \int M \cdot dH_e + \mu_0 k\delta(1-c) \int \left(\frac{dM_{\mathrm{irr}}}{dH_e}\right) \cdot dH_e \\ &+ \mu_0^2 k_{\mathrm{eddy}} \int \left(\frac{dM}{dt}\right)^2 \cdot dt + \mu_0^{1.5} k_{\mathrm{ano}} \int \left(\frac{dM}{dt}\right)^{1.5} \cdot dt\end{aligned} \tag{6-17}$$

where the first two terms in the right-side of (6-17) are responsible for the field variation under quasi-static condition, and the latter two terms are added to account for dynamic eddy current loss.

Differentiate both side of (6-17) with respect to H_e gives the following expression:

$$M_{\text{an}} = M + k\delta(1-c)\left(\frac{dM_{\text{irr}}}{dH_e}\right) + \mu_0^2 k_{\text{eddy}}\left(\frac{dM}{dH_e}\right)\left(\frac{dM}{dt}\right) + \mu_0^{1.5} k_{\text{ano}}\left|\frac{dM}{dt}\right|^{\frac{1}{2}}\left(\frac{dM}{dH_e}\right) \tag{6-18}$$

where (6-18) can be formulated to give another solution as the one shown in (6-16).

Another approach based on field separation converts the static hysteresis loop to its dynamic version by introducing additional terms to adjust the total magnetic field strength

$$H_{\text{tot}}(t) = H_{\text{stat}}\big(B(t)\big) + k_{\text{eddy}}\left(\frac{dB}{dt}\right) + k_{\text{ano}}\delta\left|\frac{dB}{dt}\right|^{\frac{1}{2}} \tag{6-19}$$

where $H_{\text{stat}}(B(t))$ is the solution calculated from the static *J-A* model, k_{eddy} is coefficient of the classical eddy current loss, and k_{ano} is the coefficient of the residual anomalous loss.

Knowing the iron loss coefficients is the prerequisite to properly include the impact of dynamic loss, and the statistical theorem [39] is commonly adopted to calculate those two coefficients

$$k_{\text{eddy}} = \frac{d^2}{12\rho_{\text{iron}}} \qquad\qquad k_{\text{ano}} = \sqrt{\frac{SGV_0}{\rho_{\text{iron}}}} \tag{6-20}$$

where d is the thickness of lamination sheet, ρ_{iron} is the material resistivity, S is the cross-section area of the lamination sheet, $G \approx 0.136$ is a dimensionless coefficient, and V_0 is a parameter representing the statistical distribution of internal domain walls.

However, the expressions in (6-20) pertain to low-frequency operating conditions, and as indicated by Figure 6-10(a) and (b), the iron loss coefficients are functions of both the dc-bias field and excitation frequency, which makes impractical to run the parameter identification of the static *J-A* model and dynamic loss terms separately. To simplify the parameter estimation process, a modified dynamic *J-A* model is proposed:

$$H_{\text{tot}}(t) = H_{\text{stat}}\big(B(t)\big) + k_{\text{dyn}}\delta\left|\frac{dB}{dt}\right|^{\nu_{\text{dyn}}} \tag{6-21}$$

where k_{dyn} and ν_{dyn} are the lumped dynamic loss coefficient and its time-dependence coefficient.

There are seven parameters (a, α, c, k, and M_s, $k_{\text{dyn,}}$ and v_{dyn}) to be identified for each measured dynamic hysteresis loop for a given operating condition including the dc-bias field. As noted previously, the small-amplitude minor loops have symmetrical shapes under the influence of varying dc-bias fields. Therefore, each minor loop is approximated as a hysteresis loop around the origin point, but with a different shape and enclosed area. In other words, the impact of the dc-bias field is not directly included in the parameter identification process or the model solution (6-21).

The seven parameters of the proposed model can be subsequently identified via available optimization techniques (e.g., nonlinear least squares, particle swarm optimization, etc.) to achieve the desired fitting performance using the hysteresis loop data collected from the toroidal core tests discussed in the preceding section.

6.4.3 Identification of Hysteresis Model Parameters

In the process of fitting a hypothetical function $\widehat{H}(B_i; \mathbf{p})$ of the input magnetic flux density waveform B_i and a group of model parameters $\mathbf{p}$, least squares problems arise to iteratively reduce the sum of the square of the errors between the measured and values calculated by the proposed estimation model. Therefore, the chi-squared error criterion $\chi^2(\mathbf{p})$ serves as a valuable measure to determine the goodness-of-fit [185], [186]

$$\chi^2(\mathbf{p}) = \sum_{i=1}^{m} \left[\frac{H(B_i) - \widehat{H}(B_i; \mathbf{p})}{\sigma_{yi}} \right]^2 \tag{6-22}$$

where σ_{yi} is the measurement error for measurement $H(B_i)$. However, for common operating conditions, σ_{yi} is not known in advance of analysis.

As a result, σ_{yi} is typically transformed into the weighting matrix $\mathbf{W}$, in which the diagonal element is defined as

$$W_{ii} = \frac{1}{\sigma_{yi}^2} \tag{6-23}$$

Subsequently, (6-22) can be written as

$$\chi^2(\mathbf{p}) = \left(H - \widehat{H}(\mathbf{p})\right)^T \mathbf{W}(H - \widehat{H}(\mathbf{p})) \tag{6-24}$$

Since the proposed dynamic hysteresis model is highly nonlinear, it takes multiple iterations to minimize the value of χ^2 with respect to the parameters. Therefore, a stable and reasonably fast optimization tool is needed to find a perturbation **h** of each parameter in each iteration that can provide a smaller value of χ^2.

Among a variety of available methodologies, the Levenberg-Marquart algorithm (LMA) is considered as a standard technique to solve the nonlinear least squares problems [187]–[189] and is selected as the preferred parameter identification tool. LMA operates as the combination of two optimization method, namely, the gradient descent method and the Gauss-Newton method.

The LMA acts more like a gradient descent method when the initial guess of parameters deviates much from the optimal value, where the gradient of the chi-squared objective function with respect to the model parameters is given as [190]

$$\frac{\partial}{\partial \mathbf{p}}\chi^2 = -2\left(H - \widehat{H}(\mathbf{p})\right)^{\mathrm{T}} \mathbf{W}\left[\frac{\partial \widehat{H}(\mathbf{p})}{\partial \mathbf{p}}\right] = -2\left(H - \widehat{H}(\mathbf{p})\right)^{\mathrm{T}} \mathbf{WJ} \tag{6-25}$$

where the Jacobian matrix **J** denotes the local sensitivity of hypothetical function $\widehat{H}(\mathbf{p})$ to the variations of parameters.

The parameter update **h** moving in the steepest descent is expressed as

$$\mathbf{h} = \alpha_{\mathrm{gd}}\mathbf{J}^{\mathrm{T}}\mathbf{W}(H - \widehat{H}(\mathbf{p})) \tag{6-26}$$

where α_{gd} is the length of the step in the steepest-descent direction.

The LMA behaves as the Gauss-Newton method when the parameters are close to their optimal values. The function is approximated through a first-order Taylor series expansion in (6-27), and the resulting normal equation for the Gauss-Newton update is given in (6-28)

$$\widehat{H}(\mathbf{p}+\mathbf{h}) \approx \widehat{H}(\mathbf{p}) + \left[\frac{\partial \widehat{H}(\mathbf{p})}{\partial \mathbf{p}}\right]\mathbf{h} = \widehat{H}(\mathbf{p}) + \mathbf{J}\mathbf{h} \tag{6-27}$$

$$[\mathbf{J}^{\mathrm{T}}\mathbf{W}\mathbf{J}]\mathbf{h} = \mathbf{J}^{\mathrm{T}}\mathbf{W}(H - \widehat{H}(\mathbf{p})) \tag{6-28}$$

Combing two solutions demonstrated in (6-26) and (6-28) gives the updating equation of LMA

$$[\mathbf{J}^{\mathrm{T}}\mathbf{W}\mathbf{J} + \lambda \mathrm{diag}(\mathbf{J}^{\mathrm{T}}\mathbf{W}\mathbf{J})]\mathbf{h} = \mathbf{J}^{\mathrm{T}}\mathbf{W}(H - \widehat{H}(\mathbf{p})) \tag{6-29}$$

where the algorithmic parameter λ is initially set to a relatively large value so that the LMA acts more like the gradient descent method. As the solution improves and the value of χ^2 goes down, the λ is decreased, and then the LMA approaches the Gauss-Newton method to accelerate the convergence. The detailed implementation procedure of the LMA is documented in [189].

Next, the LMA is employed to determine the coefficients of the static *J-A* model and the proposed dynamic *J-A* model with the measured dynamic hysteresis loops data. It is worth noting that, since the amplitude of collected minor loops is much smaller than the saturation level of the major loop (usually larger than 1.8 T) defined in the original *J-A* model, the initial value of M_s is set to be in the vicinity of the magnetization value required to generate a magnetic flux density of 0.1 T to mimic the impact of saturation on the shape of each minor loop.

Firstly, the static *J-A* model is applied to fit the measured data. The key metrics of curve-fitting performance- chi-squared error criterion χ^2 over two dc-bias conditions (i.e., B_{dc} = 0 and 1.4 T) of the minor loop at 10 mT, 5 kHz are plotted in Figure 6-12(a)-(b). For both cases, χ^2 starts with large amplitudes due to the relatively poor initial guess of model parameters. As the number of iterations increases, χ^2 drops over two orders of amplitude within the first fifty calls of updating

function, where the LMA behaves like the gradient descent method. After that, χ^2 slowly goes down and reaches its minimum value as the iteration number approaches two hundred.

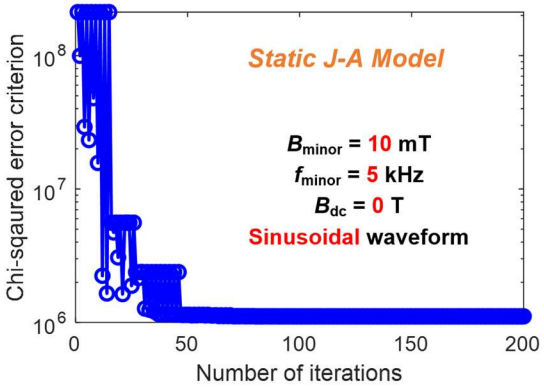

(a) Chi-squared error criterion χ^2

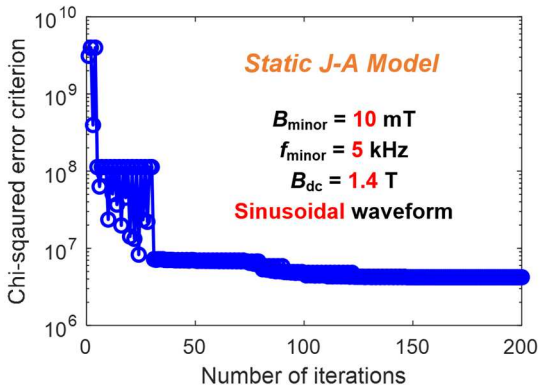

(b) Chi-squared error criterion χ^2

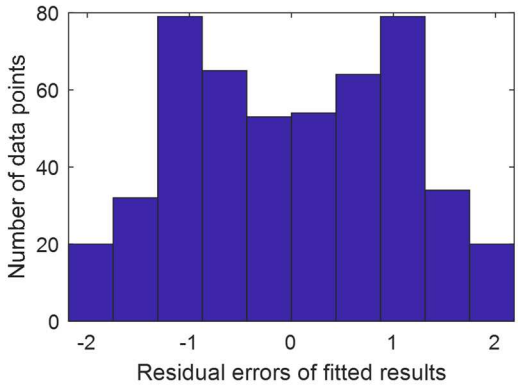

(c) Residual errors distribution

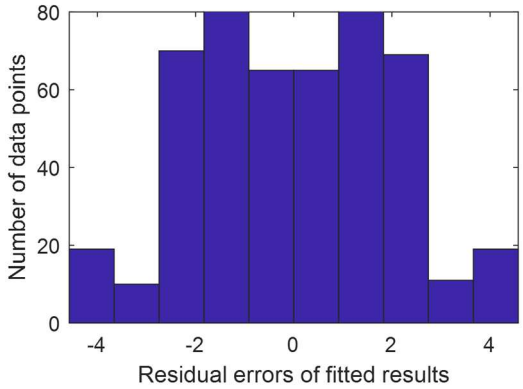

(d) Residual errors distribution

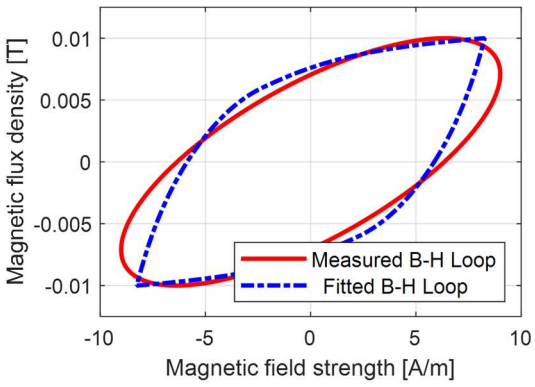

(e) Measured and fitted *B-H* loops

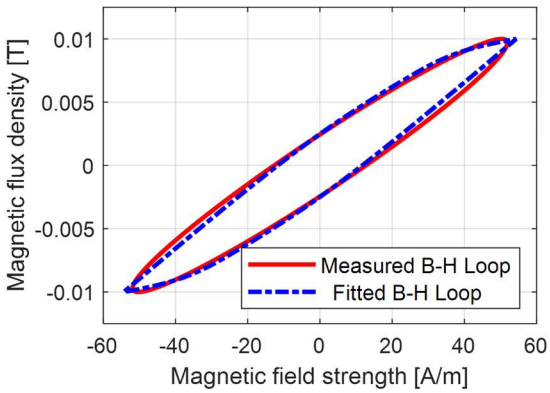

(f) Measured and fitted *B-H* loops

Figure 6-12: Evaluation of curve fitting performance on high-frequency minor loop over two values of dc-bias fields using the static *J-A* model.

However, as can be seen from Figure 6-12(c)-(d), relatively large residual errors are observed even after running the optimization process. For both cases, a large number of data points deviate from the measured significantly (i.e., $\left|H - \widehat{H}(\mathbf{p})\right| > 1$). Furthermore, Figure 6-12(e)-(f) compares the measured and fitted *B-H* hysteresis loops, further suggesting that the static *J-A* model is insufficient to emulate the dynamic hysteresis loops with high excitation frequency.

Next, the proposed dynamic *J-A* model is employed to model the dynamic hysteresis loops. Similarly, as depicted in Figure 6-13(a)-(b), the value of χ^2 decreases substantially in the first fifty iterations and then gradually reaches its optimum value. Although the initial values of χ^2 for both models are in the similar range (i.e., 10^8- 10^9), the minimum value of χ^2 in each case of the proposed dynamic *J-A* model is about two orders of amplitude better than that of the static *J-A* model. As a result, the residual errors of the fitted results shown in Figure 6-13(c)-(d) are much smaller and almost negligible, where the absolute values of the residual errors for the majority of data points are below 0.2. The fitted hysteresis loops have achieved excellent agreement with the measured data given in Figure 6-13(e)-(f), indicating that the proposed dynamic *J-A* model has better performance, less steady-state residual error than the static *J-A* model. Therefore, the modified dynamic *J-A* model is adopted in this project for the PWM-induced iron loss estimation.

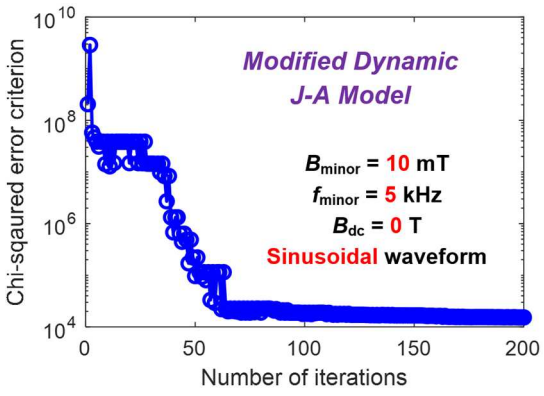

(a) Chi-squared error criterion χ^2

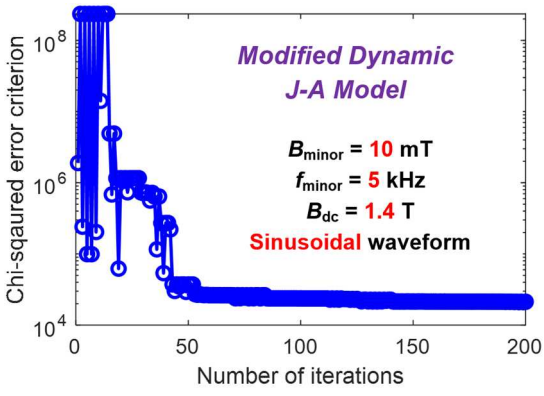

(b) Chi-squared error criterion χ^2

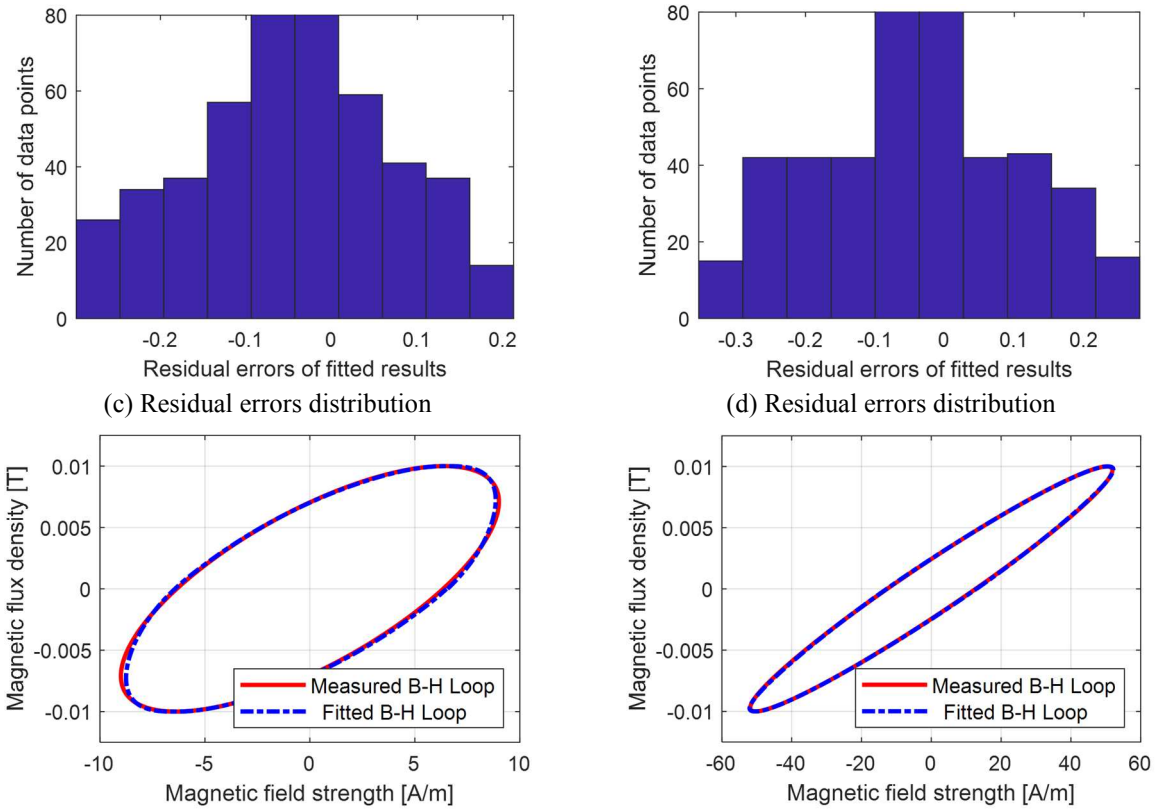

(c) Residual errors distribution

(d) Residual errors distribution

(e) Measured and fitted *B-H* loops

(f) Measured and fitted *B-H* loops

Figure 6-13: Evaluation of curve fitting performance on high-frequency minor loop over two values of dc-bias fields using the modified dynamic *J-A* model.

6.5 Experimental Evaluation of Proposed PWM-Induced Iron Loss Estimation Model

In a real machine, it is the instantaneous voltage difference between the inverter-side PWM voltage and machine-side fundamental voltage that causes the high-frequency current and flux ripple. PWM-induced current ripple data are available from both experiments and analytical predictions as presented in Chapter 5. The amplitude, frequency spectrum and waveshape of PWM-induced current ripple can vary a lot depending on the PWM switching frequency, inverter dc-bus voltage, machine saturation level, and several other influencing factors. Such complexity makes it desirable to use the parameters obtained from a limited number of tests to estimate the PWM-induced iron loss for the entire machine. In this section, the accuracy and scalability of the proposed estimation model are investigated.

6.5.1 Impact of AC Flux Ripple Amplitude

With a sufficiently large ratio between the PWM switching frequency f_{PWM} and the machine fundamental frequency f_{fund} (e.g., > 50), the amplitude of the PWM-induced flux ripple typically falls into the range from 1 to 50 mT. In this case, for a given dc-bias field and excitation frequency, three sets of hysteresis model parameters are pre-characterized for three different flux amplitudes: 10 mT, 20 mT, and 50 mT. Each set of parameters is responsible for predicting the hysteresis loop and corresponding iron loss based on the following rule:

$$\begin{cases} \text{Parameters from 10 mT ref. case, if } B_{\mathrm{minor}} \leq 15 \text{ mT}, \\ \text{Parameters from 20 mT ref. case, if } 15 \text{ mT} < B_{\mathrm{minor}} < 30 \text{ mT}, \\ \text{Parameters from 50 mT ref. case, if } B_{\mathrm{minor}} \geq 30 \text{ mT}. \end{cases} \tag{6-30}$$

It is worth noting that, for the reference minor loop at 50 mT amplitude, the measured dynamic hysteresis loop is no longer in the pure symmetrical shape, indicating that the minor loop itself exerts a noticeable impact on the minor loop's magnetic condition. As a result, in large amplitude regions (i.e., $B_{\mathrm{minor}} \approx 50$ mT), the minor loop is approximated as the symmetrical one which shares the similar shape and the identical enclosed area with the measured unsymmetrical loop.

In the example case, the parameters required for the modified dynamic *J-A* model are determined for f_{PWM} = 5 kHz, three reference amplitudes of ac flux density noted above, and 1.38 T dc-bias field where the peak iron loss occurs in Figure 6-8. The parameters obtained from these reference cases are subsequently applied to the modified dynamic *J-A* model and used to predict the hysteresis loops for the range of B_{minor} values from 5 to 50 mT. The comparison of the measured and simulated hysteresis loops and iron losses are shown in Figure 6-14.

As can be seen in Figure 6-14(a) to (e), both the shape end enclosed areas (i.e., iron loss) of the hysteresis loops can be accurately estimated using the proposed model. However, if the amplitude of minor loop ac flux density approaches 50 mT (Figure 6-14(f)), the ac flux ripple

exerts a noticeable impact on the magnetic condition, making the minor hysteresis loop unsymmetrical. Although the asymmetrical property of the minor loop is ignored in the proposed model, the iron loss estimation model provides promising accuracy.

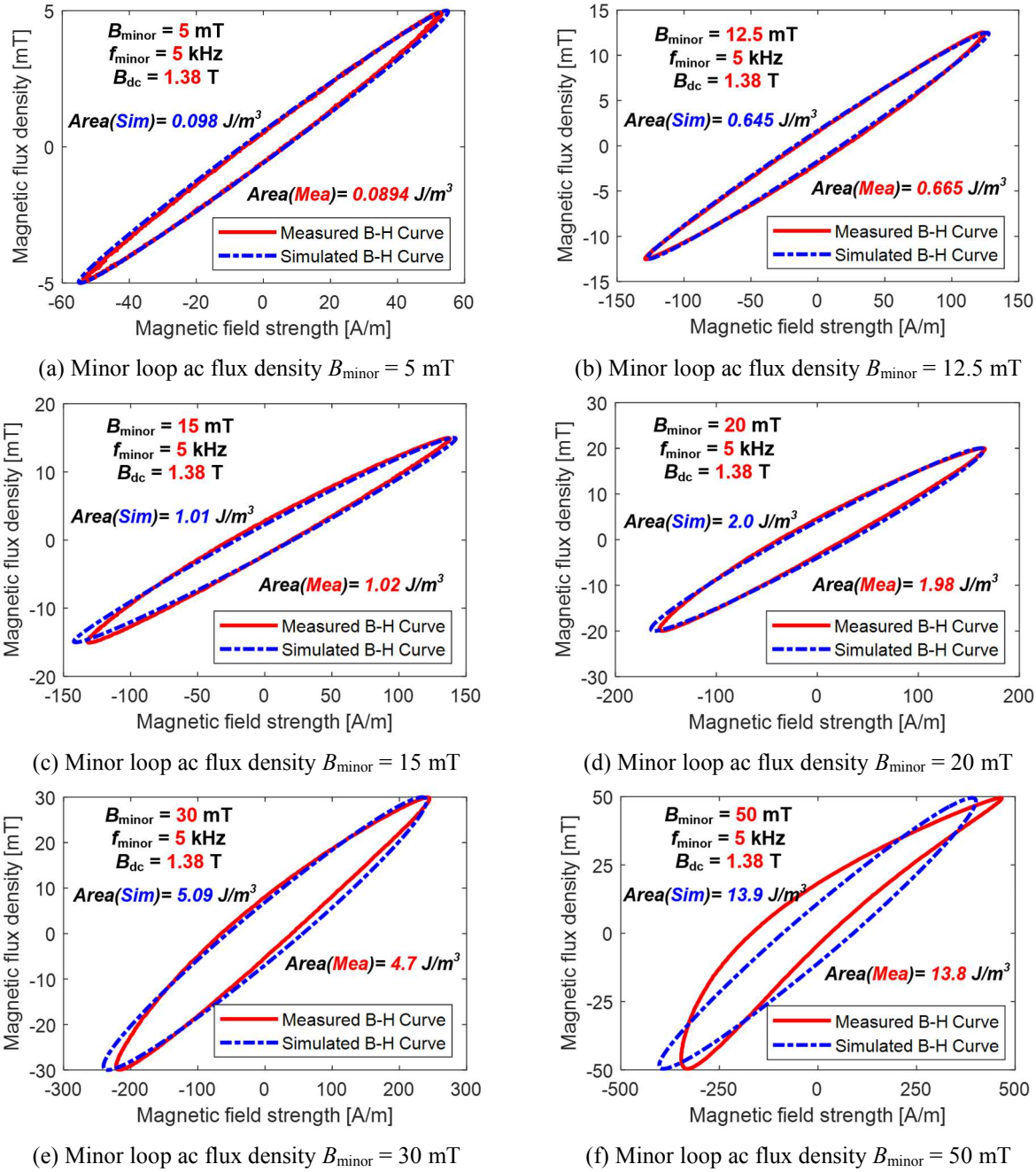

(a) Minor loop ac flux density B_{minor} = 5 mT

(b) Minor loop ac flux density B_{minor} = 12.5 mT

(c) Minor loop ac flux density B_{minor} = 15 mT

(d) Minor loop ac flux density B_{minor} = 20 mT

(e) Minor loop ac flux density B_{minor} = 30 mT

(f) Minor loop ac flux density B_{minor} = 50 mT

Figure 6-14: Comparison of measured and simulated *B-H* curves and their enclosed areas for 1.38 T dc-bias field with six different minor loop ac flux density amplitudes.

The results of these tests and comparisons demonstrate that the dynamic J-A model using the parameters determined from the reference operating point offers appealing capabilities for predicting the *B*-*H* curves and iron loss for ac flux ripple under similar operating conditions, where the average error in Figure 6-15 is below 5%. This technique can be extended to other dc-bias field values following the same estimation procedure. This technique can be extended to other dc-bias field values following the same estimation procedure. Compared to the classical iron loss models based on Steinmetz equation, the proposed model requires a much smaller number of measured data points for model characterization.

To further investigate the impact of magnetic flux amplitude on the high-frequency iron loss in the presence of dc-bias fields, the dc-bias iron loss scaling factor is defined in (6-31) as the ratio of the iron loss with and without a dc-bias field.

$$k_{\text{scaling}} = \frac{\text{Measured or predicted iron loss } (@\ B_{\text{dc}})}{\text{Measured or predicted iron loss } (B_{\text{dc}} = 0\ T)} \tag{6-31}$$

Figure 6-16 shows both the measured and predicted variation trend of the dc-bias iron loss scaling factor versus the dc-bias field for three different ac flux density amplitudes. It can be seen that similar responses to the dc-bias fields are observed for all three flux density amplitudes.

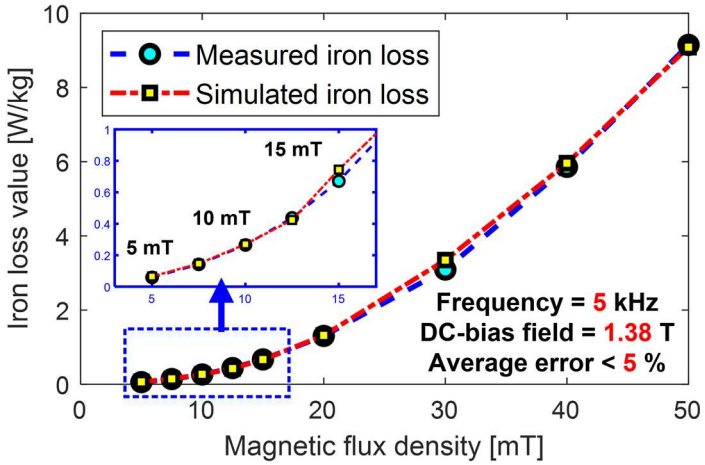

Figure 6-15: Comparison between the predicted and measured iron losses of minor loops at f_{minor} = 5 kHz and B_{dc} = 1.38 T dc-bias field with different minor loop ac flux density amplitudes (B_{minor} from 5 to 50 mT).

The peak amplitude of the dc-bias iron loss scaling factor increases substantially as the ac flux amplitude goes up. The peak value for the 40 mT case (≈ 3) is approx. 1.5x the peak value for the 7.5 mT case (≈ 2). A possible explanation for this observed phenomenon is that the hysteresis loss which is closely related to the magnetic domain condition is more susceptible to the dc-bias field compared to the classical eddy current loss, and it accounts for a larger fraction of the total iron loss as the ac flux amplitude increases.

Another significant iron loss component, the excess/anomalous loss, is attributable to the damping of domain wall movement, spin relaxation, etc. [12], [20]. These microstructure characteristics are almost impossible to model in the iron loss estimation, making it critical and necessary to experimentally pre-characterize the iron loss properties of the studied soft magnetic materials over varying dc-bias fields. Taking advantage of the measured data, the proposed dynamic *J-A* is capable of accurately estimating the high-frequency iron loss with different ac flux density amplitudes, as indicated by the high agreement between the measured and predicted loss curves in Figure 6-15 and Figure 6-16.

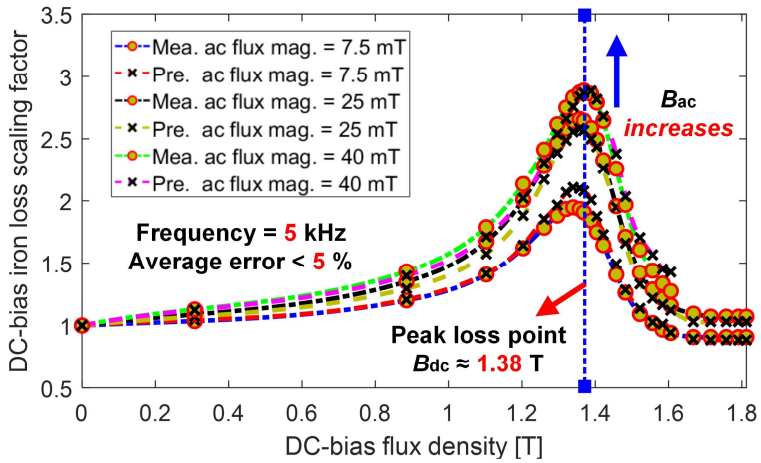

Figure 6-16: Comparison of the measured and predicted dc-bias iron loss scaling factor at 5 kHz minor loop excitation frequency f_{minor} for three values of ac flux density amplitude.

6.5.2 Impact of AC Flux Ripple Frequency

Next, the impact of ac flux ripple frequency is investigated. One of the motivations is the growing capability of wide bandgap power switches that are making it more feasible to consider high PWM switching frequency f_{PWM}. Even if f_{PWM} is held constant, the dominant PWM harmonic components are in the vicinity of twice the PWM frequency (2x f_{PWM}) when the value of modulation index is small, which makes it desirable to have the capability to estimate the iron loss at different frequencies.

Figure 6-17 presents the comparison of the measured and predicted dc-bias iron loss scaling factor for 10 kHz minor loop frequency. Similar to the 5 kHz case, as the amplitude of ac flux ripple increases, the dc-bias field has a significant impact on the iron loss especially when the dc-bias field is in the vicinity of knee region of material's dc *B-H* curve. However, it is interesting to note that the peak values of the scaling factor are lower at 10 kHz than they are at 5 kHz for the same conditions. Overall, the proposed iron loss model has exhibited excellent scalability for implementing the loss estimation over a wide range of frequencies.

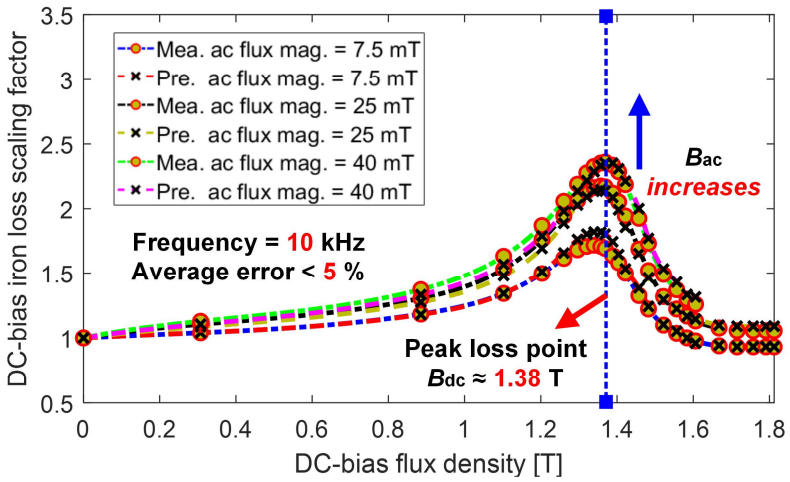

Figure 6-17: Comparison of the measured and predicted dc-bias iron loss scaling factor at 10 kHz minor loop excitation frequency for three values of ac flux density amplitude.

The dc-bias iron loss scaling factors from the measured data have been plotted in Figure 6-18 for five minor loop frequencies ranging from 3.5 to 20 kHz with an ac flux amplitude at 20 mT. Consistent with the trend exhibited in Figure 6-16 and Figure 6-17, the peak value of dc-bias iron loss scaling factor drops significantly as the frequency increases, reducing the iron loss variation over the tested dc-bias field range. Although the peak value varies, the general trend of each case is very similar, and the peak point of iron loss occurs at almost the same dc-bias field $B_{dc} \approx 1.38$ T over a wide frequency range.

Furthermore, the significant differences in the peak value of dc-bias iron loss scaling factors have provided deeper insight into iron loss segregation under conditions of high excitation frequency and dc-bias field. Consistent with the conclusion drawn in the preceding subsection, the hysteresis loss is responsible for a larger proportion of iron loss contribution at a lower excitation frequency, leading to a much larger iron loss growth around the knee region of dc *B-H* curve. In contrast, at higher excitation frequencies ($f_{minor} > 10$ kHz), the dynamic loss components (i.e., the sum of the classical eddy current loss and anomalous loss) exceeds the hysteresis loss. As a result, the dc-bias field exerts a progressively smaller impact on the iron loss.

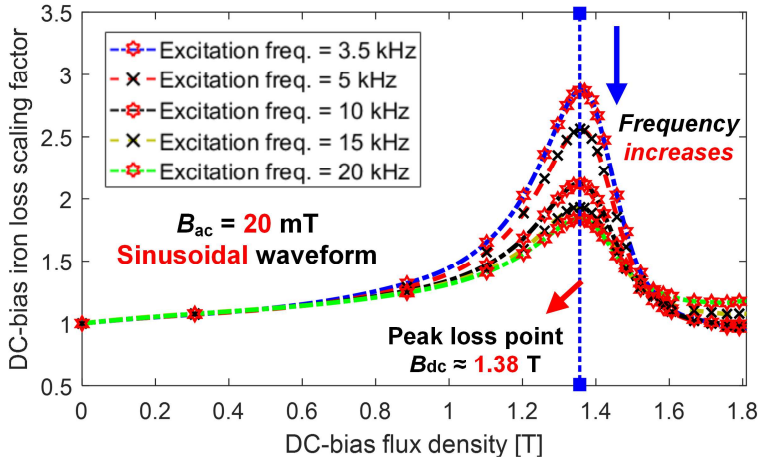

Figure 6-18: Measured dc-bias iron loss scaling factor for five excitation frequencies (f_{minor} from 3.5 to 20 kHz) with ac flux amplitude at 20 mT.

Although the machine-level PWM-induced iron loss calls for further analysis, the available results shed some light on the impact of PWM switching frequency on the PWM-induced iron loss in the electric machines. As the PWM frequency increases, the flux ripple frequency goes up, and the amplitude of ac flux variation decreases. Both of these two factors tend to reduce the iron loss increase caused by the dc-bias field, resulting in a smaller PWM-induced iron loss.

6.5.3 Impact of AC Flux Ripple Waveshape

Due to the intrinsic properties of VSIs, the PWM-induced current and flux ripple are typically shaped much more like the triangular waveforms rather than pure sinusoidal waveforms. To better understand the range and limits of the proposed model, the parameters determined from sinusoidal excitation have been applied to predict the hysteresis loop for a symmetrical triangular waveform (i.e., Duty cycle $D = 0.5$). The predicted and measured *B*-*H* curves and their areas (i.e., iron loss) at 10 mT, 5 kHz are compared in Figure 6-20(a)-(d) for four dc-bias field values. The *B*-*H* loops and areas exhibit excellent agreement, providing encouraging results in support of the model's scalability to different flux density waveshapes.

Next, the proposed model with characterized coefficients is applied to investigate the dc-bias iron loss scaling factor with triangular input waveform. As depicted in Figure 6-19, the proposed model can accurately emulate the variation trend of iron loss over the entire dc-bias field range. Compared to the measured results with sinusoidal input, the dc-bias field exerts a similar influence on the resulting iron loss. In addition, the peak iron loss point is again observed in the vicinity of 1.38 T, indicating that the location of this peak loss point is mainly determined by the magnetic properties of the testing material rather than the characteristics of superimposed harmonics (i.e., frequency, waveshape, etc.). Future plans call for the same material investigation to be extended to other magnetic materials with different lamination thicknesses and compositions.

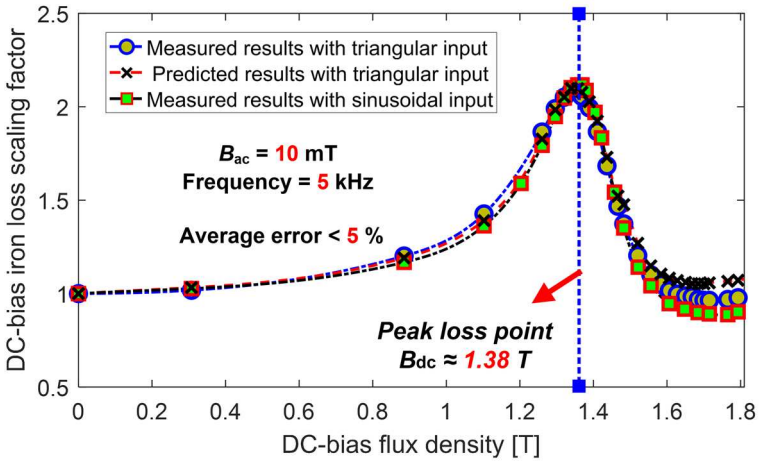

Figure 6-19: Comparison of measured and predicted dc-bias iron loss scaling factor (f_{minor} = 5 kHz) with triangular waveform excitation with B_{ac} at 10 mT.

Based on the current ripple analysis presented in the prior chapter, when the IPM machine operates at low-speed (i.e., low modulation value) or deep flux weakening region (i.e., large current control angle γ), the waveshape of the current ripple is in asymmetrical triangular shape. Therefore, evaluating the ability of the modified dynamic *J-A* model to estimate the iron loss with varying duty cycles is critically important for evaluating the accuracy of the machine-level PWM-induced iron loss estimation.

Square-wave voltage waveforms with an adjustable duty cycle are generated by the signal generator to induce triangular flux density waveforms in the tested toroids. The iron loss is measured using either a power analyzer which is supplied with the measured sensing-coil voltage

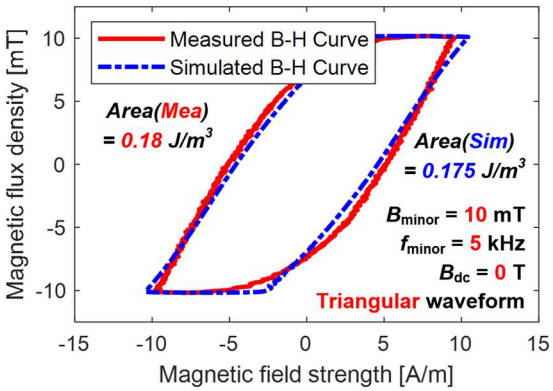

(a) External dc-bias field B_{dc} = 0 T

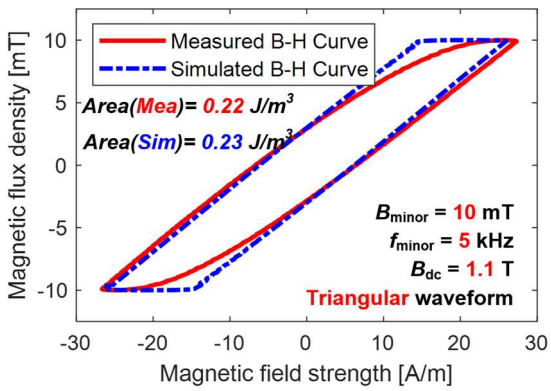

(b) External dc-bias field B_{dc} = 1.1 T

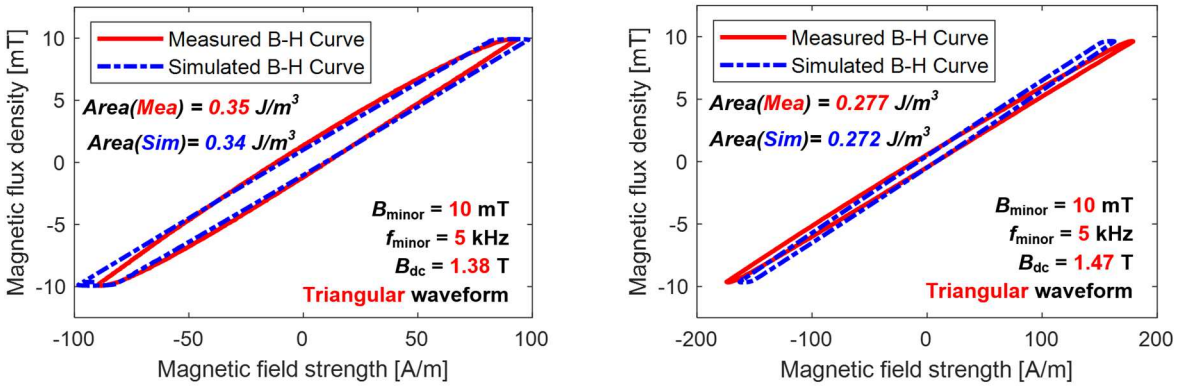

(c) External dc-bias field B_{dc} = 1.38 T (d) External dc-bias field B_{dc} = 1.47 T

Figure 6-20: Comparison of measured and simulated hysteresis loops and their enclosed areas with triangular waveform excitation for four values of dc-bias fields at 5 kHz, 10 mT.

and primary-coil current waveforms or from the equivalent net area of the measured dynamic hysteresis loop.

To evaluate the model's performance for a selected dc-bias field condition of 1.38 T, corresponding to the highest iron loss value over the tested dc-bias field range up to 1.8 T, the same set of parameters characterized with sinusoidal supply is subsequently extended to estimate the iron loss of triangular waveforms with nonsymmetrical waveshapes, where the duty cycle varies from 0.2 up to 0.8.

As depicted in Figure 6-21(a) to (d), the proposed dynamic *J-A* model can predict the triangular waveform quite accurately for four different duty cycle values when the dc-bias field is in the vicinity of the knee region of the dc *B-H* curve. These comparison results confirm that the dynamic *J-A* model can be used to accurately predict the hysteresis loop of the triangular flux waveform with duty cycle values deviating substantially from the baseline symmetrical condition.

Next, the iron loss is determined by calculating the enclosed area of the measured and predicted hysteresis loops and then multiplying the area by the excitation frequency. As shown in Figure 6-22(a)-(d), for all four tested dc-bias field conditions, the iron loss increases considerably (> 50 %) as the duty cycle value deviates in either direction from its value with symmetrical excitation (i.e.,

D = 0.5) and approaches 0.2 or 0.8 where the waveforms become highly asymmetrical. The proposed model has exhibited excellent scalability for predicting the iron loss of triangular waveforms with varying duty cycles, where the average estimation for each studied case is less than 5 %. As a result, Fourier analysis of asymmetrical triangular waveforms and material iron loss data beyond the ripple frequency are no longer necessary, enabling model implementation more convenient.

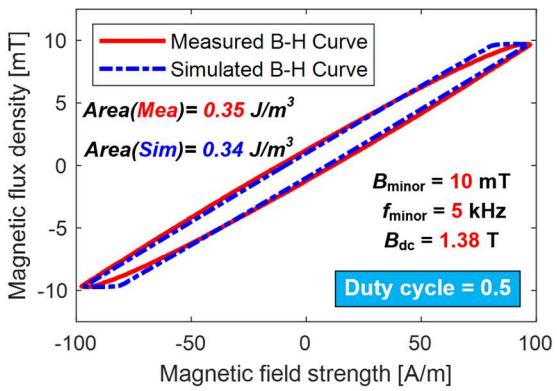

(a) Triangular waveform duty cycle D = 0.5

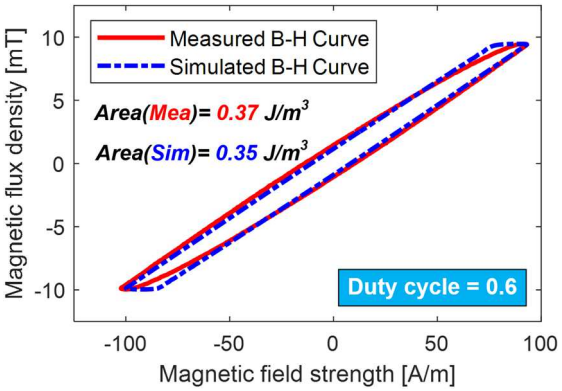

(b) Triangular waveform duty cycle D = 0.6

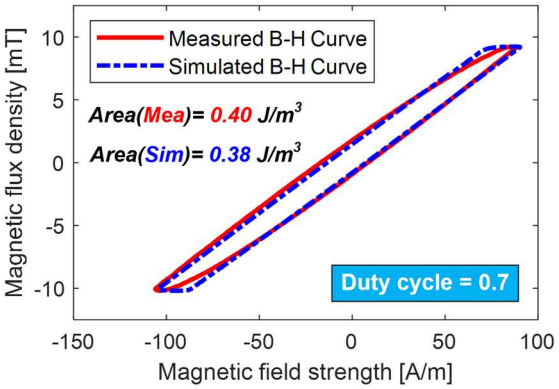

(c) Triangular waveform duty cycle D = 0.7

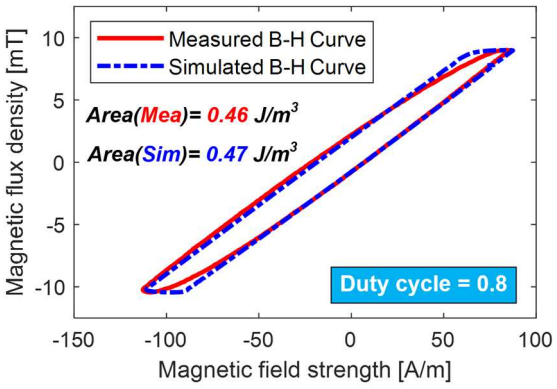

(d) Triangular waveform duty cycle D = 0.8

Figure 6-21: Comparison of measured and predicted dynamic hysteresis loops for triangular flux ripple waveforms with four values of duty cycle ranging from 0.5 to 0.8.

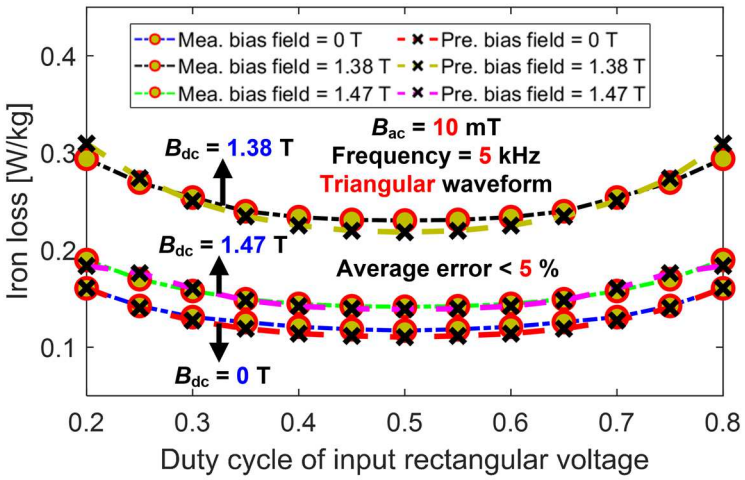

Figure 6-22: Comparison of measured and predicted iron loss of triangular waveforms with different duty cycles for three dc-bias field values.

6.6 Total Iron Loss Investigation under Inverter Excitation

In the previous sections, iron losses of high-frequency minor loops are investigated based on the equivalent dc-bias field assumption. In this section, the PWM-induced iron loss is further evaluated when the PWM-induced harmonics are riding on top of the ac fundamental field. Also, a generalized dynamic hysteresis model developed in Chapter 3 for fundamental and low-order harmonic field iron loss estimation is implemented together with the proposed PWM-induced iron loss model to determine the total iron loss for PWM-based ac voltage excitation.

Figure 6-23 shows the equivalent circuit schematic for iron loss evaluation under inverter excitation. The GaN-based H-bridge inverter operates in bipolar PWM switching mode to deliver modulated two-level output voltage (i.e., $\pm V_{dc}$) to the toroidal core under test, where the PWM gate signals are generated by a DSP microcontroller. As a result, PWM harmonics are induced in the output voltage and current waveforms. Compared to the unipolar PWM mode with 0 and + V_{dc} or 0 and - V_{dc} active during any time interval, the contribution of PWM-induced iron loss to the total iron loss is amplified significantly by using the bipolar mode, making it more convenient to evaluate the PWM-induced iron loss.

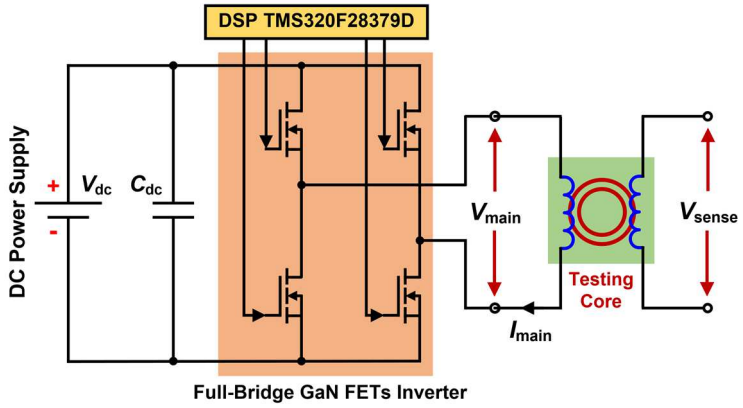

Figure 6-23: Equivalent circuit of test configuration for iron loss evaluation under PWM voltage excitation.

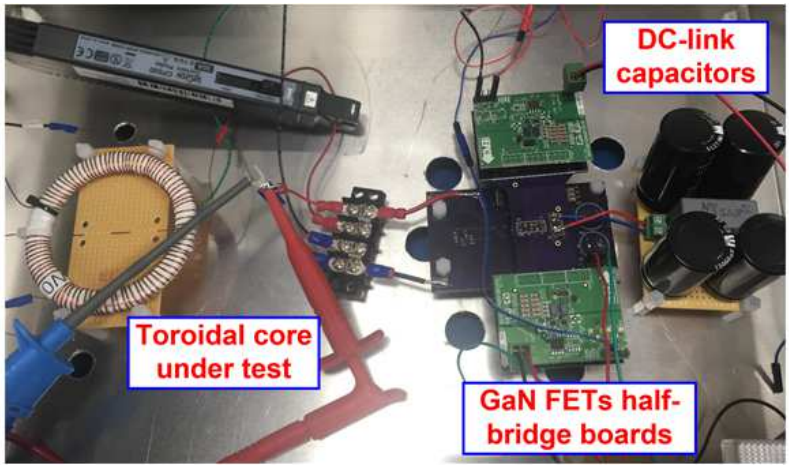

Figure 6-24: Close-up view of the inverter setup and toroidal core under test.

Figure 6-24 provides a close-up view of the GaN-FET single-phase inverter. A toroidal core fabricated with the same lamination steel material is directly connected to the inverter output with short leads to minimize the parasitic inductance. To comprehensively evaluate the iron loss characteristics under PWM voltage excitation, the tests are conducted by sweeping both the PWM switching frequency (5 kHz ~ 20 kHz), and inv-erter modulation index (0.6 ~ 0.9). The flux density amplitude of the fundamental field is maintained at 1.3 T, and the funda-mental frequency is tested at 50 and 100 Hz. As a result, the lowest PWM to fundamental frequency ratio is 50.

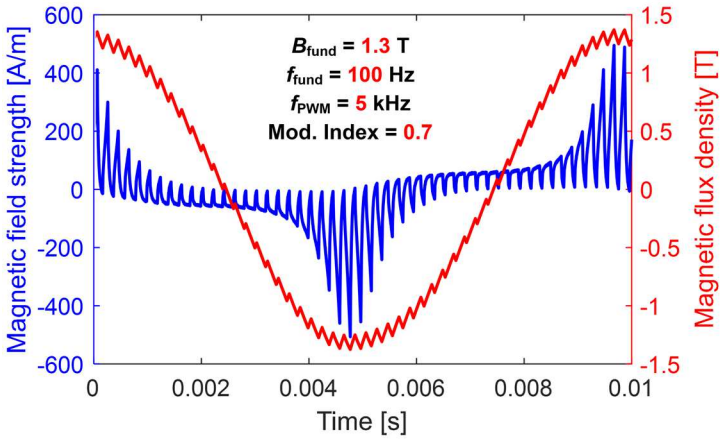

Figure 6-25: Example of the collected magnetic field strength and flux density waveforms under PWM voltage excitation.

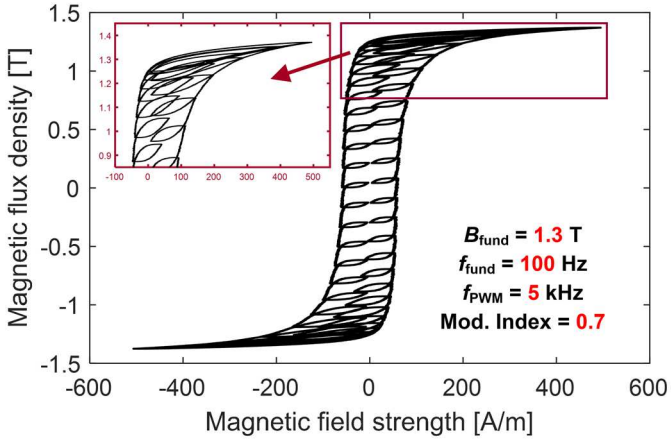

Figure 6-26: Example of the measured hysteresis loop including the PWM-induced harmonics.

An example of acquired waveform data is shown in Figure 6-25, where the PWM-induced harmonics are visible in both *H*- and *B*-field waveforms. As demonstrated in Figure 6-26, the data can be subsequently used to plot the dynamic hysteresis loop including the PWM-induced harmonics. The high-frequency harmonics result in a large number of minor loops inside the major field B-H waveform, which, in turn, significantly increases the net area of the resulting hysteresis loop and corresponding total iron loss. Moreover, the shapes and enclosed areas of minor loops operating in the saturated region (i.e., $B_{ac} > 1.1$ T) exhibit notable differences compared to those inside the linear region, indicating that the existence of external magnetic fields (i.e., ac fundamental field) have a significant impact on the minor loops.

The total iron loss estimation is implemented by the field segregation flow diagram presented in Figure 6-27. The Fast Fourier transformation (FFT) is used to segregate and subtract the fundamental field component from the measured total field waveform $B_{\text{mea}}(t)$ up to first n_{main} low-order components,

$$B_{\text{PWM}}(t) = B_{\text{mea}}(t) - \sum_{n=1}^{n_{\text{main}}} A_n \cos(2\pi n f_{\text{fund}} t + \varphi_n) \tag{6-32}$$

where A_n and φ_n are Fourier amplitude and phase coefficients.

Unlike the conventional FFT method that calculates the loss individually for every harmonic component in the PWM the waveform (e.g., up to 50x f_{PWM}), the proposed approach better accounts for the actual PWM waveshape characteristics (i.e., duty cycle) during each switching cycle. As the zoom-in results in Figure 6-28 show, the waveshape of the PWM-induced ripple varies considerably within one fundamental cycle, even though the PWM switching frequency is unchanged (i.e., 5 kHz for this example). As a result, the associated PWM iron loss changes as the PWM waveform changes (See Figure 6-22). In addition, the equivalent dc-bias field of each PWM-induced ripple is calculated individually by (6-4), where the major magnetic field is assumed to be responsible for the dc-bias field amplitude.

Next, the segregated PWM-induced ripple waveform in each switching cycle and its equivalent dc-bias field amplitude are fed into the proposed dynamic *J-A* model. The iron loss of each PWM ripple is calculated individually. The summed iron loss from all of the PWM cycles is added to the fundamental field iron loss calculated for the extracted major hysteresis loop to determine the total estimated iron loss under inverter voltage excitation.

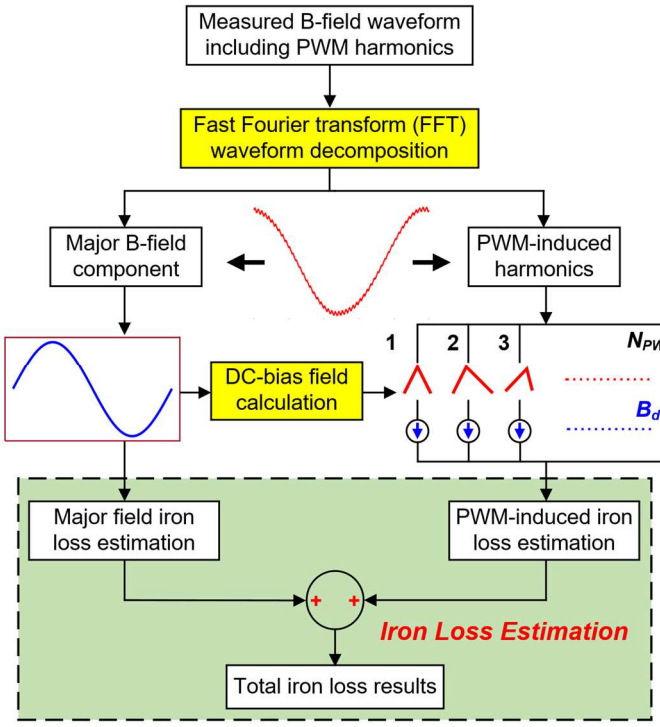

Figure 6-27: Flow-chart of the total iron loss segregation and estimation algorithm.

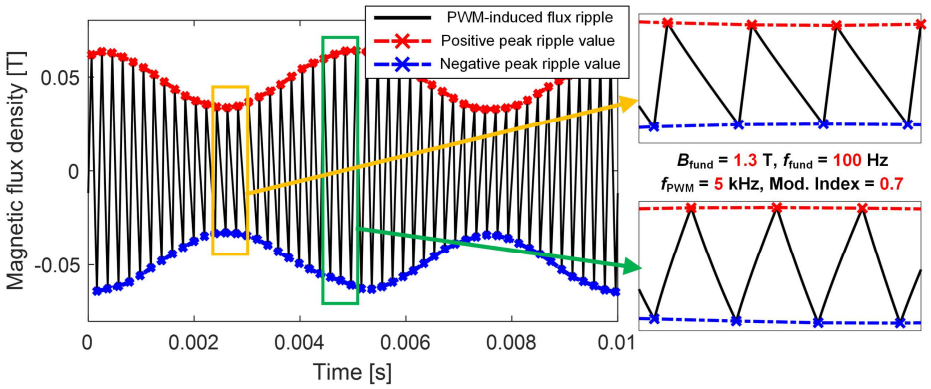

Figure 6-28: Example of segregated PWM harmonics from the measured *B*-field data using the proposed field segregation technique.

Figure 6-29 provides a comparison of measured and predicted total iron loss results under PWM voltage excitation over varying PWM frequencies at two selected modulation indexes (i.e., 0.7 and 0.9), and the fundamental field is at 1.3 T and 50 Hz. It can be observed that the predicted total iron loss exhibits excellent agreement with the measured data, building confidence in the ability of the proposed model to address the additional iron loss contributed by PWM-induced harmonics with different ripple amplitudes and frequency compositions.

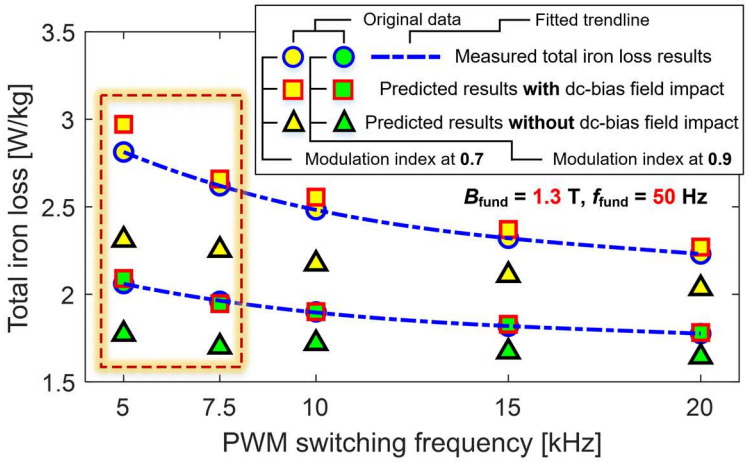

Figure 6-29: Comparison of measured total iron loss at 1.3 T and 50 Hz with the predicted values with and without considering the dc-bias field effect.

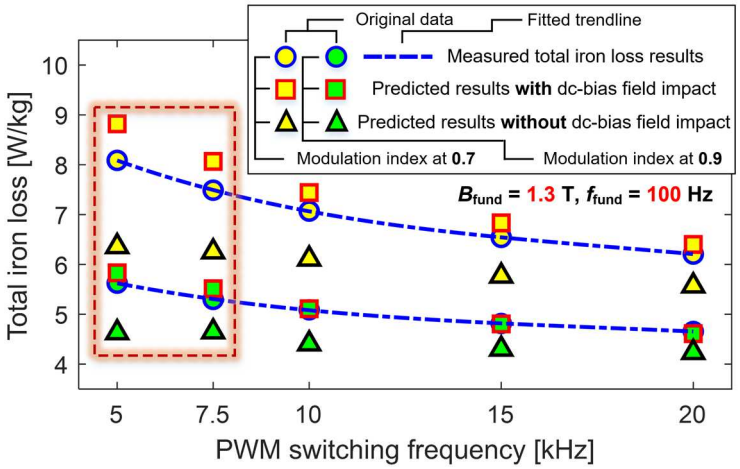

Figure 6-30: Comparison of measured total iron loss at 1.3 T and 100 Hz with the predicted values with and without considering the dc-bias field effect.

In order to quantify the impact of external dc-bias fields, the PWM-induced iron loss is then estimated without considering any dc-bias field impact (i.e., B_{dc} = 0 T). As shown in Figure 6-29, there is a significant discrepancy between the predicted results and the measured data, especially in the highlighted region where the PWM switching frequency is relatively low. Moreover, the iron loss underestimation is further aggravated when the ripple amplitude increases with a smaller modulation index (i.e., 0.7). Consistent with the key conclusions drawn in preceding sections, impact of the dc-bias field on minor loop iron loss is more pronounced at lower PWM frequencies and larger flux ripple amplitudes. Also, the predicted total iron loss excluding dc-bias field impact

produces a trendline that is almost independent of the PWM switching frequency. In other words, the existence of the ac fundamental field is one of the major influencing factors that leads to a higher PWM-induced and total iron loss at low PWM switching frequencies.

Next, while keeping the PWM switching frequency and modulation index the same, the excitation frequency of the fundamental field is extended to 100 Hz. As a result, the PWM to fundamental frequency ratio is halved, and the inverter dc-bus voltage increases proportionally to the fundamental frequency, leading to a doubling of the PWM ripple amplitude. Figure 6-30 shows the results of the model accuracy assessment by sweeping the same variables. Despite the fact that modest iron loss overestimation is observed in the low PWM frequency region, the proposed iron loss prediction model demonstrates a very promising capability to accurately model the nonlinear iron loss characteristics. Here again, ignoring the dc-bias field impact result in a significant error. Similar to the results shown in Figure 6-29, the predicted values without considering the dc-bias are always below the measured values, and the estimation errors shrinks as the PWM switching frequency increases.

Figure 6-31 and Figure 6-32 present the estimation error distribution within the analyzed operating range at 50 and 100 Hz, respectively. The average estimation error for each is below 5%, and the largest error is under 10%, confirming that the proposed model is capable of providing useful iron loss estimation for PWM-based ac voltage excitation over broad operating conditions.

Although the model performance is appealing, one of the implicit assumptions for the proposed scheme is that the shape of the major field waveform is independent of the PWM-induced harmonics regardless of the PWM switching frequency or the modulation index. However, as waveforms presented in Figure 6-33(a), corresponding to the largest error case in Figure 6-32, show that the profile of the predicted major field hysteresis loop noticeably diverges from the

measured PWM waveform, particularly in the region of heaviest saturation. One way of interpreting these results is that the large-amplitude (e.g., B_{ac} > 50 mT) PWM harmonics in this case exert a significant impact on the major field waveform, degrading the accuracy of the proposed frequency-domain iron loss segregation approach. Nevertheless, the assumption of independence of the PWM and major field waveforms is reasonably accurate when the modulation index and PWM switching frequency increase to higher levels, as confirmed by the closer waveform comparisons shown in Figure 6-33(b)-(c).

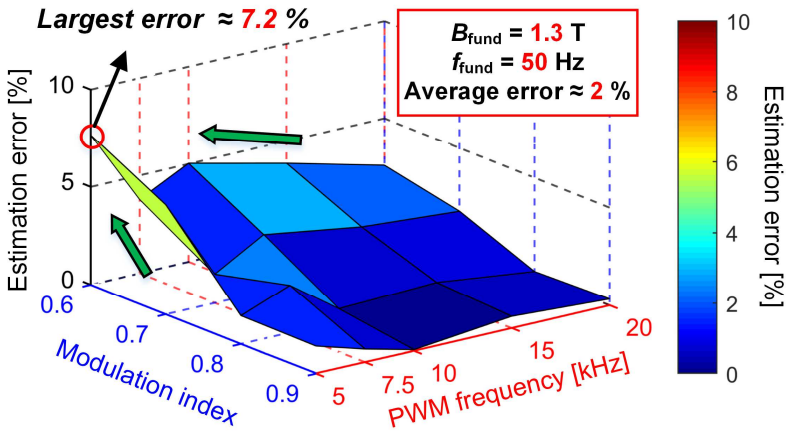

Figure 6-31: Total iron loss estimation error distribution at 1.3 T and 50 Hz.

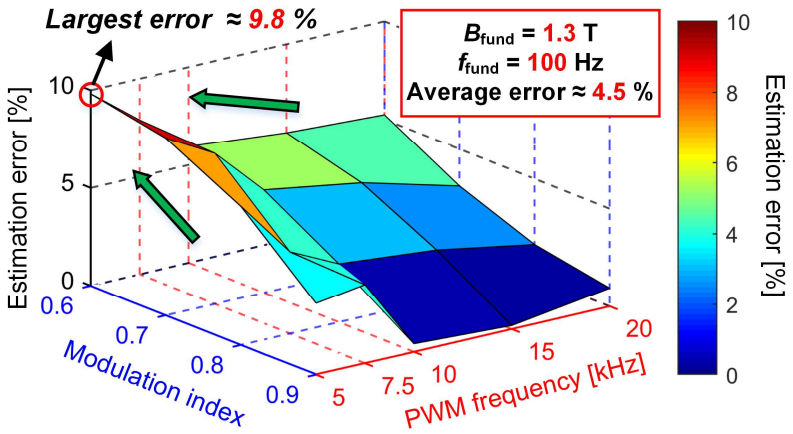

Figure 6-32: Total iron loss estimation error distribution at 1.3 T and 100 Hz.

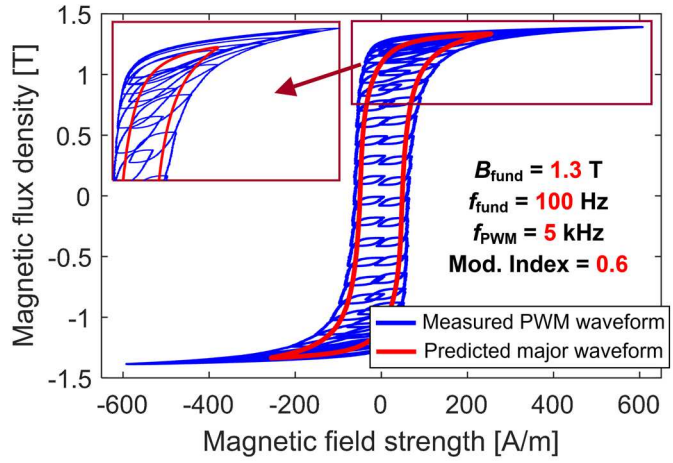

(a) Modulation index value = 0.6, and f_{PWM} = 5 kHz

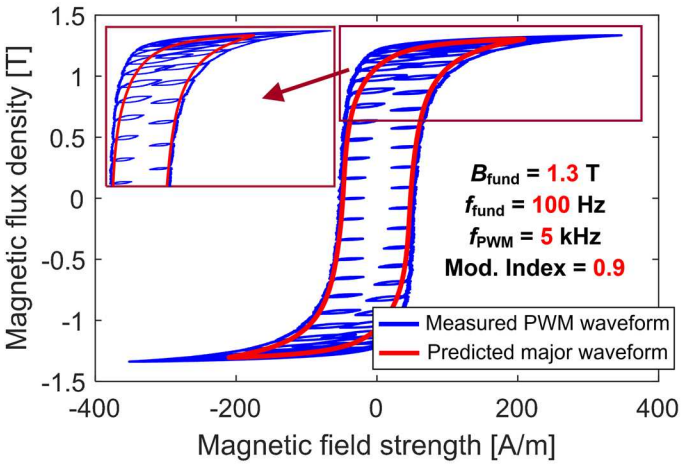

(b) Modulation index value = 0.9, and f_{PWM} = 5 kHz

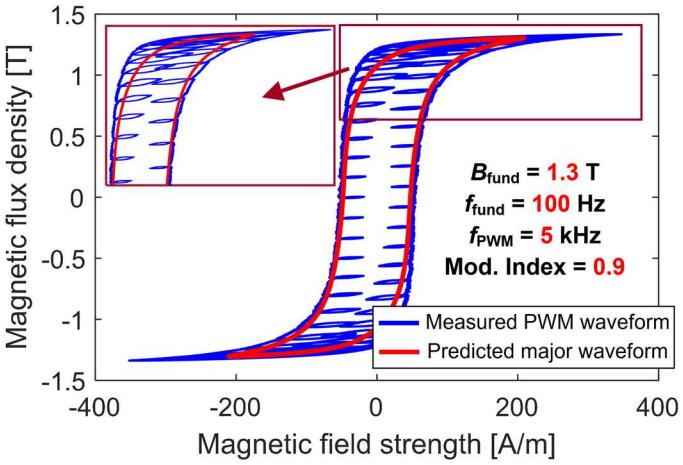

(c) Modulation index value = 0.9, and f_{PWM} = 20 kHz

Figure 6-33: Comparison of measured waveforms under PWM voltage excitation and predicted major field waveforms over different operating conditions.

The fundamental field amplitude has been elevated to 1.4 T with 100 Hz frequency, extending beyond the peak iron loss point observed in the preceding sections (i.e., B_{dc} = 1.38 T). Figure 6-34 presents the variation of total iron loss versus PWM switching frequency at two same modulation index values (i.e., 0.7 and 0.9). Once the dc-bias field impact is properly incorporated into the PWM iron loss estimation, the predicted total iron loss results closely match the measured data, validating the ability of the proposed model to estimate the total iron loss for different fundamental field amplitudes. However, if the dc-bias field is ignored, the PWM iron loss underestimation is even more significant compared to that with 1.3 T fundamental field over the entire PWM frequency range. For the low PWM frequency region, the estimation errors without including the impact of the dc-bias field impact range from 20 to 30%, substantially affecting accuracy of the total iron loss estimation.

To better reveal the relationship between the PWM-induced iron loss with the fundamental field, Figure 6-35(a)-(c) present the predicted PWM iron loss value in each switching cycle with and without considering the dc-bias field impact for 3 selected testing conditions given in Figure 6-34. A plot of the fundamental field during the period of each PWM cycle is overlaid with corresponding iron loss values.

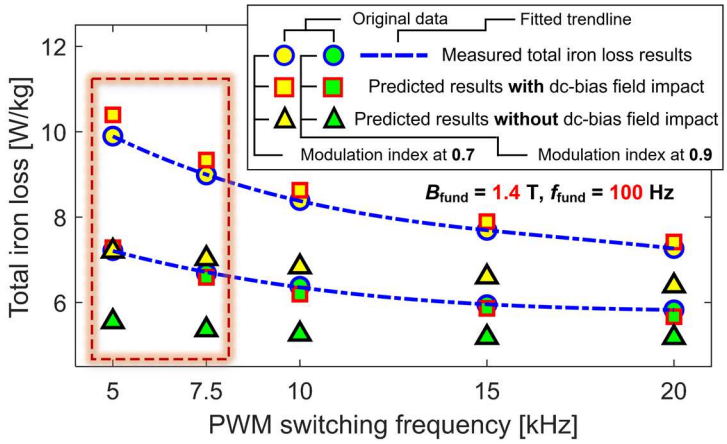

Figure 6-34: Comparison of measured total iron loss at 1.4 T and 100 Hz to the predicted values with and without considering the dc-bias field effect.

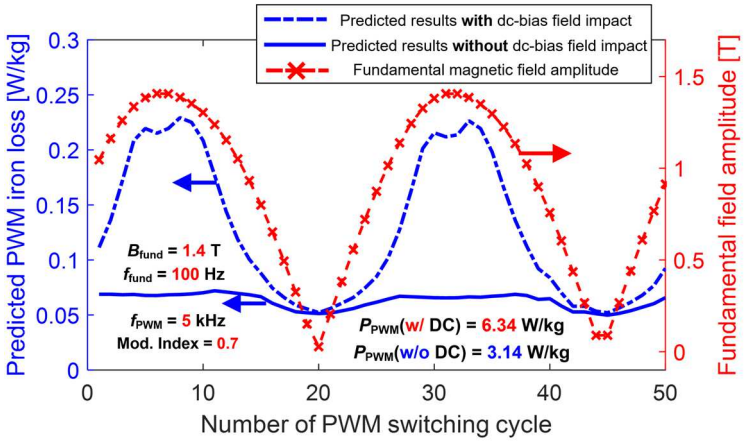

(a) Modulation index = 0.7 and f_{PWM} = 5 kHz

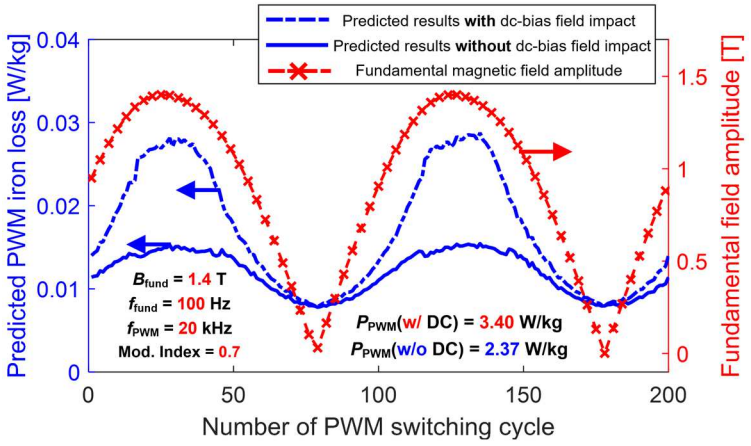

(b) Modulation index = 0.7 and f_{PWM} = 20 kHz

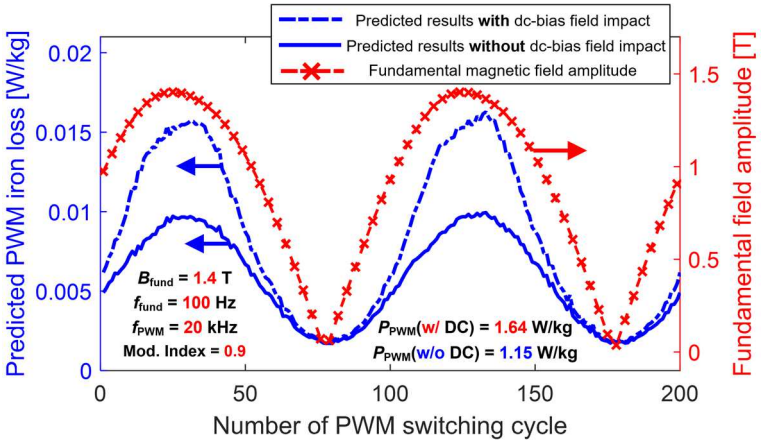

(c) Modulation index = 0.9 and f_{PWM} = 20 kHz

Figure 6-35: Predicted PWM-induced iron loss and corresponding fundamental field amplitude in each PWM switching cycle at 1.4 T and 100 Hz.

When both the PWM switching frequency and modulation index are low (i.e., Figure 6-35(a)), the presence of the fundamental field exerts a significant influence on the PWM iron loss, especially when the fundamental field B_{fund} is larger than 1 T. Based on the calculated results, incorporating the dc-bias field leads to more than twice of the total PWM iron loss value (i.e., 6.34 W/kg vs. 3.14 W/kg). Moreover, the predicted PWM-induced iron loss makes up over 60% of the total iron loss, making it the dominant iron loss component.

As the PWM frequency and modulation index are increased to higher values in Figure 6-35(b) and Figure 6-35(c), the difference in PWM iron loss caused by dc-bias field shrinks, suggesting that the impact of the dc-bias field is less for PWM harmonics with lower amplitudes and higher frequencies. Nevertheless, the predicted PWM iron loss with dc-bias field impact is still ~30% higher than that without it since the flux ripple amplitude is non-uniformly distributed within a fundamental cycle.

Finally, the suitability of the proposed modeling technique for IPM machines merits comment. Since the rotor of IPM machines rotates synchronously with the frequency of the stator supply current, the major magnetic field in the rotor side is the dc field except for the slotting harmonics that appear in the rotor surface regions. Therefore, the dc-bias field assumption is fully valid. On the other hand, the major magnetic flux density in the stator iron core varies periodically with the supply current frequency. As the PWM-to-fundamental frequency ratio is reduced and the amplitudes of the PWM harmonics increase, the nonlinear mutual coupling between the fundamental field and PWM harmonics gradually grows, degrading the accuracy of the proposed iron loss segregation approach.

Nevertheless, for general applications with sufficiently-high PWM-to-fundamental frequency ratio values (e.g., ≥ 50), the proposed method is expected to offer good accuracy over a wide range

of excitation conditions. Furthermore, it should be noted that, even though a sinusoidal waveshape has been adopted for the major magnetic field in this analysis, the same technique can be readily extended to more complicated major field waveforms consisting of combinations of several low-order harmonic components. As a result, the proposed technique offers great potential to serve as a generalized tool for conducting machine-level PWM-induced iron loss analysis.

6.7 Summary

This chapter presents a promising technique to predict the PWM-induced iron loss with high-frequency ac flux density, varying dc-bias fields, and non-sinusoidal excitation of soft magnetic materials used in the electric machines. Versatile *B-H* measurement equipment has been built to investigate the iron loss variation over a wide range of ac and dc excitation, providing valuable data and insights into high-frequency ac iron loss characteristics in the presence of a dc-bias field. A modified dynamic Jiles-Atherton (*J-A*) model has been proposed to better emulate the iron loss variation trends over a wide range of operating conditions. Several influencing factors on high-frequency iron loss have been thoroughly investigated and verified using measured results, including the magnitude of the ac flux ripple, PWM excitation frequency, and duty cycle of the PWM excitation waveform. This PWM iron core loss model has subsequently been combined with a separate dynamic hysteresis model developed for low-frequency iron loss estimation, making it possible to estimate the total iron loss characteristics under a wide variety of PWM-based ac voltage excitation conditions.

The proposed modified dynamic *J-A* model has exhibited appealing accuracy and scalability for predicting the PWM-induced iron loss. Results from many tests demonstrate that parameters obtained from a limited number of tests can be used to predict the iron loss over a broad operating range, making this model a promising tool for machine-level PWM-induced iron loss estimation. At last, the proposed PWM-induced iron loss model developed in this thesis can be applied to conduct machine-level PWM-induced iron loss estimation in IPM machines, and machine-level analysis will be presented in the next chapter.

Chapter 7
Estimation and Investigation of PWM-Induced Iron Loss in IPM Machines

7.1 Introduction

Most interior permanent magnet (IPM) synchronous machines used in industry are fed by current-regulated voltage source inverters (VSIs) using high-frequency PWM that delivers several desirable features including high-performance control capabilities, high system efficiency, etc. The electric machine behaves as an inductive filter that attenuates the harmonic components induced by the applied switched voltage waveforms. However, there are still PWM-induced ripple components that survive this filtering and appear in the machine phase currents, causing additional losses in the copper windings, iron cores, and permanent magnets.

The conventional approach [5] based on Fourier analysis and the Steinmetz equation has notable limitations for PWM-induced iron loss estimation. PWM-induced minor loops in an electric machine are superimposed on the slowly-varying fundamental field. The hysteresis properties and iron losses of minor loops are affected by the dc-bias field, highlighting the inaccuracy that results from using iron loss data collected in the absence of the dc-bias field (i.e., Epstein frame test).

In this chapter, the proposed modified dynamic *J-A* model is combined with the predicted PWM-induced current ripple and material iron loss properties over a wide range of dc-bias fields to estimate the machine-level PWM-induced iron loss. After the introduction, an overview of PWM-induced current ripple in IPM machines is provided. Subsequently, the proposed analytical model for calculating PWM-induced iron loss is presented. A special frequency segregation method is proposed to analytically separate the PWM-induced flux ripple into either a 1x or 2x

PWM switching frequency component with specific duty cycles. The acquired information is then fed into the proposed hysteresis model to predict the iron loss induced by each frequency individually and summed for the total iron loss. Finally, the proposed PWM-induced iron loss model is evaluated by comparing with the experimental results to build confidence in the model's performance and to investigate the impact of several influencing factors on PWM-induced iron and magnet losses.

7.2 PWM-Induced Current Ripple in IPM Machines

Since the PWM-induced current ripple intrinsically determines the shape and amplitude of the resulting PWM-induced flux ripple, investigation of PWM-induced current ripple is considered to be the foundation for revealing the true nature of the PWM-induced iron loss.

Although it is possible to pre-calculate the PWM voltage waveform and run the FEA with voltage input [5], it is commonly acknowledged that the FEA is much preferable to run with the current input data rather than voltage [191]. Otherwise, it requires very fine time steps to adequately represent the essence of the input voltage waveforms (i.e., sequences of stepped voltages). For example, with 100 Hz machine fundamental frequency and 5 kHz PWM switching frequency, it at least requires 5000 time steps during one fundamental cycle to ensure the simulation accuracy (i.e., 100 points within one PWM cycle). As a further complication, when the voltage source is used as the input, multiple fundamental periods/iterations are required (larger than 3) to achieve steady-state simulation results.

Alternatively, the PWM-induced flux ripple can be estimated using 2-D FEA with the measured current data including PWM harmonics. However, measured data typically contain additional noises including current spikes that appear around the PWM switching instants, making it difficult to precisely identify the PWM switching instants and to reconstruct the actual

waveshape during each PWM switching cycle. Furthermore, a fully-calibrated prototype machine is required to secure the measured phase current data, which is typically not feasible to build during the machine's initial design stage. As a result, it is highly desirable to have an analytical model to predict the PWM-induced current ripple over a wide range of operating conditions.

Therefore, the analytical model that has been presented in Chapter 5 appears as a promising candidate for predicting the current ripple waveshapes resulting from PWM voltage excitation for the same baseline IPM machine specified in Table 4-3. A comparison of the predicted and measured current ripple demonstrates excellent agreement for the current waveform shown in Figure 7-1 as well as the Fourier analysis results shown in Figure 7-2, which builds confidence in the estimation model for predicting the current ripple in IPM machines.

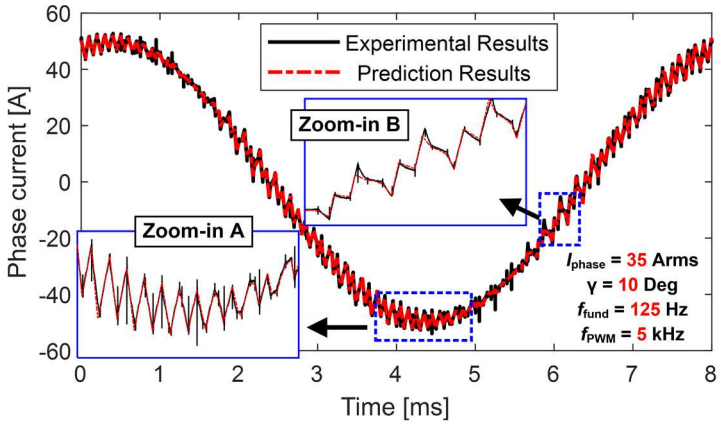

Figure 7-1: Example of measured current waveform including the PWM harmonics.

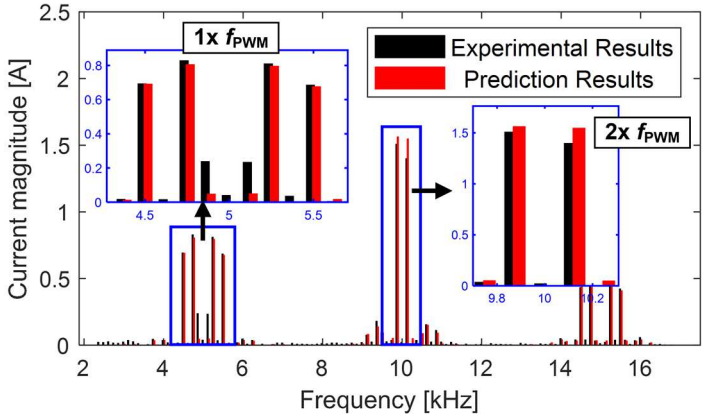

Figure 7-2: Frequency decomposition of predicted and measured phase current.

As shown in the zoom-in plots in Figure 7-1, the waveshape of current ripple varies significantly for different regions of the fundamental current, indicating that the current ripple is not uniformly distributed. Furthermore, the results in Figure 7-2 showing the complex harmonic distribution in the frequency domain suggest that the dominant current ripple frequency in each PWM switching cycle is either 1x f_{PWM} or 2x f_{PWM}. Therefore, accurate PWM-induced iron loss estimation calls for the detailed analysis of the iron loss contribution attributed to the PWM-induced flux ripple during each PWM switching cycle.

The overall current ripple prediction process is summarized in Figure 7-3. For a given current command (i.e., i_d and i_q), the machine flux linkages, as well as the dynamic inductances in two axes, are assumed to be unchanged over a range of different PWM switching frequencies and machine rotating speeds. Therefore, the proposed model can quickly sweep over a wide range of test cases with very low computational costs, and the calculation speed benefits of the proposed technique are significant.

Summarizing, analytical evaluation of the current ripple lays the foundation for enabling a deeper understanding of the PWM-induced iron loss phenomena, and the predicted current waveforms will be used for flux ripple estimation.

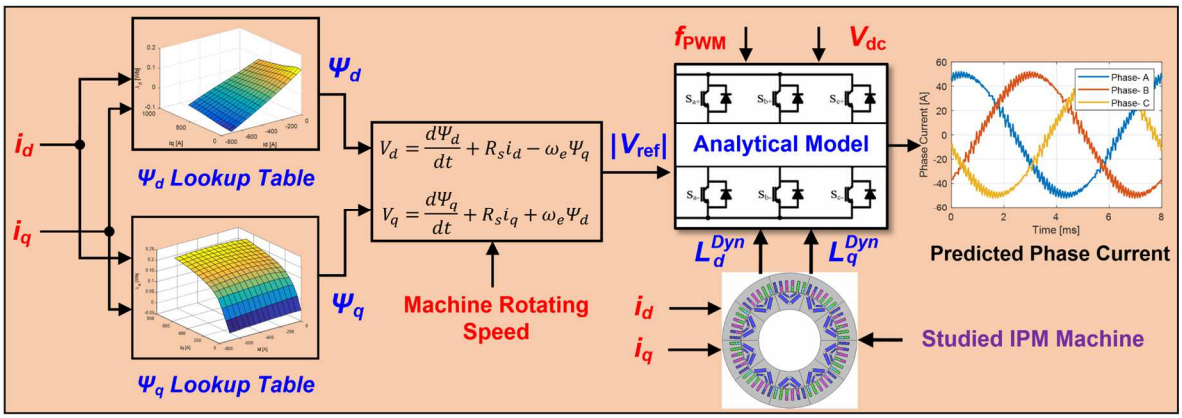

Figure 7-3: Diagram of proposed PWM-induced current ripple prediction model.

7.3 Development of PWM-Induced Iron Loss Model for IPM Machines

7.3.1 PWM-Induced Flux Ripple Identification

Estimation of the PWM-induced iron loss in an electric machine requires knowledge of the flux density distribution throughout the entire machine. Due to the complicated stator and rotor structure of an IPM machine such as the studied baseline IPM machine, 2-D FEA can play a crucial role in implementing element-based magnetic flux density predictions that offer sufficient high accuracy with reasonable calculation efforts. A single pole used in the 2-D FEA with 5474 mesh elements is shown in Figure 7-4.

Using the estimated PWM-induced current ripple data, the flux ripple distribution in the studied IPM machine is first calculated using 2-D FEA. Although the magnetic flux density distribution is complex in rotating machines, the majority of the dominant flux density components align with either the radial direction (e.g., stator teeth) or the circumferential direction (e.g., stator back iron). As a result, the decision was made to segregate the predicted flux density in each mesh element into these two axis components, and each component is analyzed separately.

The calculated magnetic flux density results in both decomposed directions during a complete fundamental period for a mesh element selected in the middle of machine's stator tooth (See Point-

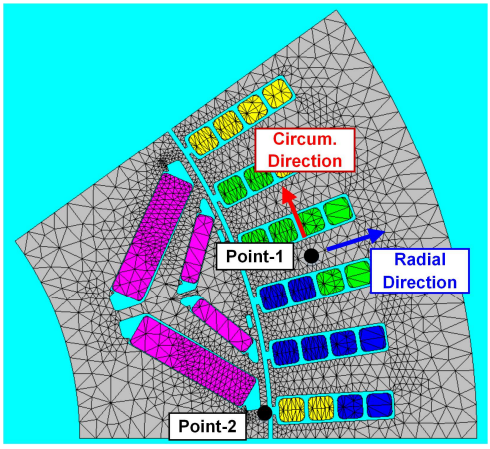

Figure 7-4: Mesh elements of a single pole in the baseline Spark machine.

1 in Figure 7-4) are presented in Figure 7-5(a)-(b), respectively. High-frequency flux ripple components are superimposed on the fundamental field.

As discussed in Chapter 6, the dc-bias field exerts a major influence on the magnetic domain distribution, significantly affecting the ac iron loss. Since the PWM frequency is much higher than the fundamental frequency, the average value of the fundamental field over the period of each PWM switching cycle ΔT_{minor} is approximated as a constant dc-bias field. For a specific mesh element, the two orthogonal directions are assumed to share the same value of dc-bias field calculated using (7-1) and (7-2) to account for the cross-coupling of magnetic saturation effects in the 2 axes.

$$B_{\text{major}} = \sqrt{B_{\text{radial}}^2 + B_{\text{circum.}}^2} \quad \text{[T]} \qquad (7\text{-}1)$$

$$B_{\text{dc}} = \frac{1}{\Delta T_{\text{minor}}} \int_0^{\Delta T_{\text{minor}}} B_{\text{major}} \cdot dt \quad \text{[T]} \qquad (7\text{-}2)$$

As shown in Figure 7-5(c), the fundamental and the low-order harmonic components can be suppressed by means of Fourier analysis, leaving the flux ripple waveform containing the harmonic components that lie in the PWM frequency range. The PWM switching instants are all pre-identified in the waveforms, where each square marker represents a switching instant. The detailed flux ripple waveshape can be recon-structed by connecting each of these switching instant values with a straight line, under the assumption that the PWM-induced flux varies linearly during each switching cycle. The reconstructed waveform closely matches the simulated flux ripple that was calculated using very small 1 μs time steps.

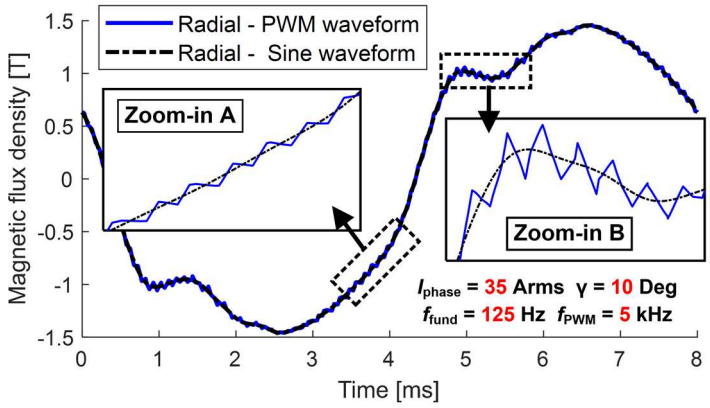

(a) Simulated magnetic flux density in radial direction

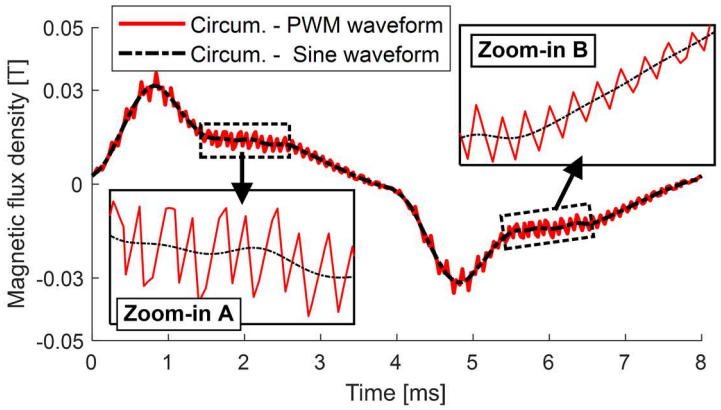

(b) Simulated magnetic flux density in circumferential direction

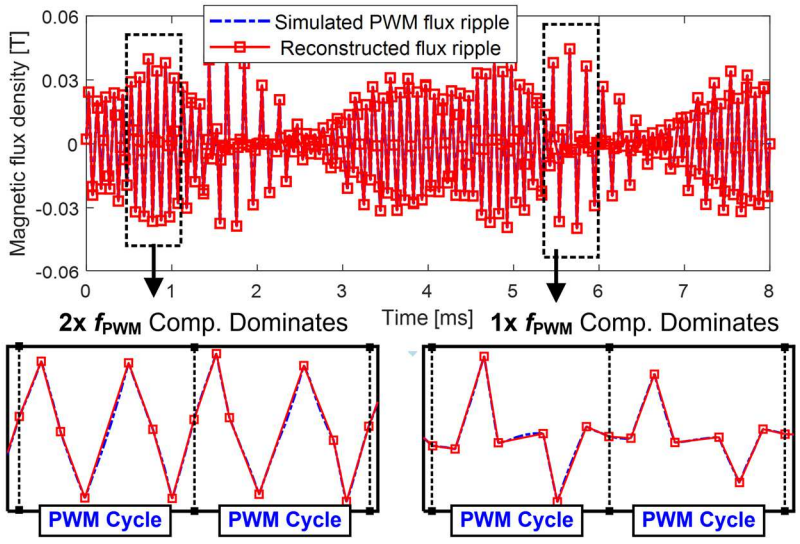

(c) Evaluation of PWM-induced flux ripple in radial direction

Figure 7-5: Predicted flux density waveforms in the middle of the stator tooth.

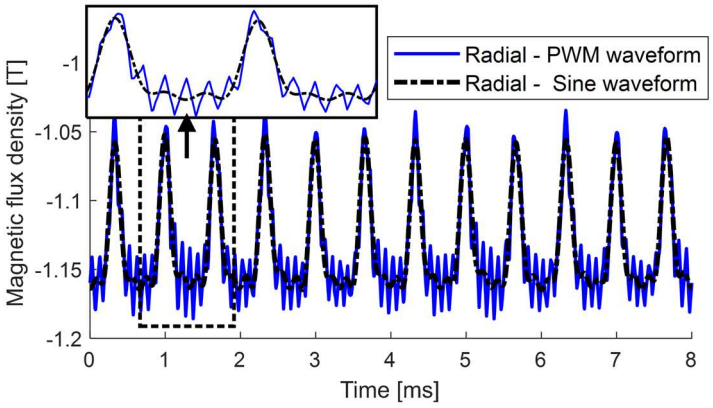

(a) Simulated magnetic flux density in radial direction

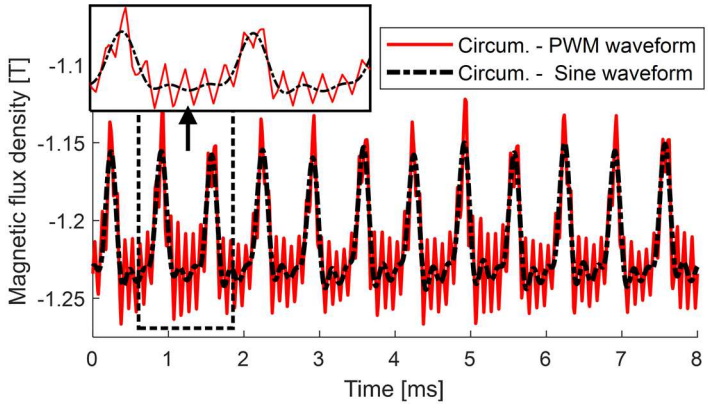

(b) Simulated magnetic flux density in circumferential direction

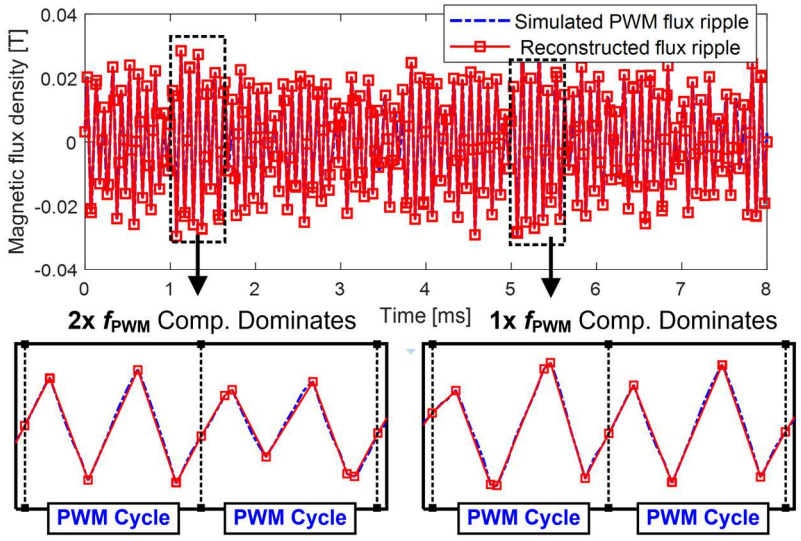

(c) Evaluation of PWM-induced flux ripple in radial direction

Figure 7-6: Predicted flux density waveforms in the machine rotor surface.

Next, the simulated PWM flux density waveforms and their fundamental field components in two orthogonal directions are provided in Figure 7-6(a)-(b) for another mesh element located in the rotor surface (Point-2 in Figure 7-4). Except for the low-amplitude slotting harmonics, the fundamental field consists of a dc field, making the PWM-induced flux ripple the dominant ac flux density component in the rotor side. In the proposed model, this analytical technique has been applied to each mesh element to ensure accurate and rapid ripple waveshape estimation. The zoomed-in regions in Figure 7-5(c) and Figure 7-6(c) show that the PWM-induced flux ripple exhibits varying frequency and waveshape properties in different regions, making it important to develop a generalized iron loss model.

For the sake of completeness, a 3-D FEA has also been conducted to investigate the impact of the end winding leakage flux on the estimation accuracy of the 2-D FEA. As depicted in Figure 7-7, a single-pole machine model with half stack length was built to save simulation time, where the symmetry boundary has been added on the machine center plane to account for the symmetry along the axial axis direction. A comparison of the simulated flux density waveforms at the same 2-D stator tooth point using 2-D and 3-D FEA tools is presented in Figure 7-8 for 4 z-axis axial positions. Although minor deviations in the 3-D FEA results are observed for Point-1 on machine's outer (i.e., end) surface compared to the 2-D FEA results, the PWM-induced flux ripple in both simulations exhibit very similar waveshapes and amplitudes. Moreover, the difference shrinks considerably as the mesh element's z-axis position moves towards the center plane. The simulation results from 3-D FEA are almost identical to the 2-D results as long as the distance to the outer surface is >5 mm, indicating that only a modest fraction of the 3-D mesh elements is influenced by end effects.

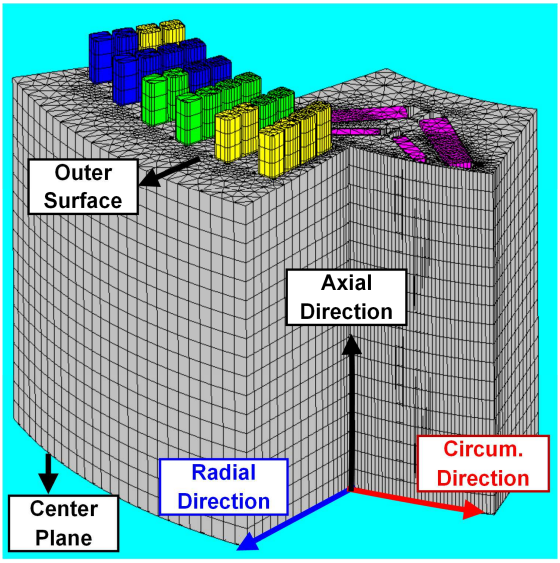

Figure 7-7: Single-pole 3-D FEA model with half machine stack length.

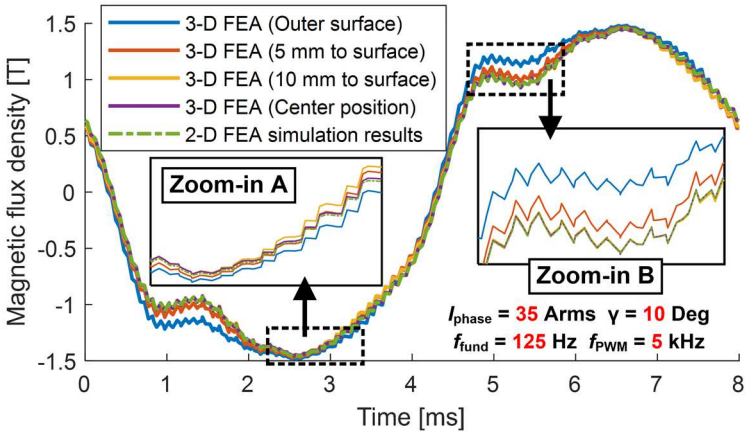

Figure 7-8: Comparison of simulated magnetic flux density waveforms in radial direction using 2-D and 3-D FEA at a selected stator-side point (See Point- 1 in Figure 7-4 for its location in 2-D space).

TABLE 7-1: COMPARISON OF 2-D AND 3-D FINITE ELEMENT ANALYSIS METRICS FOR IPM MACHINES

	2-D FEA	3-D FEA
Number of fundamental cycles	1	1
Number of time steps	1401	1401
Number of mesh elements	5474	146517
Calculation time	7.36 mins	7.6 hours
Average torque	46.18 N·m	45.54 N·m

In addition, a detailed comparison between 2-D and 3-D FEA calculation metrics is summarized in Table 7-1. Owing to a much large number of mesh elements, the simulation time of the 3-D FEA is >60x longer than for 2-D FEA. However, consistent with the fact that the flux density waveforms exhibit no notable differences between the two cases, the average output torque is almost identical. Since the much longer calculation time using 3-D FEA is undesirable for practical applications, all of the PWM-induced flux ripple and iron loss analytical results that follow in this research have been calculated using 2-D FEA. This choice cannot be generalized to all machines since it depends on whether the end effects in the machine selected for study are sufficiently small to justify it.

7.3.2 Frequency Decomposition of PWM-Induced Flux Ripple

Having the reconstructed PWM-induced flux ripple waveshape available makes it possible to take the impact of nonlinear hysteresis properties on iron loss consideration. However, the waveshape and the frequency spectrum of the PWM-induced flux ripple vary significantly with the machine's operating condition. It has been found in Chapter 5 that, although the f_{PWM} is maintained constant, the PWM-induced flux ripple during one switching cycle is dominant by one of two frequencies, 1x or 2x f_{PWM}, depending on the modulation index value. When the SVPWM modulation scheme is adopted, there are seven linear sections during each PWM switching cycle (The zero-crossing point in the middle of the cycle identifies the middle of the zero state associated with the fourth segment). With balanced zero-state intervals, the first, fourth, and last sections correspond to the zero states, and the remaining four states are active states. Moreover, the slope and polarity of each linear part depends on the relationship between the instantaneous inverter- and machine-side voltage.

Therefore, it is critically important to decompose the PWM-induced flux ripple from each cycle into different frequency components which can be directly fed into the developed dynamic *J-A* model for PWM-induced iron loss estimation.

The frequency separation process can be sub-divided into two categories: 1) The 1x f_{PWM} harmonic is dominant, and 2) The 2x f_{PWM} harmonic component is dominant. It is the dominant component that primarily determines the duty cycle properties of the overall flux ripple waveshape, and the secondary frequency component is assumed to be symmetrical. By considering either the 1x or 2x f_{PWM} as the dominant harmonic component, a unique analytical solution can be determined correspondingly.

7.3.2.1 1x PWM Frequency Component Dominates

Two example waveforms of PWM-induced magnetic flux ripple are shown in Figure 7-9(a) and (b), respectively, where the 1x f_{PWM} component at 5 kHz dominates in both cases. Each of them consists of seven linear segments, which is the same flux ripple characteristics described in the last section. Owing to the intrinsic property of the PWM-induced current ripple, the first- and second-half cycles of the ripple waveforms are inversely symmetrical to each other (i.e., mirror-image about the half-cycle time instant and reverse in polarity).

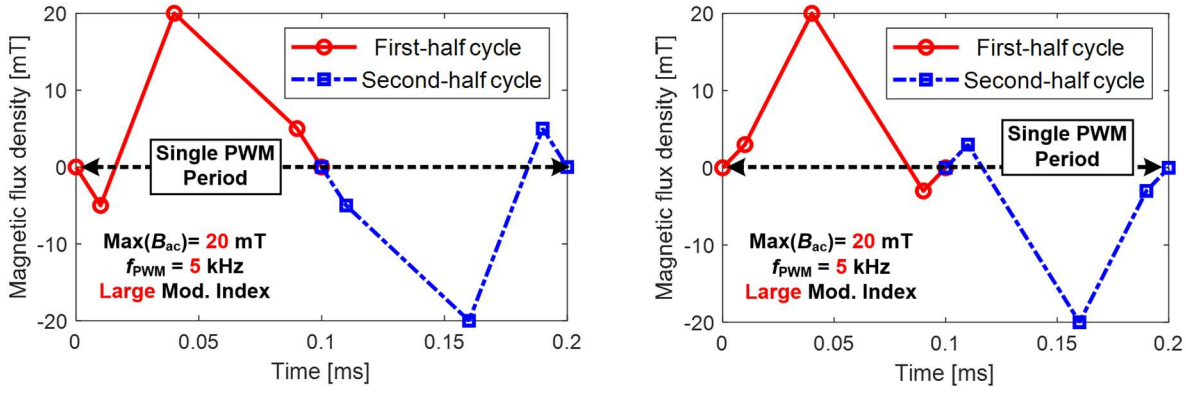

(a) Example flux ripple waveform- 1 (b) Example flux ripple waveform- 2

Figure 7-9: Two example flux ripple waveforms for the case when the 1x f_{PWM} component dominates.

It is worth noting that the waveforms shown in Figure 7-9 are not directly compatible with the dynamic *J-A* model. Even though the dominant frequency is at 1x f_{PWM}, the ripple waveforms contain higher-order harmonics including a 2x f_{PWM} component. Therefore, frequency decomposition is necessary before initiating the iron loss estimation. One popular method of analyzing the frequency composition of the complex waveform is to use FFT decomposition method. However, that method cannot emulate the most essential waveshape properties of the PWM-induced flux ripple during each PWM switching cycle. Furthermore, it typically requires a large amount of data, demanding the iron loss data for frequencies as high as 10x f_{PWM}, making it unpractical for machine-level PWM-induced iron loss estimation.

To simplify the frequency decomposition process and better emulate the key waveshape properties of each cycle of PWM-induced flux ripple, it is assumed that each cycle of the ripple waveform consists of a combination of 1x and 2x f_{PWM} piece-wise linear waveform components with different duty cycles. Here, Figure 7-9(a) is selected here as the example case. Owing to the inverse symmetry of the first- and second-half cycles, only one half-cycle data is needed for frequency decomposition. For the half-cycle waveform shown in Figure 7-10, it is apparent that the dominant frequency component is at 1x f_{PWM}. It is assumed that the location of the peak point of the triangular component at 1x f_{PWM} is the same as the peak point location in the original wave-form (i.e., $t = T_1 + T_2$ in Figure 7-10). The triangular ripple component at 2x f_{PWM} is then determined by subtracting the 1x f_{PWM} triangular waveform from the original half-cycle waveform, through linear decomposition theorem. As a result, summing up the flux ripple components at the two frequencies together produces the original ripple waveform.

The two decomposed ripple waveform components shown in Figure 7-10 include a total of seven linear segments. To apply the linear superposition theorem, the following equations are

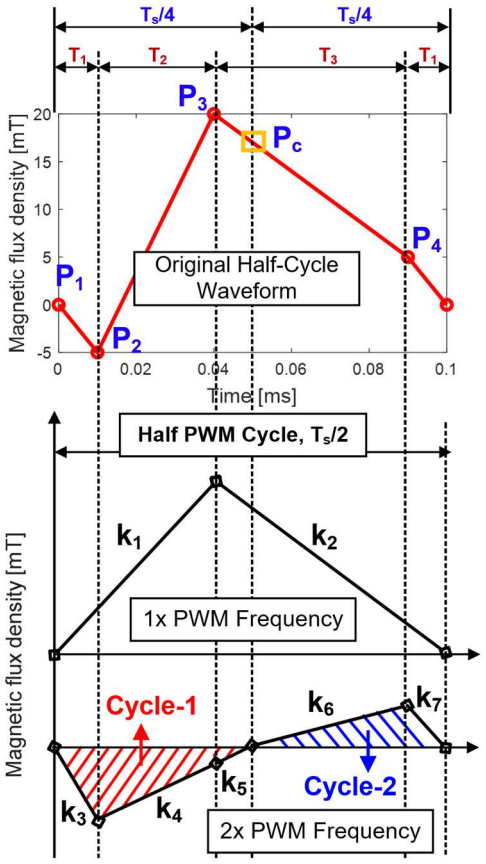

Figure 7-10: Process of frequency decomposition for dominant 1x f_{PWM} component case.

written to meet the boundary conditions at each PWM switching instant as well as one-fourth of the PWM switching cycle:

$$(k_1 + k_3) \cdot T_1 = P_2 \tag{7-3}$$

$$P_2 + (k_1 + k_4) \cdot T_2 = P_3 \tag{7-4}$$

$$P_3 + (k_2 + k_5) \cdot \left(\frac{T_s}{4} - T_1 - T_2\right) = P_c \tag{7-5}$$

$$P_c + (k_2 + k_6) \cdot \left(\frac{T_s}{4} - T_1\right) = P_4 \tag{7-6}$$

$$P_4 + (k_2 + k_7) \cdot T_1 = 0 \tag{7-7}$$

$$k_3 T_1 + k_4 T_2 + k_5 \cdot \left(\frac{T_s}{4} - T_1 - T_2\right) = 0 \tag{7-8}$$

$$k_6 \cdot \left(\frac{T_s}{4} - T_1\right) + k_7 T_1 = 0 \tag{7-9}$$

where $2T_1 + T_2 + T_3 = T_s/2$, and P_c is the value of the original flux density ripple at the midpoint of the first-half cycle (i.e., $T_s/4$).

With seven linear equations regulating the frequency of each triangular component, the unique solution of slope in each linear segment can be determined through the matrix forms presented in (7-10)-(7-12).

$$\begin{bmatrix} T_1 & 0 & T_1 & 0 & 0 & 0 & 0 \\ T_2 & 0 & 0 & T_2 & 0 & 0 & 0 \\ 0 & \lambda & 0 & 0 & \lambda & 0 & 0 \\ 0 & \tau & 0 & 0 & 0 & \tau & 0 \\ 0 & T_1 & 0 & 0 & 0 & 0 & T_1 \\ 0 & 0 & T_1 & T_2 & \lambda & 0 & 0 \\ 0 & 0 & 0 & 0 & 0 & \tau & T_1 \end{bmatrix} \begin{bmatrix} k_1 \\ k_2 \\ k_3 \\ k_4 \\ k_5 \\ k_6 \\ k_7 \end{bmatrix} = \begin{bmatrix} P_2 - P_1 \\ P_3 - P_2 \\ P_c - P_3 \\ P_4 - P_c \\ P_5 - P_4 \\ 0 \\ 0 \end{bmatrix} \tag{7-10}$$

$$\mathbf{TK} = \mathbf{\Delta P} \tag{7-11}$$

$$\mathbf{K} = (\mathbf{T})^{-1}\mathbf{\Delta P} \tag{7-12}$$

Using the identified slope of each linear segment, the original PWM ripple waveform can be uniquely decomposed into two frequency components (i.e., 1x and 2x f_{PWM}) using the slope values calculated from (7-12) and time intervals defined by the original flux density waveform given in Figure 7-10. Figure 7-11(a)-(b) show the decomposed components as well as original waveform depicted in Figure 7-9. Having the amplitude and duty cycle information available for each frequency component makes it possible to predict the iron loss separately from the 1x and 2x PWM switching frequency before being summed to estimate the total PWM-induced iron loss.

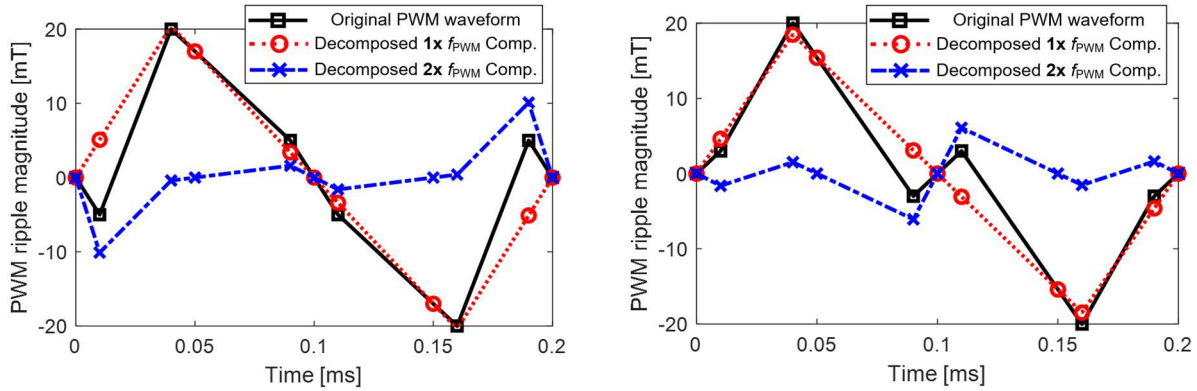

(a) Example flux ripple waveform- 1 (b) Example flux ripple waveform- 2

Figure 7-11: Frequency decomposition results for two example flux ripple waveforms shown in Figure 7-9.

7.3.2.2 2x PWM Frequency Component Dominates

When the value of modulation index is relatively small (i.e., < 0.3) and the harmonic component at 2x f_{PWM} dominates, the waveshape of the ripple exhibits approximately the same positive and negative areas during each half cycle, with nearly the same peak positive and negative values within each half-cycle intervals. Under these conditions, the roles reverse from the previous case so that the 2x f_{PWM} component mainly determines the shape of the original waveform and the waveshape of the 1x f_{PWM} component is assumed to be symmetrical.

Figure 7-12 shows the frequency decomposition procedure for the example original waveform with the dominant 2x f_{PWM} ripple component, where the absolute value positive peak value- P_2 is identical to that of the negative peak value- P_4.

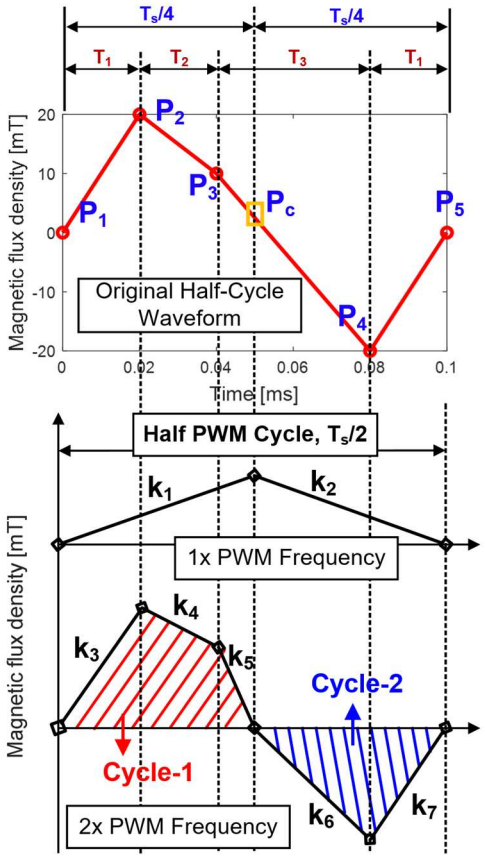

Figure 7-12: Frequency decomposition when the 2x f_{PWM} ripple component dominates.

To account for the symmetrical waveshape property of the 1x f_{PWM} component, the time interval matrix **T** is reconfigured as expressed in (7-13). Similarly, the slope matrix **K** is summarized as the product of the inverse time interval matrix $(\mathbf{T})^{-1}$ and the differences between two adjacent switching instants **ΔP**. The resulting decomposed components at 1x and 2x f_{PWM} are presented in Figure 7-13. Consistent with the waveshape property of the original waveform, it is the 2x f_{PWM} that appears as the dominant component. Nevertheless, the existence of 1x f_{PWM} component plays as an important role to meet the requirement of linear superposition approach.

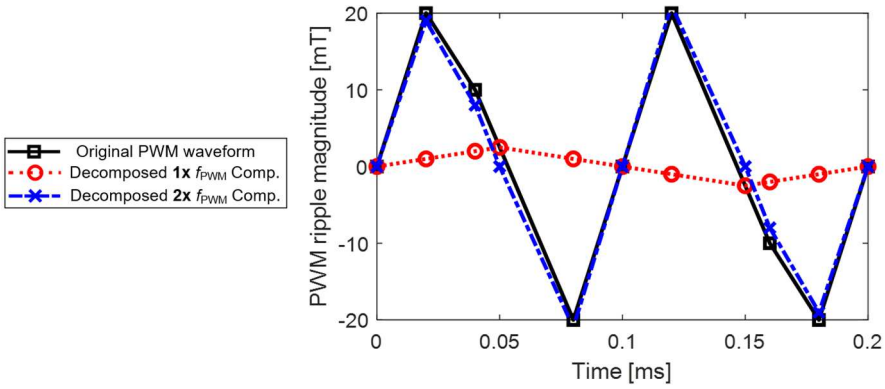

Figure 7-13: Frequency decomposition results for the example flux ripple waveform shown in Figure 7-12.

$$\begin{bmatrix} T_1 & 0 & T_1 & 0 & 0 & 0 & 0 \\ T_2 & 0 & 0 & T_2 & 0 & 0 & 0 \\ \lambda & 0 & 0 & 0 & \lambda & 0 & 0 \\ 0 & \tau & 0 & \tau & 0 & 0 & 0 \\ 0 & T_1 & 0 & 0 & 0 & 0 & T_1 \\ 0 & 0 & T_1 & T_2 & \lambda & 0 & 0 \\ 0 & 0 & 0 & 0 & 0 & \tau & T_1 \end{bmatrix} \begin{bmatrix} k_1 \\ k_2 \\ k_3 \\ k_4 \\ k_5 \\ k_6 \\ k_7 \end{bmatrix} = \begin{bmatrix} P_1 - P_2 \\ P_3 - P_2 \\ P_c - P_3 \\ P_4 - P_c \\ P_5 - P_4 \\ 0 \\ 0 \end{bmatrix} \tag{7-13}$$

The proposed frequency decomposition method makes it possible to analytically segregate the complex waveforms into 1x and 2x f_{PWM} components without losing the properties of the original waveform. Using the results of this flux ripple decomposition process, the PWM-induced iron loss of the IPM machine can be estimated element-by-element using the modified dynamic *J-A* model.

7.3.3 Implementation Procedure of the Proposed Estimation Model

Figure 7-14 shows the flow chart of the proposed machine-level PWM-induced iron loss estimation algorithm. The PWM-induced current ripple is first predicted for a given machine and inverter operating condition. The collected current waveforms including PWM harmonics are then used as inputs to 2-D FEA to determine the flux density distributions in all mesh elements. The predicted flux density in each element is then decomposed into two orthogonal components. Assuming a cylindrical coordinate system, the field components in the PWM frequency range are segregated from the total magnetic field in both the radial and circumferential directions. The PWM flux waveform in each direction is next decomposed into its 1x and 2x f_{PWM} components, and the modified dynamic *J-A* model presented in Chapter 6 is used to estimate the iron loss for each of these components based on the predicted dynamic hysteresis loops. The four predicted loss values are summed to yield the element's total PWM iron loss, and the same procedure is then applied to all machine elements to estimate the total machine PWM iron loss.

Without decomposing the PWM-induced flux ripple into a large number of high-frequency components through Fourier analysis, the triangular PWM flux ripple waveforms at 1x and 2x f_{PWM} are directly utilized to estimate the PWM iron loss. As a result, the influencing iron loss factors including the ac flux density amplitudes, excitation frequencies, triangular waveshapes, and pre-magnetized dc-bias fields are all appropriately incorporated into the iron loss estimation. This proposed algorithm can be easily extended to different types of electric machines including but not limited to the IPM machines (e.g., induction machines). Experimental test results are presented in the next section to investigate the key properties of the PWM-induced iron loss and to evaluate the performance of the proposed PWM iron loss estimation approach.

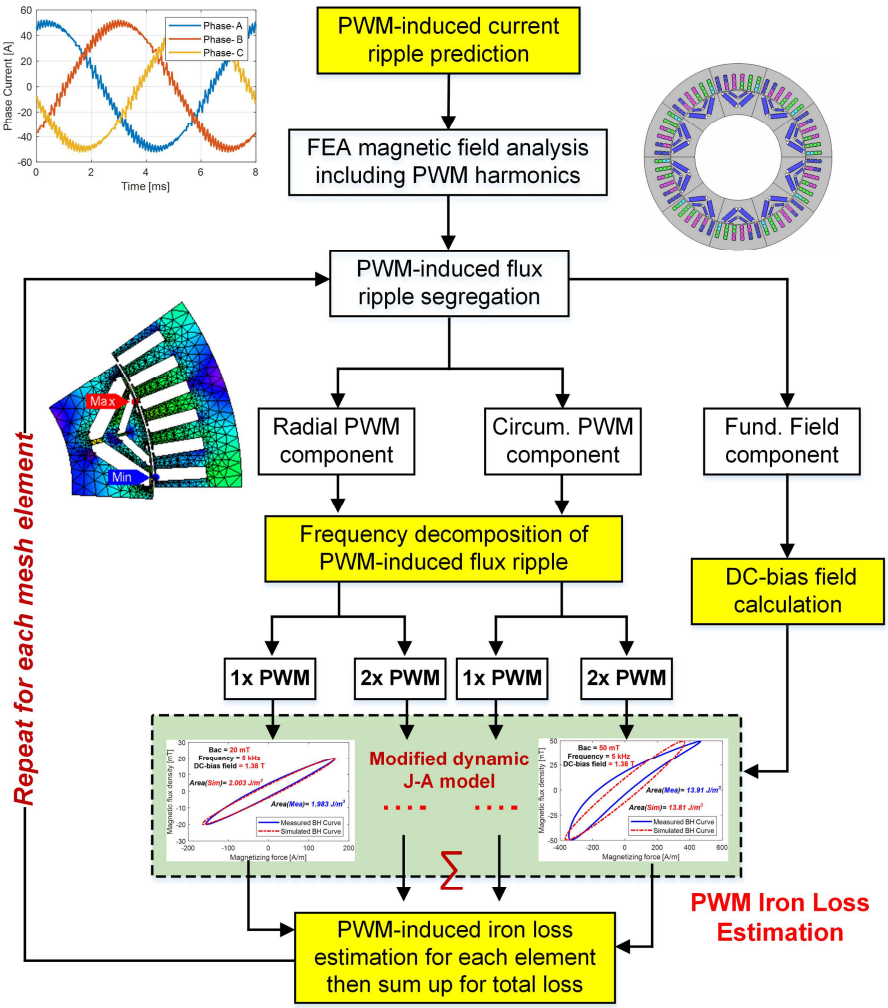

Figure 7-14: Flowchart of implementation procedure of machine-level PWM-induced iron loss estimation.

7.4 Verification and Evaluation of PWM-Induced Core Losses in IPM Machines

In this section, the improved machine-level PWM-induced iron loss estimation model, combined with a 3-D FEA model for magnet loss estimation, is utilized to investigate the additional losses due to PWM switching. Integrating the flux ripple calculation method with the predicted current input and analytical frequency decomposition method, the improved analytical model is capable of estimating the PWM-induced iron loss contributed by the 1x and 2x f_{PWM} components individually. After the introduction to segregation principle PWM-induced core losses in IPM

machines, the estimated results are compared with the measured data to verify the proposed estimation model. Effect of several influencing variables on the machine's PWM-induced core losses are investigated including PWM switching frequency f_{PWM}, machine speed (i.e., fundamental frequency), inverter dc-bus voltage V_{dc}, and current control angle γ.

7.4.1 Experimental Segregation of PWM-Induced Core Losses in IPM Machines

In this section, the improved PWM-induced iron loss estimation model, combined with a 3-D FEA model for magnet loss estimation, is utilized to investigate the additional losses due to PWM switching. To experimentally segregate the PWM-induced iron and magnet losses, an A/B test is proposed as illustrated in Figure 7-15.

A 3-phase *L-C* low-pass filter shown in Figure 7-16(a) is utilized to eliminate the high-frequency harmonics induced by PWM switching for one of the tests, providing a baseline reference case for segregating the PWM-induced losses. The 106 kW "pseudo-litz" strand-wound IPM machine (i.e., negligible ac PWM-induced copper loss) in Table 4-3 is excited with PWM and sinusoidal voltage excitation having the same fundamental component amplitude. A high-bandwidth (i.e., up to 1 MHz) power-meter is used to measure the total electrical input power delivered by the inverter. In order to minimize the influence of measurement noise, the mechanical output power is obtained using a high-precision torque-meter by averaging the measured data over a 10s time period. As a result, the PWM-induced core loss in the electric machine can be segregated by calculating the power loss difference between the two tests with and without the low-pass *L-C* filter, and a close-up view of the experimental test configuration is provided in Figure 7-16(b).

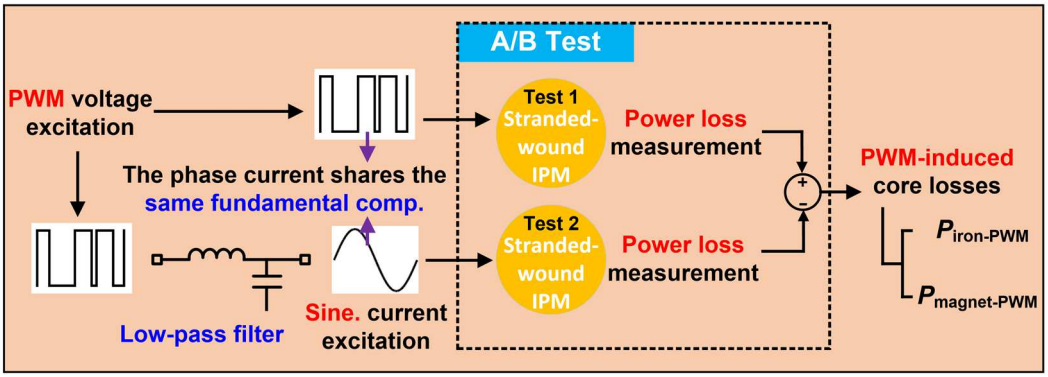

Figure 7-15: Experimental procedure of A/B test for PWM-induced core losses segregation.

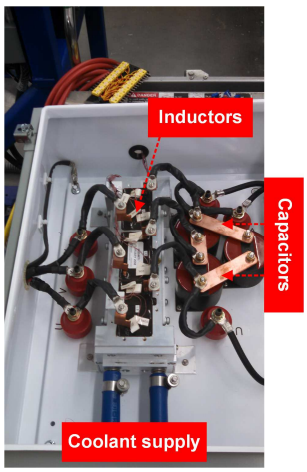

(a) Three-phase *L*-*C* filter

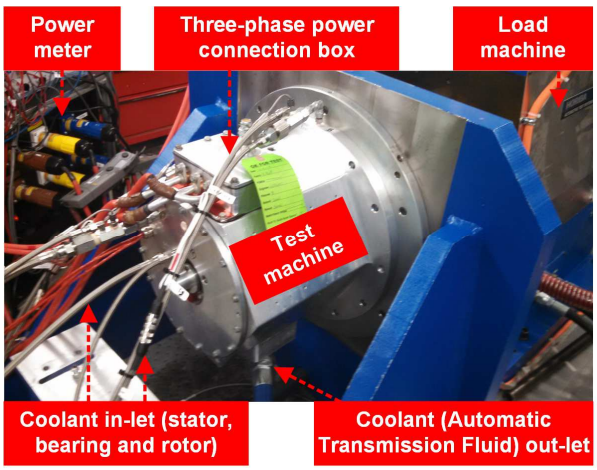

(b) IPM traction machine under test

Figure 7-16: Experimental test configuration for PWM core loss measurement.

Figure 7-17 provides an overlaid comparison of three measured machine phase current waveforms: one filtered by the *L*-*C* low-pass filter, and two current waveforms from PWM voltage excitation with different switching frequencies (i.e., f_{PWM} = 5 and 10 kHz). It can be observed that the low-pass filter is effective at suppressing the amplitude of PWM harmonics while leaving the fundamental current component unaffected.

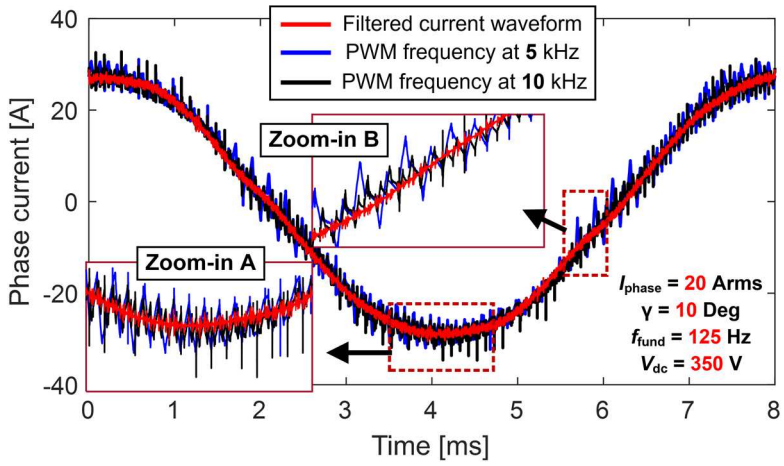

Figure 7-17: Comparison of measured current waveform filtered by *L*-*C* filter and waveforms under PWM supply with different switching frequencies.

It should be noted that, for a given operating point, both tests are conducted under identical excitation, output torque, and armature winding temperature conditions to ensure the integrity of the A/B tests. However, since the PWM-induced power loss only accounts for a very small fraction of the total input power (i.e., < 1 %), it is susceptible to measurement errors. Even with precision instrumentation, it is hard to eliminate all fluctuations in the measured power loss data. Therefore, the PWM-induced loss analysis in this research has been purposely focused on light-load (i.e., $I_{phase} \leq 35$ Arms) and low-speed (i.e., < 2,000 rpm) conditions to maximize the proportion of total machine losses attributable to PWM effects. Under these test conditions, the PWM-induced loss can be as large as 10 to 30% of the total machine loss, making it considerably easier to confidently segregate the PWM core loss component. It is also important to note that these test conditions are highly relevant for automotive traction drives since electric traction machines typically spend much of their time operating under partial/light-load conditions (e.g., city driving cycles), where the PWM-induced core loss can impose a significant penalty on the machine's average efficiency.

Even with low-amplitude phase currents, the peak value of the fundamental field approaches 1.5 T in the middle of stator teeth. The rotor core always operates under high-field conditions due to the presence of rare-earth permanent magnets, regardless of loading. Therefore, the equivalent dc-bias field during each PWM switching cycle can exert a significant impact on the PWM-induced iron loss. In the process of evaluating the estimation accuracy of the proposed estimation model, several influencing factors were selected to investigate their individual impacts on the iron core losses.

7.4.2 Impact of PWM Switching Frequency

In order to investigate the PWM switching frequency's impact on the resulting PWM-induced core losses (i.e., sum of iron and magnet loss) in the Spark machine, the measured machine power losses with and without the *L*-*C* low-pass filters are shown in Figure 7-18 at four PWM switching frequencies (i.e., 3.5, 5, 7.5, and 10 kHz). Under sinusoidal excitation (i.e., with *L*-*C* filters), the power losses induced by the fundamental loss components are assumed to be unchanged regardless of the PWM switching frequency. As a result, the power loss differences between two cases (i.e., yellow-color filled area) provide the losses that are attributable to the PWM-induced harmonics.

The measured total PWM-induced machine losses and predicted PWM-induced magnet loss from 3-D FEA are plotted vs. f_{PWM} in Figure 7-19(a). Under sinusoidal excitation, the magnet loss is negligible due to the fact that the permanent magnets are deeply embedded in the rotor cavities (i.e., no slotting harmonics). Therefore, the PWM-induced magnet loss is the principal magnet loss contributor in the IPM machines for the selected test conditions. After subtracting the predicted magnet loss from the total measured PWM-induced loss, the remained loss is considered to be the measured PWM-induced iron loss because of the low ac winding loss.

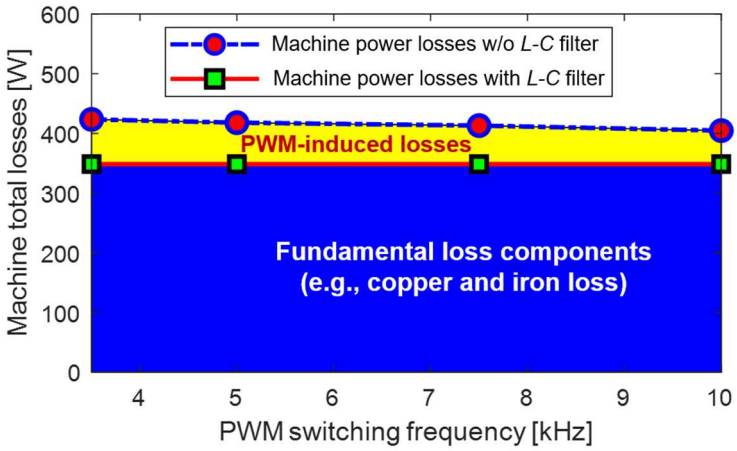

Test conditions:

Phase current I_{phase} = 35 Arms

Machine speed = 1,500 rpm (125 Hz)

Current control angle γ = 10 Deg

Inverter dc-bus voltage V_{dc} = 350 V

Figure 7-18: Experimentally segregated loss components for the Spark machine at four PWM switching frequencies: f_{PWM} = 3.5, 5, 7.5, and 10 kHz.

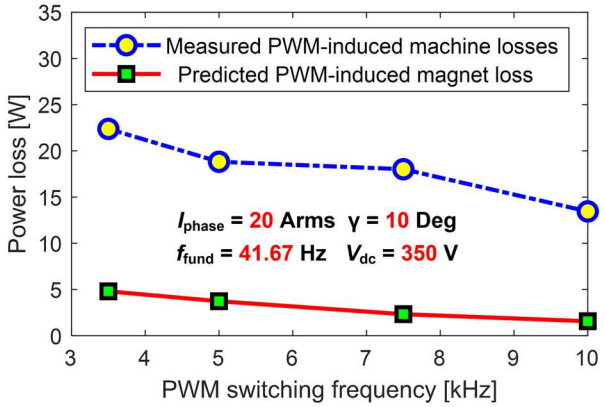

(a) Measured PWM-induced total machine loss and predicted magnet loss vs. f_{PWM}

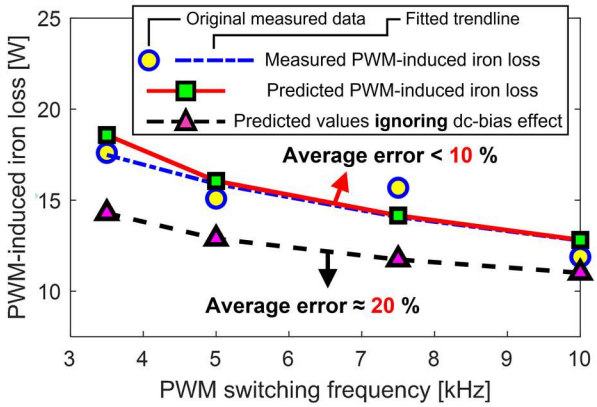

(b) Predicted and measured PWM-induced iron loss vs. switching frequency f_{PWM}

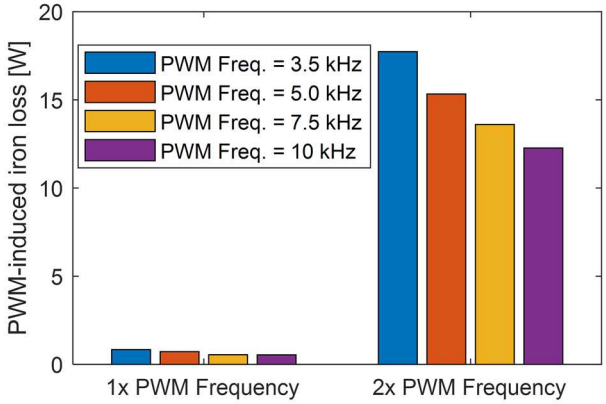

(c) Predicted PWM-induced loss from 1x and 2x f_{PWM} flux ripple for 4 f_{PWM} values

Figure 7-19: PWM-induced loss prediction model evaluation at low-speed (500 rpm) conditions using measured loss data vs. PWM switching frequency f_{PWM}.

This measured PWM induced iron loss is sub-sequently compared with the predicted values under varying PWM frequencies in Figure 7-19(b). This figure shows that the predicted PWM-induced iron loss closely matches the measured loss and the average error is below 10%, building confidence in the ability of proposed model to predict the PWM-induced iron loss for different PWM frequencies. However, if the dc-bias field impact is ignored during the iron loss estimation, the average estimation error reaches 20%.

The PWM-induced iron loss decomposition results from analytical predictions are presented in Figure 7-19(c), indicating that the loss reduction for the 2x f_{PWM} components is primarily responsible for the decreasing PWM core loss trend vs. f_{PWM}. The Fourier decomposition results of the current waveform with 5 kHz PWM switching frequency are provided in Figure 7-20. These results make it clear that the dominant harmonic components are sidebands of 2x f_{PWM}. This example confirms that the proposed frequency segregation method is important for accurately predicting the total PWM-induced core losses.

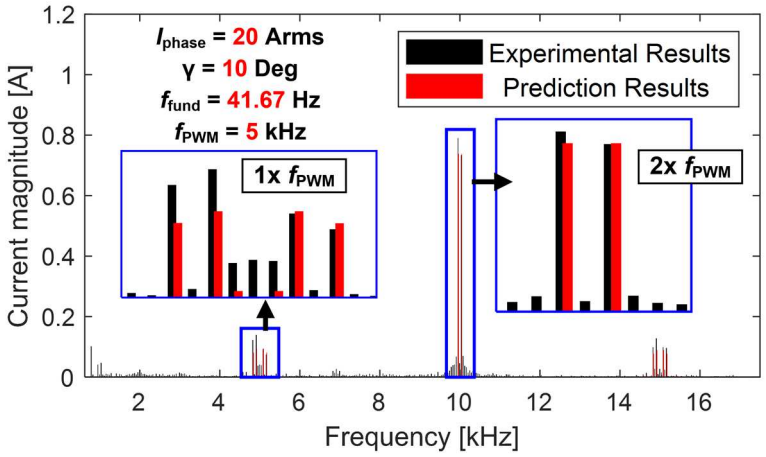

Figure 7-20: PWM current ripple spectral analysis at 500 rpm and 5 kHz f_{PWM}.

Analytical results are shown in Figure 7-21 for the case when the machine speed is increased to 1,500 rpm while keeping other operating conditions unchanged. First, compared to the 500 rpm case, the magnet eddy current loss induced by PWM switching is more significant, and it exhibits a clear decreasing trend as the PWM switching frequency increases. The 3-D FEA simulation results for magnet eddy current density shown in Figure 7-22 indicate that the eddy current distribution in each segmented magnet is strongly affected by skin effect, causing the eddy current distribution to become less uniform as the PWM frequency increases. Although the magnet's effective resistance increases at higher PWM frequencies, the PWM-induced harmonic field that passing through the PMs, which is proportional to the PWM current ripple, shrinks at a much faster rate. As a result, a notable magnet eddy current loss reduction vs. f_{PWM} is observed, and this decreasing trend is expected to continue as the PWM switching frequency keeps increasing.

The PWM-induced iron loss shows a similar decreasing trend vs. f_{PWM}. The predicted values of PWM-induced iron loss have exhibited good agreement with the measured data (i.e., average error < 10%). Here again, ignoring the dc-bias field impact leads to approx. 20% iron loss underestimation.

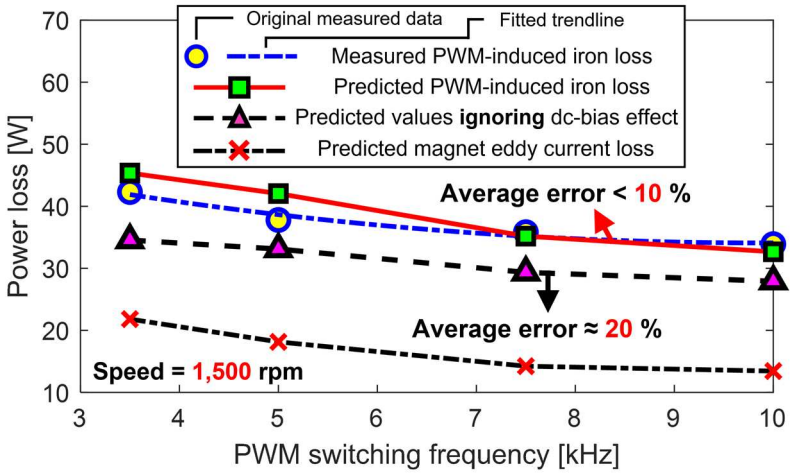

Figure 7-21: Comparison of measured PWM-induced iron loss with the predicted values with and without considering the dc-bias field effect.

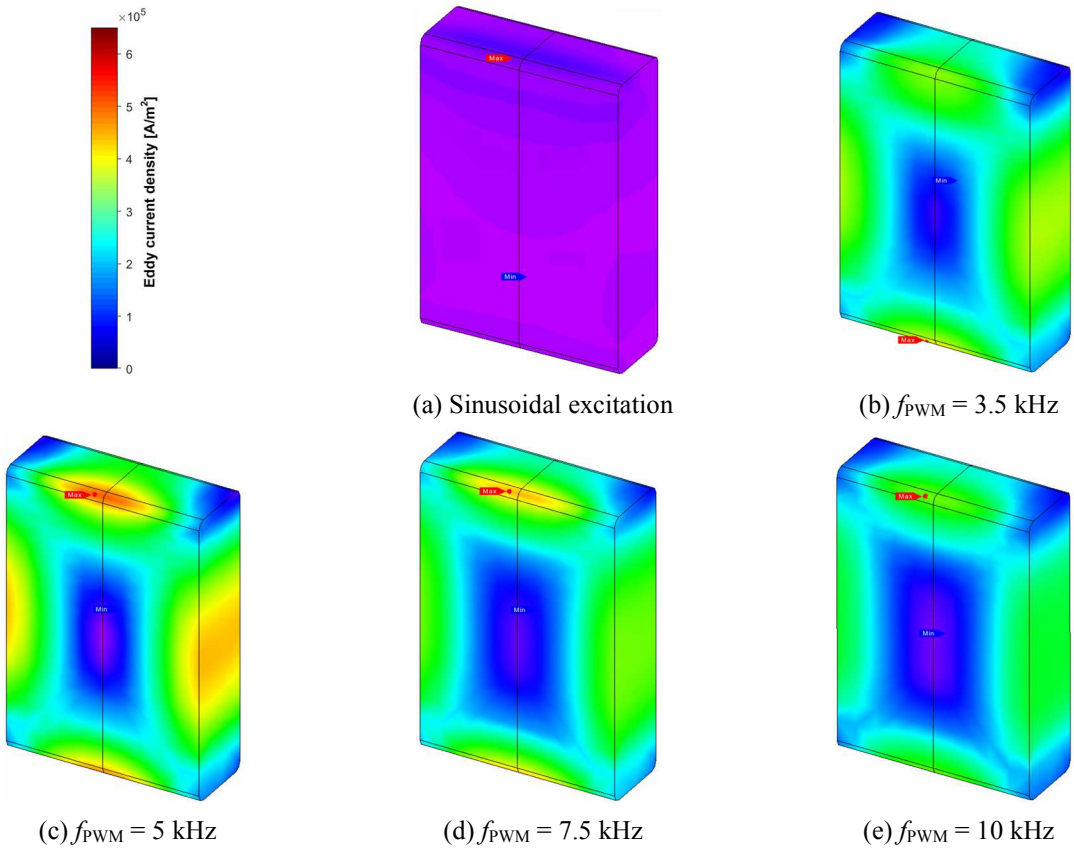

(a) Sinusoidal excitation (b) f_{PWM} = 3.5 kHz

(c) f_{PWM} = 5 kHz (d) f_{PWM} = 7.5 kHz (e) f_{PWM} = 10 kHz

Figure 7-22: Predicted magnet eddy current density distribution analysis using 3-D FEA with 35 Arms machine phase current and 10-deg γ angle.

Although the predicted core loss values shown in Figure 7-21 are always underestimated when the dc-bias field effect is ignored, the estimation error shrinks as the PWM switching frequency increases. This trend is consistent with the material-level results presented in Chapter 6, where the dc-bias field impact is more significant at lower excitation frequencies and larger flux ripple amplitudes (i.e., lower PWM frequencies). Although physically decomposing the iron loss remains a formidable task, the static hysteresis loss, which contributes a larger portion of the total iron loss at lower frequencies and larger amplitudes, is more susceptible to the presence of external dc-bias fields. As the PWM frequency increases, the dynamic eddy current loss becomes the more dominant iron loss component, making the dc-bias field impact less significant. Assuming that this trend holds for higher PWM frequency values, the PWM-induced iron loss in IPM machines is likely to come down further when the PWM switching frequency is increased beyond 10 kHz.

As noted in Chapter 2, the PWM-induced ac copper loss also decreases with the switching frequency. Therefore, there is reason to speculate that adoption of wide-bandgap (WBG) switches in future machine drives operating at much higher f_{PWM} values can reduce the total machine loss. However, the final selection of the PWM switching frequency must consider other key machine drive metrics including the inverter conduction and switching losses, stator winding voltage stress, etc. More detailed power losses analysis in IPM machines involving WBG-based inverters will be presented in next two chapters.

7.4.3 Impact of Machine Rotating Speed (i.e., Fundamental Frequency)

Next, the impact of machine speed on PWM-induced losses is evaluated. The measured total PWM-induced power loss and predicted magnet eddy current loss are plotted in Figure 7-23(a) as a function of the machine speed (from 500 to 2,000 rpm) under the same light-load conditions (i.e., I_{phase} = 20 Arms), with the PWM frequency maintained at 10 kHz. It can be observed that both losses depicted in Figure 7-23(a) increase with the machine speed. Following the same procedure described in the prior section to determine the measured PWM-induced iron loss, the results shown in Figure 7-23(b) present that the predicted values of the PWM-induced iron loss agree quite well with the measured values. For a lower rotor speed (500 rpm), the dominant PWM harmonic components are concentrated around 1x f_{PWM} and their amplitudes are relatively small, resulting in the lowest PWM-induced iron loss over the entire measured speed range. As the speed increases, increasing harmonics are observed in the vicinity of 1x and 2x f_{PWM}, leading to gradually increasing amplitudes of both the PWM-induced magnet and iron loss components. It is worth noting that, when the rotor speed is higher than 1,500 rpm, although the PWM-induced iron loss from 1x f_{PWM} components keeps increasing, the PWM-induced iron loss attributable to the harmonics in the vicinity of 2x f_{PWM} almost maintains constant. The analytical loss decomposition results shown in

Figure 7-23(c) are well consistent with the current ripple variation trend presented in Figure 5-12. The machine speed plays a vital role in determining the value of the modulation index, which, in turn, determines the current ripple spectra.

Similarly, the PWM-induced magnet loss increases monotonically as the speed grows. At higher speeds, the PWM harmonic current components progressively shift from 2x to 1x f_{PWM} which increases the magnet skin-effect losses, making the magnet loss a major contributor to the machine's total PWM-induced core losses.

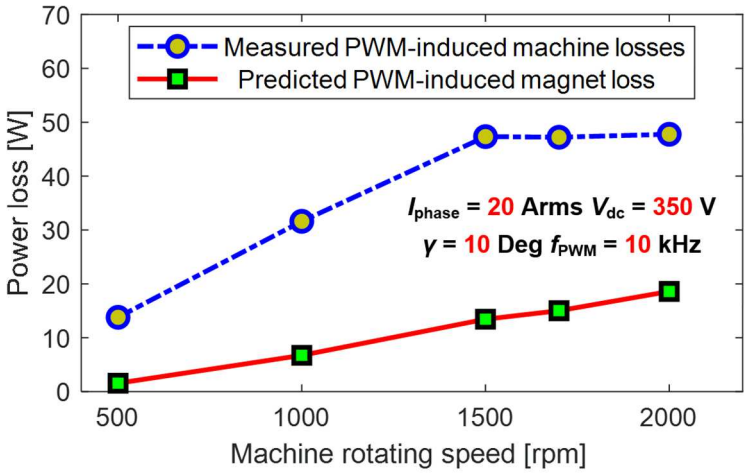

(a) Measured PWM-induced total machine losses and predicted magnet loss from 3-D FEA vs. machine speed

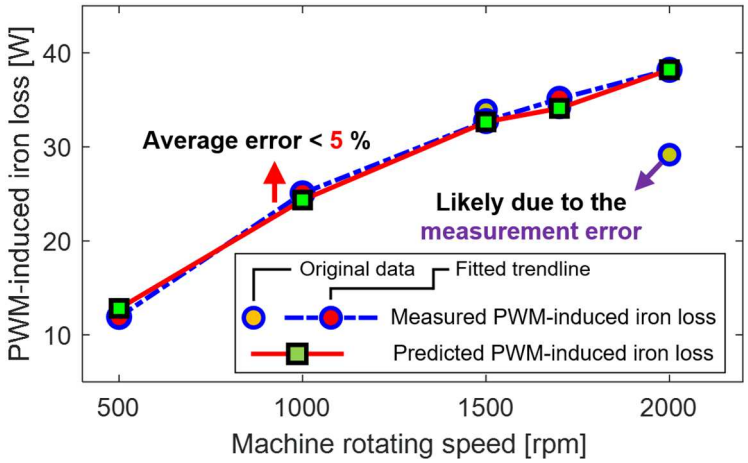

(b) Predicted and measured PWM-induced iron loss vs. machine rotating speed

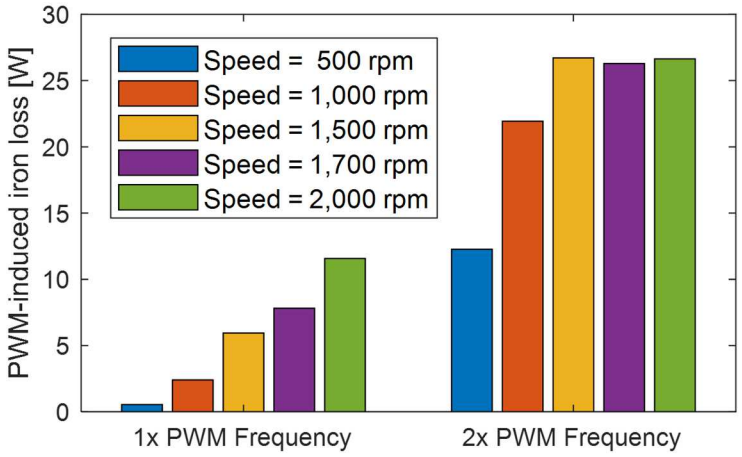

(c) Predicted PWM-induced iron loss from 1x and 2x f_{PWM} current ripple for 5 machine speed values

Figure 7-23: Experimental evaluation of the PWM-induced iron loss prediction model using measured loss data vs. machine rotating speed.

However, as can be seen from Figure 7-23(b), the measured PWM-induced iron loss at 2,000 rpm is much lower than that at 1,500. To better explain the discrepancy between the measured and predicted results, the Fourier decomposition of the current ripple at these two speeds is presented in Figure 7-24. It shows that a similar amount of the current ripple is observed at 2x f_{PWM} frequency ranges, which matches the prediction results shown in Figure 7-23(c) that the PWM- induced iron loss from the 2x f_{PWM} component are close at 1,500 and 2,000 rpm.

In contrast, current ripple harmonics in the vicinity of 1x f_{PWM} increase considerably by a ratio close to 2:1 as the machine speeds shifts from 1,500 to 2,000 rpm. This explains the notable

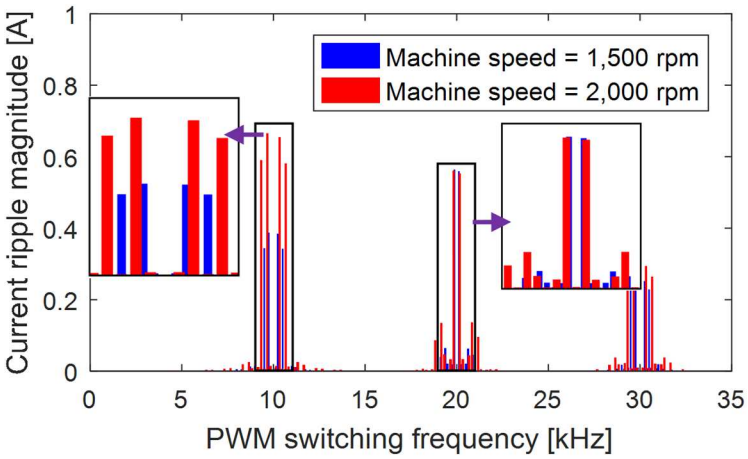

Figure 7-24: Current ripple spectra analysis for machine speeds under the same load conditions.

increase in the predicted iron loss contribution from the 1x f_{PWM} component as the speed increases from 1,500 to 2,000 rpm. That is why the observed PWM-induced iron loss drop at 2,000 rpm from experimental segregation in Figure 7-23(b) is more likely due to the measurement error.

7.4.4 Impact of Inverter DC-Bus Voltage

The impact of the inverter dc-bus voltage on the machine PWM-induced iron loss is expected to share a certain degree of similarity to that of machine rotation speed since the dc-bus voltage is also tightly related to the modulation index and the harmonic spectrum of the PWM-induced current ripple. For this study, the machine rotor speed is fixed at 1,500 rpm (i.e., f_{fund} = 125 Hz) with γ = 10 degree and 35 Arms phase current.

The predicted and measured PWM-induced iron loss results as a function of the V_{dc} are overlaid in Figure 7-25(a). The predicted loss variation trend matches the measured data quite well with the average error < 10 %, further validating the performance of the proposed model. The iron loss decomposition results plotted in Figure 7-25(b) show that the PWM-induced iron loss contributed by the 2x f_{PWM} flux ripple increases monotonically with V_{dc}, yielding a much higher PWM-induced iron loss at larger V_{dc}. In contrast, the predicted iron loss from the 1x f_{PWM} component exhibits the opposite trend.

In addition, the current ripple variation trend due to the change of the inverter dc-bus voltage in Figure 7-26 is accurately captured by the proposed iron loss prediction model. The amplitude of the PWM-induced current harmonics at twice the PWM switching frequency increases with the dc-bus voltage, consequently resulting in larger amounts of the PWM-induced iron loss. In contrast, the predicted iron loss from the 1x f_{PWM} component decreases monotonically with dc-bus voltage. Therefore, if the machine drive system allows dynamic inverter dc-bus voltage regulation, higher utilization of the dc-bus voltage (i.e., higher modulation index with lower bus voltage) can increase

the machine efficiency, especially when the electric machine operates under light-load and low-speed conditions.

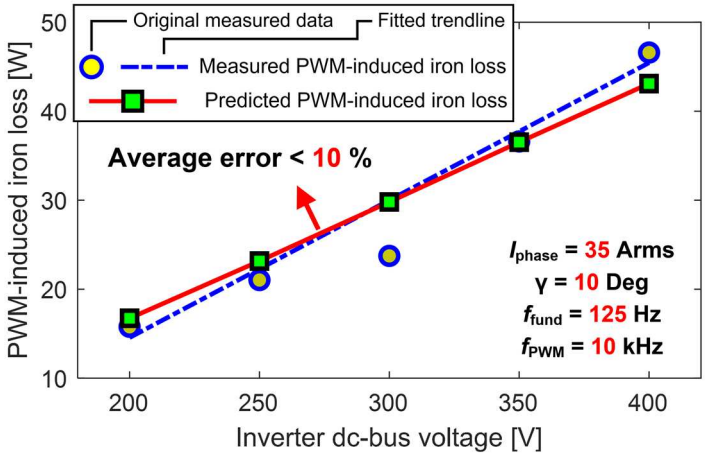

(a) Predicted and measured PWM-induced iron loss vs. inverter dc-bus voltage

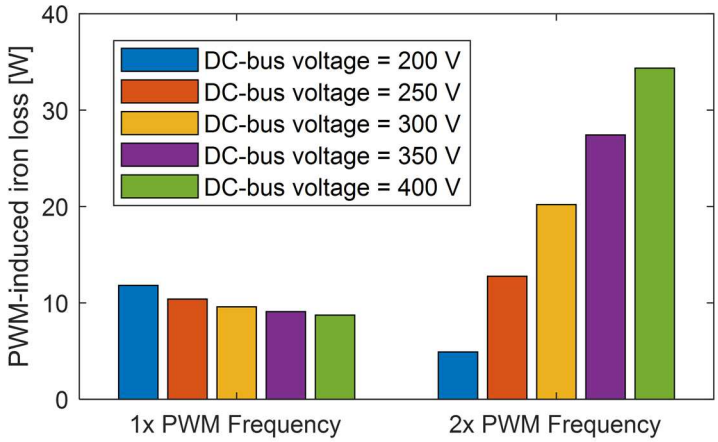

(b) Predicted PWM-induced iron loss from 1x and 2x f_{PWM} current ripple for five inverter dc-bus voltages

Figure 7-25: Machine-level analysis of PWM-induced iron loss with varying inverter dc-bus voltages.

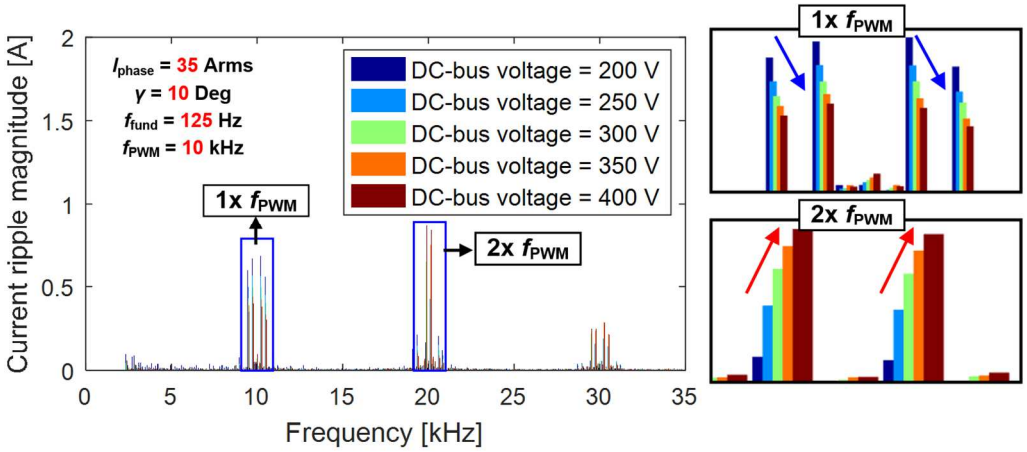

Figure 7-26: Measured current ripple spectra analysis with varying inverter dc-bus voltages at 10 kHz f_{PWM}.

7.4.5 Impact of Current Control Angle γ

It has been found from the PWM-induced current ripple analysis that the current ripple waveshape varies significantly with different current control angle γ. In addition, the modulation index decreases as the γ increases, in turn, the PWM-induced current ripple changes. This is confirmed by a comparison of the measured current spectra results presented in Figure 7-27 for γ = 10, 30, 50, and 80 degree. Both the 1x and 2x f_{PWM} current ripple components monotonically decrease as the γ angle increases, but most of the drop in the 2x f_{PWM} component occurs when the value of γ angle is larger than 50 degree.

The total measured machine loss as a function of the current control angle (with γ varying from 10 to 80 degree) for the operating condition with 35 Arms phase current and 1,700 rpm machine speed (i.e., f_{fund} = 141.7 Hz) are plotted in Figure 7-28. The measured machine loss includes the fundamental copper loss, friction and windage loss, fundamental iron loss, and PWM-induced magnet and iron loss. The machine total losses for four different PWM switching frequencies are measured, indicating that the PWM-induced losses exhibit a clear decreasing trend over the entire measured γ range. As can be seen from Figure 7-28, the measurement results are fluctuating due to the measurement errors. Therefore, linear fitted functions are provided to represent the general

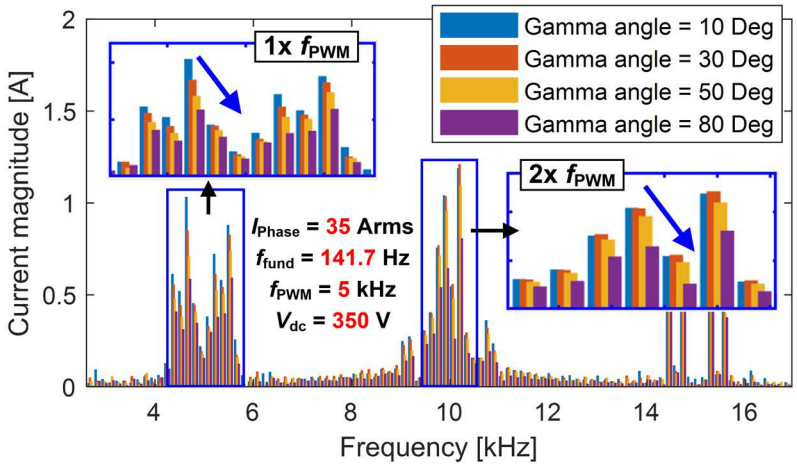

Figure 7-27: Measured current spectra analysis with four selected current control angles.

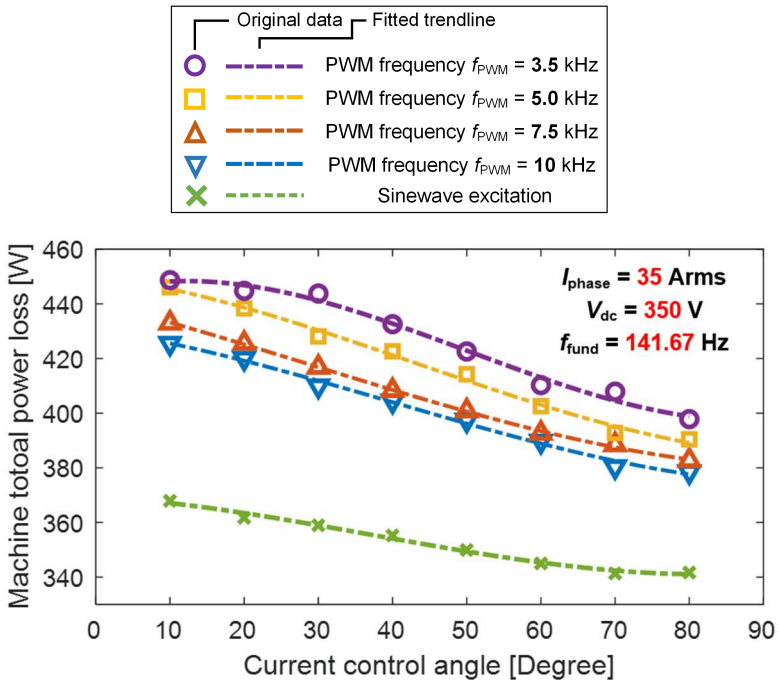

Figure 7-28: Machine total losses with and without *L-C* filters for current control angle varied from 0 to 90 degree.

variation trend of different excitations, and the fitted results will be subsequently employed to determine the measured PWM-induced power losses. Moreover, the machine power losses with the *L-C* filters (i.e., sinewave excitation) are included in the figure, providing useful reference values for identifying the PWM-induced loss components.

As seen in Figure 7-28 waveforms, the total machine loss experiences a clear decreasing trend as the current control angle increases under all excitation conditions (PWM or sinusoidal supply). Since the copper loss, as well as the friction and windage loss, can be assumed constant for any value of γ angle, it is the core loss (i.e., the sum of the fundamental and PWM-induced components) that decreases as more winding current is shifted from the positive *q*-axis to negative *d*-axis as the γ angle increases from 10 to 80 degree. Part of the reason is that the fundamental iron loss decreases as the negative *d*-axis current increases in the excitation, resulting, in turn, in a smaller fundamental flux component (i.e., flux-weakening effect).

Regarding the PWM-induced iron loss, the variation of the fundamental flux component at different γ angles affects the dc-bias condition, but more importantly, it is expected that lower current ripple amplitudes of both the 1x and 2x f_{PWM} components (see Figure 7-27) will lead to a decreasing trend of the PWM-induced iron loss as the γ angle increases.

To evaluate the prediction performance of the proposed model as well as to investigate the magnet loss variation trend with γ angle, the predicted magnet loss from 3-D FEA and a comparison of the measured and predicted PWM-induced iron loss versus γ angle for two PWM switching frequencies are plotted in Figure 7-29 and Figure 7-30, respectively. Both the magnet and iron loss components drop over the γ angle range from 10 to 80 degree, consistent with the decrease in the current ripple amplitude over this range.

The PWM-induced magnet loss exhibits a very interesting trend versus gamma angle. Initially, as the current is gradually shifted from the *q*-axis to the *d*-axis, the PWM-induced magnet loss increases. When the gamma angle is larger than 30 degree, the predicted magnet loss begins to decrease, which is attributed to smaller current ripple amplitude.

Regarding the predicted PWM-induced iron loss, the general variation trend of the measured PWM-induced iron loss is captured by the prediction model, and a monotonically decreasing trend versus γ angle is observed at two studied PWM frequencies. The average error between the predicted and measured loss versus γ angle for each case is 5 % for both PWM frequencies, adding confidence that the proposed model is capable of accurately predicting the PWM-induced iron loss with complex flux ripple waveshape properties.

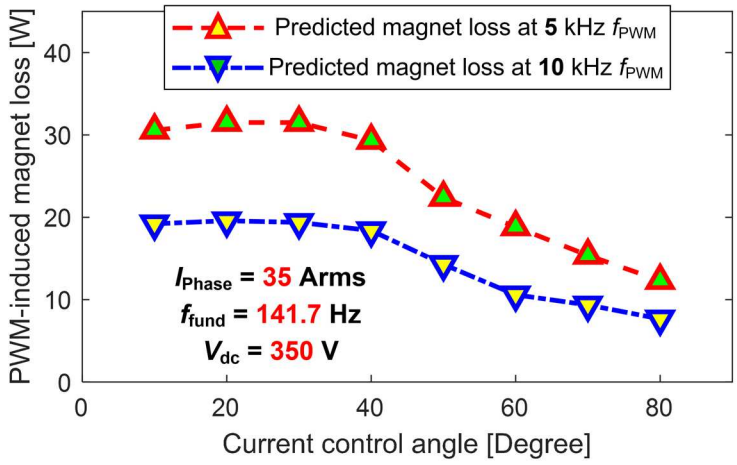

Figure 7-29: Predicted magnet eddy current loss from 3-D FEA with different current control angles.

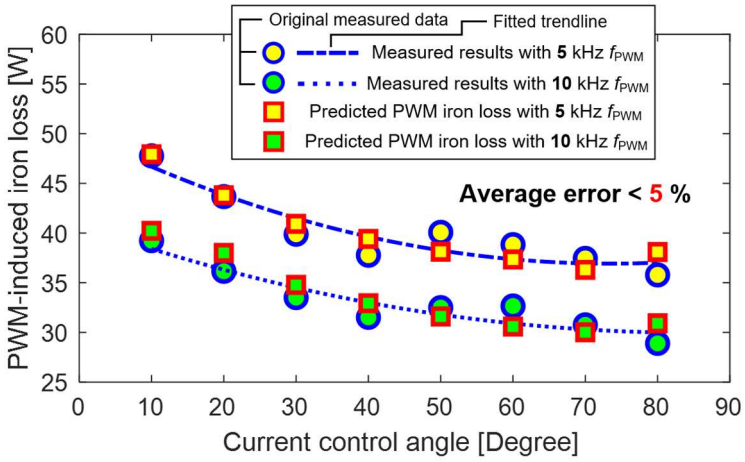

Figure 7-30: Measured and predicted PWM-induced iron loss versus current control angle γ.

7.5 Summary

A complete model for improved machine-level PWM-induced iron loss prediction has been developed in this chapter including capabilities for PWM-induced current and magnetic flux ripple prediction, flux ripple frequency decomposition, and iron PWM-induced iron loss calculation. This model provides an appealing analytical technique for estimating and characterizing the PWM-induced iron loss in both the existing and future electric IPM machine designs, and 3-D FEA has been utilized to predict the PWM-induced magnet loss in the IPM machine. Combining these two techniques offers a practical and accurate approach to estimating the total PWM-induced core losses, which is promising for use in the future IPM machine design optimization tool.

It has been found that the amplitude of the fundamental field during each PWM switching cycle can be approximated as an equivalent dc-bias field, exerting a substantial impact on the iron loss caused by PWM-induced flux ripple. Ignoring the dc-bias field leads to approx. 20% underestimation errors in the PWM-induced iron loss over a range of PWM frequencies and machine speeds for the investigated machine.

With the analytical approaches developed in this thesis, the PWM-induced iron loss in IPM machines can be predicted over a wide range of operating conditions, providing a valuable tool for future machine efficiency optimization.

Chapter 8
High-Frequency Iron Loss in Lamination Steels Driven by VSIs Using Wide-Bandgap Switches

8.1 Introduction

Adoption of the new-generation of wide-bandgap (WBG) power semiconductor devices (i.e., SiC or GaN) in voltage-source inverters (VSI) has exhibited promising capabilities for a variety of industrial and traction applications owing to their high efficiency, fast switching speed, high-temperature operating capability, etc. Although the electric motor load serves as an inductive filter, the residual harmonics induced by pulse-width modulation (PWM) result in additional high-frequency current ripple and iron loss in both the stator and rotor iron cores. Moreover, electric machines in automotive industry have been pushed in the direction of higher speed (i.e., higher fundamental frequency) to boost machine power/torque density with smaller size and weight, which further aggravates the problem. As a result, introducing the WBG power devices and then elevating the inverter PWM switching frequency substantially (e.g., $f_{PWM} > 50$ kHz) serve as an effective means to minimize the current ripple amplitude and enhance the machine performance. However, it raises questions about the iron loss properties of lamination steels when exposed to such elevated switching frequencies.

PWM-induced iron loss analysis and characterization presented in Chapter 6 has shown that the pre-magnetized dc-bias field exerts a significant impact on both the shape and enclosed area (i.e., iron loss) of the PWM-induced minor loop. However, the material loss data from the available power amplifier are restricted to low-frequency ranges (i.e., $f_{PWM} \leq 20$ kHz). Therefore, the objective of this chapter is: 1) to investigate the properties of iron loss in lamination steel generated by VSIs using wide-bandgap power switches; and 2) to a develop a more generalized material-

level model that can be conveniently used to estimate the total iron loss over broad ranges of operating conditions.

8.2 Lamination Steels Characterization for High Excitation Frequencies over Varying DC-Bias Fields

It has been discussed in Chapter 6 that, for VSI excitation with a relatively high ratio between the fundamental frequency f_{fund} and PWM switching frequency f_{PWM} (e.g., ratio > 40), the PWM-induced flux ripple is often sufficiently small (e.g., B_{minor} < 50 mT) that its impact on the major (referred to henceforth as fundamental) field is negligible. Also, it has been demonstrated via experimental tests in previous chapters that the iron loss contributions from these two widely-separated frequency components can be estimated independently. Since the PWM-induced minor loops are riding on top of the fundamental field, the average field during each PWM switching cycle can be approximated as an equivalent dc-bias field B_{dc} that exerts a significant impact on the minor loop's shape and enclosed area (i.e., iron loss) as depicted in Figure 8-1. Therefore, the total iron loss generated by a VSI can be expressed by (8-1), determined by summing up the major loop and minor loop loss components.

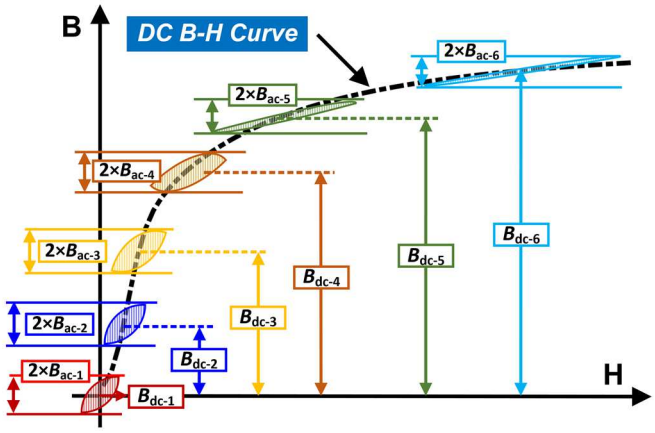

Figure 8-1: Minor loops in the presence of pre-magnetized dc-bias fields.

$$P_{\text{tot}} = P_{\text{major}}(B_{\text{major}}, f_{\text{fund}}) + \sum_{i=1}^{n} P_{\text{minor}_i}(B_{\text{minor}_i}, f_{\text{PWM}}, B_{\text{dc}_i}) \quad \text{[W]} \quad (8\text{-}1)$$

$$B_{\text{dc}_i} = \frac{1}{\Delta T_{\text{minor}}} \int_{t_{\text{minor}_i}}^{t_{\text{minor}_i}+\Delta T_{\text{minor}}} B_{\text{major}_i} \cdot dt \quad \text{[T]} \quad (8\text{-}2)$$

where B_{major} is the fundamental field amplitude, n is the total number of minor loops within a fundamental cycle, B_{minor_i} and B_{dc_i} are the amplitude and dc-bias field for the i-th PWM minor loop, t_{minor_i} is the time when i-th PWM minor loop appears, and ΔT_{minor} is the PWM time period.

In summary, the flux ripple amplitude, PWM switching frequency, and equivalent dc-bias field are three key variables that determine the iron loss associated with the PWM-induced flux ripple. Their influences on iron loss are explored in more detail in the following section.

Figure 8-2 shows the schematic adopted for high-frequency iron loss characterization. The H-bridge inverter with GaN field effect transistors (FETs) operates in bipolar mode to deliver two-level (i.e., $\pm V_{\text{dc}}$) square-wave voltage to the toroidal core under test, generating symmetrical triangular-shaped flux density waveforms (i.e., 50% duty cycle). The exceptionally high electron mobility and low on-state resistance of GaN devices make it possible to deliver high PWM switching frequencies to evaluate the iron loss characteristics over a broad frequency range. The inverter key parameters are provided in Table 8-1. During these tests, the amplitude of the input dc-bus voltage supplied by the external dc voltage source is manually adjusted to vary the ac flux density ripple amplitude. The dc-bias winding excited by the dc current source enables magnetic material characterization over a wide range of dc-bias field values. Referring to (8-3) and (8-4), the measured primary winding current I_{main} and sensing winding voltage V_{sense} provide the required data to define the dynamic hysteresis loop. The corresponding iron loss is evaluated from the enclosed hysteresis loop area via (8-5) which incorporates both the static hysteresis loss and the dynamic eddy-current loss.

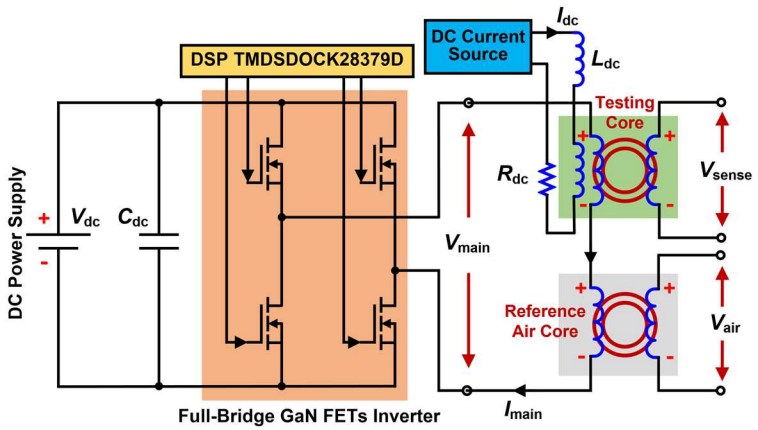

Figure 8-2: Basic schematic of the test configuration for PWM-induced iron loss characterization with GaN-FET single-phase inverter.

TABLE 8-1: KEY PARAMETERS OF GAN FETS VOLTAGE SOURCE INVERTER

Maximum dc-bus voltage	140 V
Maximum output current	12 A
Switch turn-on deadtime	< 20 ns
Output voltage rise time	< 10 ns
Output voltage fall time	< 10 ns
PWM switching frequency	10 - 200 kHz

$$H = \frac{N_{\text{main}} I_{\text{main}}}{l_{\text{core}}} \quad \text{[A/m]} \quad (8\text{-}3)$$

$$B = \frac{1}{A_{\text{core}} N_{\text{sense}}} \int V_{\text{sense}} \cdot dt \quad \text{[T]} \quad (8\text{-}4)$$

$$\overline{P_{\text{iron}}} = \frac{f_{\text{PWM}}}{\rho_{\text{iron}}} \int_0^{1/f_{\text{PWM}}} H \frac{dB}{dt} \cdot dt \quad \text{[W/kg]} \quad (8\text{-}5)$$

where l_{core} is the mean magnetic path of the toroidal core, A_{core} is the core cross section area, and other key specifications of the toroidal core made from non-oriented lamination silicon-steel with thin sheet thickness are provided in Table 8-2.

The dc-bias field strength H_{dc} in the toroidal core can be calculated with a dc current I_{dc} using (8-6) and then converted into a dc-bias field value B_{dc} using the material's dc *B*-*H* curve.

$$H_{\text{dc}} = \frac{I_{\text{dc}} N_{\text{dc}}}{l_{\text{core}}} \quad \text{[A/m]} \quad (8\text{-}6)$$

TABLE 8-2: KEY SPECIFICATIONS OF MANUFACTURED TOROIDAL CORE

Primary winding turns N_{main}	95
Sensing winding turns N_{sense}	61
DC-bias winding turns N_{dc}	90
Lamination thickness	0.3 mm
Number of sheets	11
Outer/inner diameter (**OD/ID**)	76.2/64.77 mm
Material mass density ρ_{iron}	7600 kg/m^3
Stress relief annealing process	Yes

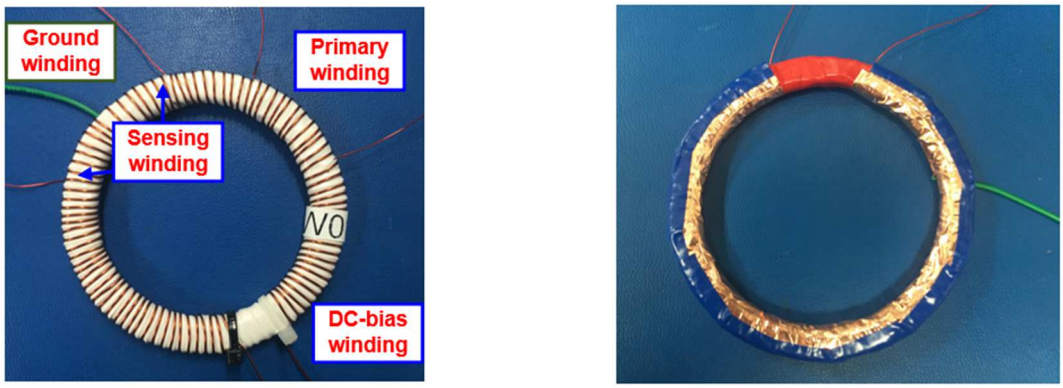

(a) Tested toroidal core (b) Electrostatic shield layer

Figure 8-3: Fabricated toroidal core for iron loss testing with extremely high PWM switching frequency.

Figure 8-3 shows the fabricated toroidal core. Due to the high switching speed of GaN FETs with V_{PWM} rise and fall time less than 10 ns, high *dv/dt* voltage slew rates can lead to transient over-voltages, causing severe winding insulation stress. Therefore, extra space is left between adjacent turns within each layer to minimize the turn-to-turn capacitance. In addition, a grounded copper-foil electrostatic shield shown in Figure 8-3(b) is inserted between the primary and sensing layer to suppress the layer-to-layer stray capacitance as much as possible.

Figure 8-4(a) shows a view of the PWM-induced iron loss test configuration, and a close-up view of the GaN FETs single-phase inverter is provided in Figure 8-4(b). 50 MHz high-bandwidth probes and a 2.5 GS/s oscilloscope are utilized for data collection to enhance the measurement accuracy under high-frequency PWM voltage excitation. In addition, a 2 MHz power analyzer and a 20 MHz power scope are employed for power loss measurement. An example of acquired voltage

and current data is shown in Figure 8-5, where the ringing ripple induced at the voltage steps is visible. Equivalent to (8-5), the total iron loss can also be directly expressed by

$$\overline{P_{\text{iron}}} = \frac{N_{\text{main}}}{N_{\text{sense}} V_{\text{core}} \rho_{\text{iron}}} \int_0^{1/f_{\text{PWM}}} V_{\text{sense}} I_{\text{main}} \cdot dt \qquad \text{[W/kg]} \qquad (8\text{-}7)$$

where the V_{core} is the toroidal core volume.

To ensure the measurement accuracy, a modified iron loss measurement method based on partial cancellation concept [192] is implemented. As shown in Figure 8-2, a reference air core is connected in series with the toroidal core under test.

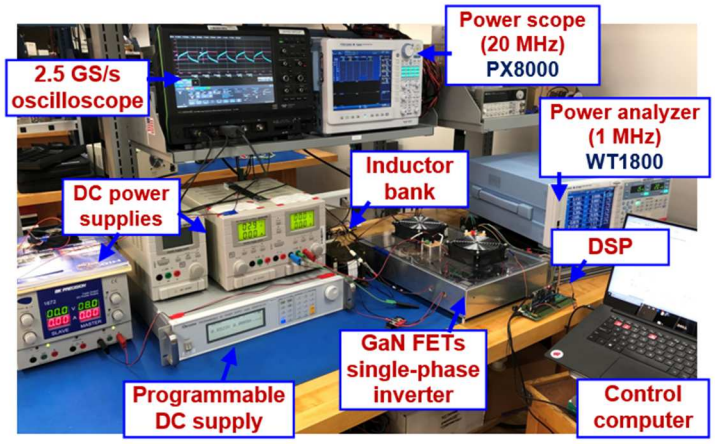

(a)

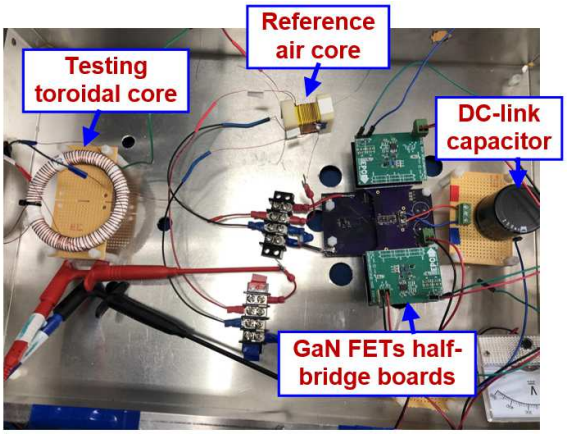

(b)

Figure 8-4: (a) Experimental test configuration; (b) Expanded view of the GaN-FET single-phase inverter and toroidal core under test.

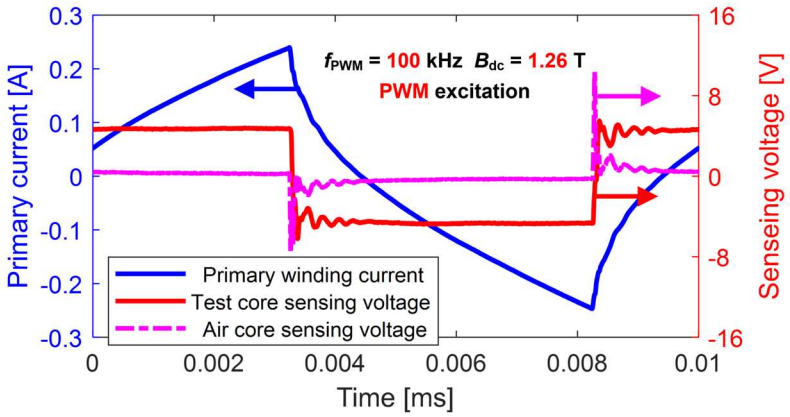

Figure 8-5: Collected current and voltage waveform data from the GaN-based measurement system for an operating condition with 100 kHz f_{PWM}.

Once two voltage probes for V_{sense} and V_{air} are properly calibrated using the de-skew function, the measurement error caused by the voltage and current phase shift deviation can be minimized using (8-8), where the correction factor k_{cor} is determined by the ratio of two voltages in their rms values. The air core sensing voltage V_{air} is depicted in Figure 8-5 for the same example case.

$$\overline{P_{iron}} = \frac{N_{main}}{N_{sense} V_{core} \rho_{iron}} \left(\int_0^{1/f_{PWM}} V_{sense} I_{main} \cdot dt - k_{cor} \int_0^{1/f_{PWM}} V_{air} I_{main} \cdot dt \right) \quad (8\text{-}8)$$

$$k_{cor} = \frac{rms(V_{sense})}{rms(V_{air})} \quad (8\text{-}9)$$

Figure 8-6 presents the measured iron loss vs. dc-bias field B_{dc} at 50 and 200 kHz, respectively, and the ac magnetic flux density amplitude B_{ac} is 10 mT. The results collected from the 20 MHz power-scope show very good agreement with the iron loss values given by oscilloscope using (8-6) or (8-7) over the entire analyzed PWM frequency range, where the average difference is around 3%. In addition, a 5-degree fictitious phase error $\Delta\varphi_i$ has been added to the measured current waveforms, and the calculated results using (8-8) are overlaid. As can be seen, the results from (8-8) are not sensitive to the phase shift error, validating the system measurement accuracy even in heavily saturated regions. To minimize the impact of potential phase shift errors, the phase shift between the voltage and current data collected from the oscilloscope is compensated during post-processing to deliver the same power loss value given by (8-8).

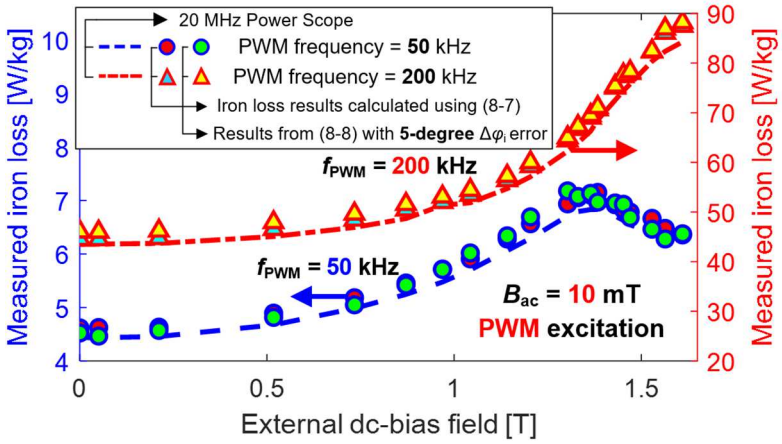

Figure 8-6: Measured iron loss values vs. dc-bias field B_{dc} for two PWM frequencies (f_{PWM} = 50 & 200 kHz) and flux ripple amplitude B_{ac} = 10 mT.

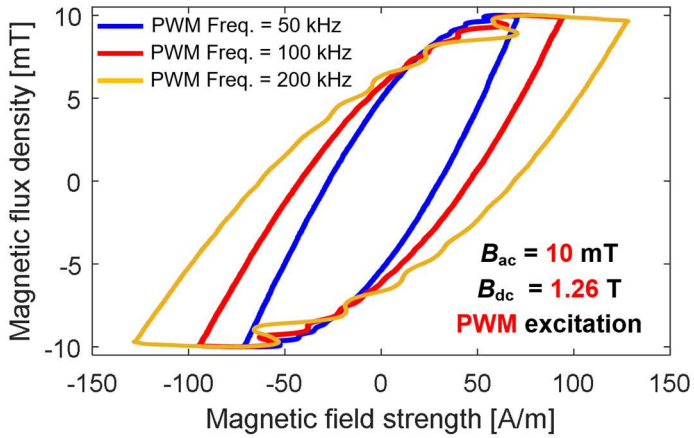

Figure 8-7: Example of measured dynamic hysteresis loops at 3 f_{PWM} values (B_{ac}=10 mT).

Next, the dynamic hysteresis loops (Figure 8-7) can be constructed using (8-3) and (8-4) over a wide range of frequencies and dc-bias fields. As shown in Figure 8-7, the loop enclosed area expands significantly as the frequency increases, indicating that the dynamic eddy-current loss becomes dominant in the high PWM frequency range (i.e., $f_{PWM} \geq 50$ kHz).

To better investigate the iron loss variation trend over a wide frequency range, normalized dc-bias iron loss scaling factors $k_{scaling}$ defined by (8-10) are presented in Figure 8-8 at four selected PWM frequencies, where the iron loss values are calculated by (8-8) using oscilloscope data.

$$k_{\text{scaling}} = \frac{\text{Measured/predicted iron loss } (@\ B_{\text{dc}})}{\text{Measured/predicted iron loss } (@\ B_{\text{dc}} = 0)} \tag{8-10}$$

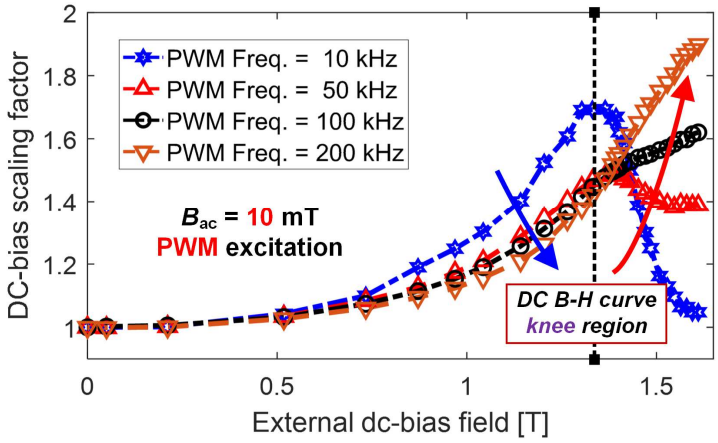

Figure 8-8: Measured dc-bias iron loss scaling factor $k_{scaling}$ vs. dc-bias field B_{dc} for four PWM switching frequency f_{PWM} values with B_{ac} = 10 mT.

As can be observed in Figure 8-8, the iron loss gradually increases for all the cases until the dc-bias field reaches the knee of the *B*-*H* curve at ~1.38 T, and the iron loss for the lowest frequency (i.e., f_{PWM} = 10 kHz) is the most susceptible to the external dc-bias field. However, the loss curves behave much differently after the knee point is reached for the four frequencies. While the iron loss value decreases sharply beyond the knee region at lower frequencies, it continues increasing when the frequency is over 100 kHz, confirming that frequency has a major impact on the iron loss properties of magnetic materials.

There is a general tendency observed in Figure 8-8 for the iron loss scaling factors to asymptote to a constant value as the dc-bias field drives the material into the heavily saturated region (i.e., $B_{dc} \geq 1.6$ T) except for the f_{PWM} = 200 kHz case. A possible explanation for this asymptote phenomenon is that the magnetic domain structure remains almost unchanged in that region as f_{PWM} varies, making the material less sensitive to the B_{dc} value.

Next, Figure 8-9 presents the iron loss variation trend vs. dc-bias field with varying flux density amplitudes at f_{PWM} = 100 kHz. Generally, the iron loss increases with the dc-bias field for all five amplitudes, but the rate of the iron loss increase drops noticeably after B_{dc} exceeds the knee value.

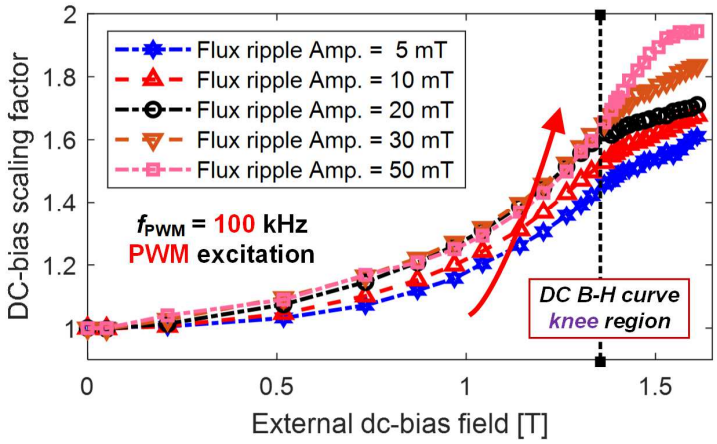

Figure 8-9: Measured dc-bias iron loss scaling factor $k_{scaling}$ vs. dc-bias field B_{dc} for four flux ripple amplitude Bac values with f_{PWM} = 100 kHz.

Although the impact of the dc-bias field is similar for all 4 amplitudes, the ac flux ripple with larger amplitude is more sensitive to the external magnetic field, indicating that it is necessary to analyze each minor loop individually rather than using the Fourier decomposition method in the frequency domain.

In summary, both the external dc-bias field and high PWM frequency exert a substantial impact on the material's magnetic and iron loss properties. However, the complex magnetic domain properties and the nonlinear cross-coupling exhibited by high-frequency skin-effect behavior make it challenging to execute physics-based iron loss modeling. Instead, experimental material characterization turns out to be a more practical approach.

Furthermore, the same analysis has been extended to two more lamination steel samples given in Figure 4-17(a)-(b) (Two toroidal samples with fewer windings turns) with different single sheet thickness at 0.25 and 0.27 mm, respectively. Although these two materials are designed for traction applications, the same as the 0.3 mm material, the material magnetic and iron loss properties (e.g., magnetic domain size, material compositions, etc.) can be somewhat different, which in turn, lead to different responses to the external dc-bias field over varying PWM frequencies and flux ripple amplitudes.

TABLE 8-3: KEY SPECIFICATIONS OF 0.25 MM TOROIDAL CORE FOR HIGH PWM FREQUENCY ANALYSIS

Primary winding turns N_{main}	101
Sensing winding turns N_{sense}	98
DC-bias winding turns N_{dc}	106
Lamination thickness	0.25 mm
Number of sheets	12
Outer diameter (**OD**)	76.2 mm
Inner diameter (**ID**)	64.7 mm
Material mass density ρ_{iron}	7600 kg/m^3
Stress relief annealing process	No

TABLE 8-4: KEY SPECIFICATIONS OF 0.27 MM TOROIDAL CORE FOR HIGH PWM FREQUENCY ANALYSIS

Primary winding turns N_{main}	104
Sensing winding turns N_{sense}	103
DC-bias winding turns N_{dc}	117
Lamination thickness	0.27
Number of sheets	11
Outer diameter (**OD**)	76.2 mm
Inner diameter (**ID**)	64.7 mm
Material mass density ρ_{iron}	7600 kg/m^3
Stress relief annealing process	No

The key specifications of the toroidal cores are provided in Table 8-3 and Table 8-4. It is worth noting that, since both cores are fabricated via wire electrical discharge machining (WEDM), the negative impacts brought by the cutting process are minimized. As a result, additional stress relief annealing (SRA) process is not implemented. Nevertheless, it has been verified that the material magnetic and iron loss properties match the data provided by the steel manufacturer, confirming the validity of the WEDM approach.

Similar to the toroidal core shown in Figure 8-3(a), relatively small number of turns (i.e., N_{main} around 100 turns) are wound in the primary winding to save sufficient space in between adjacent turns to minimize the stray capacitance. Since the amplitude of the PWM flux ripple under test is relatively small (typically less than 50 mT), the requirement for the total magnetic field strength can be met even with a fewer number of turns compared to the toroidal core designed for fundamental field analysis presented in Chapter 3 and 4 (i.e., $N_{main} > 300$ turns).

Figure 8-10(a)-(d) present the comparisons of the measured iron loss values versus the external dc-bias field for those three steel samples under evaluation over four selected high-frequency testing conditions. In general, three materials exhibit similar but not identical variation trends within the studied dc-bias field range. Initially, as the dc-bias field increases, the iron loss values

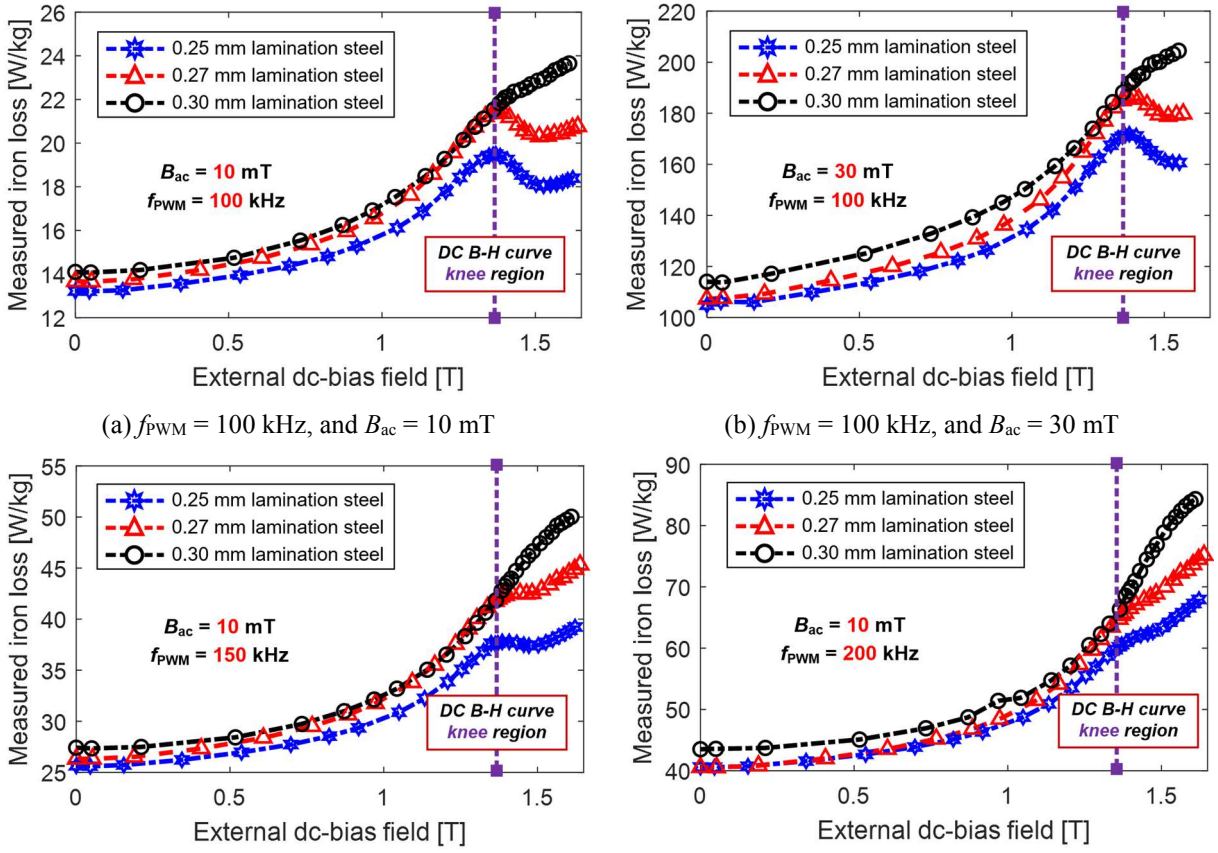

(a) f_{PWM} = 100 kHz, and B_{ac} = 10 mT

(b) f_{PWM} = 100 kHz, and B_{ac} = 30 mT

(c) f_{PWM} = 150 kHz, and B_{ac} = 10 mT

(d) f_{PWM} = 200 kHz, and B_{ac} = 10 mT

Figure 8-10: Comparisons of the measured iron loss value versus external dc-bias filed B_{dc} of small-amplitude PWM flux ripple for three different lamination steels over four selected operating conditions.

for all the studied materials become larger, while the specific variation trend of each material beyond the dc *B-H* curve knee point exhibits notable differences. It should be noted that, with extremely high PWM excitation frequencies (i.e., $f_{PWM} \geq 100$ kHz), the lamination sheet thickness appears to be a major factor determining the iron loss values. Since the eddy current loss is considered as the dominant iron loss component, shrinking the sheet thickness can effectively reduce the iron loss values over the entire studied dc-bias field range. However, despite the fact that iron loss values decrease with the sheet thickness, the existence of the external dc-bias field applies a significant impact on the resulting iron loss, making it critically important to consider the dc-bias field impact during the iron loss estimation.

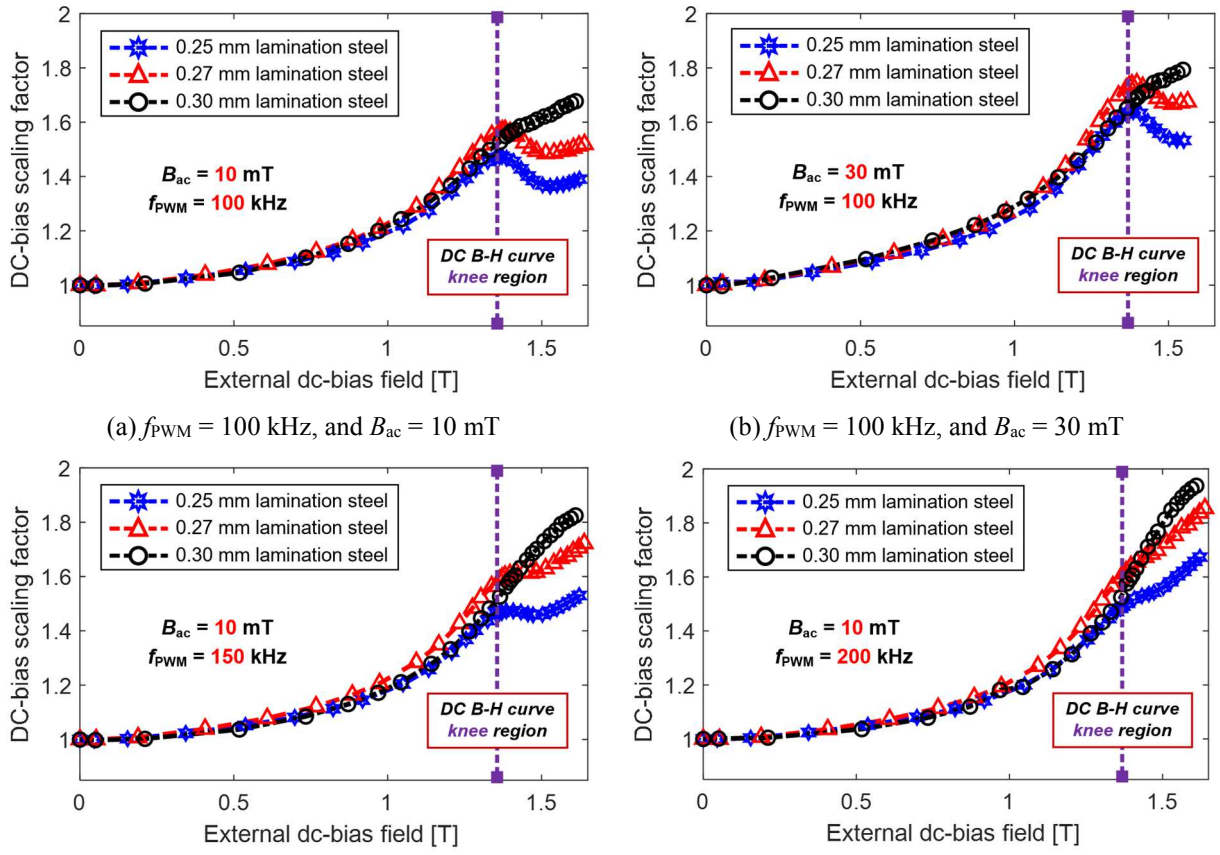

(a) f_{PWM} = 100 kHz, and B_{ac} = 10 mT

(b) f_{PWM} = 100 kHz, and B_{ac} = 30 mT

(c) f_{PWM} = 150 kHz, and B_{ac} = 10 mT

(d) f_{PWM} = 200 kHz, and B_{ac} = 10 mT

Figure 8-11: Comparisons of the measured iron loss scaling factor $k_{scaling}$ versus external dc-bias filed B_{dc} of small-amplitude PWM flux ripple for three different lamination steels over four selected operating conditions.

To better reveal the variation trend of high-frequency iron loss values in the presence of dc-bias fields, Figure 8-11(a)-(d) demonstrates the comparison of the iron loss scaling factor $k_{scaling}$ defined in (8-10) under the same testing conditions given in Figure 8-10. As can be seen from Figure 8-11, the values of the scaling factor $k_{scaling}$ are almost identical for three candidate materials within the linear region regardless of the excitation frequency and flux ripple amplitude. However, different behaviors are observed as the dc-bias field moves into the heavily saturated region (i.e., B_{dc} > 1.35 T). The material with a thicker thickness (e.g., 0.30 mm vs. 0.25 mm material) is more sensitive to the dc-bias field, indicating that the material iron loss properties in the saturated region are tightly related to the lamination sheet thickness.

In summary, both the external dc-bias field and high PWM frequency exert a substantial impact on the material's magnetic and iron loss properties. However, the complex magnetic domain properties and the nonlinear cross-coupling exhibited by high-frequency skin-effect behavior make it challenging to execute physics-based iron loss modeling. Also, lamination sheet thickness can apply different such impacts on the material iron loss characteristics in the linear and saturated region, involving more considerable uncertainties in the iron loss analysis. Instead, experimental material characterization turns out to be a more practical approach. In the next section, a new frequency-interconnected *J-A* model is presented explicitly for PWM iron loss estimation during excitation with WBG-based inverters.

8.3 Development of Frequency-Interconnected Dynamic Jiles-Atherton Model

A modified dynamic *J-A* model based on the static *J-A* model [57] is proposed in Chapter 6, providing insight into the magnetization process and enabling the PWM-induced iron loss estimation for given PWM frequency and dc-bias field. However, that model exhibits no sensitivity to frequency. Therefore, a new dynamic *J-A* model is proposed in this section that incorporates the effects of high excitation frequencies and varying dc-bias fields on PWM-induced minor loops.

The proposed model retains the key features of the static *J-A* model, which decomposes the total magnetization M into a reversible component M_{rev} due to the domain wall bowing, and an irreversible component M_{irr} responsible for the domain wall pinning effect. The key *J-A* model equations include [57]:

$$M = M_{\text{rev}} + M_{\text{irr}} \tag{8-11}$$

$$M_{\text{rev}} = c \cdot (M_{\text{an}} - M_{\text{irr}}) \tag{8-12}$$

where the reversibility coefficient c determines the relative proportion of the reversible magnetization, and M_{an} is the anhysteretic magnetization given by the Langevin function:

$$M_{\mathrm{an}} = M_s \cdot [\coth\left(\frac{H_e}{\boldsymbol{a}(f_{\mathrm{PWM}})}\right) - \frac{\boldsymbol{a}(f_{\mathrm{PWM}})}{H_e}] \tag{8-13}$$

$$H_e = H + \alpha \cdot M \tag{8-14}$$

where M_s is the saturation magnetization, $\boldsymbol{a}(f_{\mathrm{PWM}})$ is the form factor that influences the slope and shape of the anhysteretic magnetization, H_e is the effective magnetic field strength, and α represents intensity of the magnetic domain interaction.

The irreversible magnetization component is defined as

$$\frac{dM_{\mathrm{irr}}}{dH_e} = \delta_M \cdot \frac{M_{\mathrm{an}} - M_{\mathrm{irr}}}{\boldsymbol{k}(f_{\mathrm{PWM}})\delta} \tag{8-15}$$

$$\delta_M = \frac{1}{2} \cdot (1 + \mathrm{sign}(M_{\mathrm{an}} - M) \cdot \frac{dH}{dt}) \tag{8-16}$$

where the δ_M parameter avoids a nonphysical solution when the incremental susceptibility becomes negative [16], $\boldsymbol{k}(f_{\mathrm{PWM}})$ is the pinning parameter that determines the coercive field and energy dissipation of the hysteresis loop, and $\delta = \mathrm{sign}(dH/dt)$ is the direction parameter.

Considering the physical definition of the magnetic flux density, $B = \mu_0(H + M)$, equations (12)-(17) summarizing the general magnetization process can be reduced to (18) which adopts the magnetic flux density B as the input variable:

$$\frac{dM}{dB} = \frac{\delta_M(M_{\mathrm{an}} - M) + c\boldsymbol{k}\delta\frac{dM_{an}}{dH_e}}{\mu_0[\boldsymbol{k}\delta + (1 - \alpha) \cdot \left(\delta_M(M_{an} - M) + c\boldsymbol{k}\delta\frac{dM_{an}}{dH_e}\right)]} \tag{8-17}$$

Next, the hysteresis loop expansion due to the dynamic field dB/dt is incorporated into the final solution via (19):

$$H_{\mathrm{tot}}(t) = H\big(B(t)\big) + \boldsymbol{k_d}(f_{\mathrm{PWM}})\left|\frac{dB(t)}{dt}\right|^{v_d} \tag{8-18}$$

where $H(B(t))$ is the solution calculated from the static *J-A* model, and $\boldsymbol{k_d}(f_{\mathrm{PWM}})$ and v_{d} are the lumped dynamic loss coefficient and its time dependence coefficient, respectively.

Summarizing, seven parameters a, c, α, k, M_s, k_d, and ν_d must be identified in the proposed model. The PWM frequency range selected in this analysis is from 10 to 200 kHz, making it possible to thoroughly investigate the iron loss properties of lamination steels and electric motors excited by WBG-based VSIs. The reference ac flux ripple amplitude B_{ref} is maintained at 10 and 30 mT, which is consistent with the underlying assumption that the impact of the PWM-induced flux ripples on the major magnetic field condition is negligible. Also, the small-amplitude minor loop itself can be assumed to have a symmetrical shape over varying dc-bias fields up to 1.61 T. Moreover, since the dc-bias field B_{dc} plays a critical role in determining the magnetic conditions, these parameters have been characterized for each dc-bias field via measured dynamic hysteresis loops using nonlinear least-square optimization.

As suggested in Figure 8-7, the anhysteretic curve, coercive field, and enclosed area (i.e., energy dissipation) all vary substantially with f_{PWM}. As a result, parameters a, k, and k_{d} are considered to be frequency-dependent in the proposed model and are updated at each PWM frequency. The remaining coefficients except M_s are evaluated at the lowest PWM frequency (i.e., 10 kHz) and held constant throughout the entire frequency range. Instead of retaining the definition of M_{s} in the original *J-A* model as the major field saturation magnetization, the value of M_{s} is maintained constant to generate an equivalent magnetic flux density at 0.1 T (B_{ref} = 10 mT) or 0.3 T (B_{ref} = 30 mT) for all of the cases to mimic the impact of saturation on the shape of minor loops. Figure 8-12(a)-(c) plot the values of the three frequency-dependent parameters with B_{ref} at 10 mT for six selected PWM frequencies including 10, 30, 50, 100, 150, and 200 kHz and varying dc-bias fields up to 1.61 T. The variation trends of these parameters reflect key characteristics of the measured hysteresis loop shapes and enclosed areas, providing an appealing physics-based modeling perspective.

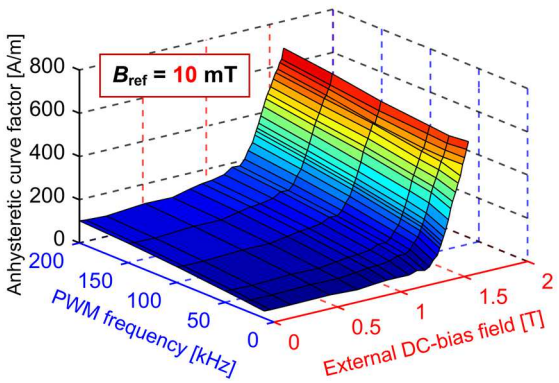

(a) Anhysteretic curve form factor a

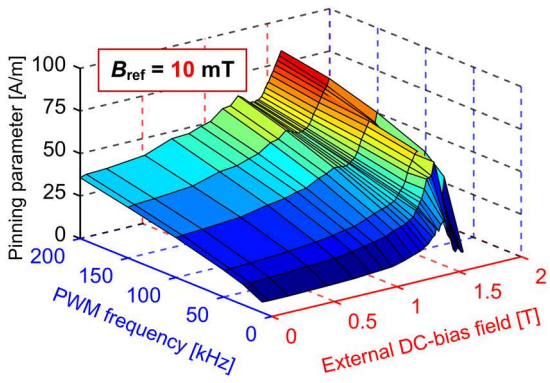

(b) Pinning effect parameter k

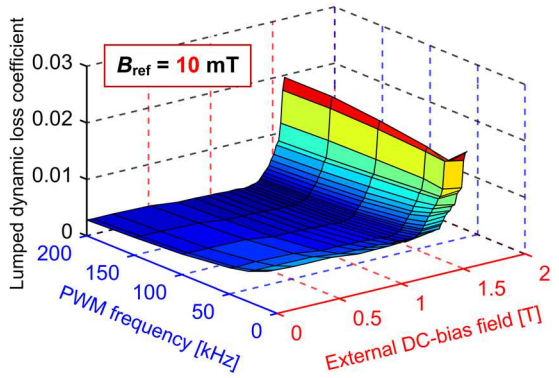

(c) Lumped dynamic loss coefficient k_d

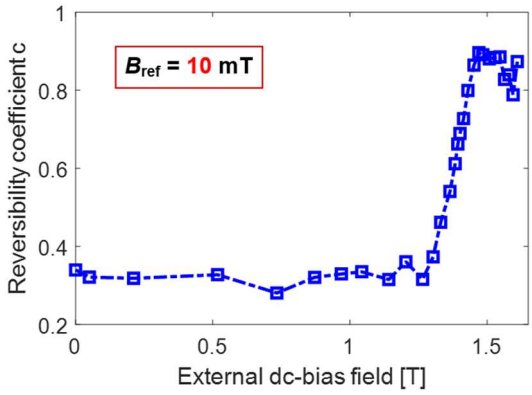

(d) Reversibility coefficient c

Figure 8-12: Measured frequency-dependent parameters of the proposed frequency-interconnected dynamic *J-A* model plotted vs. PWM switching frequency f_{PWM} and dc-bias field B_{dc}.

In addition, 2-D interpolation techniques can be applied to these data to extract the parameter values for any desired operating point that falls inside the plotted surface, reducing the stored data requirements significantly and making the model easily applicable over a wide range of f_{PWM} values. A similar 1-D interpolation approach can be utilized to determine the values of the other three dc-bias field dependent parameters c, α, and ν_d, and an example is provided in Figure 8-12(d) for reversibility coefficient c. As a result, the proposed *J-A* model is well suited for fast and convenient PWM iron loss modeling, and its accuracy and extendability will be evaluated in the next section. Since the surface data properties and parameter identification process with B_{ref} at 30 mT are very similar to the results presented in Figure 8-12, they are not provided in this thesis.

8.4 Experimental Evaluation of Proposed PWM-Induced Iron Loss Estimation Model

8.4.1 Model's scalability to different flux ripple amplitudes

In the preceding section, the parameters of the proposed frequency-interconnected *J-A* model have been experimentally identified over varying PWM frequencies with the reference ac flux ripple amplitude B_{ref} maintained at 10 and 30 mT. However, in actual applications, the ripple amplitude can vary significantly as the operating conditions change, including but not limited to changes in fundamental field amplitude and frequency, PWM switching frequency, and inverter modulation index. Therefore, it is critically important to evaluate the model's performance when the analyzed ripple amplitude deviates from that of the reference case. Depending on the flux ripple amplitude, a specific set of parameters is selected based on the following rule for predicting the dynamic hysteresis loop and its corresponding iron loss,

$$\begin{cases} \text{Parameters from 10 mT ref. case, if } B_{\text{ac}} < 20 \text{ mT}, \\ \text{Parameters from 30 mT ref. case, if } B_{\text{ac}} \geq 20 \text{ mT}. \end{cases} \tag{8-19}$$

The parameters obtained at 10 and 30 mT have been applied to estimate the hysteresis loops and iron losses for different flux ripple amplitudes (i.e., B_{ac} ranges from 5 up to 50 mT) for 0.30 mm lamination steel at 100 kHz. For a selected dc-bias field at 1.38 T, comparison results from Figure 8-13(a)-(b) have confirmed that the proposed model can accurately emulate the actual shape and enclosed area of the hysteresis loops for varying amplitudes. Despite the increase of flux ripple amplitude, the overall shape (e.g., slope) is almost identical, indicating that the key properties of the minor loop are dominated by the external dc-bias field. As a result, these observations suggest that the parameters identified from the reference case can be extended to other flux ripple amplitudes since they share similar magnetic properties.

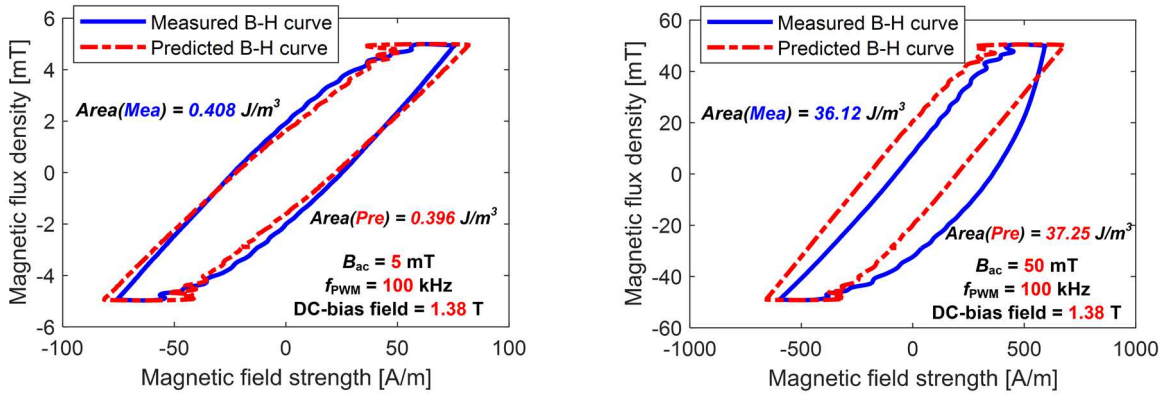

(a) B_{ac} = 5 mT, f_{PWM} = 100 kHz, and B_{dc} = 1.38 T (b) B_{ac} = 50 mT, f_{PWM} = 100 kHz, and B_{dc} = 1.38 T

Figure 8-13: Model evaluation comparing measured and simulated dynamic hysteresis loops and iron losses for f_{PWM} = 100 kHz minor loop at 1.38 T dc-bias field B_{dc} with varying ac flux ripple amplitudes.

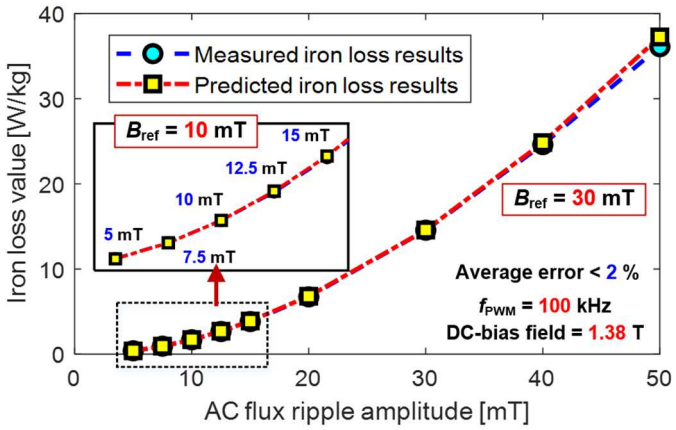

Figure 8-14: Comparison of measured and predicted PWM iron loss values vs. ac flux ripple amplitude B_{ac} from 5 to 50 mT at f_{PWM} = 100 kHz and 1.38 T B_{dc}.

This hypothesis has been validated by the results presented in Figure 8-14 using measured data, where the average error of the proposed model over a wide range of amplitudes is < 2%, where the parameters obtained from 10 and 30 mT reference case are applied to two different region as expressed by (8-19).

Furthermore, the measured and predicted iron loss results with 5 and 50 mT ac flux ripple at 100 kHz have been compared over the entire dc-bias field range in Figure 8-15. The average error between the measured and predicted iron loss values is < 3% for both cases, validating the model's promising scalability. The proposed model well captures the monotonically increasing trends at both flux ripple amplitudes. In addition, the model accuracy has been thoroughly verified at other

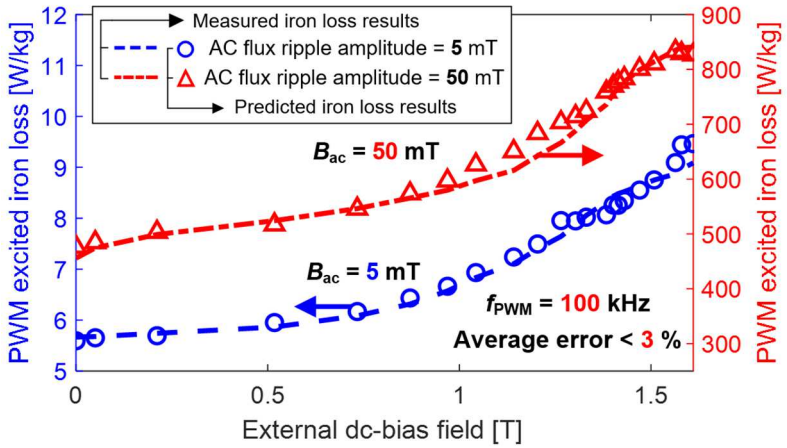

Figure 8-15: Comparison of measured and predicted PWM-induced iron loss with ac flux ripple B_{ac} = 5 & 50 mT and f_{PWM} = 100 kHz vs. external dc-bias field B_{dc}.

amplitudes (e.g., B_{ac} = 20 and 40 mT), making it possible to predict the PWM-induced iron loss over varying operating conditions with limited input characterization data. In general, the model shows preferable accuracy when the studied ripple amplitude is closer to the reference value. However, introducing more reference cases add the burden on material characterization effort.

8.4.1 Model's extendability to different flux ripple frequencies

Next, the model's frequency extendability is investigated. One of the motivations is the growing availability of WBG-based inverters that is making it more feasible to adjust the PWM switching frequency over a much wider range. In order to achieve optimum system-level efficiency, it calls for an iron loss tool that can be applied to any desired PWM frequency.

Figure 8-16 plots the measured and predicted iron loss results over the analyzed dc-bias field range with 10 mT ac flux ripple at f_{PWM} = 75 and 175 kHz. As noted previously, the 'static' coefficients are characterized at 10 kHz and only the 3 frequency-dependent parameters in Figure 8-12(a)-(c) are used for *B*-*H* curve prediction, and the loop area provides the iron loss predictions. The comparison results confirm that the model is not only capable of accurately predicting the PWM iron loss, but also presenting the measured trends in iron loss variation vs. dc-bias field B_{dc} over a wide range of f_{PWM} values, where the iron loss behaviors are much different in saturated

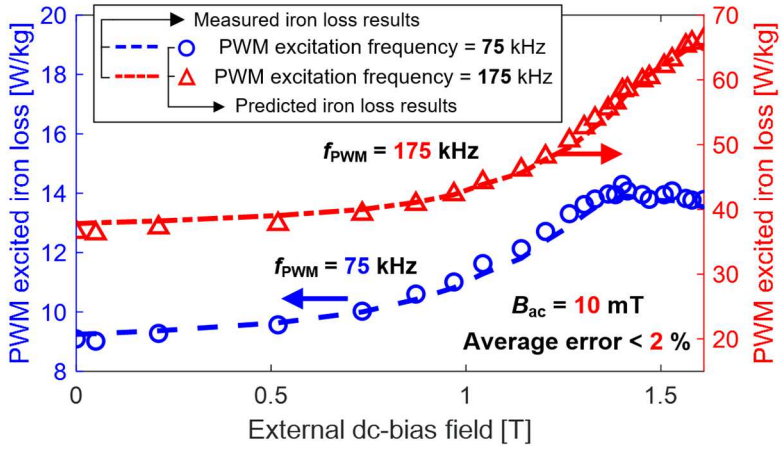

Figure 8-16: Comparison of measured and predicted PWM-induced iron loss with flux ripple B_{ac} = 10 mT and f_{PWM} = 75 & 175 kHz vs. external dc-bias field B_{dc}.

region at two PWM frequencies. The average error for both cases is below 2%, validating the model's appealing frequency extendability.

8.5 Total Iron Loss Analysis for WBG-Based Inverter Excitation

After confirming that the proposed model can be applied to estimate the PWM-induced iron loss over a wider range of different flux ripple amplitudes and frequencies, the technique is now extended to estimate the PWM-induced iron loss in the presence of a fundamental frequency field.

8.5.1 Prediction of total iron loss under PWM voltage excitation

To produce the example *B* and *H* time-domain waveforms shown in Figure 8-17, the GaN-FET single-phase inverter presented in Figure 8-4(b) delivers a bipolar PWM voltage that results in peak fundamental field of 1.3 T at 200 Hz with f_{PWM} =100 kHz. While though the fundamental *B* flux density has a sinusoidal waveshape, PWM operation adds 100 kHz high-frequency flux ripple riding on top of the fundamental field. The zoomed-in region in Figure 8-17 shows that the amplitude of the fundamental *B* field remains nearly constant during each PWM cycle, consistent with the dc-bias field assumption made in (8-2).

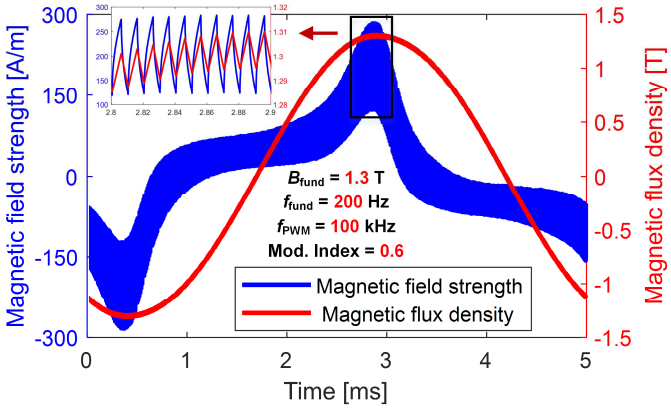

Figure 8-17: Example of collected magnetic field strength (H) and flux density (B) data for bipolar PWM voltage excitation with 100 kHz switching frequency.

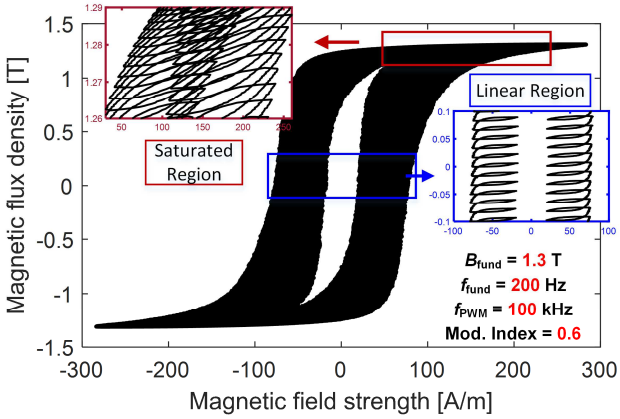

Figure 8-18: Measured hysteresis loop under bipolar PWM voltage excitation with 100 kHz PWM switching frequency (B_{fund} = 1.3 T & f_{fund} = 200 Hz) and 0.6 modulation index.

The corresponding hysteresis loop is given in Figure 8-18, including two zoomed-in regions that illustrate the minor loop properties in localized B-H curve regions. It can be seen that although the PWM switching frequency f_{PWM} is maintained constant, the amplitude and waveshape of the minor loops varies significantly in these two regions. In order to better incorporate the minor loop's actual characteristics into the PWM iron loss modeling, a generalized total iron loss estimation algorithm developed in Chapter 6 (See Figure 6-27) is implemented, where the PWM-induced field B_{PWM} is segregated from the measured magnetic field B_{mea} via (8-20).

$$B_{\mathrm{PWM}}(t) = B_{\mathrm{mea}}(t) - \sum_{n=1}^{n_{\mathrm{main}}} A_n \cos(2\pi n f_{\mathrm{fund}} t + \phi_n) \tag{8-20}$$

where n_{main} is the number of Fourier components that can sufficiently represent the fundamental field, and A_n and ϕ_n are the amplitude and phase information from Fourier decomposition.

Different from conventional Fourier analysis, only the fundamental field is subtracted from the total magnetic field, permitting the proposed algorithm to preserve the ripple waveshape for its input. The equivalent dc-bias field for each PWM cycle is calculated based on the identified major field using (8-2). In order to determine the total iron loss, a generalized dynamic hysteresis model developed in Chapter 3 and 4 is employed for fundamental field iron loss estimation. The sum of predicted loss values from these two widely-separated frequency regions represents the total predicted iron loss for PWM voltage excitation.

8.5.2 Impact of fundamental field amplitude

For electric machine applications, the magnetic field distribution is complicated and varies significantly in different areas. The fundamental field is typically driven to the saturated region in stator teeth (i.e., $B_{\text{fund}} \geq 1.5$ T), whereas it falls within the linear region in stator back iron. Therefore, in this section, the impact of the fundamental field amplitude on PWM-induced iron loss is investigated.

Figure 8-19(a)-(c) provide a comparison of the measured total iron loss results at 200 Hz fundamental frequency over a broad PWM switching frequency range with the predicted values at two selected modulation index values (i.e., different flux ripple amplitudes). The fundamental field amplitude B_{fund} ranges from 0.62 to 1.52 T, covering both the linear and saturated region. It should be noted that, in order to drive the fundamental field into the saturated region while maintaining the flux density waveform in sinusoidal shape, the input winding voltage command is compensated via close-loop feedback control discussed in Chapter 3 to account for the nonlinear voltage drop due to the primary winding resistance.

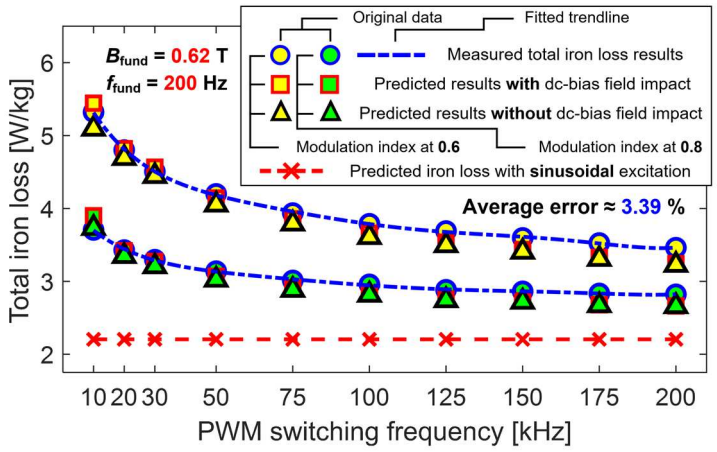

(a) B_{fund} = 0.62 T and f_{fund} = 200 Hz

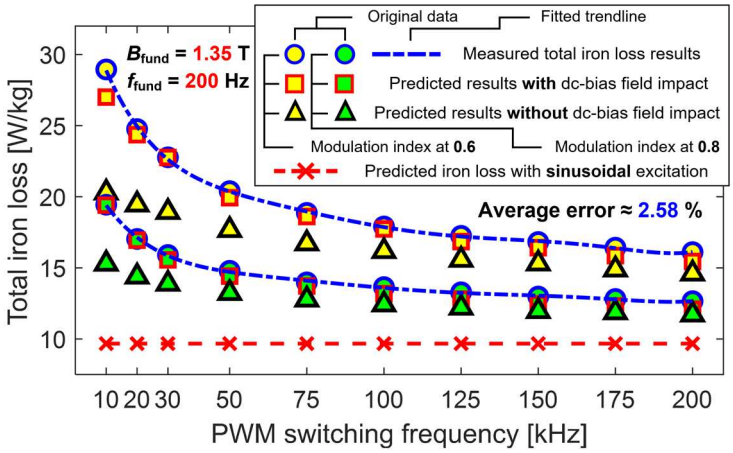

(b) B_{fund} = 1.35 T and f_{fund} = 200 Hz

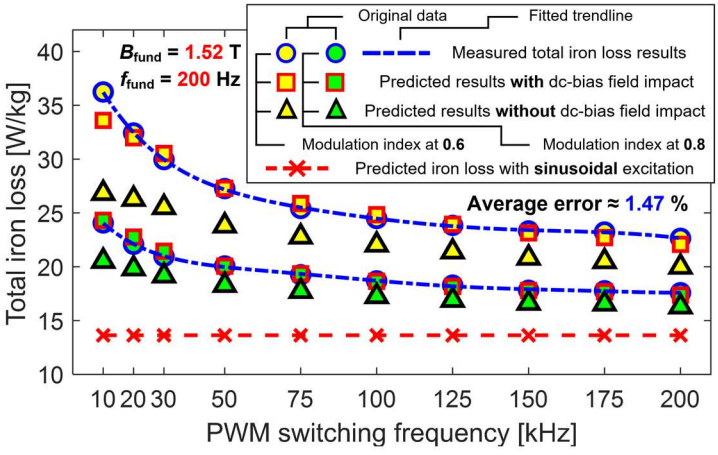

(c) B_{fund} = 1.52 T and f_{fund} = 200 Hz

Figure 8-19: Comparison of measured and predicted total iron loss results under PWM voltage excitation over different fundamental field amplitudes at f_{fund} = 200 Hz with and without including the dc-bias field effect.

These results show that the proposed model can accurately estimate the total iron loss over the entire PWM frequency range with an average error below 5% over different fundamental field amplitudes. When the fundamental field operates in its linear region with B_{fund} at 0.62 T (See Figure 8-19(a)), the impact of the external dc-bias field is negligible, where the prediction results with and without considering dc-bias field are almost identical. Both measured and predicted results are consistent with the trends depicted in Figure 8-8 and Figure 8-9. However, as the fundamental field increases, large iron loss underestimation is observed for prediction values without considering the dc-bias field effect. Moreover, lower PWM frequency and modulation index values both increase the flux ripple amplitude, which, in turn, aggravates the impact of ignoring the dc-bias field on the resulting error. As a result, the iron loss underestimation is more considerable when the PWM frequency f_{PWM} is below 50 kHz. However, the prediction error diminishes substantially as f_{PWM} increases, indicating that the dc-bias field effect is less significant at higher PWM switching frequencies.

Figure 8-20(a)-(c) depict the comparison of the measured waveforms under PWM excitation with the predicted dynamic hysteresis loop over different fundamental field amplitudes. It has confirmed that the model proposed in Chapter 3 and 4 exhibits an appealing capability to determine the overall hysteresis loop shape. Also, as shown in three zoomed-in plots, the fundamental field amplitude can apply a great influence on the resulting minor loop shape, enclosed area, and iron loss value.

Despite the fact that the impact of the fundamental field varies, the total iron loss for each case decreases monotonically as f_{PWM} goes up. Taking the case in Figure 8-19(b) with 10 kHz f_{PWM} and 0.6 modulation index as an example, the PWM-induced iron loss accounts for more than 65% of the total iron loss. While, raising the PWM frequency serves as an effective means to minimize

the total iron loss by reducing the PWM harmonic losses, where the maximum loss reduction from 10 to 200 kHz approaches 50%. However, the total iron loss curves in Figure 8-19 flattens when f_{PWM} is beyond 75 kHz, diminishing the efficiency benefits from adopting an extremely high PWM frequency.

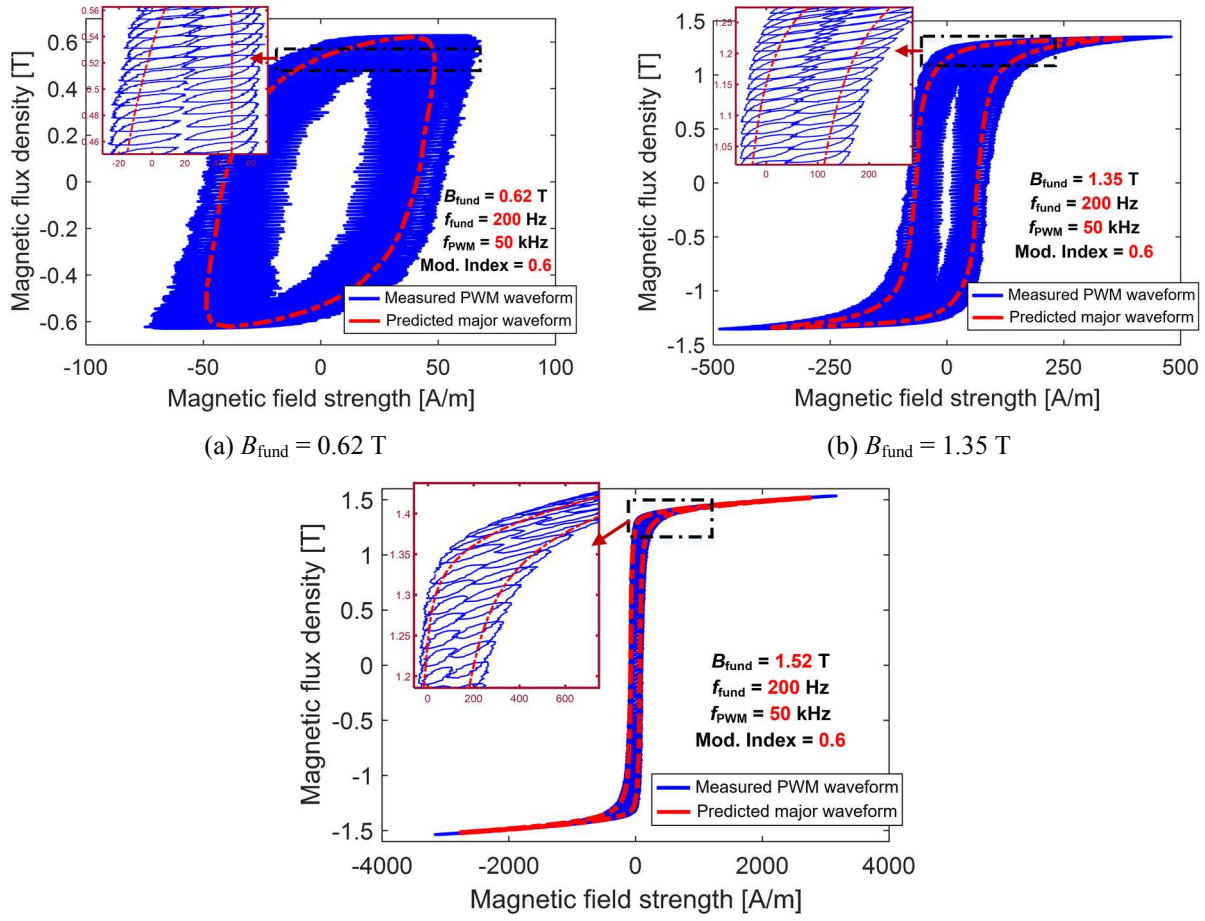

(a) B_{fund} = 0.62 T

(b) B_{fund} = 1.35 T

(c) B_{fund} = 1.52 T

Figure 8-20: Comparison of measured waveforms under PWM voltage excitation and predicted major field dynamic hysteresis loops over different fundamental field amplitudes at f_{fund} = 200 Hz and f_{PWM} = 50 kHz.

To better reveal the efficiency benefit brought by WBG-based inverters with high PWM switching frequency capability, the maximum reduction ratio of the total iron loss (i.e., iron loss value at 200 kHz f_{PWM} vs. that at 10 kHz f_{PWM}) is presented in Figure 8-21 over different fundamental field amplitudes and modulation index values. It can be seen that the iron loss reduction ratio initially increases with fundamental field and reaches its maximum value in the vicinity of the 1.35 T. After passing the peak point, the iron loss decreases sharply. This result is consistent with the observation in Figure 8-8 that the PWM-induced iron loss at 10 kHz attains its peak loss value around 1.38 T and falls rapidly after that. On the other hand, the high-frequency iron loss at 200 kHz keeps increasing over the entire dc-bias field. Therefore, the maximum total iron loss reduction ratio occurs when the fundamental field amplitude is around 1.35 T. The same trends have been observed for different modulation index values. Since the fundamental field induced iron loss can be assumed identical, the loss reduction ratio shifts downward as the PWM-induced ripple becomes smaller at higher modulation index values.

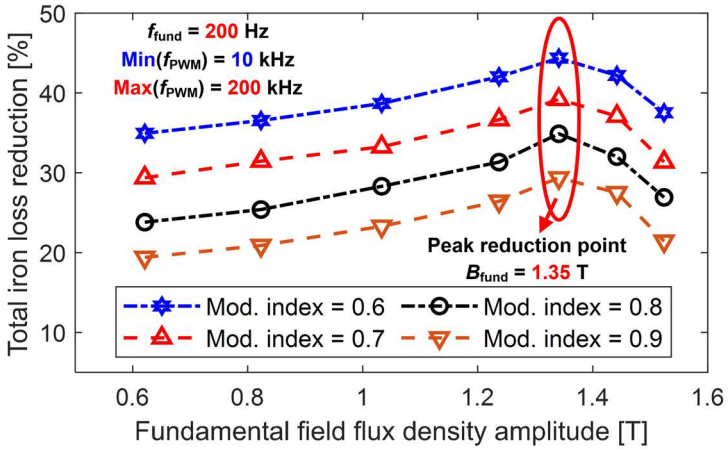

Figure 8-21: Percentage of the maximum total iron loss reduction between 10 and 200 kHz PWM switching frequency over different fundamental field amplitudes and inverter modulation index values.

8.5.3 Impact of fundamental field frequency

Next, the fundamental frequency f_{fund} has been raised to a much higher value, and the total iron loss results at 500 Hz and 1 kHz f_{fund} are presented in Figure 8-22(a)-(b), respectively. The fundamental field amplitude B_{fund} is maintained at 1.35 T. For both cases, the PWM-induced iron loss is the dominant iron loss component, which accounts for more than 50 % when the modulation index is at 0.6 even operating at the highest PWM frequency (i.e., f_{PWM} = 200 kHz). Again, the measured results match the prediction values reasonably well, confirming that the proposed model is capable of providing appealing total iron loss estimation accuracy over a broad range of fundamental frequencies.

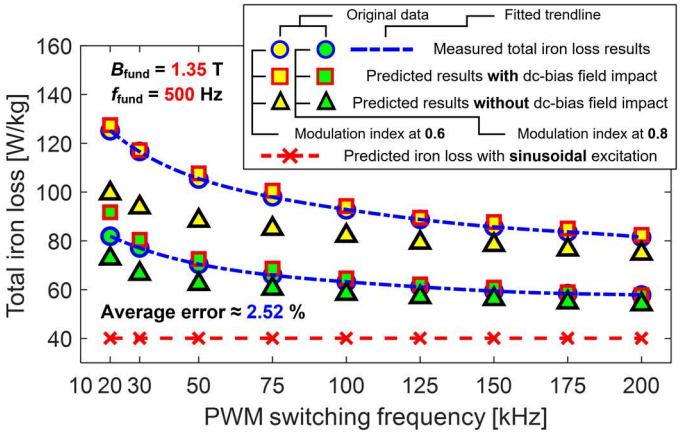

(a) B_{fund} = 1.35 T, and f_{fund} = 500 Hz

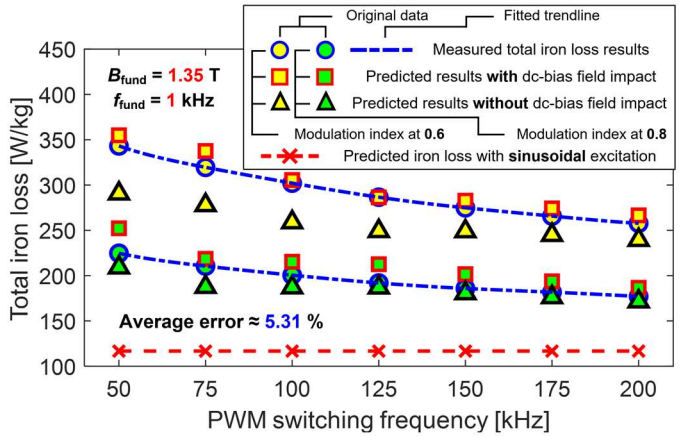

(b) B_{fund} = 1.35 T, and f_{fund} = 1 kHz

Figure 8-22: Comparison of measured and predicted total iron loss results under PWM excitation over different fundamental frequencies at Bfund = 1.35 T with and without including the dc-bias field effect.

Moreover, the results at both frequencies suggest that incorporating the dc-bias field impact into iron loss estimation is critically important to achieve satisfying accuracy. Otherwise, noticeable iron loss underestimation is observed, especially at the lower modulation index value (i.e., 0.6) with larger PWM-induced flux ripple amplitudes.

However, compared to the promising estimation accuracy at 500 Hz f_{fund} (i.e., average error ≈ 2.52%), the average error exceeds 5% at 1 kHz. One possible explanation of this phenomenon is that the fundamental field impact at such a high excitation frequency starts deviating from that at lower frequencies or dc conditions. As depicted in Figure 8-23, the major field waveform expands significantly at 1 kHz due to the eddy current. Also, the PWM harmonics apply a more substantial impact on the fundamental field compared to that under 200 Hz given in Figure 8-20(b). Therefore, the discrepancies between the predicted major waveform and measured PWM waveforms become larger in the top and bottom corner, where the magnetic field reaches its peak value. Even for the minor loops operating in the same fundamental field region (See zoomed-in plot in Figure 8-23), the shape and enclosed area are much different.

Furthermore, although the total iron loss value decreases with f_{PWM} regardless of the fundamental frequency (e.g., f_{fund} = 200 Hz or 1 kHz), the rate of decline over the studied PWM frequency is different. At lower frequencies (i.e., f_{fund} ≤ 500 Hz), the total iron loss initially decreases at a faster rate and then asymptotes to a nearly constant value. Whereas at 1 kHz, a linear dropping trend is observed. In Figure 8-24, the rate of total iron loss reduction is presented as a function of the PWM to fundamental frequency (P2F) ratio. Sharing some similarities with magnetic material's *B-H* curve given in Figure 8-1, the total iron loss reduction rate goes up linearly before the P2F ratio reaches 150. After passing that point, the reduction rate curves for all

the frequencies start saturating, suggesting that the total iron loss remains almost no change when the P2F ratio is beyond 500. As a result, for electric machines operating with extremely high fundamental frequencies (e.g., $f_{fund} \geq 1$ kHz), it will be much more challenging to push the iron loss reduction rate beyond the linear region due to some practical constraints of the VSIs, including the inverter switching loss, motor winding *dv/dt* stress, electromagnetic interference (EMI), etc.

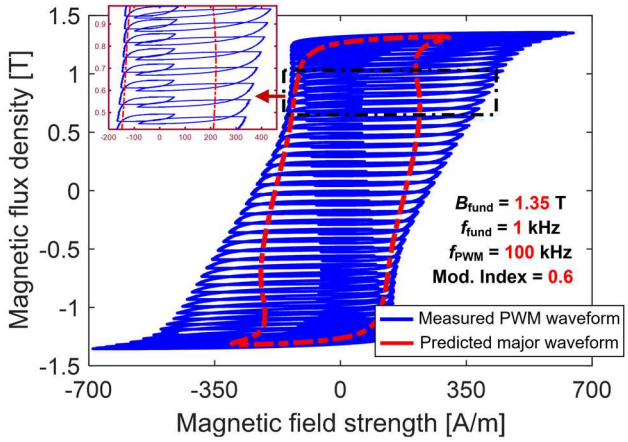

Figure 8-23: Comparison of the measured waveform under PWM voltage excitation and predicted major field dynamic hysteresis loop at B_{fund} = 1.35 T, f_{fund} = 1 kHz, and f_{PWM} = 100 kHz.

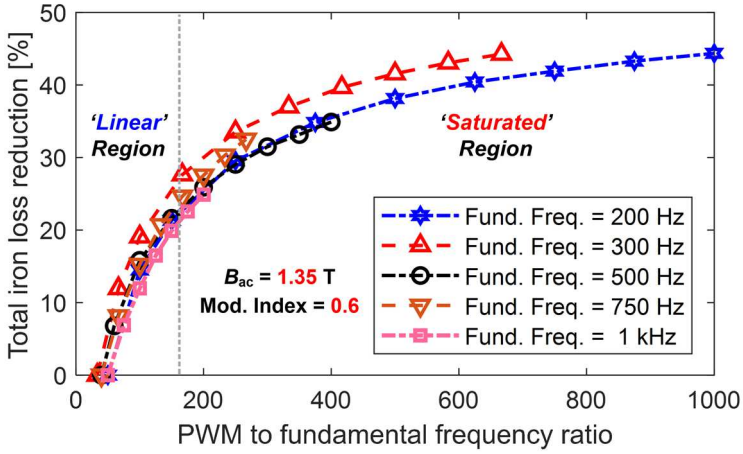

Figure 8-24: Percentage of total iron loss reduction versus PWM to fundamental frequency ratio (P2F) over different fundamental field frequencies.

8.6 Summary

This chapter has investigated the PWM-induced iron loss in lamination steels using high-frequency inverters with WBG power switches. Material characterization over a wide range of dc-bias fields and PWM frequencies has provided intriguing new insights into high-frequency iron loss characteristics as well as valuable hysteresis loop and iron loss data. Three sample materials with different sheet thicknesses have been evaluated in this study, and similar iron loss properties have been observed. By using this collected data, a new frequency-interconnected Jiles-Atherton model has been proposed that is suitable for PWM iron loss estimation under high-frequency excitation conditions with WBG-based inverters. Experimental results have confirmed the model's accuracy over a wide range of flux ripple amplitudes and frequencies with only modest input data requirements. Furthermore, the proposed model has been successfully applied to estimate the PWM-induced iron loss in the presence of fundamental frequency excitation.

It has been revealed that PWM iron loss continues to rise monotonically as the dc-bias field is increased beyond the knee point excited by extremely high PWM switching frequency (e.g., when f_{PWM} is above 100 kHz for 0.30 mm Si-steel lamination material). Even with sufficiently high PWM switching frequency, when a large amplitude fundamental field (i.e., $B_{fund} \geq 1$ T) coexists with high-frequency PWM harmonics, its average value during each switching cycle exhibits a major influence on the resulting PWM-induced iron loss. At last, WBG-based VSIs have shown promising potential to reduce the total machine iron loss by raising f_{PWM} to higher values. However, there are diminishing incremental energy savings as the P2F ratio is pushed beyond its linear region (i.e., P2F >150), making it essential to consider the combined motor and inverter losses when maximizing drive efficiency.

Chapter 9
Comparative Analysis of PWM Power Losses in IPM Machines with Different Modulation Schemes Using WBG-Based Inverters

9.1 Introduction

As presented in Chapter 7, IPM machines excited by VSIs using silicon IGBT devices have been widely adopted in traction applications. More recently, the WBG-based power switches (i.e., SiC or GaN) are experiencing increasing popularity in motor drive applications owing to a variety of promising capabilities. They enable much higher inverter-side efficiency, faster switching speeds, and elevated maximum operating temperatures, making it possible to boost the drive system power density. Although increasing the PWM switching frequency helps to suppress the PWM-induced current and torque ripple in IPM machines, the variation of machine-side PWM power loss components is not yet well understood when they are exposed to significantly higher PWM switching frequencies.

Moreover, as introduced in Chapter 2, the modulation scheme that is used to control the inverter switching events exerts a crucial impact on the resulting inverter loss, current ripple amplitude, and its frequency composition. Among available modulation schemes, space vector PWM (SVPWM) and discontinuous PWM (DPWM) are popular choices owing to their high dc-bus voltage utilization capability compared to the conventional sinusoidal PWM (SPWM). Also, the DPWM scheme leads to reduced inverter switching losses by clamping each of the output phase voltages to the positive or negative inverter bus for one-third of the fundamental cycle, resulting in increased current ripple and conduction loss as a side effect. Therefore, it is of great importance to gain deeper insights into the impact of modulation schemes on PWM power losses.

This chapter presents a comprehensive analysis of PWM power losses in IPM machines excited by WBG-based VSIs with different modulation schemes over a wide range of PWM switching frequencies. The drive system configuration and current ripple characteristics are first introduced. Then three machine-side loss estimation models are presented and subsequently applied to investigate the variation of each loss component. The predicted total PWM power losses are evaluated and subsequently compared to measured results for varying conditions to confirm the model accuracy.

9.2 PWM Current Ripple Prediction and Analysis with Different Modulation Schemes

Figure 9-1 depicts the baseline drive system configuration, including a WBG-based VSI and an IPM machine designed for traction application (Machine key specification are provided in Table 4-3). Although there are several DPWM methods (e.g., DPWM0, DPWM1, etc.) available depending on the relative timing of the zero-state clamping, DPWM2 has been adopted for this analysis since it provides minimum current ripple amplitude [141]. For DPMW2, the maximum load current in each phase coincides with its clamping period.

The voltage vector diagrams for SVPWM and DPWM2 are presented in Figure 9-2. The baseline SVPWM algorithm (i.e., symmetrical SVPWM) consists of two balanced zero voltage states (i.e., V_0 and V_7) during each switching sequence, while DPWM2 only has one zero state depending on the location of the voltage vector. Even though these two PWM algorithms provide the identical fundamental output voltage component, different zero-state distributions lead to varying current ripple amplitudes, waveshapes, and frequency compositions.

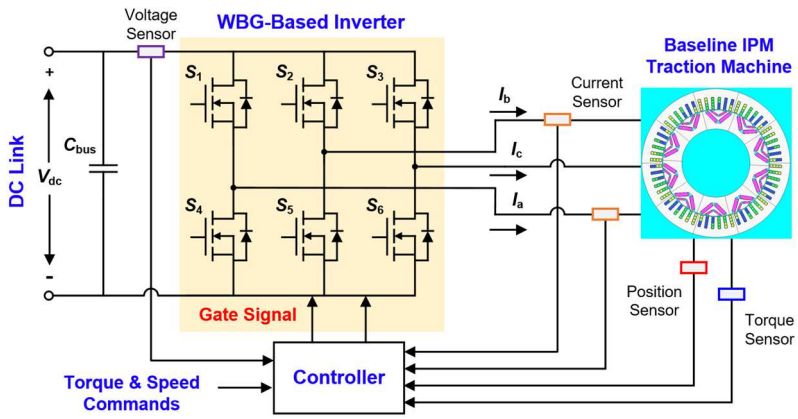

Figure 9-1: Baseline system configuration of the WBG-based ac drive system.

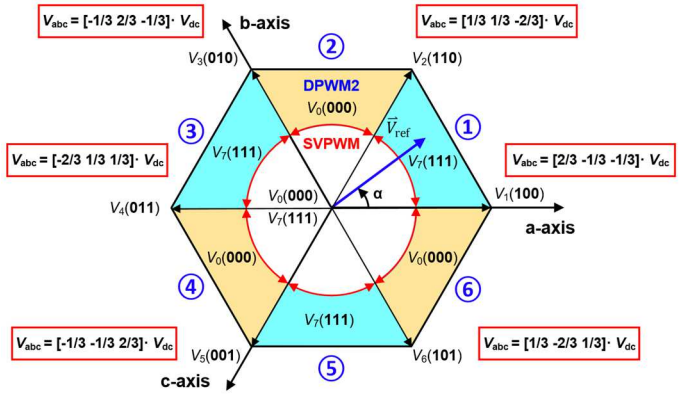

Figure 9-2: Voltage vector diagrams for SVPWM and DPWM modulation.

The analytical model developed in Chapter 5 is implemented to estimate the PWM-induced current ripple using different modulation schemes. The instantaneous voltage difference between the inverter-side output voltage and the machine-side average voltage determines the current ripple slope over a fundamental period. The key equations in the *dq* frame are:

$$\begin{bmatrix} \frac{di_d}{dt} \\ \frac{di_q}{dt} \end{bmatrix} = \left(L_{\text{IPM}}^{\text{Dyn}}\right)^{-1} \cdot \begin{bmatrix} v_{d_{\text{inv}}}(t) - \overline{v_{d\,\text{IPM}}(T_s)} \\ v_{q_{\text{inv}}}(t) - \overline{v_{q\,\text{IPM}}(T_s)} \end{bmatrix} \tag{9-1}$$

$$v_{d\,\text{IPM}}(t) = R_s i_d(t) + \frac{d\psi_d(i_d, i_q, \theta)}{dt} - \omega_e \psi_q(i_d, i_q, \theta)) \tag{9-2}$$

$$v_{q\,\text{IPM}}(t) = R_s i_q(t) + \frac{d\psi_q(i_d, i_q, \theta)}{dt} + \omega_e \psi_d(i_d, i_q, \theta) \tag{9-3}$$

where $L_{\mathrm{IPM}}^{\mathrm{Dyn}}$ is the dynamic inductance of the IPM machine calculated by 2-D FEA using a small perturbation method, $v_{d_{\mathrm{inv}}}$and $v_{q_{\mathrm{inv}}}$ are the instantaneous inverter output voltages in the *dq* rotor reference frame transformed from the *abc* frame voltages given in Figure 9-2, and $\overline{v_{d_{\mathrm{IPM}}}(T_s)}$ and $\overline{v_{d_{\mathrm{IPM}}}(T_s)}$ are the average machine *dq* voltages for a given PWM switching cycle T_s. Three-phase current ripple is obtained via the *dq0-abc* transformation by concatenating the predicted linear segments.

Next, this model is applied to predict the current waveforms during PWM voltage excitation. As shown in Figure 9-3, for a selected light-load condition, the predicted waveforms closely match the measured data for both schemes, confirming the model's promising accuracy. For any machine operating condition, the ripple waveshapes in different regions (see two zoom-in plots in Figure 9-3) exhibit considerable differences between SVPWM and DPWM2 due to differences between their switching patterns. It can also be observed from the zoom-in A plot in Figure 9-3 that, since the DPWM scheme has fewer switching states during each PWM cycle, the PWM-induced current ripple has a larger amplitude, and its dominant ripple frequency is half that of the SVPWM scheme.

To better compare their frequency composition, the Fourier analysis results are presented in Figure 9-4. Both the measured and predicted results indicate that, for this particular condition, the dominant harmonics using the SVPWM concentrate around 2x f_{PWM} while they shift towards 1x f_{PWM} with DPWM. The current ripple's rms values are plotted in Figure 9-5, showing that the DPWM amplitude is consistently higher than for SVPWM. The predicted results closely match the measured values available in the low PWM frequency range. Assuming that the machine dynamic inductances remain constant, the ripple amplitudes for both schemes drop monotonically as f_{PWM} increases.

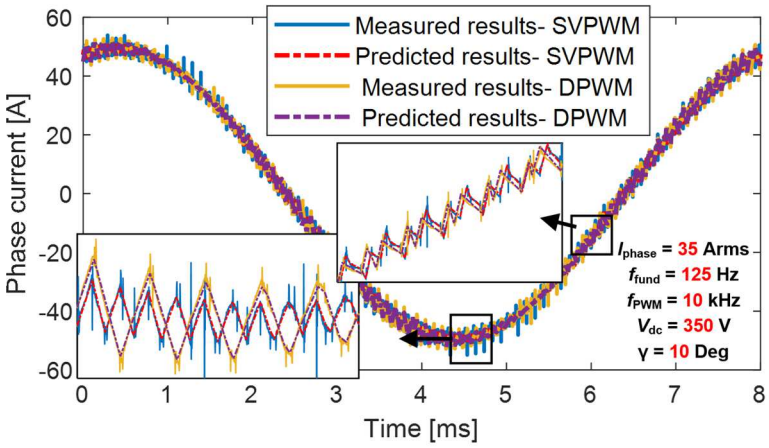

Figure 9-3: Comparison of predicted and measured IPM machine phase current waveforms with SVPWM and DPWM schemes for a light-load condition.

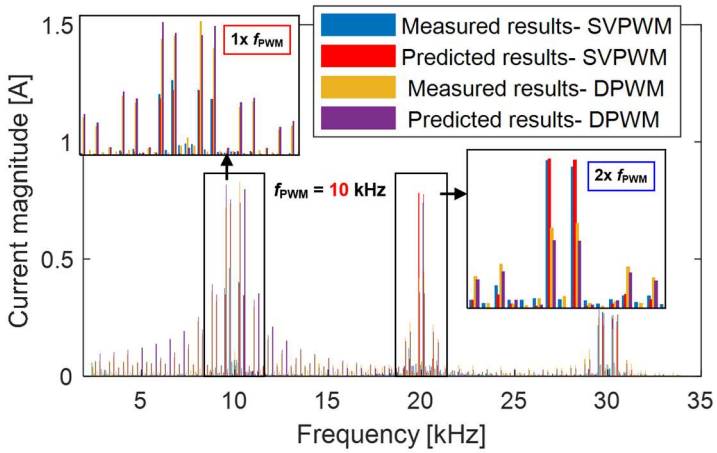

Figure 9-4: Fourier analysis of measured and predicted PWM-induced current ripple using SVPWM and DPWM modulation scheme.

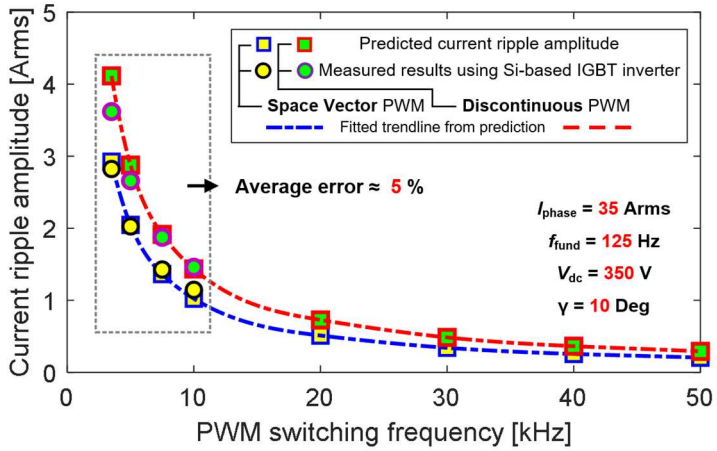

Figure 9-5: PWM-induced current ripple amplitude vs. PWM switching freq. fPWM using SVPWM and DPWM modulation scheme.

9.3 PWM Power Losses Modeling in IPM Machines

After predicting and measuring the current waveforms with PWM-induced high-frequency harmonics, the current data are used to estimate the PWM power losses in IPM machines.

9.3.1 Copper loss in form-wound windings

The total PWM copper loss in form-wound windings is subdivided into the in-slot and end-winding portions. Since the in-slot current conductors are exposed to slotting harmonics and rotor magnetic fields, an additional copper loss is induced due to both skin effect and the proximity effect. Therefore, 2-D FEA in Figure 9-6(a) with sufficiently fine mesh conditions is used to accurately predict the total in-slot copper loss by calculating the current density distribution J_z in the 2-D plane. The in-slot copper loss $P_{\mathrm{Cu}Slot}$ is obtained by integrating the local loss density:

$$P_{\mathrm{Cu}Slot} = \frac{1}{\sigma_{\mathrm{copper}}} \int_v |J_z(x,y)|^2 dv \tag{9-4}$$

where σ_{copper} is the copper conductivity.

In order to segregate the PWM loss components, an additional reference case with sinewave excitation is necessary. Based on the winding parameters specified in Table 9-1, the predicted time-domain in-slot copper loss with different current excitation waveforms are presented in Figure 9-7, where the excitation conditions are given in Figure 9-7 with f_{PWM} = 10 kHz. The PWM-induced copper loss can be determined from the difference in average loss values between PWM and sinusoidal excitation.

In order to avoid the excessive time required for end-winding loss estimation using 3-D FEA, a simplified machine end-winding model has been adopted [2] for this analysis as shown in Figure 9-6(b), approximating the current conductors in the end-winding portion as straight conductors placed side-by-side. The end-winding copper loss $P_{\mathrm{Cu}End}$ is estimated by (9-5) [193]:

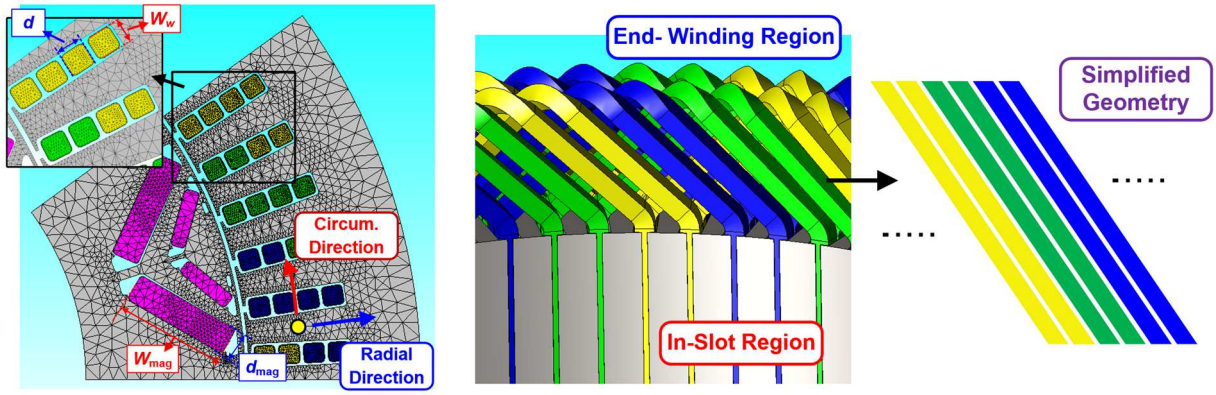

(a) 2-D FEA model (b) Simplified machine end-winding model

Figure 9-6: Estimation model for PWM-induced copper loss in IPM machines with form-wound windings.

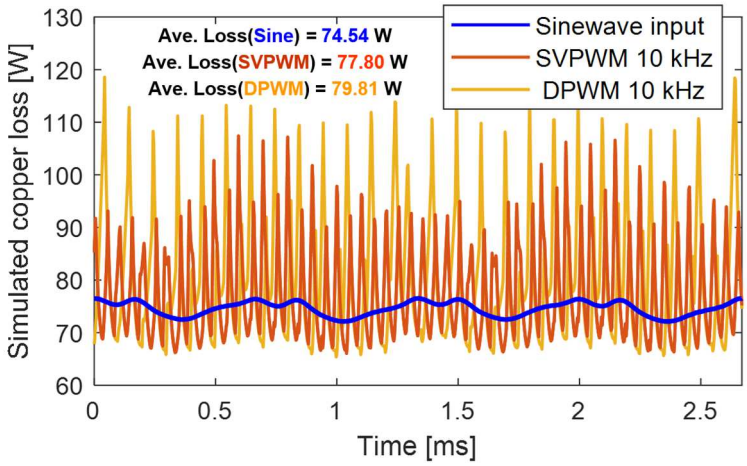

Figure 9-7: Predicted total stator PWM copper loss and end winding losses vs. f_{PWM} in the baseline IPM machine.

Excitation condition: fundamental current I_{phase} = 35 Arms, machine speed = 1,500 rpm (f_{fund} = 125 Hz), PWM switching frequency f_{PWM} = 10 kHz, inverter dc-bus voltage V_{dc} = 350 V, and current control angle γ = 10 degree.

TABLE 9-1: KEY PARAMETERS OF FORM-WOUND STATOR WINDINGS

d	W_w	l_{end}	σ_{copper}
3.5 mm	3.5 mm	8 m	4.69e7 S/m (80°C)

$$P_{\mathrm{Cu}End} = \frac{l_{\mathrm{end}} I^2}{4\delta W_w \sigma_{\mathrm{copper}}} \frac{\sinh(d/\delta) + \sin(d/\delta)}{\cosh(d/\delta) - \cos(d/\delta)} \tag{9-5}$$

where δ is the skin depth, d is the conductor radial thickness, W_w is the conductor circumferential width (see Figure 9-6(a)), and l_{end} is the machine total end winding length for each phase.

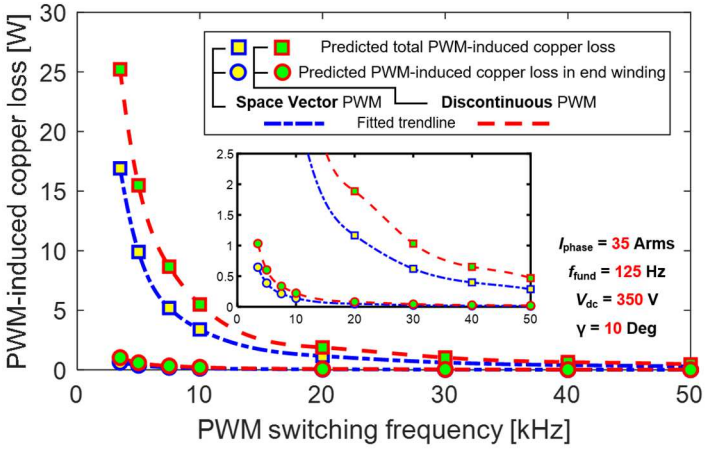

Figure 9-8: Predicted total stator PWM copper loss and end winding losses vs. f_{PWM} in the baseline IPM machine for Figure 9-7 operating point.

Next, the predicted total PWM-induced copper loss for all three stator phases using two PWM schemes are provided in Figure 9-8. Despite the fact that the conductor equivalent resistance increases with PWM frequency, the rms value of the current ripple amplitude drops, resulting in a monotonically declining PWM copper loss (i.e., I^2R) trend vs. f_{PWM}. The consistently higher current ripple amplitude with DPWM results in higher PWM copper loss than for SVPWM.

It should be noted that the PWM-induced copper loss for the DPWM scheme at $f_{PWM} = 3.5$ kHz reaches approx. one-third of the fundamental field-induced copper loss for this operating point. As the PWM switching frequency increases (i.e., $f_{PWM} \geq 20$ kHz), the loss contribution shrinks significantly for both PWM modulation schemes. The predicted results suggest that raising the PWM switching frequency serves as an effective means to suppress the PWM-induced copper loss. The end-winding copper loss is overlaid in Figure 9-8, indicating that the PWM copper loss contributed by the end-winding portion is very low compared to the in-slot values since the end-winding resistance obtained from (9-5) is not very sensitive to the PWM frequency.

9.3.2 PWM-induced iron loss in stator and rotor iron cores

As the predicted current waveforms with the PWM current ripple are fed to the IPM machine under study, high-frequency PWM-induced harmonics are found riding on top of the fundamental magnetic fields. For a mesh element selected in the middle stator tooth (See yellow point in Figure 9-6(a)), the FEA-predicted flux density waveforms in the radial direction are plotted in Figure 9-9 with different current waveforms. Since the PWM switching frequency is typically much higher than machine's fundamental frequency, changing the modulation scheme or the PWM frequency does not affect the fundamental field distribution nor its corresponding iron loss. This makes it possible to decompose these two frequency components and evaluate their iron loss contribution separately. In this analysis, the PWM-induced flux density ripple is obtained by subtracting the magnetic flux density generated by the sinusoidal input, and the resulting segregated PWM-induced flux density waveform over a fundamental cycle is presented in Figure 9-10.

The fundamental field creates an equivalent dc-bias field B_{dc} for the PWM flux density ripple in electric machines. This results in different material iron loss properties for PWM harmonics compared to what they experience in the absence of external fields. The dc-bias field during each PWM cycle is:

$$B_{\mathrm{dc}} = \frac{1}{T_s}\int_0^{T_s} B_{\mathrm{fund}} \cdot dt \tag{9-6}$$

where B_{fund} is the absolute value of the fundamental magnetic flux density in a 2-D FEA mesh element and $T_{\mathrm{s}} = 1/f_{\mathrm{PWM}}$.

As shown in the zoom-in plots in Figure 9-10, the segregated flux ripple using the two PWM schemes exhibits significant differences due to their different switching patterns and the number of switching instants per cycle. For the DPWM scheme, the ripple waveshape can be categorized into two main groups.

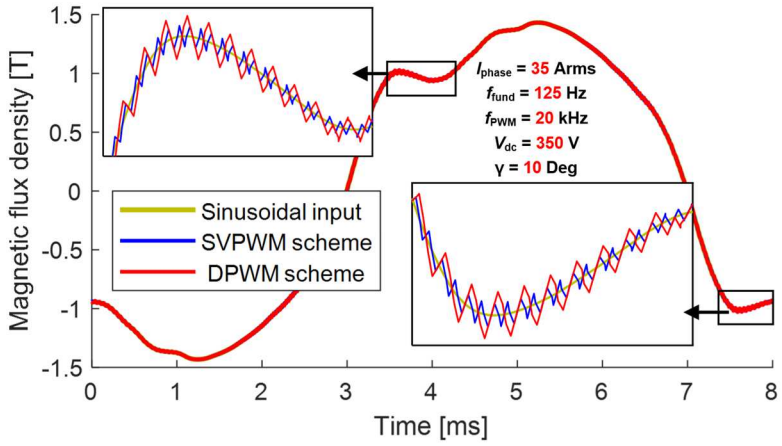

Figure 9-9: Simulated flux density waveforms of a mesh element in the middle stator tooth (See yellow point in Figure 9-6(a)) along the radial direction.

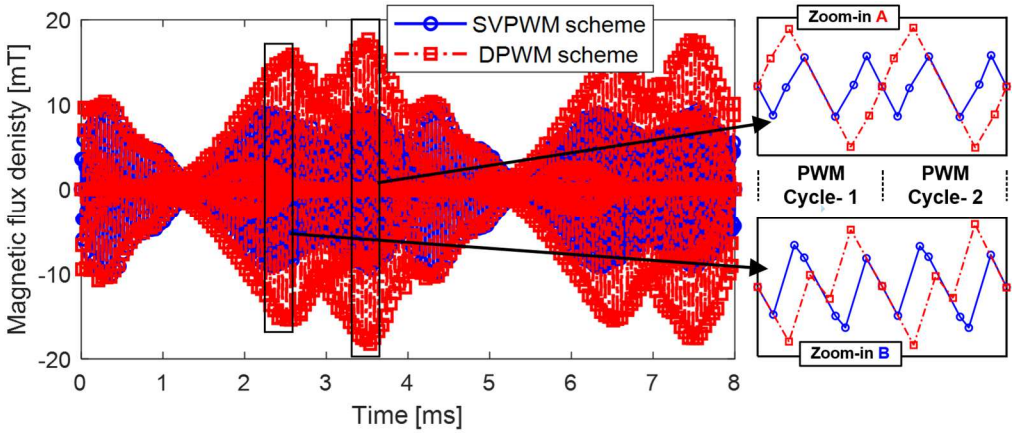

Figure 9-10: Segregated PWM-induced flux ripple over a fundamental cycle for SVPWM and DPWM scheme.

For the case illustrated in Figure 9-11(a) where the voltage vector lies in Sector 1 (See Figure 9-2), the flux density ripple is dominated by the harmonic component at f_{PWM}. In contrast, when the voltage vector moves into Sector 2, the ripple depicted in Figure 9-11(b) becomes more complicated, which can be approximated as the concatenation of two ripple waveform segments in a single switching cycle. The equivalent frequency of each segment f_{seg} is determined by its associated time period (i.e., $f_{seg} = 1/T_{seg}$). The flux ripple waveforms for all of the DPWM methods fall into those two categories in alternating Figure 9-2 segments, providing a generalized approach to decompose the DPWM flux ripple into one or two symmetrical concatenated waveforms.

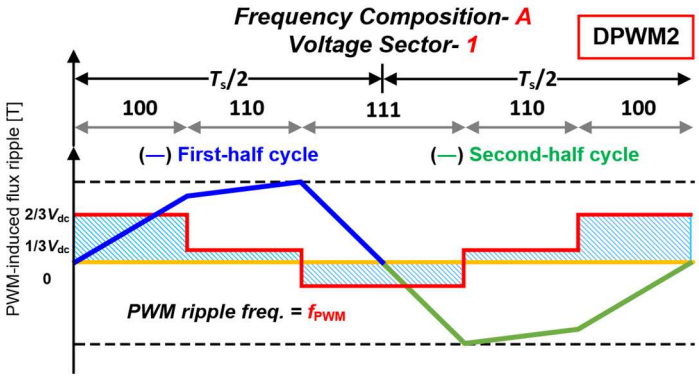

(a) PWM flux ripple in voltage sector-1

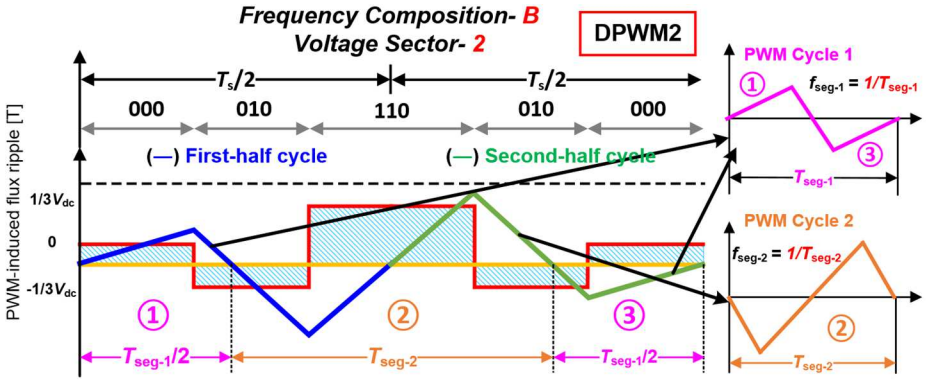

(b) PWM flux ripple in voltage sector-2

Figure 9-11: Example PWM flux ripple waveshapes with DPWM2 scheme and relationships between the inverter (—) and machine average voltage (—).

Since the zero states evenly distribute over a PWM cycle with the SVPWM scheme, the PWM flux ripple exhibits properties different from those with DPWM. Figure 9-12(a)-(b) show two example ripple waveshapes with SVPWM. Taking the ripple in voltage Sector 1 as an example, when the machine-side voltage is lower than $V_{dc}/3$ (See Figure 9-12(a)), the peak-to-peak flux ripple in the first- and second-half cycles are equal to that across the full PWM cycle (i.e., $B_{p\text{-}p}(1) = B_{p\text{-}p}(2) = B_{p\text{-}p}(T_s)$), and the dominant ripple frequency is ~2x f_{PWM}. When the machine voltage increases to > $V_{dc}/3$ in Figure 9-12(b), the ripple in each half cycle has different positive and negative peak values, driving the ripple frequency towards 1x f_{PWM}. In this analysis, a special approach developed in Chapter 7 is adopted to decompose the flux ripple with SVPWM into 1x and 2x f_{PWM} components, incorporating the decomposition method that was discussed above for DPWM in Figure 9-11(b).

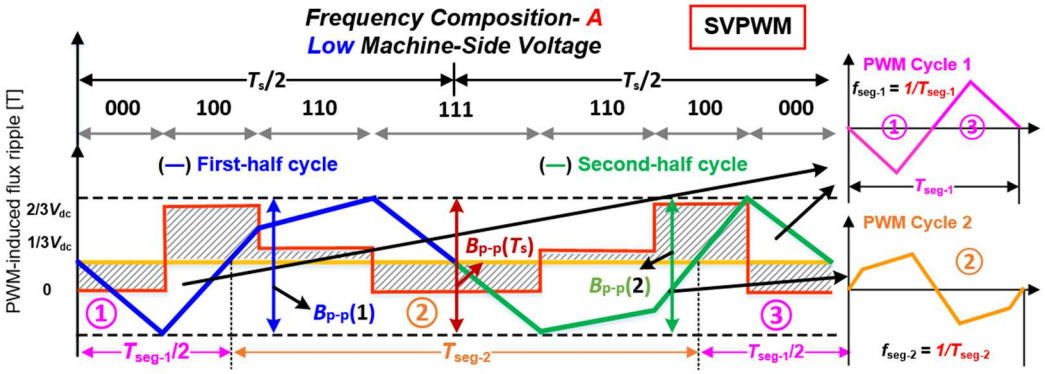

(a) PWM flux ripple in voltage sector-1 with low machine-side voltage

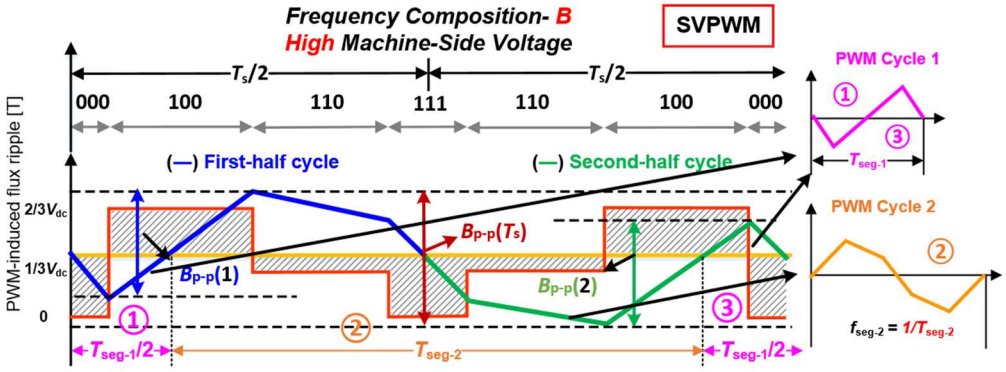

(b) PWM flux ripple in voltage sector-1 with high machine-side voltage

Figure 9-12: Example PWM flux ripple waveshapes with SVPWM scheme and relationships between the inverter (—) and machine average voltage (—).

Next, the frequency-interconnected dynamic Jiles-Atherton (*J-A*) model proposed in Chapter 8 is used in this analysis for PWM-induced iron loss estimation. As presented in preceding chapter, the total magnetic field strength H_{tot} includes the solution from the conventional static *J-A* model H_{stat}, where the key model parameters are characterized as a function of the ripple's equivalent frequency f_{seg} and dc-bias field B_{dc} induced by the fundamental field. In addition, an extra dynamic field term is introduced to better capture the impact of the dynamic eddy current loss. Incorporating the dynamic hysteresis loop term makes it possible to estimate the resulting iron loss by calculating the enclosed area of the dynamic hysteresis loop.

Figure 9-13 shows the implementation process of the proposed PWM-induced iron loss estimation algorithm. The predicted current waveforms including PWM harmonics are fed to 2-D FEA to conduct electromagnetic field analysis in the studied IPM machine. The PWM-induced flux ripple is calculated separately for the radial and circumferential directions in each element. Next, the PWM flux ripple waveform in each switching cycle is decomposed into its symmetrical sub-components. Based on the ripple's equivalent frequency f_{seg} and dc-bias field B_{dc} induced by the fundamental field, parameters for the frequency-dependent dynamic *J-A* model are extracted from the pre-characterized material database, and the PWM iron loss of each flux ripple segment is calculated via the enclosed areas of predicted minor loops. This calculation is made repeatedly for each mesh element in the IPM machine to determine the total PWM-induced iron loss.

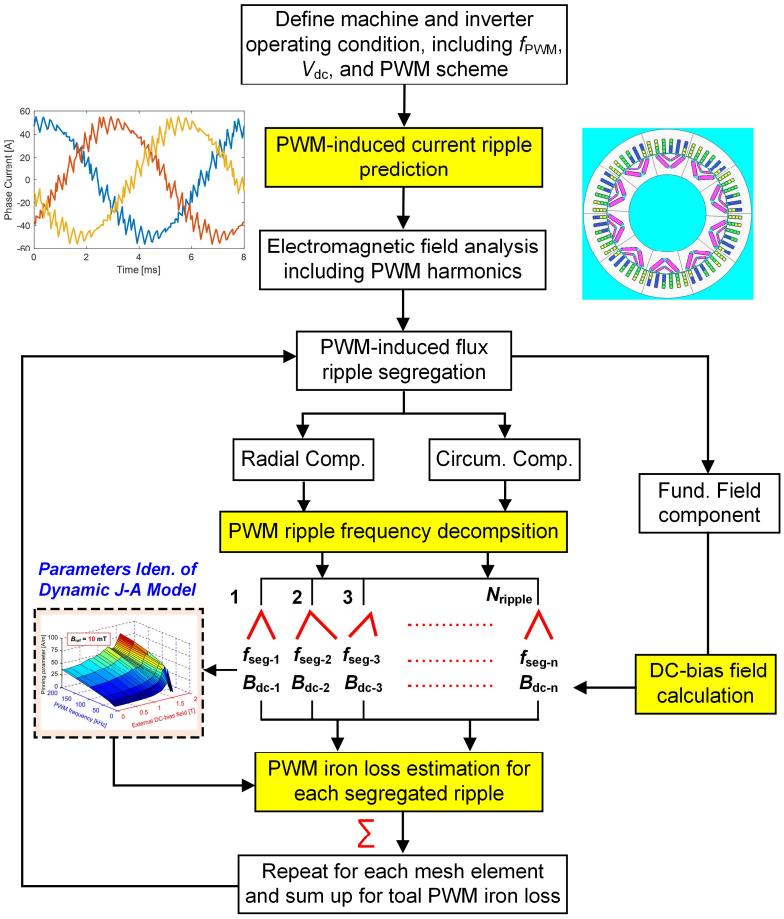

Figure 9-13: Flowchart of proposed PWM-induced iron loss estimation model.

The predicted PWM-induced iron loss results vs. f_{PWM} are presented in Figure 9-14 for both PWM schemes with and without the dc-bias field impact. The results show that increasing f_{PWM} reduces the PWM iron loss for both modulation schemes, but the rate of decline is slower compared to that of the copper loss. The results also show that the dc-bias field exerts a stronger influence on the PWM iron loss at lower frequencies, consistent with the conclusions drawn in Chapter 6 and Chapter 8. The PWM iron loss caused by DPWM is higher than that by SVPWM due, in part, to having its dominant harmonic components primarily concentrated at lower frequencies.

PWM iron loss decomposition results are plotted in Figure 9-15, showing that the PWM iron losses in both the stator and rotor are heavily affected by the dc-bias field. Even though the IPM machine rotor rotates synchronously with the stator armature current (i.e., the fundamental field is dc in the rotor except for slotting harmonics), the PWM-induced iron loss from the rotor side contributes approximately a quarter of the total PWM iron loss, making it a critical loss component in IPM machines.

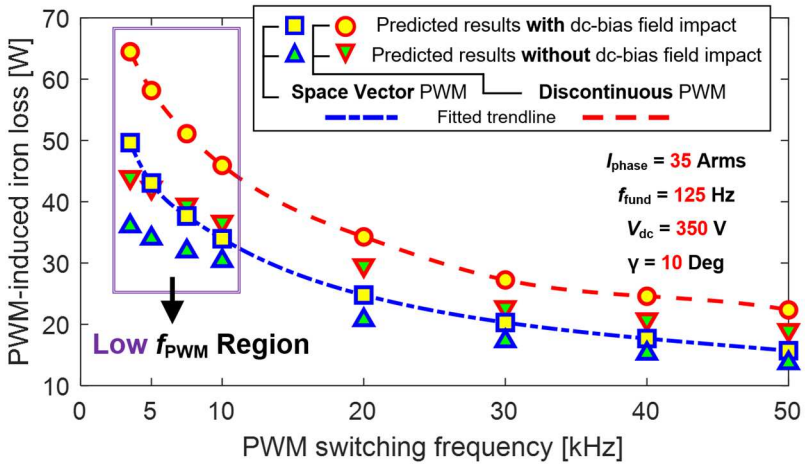

Figure 9-14: Predicted PWM-induced iron loss vs. f_{PWM} in the baseline IPM machine using different modulation schemes.

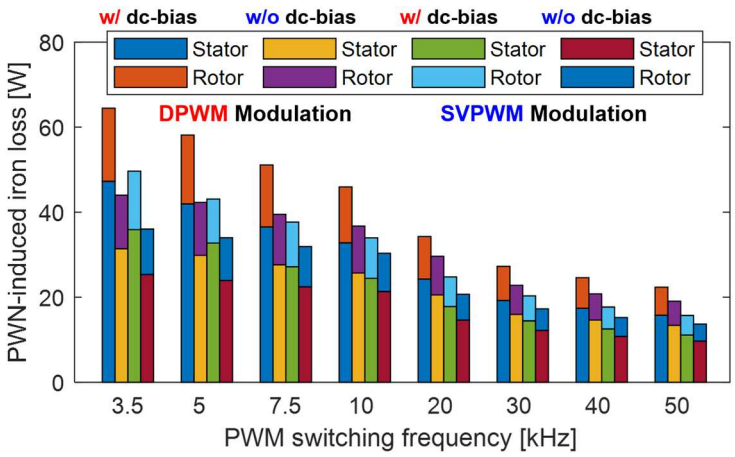

Figure 9-15: Composition of PWM-induced iron loss in the stator- and rotor-side of the baseline IPM machine with and without considering the dc-bias field impact on iron loss.

9.3.3 PWM-induced eddy current loss in permanent magnets

Eddy current loss is induced by high-frequency harmonics if the magnetic field passes through the axially-segmented magnets under PWM voltage excitation. Under a simplified assumption that the excitation field H is homogeneously distributed in time and space, the magnet eddy current loss can be determined analytically by (9-7) [5], a solution that incorporates the impact of the eddy currents on magnetic flux density B.

$$P_{\mathrm{mag}} = \frac{2bd}{\sigma\delta}|H|^2 \frac{\sinh\frac{2a}{\delta} - \sin\frac{2a}{\delta}}{\cosh\frac{2a}{\delta} + \cos\frac{2a}{\delta}} - \frac{128a^4 d}{\pi^5}\frac{|\gamma^2 H|^2}{\sigma} \times \left(\sum_{m=0}^{\infty} \frac{(\lambda_m^2 - 2\beta_{\mathrm{mi}}^2)\beta_{\mathrm{mr}}\lambda_m^3 \sinh 2\beta_{\mathrm{mr}} b}{(2m+1)^5 |\beta_m|^6 (\cosh 2\beta_{\mathrm{mr}} b + \cos 2\beta_{\mathrm{mi}} b)} - \sum_{m=0}^{\infty} \frac{(\lambda_m^2 + 2\beta_{\mathrm{mr}}^2)\beta_{\mathrm{mi}}\lambda_m^3 \sinh 2\beta_{\mathrm{mi}} b}{(2m+1)^5 |\beta_m|^6 (\cosh 2\beta_{\mathrm{mr}} b + \cos 2\beta_{\mathrm{mi}} b)} \right) \tag{9-7}$$

where a and b are the half width and length of the magnet, d is the magnet thickness, m is the number of series solutions, and λ_m, γ, β_{mr}, and β_{mi} are the functions of δ and m defined in [5].

Based on the key magnet parameters in Table 9-2, the magnet loss variation trend vs. the segment number is depicted in Figure 9-16, where the excitation field H is held constant during the analysis. With a low excitation frequency (i.e., $f_{\mathrm{input}} \leq 10$ kHz), Figure 9-16 shows that the

magnet loss continues declining as the segmentation number increases. As the frequency increases, the magnet loss initially increases and peaks at a progressively higher number of segments, indicating that magnet segmentation can be detrimental to machine efficiency in some cases. The peaking occurs because the resulting eddy current distribution is heavily affected by the relationship between the skin depth δ given in Table 9-3 and the magnet dimensions (i.e., magnet length and width). Beyond the peak loss point, the magnet loss decreases, and the rate varies with frequency.

With a low excitation frequency and large skin depth value, increasing the segmentation suppresses the circulating current, resulting in a lower magnet loss. At higher frequencies before reaching the peak loss point, increasing the segmentation number provides more circulating paths for the eddy current, leading to a higher eddy current loss. Therefore, at high PWM frequencies, a high segmentation number is necessary to effectively suppress the magnet eddy current loss compared to the loss value without introducing any magnet segmentation.

TABLE 9-2: KEY PARAMETERS OF STUDIED NDFEB MAGNETS IN THE INNER LAYER

d_{mag}	W_{mag}	l_{mag} (w/o seg.)	σ_{mag}
4.75 mm	18 mm	125 mm	5.56e5 S/m

TABLE 9-3: MAGNET SKIN DEPTH VS. FREQUENCIES

f_{input} [kHz]	5	10	20	30	50	100
δ [mm]	9.5	6.6	4.7	3.8	2.9	2.1

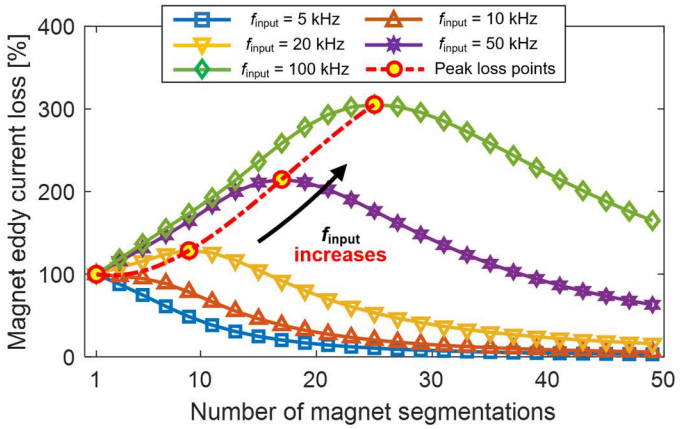

Figure 9-16: Magnet eddy current loss variation vs. number of segmentations.

Although the insights provided by the analytical solution is helpful, the PWM-induced harmonic fields passing through the permanent magnets in IPM machines vary in space and time, making 3-D FEA indispensable to secure accurate magnet loss estimation. For the same operating condition analyzed in the preceding sections, the predicted PWM-induced magnet loss results vs. PWM frequency f_{PWM} are plotted in Figure 9-17 for both schemes. The PWM magnet loss with both schemes drops monotonically as f_{PWM} increases, indicating that the harmonic field amplitude (i.e., current ripple amplitude) is the most influencing factor to the resulting magnet loss.

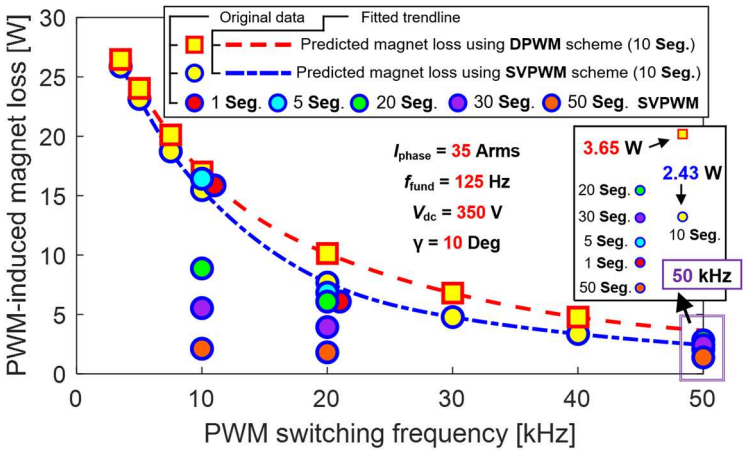

Figure 9-17: Predicted PWM-induced magnet loss vs. f_{PWM} in the baseline IPM machine with different modulation schemes and number of segmentations.

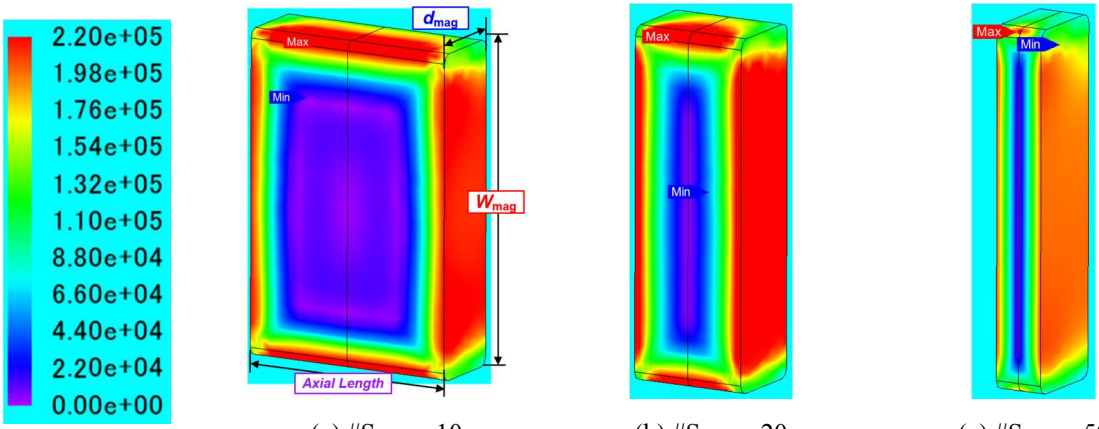

(a) #Seg. = 10 (b) #Seg. = 20 (c) #Seg. = 50

Figure 9-18: Predicted magnet eddy current distribution from 3-D FEA with different numbers of axial segments and f_{PWM} at 50 kHz using SVPWM.

It should be noted that the difference between the losses with the two PWM schemes is small in the low-frequency range (i.e., $f_{PWM} \leq 10$ kHz), but their ratio increases over the entire f_{PWM} range. The DPWM/SVPWM loss ratio approaches 1.5 at f_{PWM} = 50 kHz, mainly due to different relationships between the skin depth and magnet length for those two schemes.

The impact of magnet segment number is also included in Figure 9-17, showing that increasing the segmentation number is more beneficial to suppress the magnet loss at lower PWM frequencies, consistent with the trend presented in Figure 9-16. For the case with f_{PWM} = 50 kHz, the largest magnet loss value occurs with 20 segments, while the case without any segmentation offers the second-lowest magnet loss value. Figure 9-18 shows the 3D-FEA-predicted magnet eddy current distribution at a particular time instant, confirming that the eddy current distribution is quite low in much of the magnet volume for the lowest segmentation number (=10) at f_{PWM} = 50 kHz.

9.4 Experimental Evaluation of Proposed Estimation Model in IPM Traction Machines

In this section, the loss values in the three machine components are summed up to obtain the total predicted machine PWM-induced power losses. The test configuration in Figure 7-16(a)-(b) has been used to provide model verification in the low PWM frequency range (i.e., $f_{PWM} \leq 10$ kHz) using a silicon-based IGBT inverter. A three-phase low-pass *L-C* filter depicted in Figure 7-16(a) helps to segregate the PWM-induced power losses in the baseline IPM machine via an A/B test, where the loss difference between the sinusoidal and PWM voltage excitation test is considered to be the loss contribution from the PWM harmonics. The detailed test procedure is documented in Chapter 7.

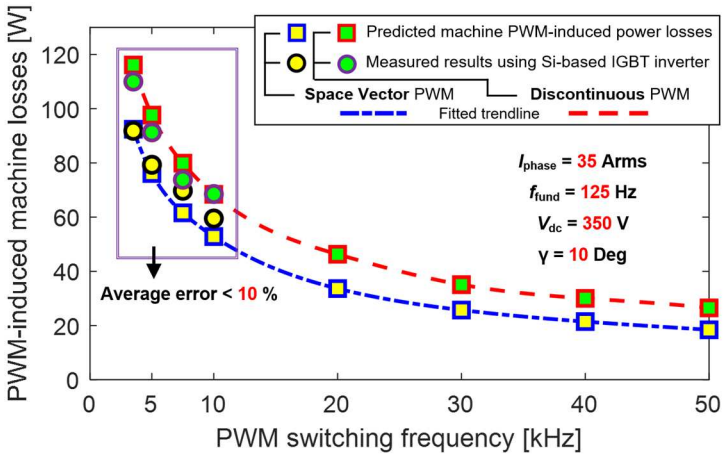

Figure 9-19: Predicted total machine PWM loss and measured loss vs. f_{PWM} for the baseline IPM machine under a low-speed and light-load condition.

The predicted and measured machine PWM power losses vs. the PWM switching frequency f_{PWM} for both PWM schemes are overlaid in Figure 9-19. It can be seen that the predicted and measured losses match within 10% over the low PWM frequency range, building confidence in the proposed model to predict total PWM losses for different frequencies and PWM schemes.

As the PWM frequency is raised to higher values enabled by a WBG-based inverter, the total machine PWM losses are predicted to decline significantly. Compared to the peak loss point at 3.5 kHz, the predicted PWM losses at 50 kHz are reduced by almost 80% for both PWM schemes. For this machine operating condition, the machine total loss with sinusoidal current excitation is approx. 292.7 W. The measured PWM power losses with the DPWM and SVPWM schemes at f_{PWM} = 3.5 kHz account for approx. 27.3% (110 W) and 23.9% (91.84 W) of the machine's total loss, respectively. The predicted results indicate that the PWM losses can be reduced to 9% (DPWM) and 6.3% (SVPWM) with f_{PWM} = 50 kHz, highlighting the potential benefits of increasing the PWM frequency for boosting the machine efficiency.

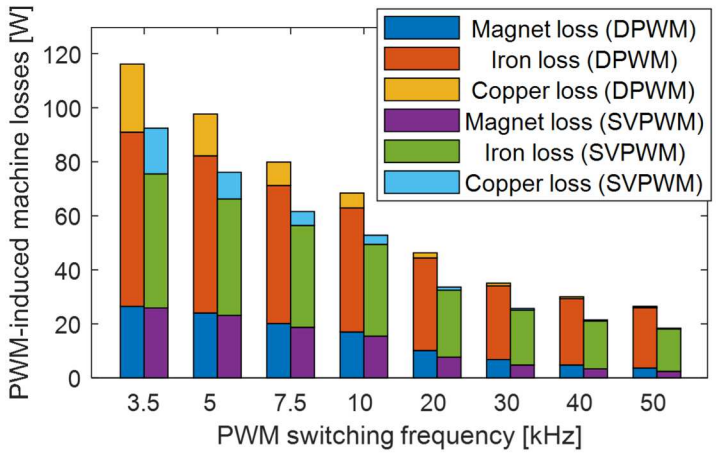

Figure 9-20: Composition of predicted machine total PWM power losses in the baseline IPM machine with both PWM modulation schemes.

The predicted loss composition results presented in Figure 9-20 suggest that the copper and magnet PWM losses become insignificant with sufficiently high PWM frequency (i.e., $f_{PWM} \geq 20$ kHz) while the PWM iron loss remains the dominant loss component. In addition, the SVPWM scheme exhibits advantage over the DPWM scheme within the studied PWM frequency range, providing smaller machine-side PWM losses. However, since the DPWM scheme requires fewer inverter switching instants per cycle, the lower inverter loss results in improved inverter-side efficiency which partially offsets the machine-side efficiency advantage held by the SVPWM scheme.

Next, to further verify the model performance in the higher PWM frequency range, the same analysis is applied to a newly designed IPM machine with form-wound windings. However, since this machine is still in the design stage, the detailed specifications are not provided in this thesis. Also, only the machine power loss results under PWM excitation are collected, with the PWM frequency ranging from 10 to 20 kHz. Therefore, a new PWM power losses factor k_{PWM} defined in (9-8) is used to quantify the relative variation of PWM losses for either modulation scheme versus the measured value at 10 kHz with the same PWM scheme.

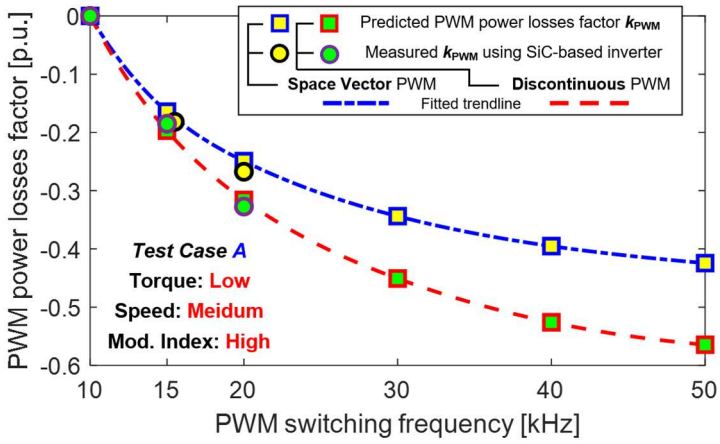

Figure 9-21: Predicted and measured PWM loss factor k_{PWM} vs. f_{PWM} for a newly-designed IPM machine at a medium-speed and light-load condition.

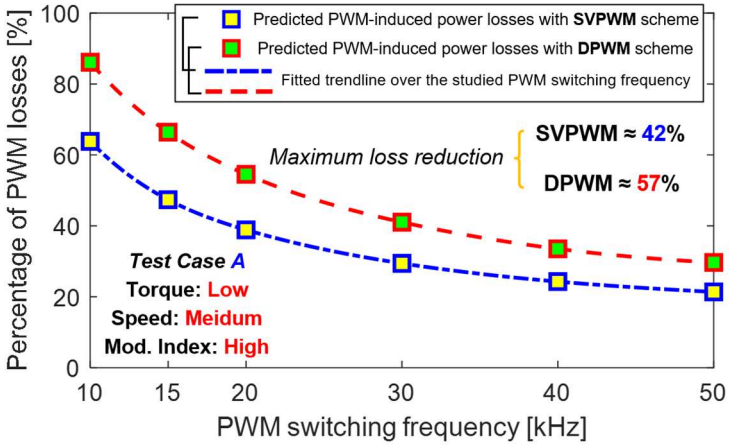

Figure 9-22: PWM losses as percentage of losses with sinusoidal excitation vs. f_{PWM} for a newly-designed IPM machine at a selected testing condition.

$$k_{\mathrm{PWM}} = \frac{P_{\mathrm{tot-fPWM}} - P_{\mathrm{tot-10kHz}}}{P_{\mathrm{tot-sine}}} \quad \text{[p.u.]} \qquad (9\text{-}8)$$

where $P_{\text{tot-fPWM}}$ is the measured/predicted machine total loss for a given PWM frequency f_{PWM} and modulation scheme, and $P_{\text{tot-sine}}$ is the predicted machine power loss with sinusoidal input.

Figure 9-21 depicts the variation trend of the factor k_{PWM} over the studied PWM frequency range when the machine operates at a medium-speed and light-load condition. Available experimental data from operation with f_{PWM} in the 10 to 20 kHz range confirm that the proposed model is capable of accurately tracking the reduction of PWM power losses f_{PWM} increases. The prediction results demonstrate the same trend exhibited in Figure 9-19 that increasing the PWM

frequency is beneficial to suppress the machine-side PWM losses. A larger fractional reduction is observed for the case with the DPWM scheme, where larger current harmonics and higher PWM losses are induced for a given switching frequency compared to those for the SVPWM scheme.

The predicted PWM losses as a percentage of the loss with sinusoidal excitation $P_{\text{tot-sine}}$ is plotted in Figure 9-22 for both schemes. The PWM losses drop monotonically with both schemes, where the maximum loss reduction rate approaches 42% for SVPWM and 57% for DPWM by increasing the switching frequency f_{PWM} from 10 to 50 kHz. It is worth noting that, for both PWM schemes, the rate of decrease gradually drops as the PWM frequency is raised (i.e., $f_{\text{PWM}} \geq 30$ kHz), indicating that there are diminishing returns for adopting a very high switching frequency.

Furthermore, the same analysis is extended to three more machine operating conditions depicted in Figure 9-23(a)-(c). Since the match between the predicted and measured results heavily depends on the accuracy of the measured data at the reference point (i.e., f_{PWM} = 10 kHz), discrepancies can be observed for a particular case, like the DPWM scheme given in Figure 9-23(b). Nevertheless, the proposed model generally presents a similar variation trend compared to the measured data, confirming that the efficiency benefit brought by high switching frequency is extendable to other machine operating conditions. It is worth noting that, although the PWM power losses reduction with DPWM scheme are typically more significant than that with SVPWM scheme, both the measured and predicted results given in Figure 9-23(a) suggest that the PWM power losses drop at a similar rate for either scheme, indicating that the machine operating condition applies a considerable impact on the PWM power losses.

In summary, it has been verified that the proposed model can be utilized to determine the PWM losses for varying conditions, which provides deeper insights into the impact of the PWM switching frequency and modulation scheme on the resulting machine efficiency.

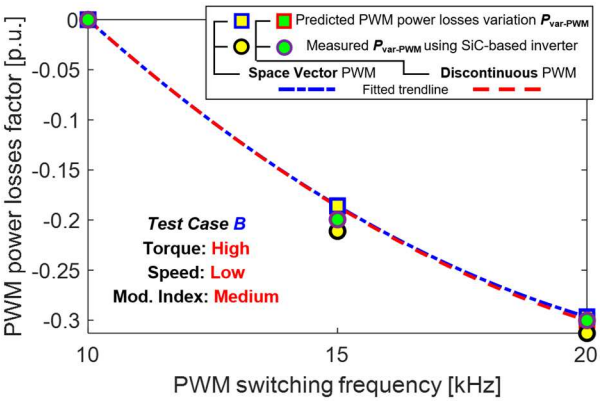

(a) Test Case **B**: High torque, low machine speed, and medium modulation index

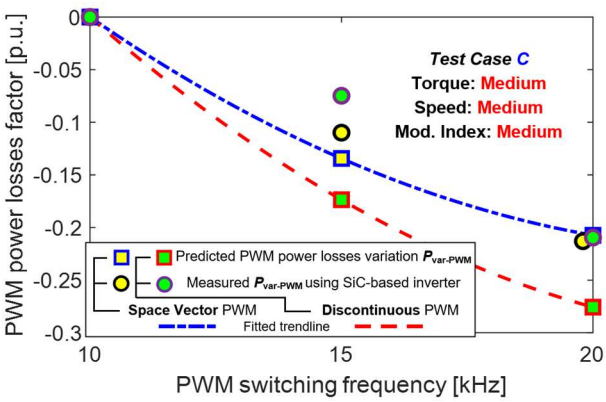

(b) Test Case **C**: Medium torque, medium machine speed, and medium modulation index

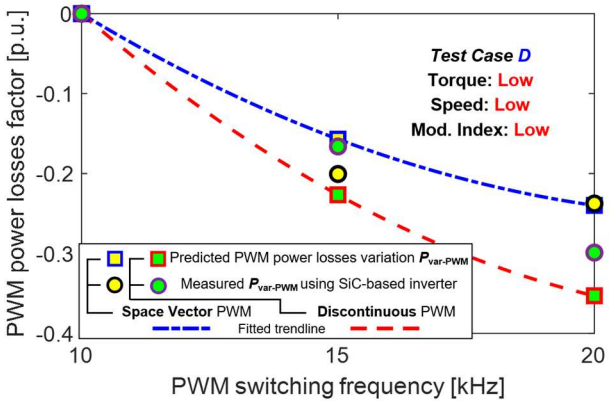

(c) Test Case **D**: Low torque, low machine speed, and low modulation index

Figure 9-23: Predicted and measured PWM loss factor k_{PWM} vs. f_{PWM} for a newly-designed IPM machine over three testing conditions.

TABLE 9-4: MACHINE TOTAL POWER LOSSES ANALYSIS IN A NEWLY-DESIGNED IPM TRACTION MACHINE FOR FOUR SELECTED OPERATING CONDITIONS

Testing Case	Torque	Speed	Mod. index	Measured results [p.u.]	Predicted results [p.u.]	Est. error [%]	Predicted PWM losses [p.u.]
A	Low	Medium	High	1.0	0.923	7.74	0.462
B	High	Low	Medium	1.0	1.006	0.62	0.468
C	Medium	Medium	Medium	1.0	1.022	2.22	0.407
D	Low	Low	Low	1.0	0.968	3.17	0.489

At last, combining with the fundamental field iron loss model discussed in Chapter 3 and Chapter 4, the machine total power losses over four selected machine testing cases are evaluated, and the comparison between the predicted and measured results are documented in Table 9-4. It should be noted all the cases are excited by regular PWM voltage with the DPWM scheme and 10 kHz f_{PWM}. In general, the proposed model shows a very promising capability in estimating the machine total power losses, where the estimation error of all the studied cases is below 10%. More importantly, the predicted PWM power losses for all the cases account for a significant proportion of total machine power losses, in between 40-50%, suggesting that properly incorporating the loss contribution from PWM-induced harmonics is critically important to secure accurate power losses estimation. After integrating with machine-level or system-level optimization tool, the proposed model can be applied to estimate the machine power losses and subsequently identify the optimum machine design topology, PWM switching frequency, and modulation scheme, which shows great potential to boost the efficiency of the future designed electric machines and electrification system.

9.5 Practical challenges involved in machine power losses estimation

Although the proposed machine power loss estimation models exhibit a promising capability for predicting the power losses in IPM traction machines over broad operating conditions, there are several practical challenges that were observed during the implementation process.

First, the parameter characterization required for the iron loss analysis model appears to be one of the most influential factors affecting model performance for both fundamental and PWM iron loss estimation. This is particularly true for the dynamic *J-A* model proposed for PWM iron loss analysis. It is commonly acknowledged that the accuracy of the *J-A* model is highly susceptible to the parameter initial guesses that are used for model performance optimization, posing challenges and uncertainties to ensure the quality of the fitted model parameters.

Second, there are several factors that influence the required calculation time for these models. Since the developed iron loss algorithms are programmed in the MATLAB environment, it is necessary to extract the simulated machine flux density information for the studied machines from FEA for post-processing in MATLAB. Depending on the total number of mesh elements, this transfer process can take several minutes, increasing the calculation time. Therefore, it would be preferable to program and implement the iron loss models inside FEA tools. Once programmed, the run-time of iron loss models is typically in the range of 1-2 minutes for a given test case with a typical personal computer. Introducing high-performance computers can significantly increase the calculation speed, making it more practical to implement the machine design optimization by sweeping over a large number of design candidates.

Finally, the 3-D FEA simulation that is necessary for the magnet eddy current loss estimation generally requires a very long calculation time (e.g., 30 mins to 6 hours), depending on the thickness of the studied magnet segment. The alternative approach of combining a 2-D FEA magnet model with an enhanced analytical model to estimate the effects of the third dimension is promising as a technique for achieving reasonable accuracy while significantly reducing the calculation time.

9.6 Summary

This chapter presents an in-depth analysis of the PWM power losses in IPM machines with different modulation schemes over a broad PWM switching frequency range enabled by a WBG-based voltage-source inverter. The variation trend of each loss component has been investigated using the best available loss prediction models. Experimental data from two IPM traction machines have confirmed the composite model's promising capabilities for PWM power loss estimation with different modulation schemes over a broad range of PWM frequencies.

Both the predicted and measured results in the studied IPM machines indicate that raising the PWM frequency reduces all three major loss components, resulting in efficiency boosts that can be large under light-load conditions. The PWM-induced copper, iron, and magnet loss all shrink significantly at higher PWM frequencies, provided that the magnet segmentation is properly adjusted. The PWM iron loss is the dominant loss component at high f_{PWM} values. The DPWM scheme induces larger machine PWM losses than the SVPWM scheme, but it exhibits a larger fractional reduction as f_{PWM} rises.

To date, the focus of this analysis has been on the machine-side loss components. However, the system-level efficiency is also tightly related to the inverter-side losses. Increasing f_{PWM} helps to constrain the current ripple amplitudes, while larger inverter switching losses are inevitable when it operates at elevated switching frequencies. Therefore, a comprehensive optimization is necessary to determine the PWM frequency and modulation scheme that delivers the optimum system-level efficiency based on the machine operating conditions.

Chapter 10
Conclusions, Contributions, and Recommended Future Work

10.1 Conclusions

This research program that has been devoted to the investigation and prediction of fundamental and PWM frequency-induced core losses in the PM synchronous traction machines. The following key conclusions can be drawn from this research to date:

10.1.1 Key Conclusions from State-of-the-Art Review

- Magnetization in ferromagnetic materials is not uniform but highly localized. Even if the external field changes at an infinitesimal rate justifying quasi-static assumptions, a change in the global magnetization of the magnetic material can only be achieved by movement of the magnetic domain walls. Therefore, there is no obvious physical distinction to be made between static hysteresis loss and dynamic eddy-current loss.
- Iron loss estimation models based on either the Steinmetz equation or the standard iron loss separation theorem offer simple and fast ways to predict the iron loss. However, when significant minor loops appear in the flux density waveforms or the excitation frequency increases to elevated levels, the estimation accuracy of these models suffers considerably.
- It has been widely recognized that obtaining accurate iron loss estimates calls for the development of hysteresis models that are capable of accurately modeling the re-magnetization process and hysteresis loop, whereby the resulting iron loss can be determined from the net enclosed area. However, incorporating the impact of dynamic field-induced eddy current into the hysteresis loop modeling requires further improvement.

- Decomposing the rotating magnetic field simulated using 2-D FEA into two orthogonal directions (e.g., radial and circumferential direction) has been commonly utilized to investigate the iron loss of non-oriented ferromagnetic materials.
- The presence of pre-magnetized dc-bias fields exhibits a significant impact on the resulting magnetic and iron loss properties of the minor loops. As a result, the conventional iron loss methods (e.g., Steinmetz equation), in which the coefficients are identified from symmetrical conditions, cannot be directly applied to estimate the minor loop losses affected by external magnetic fields.
- The total iron loss induced by magnetic flux waveforms under PWM or dc-bias conditions can be estimated by summing up the loss contributions of each major/minor loop. In contrast, Fourier analysis is not appropriate for iron loss estimation of the nonlinear materials since the instantaneous power loss function is not a linear function.
- Analytical approaches have been proposed to estimate the PWM-induced current ripple for a variety of applications (e.g., *L*-*R*-*C* and induction machine loads), enabling faster calculation speeds and deeper insights into current ripple waveshape properties.
- When the SVPWM switching algorithm is utilized, each PWM switching period can be divided into seven linear regions, while five linear regions exist for the DPWM algorithm.
- 3-D FEA simulation has been widely utilized to predict the eddy current distribution and the corresponding Joule losses in permanent magnets.
- Although several existing studies are devoted to raising the awareness of PWM-induced iron loss and experimentally investigating this loss component, a comprehensive approach for estimating the PWM-induced iron loss has not yet been presented in the literature.

- Material-level PWM iron loss analysis has been extended to very high PWM frequencies (i.e., f_{PWM} > 100 kHz) using WBG-based inverters, indicating that iron loss properties exhibit notable differences compared to lower PWM frequency conditions.

10.1.2 Iron Loss Model Development for Fundamental and Low-Order Harmonics

- Due to the inherent nonlinearities of soft magnetic materials, the actual flux observed using a sensing winding can deviate substantially from the commanded flux waveform, making it necessary to implement closed-loop regulation of the flux waveshape to minimize the error.
- The static Preisach hysteresis model is a promising candidate to model complex flux waveforms under quasi-static conditions owing to its demonstrated accuracy as well as minor loop congruency.
- A more general hypothesis has been developed to model the dynamic field, incorporating the impact of the flux density rate-of-change $dB(t)/dt$, the instantaneous magnetization state $B(t)$, and the magnetic history of the flux waveform B_{hist}.
- Two dynamic field modeling approaches have been developed in this research. One emulates the dynamic field variation rate $\Delta H_{dyn}/\Delta t$ over varying regions, and another one directly models the instantaneous dynamic field strength H_{dyn}.
- The dynamic hysteresis model characterized from symmetrical hysteresis loops can only be applied to predict a half path of the minor hysteresis loop. Therefore, it calls for an approximation of parameters for the unknown path as well as dynamic field compensation during post-processing to guarantee closure of the minor loop. The proposed minor loop compensation method has shown promising potential to emulate the minor hysteresis loop affected by ac average magnetic fields without any additional tests.

- As the amplitude of minor loop varies, the ac average field coupled with the major field and the pre-magnetized dc-bias field can exert similar but different impacts on the material's magnetic condition, especially in the region of heavy saturation. As a result, it is indispensable to take into account the actual magnetic condition in the minor loop iron loss modeling.

10.1.3 Model Application and Experimental Evaluation

- Both candidate dynamic hysteresis models have exhibited excellent accuracy for modeling both the dynamic hysteresis loops and the iron losses of sinusoidal flux waveforms within the input characterization data (i.e., 1 kHz) over a wide range of ac flux density amplitudes. When they are applied to estimate sinusoidal waveforms beyond the frequency limit, the $\Delta H_{dyn}/\Delta t$-based model exhibits a better frequency extendability.
- For non-sinusoidal flux waveforms that contain a higher-order harmonic field with harmonic order $h < 5$, the resultant hysteresis loop changes substantially as the phase shift angle between the fundamental and harmonic field varies. Owing to the nonlinearities of the magnetic materials, the iron loss experiences a correspondingly dramatic variation. However, as the order of the harmonic field increases ($h \geq 5$), the iron loss becomes less sensitive to the phase shift angle.
- In contrast, the conventional frequency-domain method based on Fourier analysis provides invariant results over different phase shift angles, leading to much larger estimation errors.
- It has been experimentally verified that the proposed H_{dyn}-based dynamic hysteresis model is capable of accurately modeling the major loop component over a wide range of conditions, whereas the $\Delta H_{dyn}/\Delta t$-based model provides overestimated major loop enclosed area with high fundamental and harmonic field frequencies (e.g., f_{fund} = 500 Hz and $f_{har\text{-}3}$ = 1.5 kHz).

- Although the method characterized from the concentric hysteresis loops cannot be directly applied to model the minor loops in the presence of external fields, the proposed minor loop compensation method bypasses this limitation successfully for the purpose of modeling the minor loop influenced by an ac average field without requiring any additional test data.
- Since the H_{dyn}-based model shows a better capability in major loop modeling, and $\Delta H_{dyn}/\Delta t$-based model is preferable for high-frequency analysis, a hybrid dynamic hysteresis model combing these two models are finally formulated. This hybrid dynamic hysteresis model has demonstrated excellent accuracy over broad testing conditions, and it has been further validated for three lamination materials with different thicknesses.
- The magnetic conditions created by the ac average field coupled with the major field and pre-magnetized dc-bias field are similar but different over varying magnetization states. Moreover, minor loops with large amplitudes further accentuate the differences. The proposed 2-D look-up table for dc-bias field corrections serves as an effective tool to determine the equivalent ac average field based on the minor loop and dc-bias field amplitudes. As a result, the minor loop can be accurately estimated using the data characterized from the concentric hysteresis loops.

10.1.4 Investigation and Prediction of PWM-Induced Current Ripple in IPM Machines

- The PWM-induced current ripple can be analytically calculated based on the terminal-to-neutral phase excitation voltage which is determined by the inverter's switching state, dc-bus voltage, and machine operating conditions.

- The value of the modulation index determines the switching pattern of the SVPWM algorithm and plays a crucial role in determining the current ripple's amplitude and frequency spectrum. In particular, the amplitude of the current ripple component at 1x f_{PWM} increases monotonically as the modulation index increases, while the corresponding component at 2x f_{PWM} initially increases and then falls back when the modulation index is > 0.3.
- The IPM machine's dynamic self- and mutual inductances in both axes are functions of rotor position (i.e., slotting effect), current control angle γ, and the phase current amplitude. The dynamic inductance must be used when calculating the current ripple, while the use of the static inductance leads to significant estimation errors when the IPM machine is heavily saturated.
- As the PWM switching frequency f_{PWM} increases, the machine operating conditions and the inverter dc-bus voltage V_{dc} are not affected. Therefore, the decrease of the current ripple amplitude is mainly attributable to the shorter time duration of each switching state at a higher PWM switching frequency.
- The impact of machine rotating speed and inverter dc-bus voltage V_{dc} share some degree of similarities since both of them directly affect the value of the modulation index. As a result, it can be observed that the dominant PWM harmonic components are shifted from 2x f_{PWM} to 1x f_{PWM} as the machine speed increases or as V_{dc} decreases.
- The rms value of the PWM-induced current ripple decreases monotonically versus the current control angle γ. Also, the waveshape of the current ripple experiences a substantial variation as the γ angle changes.

- For constant modulation index values, increasing the phase current amplitude or machine speed leads to monotonic increases in the current ripple amplitude, while the PWM switching patterns and relative current ripple harmonic distribution in the frequency domain remain unchanged.
- An alternative current ripple estimation based on time-stepped FEA simulation is proposed and compared to results from the analytical model and experimental tests. Although the model performance is acceptable when the studied machine operates in the linear region, the current ripple amplitude is underestimated as the machine is driven to heavily saturated region, which, again, indicates it is of great importance to account for the dynamic inductances.

10.1.5 Characterization and Modeling of Soft Magnetic Materials for PWM-Induced Iron Loss Estimation

- For high-frequency excitation (i.e., $f \geq 5$ kHz) and small-amplitude ac flux ripple (i.e., $B_{ac} < 50$ mT) in soft magnetic materials, the dc-bias field exerts a significant impact on its iron loss near the knee region of the material's dc *B*-*H* curve (i.e., $B_{dc} \approx 1.38$ T). After passing the peak point, the iron loss decreases sharply and then remains at a nearly constant value in the heavily-saturated region (i.e., $B_{dc} > 1.6$ T).
- As the amplitude of the ac flux ripple increases, the iron loss becomes more sensitive to the dc-bias field. For 5 kHz excitation, the peak value of the dc-bias iron loss scaling factor with $B_{dc} = 40$ mT (≈ 3) is about 1.5x its value for 7.5 mT (≈ 2). However, the iron loss is less sensitive to the dc-bias field as the frequency increases.

- As the PWM switching frequency f_{PWM} increases, the peak value of dc-bias iron loss scaling factor drops significantly, reducing the iron loss variation over the tested dc-bias field range.
- Physics-based modeling of the impact of dc-bias fields on iron loss is exceptionally challenging due to the complicated nature of iron loss phenomena in microscopic view under changing dc-bias fields. Therefore, experimental characterization of iron loss under varying dc-bias fields turns out to be the most practical approach to modeling these effects.
- The proposed modified dynamic Jiles-Atherton (*J-A*) model has exhibited appealing accuracy and scalability for predicting the PWM-induced iron loss. Results from many tests demonstrate that parameters obtained from a limited number of tests can be used to predict the iron loss over a broad operating range of flux density amplitudes, frequencies, dc-bias field values, and duty cycles of triangular waveforms. The average error estimation error is below 5 %.
- Since the ac magnetic field can exert an equivalent dc-bias impact on PWM-induced harmonics, ignoring the dc-bias field effect yields large iron loss underestimation errors. The observed discrepancies between the measured and predicted results are particularly severe at low PWM frequencies and small modulation index values, where the dc-bias field exerts a more pronounced impact on PWM-induced iron loss.
- As long as the amplitudes of PWM-induced harmonics are relatively small ($B_{ac} < 50$ mT), the total iron loss under inverter excitation can be decomposed into its fundamental and PWM-induced iron loss component. It has been verified that the proposed estimation approach exhibits promising accuracy for predicting the total iron loss over a variety of PWM switching frequency and modulation index value combinations.

10.1.6 Estimation of PWM-Induced Core Losses in IPM Machines

- Since the PWM switching frequency f_{PWM} is typically much higher than the fundamental frequency f_{fund}, the amplitude of the fundamental field within each PWM switching cycle can be approximated as an equivalent dc-bias field, exerting a substantial impact on the iron loss of PWM-induced flux ripple. Ignoring the dc-bias field leads to approximately 20% PWM-induced iron loss underestimation errors over a range of PWM frequencies and machine speeds.
- The PWM-induced magnet loss is the principal contributor to the total magnet loss in IPM machines. Higher PWM switching frequency tends to suppress the magnet loss significantly owing to the skin effect. However, the PWM-induced magnet loss increases monotonically as the machine speed increases due to an increase in the portion of harmonic components that appear in the vicinity of 1x f_{PWM}.
- The frequency decomposition method has demonstrated excellent performance for segregating complex flux ripple waveforms into 1x and 2x f_{PWM} flux ripple components over a variety of machine operating conditions (e.g., varying machine speeds or inverter dc-bus voltages). The results confirm the importance of separately calculating the core losses for these two frequency bands to accurately predict the total PWM-induced iron loss.
- It has been experimentally confirmed that the proposed estimation model is capable of predicting the PWM-induced iron loss of the studied IPM machine over a variety of test conditions with average errors below 10%. This feature makes the model an appealing technique for use in machine design exercises to more accurately incorporate PWM-induced losses into efficiency calculation, as well as for evaluating the impact of different PWM modulation schemes on the resultant PWM-induced iron loss.

- Since the proposed PWM-induced iron loss model performs element-by-element iron loss analysis, there is a basis for confidence that the same model will prove to be valuable for other types of ac machines as well without any required modifications. Also, the proposed technique can be applied to machines using different grades/thicknesses of lamination steels. Nevertheless, the same material characterization process is critically important to characterize the dynamic *J-A* model over a wide range of external dc-bias field and minor-loop excitation frequency values.

10.1.7 High-Frequency Iron Loss Characteristics with WBG-Based Inverter

- The PWM iron losses fall when dc-bias field is raised above its knee point into progressively heavier saturation with f_{PWM} values typical of Si-based inverters (i.e., $f_{PWM} \leq 20$ kHz). However, the measured PWM iron loss using a WBG-based inverter continues to rise monotonically as the dc-bias field is increased beyond the knee point when f_{PWM} is above 100 kHz for the tested 0.30 lamination material.
- When a large amplitude fundamental field (i.e., $B_{fund} \geq 1$ T) coexists with high-frequency PWM harmonics, its average value during each switching cycle can be approximated as an equivalent dc-bias field that exhibits a major influence on the PWM-induced iron loss. The PWM-induced iron loss is more sensitive to the dc-bias field when the PWM frequency and modulation index are both low, corresponding to conditions of high-amplitude flux ripple.
- When PWM harmonics are riding on top of a small amplitude fundamental field (e.g., $B_{fund} = 0.62$ T), the impact of dc-bias field on PWM iron loss is almost negligible. However, increasing the f_{PWM} (i.e., reduce the ripple amplitudes) remains effective to reduce the total iron loss by suppressing the iron loss contribution from PWM harmonics.

- WBG-based inverters offer promising potential to reduce the total iron loss by raising f_{PWM} to higher values, where the maximum total iron loss reduction rate with 0.6 inverter modulation index approx. 50%. However, there are diminishing incremental energy savings as the P2F ratio is pushed beyond its linear region (i.e., P2F >150), making it essential to consider the combined motor and inverter losses when maximizing drive efficiency.

10.1.8 PWM Power Losses in IPM Machines with WBG-Based Inverter

- Even though the SVPWM and DPWM scheme share the identical fundamental output component, different zero-state distributions in each PWM cycle lead to varying current ripple amplitudes, waveshapes, and frequency compositions, which, in turn, induce different PWM power losses in IPM machines.
- The PWM-induced copper loss in IPM machines with form-wound windings can contribute to a significant portion of the total copper loss when operating with a very low PWM switching frequency. However, as the f_{PWM} is raised up to a higher value, the copper loss contribution shrinks significantly for both PWM schemes. Also, the PWM copper loss consumed by the end-winding is very low compared to the in-slot region since the end-winding resistance is not sensitive to the PWM frequency.
- The PWM-induced iron loss caused by the DPWM scheme is higher than that by the SVWPM scheme, due, in part, to having it dominant harmonic components primarily concentrated at low frequencies with larger ripple amplitudes.
- The PWM-induced iron losses in both the stator and rotor side are heavily influenced by the dc-bias field, and the PWM iron loss from the rotor side contributes to approx. a quarter of the total PWM iron loss, making it a critical loss component in IPM machines.

- With a low excitation frequency and large skin depth value, increasing the magnet segmentation suppresses the circulating current, resulting in a lower magnet loss. At higher frequencies before reaching the peak loss point, increasing the segmentation number provides more circulating paths for the eddy current, leading to a higher loss.
- For the studied baseline IPM machine, the predicted loss composition results suggest that the copper and magnet PWM losses become insignificant with sufficiently high PWM frequency while the PWM iron loss remains the dominant loss component. Moreover, the SVPWM scheme exhibits advantages over the DPWM scheme, which exhibit smaller PWM power losses over the studied PWM frequency range.

10.2 Contributions

The principal objective of the overall project is to develop new models that improve the prediction of ac core losses in high-performance PM synchronous machines for traction applications, and then to integrate these models into machine design software for achieving loss reduction. The key contributions of this research project are summarized as follows:

- **Developed a generalized dynamic hysteresis model for improved iron loss estimation of complex flux waveforms**

  A new generalized dynamic hysteresis model has been developed for accurately modeling the complexities associated with the fundamental and low-order harmonic field-induced iron loss. Compared to the conventional model based on the Steinmetz equation or iron loss separation theorem, the new model is capable of emulating the magnetization process from the predicted dynamic hysteresis loop much more accurately. The following project accomplishments support this contribution:

  - Developed a more general hypothesis for dynamic field modeling which is applicable to flux waveforms with arbitrary waveshapes.
  - Developed a new minor loop estimation method with symmetrical B-H curve data, enabling accurate minor loop estimation without conducting any additional tests involving the dc-bias fields.
  - Determined the influence of the ac average field and dc-bias field on the minor loop over a wide range of excitation frequencies and minor loop amplitudes.
  - Developed a new dc-bias field correction technique that links the ac average field and dc-bias field via a 2-D look-up table.

- **Experimentally verified the new generalized dynamic hysteresis model and used it to investigate some important features of the iron loss characteristics**

  The proposed dynamic hysteresis model and the accompanying experimental results have been utilized to investigate key features of the iron loss characteristics and model accuracy over a wide variety of operating conditions. Key aspects of this contribution include the following:

  - Experimentally verified the model's accuracy and scalability for a range of different sinewave excitation frequencies up to 5 kHz and flux density amplitudes up to 1.6 T.
  - Applied the model to expose and characterize the significant impact of the phase shift angle between the fundamental and higher-order harmonic field on the hysteresis loop and the resulting iron loss over varying harmonic field amplitudes and frequencies.
  - Applied the model to perform a comparative study of the impact of the ac average field and dc-bias field on the minor loop over varying amplitudes and frequencies.
  - Conducted a preliminary experimental evaluation of the proposed dynamic hysteresis model on machine-level iron loss analysis with promising results.
  - Developed an element-by-element fundamental field iron loss estimation approach including a complex waveshape segregation and rotating field decomposition method.

- **Developed an enhanced PWM-induced current ripple modeling approach**

  A promising analytical model has been developed to accurately predict the PWM-induced current ripple in IPM machines. In addition to calculating the current waveforms including the PWM switching harmonics, this investigation has offered valuable insights into the frequency distribution and current ripple waveshapes over a wide range of machine and inverter working conditions. Key elements of this contribution include the following:

- Performed 2-D FEA simulation to characterize the dynamic inductances of IPM machines in both axes over a broad range of machine operating conditions.
- Incorporated the impact of slotting, magnetic saturation, and cross-coupling effects into the analytical current ripple estimation. The unique feature of this research is that the estimation accuracy is not degraded even when the machine is operating under heavy saturation conditions.
- Determined the influence of the modulation index which primarily determines the frequency composition of the current ripple induced by PWM switching.
- Investigated the impact of several influencing factors (e.g., PWM switching frequency, machine rotating speed, etc.) on the current ripple frequency composition and rms amplitude, leading to a better understanding of machine-side loss variation under different operating conditions.

- **Developed a generalized dynamic hysteresis model for PWM-induced iron loss estimation**

  A promising technique has been developed during this research to predict the PWM-induced iron loss with high-frequency ac flux density, varying dc-bias fields, and non-sinusoidal excitation of the soft magnetic materials adopted in electric machines. Key elements of this contribution include the following:

  - Developed versatile *B*-*H* measurement systems to investigate the iron loss variation over a wide range of ac and dc excitation, providing valuable data and insights into high-frequency ac iron loss characteristics in the presence of dc-bias fields.
  - Explored the power loss measurement accuracy when the tested magnetic material is operated under heavy saturation and high-frequency conditions.

- Investigated the PWM-iron loss characteristics of different lamination steels when they are driven by WBG-based VSIs with a broad range of PWM switching frequencies.
- Developed generalized dynamic Jiles-Atherton (*J-A*) hysteresis models for PWM-induced iron loss estimation, enabling a better emulation of the iron loss variation trends over varying operating conditions.
- Investigated the impact of several influencing factors on high-frequency iron loss, including the amplitude of the ac flux ripple, PWM excitation frequency, and duty cycle of the PWM excitation waveform.
- Developed a generalized and accurate approach to estimate the total iron loss in lamination steels under PWM voltage excitation over a broad range of PWM switching frequencies, fundamental field amplitudes, and excitation frequencies.

- **Developed an integrated machine-level PWM-induced iron loss estimation model**

  A complete model for improved machine-level PWM-induced iron loss prediction has been developed including capabilities for PWM-induced current and flux ripple prediction, flux ripple frequency decomposition, and iron loss calculation, enabling much improved PWM-induced iron loss estimation in both existing and newly-developed IPM machine designs. Key elements of this contribution include the following:

  - Incorporated the predicted PWM-induced current ripple into the magnetic flux ripple identification process.
  - Developed a new frequency decomposition approach to analytically decompose the PWM-induced flux ripple into 1x and 2x PWM frequency components.

- Experimentally segregated the total machine PWM-induced core losses from the machine total power losses.
- Investigated the impact of several influencing factors on the resulting PWM-induced iron loss including: PWM switching frequency, machine rotating speed, inverter dc-bus voltage, and current control angle.
- Performed 3-D FEA simulation to investigate the variation trends of PWM-induced magnet loss in IPM machines for a wide range of operating conditions.

- **Investigated the PWM-induced power losses in IPM machines with different PWM switching frequencies and modulation schemes**

  An in-depth analysis of the PWM power losses in IPM traction machines has been developed during this research program to assess the opportunities and challenges brought by WBG-based VSIs. The variation trend of each loss component has been investigated using the best available loss prediction models. Key elements of this contribution include the following:

  - Developed a generalized flux ripple decomposition approach applicable for both the SVPWM and DPWM schemes.
  - Investigated the impact of magnet segmentation on PWM-induced magnet eddy current loss with varying PWM switching frequencies.
  - Investigated the impact of the PWM modulation scheme on PWM power losses in IPM machines over a wide range of PWM frequencies enabled by WBG-based VSIs.
  - Experimentally verified the proposed composite model's promising capabilities for PWM power loss analysis and prediction in two IPM traction machines.

- Experimentally validated the total power loss estimation capabilities for IPM machines by combining the models developed throughout this research program.

10.3 Recommended Future Work

The following topics are recommended for future investigation, inspired by the results presented in this dissertation.

10.3.1 Iron Loss Investigation in Different Electric Machine Topologies

- This thesis proposes a comprehensive fundamental and PWM-induced iron loss analysis in IPM traction machines. It would be beneficial to fully understand the iron loss properties in different types of electric machines for a broad range of applications. Although some types of synchronous machines share some similarities to IPM machines (e.g., surface permanent magnet (SPM) machines, synchronous reluctance machines (SynRM), etc.) in terms of their excitation waveforms and the flux density waveshapes, notable differences exist in other electric machines. Taking the induction machines (IMs) as an example, it is the leakage inductance, rather than the dynamic magnetizing inductance in the case of IPM machines, that mainly determines the PWM-induced current ripple amplitude. Also, the fundamental frequency on the rotor side of IMs varies with the slip frequency rather than maintaining a constant value. Moreover, for some other PM machines with magnets embedded in the stator slots (flux-switching permanent magnet (FSPM) machines, doubly-salient PM (DSPM) machines, etc.), the stator magnetic field is affected by a dc-bias field created by the PMs. As a result, the iron loss on the rotor side is significantly higher than for traditional PM machines due to this flux variation effect. Therefore, the fundamental and PWM-

induced iron loss properties must be analyzed and modeled differently depending on the specific machine topology under study.

10.3.2 Emerging Materials Characterization for Future Electric Machine Applications

- In this thesis, three silicon-iron (SiFe) materials with different sheet thicknesses have been experimentally characterized over a wide range of flux density amplitudes, excitation frequencies, and pre-magnetized dc-bias fields. In light of recent development in magnetic materials for future electric machine applications, it would be useful and interesting to extend the magnetic material characterization to other emerging materials, including but not limited to ultra-thin gauge silicon-iron steels (i.e., sheet thickness approx. 0.1 mm), Cobalt-iron (CoFe) and Nickel-iron (NiFe) magnetic alloys, amorphous and nanocrystalline alloys, and soft magnetic composite (SMC) material. Although there are existing reports in the technical literature demonstrating several appealing advantages of the aforementioned magnetic materials for varying applications, their loss properties when excited by PWM voltage waveforms are not yet well understood, encouraging further investigation.

10.3.3 Incorporation of Manufacturing Influences into Iron Loss Modeling

- The magnetic materials presented in this thesis are manufactured either by mechanical stamping with a stress relief annealing process (0.30 mm material), or by wire electrical discharge machining (0.25 and 0.27 mm material). The impact of mechanical and thermal stress induced during the cutting process is minimized as much as possible to retain the materials' optimum magnetic and iron loss properties. However, in production machines, the cutting and welding processes can exert a significant impact on the resulting iron loss.

More recently, new machining technique such as additive manufacturing (i.e., metal 3-D printing) is becoming more practical and increasingly popular in various applications. Thus, incorporating the influences of the manufacturing process into the loss models is of great importance to future machine analysis.

10.3.4 Development of Iron Loss Models using Machine Learning Techniques

- The generalized dynamic hysteresis model developed in this thesis for fundamental field iron loss analysis approximates the magnetic history impact as the preceding flux density reversing point, neglecting the impact of the travel trajectory between the flux density reversing point and current modeling point. Although the proposed model shows promising accuracy when the studied waveform has a shape relatively close to sinusoidal waveforms, the model accuracy might degrade if the studied flux density waveform deviates significantly from the sinusoidal shape. Taking switched reluctance machines (SRMs) as an example, when the machine phase current waveshape is no longer sinusoidal, the resulting flux density waveshapes become much more complicated and contain rich harmonic components. Thus, the magnetic history impact will likely become much more pronounced compared to that in IPM machines. However, as discussed in this thesis, it is hard to develop a unique solution to account for arbitrary magnetic histories. One candidate approach to resolve this challenging problem is to use machine learning techniques such as artificial neural networks. By providing input *B*-*H* curves corresponding to the target applications (e.g., flux density waveforms commonly observed in SRMs) to tune the parameters in the constructed neural network, dynamic hysteresis loops can be emulated using an alternative approach.

- Regarding the PWM-induced iron loss analysis, the proposed dynamic Jiles-Atherton (*J-A*) with frequency interconnection has exhibited appealing capabilities for modeling the PWM iron loss over broad ranges of frequencies and dc-bias fields. However, a commonly-acknowledged shortcoming of the *J-A* model is that the parameter identification process is tedious and complicated. Therefore, machine learning techniques might provide the basis for an effective solution to this challenging problem.

10.3.5 Development of a Measurement System with Extended Frequency Range

- Enabled by emerging wide-bandgap (WBG) power devices (i.e., SiC and GaN), electric machines can operate at much elevated rotating speeds to boost the machine power density in applications such as aerospace. However, a major challenge associated with adopting high rotating speeds (i.e., high fundamental frequencies) is that the iron loss in electric machines also increases considerably, which can be detrimental to the machine and drive down system efficiency. Making matters worse, the ratio between the PWM and fundamental frequency (P2F) likely shrinks to a smaller ratio as the fundamental frequency increases, depending on the inverter capabilities. As presented in this thesis, the PWM-induced harmonics contribute a more substantial proportion of the total iron loss for smaller values of the P2F ratio. As a result, there are practical benefits to further extending the measurement system's frequency range to improve prediction of the iron loss during the design of high-speed electric machines.

10.3.6 Investigation of PWM-Induced Power Losses in the Over-Modulation Region

- An analytical PWM-induced current ripple estimation approach has been developed in this thesis for IPM machines operating in the linear region. Having accurate current ripple data is indispensable to develop physical insights into the PWM power losses in the studied machines. Moreover, the predicted current ripple data provide a valuable basis for implementing the frequency decomposition approach to the PWM-induced flux ripple in order to generate the input data for the proposed PWM iron loss estimation model. However, to fully utilize the inverter output voltage, the investigation of PWM power losses should be extended to the over-modulation region. The specific control algorithm implemented in the over-modulation region is likely to have a significant impact on the resulting machine PWM losses.

10.3.7 Investigation of WBG Inverter Characteristics on Electric Machine Efficiency

- In this thesis, the iron loss characteristics of three selected SiFe lamination steels excited by WBG-based VSIs have been investigated over a wide range of PWM switching frequencies and external dc-bias fields. It is worth noting that the developed GaN-based single-phase inverter reduces the switch deadtime to a very small value (approx. 20 *ns*) based on the GaN switch's ultra-fast turn-on and turn-off times. However, in practical applications, the inverter turn-on and turn-off time may be purposely extended (e.g., adjusting the values of the gate resistance) to meet the *dv/dt* regulations or to optimize the inverter switching losses. In some applications, a *L-C-R dv/dt* filter is placed between the inverter output terminals and the machine input to suppress the *dv/dt* rate of the output voltage waveforms in order to

reduce EMI noise, etc. Therefore, it is critically important to understand how the design characteristics of the WBG-based inverter affect the machine-side efficiency.

10.3.8 Development of Multi-Physics Models for System-Level Optimization

- The focus of the PWM power losses analysis presented in this thesis has been on the machine-side loss components. However, the system-level efficiency is also tightly related to the inverter-side losses. Increasing f_{PWM} helps to constrain the current ripple amplitudes, while larger inverter switching losses are inevitable when it operates at elevated switching frequencies. Therefore, a comprehensive optimization is necessary to determine the PWM frequency and modulation scheme that delivers the optimum system-level efficiency based on the machine's operating conditions. In addition, since thermal and structural analyses of both the inverter and machine are of great importance for practical applications, it is necessary to incorporate multi-physics models for system-level design optimization.

Bibliography

[1] O. Aglen, "Loss calculation and thermal analysis of a high-speed generator," in *IEEE International Electric Machines and Drives Conference, 2003. IEMDC'03.*, Madison, WI, USA, 2003, vol. 2, pp. 1117–1123.

[2] W. Zhang, "Winding losses in high-speed machines using form-wound windings," University of Wisconsin- Madison, 2015.

[3] K. Yamazaki and Y. Seto, "Iron loss analysis of interior permanent-magnet synchronous motors-variation of main loss factors due to driving condition," *IEEE Trans. Ind. Appl.*, vol. 42, no. 4, pp. 1045–1052, Jul. 2006.

[4] D. Kowal, P. Sergeant, L. Dupre, and H. Karmaker, "Comparison of frequency and time-domain iron and magnet loss modeling including PWM harmonics in a PMSG for a wind energy application," *IEEE Trans. Energy Convers.*, vol. 30, no. 2, pp. 476–486, Jun. 2015.

[5] K. Yamazaki and A. Abe, "Loss investigation of interior permanent-magnet motors considering carrier harmonics and magnet eddy currents," *IEEE Trans. Ind. Appl.*, vol. 45, no. 2, pp. 659–665, Apr. 2009.

[6] P. Roussel, "SiC market and industry update," presented at the Int. SiC Power Electron. Appl. Workshop, Kista, Sweden, 2011.

[7] J. Millan, P. Godignon, X. Perpina, A. Perez-Tomas, and J. Rebollo, "A survey of wide bandgap power semiconductor devices," *IEEE Trans. Power Electron.*, vol. 29, no. 5, pp. 2155–2163, May 2014.

[8] A. G. Sarigiannidis and A. G. Kladas, "Switching frequency impact on permanent magnet motors drive system for electric actuation applications," *IEEE Trans. Magn.*, vol. 51, no. 3, pp. 1–4, Mar. 2015.

[9] G. Bertotti, A. Boglietti, M. Chiampi, D. Chiarabaglio, F. Fiorillo, and M. Lazzari, "An improved estimation of iron losses in rotating electrical machines," *IEEE Trans. Magn.*, vol. 27, no. 6, pp. 5007–5009, Nov. 1991.

[10] A. Krings, "Iron losses in electrical machines- Influence of material properties, manufacturing processes, and inverter operation," KTH Royal Institute of Technology, 2014.

[11] F. Brailsford, "Magnetic materials: A review of progress," *Methuns Phys. Monogr.*, p. 22.

[12] J. Reinert, A. Brockmeyer, and R. A. A. De Doncker, "Calculation of losses in ferro- and ferrimagnetic materials based on the modified Steinmetz equation," *IEEE Trans. Ind. Appl.*, vol. 37, no. 4, p. 7, 2001.

[13] D. Steiner Petroviĉ, "Non-oriented electrical steel sheets," *Mater. Technol.*, vol. 44, no. 6, 2010.

[14] R. Hilzinger and W. Rodewald, "Magnetic materials: fundamentals, products, properties, applications," *Vacuumschmelze*, 2013.

[15] H. J. Williams, W. Shockley, and C. Kittel, “Studies of the propagation velocity of a ferromagnetic domain boundary,” *Phys. Rev.*, vol. 80, no. 6, pp. 1090–1094, Dec. 1950.

[16] R. H. Pry and C. P. Bean, “Calculation of the energy loss in magnetic sheet materials using a domain model,” *J. Appl. Phys.*, vol. 29, no. 3, pp. 532–533, Mar. 1958.

[17] Gordon E. Fish, “Soft magnetic materials,” *Proc. IEEE*, vol. 78, pp. 967–972, Jun. 1990.

[18] T. R. Haller and J. J. Kramer, “Model for reverse domain nucleation in ferromagnetic conductors,” *J. Appl. Phys.*, vol. 41, no. 3, pp. 1036–1037, Mar. 1970.

[19] G. Bertotti, F. Fiorillo, and P. Mazzetti, “Basic principles of magnetization processes and origin of losses in soft magnetic materials,” *J. Magn. Magn. Mater.*, vol. 112, no. 1–3, pp. 146–149, Jul. 1992.

[20] C. D. Graham, “Physical origin of losses in conducting ferromagnetic materials (invited),” *J. Appl. Phys.*, vol. 53, no. 11, pp. 8276–8280, Nov. 1982.

[21] J. J. Becker, “Magnetization changes and losses in conducting ferromagnetic materials,” *J. Appl. Phys.*, vol. 34, no. 4, pp. 1327–1332, Apr. 1963.

[22] C. Steinmetz, “On the law of hysteresis (originally published in 1892),” *Proc. IEEE*, vol. 72, no. 2, pp. 197–221, 1982.

[23] P. M. Gradzki, M. M. Jovanovic, and F. C. Lee, “Computer aided design for high-frequency power transformers,” *Proc IEEE APEC90*, pp. 336–343, 1990.

[24] R. Severns, “HF-core losses for nonsinusoidal waveforms,” *Proc HFPC*, pp. 140–148, 1991.

[25] M. Albach, T. Durbaum, and A. Brockmeyer, “Calculating core losses in transformers for arbitrary magnetizing currents a comparison of different approaches,” in *PESC Record. 27th Annual IEEE Power Electronics Specialists Conference*, Baveno, Italy, 1996, vol. 2, pp. 1463–1468.

[26] M. S. Lancarotte and A. de A. Penteado, “Estimation of core losses under sinusoidal or non-sinusoidal induction by analysis of magnetization rate,” *IEEE Trans. ENERGY Convers.*, vol. 16, no. 2, p. 6, 2001.

[27] G. Bertotti, *Hysteresis in magnetism: for physicists, materials scients, and engineers*. Academic Press, 1998.

[28] I. D. Mayergoyz, *Mathematical models of hysteresis*. Springer-Verlag, 1991.

[29] Jieli Li, T. Abdallah, and C. R. Sullivan, “Improved calculation of core loss with nonsinusoidal waveforms,” in *Conference Record of the 2001 IEEE Industry Applications Conference. 36th IAS Annual Meeting (Cat. No.01CH37248)*, Chicago, IL, USA, 2001, vol. 4, pp. 2203–2210.

[30] K. Venkatachalam, C. R. Sullivan, T. Abdallah, and H. Tacca, “Accurate prediction of ferrite core loss with nonsinusoidal waveforms using only Steinmetz parameters,” in *2002 IEEE Workshop on Computers in Power Electronics, 2002. Proceedings.*, Mayaguez, Puerto Rico, 2002, pp. 36–41.

[31] A. Brockmeyer, “Experimental evaluation of the influence of DC-premagnetization on the properties of power electronic ferrites,” in *Proceedings of Applied Power Electronics Conference. APEC ’96*, San Jose, CA, USA, 1996, vol. 1, pp. 454–460.

[32] A. Brockmeyer and J. Paulus-Neues, “Frequency dependence of the ferrite-loss increase caused by premagnetization,” in *Proceedings of APEC 97 - Applied Power Electronics Conference*, Atlanta, GA, USA, 1997, vol. 1, pp. 375–380.

[33] Wai Keung Mo, D. K. W. Cheng, and Y. S. Lee, “Simple approximations of the DC flux influence on the core loss power electronic ferrites and their use in design of magnetic components,” *IEEE Trans. Ind. Electron.*, vol. 44, no. 6, pp. 788–799, Dec. 1997.

[34] J. Muhlethaler, J. Biela, J. W. Kolar, and A. Ecklebe, “Core losses under the DC bias condition based on steinmetz parameters,” *IEEE Trans. Power Electron.*, vol. 27, no. 2, pp. 953–963, Feb. 2012.

[35] C. Simao, N. Sadowski, N. J. Batistela, and J. P. A. Bastos, “Evaluation of hysteresis losses in iron sheets under DC-biased inductions,” *IEEE Trans. Magn.*, vol. 45, no. 3, pp. 1158–1161, Mar. 2009.

[36] J. Muhlethaler, J. Biela, J. W. Kolar, and A. Ecklebe, “Improved core-loss calculation for magnetic components employed in power electronic systems,” *IEEE Trans. Power Electron.*, vol. 27, no. 2, pp. 964–973, Feb. 2012.

[37] A. Van den Bossche, V. C. Valchev, and G. B. Georgiev, “Measurement and loss model of ferrites with non-sinusoidal waveforms,” in *2004 IEEE 35th Annual Power Electronics Specialists Conference (IEEE Cat. No.04CH37551)*, Aachen, Germany, 2004, pp. 4814–4818.

[38] H. Jordan, “Die ferromagnetischen Konstanten für schwache Wechselfelder,” *Elektr Nach Techn*, 1924.

[39] G. Bertotti, “General properties of power losses in soft ferromagnetic materials,” *IEEE Trans. Magn.*, vol. 24, no. 1, pp. 621–630, Jan. 1988.

[40] G. Bertotti, G. Di Schino, A. Ferro Milone, and F. Fiorillo, “On the effect of grain size on magnetic losses of 3 % non-oriented SiFe,” *J. Phys. Colloq.*, vol. 46, no. C6, pp. C6-385-C6-388, Sep. 1985.

[41] K. Chwastek, “Prediction of loss in non-oriented steel laminations,” *Elect Rev*, vol. 88, no. 5a, pp. 5–9, 2012.

[42] A. Broddefalk and M. Lindenmo, “Dependence of the power losses of a non-oriented 3% Si-steel on frequency and gauge,” *J. Magn. Magn. Mater.*, vol. 304, no. 2, pp. e586–e588, Sep. 2006.

[43] J. E. L. Bishop, “Accomadation of the speed distribution of magnetic domain walls with speeds in field equilibrium,” *J Magn Magn Mater*, vol. 86, pp. 341–348, 1990.

[44] J. E. L. Bishop, “Eddy current interaction loss of randomly distributed magnetic domain walls with speeds in field equilibrium,” *IEEE Trans Magne*, vol. 26, pp. 2217–2219, Sep. 1990.

[45] H. Pfutzner, P. Schonhuber, B. Erbil, G. Harasko, and T. Klinger, “Problems of loss separation for crystalline and consolidated amorphous soft magnetic materials,” *IEEE Trans. Magn.*, vol. 27, no. 3, pp. 3426–3432, May 1991.

[46] D. J. Seagle and S. H. Charap, “Frequency dependent hysteresis loss in SiFe,” *J. Appl. Phys.*, vol. 53, no. 11, pp. 8299–8301, Nov. 1982.

[47] M. Ibrahim and P. Pillay, “Advanced testing and modeling of magnetic materials including a new method of core loss separation for electrical machines,” *IEEE Trans. Ind. Appl.*, vol. 48, no. 5, pp. 1507–1515, Oct. 2012.

[48] Y. Zhang, R. Guan, P. Pillay, and M.-C. Cheng, "General core loss models on a magnetic lamination," in *2009 IEEE International Electric Machines and Drives Conference*, Miami, FL, USA, May 2009, pp. 1529–1534.

[49] Y. Gao, Y. Matsuo, and K. Muramatsu, "Investigation on simple numeric modeling of anomalous eddy current loss in steel plate using modified conductivity," *IEEE Trans. Magn.*, vol. 48, no. 2, pp. 635–638, Feb. 2012.

[50] D. M. Ionel, M. Popescu, M. I. McGilp, T. J. E. Miller, S. J. Dellinger, and R. J. Heideman, "Computation of core losses in electrical machines using improved models for laminated steel," *IEEE Trans. Ind. Appl.*, vol. 43, no. 6, pp. 1554–1564, Dec. 2007.

[51] S. Zhu, M. Cheng, J. Dong, and J. Du, "Core loss analysis and calculation of stator permanent-magnet machine considering DC-biased magnetic induction," *IEEE Trans. Ind. Electron.*, vol. 61, no. 10, pp. 5203–5212, Oct. 2014.

[52] S. Yanase, Y. Okazaki, and T. Asano, "AC magnetic properties of electrical steel core under DC-biased magnetization," *J. Magn. Magn. Mater.*, vol. 215–216, pp. 156–158, Jun. 2000.

[53] E. Barbisio, O. Bottauscio, M. Chiampi, and C. Ragusa, "Analysis of AC magnetic properties in SiFe laminations under DC-biased magnetisation," *Phys. B Condens. Matter*, vol. 343, no. 1–4, pp. 127–131, Jan. 2004.

[54] S. Xue *et al.*, "Iron loss model under DC bias flux density considering temperature influence," *IEEE Trans. Magn.*, vol. 53, no. 11, pp. 1–4, Nov. 2017.

[55] B. Tekgun, Y. Sozer, and I. Tsukerman, "Measurement of core losses in electrical steel in the saturation region under DC bias conditions," *IEEE Trans. Ind. Appl.*, vol. 53, no. 1, pp. 88–96, Jan. 2017.

[56] T. Taitoda, Y. Takahashi, and K. Fujiwara, "Iron loss estimation method for a general hysteresis loop with minor loops," *IEEE Trans. Magn.*, vol. 51, no. 11, pp. 1–4, Nov. 2015.

[57] D. C. Jiles and D. L. Atherton, "Theory of ferromagnetic hysteresis," *J. Magn. Magn. Mater.*, vol. 61, no. 1–2, pp. 48–60, 1986.

[58] D. C. Jiles, J. B. Thoelke, and M. K. Devine, "Numerical determination of hysteresis parameters for the modeling of magnetic properties using the theory of ferromagnetic hysteresis," *IEEE Trans. Magn.*, vol. 28, no. 1, pp. 27–35, Jan. 1992.

[59] J. Izydorczyk, "A new algorithm for extraction of parameters of Jiles and Atherton hysteresis model," *IEEE Trans. Magn.*, vol. 42, no. 10, pp. 3132–3134, Oct. 2006.

[60] F. R. Fulginei and A. Salvini, "Softcomputing for the identification of the Jiles-Atherton model parameters," *IEEE Trans. Magn.*, vol. 41, no. 3, pp. 1100–1108, Mar. 2005.

[61] D. Lederer, H. Igarashi, A. Kost, and T. Honma, "On the parameter identification and application of the Jiles-Atherton hysteresis model for numerical modelling of measured characteristics," *IEEE Trans. Magn.*, vol. 35, no. 3, pp. 1211–1214, May 1999.

[62] P. R. Wilson, J. N. Ross, and A. D. Brown, "Optimizing the Jiles-Atherton model of hysteresis by a genetic algorithm," *IEEE Trans. Magn.*, vol. 37, no. 2, pp. 989–993, Mar. 2001.

[63] E. D. M. Hernandez, C. S. Muranaka, and J. R. Cardoso, “Identification of the Jiles-Atherton model parameters using random and deterministic searches,” *Phys. B*, vol. 275, pp. 212–215, 2000.

[64] L. A. L. Almeida, G. S. Deep, Lima A. M. N., and F. H. Nef, “Modeling a magnetostrictive transducer using genetic algorithm,” *J Magn Magn Mater*, vol. 266–230, pp. 1262–1264, 2001.

[65] S. Cao, B. Wang, R. Yan, W. Huang, and Q. Yang, “Optimization of hysteresis parameters for the Jiles-Atherton model using a genetic algorithm,” *IEEE Trans. Appiled Supercond.*, vol. 14, no. 2, pp. 1157–1160, Jun. 2004.

[66] K. Chwastek and J. Szczyglowski, “Identification of a hysteresis model parameters with genetic algorithms,” *Math Comput Simulat*, vol. 71, no. 3, pp. 206–211, May 2006.

[67] A. Salvini and F. R. Fulginei, “Genetic algorithms and neural networks generalizing the Jiles-Atherton model of static hysteresis for dynamic loops,” *IEEE Trans. Magn.*, vol. 38, no. 2, pp. 873–876, Mar. 2002.

[68] D. Grimaldi, L. Michaeli, and A. Palumbo, “Automatic and accurate evaluation of the parameters of a magnetic hysteresis model,” *IEEE Trans. Instrum. Meas.*, vol. 49, no. 1, pp. 154–160, Feb. 2000.

[69] R. Marion, R. Scorretti, N. Siauve, M.-A. Raulet, and L. Krahenbiihl, “Identification of Jiles–Atherton model parameters using particle swarm optimization,” *IEEE Trans. Magn.*, vol. 44, no. 6, pp. 894–897, Jun. 2008.

[70] J. V. Leite, N. Sadowski, P. Kuo-Peng, N. J. Batistela, and J. P. A. Bastos, “The inverse Jiles-Atherton model parameters identification,” *IEEE Trans. Magn.*, vol. 39, no. 3, pp. 1397–1400, May 2003.

[71] A. Benabou, J. V. Leite, S. Clénet, C. Simão, and N. Sadowski, “Minor loops modelling with a modified Jiles–Atherton model and comparison with the Preisach model,” *J. Magn. Magn. Mater.*, vol. 320, no. 20, pp. e1034–e1038, Oct. 2008.

[72] M. Hamimid, S. M. Mimoune, M. Feliachi, and K. Atallah, “Non centered minor hysteresis loops evaluation based on exponential parameters transforms of the modified inverse Jiles–Atherton model,” *Phys. B Condens. Matter*, vol. 451, pp. 16–19, Oct. 2014.

[73] D. C. Jiles, “A self consistent generalized model for the calculation of minor loop excursions in the theory of hysteresis,” *IEEE Trans Mag*, vol. 28, no. 5, pp. 2602–2604, 1992.

[74] M. Hamimid, S. M. Mimoune, and M. Feliachi, “Evaluation of minor hysteresis loops using Langevin transforms in modified inverse Jiles–Atherton model,” *Phys. B Condens. Matter*, vol. 429, pp. 115–118, Nov. 2013.

[75] F. Preisach, “On the magnetic aftereffect,” *IEEE Trans. Magn.*, vol. 53, no. 3, pp. 1–11, Mar. 2017.

[76] I. Mayergoyz, “Mathematical models of hysteresis,” *IEEE Trans. Magn.*, vol. 22, no. 5, pp. 603–608, Sep. 1986.

[77] M. Krasnoselskii and A. Pokrovskii, *Systems with Hysteresis*. Nauka, Moscow, 1983.

[78] S. E. Zirka, Y. I. Moroz, P. Marketos, and A. J. Moses, “Congruency-based hysteresis models for transient simulation,” *IEEE Trans. Magn.*, vol. 40, no. 2, pp. 390–399, Mar. 2004.

[79] E. Dlala, “Inverted and forward Preisach models for numerical analysis of electromagnetic field problems,” *IEEE Trans Mag*, vol. 42, pp. 1963–1973, 2006.

[80] S. R. Naidu, “Simulation of the hysteresis phenomenon using Preisach’s theory,” *IEE Proc. Phys. Sci. Meas. Instrum. Manag. Educ.*, vol. 137, no. 2, pp. 73–79, Mar. 1990.

[81] A. A. Adly and S. K. Abd-El-Hafiz, “Using neural networks in the identification of Preisach-type hysteresis models,” *IEEE Trans. Magn.*, vol. 34, no. 3, pp. 629–635, May 1998.

[82] C. Serpico and C. Visone, “Magnetic hysteresis modeling via feed-forward neural networks,” *IEEE Trans. Magn.*, vol. 34, no. 3, pp. 623–628, May 1998.

[83] E. Dlala and A. Arkkio, “A neuro-fuzzy-based Preisach approach on hysteresis modeling,” *Phys. B Condens. Matter*, vol. 372, pp. 49–52, 2006.

[84] E. Dlala, J. Saitz, and A. Arkkio, “Hysteresis modeling based on symmetric minor loops,” *IEEE Trans. Magn.*, vol. 41, no. 8, pp. 2343–2348, Aug. 2005.

[85] P. Kis, M. Kuscmann, J. Fuzi, and A. Iványi, “Hysteresis measurement in LabView,” *Phys. B Condens. Matter*, vol. 343, no. 1–4, pp. 357–363, Jan. 2004.

[86] M. Kuczmann, “Dynamic Preisach hysteresis model,” p. 6, 2010.

[87] D. A. Philips, “Comparison of Jiles and Preisach hysteresis models in magnetodynamics,” *IEEE Trans Mag*, vol. 31, no. 6, pp. 3551–3553, 1995.

[88] A. Benabou, S. Clénet, and F. Piriou, “Comparison of Preisach and Jiles–Atherton models to take into account hysteresis phenomenon for finite element analysis,” *J. Magn. Magn. Mater.*, vol. 261, no. 1–2, pp. 139–160, Apr. 2003.

[89] D. C. Jiles, “Frequency dependence of hysteresis curves in conducting magnetic materials,” *J. Appl. Phys.*, vol. 76, no. 10, pp. 5849–5855, Nov. 1994.

[90] R. Du and P. Robertson, “Dynamic Jiles-Atherton model for determining the magnetic power loss at high frequency in permanent magnet machines,” *IEEE Trans Mag*, vol. 51, no. 6, pp. 1–10, Jun. 2015.

[91] A. P. S. Baghel and S. V. Kulkarni, “Dynamic loss inclusion in the Jiles–Atherton (JA) hysteresis model using the original JA approach and the field separation approach,” *IEEE Trans. Magn.*, vol. 50, no. 2, pp. 369–372, Feb. 2014.

[92] R. M. Del Vecchio, “Computation of losses in nonoriented electrical steels from a classical viewpoint (invited),” *J. Appl. Phys.*, vol. 53, no. 11, pp. 8281–8286, Nov. 1982.

[93] D. H. Gillott and J. F. Calvert, “Eddy current loss in saturated solid magnetic plates, rods, and conductors,” *IEEE Trans Mag*, vol. 1, pp. 126–137, 1965.

[94] I. D. Mayergoyz, “Dynamic Preisach models of hysteresis,” *IEEE Trans. Magn.*, vol. 24, no. 6, pp. 2925–2927, Nov. 1988.

[95] G. Bertotti, “Dynamic generalization of the scalar Preisach model of hysteresis,” *IEEE Trans Mag*, vol. 28, pp. 2559–2601, Sep. 1992.

[96] D. A. Philips, L. R. Dupré, and J. A. A. Melkebeek, "Magneto-dynamic field computation using a rate-dependent Preisach model," *IEEE Trans Mag*, vol. 30, pp. 4377–4379, Nov. 1994.

[97] Y. Bernard, E. Mendes, and F. Bouillault, "Dynamic hysteresis modeling based on Preisach model," *IEEE Trans. Magn.*, vol. 38, no. 2, pp. 885–888, Mar. 2002.

[98] S. E. Zirka, Y. I. Moroz, P. Marketos, A. J. Moses, D. C. Jiles, and T. Matsuo, "Generalization of the classical method for calculating dynamic hysteresis loops in grain-oriented electrical steels," *IEEE Trans. Magn.*, vol. 44, no. 9, pp. 2113–2126, Sep. 2008.

[99] S. Steentjes, S. E. Zirka, Y. E. Moroz, E. Y. Moroz, and K. Hameyer, "Dynamic magnetization model of nonoriented steel sheets," *IEEE Trans. Magn.*, vol. 50, no. 4, pp. 1–4, Apr. 2014.

[100] E. Dlala, "A simplified iron loss model for laminated magnetic cores," *IEEE Trans. Magn.*, vol. 44, no. 11, pp. 3169–3172, Nov. 2008.

[101] T. Chevalier, A. Kedous-Lebouc, B. Cornut, and C. Cester, "A new dynamic hysteresis model for electrical steel sheet," *Phys. B Condens. Matter*, vol. 275, no. 1–3, pp. 197–201, Jan. 2000.

[102] S. E. Zirka, Y. I. Moroz, P. Marketos, and A. J. Moses, "Viscosity-based magnetodynamic model of soft magnetic materials," *IEEE Trans. Magn.*, vol. 42, no. 9, pp. 2121–2132, Sep. 2006.

[103] A. Bergqvist, "Magnetic vector hysteresis model with dry friction-like pinning," *Phys. B Condens. Matter*, vol. 233, no. 4, pp. 342–347, 1997.

[104] R. Linkous, A. W. Kelley, and K. C. Armstrong, "An improved calorimeter for measuring the core loss of magnetic materials," in *APEC 2000. Fifteenth Annual IEEE Applied Power Electronics Conference and Exposition (Cat. No.00CH37058)*, New Orleans, LA, USA, 2000, vol. 2, pp. 633–639.

[105] M. Mu, "High frequency magnetic core loss study," Virginia Polytechnic Institute and State University, 2013.

[106] V. J. Thottuvelil, T. G. Wilson, and H. A. Owen JR, "High-frequency measurement techniques for magnetic cores," *IEEE Trans. Power Electron.*, vol. 5, no. 1, pp. 41–53, 1990.

[107] W. L. Soong, "B-H curve and iron loss measurements for magnetic materials," *Power Eng. Brief. Note Ser.*, p. 2, May 2008.

[108] M. Mu, Q. Li, D. J. Gilham, F. C. Lee, and K. D. T. Ngo, "New core loss measurement method for high-frequency magnetic materials," *IEEE Trans. Power Electron.*, vol. 29, no. 8, pp. 4374–4381, Aug. 2014.

[109] "Magnetic materials—Part 2: Methods of measurements of the magnetic properties of electrical steel sheet and strips by means of an Epstein frame." IEC 60404-4, 2008.

[110] L. T. Mthombeni and P. Pillay, "Core losses in motor laminations exposed to high-frequency or nonsinusoidal excitation," *IEEE Trans. Ind. Appl.*, vol. 40, no. 5, pp. 1325–1332, Sep. 2004.

[111] F. Fiorillo, *Measurement and Characterization of Magnetic Materials*. Elsevier Academic Press, 2005.

[112] A. J. Clerc and A. Muetze, “Measurement of stator core magnetic degradation during the manufacturing process,” *IEEE Trans. Ind. Appl.*, vol. 48, no. 4, pp. 1344–1352, Jul. 2012.

[113] S. Zurek, P. Marketos, T. Meydan, and A. J. Moses, “Use of novel adaptive digital feedback for magnetic measurements under controlled magnetizing conditions,” *IEEE Trans. Magn.*, vol. 41, no. 11, pp. 4242–4249, Nov. 2005.

[114] P. Anderson, “Measurement techniques for the assessment of materials under complex magnetising conditions,” *Przeglad Elektrotechniczny Electr. Rev.*, vol. 87, no. 9b, pp. 61–64, 2011.

[115] J. Geisinger and A. M. Knight, “Investigation of iron losses in mixed frequency flux density waveforms,” *IEEE Trans. Magn.*, vol. 50, no. 11, pp. 1–4, Nov. 2014.

[116] A. J. Moses, N. Derebasi, G. Loisos, and A. Schoppa, “Aspects of the cut-edge effect stress on the power loss and flux density distribution in electrical steel sheets,” *J. Magn. Magn. Mater.*, vol. 215–216, pp. 690–692, 2000.

[117] A. Boglietti, A. Cavagnino, L. Ferraris, and M. Lazzari, “The annealing influence onto the magnetic and energetic properties in soft magnetic material after punching process,” in *IEEE International Electric Machines and Drives Conference (IEMDC)*, Madison, WI, USA, 2003, vol. 1, pp. 503–508.

[118] A. Schoppa, J. Schneider, and C. D. Wuppermann, “Influence of the manufacturing process on the magnetic properties of non-oriented electrical steels,” *J. Magn. Magn. Mater.*, vol. 215, pp. 74–78, 2000.

[119] P. Beckley, *Electrical Steels for Rotating Machines*. The Institution of Engineering and Technology, 2002.

[120] A. Daikoku *et al.*, “An accurate magnetic field analysis for estimating motor characteristics taking account of stress distribution in the magnetic core,” *IEEE Trans. Ind. Appl.*, vol. 42, no. 3, pp. 668–674, May 2006.

[121] K. Yamazaki and H. Takeuchi, “Impact of mechanical stress on characteristics of interior permanent magnet synchronous motors,” *IEEE Trans. Ind. Appl.*, vol. 53, no. 2, pp. 963–970, Mar. 2017.

[122] I. Bogdanov and I. Protvino, “Study of electrical steel magnetic properties for fast cycling magnets of SIS100 and SIS300 rings,” p. 3, 2004.

[123] N. Takahashi, M. Morishita, D. Miyagi, and M. Nakano, “Examination of magnetic properties of magnetic materials at high temperature using a ring specimen,” *IEEE Trans. Magn.*, vol. 46, no. 2, pp. 548–551, Feb. 2010.

[124] M. Nakano, A. Fukuma, H. Nakaya, D. Miyagi, M. Nakano, and N. Takahashi, “Examination of temperature characteristics of magnetic properties using a single sheet tester,” *IEEJ Trans. Fundam. Mater.*, vol. 125, no. 1, pp. 63–68, 2005.

[125] H. Domeki *et al.*, “Investigation of benchmark model for estimating iron Loss in rotating machine,” *IEEE Trans. Magn.*, vol. 40, no. 2, pp. 794–797, Mar. 2004.

[126] S. Hawkins, A. Holmes, D. Ames, K. Rahman, and R. Malone, “Design optimization, development and manufacturing of general motors new battery electric vehicle drive unit (1ET35),” *SAE Int. J. Altern. Powertrains*, vol. 3, no. 2, pp. 213–221, Apr. 2014.

[127] W. Zhang and T. M. Jahns, “Analytical model for predicting AC losses in form-wound machine windings due to stator current interactions,” in *Proc. IEEE Int. Elect. Mach. Drives Conf. (IEMDC)*, 2015, pp. 1131–1137.

[128] K. Yamazaki, T. Fukuoka, K. Akatsu, N. Nakao, and A. Ruderman, “Investigation of locked rotor test for estimation of magnet PWM carrier eddy current loss in synchronous machines,” *IEEE Trans. Magn.*, vol. 48, no. 11, pp. 3327–3330, Nov. 2012.

[129] JSOL, “JMAG Application Note- Analysis of eddy current in the magnet of IPM machine.” .

[130] Y. Aoyama, K. Miyata, and K. Ohashi, “Simulations and experiments on eddy current in Nd-Fe-B magnet,” *IEEE Trans. Magn.*, vol. 41, no. 10, pp. 3790–3792, Oct. 2005.

[131] C. Mi, G. R. Slemon, and R. Bonert, “Modeling of iron losses of permanent-magnet synchronous motors,” *IEEE Trans. Ind. Appl.*, vol. 39, no. 3, pp. 734–742, May 2003.

[132] R. K. Járdán, P. Stumpf, Z. Varga, C. Endisch, P. Sipos, and M. Simon, “Laboratory system for measurement of iron losses in high speed drives,” *Int. J. Hydrog. Energy*, vol. 41, no. 29, pp. 12650–12658, Aug. 2016.

[133] K. Yamazaki, “Torque and efficiency calculation of an interior permanent magnet motor considering harmonic iron losses of both the stator and rotor,” *IEEE Trans. Magn.*, vol. 39, no. 3, pp. 1460–1463, May 2003.

[134] J. H. Seo, T. K. Chuang, C. G. Lee, S. Y. Jung, and H. K. Jung, “Harmonic iron loss analysis of electrical machines for high-speed operation considering driving condition,” *IEEE Trans. Magn.*, vol. 45, no. 10, pp. 4656–4659, Oct. 2009.

[135] P. A. Hargreaves, B. C. Mecrow, and R. Hall, “Calculation of iron loss in electrical generators using finite-element analysis,” *IEEE Trans. Ind. Appl.*, vol. 48, no. 5, pp. 1460–1466, Sep. 2012.

[136] E. Dlala, “Comparison of models for estimating magnetic core losses in electrical machines using the finite-element method,” *IEEE Trans. Magn.*, vol. 45, no. 2, pp. 716–725, Feb. 2009.

[137] D. Lin, P. Zhou, W. N. Fu, Z. Badics, and Z. J. Cendes, “A dynamic core loss model for soft ferromagnetic and power ferrite materials in transient finite element analysis,” *IEEE Trans. Magn.*, vol. 40, no. 2, pp. 1318–1321, Mar. 2004.

[138] B. Tekgun, “Analysis, measurement and estimation of the core losses in electrical machines,” University of Akron, 2016.

[139] D. G. Holmes and T. A. Lipo, *Pulse Width Modulation for Power Converters- Principles and Practice*. Piscataway, NJ, USA: IEEE Press, 2003.

[140] Y. Wu, C. Y. Leong, and R. A. McMahon, “A study of inverter los reduction using discontinuous pulse width modulation techniques,” in *Proc. 3rd IET Int. Conf. Power Electron., Machines Drives*, Mar. 2006, pp. 596–600.

[141] Y. Wu, M. A. Shafi, A. M. Knight, and R. A. McMahon, “Comparison of the effects of continuous and discontinuous PWM schemes on power losses of voltage-sourced inverters for induction motor drives,” *IEEE Trans. Power Electron.*, vol. 26, no. 1, pp. 182–191, Jan. 2011.

[142] A. M. Hava, R. J. Kerkman, and T. A. Lipo, "Simple analytical and graphical methods for carrier-based PWM-VSI drives," *IEEE Trans. Power Electron.*, vol. 14, no. 1, pp. 49–61, Jan. 1999.

[143] R. Ghosh and G. Narayanan, "Control of three-phase, four-wire PWM rectifier," *IEEE Trans. Power Electron.*, vol. 23, no. 1, pp. 96–106, Jan. 2008.

[144] D. Zhao, V. S. S. Pavan Kumar Hari, G. Narayanan, and R. Ayyanar, "Space-vector-based hybrid pulsewidth modulation techniques for reduced harmonic distortion and switching loss," *IEEE Trans. Power Electron.*, vol. 25, no. 3, pp. 760–774, Mar. 2010.

[145] D. Jiang and F. Wang, "Current-ripple prediction for three-phase PWM converters," *IEEE Trans. Ind. Appl.*, vol. 50, no. 1, pp. 531–538, Jan. 2014.

[146] D. Jiang and F. Wang, "A general current ripple prediction method for the multiphase voltage source converter," *IEEE Trans. Power Electron.*, vol. 29, no. 6, pp. 2643–2648, Jun. 2014.

[147] G. Grandi and J. Loncarski, "Evaluation of current ripple amplitude in three-phase PWM voltage source inverters," in *Compatibility and Power Electronics (CPE), 2013 8th International Conference on*, 2013, pp. 156–161.

[148] G. Grandi, J. Loncarski, and O. Dordevic, "Analytical evaluation of output current ripple amplitude in three-phase three-level inverters," *IET Power Electron.*, vol. 7, no. 9, pp. 2258–2268, Sep. 2014.

[149] F. Yang, A. R. Taylor, H. Bai, B. Cheng, and A. A. Khan, "Using d-q transformation to vary the switching frequency for interior permanent magnet synchronous motor drive systems," *IEEE Trans. Transp. Electrification*, vol. 1, no. 3, pp. 277–286, Oct. 2015.

[150] P. B. Reddy, T. M. Jahns, and T. P. Bohn, "Transposition effects on bundle proximity losses in high-speed PM machines," in *2009 IEEE Energy Conversion Congress and Exposition*, San Jose, CA, Sep. 2009, pp. 1919–1926.

[151] M. van der Geest, H. Polinder, J. A. Ferreira, and D. Zeilstra, "Current sharing analysis of parallel strands in low-voltage high-speed machines," *IEEE Trans. Ind. Electron.*, vol. 61, no. 6, pp. 3064–3070, Jun. 2014.

[152] M. van der Geest, H. Polinder, and J. A. Ferreira, "Influence of PWM switching frequency on the losses in PM machines," in *Proc. 2014 Int. Conf. on Elect. Mach. (ICEM)*, Berlin, Germany, Sep. 2014, pp. 1243–1247.

[153] M. J. Islam and A. Arkkio, "Effects of pulse-width-modulated supply voltage on eddy currents in the form-wound stator winding of a cage induction motor," *IET Electr. Power Appl.*, vol. 3, no. 1, p. 50, 2009.

[154] K. Atallah, D. Howe, P. H. Mellor, and D. A. Stone, "Rotor loss in permanent-magnet brushless AC machines," *IEEE Trans. Ind. Appl.*, vol. 36, no. 6, p. 7, 2000.

[155] M. Markovic and Y. Perriard, "A simplified determination of the permanent magnet (PM) eddy current losses due to slotting in a PM rotating motor," p. 6.

[156] L. J. Wu, Z. Q. Zhu, D. Staton, M. Popescu, and D. Hawkins, "Analytical modeling and analysis of open-circuit magnet loss in surface-mounted permanent-magnet machines," *IEEE Trans. Magn.*, vol. 48, no. 3, pp. 1234–1247, Mar. 2012.

[157] Z. Q. Zhu, K. Ng, N. Schofield, and D. Howe, "Improved analytical modelling of rotor eddy current loss in brushless machines equipped with surface-mounted permanent magnets," *IEE Proc. - Electr. Power Appl.*, vol. 151, no. 6, p. 641, 2004.

[158] J. Pyrhönen, *et al.*, "Hysteresis losses in sintered NdFeB permanent magnets in rotating electrical machines," *IEEE Trans. Ind. Electron.*, vol. 62, no. 2, pp. 857–865, Feb. 2015.

[159] A. Jassal, H. Polinder, and J. A. Ferreira, "Literature survey of eddy-current loss analysis in rotating electrical machines," *IET Electr. Power Appl.*, vol. 6, no. 9, p. 743, 2012.

[160] K. Yamazaki and Y. Fukushima, "Effect of eddy-current loss reduction by magnet segmentation in synchronous motors with concentrated windings," *IEEE Trans. Ind. Appl.*, vol. 47, no. 2, pp. 779–788, Mar. 2011.

[161] Wan-Ying Huang, A. Bettayeb, R. Kaczmarek, and J.-C. Vannier, "Optimization of Magnet Segmentation for Reduction of Eddy-Current Losses in Permanent Magnet Synchronous Machine," *IEEE Trans. Energy Convers.*, vol. 25, no. 2, pp. 381–387, Jun. 2010.

[162] M. Cheng and S. Zhu, "Calculation of PM eddy current loss in IPM machine under PWM VSI supply with combined 2-D FE and analytical method," *IEEE Trans. Magn.*, vol. 53, no. 1, pp. 1–12, Jan. 2017.

[163] A. Krings, J. Soulard, and O. Wallmark, "Influence of PWM switching frequency and modulation index on the iron losses and performance of slot-less permanent magnet motors," in *2013 International Conference on Electrical Machines and Systems (ICEMS)*, Busan, Oct. 2013, pp. 474–479.

[164] A. Boglietti, A. Cavagnino, and A. M. Knight, "Isolating the impact of PWM modulation on motor iron losses," in *Conf. Rec. IEEE IAS Annu. Meeting*, Edmonton, AB, Canada, 2008, pp. 1–7.

[165] L. Masisi, M. Ibrahim, J. Wanjiku, A. M. Aljehaimi, and P. Pillay, "The effect of two- and three-level inverters on the core loss of a synchronous reluctance machine (SynRM)," *IEEE Trans. Ind. Appl.*, vol. 52, no. 5, pp. 3805–3813, Sep. 2016.

[166] M. S. Lancarotte, C. Goldemberg, and A. d. A. Penteado, "Estimation of FeSi core losses under PWM or DC bias ripple voltage excitations," *IEEE Trans. Energy Convers.*, vol. 20, no. 2, pp. 367–372, Jun. 2005.

[167] Z. Gmyrek, "Prediction of iron loss in magnetic laminations under PWM voltage supply," *COMPEL - Int. J. Comput. Math. Electr. Electron. Eng.*, vol. 28, no. 6, pp. 1672–1687, Nov. 2009.

[168] Z. Gmyrek, A. Boglietti, and A. Cavagnino, "Iron Loss prediction with PWM supply using low- and high-frequency measurements: analysis and results comparison," *IEEE Trans. Ind. Electron.*, vol. 55, no. 4, pp. 1722–1728, Apr. 2008.

[169] S. Xue *et al.*, "Iron loss model for electrical machines fed by low switching frequency PWM," in *2017 IEEE International Magnetics Conference (INTERMAG)*, Dublin, Ireland, Apr. 2017, pp. 1–1.

[170] Y. Takeda, Y. Takahashi, K. Fujiwara, A. Ahagon, and T. Matsuo, "Iron loss estimation method for rotating machines taking account of hysteretic property," *IEEE Trans. Magn.*, vol. 51, no. 3, pp. 1–4, Mar. 2015.

[171] W. Martinez, S. Odawara, and K. Fujisaki, "Iron loss characteristics evaluation using a high-frequency GaN inverter excitation," *IEEE Trans. Magn.*, vol. 53, no. 11, pp. 1–7, Nov. 2017.

[172] J. Millinger, O. Wallmark, and J. Soulard, "High-frequency characterization of losses in fully assembled stators of slotless PM motors," *IEEE Trans. Ind. Appl.*, vol. 54, no. 3, pp. 2265–2275, May 2018.

[173] F. Briz, M. W. Degner, and R. D. Lorenz, "Analysis and design of current regulators using complex vectors," *IEEE Trans. Ind. Appl.*, vol. 36, no. 3, pp. 817–825, Jun. 2000.

[174] R. Zhang, M. Cardinal, P. Szczesny, and M. Dame, "A grid simulator with control of single-phase power converters in D-Q rotating frame," in *2002 IEEE 33rd Annual IEEE Power Electronics Specialists Conference. Proceedings (Cat. No.02CH37289)*, Cairns, Qld., Australia, 2002, pp. 1431–1436.

[175] M. Gonzalez, V. Cirdenas, and F. Pazos, "DQ transformation development for single-phase systems to compensate harmonic distortion and reactive power," in *9th IEEE International Power Electronics Congress, 2004. CIEP 2004*, Celaya, Mexico, 2004, pp. 177–182.

[176] Kai Zhang, Yong Kang, Jian Xiong, and Jian Chen, "Direct repetitive control of SPWM inverter for UPS purpose," *IEEE Trans. Power Electron.*, vol. 18, no. 3, pp. 784–792, May 2003.

[177] H. Deng, R. Oruganti, and D. Srinivasan, "Analysis and Design of Iterative Learning Control Strategies for UPS Inverters," *IEEE Trans. Ind. Electron.*, vol. 54, no. 3, pp. 1739–1751, Jun. 2007.

[178] J. P. Boyd, "Computing the zeros, maxima and inflection points of Chebyshev, Legendre and Fourier series: solving transcendental equations by spectral interpolation and polynomial rootfinding," *J. Eng. Math.*, vol. 56, no. 3, pp. 203–219, Jan. 2007.

[179]J. P. Boyd, "A comparison of companion matrix methods to find roots of a trigonometric polynomial," *J. Comput. Phys.*, vol. 246, pp. 96–112, Aug. 2013.

[180] T. Okubo, G. Shilyashki, H. Pfutzner, A. Kenov, and Y. Oda, "Can circular rotational losses of non-oriented soft magnetic materials be estimated from alternating losses?," *IEEE Trans. Magn.*, vol. 54, no. 12, pp. 1–6, Dec. 2018.

[181] K. Zhou and D. Wang, "Relationship between space-vector modulation and three-phase carrier-based PWM: a comprehensive analysis [three-phase inverters]," *IEEE Trans. Ind. Electron.*, vol. 49, no. 1, pp. 186–196, 2002.

[182] J. Liu *et al.*, "Design of the Chevrolet bolt EV propulsion system," *SAE Int. J. Altern. Powertrains*, vol. 5, no. 1, Apr. 2016.

[183] Y. Li, L. Zhu, and J. Zhu, "Calculation of core losses under DC bias and harmonics based on Jiles-Atherton dynamic hysteresis model combined with finite element analysis," in *Electrical Machines and Systems (ICEMS), 2017 20th International Conference on*, 2017, pp. 1–5.

[184] J. H. B. Deane, "Modeling the dynamics of nonlinear inductor circuits," *IEEE Trans. Magn.*, vol. 30, no. 5, pp. 2795–2801, Sep. 1994.

[185] Y. Bard, *Nonlinear parameter estimation*. New York: Academic Press, 1974.

[186] A. Bjorck, *Numerical methods for least squares problems*. SIAM, Philadelphia, 1996.

[187] K. Levenberg, “A method for the solution of certain non-linear problems in least squares,” *Q. Appl. Mathmatics*, vol. 2:, pp. 164–168, 1944.

[188] D. W. Marquardt, “An algorithm for least-squares estimation of nonlinear parameters,” *J. Soc. Ind. Appl. Math.*, vol. 11, no. 2, pp. 431–441, 1963.

[189] H. Garvin, *The Levenberg-Marquardt method for nonlinear least squares curve-fitting problems*. Durham, NC: Dept. Civil and Enviromental Engineering, Duke Univ., 2011.

[190] K. Madsen, N. B. Nielsen, and O. Tingleff, *Methods for non-linear least squares problems*. Lyngby, Denmark: Informatics and Mathematical Modelling, Technical University of Denmark, 2004.

[191] T. J. E. Miller, M. Popescu, C. Cossar, and M. McGilp, “Performance estimation of interior permanent-magnet brushless motors using the voltage-driven flux-MMF diagram,” *IEEE Trans. Magn.*, vol. 42, no. 7, pp. 1867–1872, Jul. 2006.

[192] D. Hou, M. Mu, F. C. Lee, and Q. Li, “New high-frequency core loss measurement method with partial cancellation concept,” *IEEE Trans. Power Electron.*, vol. 32, no. 4, pp. 2987–2994, Apr. 2017.

[193] R. L. Stoll, *The analysis of eddy currents*. Oxford: U.K.: Clarendon, 1974.